STRUCTURAL AND ELECTRONIC INVESTIGATIONS INTO SUBNANOMETRE METALLIC CLUSTERS

by

HEIDER A. ABDULHUSSEIN

A thesis submitted to
The University of Birmingham
for the degree of
DOCTOR OF PHILOSOPHY

School of Chemistry
College of Engineering and Physical Sciences
The University of Birmingham
June 2019

ABSTRACT

This thesis presents computational studies of the geometric and electronic structures and energetic properties of homo- and heterometallic subnanometre clusters (SNCs). The first two chapters give an introductory overview of nanoparticles and the basics of the sophisticated search algorithms, Genetic Algorithms (GAs), as applied to clusters, and outline a general introduction to the computational methodologies applied in this work, the coupling of the recently developed combination of GAs with Density Functional Theory (DFT) calculations. This is followed by four results chapters, in which these computational methods are adapted to several SNC systems to elucidate their applicability in catalysis. Six publications are documented in the results chapters. Gold-palladium SNCs, which are promising catalysts for a wide variety of chemical reactions, are studied extensively in chapters 3 and 4. Chapter 3 considers the evolution of structural motifs as a function of size and composition for neutral Au-Pd clusters in the gas-phase and supported on a MgO(100) surface. Quantum-regime effects are observed and energetics are further studied. In chapter 4, a rigorous approach is presented to explore structure and stability of mono-cationic Pd-doped Au clusters and their reactivity with CO gas. The Birmingham Parallel Genetic Algorithm BPGA-DFT approach is combined with experimental techniques, including mass spectrometry, and infra-red multiphoton dissociation spectroscopy. This study gives unique insights into Pd dopant effects on cluster stability, as measured by their photo-fragmentation properties, and on their CO adsorption properties. Computational investigations into AuCu SNCs, using the Mexican Enhanced Genetic Algorithm MEGA-DFT code to rationalize the efficient catalytic properties, are presented in chapter 5. Free clusters and those supported on a MgO(100) surface are

compared in this approach. The interactions with the support are extensively probed in order to better understand their role in catalysis at the atomistic level. Chapter 6 is dedicated to the structural characterisation, which is vital first step in order to understanding catalytic activity, of Ru-Pt clusters, which are electrode catalysts in direct methanol fuel cells. Ru@Pt core-shell chemical ordering is predicted. Finally, overall conclusions and outlook are presented in chapter 7.

To Roy, for his human touch and love for science;
Rusul, for her love;
and Adam, for being in my life.

ACKNOWLEDGEMENTS

This work would not have been possible without the boundless enthusiasm, scientific insight, support and guidance of my supervisor Prof. Roy Johnston. Roy, there are no words can express my gratitude to you. Truly you are an excellent supervisor.

I would like to thank my former second supervisor Prof. Graham Worth (University College London) and current second supervisor Dr. Sarah Horswell, whose guidance and ideas helped me throughout my PhD.

My thanks must go to past and present members of the Johnston and Chakrabarti groups, and in particular Dr. Jack Davis, Dr. Ilker Demiroglu, Dr. Daniel Morphew, Dr. Marcus Taylor, John Hey, Abhishek Rao, James Shaw, Christopher Avins, and Andreas Neophytou, for making our office such a pleasant work environment. Particularly John Hey, for the endless invitations for tea and of course for his constant support.

Much of the work presented in this thesis was carried out in collaboration with experimental and theoretical research groups, and I particularly thank the participants: Drs Piero Ferrari, Jan Vanbuel, Prof. Peter Lievens, and Prof. Ewald Janssens (the Catholic University of Leuven); Dr Christopher Heard (Charles University, Prague); and Prof. André Fielicke (the Fritz Haber Institute of the Max Planck Society, Berlin). Acknowledgments also for the Gaston group at the University of Auckland in New Zealand, especially to Associate Professor Nicola Gaston for giving me the opportunity to visit her group and develop calculations using the supercomputer facilities in Auckland.

I also acknowledge those organisations and bodies which have supported my PhD studies, including the University of Kufa and the Ministry of Higher Education and Scientific Research (Iraq) for financial support through the award of a PhD scholarship

and the facilities (and people associated) of the University of Birmingham's BlueBEAR high-performance computer (http://www.bear.bham.ac.uk/bluebear), ATHENA at HPC Midlands Plus, which is funded by the EPSRC through grant (EP/P020232), THOMAS, the UK Materials and Molecular Modelling Hub for computational resources, which is partially funded by EPSRC (EP/P020194/1), ARCHER, the UK National Supercomputing Service (http://www.archer.ac.uk) via membership of the UK's HPC Materials Chemistry Consortium, which is funded by EPSRC (EP/L000202), and "TOUCAN: Towards an Understanding of Catalysis on Nanoalloys" membership, which is funded by EPSRC under Critical Mass Grant (EP/J010804/1), and NeSI, the New Zealand eScience Infrastructure.

I express my gratitude to all those people who made my time in Birmingham one of the most important experiences in my life. First of all, I have to thank Badr Aldhafri, for standing right beside me in every moment. Then, I would like to say thanks to my friends, Dana Noory and Wisam Alshohani and their families with whom I (and my family) shared a part of our life in Birmingham and whose presence we will definitely miss.

Finally, I cannot omit to acknowledge my parents, sisters, and brothers for all the support I received from them. I would like to thank them all for encouraging and always believing in me. Last among mentions but first among people, my wife, Rusul, and my kid, Adam, the courage and significance you give me every day are unparalleled. You are the two people in my life who I want to make them most proud of me. Thank you for the constant support and love.

PUBLICATIONS

List of publications contained in this thesis:

1. DFT global optimisation of gas-phase and MgO-supported sub-nanometre AuPd clusters; Heider A. Hussein, Jack B. Davis and Roy L. Johnston, *Physical Chemistry Chemical Physics*, 2016, **18**, 26133.

2. DFT global optimization of gas-phase subnanometer Ru-Pt clusters; Ilker Demiroglu, Kezi Yao, Heider A Hussein, and Roy L. Johnston, *The Journal of Physical Chemistry C*, 2017, **121**, 10773.

3. Application of a Parallel Genetic Algorithm to the Global Optimization of Medium-sized Au-Pd Sub-nanometre Clusters; Heider A. Hussein, Ilker Demiroglu, and Roy L. Johnston, *The European Physical Journal B*, 2018, **91**, 34.

4. Effect of palladium doping on the stability and fragmentation patterns of cationic gold clusters; Piero Ferrari, Heider A. Hussein, Christopher Heard, Jan Vanbuel, Roy L. Johnston, Peter Lievens and Ewald Janssens, *Physical Review A*, 2018, **97**, 052508.

5. The DFT-Genetic Algorithm Approach for Global Optimization of Subnanometer Bimetallic Clusters; Heider A. Hussein and Roy L. Johnston, In *Computational Modelling of Nanoparticles* (Eds. Stefan T. Bromley and Scott M. Woodley), *Frontiers of Nanoscience*, 2018, **12**, Ch. 4, 145-169.

6. Physico-chemical insights into gas-phase and oxide-supported sub-nanometre AuCu clusters; Heider A. Hussein, Mansi Gao, Yiyun Hou, Sarah L. Horswell, and Roy L.

Johnston, *Zeitschrift für Physikalische Chemie*, Special issue on "Gas Phase Model Systems for Catalysis", Published Online, 2019. DOI: 10.1515/zpch-2018-1356

7. Altering CO binding on Gold Cluster Cations by Pd-doping; Heider A. Abdulhussein, Piero Ferrari, Jan Vanbuel, Christopher Heard, André Fielicke, Peter Lievens, Ewald Janssens and Roy L. Johnston, 2019, **Submitted**.

In addition, the publications undertaken during my PhD studies but not contained in this thesis are listed below:

1. DFT study of the structure, chemical ordering and molecular adsorption of Pd-Ir nanoalloys; Tian-E Fan, Ilker Demiroglu, Heider A. Hussein, Tun-Dong Liu and Roy L. Johnston, *Physical Chemistry Chemical Physics*, 2017, **19**, 27090.

2. The electronic properties of N = 3-20 $Sc_N{}^{0,+}$ clusters; Heider A. Abdulhussein, James Thomas Alan Gilmour, Nicola Gaston and Roy L. Johnston, **In Prep**.

ABBREVIATIONS

NA Nanoalloy

NP Nanoparticle

MNP Metal Nanoparticle

SNC Subnanometre Cluster

GO Global Optimisation

GA Genetic Algorithm

BCGA Birmingham Cluster Genetic Algorithm

S-BCGA Surface Birmingham Cluster Genetic Algorithm

BPGA Birmingham Parallel Genetic Algorithm

MEGA Mexican Enhanced Genetic Algorithm

GIGA German Improved Genetic Algorithm

GM Global Minimum

DFT Density Functional Theory

VASP Vienna Ab initio Simulation Package

GGA Generalised Gradient Approximation

LDA Local Density Approximation

PBE Perdew-Burke-Ernzerhof Exchange-Correlation Functional

XC Exchange-Correlation

CONTENTS

CHAPTER 1

INTRODUCTION

1.1 Nanoparticles

Nanoparticles (NPs) are clusters of atoms, ions or molecules in the size range from one to several hundred nanometres, filling the gap between discrete atoms (or molecules) and bulk materials [1]. They have distinct properties due to their high surface-to-volume ratios. NPs composed of one metal element, i.e. metal nanoparticles (MNPs), are of particular interest, due to the importance of quantum effects [2]. The ability to control and tune the physical and chemical properties of MNPs including optical [3], magnetic and electronic properties [4], and catalytic activity [5, 6], has led to their use in many emerging technological applications, such as nanobiology, nanodevices, nanofabrication, and nanocatalysis [7–11].

A number of technological advances have allowed better understanding and control of the synthesis, structures and properties of MNPs [12–14]. Synthetic methods either follow a bottom-up approach, which builds nanostructures up from the atomic level, or a top-down approach, to achieve the miniaturization of materials down to the nanoscale. [15]. Characterisation involves a myriad of techniques, including mass spectrometry, electron microscopy, atomic force microscopy, infra-red and UV-visible spectroscopy, and X-ray diffraction (XRD), yielding information on, for example, particle size, morphology, surface area, porosity, aggregation, and crystallinity [12, 16].

Theory plays a significant role in the study of NPs, as many of their properties are difficult to measure experimentally and some of them (e.g. mass spectrometric and spectroscopic data) need to be interpreted using theoretical techniques [17]. The exponential growth of computer power has been aided by the development of efficient algorithms for predicting and describing the physical and chemical properties of NPs [18]. For example, many optimisation strategies (e.g. Monte Carlo, basin-hopping, simulated annealing, parallel tempering, and evolutionary algorithms) have been developed to identify the lowest energy configurations for different sizes and compositions of NPs [19].

1.1.1 Nanoalloys

The range of properties of MNPs can be expanded by combining two or more metallic elements, resulting in the sub-class of nanoalloys (NAs) [20, 21]. For example, Fe NPs exhibit giant magneto-resistance behaviour when embedded in a Ag host [22]. Despite the expense and rarity of the noble metals in the earth's crust [23], they have been used extensively in NAs which are applied in many high-tech fields due to their remarkable magnetic, electronic, and catalytic properties [24, 25]. These properties can be enhanced and tuned by changing the size, shape, composition, and chemical order (the arrangement of the component metal atoms) of the NAs [26,27]. There are also economic reasons which favour mixing two or more metals: for example reducing the amount of the expensive noble metal (e.g. Rh, Pd, Pt, Au) in nanocatalysts by adding low cost metals (e.g. Fe, Co, Ni, Cu) which may also enhance the stability, selectivity, and activity of the catalysts [28,29]. NAs show novel properties and structures, not only compared to the corresponding bulk alloys, but also relative to the corresponding monometallic NPs [30].

It is well-known that mixing two metals can lead to four fundamental patterns of chemical ordering; core-shell, multishell (onion-like), Janus (layered-segregated) and mixed (with subgroups either random or ordered mixing), as shown in Figure 1.1 [31,32].

At low temperatures, MNPs and NAs tend to adopt structures which minimise the total potential energy [21], with minimisation of the surface energy being important

due to the high surface-to-volume ratio. Pseudo-crystalline structures, including fcc-type truncated octahedra and octahedra are typically observed for larger clusters, while non-crystalline structures, such as polytetrahedra, icosahedra, and Marks' decahedra are commonly observed for smaller NAs [33, 34]. Examples of such geometries are shown in Figure 1.2 [35].

For technological applications (e.g. in catalysis and magnetics), it is generally necessary to isolate and immobilise the MNPs and NAs on a support, such as a metal oxide or carbon (e.g. graphene or amorphous carbon). However, the geometries and electronic structures (and chemical ordering for NAs) of MNPs and, hence, their physical and chemical properties may be altered by supporting them on a surface. For example, Weiher et al. have enhanced the catalytic activity of Au NPs for the oxidation of CO using Al_2O_3 as the support [36]. Pt NPs on a MgO support have also proved very active in catalysing the production of CO_2 from methanol [37]. In contrast, the magnetic moments of Co-Ag clusters are reduced (quenched) when they are deposited on a MgO support [38].

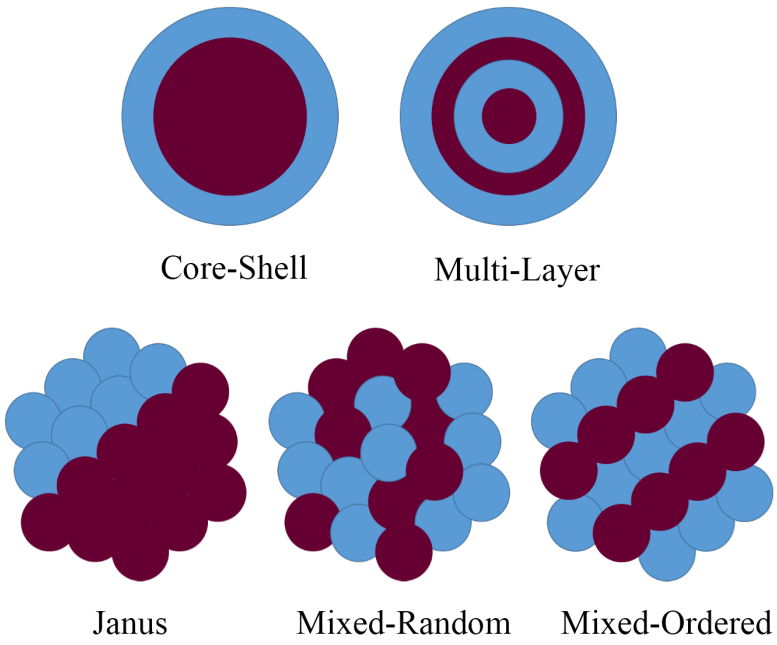

Figure 1.1: Common mixing patterns seen in nanoalloys [39].

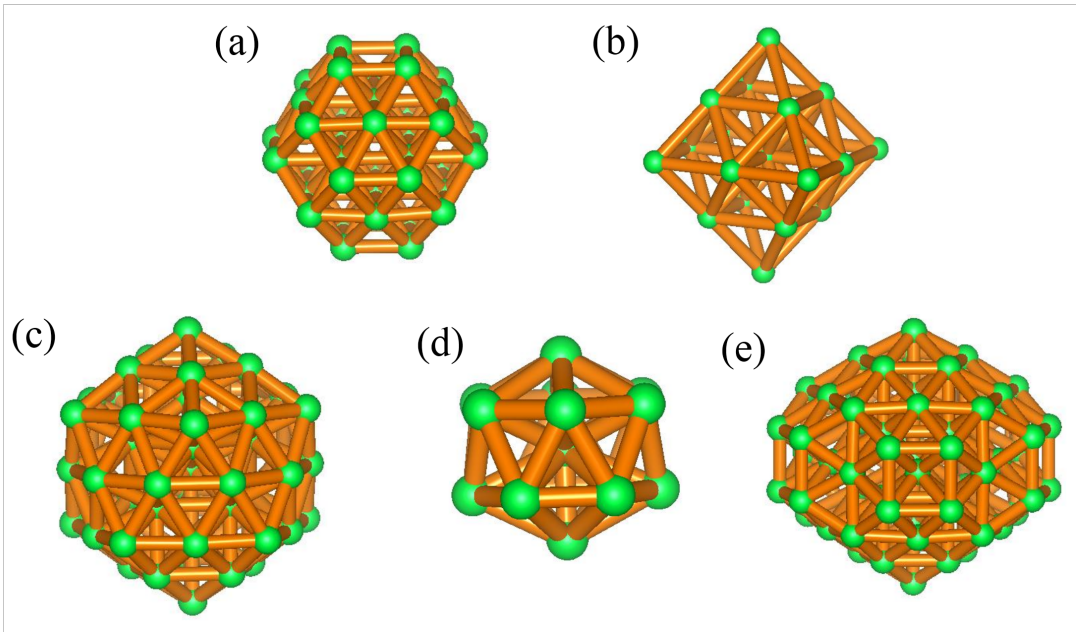

Figure 1.2: High symmetry cluster structures: (a) 38-atom truncated octahedron, (b) 19-atom octahedron, (c) 55-atom icosahedron, (d) 15-atom polytetrahedron, and (e) 75-atom Marks' decahedron [35].

1.1.2 Subnanometre Clusters

There is considerable interest in the chemistry and physics of small metal clusters, up to a few tens of atoms in size - i.e. in the subnanometre domain, particularly for catalysis [40]. Such subnanometre (metal) clusters (SNCs) occupy a region where cluster properties do not vary monotonically with size - i.e. where "every atom counts" and unique quantum size effects can be observed [41]. SNCs are also interesting as they are accessible to both high-level theory and state-of-the-art experimental investigation. Cluster beam experiments are used for determining the structures and electronic, vibrational, optical and magnetic properties of isolated SNCs. For technological applications, however, SNCs have to be stabilised against aggregation, either by passivating them with surface-bound ligands [42] or by immobilising them on a substrate (such as carbon, silicon, silica or a metal oxide) or inside zeolites or other porous solids [43]. Such experiments allow individual clusters to be studied by spectroscopic, diffraction and microscopy techniques, but it is possible that the structure may be perturbed by the substrate or coordinated ligands.

Strategies for the synthesis and characterization of SNCs have revealed some difficulties due to their small size, compared to methods used for larger metal NPs. These difficulties are represented by challenges in tuning experimental conditions, such as pH, time, pressure and temperature, to provide the fine control of sizes, shapes, and compositions of SNCs [44]. In some instances, molecular beam techniques have been used to produce SNCs in a cluster molecular beam. Molecular beam methods involve evaporation, condensation, and then growth of the cluster nuclei [17]. As an example, silicon clusters with 8 and 11 atoms have been reported by Götz et al., using a laser vaporization source, with gas-phase uv photo-depletion spectroscopy coupled with theoretical calculations enabling structural characterization of the Si_8 and Si_{11} clusters [45].

Theoretical models and computational methods are essential in helping to interpret spectroscopy and other experiments performed on SNCs [21]. For an accurate treatment, quantum mechanical methods are required. Density Functional Theory (DFT) calculations have therefore become increasingly popular for performing local geometry optimisation of metal clusters [46]. With increasing computing power and the availability of more efficient DFT codes there has been a significant increase in the size and complexity of systems that can be studied, including surface-passivated and substrate-supported clusters, and the adsorption and reactions of small molecules on metal clusters, which is critical to understanding sub-nanocatalysis. An important advantage of SNCs is that for these sizes it is generally possible to carry out high level calculations: DFT, Time Dependent-DFT and even correlated Molecular Orbital methods. SNCs present a synergistic combination of quantum size effects, which require electronic structure methods to be employed, and sufficiently small particle sizes to allow direct global optimisation at the DFT level.

1.2 Genetic Algorithms

A considerable number of global optimization algorithms have been utilized to determine locally stable structures on the energy landscape [32,47–52], i.e. the global minimum (GM)

and low-lying minima (LM). A genetic algorithm (GA) is an example of an evolutionary algorithm which mimics the natural evolution process. It is the most popular search technique among these algorithms, which also include differential evolution, evolution strategies, and genetic programming [53].

GA has been employed for structure prediction of a wide variety of systems ranging from zero- to 3-Dimensional Systems. GA studies have been performed on single-species systems [54, 55] and on conformations of molecules [56] and polymers [57]. Series of nanowires for gold [58], zirconium [59], and titanium [60] were predicted by Wang et al., suggesting a bulk-like character within the wires. Employing a tight binding scheme, GA has been used by Fu et al. [61] to study the Si(001) surface. Landree et al. [62] have utilized surface diffraction data in GA application in order to surface structure identifications. GA has also been extensively developed and applied to solving structures of dense and microporous oxide structures by Woodley and co-workers [49, 50, 63–65], molecular crystals by Harris and co-workers [66–71], and metallic and alloy clusters by Johnston and co-workers [19, 32, 47, 48]. Owing to that our project is concerning on nanoclusters, the next paragraphs focus on employing GA for structural investigations for several nanocluster systems.

The optimisation of nanocluster structures is not a trivial task. As the cluster size of monometallic nanoclusters increases, the number of local minima on the corresponding potential energy surface increases exponentially [72]. In bimetallic nanoclusters (nanoalloys), an additional problem arises due to the presence of homotops (i.e. isomers having the same geometric structure but with different chemical ordering for a given size and composition) [73]. Although the GM is the energetically preferred isomer, which is generally found in experiments, other metastable isomers may also be observed due to kinetic effects. This has increased the computational efforts in mapping the PES. Due to the difficulty of identifying the GM structure for clusters, many optimisation strategies, including search techniques such as genetic algorithms (GA), have been developed to locate the lowest energy isomers [19].

The use of GAs for optimising cluster geometries can be traced back to the early 1990s, when clusters of benzene, naphthalene and anthracene molecules were optimised by Xiao and Williams [74], followed by GA geometry optimisation of small clusters of silicon [55], water [75] and mercury [76] conducted by Hartke [54].

Zeiri [77] introduced real-valued cartesian coordinates (rather than binary coding) to represent the clusters in a GA. The next significant step in the evolution of GAs for cluster optimisation was introduced by Deaven and Ho [78] in 1995, when they implemented the gradient-driven local minimisation of the cluster energy after each GA operation. As in the basin-hopping approach [79], local minimisation transforms the cluster potential energy hypersurface into a stepped surface, where each step corresponds to a basin of attraction of a local minimum on the PES, as explained by Figure 2.1 in section 2.1. The simplified surface now reduces the space that the GA has to search thereby improving the efficiency of the GA (which is formally known as a Lamarckian GA [80]). Deaven and Ho [78] introduced another important development into GA cluster optimisation by including a 3D cut-and-splice operation for mating (crossover). This method has been employed in most subsequent GA optimisations of clusters.

Over the past two decades, together with a number of collaborators, the Johnston group have developed a series of in-house GA codes for the global geometry optimization of metal clusters and nanoparticles, including nanoalloys, ranging in size from a few atoms to several tens of atoms [19,32,81,82]. The Birmingham Cluster Genetic Algorithm (BCGA) [32], which was the first version of the GA program, employed empirical potentials to search for the GM. The validity of the BCGA programme for the global optimization of NPs was tested on Morse clusters by Roberts et al. [83], when the efficiency and reliability of the code have been demonstrated by comparing the newly calculated (by BCGA) structures and their energies with the database of structures and energies for such clusters previously reported [84] and stored in the Cambridge Cluster Database [35].

BCGA was then modified to permit the global optimization of SNCs directly at the DFT level of theory by combining every GA step with a local energy minimization

using DFT, as explained in section 2.1. The optimization in the BCGA-DFT approach is applied to smaller populations than used for empirical potentials, due to the increased computational cost of the local minimization step, although this is typically carried out on multiple processors due to the parallelization of the DFT codes [85, 86]. The first application of the BCGA-DFT approach was the study of 8-atom Au-Ag clusters [87]. The plane wave PWscf method within the Quantum Espresso package [85] was used in this application.

The Surface Birmingham Cluster Genetic Algorithm (S-BCGA) [88, 89] is a modification of the BCGA developed for the global optimisation of clusters in the presence of a surface. The global optimization of supported clusters in this case can be considered as modelling the structures produced by the interaction between clusters adsorbed on the surface, as the structure of the free cluster does not always reflect the stable configuration on deposition. Hence, S-BCGA is applicable for clusters supported on active substrates (i.e. supports which interact strongly with bound clusters). This optimisation represents deposition and growth of a cluster on a surface after annealing, overcoming energetic barriers to generate new supported-clusters, and distorting the free cluster structure. This is in contrast to ultrasoft landing, where the cluster experiences only small rearrangements when deposited on the support [89].

The Birmingham Parallel Genetic Algorithm (BPGA) [82] was developed to enable the GA-DFT approach to be extended to larger cluster sizes, for pure metals and nanoalloys. This programme is an open-source genetic algorithm written in the Python language, with an interface to the Vienna Ab initio Simulation Package (VASP) [90–93], improving on the BCGA [32]. The BPGA-DFT approach [82] was used to confirm the simple-cubic growth pattern for pure Ir clusters with 10-20 atoms. The putative global minima from this study were evaluated and compared with previous findings [94–96], indicating the efficiency of BPGA for finding the putative GM at a given level of theory (PAW/PBE), although some Ir cluster structures were predicted for the first time [82]. BPGA can also be applied to supported clusters (as in S-BCGA) and has been applied

to the global optimization of various clusters supported on the MgO(100)- surface. The effect of the MgO(100) surface on the structural properties and stability of of AuIr [97] and AuPd [98] subnanometre clusters have been captured by this approach. Such effects are illustrated in Figure 1.3, which compares the free (gas phase) and MgO-supported GM structures for Pd_6, Au_3Pd_2 and Au_9 clusters [39, 98].

The Mexican Enhanced Genetic Algorithm (MEGA) was developed from the BPGA, with an interface to the VASP code [90–93], written in the Python language by Vargas et al. [99]. Several new characteristics were introduced, improving the efficiency and accuracy of the method, and providing new output-analysis files. The MEGA developers have studied the neutral and mono-anionic Au clusters with 27-30 atoms [99], to validate the performance of the MEGA code. The new geometries were predicted and confirmed by comparison with the available experimental and theoretical data reported previously by Shao et al. [100].

Due to advances in the GA methodology [39, 48], including coupling the GA to electronic structure methods (especially DFT), employing various new mutation operators, and incorporating parallel computing techniques, a wide range of SNCs have been studied. Therefore, GA applications have become possible for a range of metal clusters, of various sizes, for pure and heteroatomic clusters, both for free clusters and those supported on an extended surface. Further developments are currently being carried out on the cluster GA program. The most recent version is the German Improved Genetic Algorithm (GIGA) [101], a collaboration between the Johnston group and the Schäfer group from T. U. Darmstadt, which includes a wider variety of electronic structure methods, optimisation of cluster spin, and optimisation of ligand binding and reactant adsorption sites.

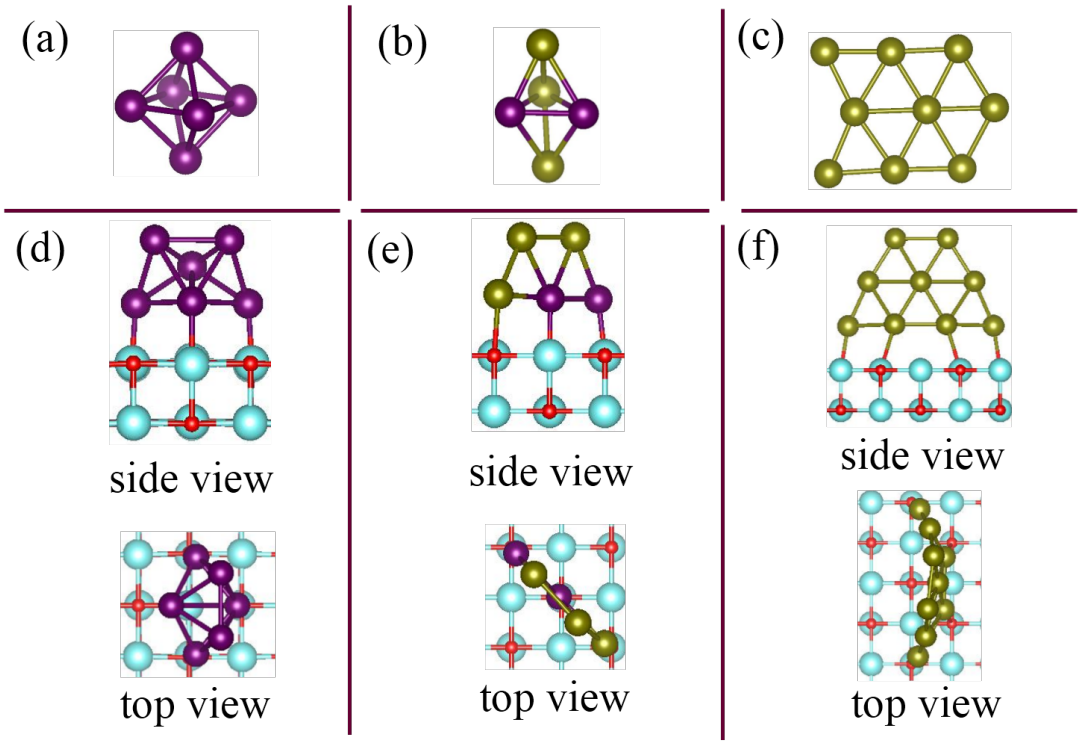

Figure 1.3: (a), (b), and (c) are putative global minimum structures of free (gas phase) Pd_6, Au_3Pd_2 and Au_9 clusters, respectively, while (d), (e), and (f) are side- and top-view of putative global minimum structures of the corresponding MgO(100)-supported clusters [39,98]. Pd, Au, Mg and O are shown in purple, green, blue and red, respectively. The gas-phase structure of Pd_6 is an octahedron, while it is a bicapped tetrahedron on the surface. A 3D-2D structural transition occurs for the gas-phase Au_3Pd_2 cluster when supported on the surface. Au_9 adopts a pseudo-planar configuration on the surface which is different from the 2D structure in the gas-phase.

1.3 Research Objectives

Following recent demonstrations of the utility of nanoalloys to environmental, energy, technological and engineering applications [1,31,102,103] which use composition, temperature and other parameters for tuning the properties of the conventional alloys, particle size has emerged as an effective parameter for property optimisation. This has led to research efforts focussed on investigating and improving the structural characterisation of clusters at sub-nanoscale by both theory and experiment.

The initial aim of the project was the prediction of the structures of Au and Pd and their nanoalloys using genetic algorithm global optimization at the Density Functional

Theory level (GA-DFT). The research involves catalytic studies of the clusters, treating them as adsorbates on oxide surfaces (e.g. MgO, Al_2O_3, TiO_2 and CeO_2 surfaces).

To achieve this aim, neutral AuPd subnanometre clusters have been characterized theoretically to understand better the underlying segregation effects in/without the presence of a MgO(100) surface. This research, which has used global optimization calculations employing the Birmingham Parallel Genetic Algorithm at Density Functional Theory level (BPGA-DFT), has established the structures and energetics of AuPd nanoalloy at the subnanometre.

AuCu clusters were then suggested by the author to be studied, trying to investigate the effect of replacing the closed-shell metal (Pd) by an open-shell metal (Cu) on the structural, energetic and adsorption properties. Such elemental replacement is of potential industrial importance due the natural abundance of Cu and its consequent low cost, in addition to the distinct catalytic role of copper-based catalysts in oxidation and hydrogenation reactions [104, 105]. For this study, the Mexican Enhanced Genetic Algorithm (MEGA-DFT) code has been applied to ultrasmall AuCu clusters to conduct an extensive structural search, for a wide variety of compositions, and the exploration of quantum-regime effects.

The author has considered gold as a common theme throughout the studied nanoalloy systems, due to its curious characteristics at the nanoscale such as absorbing green light and appearing red rather than yellow (as in the bulk), exhibiting considerable catalytic activity, and the size-dependant structural behaviour [106]. Bimetallic derivatives of gold are also considered in the research to equivalent features and/or novel new properties.

The interesting outcomes of the AuPd and AuCu studies, mentioned above, which show a clear effect of doping Pd or Cu atoms on the alloying, stability and structures of Au clusters, led us to focus on studying dopant effects on the stability, electronic structure, and catalytic activity and selectivity of subnanometre gold clusters. Our close collaboration with experimental research groups: Lievens group (K. U. Leuven) and Fielicke group (T. U. Berlin) who employ state of the art experiments for the synthesis and characteri-

zation of gold cluster cations, has led us to probe Pd dopant influences on the properties of cationic gold clusters.

Our findings highlight the subtle variations of adsorption preference and reactivity of clusters in the sub-nanometre "every-atom-counts" size regime, and the need for the synergistic application of multiple analysis techniques to understand metal cluster-CO interactions at the atomic level. These observations have significance for the rapidly growing fields of sub-nanoscale and single atom catalysis, for which a fundamental understanding of archetypal gas-cluster interactions is required.

Finally, trying to answer the outstanding question of the choice of optimal parameters required to optimise effective RuPt electrocatalysts, a combination of DFT for energy calculations and a genetic algorithm for structure optimization is employed. This study involves determining the geometric structures and energies of RuPt clusters in the size range N=2-8, for all possible compositions.

CHAPTER 2

METHODOLOGY

2.1 Energy Landscapes and Local Optimisation

The energetic response to structural rearrangements in many-body systems is described by the conceptual framework of energy landscapes. An energy landscape can be constructed by mapping the system energy as a function of its spatial coordinates. This mapping is generally defined as an energy function of the coordinate vector $\mathbf{R}$ with general expression $E = E(\mathbf{R})$, where $\mathbf{R}$ is a D-dimensional vector. For chemical systems, including clusters, Cartesian coordinates are generally used, where $\mathbf{R}$ becomes a $3N$-dimensional vector corresponding to the position of the atoms.

Special points can be recognised on such high-dimensional hypersurfaces, reflecting physically important features. Local minima, which are stationary points with no negative Hessian eigenvalues, correspond to the possible stable isomers available to the system. Saddle points are stationary points with one or more negative Hessian eigenvalues, determining barriers (energy maxima) between pairs of minima. The stationary point with a single negative Hessian eigenvalue (i.e. single imaginary normal mode frequency) represents a transition state. Across the landscape, the paths that interconvert two minima, navigating the lowest possible saddle point, indicate minimum energy pathways (MEP). Such analyses can be employed to elucidate physical (e.g. interconversion between locally stable isomers and homotops and inversion of the chemical ordering for nanoalloys) and

chemical processes (e.g. reactions and chemisorption) of the clusters. To exploit such features, sophisticated search methods have been developed, as described in section 2.2. The energy barriers, energy minima, phase volumes and the energy landscape pathways can be respectively employed to elucidate the activation energies, enthalpies, ergodicity, and rate constants of a system [107–114].

The potential energy of a cluster (E) can be represented on a PES diagram. High numbers of local-minima can be obtained in the PES of a small cluster, corresponding to their high-energy arrangements. Any displacement of the atomic coordinates of a local minimum in the PES will lead to configurations with higher potential energy (E). The gradients at the local minimum are all zero, ∇E_{clus}=0; and all the second derivatives (curvatures) are positive. The lowest energy configuration (lowest minimum) is called the global-minimum (GM) [107]. The pictorical representation of a PES shown in Figure 2.1 demonstrates how the potential energies of clusters with the same composition and size are affected by the different segregation patterns of their metals.

The atoms in a general configuration may experience non-zero net forces (Hellmann-Feynman forces) [115–117], resulting in movement of the atoms. Relaxing the atoms (until the net forces disappear) to their more stable configuration (i.e. minimum energy with respect to the atomic coordinates) is known as local optimisation. The resulting configuration is a valid solution (isomer), though it may not be the best (lowest energy) configuration overall. The energy of the structure is minimised by a local minimisation algorithm to the minimum of the local basin of attraction. A conjugate-gradient algorithm is used for the minimization of the cluster potential energy as a function of the cluster coordinates. For our local optimizations stages in the GA-DFT calculations, we have tested some convergence criteria. The stopping condition for the ionic relaxation runs and the global stopping condition for the electronic self-consistency loop were evaluated using various values. If the force convergence tolerance > 0, the ionic-relaxation stops when the energy change between ionic iterations is smaller than the magnitude of the force convergence tolerance. The thresholds for the electronic energy and forces were

set to 10^{-6} eV and 10^{-5} eV/Å, respectively. We have compared these thresholds with $10^{-5}/10^{-4}$ and $10^{-4}/10^{-3}$ thresholds, showing that all are fine for the optimization of our metallic systems, though the $10^{-4}/10^{-3}$ thresholds relatively speed up the optimization. The thresholds ($10^{-6}/10^{-5}$) were employed in our calculations to make the total energy significant to 6 figures and, thus, relatively more accurate.

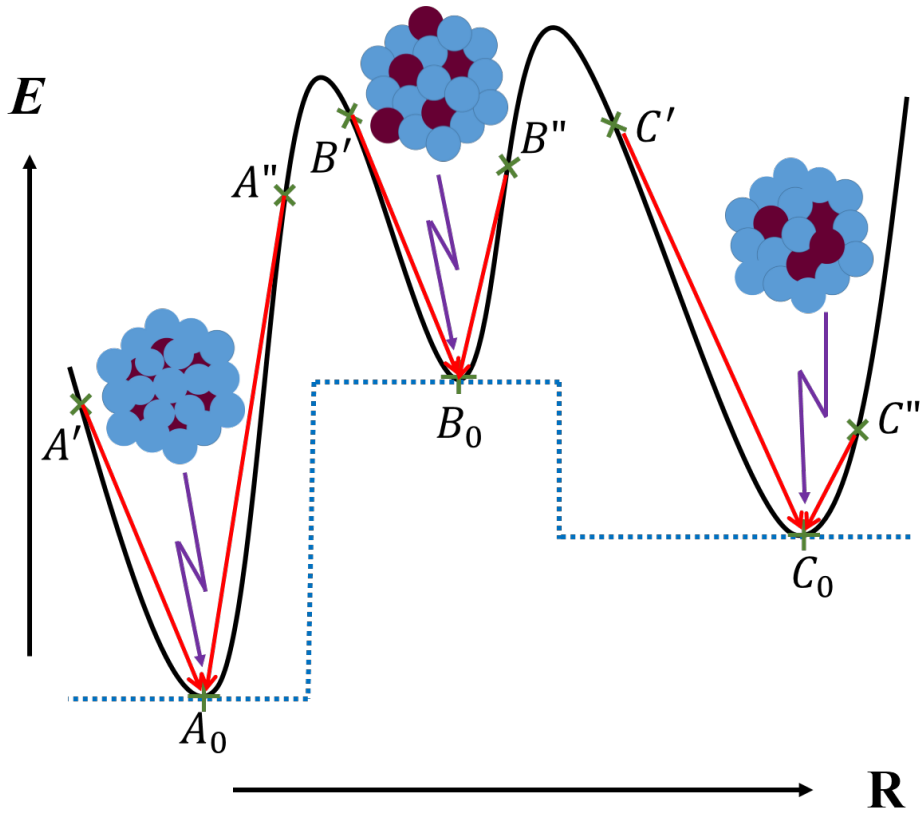

Figure 2.1: Schematic representation of a PES, with three basins of attraction having minimum energy solutions of A_0, B_0, and C_0. The black curve represents the true potential function, while the dashed blue line represents the converted potential energy surface (stepped surface). A', A'', B', B'', C', and C'' are six initial structures on the PES. After minimisation, the number of structures is reduced to three structures, A_0, B_0, and C_0. These represent three patterns of chemical ordering for the same nanoalloy (same size, composition and geometry). The two types of atoms are represented in blue and purple colours.

2.2 Global Optimisation

One of the most studied problems in computational nanoscience is locating the most favourable structure, corresponding to the lowest energy configuration or global minimum (GM), since the structure of a given nanoparticle (NP) strongly influences its physical and chemical properties. It is, therefore, necessary to search the potential energy surface (PES), or free energy surface if thermal effects are to be included [107]. However, an exhaustive search for the GM is still impossible for all but trivial cases. This indicates that the efficient and complete exploration of an energy landscape (i.e. the energetic mapping of structural rearrangements in cluster systems) cannot be guaranteed by an exact algorithmic approach and, therefore, sampling efficiency and heuristic improvement are important factors for effective global optimisation. Many global optimisation techniques, including Monte Carlo [118], basin-hopping [79] and evolutionary algorithms [32, 119], have been applied to search for the GM of NPs. In the class of nature-inspired evolutionary algorithms, genetic algorithms (GAs) have found widespread use throughout chemistry, physics, materials science and beyond.

2.2.1 Birmingham Parallel Genetic Algorithm (BPGA)

BPGA, as shown in Figure 2.2, employs a pool methodology to optimize and evaluate structures in parallel. Each run implements multiple BPGA instances, which in turn run a set of processes in parallel and independently [82, 120]. For a given cluster size, numerous random geometries (typically ranging from 10 to 30) are generated to form an initial pool using real-valued cartesian coordinates. The xyz coordinates are randomly chosen in the range $[0,\ N^{1/3}]$. This guarantees the correct scale between the cluster volume and the number of cluster atoms (N). In addition, constraints are placed on minimum and maximum nearest-neighbour distances so that $r_{nn} \leq r_{max}; r_{nn} \geq r_{min}$, where $r_{max} = 1.1 \times r_{nn}$ (atomic) and $r_{min} = 0.9 \times r_{nn}$ (atomic). These structures are then geometrically relaxed (locally energy minimized). Once the local minimization of the

initial pool structures is completed, offspring and mutants are produced through crossover and mutation operations. In our current work, the mutation rate is set to 10% of the pool size.

Clusters are selected for crossover using tournament selection, with crossover being performed using the cut-and-splice method introduced by Deaven and Ho [78]. The number of crossovers is predefined as a percentage (typically 90%) of the pool size. The fitness of each of the selected clusters is used to weight the cutting plane. A lower energy is represented by a higher fitness. The mutation operation consists of the random selection of a cluster from the pool, followed by a random displacement of two of the cluster atoms by up to 1Å for pure clusters or swapping unlike atoms (homotop-swap) for nanoalloys. After local minimisation, the energy of the newly created structures is compared with those of the other structures in the pool. The highest-energy isomer is replaced with a new lower energy isomer.

BPGA can also be applied to supported clusters and has been adapted to the global optimization of various clusters supported on the MgO(100) surface. The optimisation of the supported cluster is performed within a sphere placed at 1.5 Å over a slab of MgO(100) with specific dimensions (e.g. $6 \times 6 \times 2$, $8 \times 8 \times 2$, $6 \times 6 \times 3$, $6 \times 6 \times 4$, etc.) can be tuned manually. As shown in Figure 2.3, the repeat unit cells are set at 14.7, 14.7, and 21.1 Å with a minimum spacing of 8.7 Å in the z-direction (between the individual clusters) in order to avoid any non-physical or cluster-cluster interactions which may arise due to the periodic boundary conditions [97, 98]. Hence, the centre of the sphere is not constrained to lie above a specific atom (Mg or O) of the substrate. The surface effects can be increased quadratically by employing a two-layer MgO(100) slab [121–124]. The slab can be relaxed or fixed during the optimisations, but the fixing is the more popular due to the high computational cost of MgO(100) slab relaxation. The mutation operation for such systems is achieved by the random rotation of the cluster relative to the fixed surface [97, 98].

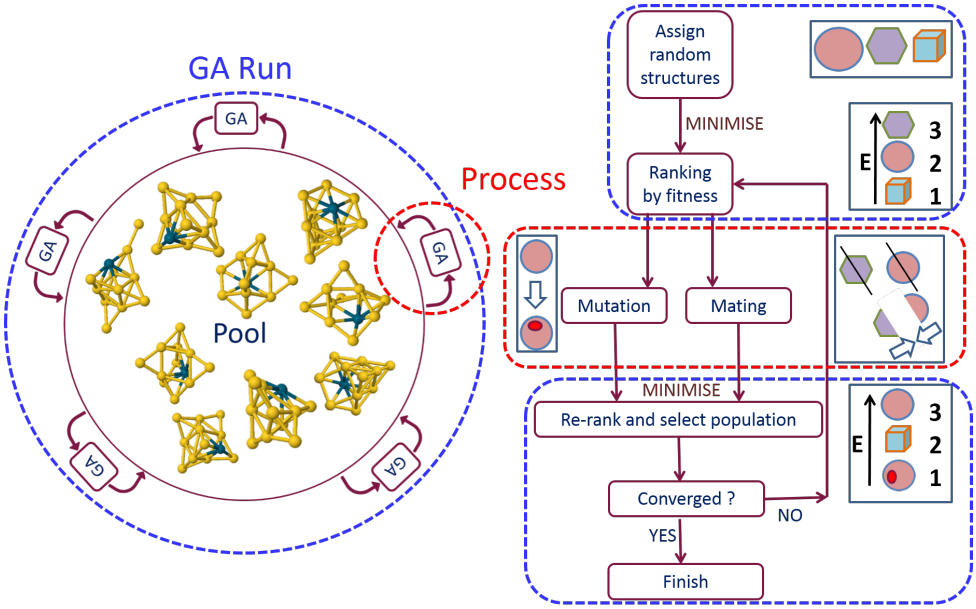

Figure 2.2: Schematic representation of the BPGA programme [39]. The left side illustrates the pool methodology, containing structural information (global database) and defines the run (dashed blue circle and boxes), and process (dashed red box) concepts. The right side shows a flow chart of the GA-method. The initialisation of the pool (random generation of structures), ranking for fitness (both at the beginning and later in the run) and the decision to carry out mutation or crossover (and what type) are done outside of the process. The process represents either mutation or crossover operation and takes input from the run and puts the output back into the run (where it may or may not be accepted). The overall convergence applies to the whole pool (i.e. the run), not the individual GA process. The instance consists of carrying out the specified type of mutation or crossover (process), followed by DFT local minimization.

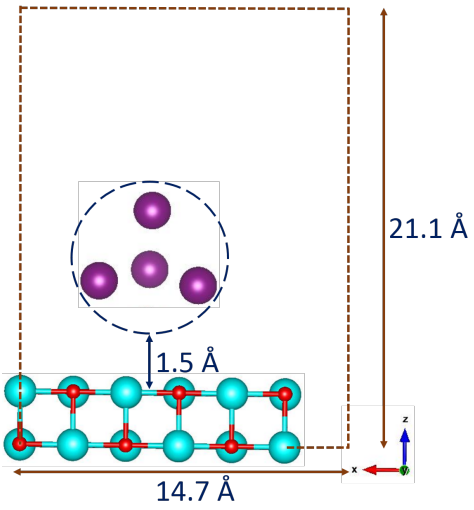

Figure 2.3: Schematic representation of BPGA optimisation of a supported cluster over a $6 \times 6 \times 2$ slab of MgO(100) [39]. Fixed height and vacuum spacing for an initial random geometry of the supported cluster are shown. Mg and O are shown in blue and red, respectively, while the cluster atoms are shown in purple.

2.2.2 Mexican Enhanced Genetic Algorithm (MEGA)

As in BPGA [82], MEGA [39, 99] employs the pool methodology for conducting parallel DFT relaxations for chosen individuals, following crossover or mutation (i.e. the main functionalities are same in both codes - e.g. both are written in Python, capable of conducting parallel and independent relaxations synchronized with a pool). The pool (global database), which contains the atomic coordinates and the energies of the most stable isomers for a given size and composition, is the central repository, where these implementations are achieved. A pool size is set at the beginning and remains at same size throughout the whole process. For a given cluster size, new geometries are generated and relaxed, and then their atoms are checked to ensure all atoms are connected to the cluster. In MEGA, the new structures forming the initial pool can be generated from scratch or previously found structures can be fed in. The origin of each cluster is located at its centre of mass. MEGA employs the same fitness criterion and roulette-wheel selection method used in previous GA versions [19, 32, 81]. The highest and lowest fitness of clusters in the population are used to re-scale the potential energy (V_i) of a specific cluster i:

$$\rho_i = \frac{(V_i - V_{min})}{(V_{max} - V_{min})}, \tag{2.1}$$

where ρ_i is the normalised value of the energy, and V_{min} and V_{max} are the lowest and highest potential energies of clusters in the population, respectively. The members in the next GA run are determined by a fitness function, f_i, which gives the probability of a member of the population being chosen to take part in crossover. Typically, a hyperbolic tangent function is adopted:

$$f_i = \frac{1}{2}[1 - tanh(2\rho_i - 1)]. \tag{2.2}$$

In roulette-wheel selection, a member of the pool (cluster) is randomly chosen for crossover if its (f_i) is higher than a randomly generated number between zero and 1, otherwise another pool member is selected and evaluated. Deaven-Ho [78] crossover is used (see

Section 2.2.1). The crossover operation generates 80% of the new clusters in the pool and the rest are produced by mutation.

As shown in Figure 2.4, different mutation operations, including "move", "rotate", "twist", and "atom inversion", are adopted in MEGA and the relative probability of each type of mutation can be predefined. "Move" mutation displaces 25% of total number of atoms of cluster shifting their coordinates by a certain value, x, $(-r_a \leq x \leq +r_a)$, where r_a is the atomic radius. "Rotate" mutation rotates 25% of the cluster atoms rigidly around an axis passing through the centre of mass and directed randomly. Similar to "rotate" mutation, "twist" mutation also rotates the cluster atoms rigidly but 50% of the atoms are rotated through a random angle relative to the other half of the cluster, retaining the same geometry within each half. "Atom inversion" mutation inverts one atom through the cluster centre of mass from one side to the other. This operation can be simply achieved by changing the signs of the coordinates of the relevant atom.

In addition to methods for selecting clusters and comparing the energies of competitive isomers, MEGA introduced a new criterion to maintain the pool diversity by including structural comparisons, to avoid rejecting significantly different configurations which happen to have very similar energies [99]. Structural comparisons can be acheived by comparing the variance of atomic distances, the radial distribution of atoms, or the eigenvalues of inertia tensors. In our work, we have utilised the interatomic distances to perform the geometric check without any additional energy check. Such checks have been previously introduced by Vilhelmsen and Hammer [125] with and without an additional energy check, showing that employing only the geometric check results in better performance. All the above improvements have enhanced the diversity, improved the exploration of the PES, and decreased the probability of being trapped in a sub-optimal local minimum (stagnation), in addition to finding new geometries with diverse properties and energetics using different exchange-correlation functionals or different levels of theory.

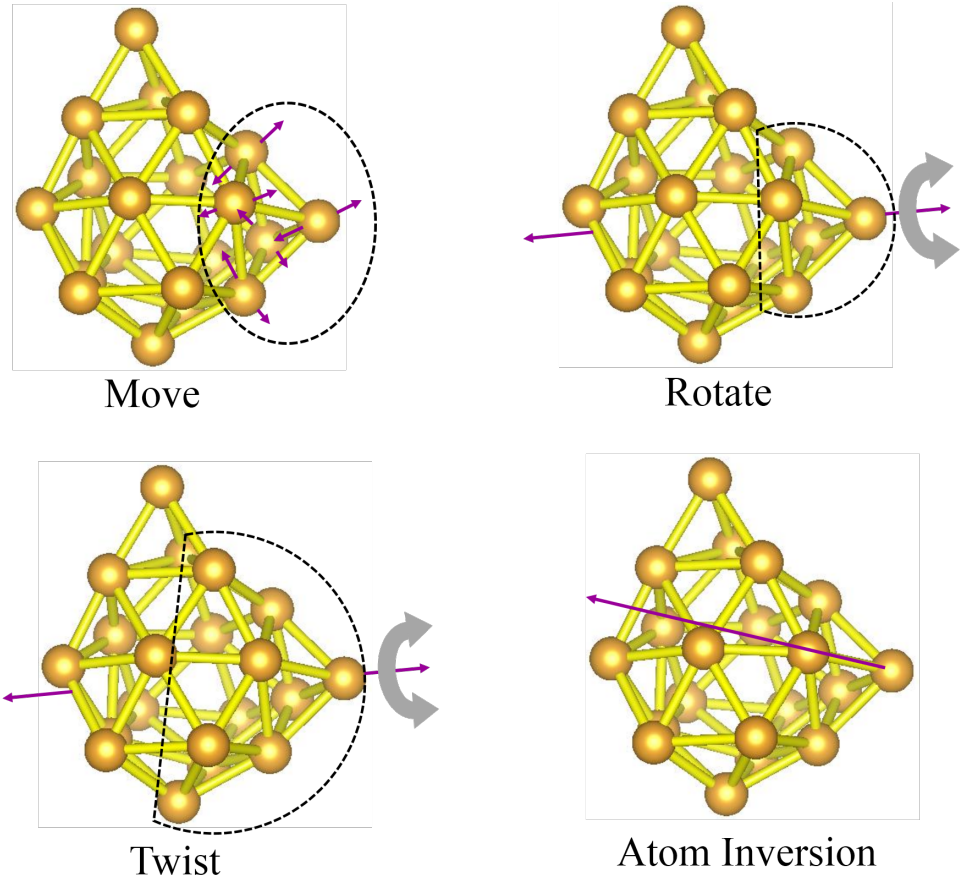

Figure 2.4: Schematic representation of four mutation operations applied to a 20-atom cluster within MEGA programme. The operations include "move" (where 1/4 of the cluster atoms, 5 atoms, are shifted by the x value, mentioned above), "rotate" (where 1/4 of the cluster atoms, 5 atoms, are rigidly rotated around a central axis), "twist" (where half of the cluster, 10 atoms, is rigidly rotated through a random angle relative to the fixed half), and "atom inversion" (where one atom is inverted from one side of the cluster to the other). The atoms are shown in gold, while the bonds are shown in yellow.

2.3 Density Functional Theory (DFT)

DFT is one of the main methods currently used to investigate the electronic structures of various materials, due to the combination of the accuracy and the efficiency provided by this method [126]. Although a wide range of theoretical methods have been developed to solve the Schrödinger equation based on the wave function theory (WFT) approach [127–129], DFT has presented a significant simplification by employing the electron density as a central concept instead of the wavefunction. This leads to a reduction of the

dimensionality from $3N$ for an N-electron system to 3 [130]. The electron density can be defined as the probability of an electron being located within a volume element $d\mathbf{r}$. The integral of the electron density then represents the total number of electrons N.

$$\int \rho(\mathbf{r}) d\mathbf{r} = N \tag{2.3}$$

To replace the wave function by the electron density, the Hamiltonian should be constructed from it. Three variables, including the number of electrons N, the nuclear charges Z_a and the position of the nuclei in space R_A, are employed to define the Hamiltonian of a given system. DFT is based on the two Hohenberg-Kohn (HK) theorems [131], where they formulated the construction of the Hamiltonian of a molecular system from the electron density. The first theorem states: '*the external potential, $V_{ext}(\boldsymbol{r})$ is a unique functional of $\rho(\boldsymbol{r})$; since, in turn V_{ext} fixes $\hat{H}$ we see that the full many particle ground state is a unique functional of $\rho(\boldsymbol{r})$*'. Through a functional of the ground state electron density, the ground state energy (external potential V_{ext}) of a system is, therefore, available. The second HK theorem states that the ground-state total energy for a given system can be represented as a functional of electron density $\rho(\mathbf{r})$.

The ground-state energy functional, according to the Kohn-Sham approach, which assumes that electron density $\rho(\mathbf{r})$ of the interacting system is the same as that of a fictitious n-electron non-interacting system, can be obtained from Equation 2.4 [132]:

$$\begin{aligned} E[\rho] = -\frac{\hbar}{2m_e}\sum_{i=1}^{n}\int \psi_i^*(\mathbf{r}_1)\nabla_1^2\psi_i(\mathbf{r}_1)d\mathbf{r}_1 - \sum_{I=1}^{N}\int \frac{Z_I e^2}{4\pi\epsilon_0 \mathbf{r}_{I1}}\rho(\mathbf{r}_1)d\mathbf{r}_1 \\ +\frac{1}{2}\int \frac{\rho(\mathbf{r}_1)\rho(\mathbf{r}_2)e^2}{4\pi\epsilon_0\mathbf{r}_{12}}d\mathbf{r}_1 d\mathbf{r}_2 + E_{XC}[\rho], \end{aligned} \tag{2.4}$$

where the first term is the independent particle kinetic energy, the second term is the interaction potential between an electron and the atomic nuclei, the third term is the Hatree potential, which is the Coulomb repulsion between an electron and the total electron density and involves a self-interaction contribution, and the fourth term is the exchange-correlation potential. $\hbar = h/2\pi$ (where h is Planck's constant), m_e is the electron mass, n

is the number of electrons, ψ_i is the electronic wave function, ∇^2 is the Laplacian operator (second derivative with regard to cartesian displacements), N is the number of nuclei, Z_I is the atomic number of the I^{th} nucleus, e is the elementary charge ($e = 1.602177 \times 10^{-19}\text{C}$), and ϵ_0 is the vacuum permittivity ($\epsilon_0 = 1/c^2\mu_0 = 8.854187816 \times 10^{-12}\text{J}^{-1}\text{C}^2\text{m}^{-1}$, where c is the speed of light and μ_0 is the vacuum permeability).

The Kohn-Sham approach typically replaces $3n$ coordinate problem for an n-electron system by only 3 spatial coordinates by using so-called Kohn-Sham orbitals. The non-classical electron-electron interactions are represented by the exchange-correlation energy which is analytically an unknown expression, thus it needs to be approximated. The exact ground state electron density of interacting system can be calculated from the summing over all occupied Kohn-Sham orbitals ψ_i ($i = 1, 2, ..., n$), as shown in Equation 2.5:

$$\rho(\mathbf{r}) = \sum_{i=1}^{n} |\psi_i(\mathbf{r})|^2 \tag{2.5}$$

The Kohn-Sham equations can be solved by making an initial guess for the electron density. The equations are then subjected to self-consistent solution by first computing E_{XC} as a function of ($\mathbf{r}$). An improved density is computed (using Equation 2.5) based on an initial set of orbitals obtained from solving the equations. This process is performed repeatedly until the density and exchange-correlation energy are converged. The ground state energy can then be found utilising Equation 2.4.

2.3.1 Exchange-Correlation Functionals

Because the accuracy of an exchange-correlation functional is controlled by their parameters, the research in development of efficient and accurate forms of the functional is a key field for DFT [133–135]. The extent of accuracy (and the computational cost) scales with the level of the sophistication of the approximations.

Local density approximation (LDA) functionals, which assume uniformity of the electron density throughout the molecule [136], are the simplest exchange-correlation

functionals employed in DFT. LDA has been employed successfully for solid systems, for which cohesive energies and lattice spacings are calculated with impressive accuracy. LDA is less important for heavy metals, conjugated molecules, and many metal oxides due to their high electron correlation effects. Due to the LDA assumption that the system as a uniform electron gas embedded into a positive background charge distribution, the exchange and correlation energies are known. Equation 2.7 defines that the total energy E_{XC} is equal to the integral of the exchange and correlation energies per atom, which are defined individually as $\epsilon_X(\rho(\mathbf{r}))$ and $\epsilon_C(\rho(\mathbf{r}))$, respectively, weighted by their densities. This means that the density is stationary at each point.

$$E_{XC} = \int \rho(\mathbf{r})(\epsilon_X(\rho(\mathbf{r})) + \epsilon_C(\rho(\mathbf{r})))d\mathbf{r}. \tag{2.6}$$

The generalised gradient approximation (GGA) improves on the LDA, including the gradient of the electron density over the particle (non-uniformity). This assumption is more consistent with the realistic distribution of the electron density in a molecule. The Perdew-Burke-Ernzerhof (PBE) functional [137] is a popularly employed example of a GGA functional. It is used as a standard functional for the treatment of metallic systems, including bulk metals and gas-phase and supported metal clusters and NPs [138–143].

Long-range corrected (LC) functionals [144], which are derived from GGA functionals, are typically used for systems that exhibit long range charge transfer, due to the improved asymptotic behaviour of the exchange energy at long range and correction for the self-interaction energy. Binary metallic clusters, where the electronegativities of the two metals are significantly different [144, 145], and organic photovoltaic materials with spatial charge separation [146, 147], are prime examples of such systems. These LC functionals increase the accuracy of the description of electron-electron interactions by the separation of the Coulomb term into a short-range (SR) component, which is DFT exchange, and a long-range (LR) component, which has a degree of exact Hartree-Fock (HF) exchange. The extent of HF exchange is determined by a tunable parameter which can be optimized. The long-range corrected LC-ωPBEh functional [144, 148], which has

been used in this work, is a hybrid functional, so it also contains some HF exchange in the short-range component. The form of the LC-ωPBEh functional is given by:

$$\begin{aligned} E_{XC}^{LC-DFT} &= \alpha E_X^{SR-HF}(\omega) + (1-\alpha)E_X^{SR-DFT}(\omega) \\ &+\beta E_X^{LR-HF}(\omega) + (1-\beta)E_X^{LR-DFT}(\omega) + E_C^{DFT}, \end{aligned} \tag{2.7}$$

where α and β represent the magnitudes of the HF and DFT exchange, respectively, in the short-range (SR) and long-range (LR) components of the Coulomb term, with $\alpha = 0.2$ and $\beta = 0.8$, while ω refers to the range separation.

2.3.2 Basis Sets

To describe where the electrons are in the KS orbital, an appropriate choice of basis sets is required. Two methods are widely used, the linear combination of atomic orbitals (LCAO) technique, and the plane wave (PW) approach. LCAO linearly combines the basis sets χ_μ with expansion coefficients $c_{\mu j}$ to expand the KS orbitals required to define the electron density. KS orbitals ψ_j are described by Equation 2.9:

$$\psi_j = \sum_{\mu=1}^{D} c_{\mu j}\chi_\mu, \tag{2.8}$$

such that the KS orbital ψ_j is a linear combination of the D basis sets χ_μ weighted by their contribution $c_{\mu j}$.

The quality and accuracy of such a method cannot be guaranteed to be improved by increasing the number of basis functions (as DFT is not a variational method), instead, the quality of the chosen basis function could provide a reasonable contribution. Two types of atomic orbital basis sets are commonly employed in DFT calculations: Slater type orbitals (STOs) and Gaussian type orbitals (GTOs) [149]. STO basis functions look like atomic orbitals (hydrogen-like in form). However, GTO basis functions are more computationally efficient. Combining both classes, a commonly applied approach for DFT calculations, the contracted Gaussian functions (CGF) basis functions were developed [150]. CGF

combines fixed Gaussian functions to generate a set of χ_μ to reproduce STOs.

The efficiency and computational cost are highly dependent on the size of the basis set. A minimal basis set, where each atomic orbital is represented by a small number of functions, is the simplest. Such basis sets have lower accuracy but are much cheaper than the other larger basis sets. This type of basis set is used to provide an approximate first estimation of specific molecular properties. Performance can be enhanced by splitting the basis into valence (where the electrons are involved in chemical reactions) and core regions, generating split-valence basis sets. The threshold of the splitting is controlled by considering an energy cutoff, such that the orbitals below it are treated with a quick and lower quality approximation (reduced cost). Conversely, a more careful and thorough treatment is applied to the valence electrons. This requires a more accurate (but more expensive) basis set which can also increase its quality by employing multiple sets for each orbital. Triple-zeta bases, which are used extensively in the work presented in Chapter 4, use three functions to represent each orbital. Inclusion of additional polarization and diffuse functions sets is commonly used to improve the performance by increasing the flexibility of the electron distribution. In the present work, the def2-TZVPP [151] basis set, which has triple-zeta and two additional polarization functions, is employed.

Plane wave basis sets were developed to be used for periodic systems, such as solid state materials and extended surfaces. The KS equations are produced from an expansion of the naturally periodic PW functions. Because each PW is constructed to be orthogonal to the others, a PW basis set can be improved qualitatively by expanding the wavefunctions to higher wave vector ($\mathbf{G}$) (and thus higher energy). Controlling such qualitative improvement in the basis set can systematically be achieved by employing a kinetic energy cutoff parameter. This parameter determines the number of PWs; as higher frequency PWs can be added to the calculation by using a higher kinetic energy cutoff (giving higher accuracy but being computationally more expensive). The PW approach follows Bloch's theorem and utilizes periodic boundary conditions to generate the KS wavefunctions.

As the core electrons oscillate rapidly with $\mathbf{r}$, employing PW methods for core

regions requires a large number of functions (larger even those required for LCAO methods), or a large kinetic energy cutoff, to allow to an accurate description. An effective potential, pseudopotential, is employed to avoid such drawbacks by merging the nucleus-electron interactions and the core electron states in the same term. Accordingly, PW basis functions are utilized to model only valence electronic states while pseudopotentials are used for frozen core states. The pseudopotential corresponds to the effective core potential approximation used in LCAO methods, such as the def2-ECP of Weigend and Ahlrichs [144, 148, 152] used in the present work. These potentials are introduced to replace the strong true ionic potential with a flexibly varying, feasible potential function. The pseudopotential is constructed in such a way that it and the correct form are identical to the all-electron states and potential as the distance approaches the radius cut-off, $\mathbf{r}_c$.

The projector augmented wave (PAW) [153] is another method that can be used to address the core electron problem. The PAW approach allows the modelling of all-electron properties by transforming the rapidly oscillating core region wavefunctions into smoother wavefunctions, providing a more computationally convenient method. The smooth pseudo-wavefunction of the core states can be locally optimized and described by plane waves to recover all-electron states. In the PAW method, effective calculations can be conducted with a performance similar to that provided by the pseudopotential approach. Moreover, the PAW approach provides a high degree of transferability and gives a clearer picture of the wavefunctions near the nuclei.

CHAPTER 3

STRUCTURAL CHARACTERISATION OF FREE AND MGO(100)-SUPPORTED NEUTRAL GOLD-PALLADIUM NANOALLOYS

3.1 Introduction

The impressive activity and stability of subnanometre metallic particles have been discovered due to the increasing interest in their catalytic activity for a wide range of chemical reactions [154–157], promising a great future of industrial applications. To investigate and design such materials with high activity and selectivity, a comprehensive understanding of their atomic structures is required. The nature of the nanoparticle atoms' coordination, including the undercoordination is important in adjusting their electronic properties and consequently their reactivity [5, 6, 158]. Moreover, the presence of the support is known to be highly influential and contributes effectively in improving the catalytic performance [5, 159, 160]. The direct bonding of the support to atoms of the particle and possible alteration in further layers can induce structural modulations in the deposited particles, thereby changing their reactive properties [123, 161, 162]. However, the support may drive epitaxial growth of the nanoparticle and, sometimes, crystallisation can occur [163, 164].

Experimentally, the products of the deposition process are highly affected by its mechanism and the environment. The structures of clusters, which are soft-landed on

the surface after their generation in the gas-phase, are expected to be largely similar to their low energy minima in the gas phase [165]. On the contrary, clusters, which grow or agglomerate upon the surface, are found to be strongly affected by the surface [166, 167], producing structures different to those found in the gas phase. A set of variables, including the size and composition of the cluster, the electronic and chemical behaviour of the support, and the deposition process, are required to be studied to determine the unbiased structure. Such complex issues are hard to solve experimentally, due to the small size of the reactants as well as variable reaction conditions. Theoretical screening is, therefore, considered to be the ideal solution and introduces an effective way to treat and tune the various factors, determining the cluster structures.

In Publication 1, several factors that influence the structures of ultra-small (sub-nanometre) AuPd clusters on the MgO(100) surface are considered based on a BPGA-DFT study. Structural transitions and alterations as a function of size, composition, and support effects are predicted and discussed. The extent of the size contribution to the stability of the clusters are explained. The underlying synergistic mechanisms of mixing that play a significant role in controlling geometric structures are investigated. The energetics are employed for evaluation of several observations, including homotops, alloying, and the adsorption on the surface. The direct DFT global optimisation of AuPd clusters are extended up to N=18 for clusters in the gas-phase (Publication 2). From their combined findings, the quantum-size effects are revealed. As shown in Figure 3.1, the evolution of the structural motifs has been elucidated as function of the cluster sizes. The structures of pure clusters are found to be size dependent, while for mixed clusters, the structural characteristics are found to be controlled by the size and composition. The preferred connectivity sites for both Au and Pd atoms are calculated. The tendency of Au and Pd atoms to mixing is measured by the mixing (or excess) energies. Negative values of the excess energy correspond to favourable mixing, whereas de-mixing is indicated by positive values.

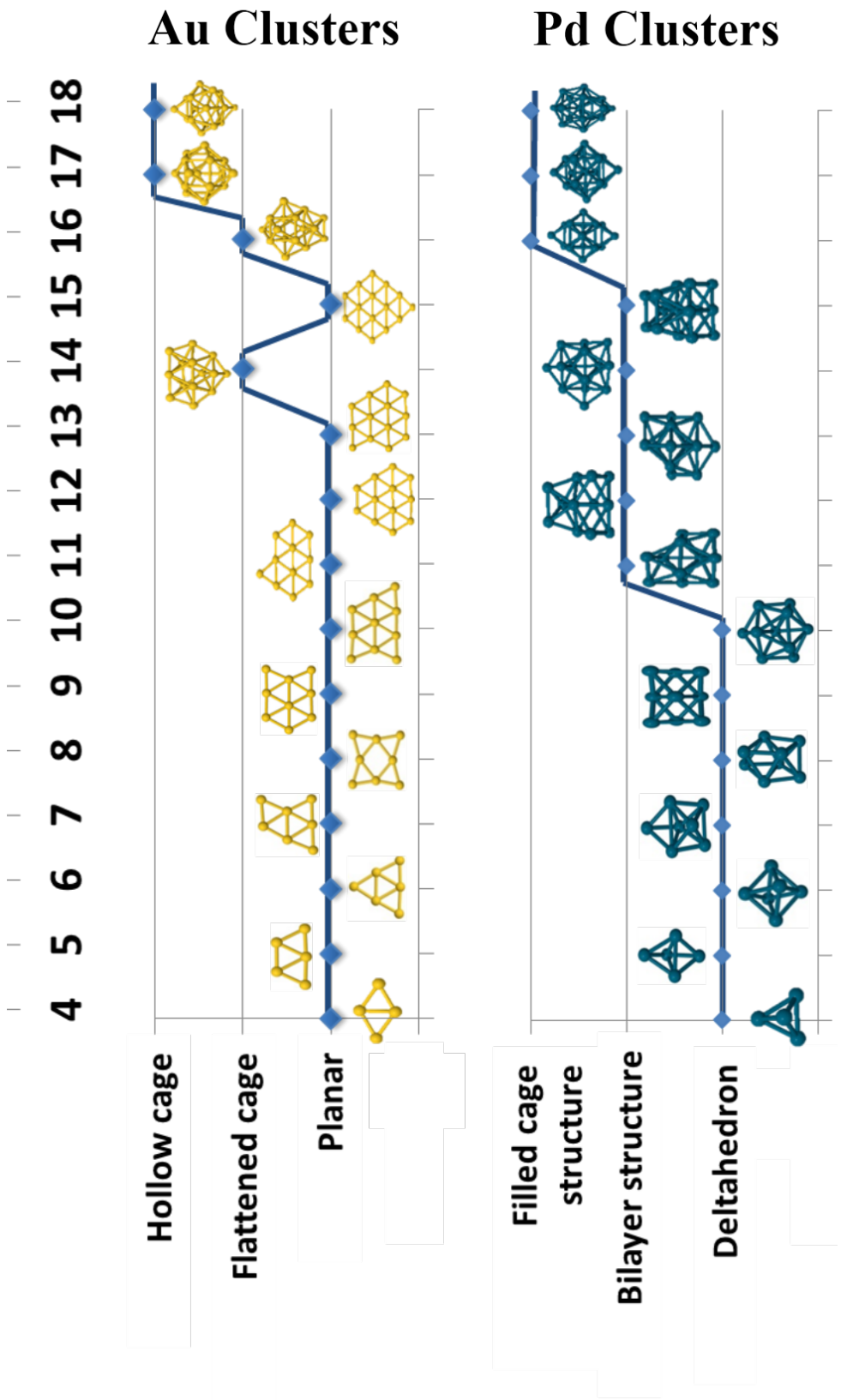

Figure 3.1: Evolution of structural motifs for pure Pd and Au clusters [39].

3.2 Publication 1

Title

DFT global optimisation of gas-phase and MgO-supported sub-nanometre AuPd clusters

Authors

Heider A. Hussein, Jack B. A. Davis and Roy L. Johnston

Journal Physical Chemistry Chemical Physics

Volume 18

Pages 26133-26143

DOI 10.1039/C6CP03958H

Submitted

7 June 2016

Accepted

25 August 2016

3.2.1 Author Contribution

The author carried out all calculations of the study, along with post-calculation acquisition and analysis of data, discussing the results and writing the article. All the figures and tables in the article and the supplemental material were created by the author.

PCCP

PAPER

Cite this: *Phys. Chem. Chem. Phys.*, 2016, **18**, 26133

DFT global optimisation of gas-phase and MgO-supported sub-nanometre AuPd clusters†

Heider A. Hussein,[ab] Jack B. A. Davis[a] and Roy L. Johnston*[a]

Received 7th June 2016,
Accepted 25th August 2016

DOI: 10.1039/c6cp03958h

www.rsc.org/pccp

The Birmingham Parallel Genetic Algorithm (BPGA) has been adopted for the global optimization of free and MgO(100)-supported Pd, Au and AuPd nanocluster structures, over the size range N = 4–10. Structures were evaluated directly using density functional theory, which has allowed the identification of Pd, Au and AuPd global minima. The energetics, structures, and tendency of segregation have been evaluated by different stability criteria such as binding energy, excess energy, second difference in energy, and adsorption energy. The ability of the approach in searching for putative global minimum has been assessed against a systematic homotop search method, which shows a high degree of success.

1 Introduction

Nanomaterials have at least one dimension on the nanometer scale (1–100 nm). They have recently emerged as new materials that bridge the gap between atoms or molecules and bulk materials, and they have attracted remarkable interest owing to their numerous potential applications.[1] Nanomaterials contribute to many new technological applications in various fields, such as medicine, materials, physics, and chemistry. These new applications came as a consequence of their novel chemical and physical properties which are due to electronic and quantum effects and the high surface-area-to-volume ratio.[1–3]

The ability to control the surface and structural properties of nanostructures in the nanometre range and their suitable integration with different scientific research concepts have attracted widespread interest from researchers because of their use in many emerging technological applications.[4–7] AuPd nanostructures, in particular, have been investigated previously for a number of applications, including catalytic applications. AuPd catalysts have been found to be promising candidates for a wide variety of chemical reactions, such as cyclohexane oxidation,[8] NO reduction,[9] CO oxidation,[10,11] direct synthesis of hydrogen peroxide,[12,13] and synthesis of aldehydes from primary alcohols.[14]

Theoretically, AuPd systems have been studied to rationalize their catalytic activities. Studies have been conducted on some of the AuPd clusters in the gas phase[15] and supported on surfaces (*e.g.* MgO(100) and TiO_2(110) slabs)[16–18] in addition to the simulation of the interaction of pure Au and Pd nanoparticles and AuPd nanoparticles with atoms or small molecules such as S, H, NO, and CO.[9,10,19,20] However to date there have been few studies of small AuPd clusters supported on MgO. Subnanometre clusters are groups or aggregates of a few to tens of metal atoms which are (<1.0 nm) in size. These smaller clusters are of interest in catalysis due to the potential for enhanced activity and selectivity.

The rarity of theoretical studies concerned with N = 4–10 AuPd nanoalloys, whether in the gas phase or supported on MgO, has led us to select the Au–Pd system to be studied. In order to find the global minima for the pure and mixed AuPd clusters in the gas phase and on MgO, we have used the Birmingham Parallel Genetic Algorithm (BPGA) to enable global optimisation directly at the DFT level.[21]

2 Methodology

2.1 BPGA-DFT

The BPGA-DFT approach was applied for cluster sizes ranging from N = 4–10 for all compositions of free and MgO(100)-supported AuPd nanoalloys, as well as the pure Au and Pd clusters. Gamma-point DFT calculations were performed with the Vienna *ab initio* Simulation Package (VASP) code[22] utilising projected-augmented wave (PAW) pseudopotentials and the PBE exchange correlation functional.[23,24] A plane-wave basis set was used. The energy was truncated at 400 eV. Methfessel–Paxton smearing, with a sigma value of 0.01 eV, was implemented to improve convergence.[25]

The Birmingham Parallel Genetic Algorithm (BPGA) has been adopted for the evaluation of potential cluster structures. This method is the latest open-source genetic algorithm[26] improving on the Birmingham Cluster Genetic Algorithm

[a] *School of Chemistry, University of Birmingham, Birmingham, B15 2TT, UK. E-mail: r.l.johnston@bham.ac.uk; Tel: +44 (0)1214 147477*
[b] *Department of Chemistry, College of Science, University of Kufa, Najaf, Iraq*

† Electronic supplementary information (ESI) available. See DOI: 10.1039/c6cp03958h

(BCGA), a genetic algorithm for determining the lowest energy isomers of nanoparticles and nanoalloys up to approximately 100 atoms.[27]

BPGA employs a pool methodology to evaluate structures in parallel. In each run, multiple BPGA instances are implemented, and in each instance, a set of processes are run in parallel and independently.[15,28] Numerous random geometries are initially generated to form a population.[21] The generated structures of a given population are then geometrically relaxed (local energy minimized).[15] Once the local minimization of the initial pool structures is completed, crossover and mutation are conducted on the lowest energy individuals in the population.

Clusters are selected for crossover using tournament selection with crossover being performed using the cut-and-splice method introduced by Deaven and Ho.[29] The mutation operators are set as a homotop-swap for nanoalloys and a random atom displacement for the pure clusters. The energy of any newly created structure is compared with those of the other structures in the pool. The highest-energy isomer is replaced with the new lower energy isomer.

For the supported clusters, owing to the high computational cost of MgO(100) slab relaxation, the slab is not relaxed during the local minimization, but the cluster geometries are optimised in the presence of the fixed slab. The supported cluster is optimised within a sphere placed at 1.5 Å over a 6 × 6 × 2 slab of MgO(100) with a 14.7 Å vacuum spacing (as shown in Fig. 1), to ensure that there are no cluster–cluster or other non-physical interactions arising due to the periodic boundary conditions. The interactions between the cluster and the surface have been replicated using two layers of MgO(100).[17,30–32] The efficacy of replicating a surface behaviour and the cluster properties by using two layers of the MgO slab has previously been confirmed.[33,34] Random rotation of the cluster regarding the fixed surface is used as a mutation operator when optimising the supported clusters.

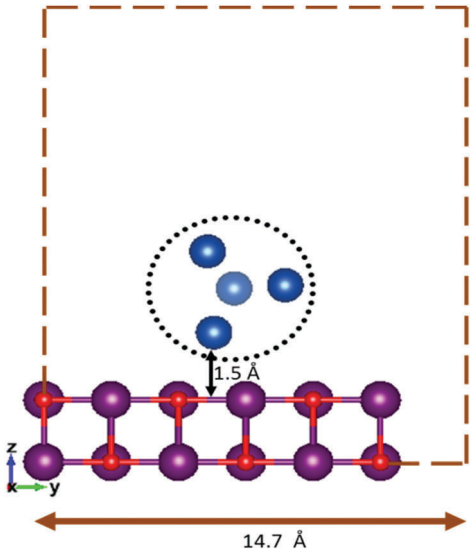

Fig. 1 Fixed height and vacuum spacing for an initial random geometry of the surface-supported cluster.

2.2 Energy calculations

The average binding energy per atom E_b is given by

$$E_b = \frac{1}{N}\left[E_{(Au_mPd_n)} - mE_{Au} - nE_{Pd}\right] \quad (1)$$

where m, n, E_{Au}, and E_{Pd} are the numbers of Au and Pd atoms and the electronic energies of a single Au or Pd atom, respectively, and N is the total number of atoms ($N = m + n$).

The stability of each cluster, relative to its neighbours, is indicated by the second difference in energy Δ_2E which is given by

$$\Delta_2E = E_{(A_{(N+1)})} + E_{(A_{(N-1)})} - 2E_{(A_N)} \quad (2)$$

where A is Au or Pd, $E_{(A_N)}$ corresponds to the total energy of the N-atom cluster and $E_{(A_{(N+1)})}$ and $E_{(A_{(N-1)})}$ are the neighbouring clusters, with one atom more and one atom less, respectively.

Evaluation of the effect of mixing in binary nanoalloys has been achieved by calculating the excess energy Δ which is given by

$$\Delta = NE_{(Au_mPd_n)} - mE_{(Au_N)} - nE_{(Pd_N)} \quad (3)$$

where $E_{(Au_mPd_n)}$ is the total energy of the nanoalloy and $E_{(Au_N)}$ and $E_{(Pd_N)}$ are the energies of the pure Au and Pd clusters with the same total number of atoms as Au_mPd_n.

The adsorption energy, E_{ads}, of the Au_mPd_n cluster on the MgO(100) support was calculated by

$$E_{ads} = E_{(slab+Au_mPd_n)} - E_{(slab)} - E_{(Au_mPd_n)} \quad (4)$$

where $E_{(slab+Au_mPd_n)}$ is the energy of the MgO(100)-supported cluster, $E_{(slab)}$ is the energy of the MgO(100) surface, and $E_{(Au_mPd_n)}$ is the energy of the free Au_mPd_n cluster, locally minimized in the gas phase.

3 Results and discussion

3.1 Global optimisation of free and supported Au, Pd, and AuPd clusters

3.1.1 Gold clusters. The putative global minima for pure Au clusters, $4 \leq N \leq 10$, are shown in Fig. 2 and their energies, structures, and point groups are listed in Table S1 (see the ESI†). Putative global minima for the MgO(100)-supported Au clusters, $4 \leq N \leq 10$, are shown in Fig. 3 and 4.

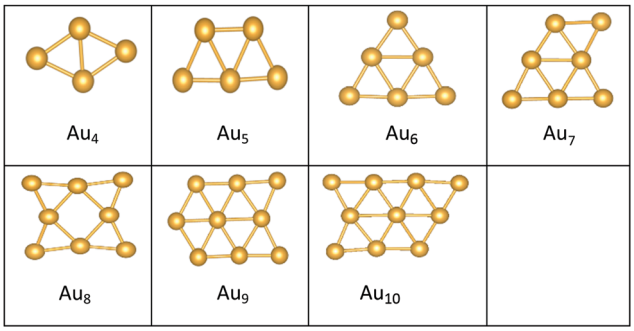

Fig. 2 Putative global minimum structures of free Au_N clusters, N = 4–10.

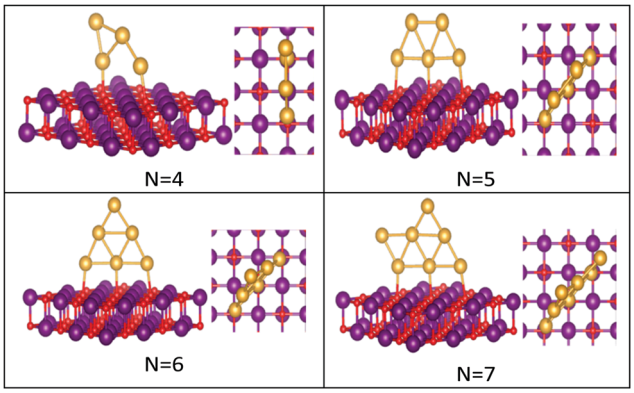

Fig. 3 Putative global minimum structures of MgO(100)-supported Au_N clusters, N = 4–7. Au, Mg and O are shown in gold, purple, and red, respectively.

The best structures obtained for all studied free Au clusters in this size range show planar configurations, as previously reported.[35–37] Our results satisfactorily concur with those presented by previous theoretical studies on Au clusters up to 10 atoms[38–40] and by experimental research on Au cation clusters up to 7 atoms.[41] In addition, our results agree with the findings of Zhao and co-workers[42] concerning the planar structures of small Au clusters up to 6 atoms. However, some differences are observed for Au_7, Au_8, and Au_9, which are predicted to be 3D by Zhao.[42]

Global minima for the supported Au clusters are all found to be still planar, with some slight deviation from the planarity for Au_9 and Au_{10}. They are found to lie roughly perpendicular to the MgO surface, due to the "metal-on-top" effect.[32] Bonding of two atoms of Au to O atoms has led to an increase in the Au–Au distance from (2.68) to (3.76) Å, forming an elongated Au_4 cluster on the surface.[43] N = (5–8) Au clusters on the surface have similar structures to that in the gas phase, whereas Au_9 adopts a different pseudo-planar configuration and Au_{10} keeps the gas phase structure but with a bend in one of its edges.

The preference for Au clusters with planar structures may be attributed to the non-additive many-body interactions in comparison with the additive two-body forces in Au atoms,[44] and the involvement of the d electrons of Au in bonding in planar structures is higher than in 3D ones.[39] Some researchers have considered "relativistic effects"[45] in interpreting the preference for planar structures, attributing such a preference to the decrease in the 5d–6s orbital spacing that strengthens s–d hybridization.[46]

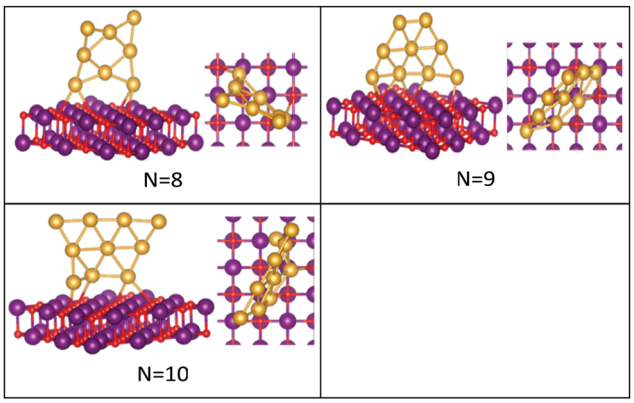

Fig. 4 Putative global minimum structures of MgO(100)-supported Au_N clusters, N = 8–10. Au, Mg and O are shown in gold, purple, and red, respectively.

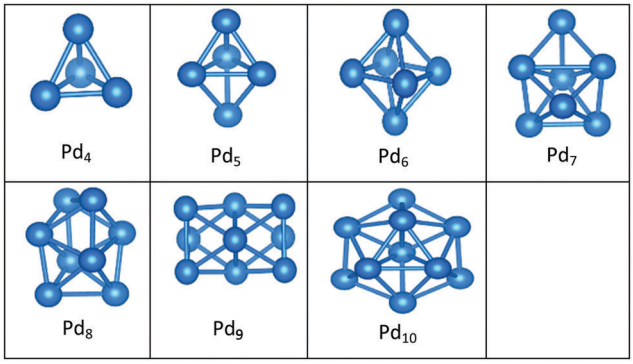

Fig. 5 Putative global minimum structures of free Pd_N clusters, N = 4–10.

3.1.2 Palladium clusters. Fig. 5 and 6 show the putative global minima for free and supported pure Pd clusters, and Table S1 lists the energies, structures, and point groups for free clusters (see the ESI†).

In contrast to Au clusters, Pd clusters do not adopt 2D structures; instead, they all have 3D motifs that mostly favour

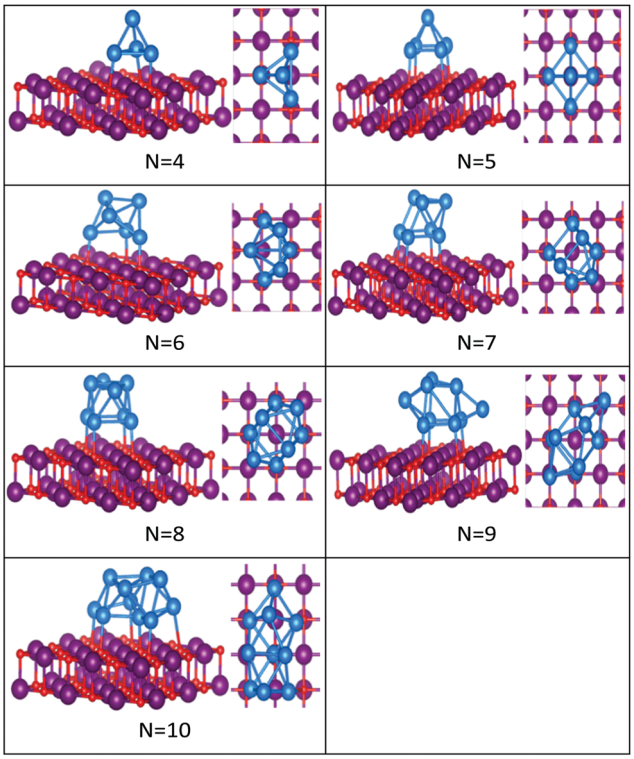

Fig. 6 Putative global minimum structures of MgO(100)-supported Pd_N clusters, N = 4–10. Pd, Mg and O are shown in blue, purple, and red, respectively.

deltahedral (triangular faced) compact structures as lowest-energy configurations. Global minima for the gas phase Pd clusters are all found to be different from their supported structures with the exception of Pd_4 which remains a tetrahedron.

Landman *et al.*[47] investigated the structural properties of neutral Pd_N isomers with $N = 1$–7 using DFT. These researchers clarified that the global minima are 3D for clusters with more than 3 atoms, which is in full agreement with the gas-phase Pd clusters for sizes $4 \leq N \leq 7$ reported here. Thus, the global minimum of free Pd_5 is the trigonal bipyramid. On the surface this structure distorts to give a square-based pyramidal structure. The four Pd atoms of the square base are bonded to four different O atoms of the slab. The octahedral structure of free Pd_6 alters to form a bicapped tetrahedron on the surface, forming three Pd–O bonds.

We have previously presented BCGA-DFT studies of free Pd_8, Pd_9, and Pd_{10} clusters,[16,48] whose putative global minima were identified as a dodecahedron, an icosahedral fragment, and an incomplete centered icosahedron, respectively. These observations conform to our findings for free clusters. Our supported structures of Pd_7, Pd_8, and Pd_9 are a capped trigonal prism, a distorted square antiprism, and a distorted tricapped octahedron, respectively. The structure of Pd_{10} is an icosahedral fragment in the gas-phase. On the surface this global minimum distorts to give a more complex fused structure.

3.1.3 Gold–palladium clusters. The putative global minima for all compositions of free and supported Au_mPd_n clusters, $4 \leq (m + n) \leq 10$, are shown in Fig. 7–16 and the energies, structures, and point groups of all free clusters are given in Table S2 (see the ESI†). On going from monometallic clusters to nanoalloys, there is an increase in difficulty of identifying the global minimum (GM) structure due to the presence of "homotops" in addition to the size effect.[49]

All the favoured structures of Au_1Pd_n n = 3–9 compositions are 3D. For $N = 4$–7 and $N = 9$, doping one Au atom into the pure Pd clusters yields geometries which are similar to the pure Pd clusters, as previously reported.[35,50] Au_1Pd_n n = 7 and 9 are a bicapped octahedron and a capped face-sharing octahedron, respectively. The Au atom occupies a low-connectivity vertex or an edge position, as previously reported for larger clusters.[51] On the surface, Au_1Pd_n structures are all found to be different from their gas-phase counterparts, with the exception of Au_1Pd_3, which remains a tetrahedron.

The 2D structures of Au clusters, discussed in Section (3.1.1), remain the global minima when they are doped with a single Pd atom. The Pd atoms are located in or close to the centre of the clusters. Au_mPd_1 m = 3–5 clusters have the same structures as the corresponding pure Au clusters, as previously reported.[35,50] Au_mPd_1 m = 6 adopts a Pd-centred planar hexagon which is also the core of the clusters with 7 and 8 Au atoms. The cluster for m = 9 also has a planar global minimum. 2D–3D structural transitions take place at sizes $N = 7$–10 on the surface.

It is clear that Pd-rich nanoalloys tend to adopt 3D geometries while 2D–3D structural transitions occur for gold clusters when adding more than one Pd atom. It is worthwhile

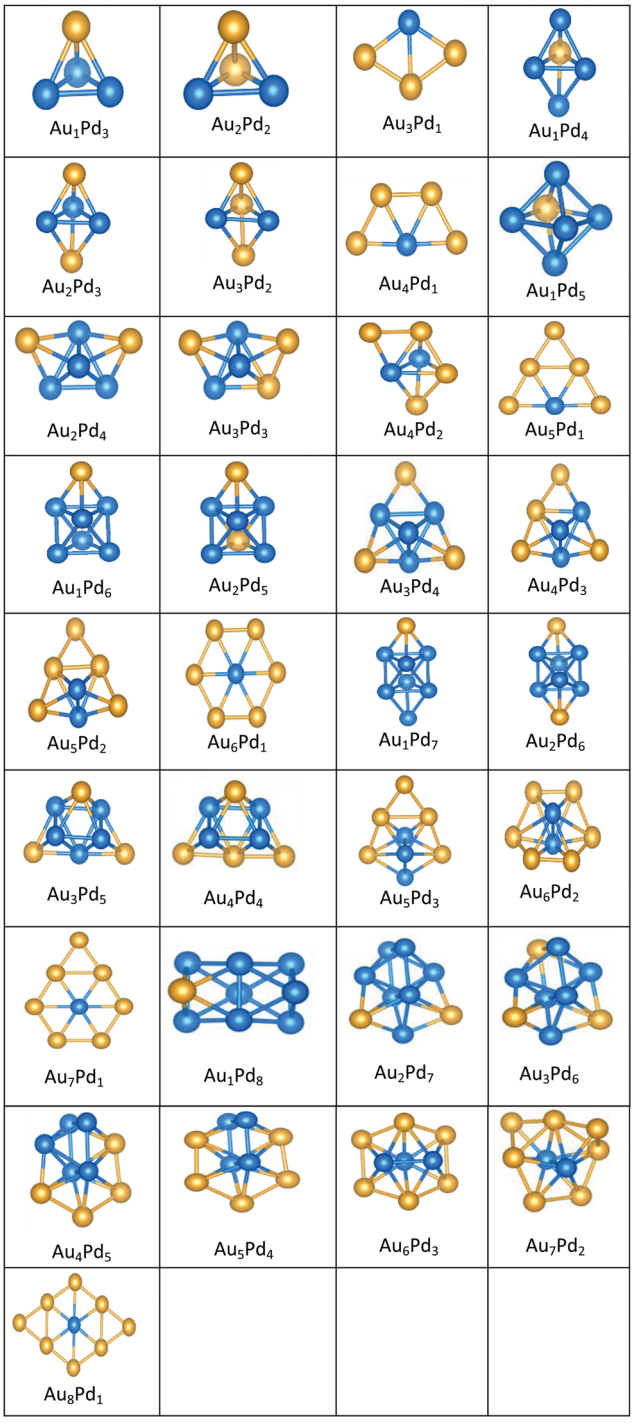

Fig. 7 Putative global minimum structures for all compositions of free AuPd nanoalloys with sizes N = 4–9, Au and Pd are shown in gold and blue, respectively.

mentioning that most of the lowest energy structures of free Au_mPd_n clusters for $(n + m)$ = 4–10, which were calculated recently by Zanti and Peeters[35] and Palagin and Doye,[50] are in good agreement with our observations.

The supported and gas-phase structures of Au_1Pd_3 and Au_2Pd_2 are both tetrahedra. For Au_3Pd_1, the supported structure is similar to that of the free cluster, both having a planar

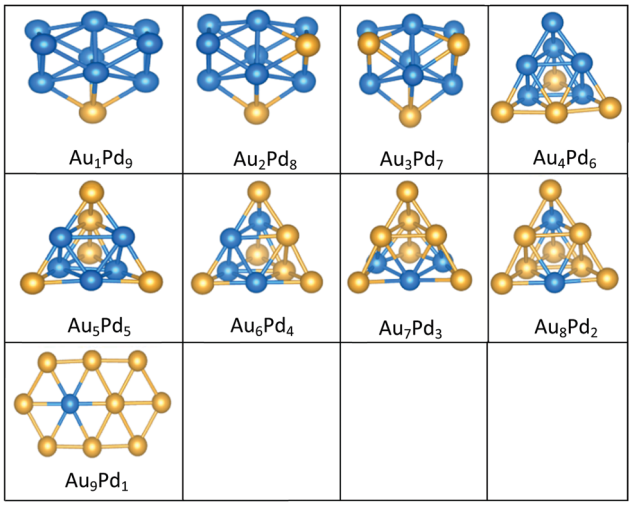

Fig. 8 Putative global minimum structures for all compositions of free AuPd nanoalloys with size N = 10, Au and Pd are shown in gold and blue, respectively.

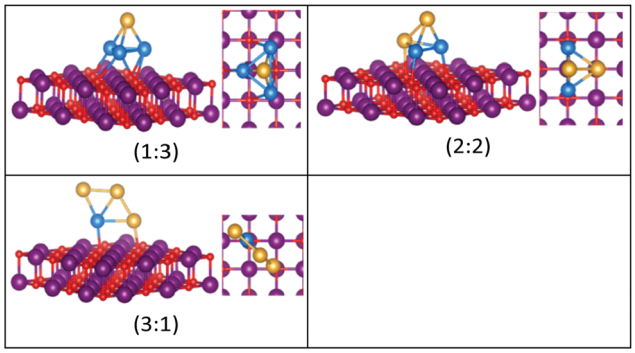

Fig. 9 Putative global minimum structures for compositions of MgO(100)-supported AuPd nanoalloys with size N = 4. Au, Pd, Mg and O are shown in gold, blue, purple, and red, respectively.

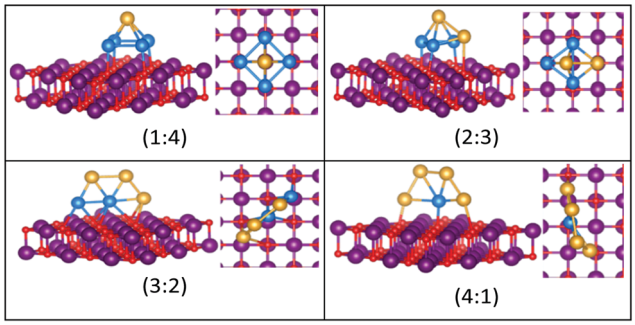

Fig. 10 Putative global minimum structures for compositions of MgO(100)-supported AuPd nanoalloys with size N = 5. Au, Pd, Mg and O are shown in gold, blue, purple, and red, respectively.

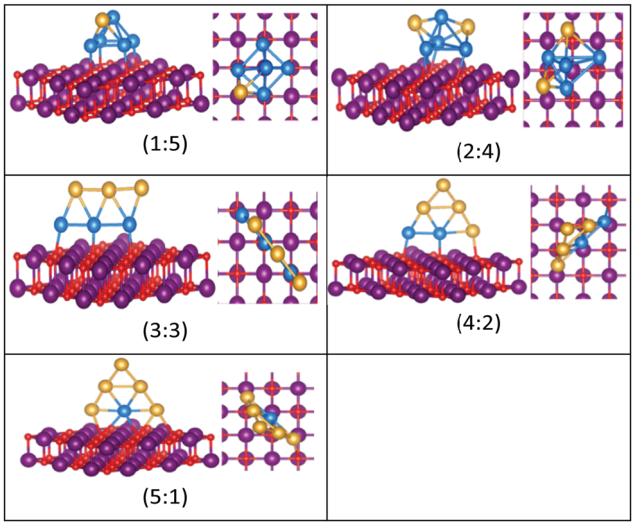

Fig. 11 Putative global minimum structures for compositions of MgO(100)-supported AuPd nanoalloys with size N = 6. Au, Pd, Mg and O are shown in gold, blue, purple, and red, respectively.

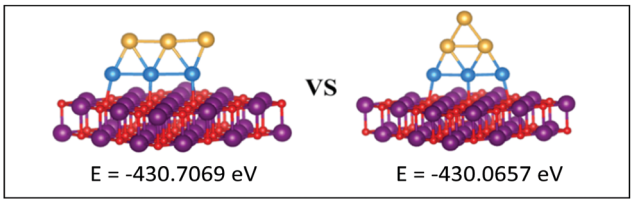

Fig. 12 Putative global minimum (left) *versus* local minimum (right) for the MgO(100)-supported Au_3Pd_3 cluster. Pd, Au, Mg and O are shown in blue, gold, purple, and red, respectively.

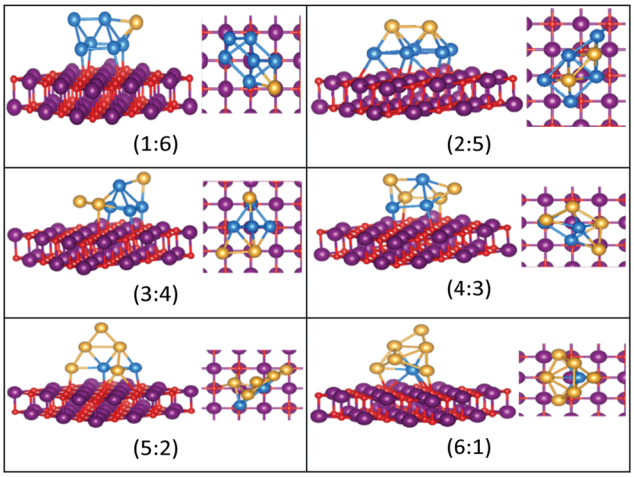

Fig. 13 Putative global minimum structures for compositions of MgO(100)-supported AuPd nanoalloys with size N = 7. Au, Pd, Mg and O are shown in gold, blue, purple, and red, respectively.

rhombic structure. For all compositions of size $N = 4$, the lowest energy conformation for the supported cluster maximises the number of the stronger Pd–O interactions.

The gas-phase global minima for Au_1Pd_4, Au_2Pd_3 and Au_3Pd_2 are all trigonal bipyramid structures, whereas Au_4Pd_1 is planar. For Au_1Pd_4, the supported structure is similar to that of supported Pd_5 (discussed above), having a square-based pyramid structure. For Au_2Pd_3, the supported cluster is a distorted homotop of the gas phase structure, which allows

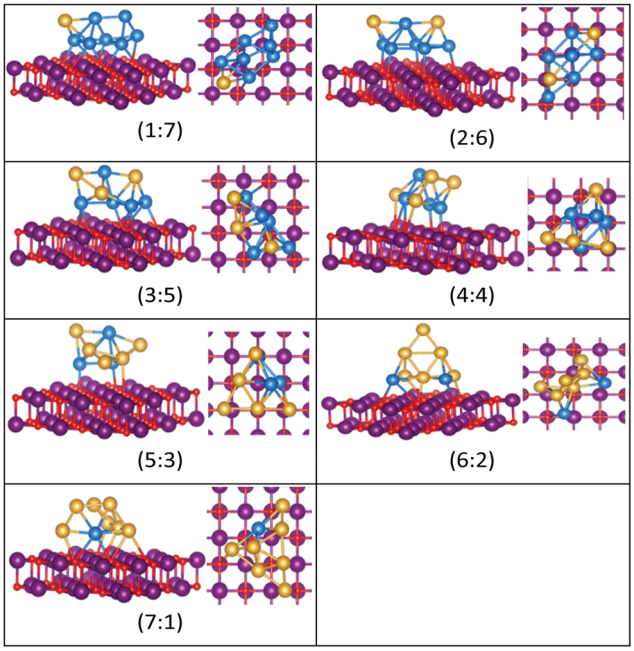

Fig. 14 Putative global minimum structures for compositions of MgO(100)-supported AuPd nanoalloys with size N = 8. Au, Pd, Mg and O are shown in gold, blue, purple, and red, respectively.

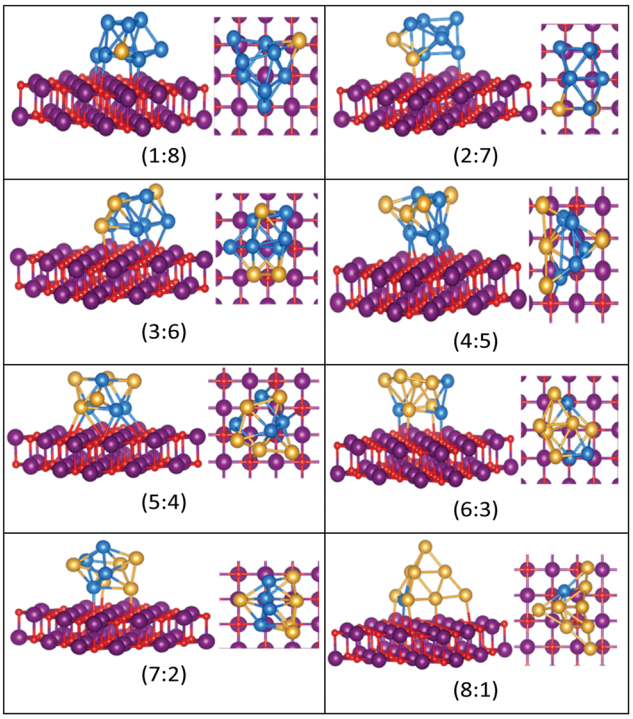

Fig. 15 Putative global minimum structures for compositions of MgO(100)-supported AuPd nanoalloys with size N = 9. Au, Pd, Mg and O are shown in gold, blue, purple, and red, respectively.

all 3 Pd atoms to bind to the surface. A structural transition occurs for the gas-phase Au_3Pd_2 cluster from 3D to 2D when supported on the surface, having a similar structure to the supported Au_4Pd_1 structure.

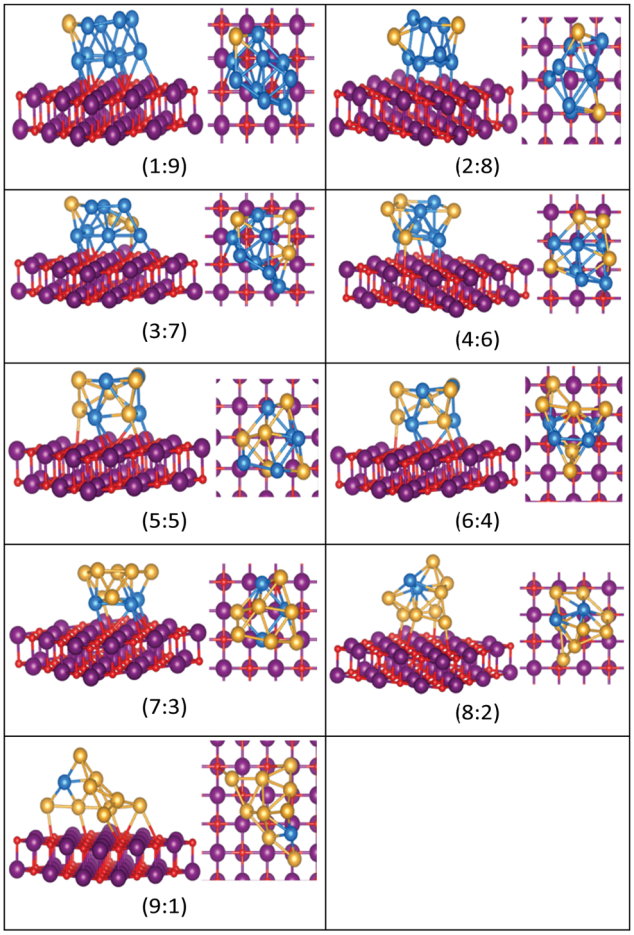

Fig. 16 Putative global minimum structures for compositions of MgO(100)-supported AuPd nanoalloys with size N = 10. Au, Pd, Mg and O are shown in gold, blue, purple, and red, respectively.

The gas-phase Au_1Pd_5 structure is an octahedron and Au_2Pd_4 and Au_3Pd_3 are both tetrahedra whereas Au_4Pd_2 and Au_5Pd_1 are an edge-bridged-capped trigonal bipyramid and planar triangle, respectively. Structural changes occur for all of these global minima on the surface except for Au_5Pd_1. The interactions between Au and Pd atoms and the MgO(100) surface favours face-capped square-based pyramid and face-capped trigonal bipyramid structures for supported Au_1Pd_5 and Au_2Pd_4 clusters, respectively. The supported configurations of Au_3Pd_3, Au_4Pd_2 and Au_5Pd_1 are all 2D structures. For Au_3Pd_3 on the surface, the three Pd atoms form a linear chain bonding to O atoms of the surface, resulting in a planar parallelogram. DFT local minimisation using the VASP code was used to confirm the parallelogram configuration by assessing an alternative planar triangular structure (as previously found for Au_3Ir_3[43]) for this composition (see Fig. 12). The minimisation showed that the putative GM parallelogram is indeed lower in energy than the triangle for this composition. However, both Au_4Pd_2 and Au_5Pd_1 are found to adopt the planar triangular structure on the surface with clear preference for Pd bonding to O atoms on the surface.

A capped octahedron is the global minimum for both Au_1Pd_6 and Au_2Pd_5, which distort on the surface to form a

bicapped square pyramid and a square pyramid fused with a trigonal bipyramid, respectively, bound to the surface by Pd–O bonds. In the gas phase, the GM for Au_3Pd_4, Au_4Pd_3 and Au_5Pd_2 all have edge-bridged bicapped tetrahedral structures, with the Pd atoms occupying the central tetrahedral core. On MgO, they all form low-symmetry fused structures. Au_6Pd_1 has a Pd-centred planar hexagonal structure in the gas phase, while on the surface a complex 3D structure is preferred.

Both Au_1Pd_7 and Au_2Pd_6 have the same bicapped octahedral structure (with the caps adopting a "*para*" position) in the gas-phase and both adopt structures similar to Au_2Pd_5, but with an additional atom capping the square pyramid. The gas-phase Au_3Pd_5 and Au_4Pd_4 clusters both have a "*meta*-" bicapped octahedral structure, but on the MgO surface Au_3Pd_5 adopts a polytetrahedral geometry, while Au_4Pd_4 keeps the bicapped octahedral structure, but adopts a different homotop so that 3 of the Pd atoms are in contact with the surface. The edge-bridged pentagonal bipyramid structure of Au_5Pd_3 distorts to a polytetrahedral structure on the surface. The gas-phase Au_6Pd_2 cluster is a hexagonal bipyramid and its global minimum on the surface is similar to that of the supported Au_5Pd_2 structure with an additional face cap. Homotop swap and structural changes occur for the edge-bridged planar hexagon structure, the global minimum of gas-phase Au_7Pd_1, giving a 3-dimensional bent triangle bonded by the single Pd atom and 4 Au atoms to the O atoms of the MgO slab.

The gas-phase Au_1Pd_8 global minimum is a face-sharing bioctahedral structure. Au_2Pd_7–Au_5Pd_4 have structures that can be described as the result of fusing an octahedron and a trigonal bipyramid, while Au_6Pd_3 and Au_7Pd_2 (bicapped pentagonal bipyramid) have structures which are fragments of the centred icosahedron. Au_8Pd_1 has a planar, bi-edge-bridged centred hexagon. On the MgO surface, complex fused structures are found, mostly consisting of 2-close packed layers of metal atoms, with Pd enrichment closest to the MgO surface.

Doping up to three Au atoms changes the structure of gas-phase Pd_{10} (discussed earlier) from an icosahedral fragment to two face-sharing octahedra, with a capping atom at the joint. The tetrahedral tetracapped octahedron is the GM for Au_4Pd_6–Au_8Pd_2, while Au_9Pd_1 has a planar, bihexagonal structure. On the MgO(100)-support, bilayer close packed structures predominate, again with the MgO-cluster interface enriched in Pd to maximise Pd–O bonding.

3.2 Energetic analysis

To evaluate the stability of free and supported clusters and predict the structural preferences for magic sizes, we have to calculate the excess energy Δ, the second difference in energy Δ_2E, the binding energy E_b, and the adsorption energy E_{ads}, which are defined in eqn (1)–(4). Tables S4 and S5 list the values of these energies for free and surface supported clusters (see the ESI†).

Looking at the elemental properties of Au and Pd (shown in Table 1),[52] such as surface energy (E_{sur}), cohesive energy (E_{coh}), atomic radius (r_a), and electronegativity (χ), we can simply predict the type of segregation in AuPd nanoalloys.

Table 1 Some elemental properties of Au and Pd[52]

	E_{coh}/eV atm^{-1}	E_{sur}/meV Å^{-2}	r_a/Å	χ
Au	3.81	96.8	1.44	2.4
Pd	3.89	131	1.38	2.2

The larger values of cohesive energy and surface energy of Pd compared with Au explain the tendency of Pd atoms to occupy the centres and cores of clusters and the preference of Au atoms for surface positions. The atomic radius of Pd is smaller than for Au. This also favours the aggregation of Pd atoms in the cores of clusters, whereas electron transfer between Pd and Au atoms supports the mixing of Au and Pd, but this is a weak effect as the electronegativities of Au and Pd are quite similar.

The effect of mixing in a cluster system can be studied by calculating the excess energy, Δ. Excess energy plots for free AuPd clusters $(m + n) = 4$–10 are shown in Fig. 17 and 18. Favourable mixing is represented by negative values of excess energies Δ, whereas positive values indicate a demixing tendency.

For $(m + n = 4)$ clusters, Au_1Pd_3 shows a strong demixing tendency, whereas Au_3Pd_1 exhibits the best mixing among clusters of this size. All $(m + n = 5)$ clusters favour mixing and the strongest mixing is for Au_2Pd_3. However, all mixed $(m + n = 6)$ clusters are energetically unfavourable relative to pure Pd and Au clusters. For $(m + n = 7)$ clusters, all clusters show favourable mixing, with the largest tendency for Au_6Pd_1. For $(m + n = 8)$ clusters, only Au_1Pd_7 shows unfavourable mixing and the most favourable mixing is for Au_3Pd_5. The clusters of $(m + n = 9$ and $10)$ favour mixing, with the most favourable mixing being for Au_8Pd_1 and Au_6Pd_4.

The mixing energy values for clusters with the same size show that variations in composition play a more important role than geometric effects in determining cluster stabilities.

The relative stabilities of clusters can be studied by calculating the second difference in energy Δ_2E, which indicates the stability of an N-atom cluster with respect to neighbouring sizes. Fig. 19 shows a plot of the second difference in energy Δ_2E for free and supported Au and Pd clusters. The most relatively stable clusters are indicated by significant positive peaks in Δ_2E.

The results show that free Au_6 (2D) and Pd_6 (3D) clusters have a high relative stability compared to their neighbours. Accordingly, $N = 6$ represents a magic size for both 2D Au and

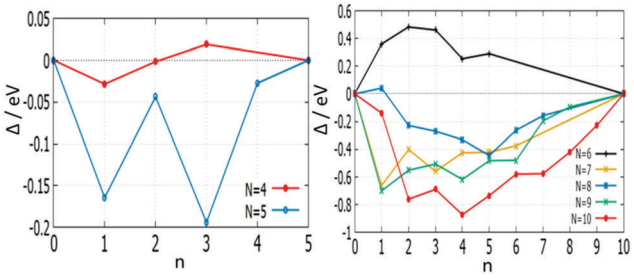

Fig. 17 Plot of mixing energy Δ against the number of Pd atoms (n) for free AuPd clusters, with $N = 4$–10.

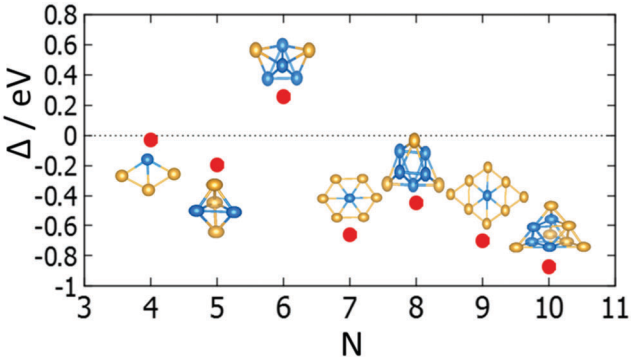

Fig. 18 For each size (N), the isomer with lowest Δ is shown for free clusters.

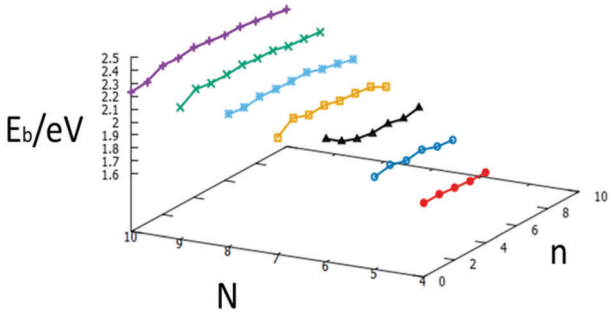

Fig. 20 Binding energies for each size N = 4–10 against the number of Pd atoms, n, for free $Au_{N-n}Pd_n$ clusters.

3D Pd structures. The magic size N = 6 for both free Au and Pd clusters explains the positive values of mixing energy of nanoalloys compared to monometallic clusters at this size. On the MgO surface, Au_6 is still found to have the highest relative stability due to it retaining the same triangular structure both when free and supported on MgO. However, Pd clusters show a noticeable (stable) positive peak in Δ_2E for the supported cluster with N = 5, rather than 6. This is because the structure of Pd_6 changes from an octahedron to a bicapped tetrahedron on the MgO surface, in addition to the cluster–substrate interaction effects mentioned in Section 3.1.2.

The relative stabilities of nanoclusters can be obtained by calculating the binding energy per atom, E_b. A plot of the binding energies for studied clusters is shown in Fig. 20. The binding energy increases with increasing cluster size, as previously reported.[35] The plot also illustrates the relative stability of nanoalloys compared to the same size of free Au and Pd clusters, with one exception for N = 6, which reinforces the ''magic size'' hypothesis mentioned above.

There are differences between the energies of the Mg(100)-supported global minima and the energies of the supported clusters with the slab removed. Tables S4 and S5 (see the ESI†) list the adsorption energies E_{ads} of the supported clusters and Fig. 21 shows a graphical representation. The plots reveal that the Pd and Pd-rich clusters tend to have the most negative E_{ads} as there are a greater number of strong Pd–O interactions. Comparing the E_{ads} values for the clusters as a function of size is more complicated, however, due to the interplay between

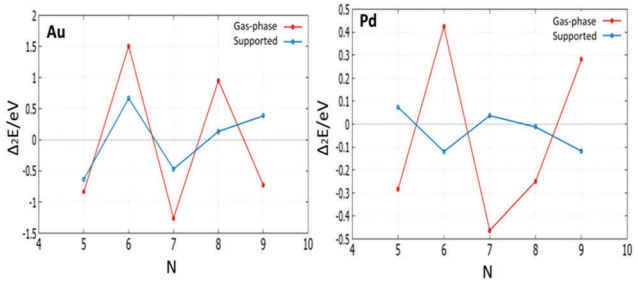

Fig. 19 The plot of the second difference in energy Δ_2E for free and supported Au and Pd clusters.

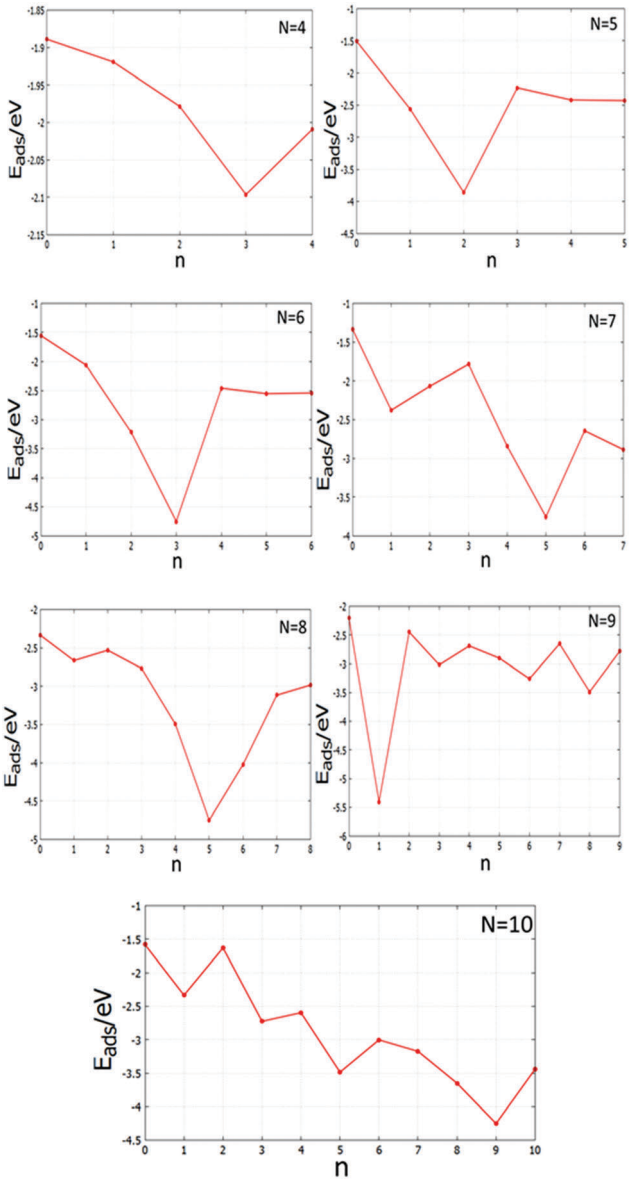

Fig. 21 Adsorption energies E_{ads} against the number of Pd atoms, n, for the MgO(100)-supported N = 4–10 clusters.

structural changes and the number of interfacial Pd atoms; as for smaller clusters a higher proportion of atoms are in contact with the oxide substrate. The higher adsorption energies of Pd-doped Au clusters can contribute to improve catalyst performance by decreasing cluster diffusion rates and, hence, suppressing sintering.

3.3 Systematic homotop search

The global minima (GM) of AuPd nanoalloys have many symmetry inequivalent homotops which may have been missed by the BPGA-DFT search. Based on the GM of monosubstituted clusters and some supported-clusters, the structural energy for each symmetry inequivalent homotop was studied by DFT local minimisation using the VASP code. Tables S6–S9 (see the ESI†) show energies and structures of homotops for free monosubstituted clusters and some MgO(100)-supported clusters. Fig. 22 and 23 show plots of the relative energy ΔE against symmetry inequivalent homotop structures for these clusters.

The BPGA-DFT search for all free monosubstituted clusters N = 4–10, successfully found the lowest energy homotop as the global minimum. For N = 4, Au_1Pd_3 does not have any symmetry inequivalent homotops whereas Au_3Pd_1 has one symmetry inequivalent homotop with a relative energy of 0.50 eV.

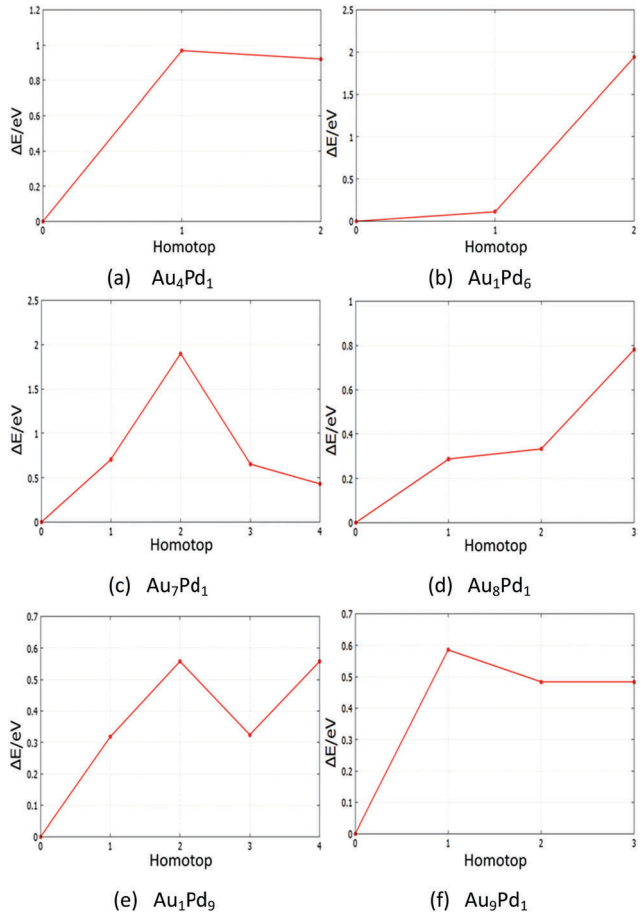

Fig. 22 Relative energies for symmetry inequivalent homotop structures of several Au- and Pd-doped clusters.

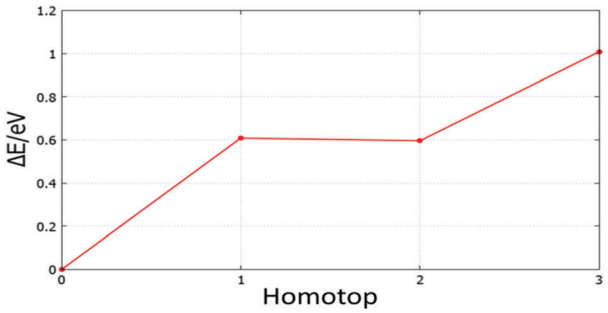

Fig. 23 Relative energy for symmetry inequivalent homotop structures of the supported Au_5Pd_1 cluster.

For N = 5, the only symmetry inequivalent homotop for Au_1Pd_4 is 1.04 eV higher in energy than the GM found by BPGA-DFT. Au_4Pd_1 has two symmetry inequivalent homotops and both are higher in energy than the GM, by 0.92 and 0.96 eV, as shown in Fig. 22(a).

For N = 6, Au_1Pd_5 does not have any symmetry inequivalent homotops whereas Au_5Pd_1 has just one symmetry inequivalent homotop which is 2.86 eV less stable than the GM. For N = 7, Au_1Pd_6 has two symmetry inequivalent homotops with relative energies of 0.11 eV and 1.93 eV, as shown in Fig. 22(b), whereas Au_6Pd_1 has one symmetry inequivalent homotop with a relative energy of 0.28 eV. For N = 8, Au_1Pd_7 has just one symmetry inequivalent homotop with a relative energy of 0.35 eV, whereas Au_7Pd_1 has four symmetry inequivalent homotops which can clearly be seen in Fig. 22(c). For N = 9, Au_1Pd_8 also has one symmetry inequivalent homotop with a relative energy of 0.15 eV, whereas Au_8Pd_1 has three symmetry inequivalent homotops which can be seen in Fig. 22(d). Finally, Fig. 22(e) and (f) shows the relative energies for symmetry inequivalent homotops of Au_1Pd_9 and Au_9Pd_1.

The BPGA-DFT search for MgO(100)-supported clusters generally successfully finds the energy homotop as the global minimum. Fig. 23, for example, shows the relative energy for symmetry inequivalent homotop structures of the supported Au_5Pd_1 cluster.

4 Conclusions

The use of the BPGA-DFT approach has successfully allowed the global optimization of free and MgO(100)-supported N = 4–10 Au, Pd, and AuPd clusters. Significant structural differences between the gas-phase and surface-supported are revealed by global optimization in the presence of a MgO slab in addition to the clear homotop swap behaviour in mixed AuPd clusters, in order to increase the number of stabilising Pd–O bonds. For singly doped clusters, the GM structures were confirmed by homotop reminimisation.

The BPGA-DFT calculations show that the Pd and Pd-rich clusters prefer 3D structures, while structural transitions occur for Au configurations from 2D to 3D upon adding more than one Pd atom. The planar structures of free Au global minima are all found to remain planar on the MgO(100) surface, with

some deviation from the planarity for supported Au_9 and Au_{10}. They are also found to lie roughly perpendicular to the MgO surface, due to the ''metal-on-top'' effect. Global minima for the gas phase Pd clusters are all found to be different from their supported structures with the exception of Pd_4, which retains its tetrahedral structure.

Mixing energies show the strong tendency of free Au–Pd clusters to alloy, with the exception of $N = 6$, which confirms the magic size hypothesis of pure Pd and Au clusters at this size (confirmed by findings of the binding energy E_b for nanoalloys compared to pure clusters and the second difference in energy Δ_2E calculations for pure Au and Pd clusters).

The adsorption energy E_{ads} results reveal that the Pd and Pd-rich clusters tend to have the most negative E_{ads} values. This could improve catalytic performance by suppressing cluster sintering.

Acknowledgements

H. A. Hussein is grateful to the University of Kufa and the Ministry of Higher Education and Scientific Research (Iraq) for the award of a PhD scholarship. Calculations were performed on the University of Birmingham's Blue-BEAR high-performance computer and ARCHER facilities, the UK National Supercomputing Service (http://www.archer.ac.uk) *via* membership of the UK's HPC Materials Chemistry Consortium, which is funded by EPSRC (EP/L000202), and ''TOUCAN: Towards an Understanding of Catalysis on Nanoalloys'' membership, which is funded by EPSRC under Critical Mass Grant EP/J010804/1. The authors acknowledge Dr Christopher Heard for helpful discussions. H. A. Hussein thanks Dr Ilker Demiroglu for his valuable advice.

References

1 G. M. Whitesides, *Small*, 2005, **1**, 172–179.
2 H. Zhang, T. Watanabe, M. Okumura, M. Haruta and N. Toshima, *Nat. Mater.*, 2012, **11**, 49–52.
3 R. Bazzi, M. Flores-Gonzalez, C. Louis, K. Lebbou, C. Dujardin, A. Brenier, W. Zhang, O. Tillement, E. Bernstein and P. Perriat, *J. Lumin.*, 2003, **102–103**, 445–450.
4 M. A. Ferrara, P. Dardano, L. De Stefano, I. Rea, G. Coppola, I. Rendina, R. Congestri, A. Antonucci, M. De Stefano and E. De Tommasi, *PLoS One*, 2014, **9**, e103750.
5 K. Vasundhara, S. N. Achary, S. K. Deshpande, P. D. Babu, S. S. Meena and A. K. Tyagi, *J. Appl. Phys.*, 2013, **113**, 194101.
6 Y. Li, Q. Liu and W. Shen, *Dalton Trans.*, 2011, **40**, 5811.
7 R. Pillarisetty, *Nature*, 2011, **479**, 324–328.
8 X. Liu, M. Conte, M. Sankar, Q. He, D. M. Murphy, D. Morgan, R. L. Jenkins, D. Knight, K. Whiston, C. J. Kiely and G. J. Hutchings, *Appl. Catal., A*, 2015, **504**, 373–380.
9 Y. Gao, W. Huang, J. Woodford, L. Wang and X. C. Zeng, *J. Am. Chem. Soc.*, 2009, **131**, 9484–9485.
10 D. W. Yuan and Z. R. Liu, *Phys. Lett. A*, 2011, **375**, 2405–2410.
11 F. Gao, Y. Wang and D. W. Goodman, *J. Phys. Chem. C*, 2010, **114**, 4036–4043.
12 J. K. Edwards, S. J. Freakley, A. F. Carley, C. J. Kiely and G. J. Hutchings, *Acc. Chem. Res.*, 2014, **47**, 845–854.
13 J. K. Edwards, B. Solsona, E. Ntainjua N, A. F. Carley, A. A. Herzing, C. J. Kiely and G. J. Hutchings, *Science*, 2009, **323**, 1037–1042.
14 D. I. Enache, J. K. Edwards, P. Landon, B. Solsona-espriu, A. F. Carley, A. A. Herzing, M. Watanabe, C. J. Kiely, D. W. Knight and G. J. Hutchings, *Science*, 2006, **311**, 362.
15 A. Shayeghi, D. Götz, J. B. A. Davis, R. Schäfer and R. L. Johnston, *Phys. Chem. Chem. Phys.*, 2015, **17**, 2104–2112.
16 C. J. Heard, S. Vajda and R. L. Johnston, *J. Phys. Chem. C*, 2014, **118**, 3581–3589.
17 R. Ismail, R. Ferrando and R. L. Johnston, *J. Phys. Chem. C*, 2013, **117**, 293–301.
18 I. Atanasov, G. Barcaro, F. R. Negreiros, A. Fortunelli and R. L. Johnston, *J. Chem. Phys.*, 2013, **138**, 224703.
19 L. Gan, R. Tian, X. Yang, S. Peng and Y.-J. Zhao, *Phys. Chem. Chem. Phys.*, 2011, **13**, 14466–14475.
20 F. Pittaway, L. O. Paz-borbon, R. L. Johnston, H. Arslan, R. Ferrando, C. Mottet, G. Barcaro and A. Fortunelli, *J. Phys. Chem. C*, 2009, **113**, 9141–9152.
21 J. Davis, A. Shayeghi, S. L. Horswell and R. L. Johnston, *Nanoscale*, 2015, **7**, 14032–14038.
22 G. Kresse and J. Hafner, *Phys. Rev. B: Condens. Matter Mater. Phys.*, 1993, **47**, 558–561.
23 J. Perdew, K. Burke and Y. Wang, *Phys. Rev. B: Condens. Matter Mater. Phys.*, 1996, **54**, 16533–16539.
24 G. Kresse, *Phys. Rev. B: Condens. Matter Mater. Phys.*, 1999, **59**, 1758–1775.
25 M. Methfessel and A. T. Paxton, *Phys. Rev. B: Condens. Matter Mater. Phys.*, 1989, **40**, 3616–3621.
26 https://bitbucket.org/JBADavis/bpga/.
27 R. L. Johnston, *Dalton Trans.*, 2003, 4193–4207.
28 B. Bandow and B. Hartke, *J. Phys. Chem. A*, 2006, **110**, 5809–5822.
29 D. Deaven and K. Ho, *Phys. Rev. Lett.*, 1995, **75**, 288–291.
30 H. Grönbeck and P. Broqvist, *J. Chem. Phys.*, 2003, **119**, 3896.
31 R. Ferrando and A. Fortunelli, *J. Phys.: Condens. Matter*, 2009, **21**, 264001.
32 G. Barcaro and A. Fortunelli, *J. Chem. Theory Comput.*, 2005, **1**, 972–985.
33 P. Frondelius, H. Häkkinen and K. Honkala, *New J. Phys.*, 2007, **9**, 339.
34 P. Frondelius, H. Häkkinen and K. Honkala, *Phys. Rev. B: Condens. Matter Mater. Phys.*, 2007, **76**, 1–4.
35 G. Zanti and D. Peeters, *J. Phys. Chem. A*, 2010, **114**, 10345–10356.
36 H. Häkkinen, B. Yoon, U. Landman, X. Li, H.-J. Zhai and L.-S. Wang, *J. Phys. Chem. A*, 2003, **107**, 6168–6175.
37 B. Assadollahzadeh and P. Schwerdtfeger, *J. Chem. Phys.*, 2009, **131**, 064306.
38 A. Walker, *J. Chem. Phys.*, 2005, **122**, 094310.
39 V. Bonačić-Koutecký, J. Burda, R. Mitrić, M. Ge, G. Zampella and P. Fantucci, *J. Chem. Phys.*, 2002, **117**, 3120.
40 D. Alamanova, Y. Dong, H. U. Rehman, M. Springborg and V. G. Grigoryan, *Comput. Lett.*, 2005, **1**, 1–12.

41 S. Gilb, P. Weis, F. Furche, R. Ahlrichs and M. M. Kappes, *J. Chem. Phys.*, 2002, **116**, 4094–4100.
42 J. Wang, G. Wang and J. Zhao, *Phys. Rev. B: Condens. Matter Mater. Phys.*, 2002, **66**, 035418.
43 J. B. A. Davis, S. L. Horswell and R. L. Johnston, *J. Phys. Chem. C*, 2016, **120**, 3759–3765.
44 G. Bravo-Pérez, I. L. Garzón and O. Novaro, *Chem. Phys. Lett.*, 1999, **313**, 655–664.
45 K. Pitzer, *Acc. Chem. Res.*, 1979, **12**, 271–276.
46 H. Häkkinen, M. Moseler and U. Landman, *Phys. Rev. Lett.*, 2002, **89**, 033401.
47 M. Moseler, H. Häkkinen, R. N. Barnett and U. Landman, *Phys. Rev. Lett.*, 2001, **86**, 2545–2548.
48 J. B. A. Davis, S. L. Horswell and R. L. Johnston, *J. Phys. Chem. A*, 2014, **118**, 208–214.
49 J. Jellinek and E. B. Krissinel, *Chem. Phys. Lett.*, 1996, **258**, 283–292.
50 D. Palagin and J. Doye, *Phys. Chem. Chem. Phys.*, 2015, **17**, 28010–28021.
51 I. V. Yudanov and K. M. Neyman, *Phys. Chem. Chem. Phys.*, 2010, **12**, 5094–5100.
52 R. Ferrando, J. Jellinek and R. L. Johnston, *Chem. Rev.*, 2008, **108**, 845–910.

Supporting Information of:

DFT Global Optimisation of Gas-phase and MgO-supported Sub-nanometre AuPd Clusters

Heider A. Hussein, Jack B. A. Davis, and Roy L. Johnston

August 2016

Tables S1 and S2 contain energies, structures and point group symmetries for all free studied clusters. Table S3 contains total energies for all compositions of MgO(100)-supported clusters. Tables S4 and S5 contain Excess Energies Δ and Binding Energies E_b (gas phase only), Adsorption Energies E_{ads} (surface supported only), and the second difference in energy $\Delta_2 E$ for the studied clusters. Tables S6-S9 contain the energies and structures for homotops of the free monosubstituted clusters and some supported clusters.

Table S1: The energies, structures, and point groups for Au_N and Pd_N clusters, N= 4-10.

Composition	E / eV	Structure	Point Group
Au_4	-6.9261	Rhombic Planar	D_{2h}
Au_5	-9.3888	M-like planar	C_{2v}
Au_6	-12.6879	Planar triangle	D_{3h}
Au_7	-14.4817	Edge-bridged planar triangle	C_s
Au_8	-17.5334	Planar	D_{4h}
Au_9	-19.6323	Planar	C_{2v}
Au_{10}	-22.4613	Planar	C_s
Pd_4	-12.6642	Tetrahedron	T_d
Pd_5	-16.4666	Trigonal bipyramid	D_{3h}
Pd_6	-20.5537	Octahedron	O_h
Pd_7	-24.2169	Capped octahedron	C_{3v}
Pd_8	-28.3425	$\triangle$-Dodecahedron	D_{2d}
Pd_9	-32.7178	Two face sharing octahedron	D_{3h}
Pd_{10}	-36.8133	Icosahedral fragment	C_{3v}

Table S2: The energies, structures, and point groups for all compositions of Au_mPd_n clusters, (m+n)= 4-10.

Composition	E / eV	Structure	Point Group
Au_1Pd_3	-11.2109	Tetrahedron	C_{3v}
Au_2Pd_2	-9.7968	Tetrahedron	C_{2v}
Au_3Pd_1	-8.3892	Planar	C_{2v}
Au_1Pd_4	-15.0785	Trigonal bipyramid	C_{2v}
Au_2Pd_3	-13.8296	Trigonal bipyramid	D_{3h}
Au_3Pd_2	-12.2638	Trigonal bipyramid	C_{2v}
Au_4Pd_1	-10.9688	M-like planar	C_{2v}
Au_1Pd_5	-18.9518	Octahedron	C_{4v}
Au_2Pd_4	-17.6879	Bicapped Tetrahedron	C_{2v}
Au_3Pd_3	-16.1603	Bicapped Tetrahedron	C_s
Au_4Pd_2	-14.8270	Edge-bridged trigonal bipyramid	C_1
Au_5Pd_1	-13.6389	Triangle Planar	C_{2v}
Au_1Pd_6	-23.2010	Capped octahedron	C_{3v}
Au_2Pd_5	-21.8573	Capped octahedron	C_s
Au_3Pd_4	-20.4696	Edge-bridged bicapped Tetrahedron	C_{2v}
Au_4Pd_3	-19.2146	Edge-bridged bicapped Tetrahedron	C_s
Au_5Pd_2	-17.6645	Edge-bridged bicapped Tetrahedron	C_2
Au_6Pd_1	-16.5348	Planar hexagon	D_{3d}
Au_1Pd_7	-27.1492	Bicapped octahedron	C_{3v}
Au_2Pd_6	-25.9037	Bicapped octahedron	D_{3d}
Au_3Pd_5	-24.7344	Meta-bicapped octahedron	C_{2v}
Au_4Pd_4	-23.2697	Meta-bicapped octahedron	C_{2v}
Au_5Pd_3	-21.8577	Edge-bridged pentagonal bipyramid	C_{2v}
Au_6Pd_2	-20.4650	Hexagonal bipyramid	C_{2v}
Au_7Pd_1	-18.8431	Edge-bridged planar hexagon	C_{2v}
Au_1Pd_8	-31.3585	Face-sharing bioctahedra	C_s
Au_2Pd_7	-30.0058	Fused octahedron with trigonal bipyramid	C_s
Au_3Pd_6	-28.8358	Fused octahedron with trigonal bipyramid	C_1
Au_4Pd_5	-27.3847	Fused octahedron with trigonal bipyramid	C_1
Au_5Pd_4	-26.0664	Fused octahedron with trigonal bipyramid	C_2
Au_6Pd_3	-24.5009	Incomplete fragment of centered icosahedra	C_{2v}
Au_7Pd_2	-23.0921	Bicapped pentagonal bipyramid	C_2
Au_8Pd_1	-21.7874	Two edge-capped planar hexagon	D_{2h}
Au_1Pd_9	-35.6073	Capped 2 face-sharing octahedron	C_{2h}
Au_2Pd_8	-34.3625	Capped 2 face-sharing octahedron	C_1
Au_3Pd_7	-33.0843	Capped 2 face-sharing octahedron	C_s
Au_4Pd_6	-31.6600	Tetrahedral tetracapped octahedron	C_1
Au_5Pd_5	-30.3728	Tetrahedral tetracapped octahedron	C_s
Au_6Pd_4	-28.97655	Tetrahedral tetracapped octahedron	D_{2d}
Au_7Pd_3	-27.4580	Tetrahedral tetracapped octahedron	C_{3v}
Au_8Pd_2	-26.0937	Tetrahedral tetracapped octahedron	C_2
Au_9Pd_1	-24.0365	Planar bihexagon	C_{2v}

Table S3: The total energies for all compositions of MgO(100)-supported clusters, N= 4-10.

Cluster	E / eV	Cluster	E / eV	Cluster	E / eV
Pd_4	-426.5281	Au_1Pd_3	-425.3348	Au_2Pd_2	-423.5336
Au_3Pd_1	-422.0454	Au_4	-420.6899		
Pd_5	-430.6890	Au_1Pd_4	-429.3689	Au_2Pd_3	-427.5820
Au_3Pd_2	-426.5624	Au_4Pd_1	-424.8570	Au_5	-422.7648
Pd_6	-434.7030	Au_1Pd_5	-433.2432	Au_2Pd_4	-431.9594
Au_3Pd_3	-430.7069	Au_4Pd_2	-428.8707	Au_5Pd_1	-427.7307
Au_6	-426.1135				
Pd_7	-438.9562	Au_1Pd_6	-437.5350	Au_2Pd_5	-436.2389
Au_3Pd_4	-434.6519	Au_4Pd_3	-433.2087	Au_5Pd_2	-431.6248
Au_6Pd_1	-429.9350	Au_7	-428.1261		
Pd_8	-443.1357	Au_1Pd_7	-441.9092	Au_2Pd_6	-440.6321
Au_3Pd_5	-439.0318	Au_4Pd_4	-437.3377	Au_5Pd_3	-436.4834
Au_6Pd_2	-433.6166	Au_7Pd_1	-432.4803	Au_8	-431.0780
Pd_9	-447.3397	Au_1Pd_8	-445.9536	Au_2Pd_7	-444.1691
Au_3Pd_6	-443.2809	Au_4Pd_5	-441.9145	Au_5Pd_4	-440.3918
Au_6Pd_3	-438.2770	Au_7Pd_2	-436.9025	Au_8Pd_1	-435.7250
Au_9	-433.7606				
Pd_{10}	-451.7787	Au_1Pd_9	-450.4100	Au_2Pd_8	-448.9302
Au_3Pd_7	-447.6585	Au_4Pd_6	-446.3715	Au_5Pd_5	-444.3350
Au_6Pd_4	-442.6103	Au_7Pd_3	-441.1485	Au_8Pd_2	-439.2605
Au_9Pd_1	-437.4065	Au_{10}	-435.6699		

Table S4: Excess Energy Δ and Binding Energy E_b (gas phase only), Adsorption Energy E_{ads} (surface supported only), and the second difference in energy $\Delta_2 E$ for 4 to 8 atoms.

	Gas Phase			Surface Supported	
	Δ/eV	Δ_2E/eV	E_b/eV	Δ_2E/eV	E_{ads}/eV
Pd_4	0.0000	—	1.6952	—	-2.0092
Au_1Pd_3	0.0187	—	1.6969	—	-2.0963
Au_2Pd_2	-0.0016	—	1.7084	—	-1.9783
Au_3Pd_1	-0.0285	—	1.7215	—	-1.9191
Au_4	0.0000	—	1.7208	—	-1.8889
Pd_5	0.0000	-0.2846	1.8225	0.0734	-2.4288
Au_1Pd_4	-0.0274	—	1.8369	—	-2.4178
Au_2Pd_3	-0.1941	—	1.8791	—	-2.2299
Au_3Pd_2	-0.0438	—	1.8601	—	-3.8606
Au_4Pd_1	-0.1644	—	1.8910	—	-2.5606
Au_5	0.0000	-0.8363	1.8670	-0.6368	-1.5048
Pd_6	0.0000	0.4238	1.9548	-0.1196	-2.5392
Au_1Pd_5	0.2909	—	1.9312	—	-2.5511
Au_2Pd_4	0.2550	—	1.9620	—	-2.4559
Au_3Pd_3	0.4604	—	1.9526	—	-4.7531
Au_4Pd_2	0.4828	—	1.9737	—	-3.2158
Au_5Pd_1	0.3599	—	2.0191	—	-2.0625
Au_6	0.0000	1.5052	2.1039	0.6680	-1.5551
Pd_7	0.0000	-0.4624	1.9887	0.0369	-2.8856
Au_1Pd_6	-0.3748	—	2.0522	—	-2.6424
Au_2Pd_5	-0.4219	—	2.0688	—	-3.7557
Au_3Pd_4	-0.4249	—	2.0791	—	-2.8437
Au_4Pd_3	-0.5607	—	2.1084	—	-1.7859
Au_5Pd_2	-0.4013	—	2.0971	—	-2.0666
Au_6Pd_1	-0.6623	—	2.1428	—	-2.3772
Au_7	0.0000	-1.2579	2.0581	-0.4697	-1.3326
Pd_8	0.0000	-0.24974	2.07199	-0.0122	-2.9827
Au_1Pd_7	-0.1578	—	2.1053	—	-3.1149
Au_2Pd_6	-0.2634	—	2.1321	—	-4.0233
Au_3Pd_5	-0.4453	—	2.1685	—	-4.7494
Au_4Pd_4	-0.3317	—	2.1679	—	-3.4934
Au_5Pd_3	-0.2708	—	2.1739	—	-2.7661
Au_6Pd_2	-0.2293	—	2.1823	—	-2.5308
Au_7Pd_1	0.0414	—	2.1621	—	-2.6648
Au_8	0.0000	0.95281	2.1809	0.1347	-2.3324

Table S5: Excess Energy Δ and Binding Energy E_b (gas phase only), Adsorption Energy E_{ads} (surface supported only), and the second difference in energy $\Delta_2 E$ for 9 and 10 atoms.

	Gas Phase			Surface Supported	
	Δ/eV	Δ_2E/eV	E_b/eV	Δ_2E/eV	E_{ads}/eV
Pd_9	0.0000	0.2797	2.1645	-0.1175	-2.7822
Au_1Pd_8	-0.0946	—	2.1757	—	-3.4869
Au_2Pd_7	-0.1958	—	2.1876	—	-2.6532
Au_3Pd_6	-0.4798	—	2.2198	—	-3.2611
Au_4Pd_5	-0.4827	—	2.2208	—	-2.9025
Au_5Pd_4	-0.6183	—	2.2366	—	-2.6899
Au_6Pd_3	-0.5519	—	2.2249	—	-3.0183
Au_7Pd_2	-0.5519	—	2.2306	—	-2.4475
Au_8Pd_1	-0.7011	—	2.2478	—	-5.4071
Au_9	0.0000	-0.7300	2.1706	0.3865	-2.2012
Pd_{10}	0.0000	—	2.2105	—	-3.4407
Au_1Pd_9	-0.2291	—	2.2359	—	-4.2517
Au_2Pd_8	-0.4196	—	2.2574	—	-3.6512
Au_3Pd_7	-0.5766	—	2.2756	—	-3.1747
Au_4Pd_6	-0.5801	—	2.2784	—	-3.0033
Au_5Pd_5	-0.7355	—	2.2965	—	-3.4862
Au_6Pd_4	-0.8743	—	2.3128	—	-2.5966
Au_7Pd_3	-0.6911	—	2.2970	—	-2.7252
Au_8Pd_2	-0.7620	—	2.3066	—	-1.6295
Au_9Pd_1	-0.1399	—	2.2469	—	-2.3352
Au_{10}	0.0000	—	2.2354	—	-1.5802

Table S6: The energies and structures for homotops of the free monosubstituted clusters, N=4-7.

Size, N	Composition	Homotop, E/eV	GM, E/eV
4	Au_3Pd_1	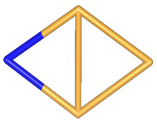 -7.8866	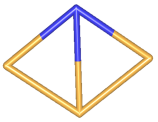 -8.3892
5	Au_1Pd_4	 -14.0342	 -15.0785
5	Au_4Pd_1	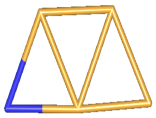 -10.0001 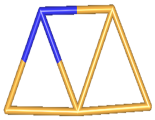 -10.0477	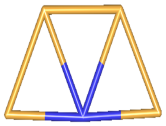 -10.9688
6	Au_5Pd_1	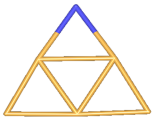 -10.7715	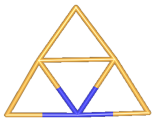 -13.6389
7	Au_1Pd_6	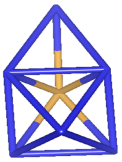 -21.2622 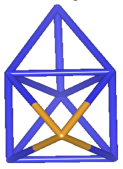 -23.0893	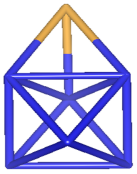 -23.2010

Table S7: The energies and structures for homotops of the free monosubstituted clusters, N=7-9.

Size, N	Composition	Homotop, E/eV	GM, E/eV
7	Au_6Pd_1	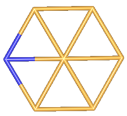 -16.2542	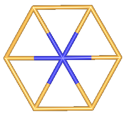 -16.5348
8	Au_1Pd_7	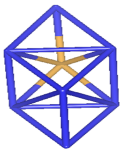 -26.7958	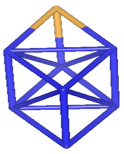 -27.1492
8	Au_7Pd_1	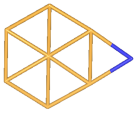 -18.1356 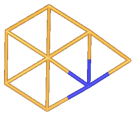 -16.9430 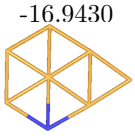 -18.1881 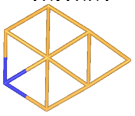 -18.4109	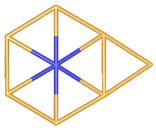 -18.8431
9	Au_1Pd_8	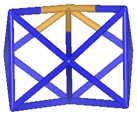 -31.2069	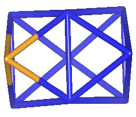 -31.3585
9	Au_8Pd_1	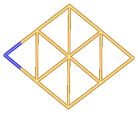 -21.5006	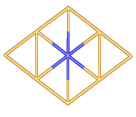 -21.7874

Table S8: The energies and structures for homotops of the free monosubstituted clusters, N=9 and10.

Size, N	Composition	Homotop, E/eV	GM, E/eV
9	Au_8Pd_1	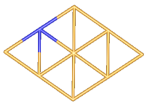 -21.4551 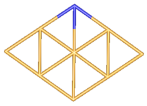 -21.0059	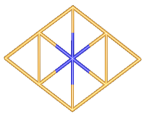 -21.7874
10	Au_1Pd_9	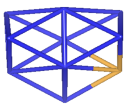 -35.2896 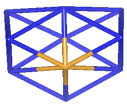 -35.0493  -35.2830 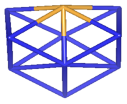 -35.0497	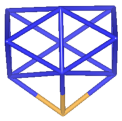 -35.6073
10	Au_9Pd_1	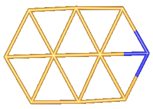 -23.4507 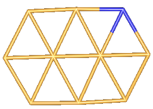 -23.5524 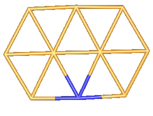 -23.5525	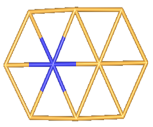 -24.0365

Table S9: The energies and structures for homotops of the MgO(100)-supported Au_5Pd_1 cluster

Size, N	Composition	Homotop, E/eV	GM, E/eV
6	MgO(100)-Au_5Pd_1	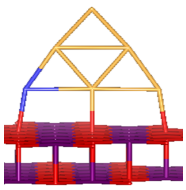 -427.1217	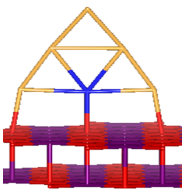 -427.7307
		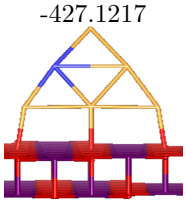 -427.1341	
		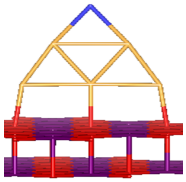 -426.7215	

3.3 Publication 2

Title

Application of a parallel genetic algorithm to the global optimization of medium-sized Au-Pd sub-nanometre clusters

Authors Heider A. Hussein, Ilker Demiroglu and Roy L. Johnston

Journal The European Physical Journal B

Volume 91

Pages 34

DOI 10.1140/epjb/e2017-80314-2

Submitted

31 May 2017

Accepted

18 July 2017

3.3.1 Author Contribution

The author carried out all the calculations (including amending the BPGA-DFT code to fit with the systems of study), acquisition and analysis of data, interpretation and discussion of results and writing the paper. All the figures and tables in the paper and the supplemental material were created by the author.

Eur. Phys. J. B (2018) 91: 34
https://doi.org/10.1140/epjb/e2017-80314-2

THE EUROPEAN PHYSICAL JOURNAL B

Regular Article

Application of a parallel genetic algorithm to the global optimization of medium-sized Au–Pd sub-nanometre clusters*,**

Heider A. Hussein[1,2], Ilker Demiroglu[1], and Roy L. Johnston[1,a]

[1] School of Chemistry, University of Birmingham, Birmingham B15 2TT, UK
[2] Department of Chemistry, College of Science, University of Kufa, Najaf, Iraq

Received 31 May 2017 / Received in final form 30 June 2017
Published online 12 February 2018

Abstract. To contribute to the discussion of the high activity and reactivity of Au–Pd system, we have adopted the BPGA-DFT approach to study the structural and energetic properties of medium-sized Au–Pd sub-nanometre clusters with 11–18 atoms. We have examined the structural behaviour and stability as a function of cluster size and composition. The study suggests 2D–3D crossover points for pure Au clusters at 14 and 16 atoms, whereas pure Pd clusters are all found to be 3D. For Au–Pd nanoalloys, the role of cluster size and the influence of doping were found to be extensive and non-monotonic in altering cluster structures. Various stability criteria (e.g. binding energies, second differences in energy, and mixing energies) are used to evaluate the energetics, structures, and tendency of segregation in sub-nanometre Au–Pd clusters. HOMO–LUMO gaps were calculated to give additional information on cluster stability and a systematic homotop search was used to evaluate the energies of the generated global minima of mono-substituted clusters and the preferred doping sites, as well as confirming the validity of the BPGA-DFT approach.

1 Introduction

Due to the environmental and energy challenges facing the world, research in catalysis is particularly important. Nanometallic catalysts, in particular, often show superior performance compared to their bulk counterparts [1,2]. These catalysts, which are widely used in the chemical industry, have motivated experiments on new materials on the nanoscale with high catalytic activity and/or selectivity [3–5] and have inspired the development of computational methods for predicting new catalyst candidates and optimizing their efficiency [6,7].

Although extensive research indicates that platinum and platinum-based nanostructures exhibit exceptional electrocatalytic activity, for example in direct alcohol fuel cells [8,9] their applications are somewhat limited due to the rarity of Pt in the earth's crust and its consequent high cost. This has motivated researchers to look for alternative metals (or alloy systems) to replace Pt, ideally keeping the high performance but at lower cost [10–12]. The much higher natural abundance of Pd relative to Pt has led to researchers fabricating nanostructures based on Pd [7,11]. Pd-based bimetallic nanostructures have also been used extensively, not only in the application to the direct alcohol fuel cells (as the cathodic catalyst) [11] but also in many high-tech fields, due to their interesting magnetic and electronic properties, as well as their catalytic properties [2,8,13,14].

Changing the chemical order and composition of the bimetallic nanostructures can enhance and enable tuning of their catalytic properties [15,16]. The chemical order effect can lead to control of the catalytic properties (e.g. modifying relevant activation energy barriers) by tuning the energy and spatial distribution of electrons at the surface of the clusters [2]. There are also economic reasons for mixing two metals, such as adding low cost metals (e.g. Co, Cu, and Ni) to balance the high cost of noble metals. The enhancement of catalytic performance and possible discovery of unique properties is still the main force driving the designing of novel nano-catalysts and sub-nanometre cluster catalysts. The Pd–Au bimetallic system, for example, exhibits high durability and catalytic activity for many interesting chemical reactions, such as the electro-oxidation of ethanol [17,18], the Suzuki coupling reaction [19], and the oxygen reduction reaction [20].

The catalytic activity and selectivity of sub-nanometre- and nano-clusters are also strongly affected by the size of the cluster and its electronic distribution. The origin of size effects are still ambiguous [21], however, they are

* Contribution to the Topical Issue "Shaping Nanocatalysts", edited by Francesca Baletto, Roy L. Johnston, Jochen Blumberger and Alex Shluger.
** Supplementary material in the form of one PDF file available from the Journal web page at https://doi.org/10.1140/epjb/e2017-80314-2.
[a] e-mail: r.l.johnston@bham.ac.uk

usually attributed to the changing surface-area-to-volume ratio and the number and nature of exposed facets/surface sites [22–24].

Gas-phase sub-nanometre clusters are simplified models that can test a system's suitability for specific applications, at a reasonably high level of theory, before dealing with more complex systems. However, even the optimisation of gas-phase structures is not a trivial task. There is usually little energy separation between many competitive isomers of metallic clusters [25], which may explain the challenges that face experimentalists in determining the preferred isomer [26,27]. In addition, charge-neutral clusters are more difficult to investigate experimentally compared with anions and cations, as most characterizations rely on mass spectrometry measurements, which creates a clear difficulty in separating and probing different size of neutral clusters [28,29].

In spite of the early investigations of neutral Au_2 [30] and Au_3 [31]. It is well known that experimental investigations of medium sized neutral Au clusters are limited for the reasons given above. Hence, a combination of experimental techniques with theoretical calculations has been used effectively: for example, Fielicke and co-workers [28] reported the gas-phase structures of neutral Au_7, Au_{19}, and Au_{20} clusters tagged with Kr atoms. The case of Pd is similar as, unlike the smaller Pd clusters, studies of medium sized clusters are relatively few and are the object of some controversy in terms of identifying the structural characteristics [32]. Turning our attention to medium-sized Au–Pd nanoalloys, a comprehensive study of structural motifs for all compositions have, to our knowledge, not been investigated before. However, Au-doped Pd clusters [33], (1:1) compositions [34], and nuclearities lower than 14 atoms [35] have previously been studied theoretically.

In the Au–Pd system, doping an atom of one metal into a pure cluster of the other metal often yields clusters with non-identical structures and properties [35–37]. This can increase the difficulty in finding global minima, in addition to the permutational isomers (homotops) effect [38]. There is additional complexity introduced by multi-directional bonding, unrestrained bond orders, and fluxional behaviour as a result of electron delocalization. In addition, alloying Pd with Au modifies the lattice distance between host atoms and the low dimensionality of Au could influence the spatial arrangement of Pd atoms [39,40].

The DFT-based Birmingham Parallel Genetic Algorithm (BPGA-DFT) computational approach has been successfully applied to search for low-lying isomers for various sub-nanometre cluster systems. Applications include: pure clusters Ir_{10}–Ir_{20} [41], Rh_4–Rh_6 [42], Au_4–Au_{10}, Pd_4–Pd_{10} [37], Ru_3–Ru_{12} and Pt_3–Pt_{10} [43]; and bimetallic clusters $(AuRh)_{4–6}$ [42]. $(AuPd)_{4–10}$ [37], $(AuIr)_{4–6}$ [44], and $(RuPt)_{3–8}$ [43] as well as surface-supported [37,44] clusters.

In this context, we present here a computational study of the structural properties of binary sub-nanometre Au–Pd clusters, including a comparison to the pure clusters. Using the BPGA-DFT approach, the lowest energy structures in the size range 11–18 atoms were calculated for all compositions. This work also sheds some light on the energetics of these clusters and the underlying mechanisms of mixing in binary metallic systems on the sub-nanometre and nanoscale. Our findings for the Au–Pd system should provide valuable information for Au–Pd catalysts and for further theoretical and experimental investigations.

2 Methodology

The Birmingham Parallel Genetic Algorithm (BPGA-DFT) approach [41,45] was applied to investigate (at the DFT level) the lowest energy structures of Au–Pd sub-nanometre clusters with total number of atoms $N =$ 11–18, as well as pure Au_N and Pd_N clusters. BPGA-DFT is an open-source genetic algorithm [45], which is a parallel extension of the Birmingham Cluster Genetic Algorithm (BCGA), a genetic algorithm for locating the global minima of small metal clusters directly at the DFT level [46].

Instead of generations, BPGA-DFT employs a pool methodology to evaluate structures in parallel. In each run, multiple BPGA instances are implemented, and in each instance, a set of processes are run in parallel and independently [47,48]. Initially, the pool population is formed by generating a number of random isomers [41]. The ten generated structures forming the initial pool are geometrically relaxed by local DFT energy minimization [47]. Once minimized structures are generated, the genetic algorithm crossover and mutation operations are applied to members of the population.

The clusters are selected for either crossover or mutation. The crossover operation involves selecting a pair of clusters from the pool, using the tournament selection method, based on a fitness criterion, where the fittest isomers (those with the lowest DFT energies) are more likely to be selected for crossover. Offspring clusters are then generated using the cut-and-splice method introduced by Deaven and Ho [49]. There are two mutation operations, in which a single cluster is randomly selected and either randomly chosen atoms are displaced or (for bimetallic clusters) the positions of a randomly chosen pair of non-identical atoms are swapped. After crossover and mutation, the structures are locally energy-minimized at the DFT level. The newly generated structures are then compared energetically with existing structures in the pool and the highest energy isomers are replaced by any lower energy isomers among the set of offspring and mutants.

All the local energy minimizations mentioned above were conducted with gamma-point DFT calculations employing the Vienna ab initio Simulation Package (VASP) code [50]. Projected-augmented wave (PAW) pseudopotentials were used, with the (GGA) Perdew–Burke–Ernzerhof (PBE) exchange correlation functional [51,52]. A plane-wave basis set was implemented including spin polarization. The plane wave cut-off energy was truncated at 400 eV. Methfessel–Paxton smearing, with a sigma value of 0.01 eV, was implemented to improve convergence [53].

For pure Au and Pd and mixed Au-Pd clusters, the stability of each cluster, relative to neighbouring sizes, is indicated by the second difference in energy ($\Delta_2 E$) which is given by:

$$\Delta_2 E = E(A_{N+1}) + E(A_{N-1}) - 2E(A_N) \quad (1)$$

where $E(A_N)$ corresponds to the energy of the N-atom cluster and $E(A_{N+1})$ and $E(A_{N-1})$ are the neighbouring clusters, with one atom more and one atom less, respectively.

The effect of mixing Au with Pd atoms in nanoalloys can be evaluated by calculating the mixing or excess energy (Δ) which is given by:

$$\Delta = E_{(\mathrm{Au}_m\mathrm{Pd}_n)} - m\frac{E_{(\mathrm{Au}_N)}}{N} - n\frac{E_{(\mathrm{Pd}_N)}}{N} \quad (2)$$

where m and n are the numbers of Au and Pd atoms, respectively, $E_{(\mathrm{Au}_m\mathrm{Pd}_n)}$ is the total energy of the nanoalloy $\mathrm{Au}_m\mathrm{Pd}_n$ whereas $E_{(\mathrm{Au}_N)}$ and $E_{(\mathrm{Pd}_N)}$ are the energy of pure metal clusters of Au and Pd, respectively, of the same size ($N = m + n$).

The average binding energy per atom (E_b) is given by:

$$E_b = -\frac{1}{N}[E_{(Au_m Pd_n)} - mE_{(Au)} - nE_{(Pd)}] \quad (3)$$

where $E_{(Au)}$ and $E_{(Pd)}$ are the electronic energies of single Au and Pd atoms, respectively.

The homotops (inequivalent permutational isomers) [38] are evaluated using:

$$\Delta E = E_{hom} - E_{GM} \quad (4)$$

where ΔE is the relative energy of the proposed homotop and E_{hom} and E_{GM} are the electronic energies of a particular homotop and the lowest energy isomer (global minimum) of the cluster, respectively.

Ignoring the symmetry, the number of homotops is given by:

$${}^N P_{Au,Pd} = \frac{N!}{m!n!} = \frac{N!}{m!(N-m)!} \quad (5)$$

where N is the total number of atoms, m is the number of Au atoms, and n is the number of Pd atoms.

3 Results and discussions

3.1 Structures

3.1.1 Au clusters

The putative global minima for pure Au clusters $11 \leq N \leq 18$, are shown in Figure 1 and their energies, coordinates, and point groups are listed in Table S1 (see the Supporting Information).

The lowest energy structures obtained for $N = 11$–13 and 15 Au clusters have planar (2D) configurations. The clusters deviate from planar to 3D structures at $N = 14$ and for 16–18 atoms. The exact 2D–3D transition point for neutral Au clusters is disputed theoretically and experimental evidence is scarce. Theoretical predictions of the 2D–3D crossover point have previously ranged from $N = 7$–14 atoms [54–57]. This range is consistence with the evolution of structure-symmetry for Au clusters reported here. The smallest 3D ground-state structure was predicted previously to be Au_{10} by David and co-workers [58], using the second-order Møller–Plesset perturbation theory (MP2) method. Employing hybrid DFT, Zanti and Peeters [35] arrived at the same conclusion showing a 3D structure for $N = 10$. This, however, disagreed with the 2D Au_{10} structure recently obtained by us [37] and previously by different research groups using semi-local density functional theory (DFT) [59] and coupled cluster singles doubles and perturbative triples [CCSD(T)] calculations [60,61]. Recently, Johansson et al., using a genetic algorithm and meta-GGA DFT, assigned a 3D structure as the GM structure at $N = 12$. However, they also suggested two isoenergetic structures (2D and 3D) for $N = 11$ atoms [62].

Three generic structure types can be identified for Au clusters (see Fig. 2): (i) a 2D close packed **planar** layer (analogous to the (111) face of fcc bulk gold) for $N = 11$–13 and 15; (ii) a condensed **flattened cage** structure for $N = 14$ and 16 clusters; (iii) a pseudo-spherical **hollow cage** structure for $N = 17$–18. To explain the difference between the flattened and hollow cage structures, we can compare the predicted structures of Au_{16} and Au_{17}, which are shown in Figure 3. For Au_{16} (flattened cage), the dimensions of the shortest two internal axes are 0.3 nm and 0.7 nm. This cage could accommodate a small atom (e.g. H, He, Ne, O or F). However, for Au_{17} (hollow cage), the dimensions are both 0.6 nm and the cage could accommodate larger atoms, even an extra Au atom.

The planar structures obtained for the global minima of Au_N ($N = 11$–13 and 15) clusters agree with the findings of Fa et al. [63] concerning Au_{11} and Au_{12}. However, a difference is observed for Au_{13} and Au_{15}, which are predicted to be 3D by Fa. The nearest low-lying isomer to our 2D Au_{13} global minimum is predicted to be 3D, with an energy 0.5 eV higher than the GM. The lowest-energy structures of Au_{14} shows flattened cage structures, as previously reported [63,64]. The competitive isomer for the 3D GM of Au_{14} (C_{2v}) is also 3D (C_{2v}), with a relative energy of only 9 meV. The lowest-energy structure of Au_{15} is a 2D close packed layer, with C_{2v} symmetry. The second most stable isomer is 3D (C_{2v}), with relative energy 0.19 eV. Having a flattened cage structure and C_{2v} symmetry, Au_{16} is similar to the case of Au_{14}, as previously reported [64]. In contrast, anionic Au_{16} has been reported to adopt a hollow cage structure [65].

The structural transition from flattened cage to hollow cage configurations occurs at $N = 17$. The lowest energy structure we have obtained for Au_{17} is similar to what has been reported for neutral [64] and anionic [65] Au_{17}, showing a pseudo-spherical hollow cage structure with C_{2v} symmetry. The nearest competitive isomer to the GM is also another hollow-cage structure, with a relative energy of 0.08 eV and C_1 symmetry. The hollow cage structure (D_{4d}) observed for Au_{18} is different from the

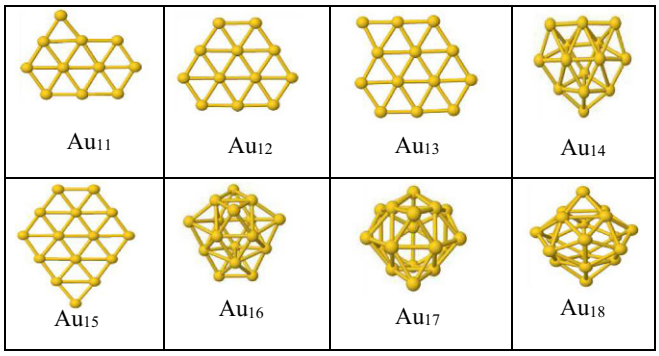

Fig. 1. Putative global minimum structures for Au_N clusters, $N = 11$–18.

hollow cage structure reported by Bulusu and Zeng [64], though the latter agrees with the energetically competitive isomer that we have found, which is only 0.08 eV higher in energy than the GM with C_S symmetry.

3.1.2 Pd clusters

Figure 4 shows the putative global minima for Pd clusters: their energies, coordinates and point groups are listed in Table S1 (see the Supporting Information).

Similar to small Pd clusters [37], the lowest energy structures obtained here for medium-sized Pd clusters are all 3D. As for pure Au clusters, the structural motifs adopted by Pd clusters are size-dependent; for medium-sized Pd clusters, a structural transition occurs at $N = 15$ atoms from **bilayer** structures to **filled cage** structures.

Global minima for the gas phase Pd_{11}, Pd_{13} and Pd_{14} clusters are found to be distorted hexagonal bilayer (HBL) structures with C_2 symmetry whereas Pd_{13} is found to be icosahedral fragment (C_2). These resemble the ground-state structures of the same sizes investigated previously [14,66]. The predicted Pd_{11} structure is energetically preferred over the next lowest-lying structure by only 2 meV. The competitive isomer for Pd_{14} also has a distorted hexagonal bilayer (HBL) structure, but with lower symmetry (C_1) and a relative energy of 0.09 eV. The global minimum of Pd_{13} reported here is found to be different from the compact icosahedron structure predicted as the GM in references [67–69].

The GM for Pd_{12} has a (C_1) buckled mono-planar (BMP) structure, which is similar to that observed recently by Xing and co-workers [32]. The GM of Pd_{15} is a buckled biplanar (BBP) structure. In the case of Pd_N clusters, $N = 16$–18 atom, the global minima are found to be pseudo-spherical filled cage structures and agree with the fcc-like growth pathway observed previously for 16–20 atoms [14,32,70].

3.1.3 Au–Pd clusters

The global minima for all compositions of Au_mPd_n clusters, $11 \leq m + n \leq 18$, are shown in Figures 5–8. Tables S2–S5 list the energies, coordinates and point groups (see the Supporting Information).

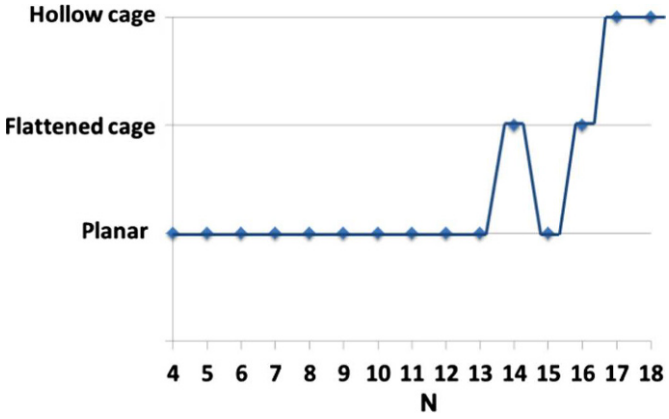

Fig. 2. Evolution of structural motifs for Au clusters. The structural properties for sizes $N = 4$–10 are taken from reference [37].

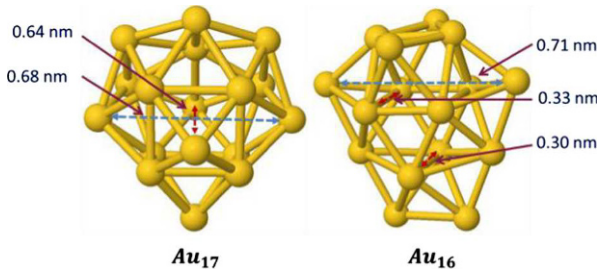

Fig. 3. The shortest-axis lengths of the predicted hollow cage structure of Au_{17} and flattened cage structure of Au_{16}.

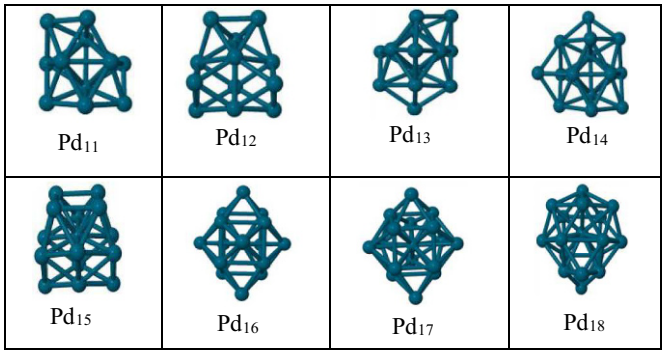

Fig. 4. Putative global minimum structures for Pd_N clusters, $N = 11$–18.

As shown in Figure 5, all the predicted structures of mono-gold-doped Pd clusters (Au_1Pd_n, $n = N - 1 = 10$–17) are 3D. For $N = 11$, 12 and 18, replacement of a single Pd atom in Pd_N by an Au atom yields geometries which are significantly distorted from the pure clusters. For sizes $N = 13$, 15 and 16, the Au-doped Pd clusters are similar to their pure Pd species whereas for $N = 14$ and 17 atoms, the Au-doped structures are quite different from the pure Pd clusters.

Au_1Pd_n $n = 10$–13 show icosahedral (Ih) derivatives; as for Au_1Pd_{10}, Au_1Pd_{11}, and Au_1Pd_{12} clusters, the most stable structure is an Ih fragment, while Au_1Pd_{13} is an Ih fragment which can be considered as an incomplete M_{19}

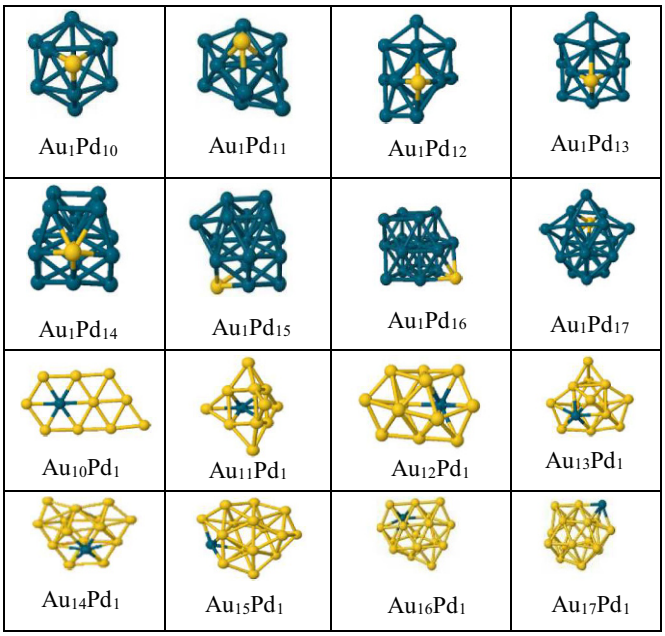

Fig. 5. Putative global minimum structures for mono-doped clusters, $N = 11$–18. Au and Pd atoms are shown (here, and in subsequent figures) in yellow and blue, respectively.

double icosahedron. Au_1Pd_{14} is found to be similar to its pure Pd counterpart (Pd_{15}) by showing a buckled biplanar (BBP) structure. GM of Au_1Pd_{15} is found to be pseudo-spherical filled cage structure and can be considered as a bicapped truncated decahedron (tDh). For Au_1Pd_{16}, the GM is a hcp-based structure. GM of Au_1Pd_{17} is a filled cage-like structure. In all cases of Au-doped Pd clusters, the unique Au is located in a low-connectivity surface site, in particular in capping sites on the Pd polyhedral cluster.

Figure 5 shows that all GM of Au_mPd_1 $m = 10$–17 clusters are 3D, except for planar $Au_{10}Pd_1$. Substitution of one Au atom by Pd in pure Au clusters is responsible for the shift of the 2D–3D transition point from 14- and 16-atom clusters to 12 atoms ($Au_{11}Pd_1$). This is in disagreement with the 2D–3D transition point suggested by Zanti and Peeters at size $N = 8$ [35]. However, in continuation with the planar structural pattern observed for $N = 4$–10 Pd-doped Au clusters previously [37], the gas-phase $Au_{10}Pd_1$ global minimum is also planar. A non-compact 3D structure is the GM for $Au_{11}Pd_1$. The other mono-substituted clusters, $Au_{12}Pd_1$–$Au_{17}Pd_1$ have flattened cage structures. $Au_{17}Pd_1$, for example, shows more condensed cage compared with a pseudo-spherical hollow cage structure of pure Au_{18}. The Pd atoms are located in or close to the centre of the clusters in high-coordination sites. The deviation from planarity generally occurs near this Pd centre, as previously reported for $N \leq 14$ clusters [35].

The putative GM for greater degrees of substitution are shown in Figures 6 ($N = 11$–14), 7 ($N = 15$–17) and 8 ($N = 18$).

For $N = 11$, doping two Au atoms into Pd_{11} clusters yields bilayer-structure, with the Au atoms in capping positions. All GM from Au_3Pd_8 to Au_5Pd_6 clusters have 3-layer hexagonal close-packed (hcp) structures, while Au_6Pd_5–Au_8Pd_3 have symmetrical or distorted Ih fragment structures which are similar to the GM found for Au_1Pd_{10}. In contrast, Au_9Pd_2 is found to be similar in shape to pure Pd_{11}, showing a hexagonal bilayer (HBL) fragment.

For $N = 12$, doping up to ten Au atoms changes the structure of gas-phase Au_1Pd_{11} and Au_2Pd_{10} from an Ih fragment to fcc-like motifs. They are 3-layer structures up to Au_7Pd_5, but they are incomplete for Au_8Pd_3–$Au_{10}Pd_2$. The structural configurations observed here for Au_3Pd_9–Au_7Pd_5 agree with the clusters reported previously by Zanti and Peeters [35], although their homotopic distributions are different.

For $N = 13$, the icosahedral fragment observed for Pd_{13} is the global minimum for Au_1Pd_{12}–Au_3Pd_{10} clusters. Au_7Pd_6 has a 3-layer hcp structure. The interactions between Au and Pd atoms favours fcc-like motifs for Au_4Pd_9–Au_6Pd_7 and Au_8Pd_5–$Au_{11}Pd_2$ clusters, having octahedral-based configurations. These fcc-like motifs were observed previously [35] for Au_4Pd_9, Au_6Pd_7 and Au_8Pd_5–$Au_{10}Pd_3$ clusters, but with different homotopic distributions, apart from Au_6Pd_7.

For $N = 14$, the gas-phase structure of Au_1Pd_{13}, Au_3Pd_{11}, Au_5Pd_9 and Au_7Pd_7 are all Ih-based fragments, whereas a distorted hexagonal bilayer (HBL) structure is the GM for Au_2Pd_{12}. For Au_4Pd_{10}, Au_6Pd_8 and $Au_{10}Pd_4$ clusters, the gas-phase global minima are fcc-fragments, and Au_8Pd_6 and Au_9Pd_5 show a continuation of the fcc structural growth, having complete octahedron motifs. These motifs have been reported previously [35] with different homotopic distributions. A clear structural transition from fcc-like structure to complex condensed cage structures occurs for $Au_{11}Pd_3$–$Au_{13}Pd_1$ clusters.

For $N = 15$, the buckled biplanar (BBP) structure of Pd_{15} remains the GM when doped with up to two Au atoms. GM of Au_3Pd_{12} is found to be hcp structure. Distorted hexagonal bilayer (HBL) structures are the lowest energy isomers when doping eight and nine atoms of Au whereas distorted fcc-like structures are found on doping 4–6 and 10–12 atoms of Au. Fused cage structures are the favoured structures for Au_7Pd_8, $Au_{13}Pd_2$ and $Au_{14}Pd_1$.

For $N = 16$, although a bicapped truncated decahedron (tDh) is the favoured structure for Pd_{16} (and also Au_1Pd_{15}), doping up to five atoms of Au results in putative GM with hcp structures. Au_6Pd_{10}, Au_7Pd_9 and Au_9Pd_7–$Au_{11}Pd_5$ clusters show compact capped pentagonal prism and icosahedral structures, whereas $Au_{12}Pd_4$ is a hcp-based fragment. A pseudo-spherical-like cage structure is the global minimum for both Au_8Pd_8 and $Au_{13}Pd_3$ while $Au_{14}Pd_2$ has a bicapped 13-atom close packed layer and $Au_{15}Pd_1$ a flattened cage structure.

For $N = 17$, doping two or three Au atoms retains the cage structure of Pd_{17}, though the mono-doped Pd cluster has a different (hcp), structure. Au_4Pd_{13} is an icosahedral fragment, which is related to the structure of $Au_{10}Pd_7$. Moving to Au_6Pd_{11}, the GM is a capped hcp structure, whereas Au_5Pd_{12} has structure intermediate between those of the Au_4Pd_{13} and Au_6Pd_{11} clusters. The predicted structure for Au_7Pd_{10} is a mixture of icosahedral and octahedral structures, while the GM for Au_8Pd_9

is a fused icosahedral structure. The GM for Au_9Pd_8 has an fcc structure, while hcp-based structures are found for $Au_{11}Pd_6$–$Au_{13}Pd_4$. Doping up to three Pd atoms into the Au_{17} cluster gives complex cage structures, though, unlike Au_{17}, they are not hollow.

For $N = 18$, as for Pd_{18}, the predicted GM for Au_2Pd_{16} is filled pseudo-spherical cage, whereas Au_3Pd_{15} and Au_4Pd_{14} are based on icosahedral fragments. The structures of Au_5Pd_{13}–Au_7Pd_{11} can be described as polytetrahedral, composed of mainly fused pentagonal bipyramids with (in some cases) hexagonal bipyramids. Fused tricapped buckled biplanar (BBP) structure is the favoured structure for $Au_{10}Pd_8$. Filled pseudo-spherical structures are the putative GM for Au_8Pd_{10}, Au_9Pd_9 and $Au_{16}Pd_2$ clusters. Fusing of hexagonal bipyramid structures generates a shell-like structure for the $Au_{11}Pd_7$ cluster. A filled spherical-like structure is also the global minima for the $Au_{12}Pd_6$ and $Au_{13}Pd_5$ clusters which are formed by fusing of hexagonal bipyramid, pentagonal bipyramid and icosahedral structures. Fusing of icosahedral fragments makes a spherical-like cage structure for the $Au_{14}Pd_4$ cluster, whereas fusing of hexagonal bipyramids and pentagonal bipyramids yields the crown-like structure for $Au_{15}Pd_3$. Finally, a capped flattened cage structure is the global minima for $Au_{17}Pd_1$, although the pure Au_{18} cluster is a hollow cage.

3.2 Stability

Generally, the observed preference of Au atoms for low coordination surface positions (especially capping sites) and Pd atoms for high coordination core and central sites can be explained with reference to bulk cohesive and surface energies which are higher for Pd: average low-index surface energies (E_{sur}) and cohesive energy (E_{coh}) are 96.8 meV Å^{-2} and 3.81 eV atm^{-1}, respectively, for Au and 131 meV Å^{-2} and 3.89 eV atm^{-1}, respectively, for Pd. The stronger Pd–Pd bonds and lower Au surface energy favours Pd-rich cores and Au-rich outer shells (though this depends on the cluster size and composition). This preference is reinforced by the sizes of the atoms, as the atomic radius of Pd is smaller than for Au by 0.06 Å, so the larger Au atoms are more easily accommodated in low coordination sites. The small difference in electronegativity values of Pd(2.2) and Au(2.4) can lead to weak (Pd to Au) s electron transfer [34,38] (favouring mixing in larger clusters), but favouring surface Au in smaller clusters, as the more electronegative Au atom can better stabilise the negative charge that tends to build up on the cluster surface [71]. However, it should be noted that for larger clusters reverse (Au to Pd) d-band electron donation can also occur [72,73].

The stabilities of the clusters, and their structural preferences, can be investigated by calculating the excess energy Δ, binding energy E_b, and second difference in energy $\Delta_2 E$, which are defined in equations (1)–(3). Tables S6–S9 list the values of these energies for all clusters studied here (see the Supporting Information).

The relative stabilities of clusters of different nuclearities can be studied by calculating the second difference in energy $\Delta_2 E$, which indicates the stability of an N-atom cluster with respect to neighbouring sizes. Figure 9 shows a plot of $\Delta_2 E$ for Au and Pd clusters and their mono-substituted clusters as a function of cluster size. The relatively stable clusters are indicated by significant positive peaks.

Compared to their neighbours, even-numbered clusters Au_{12} (2D), Au_{14} (3D) and Au_{16} (3D) have high relative

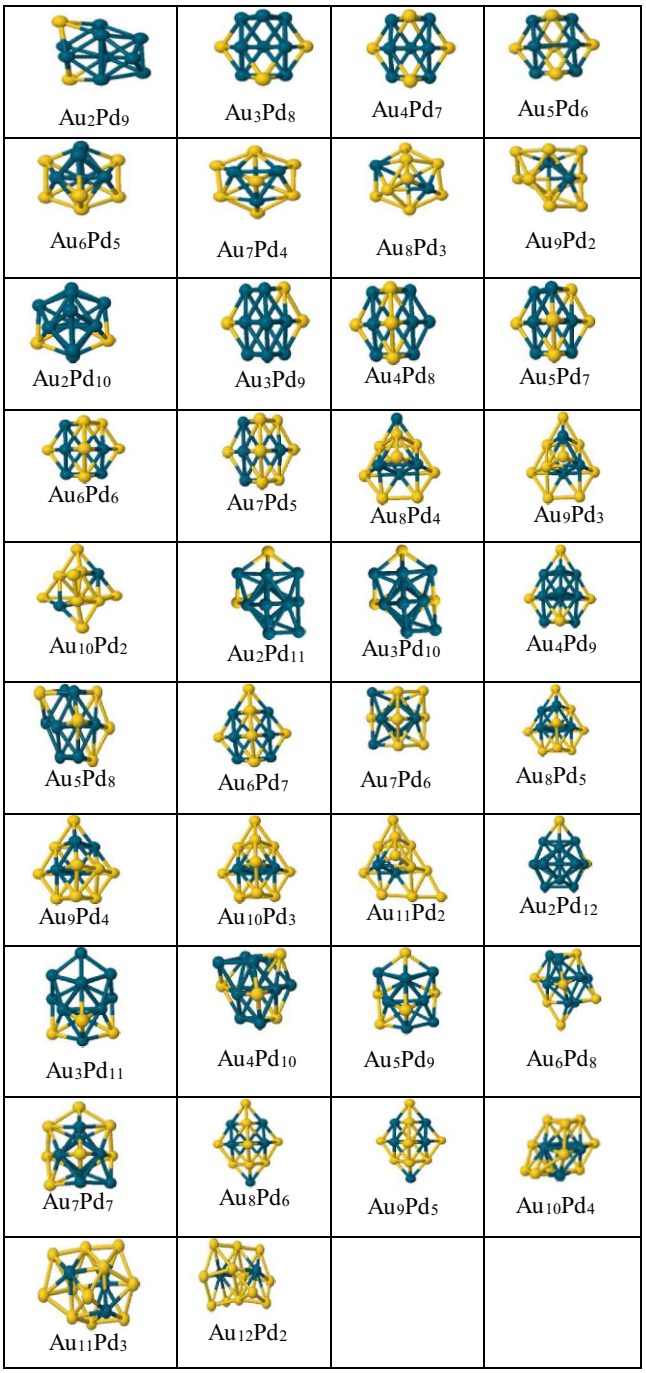

Fig. 6. Putative global minimum structures for all compositions (excluding mono-doping) of AuPd nanoalloys with sizes $N = 11$–14.

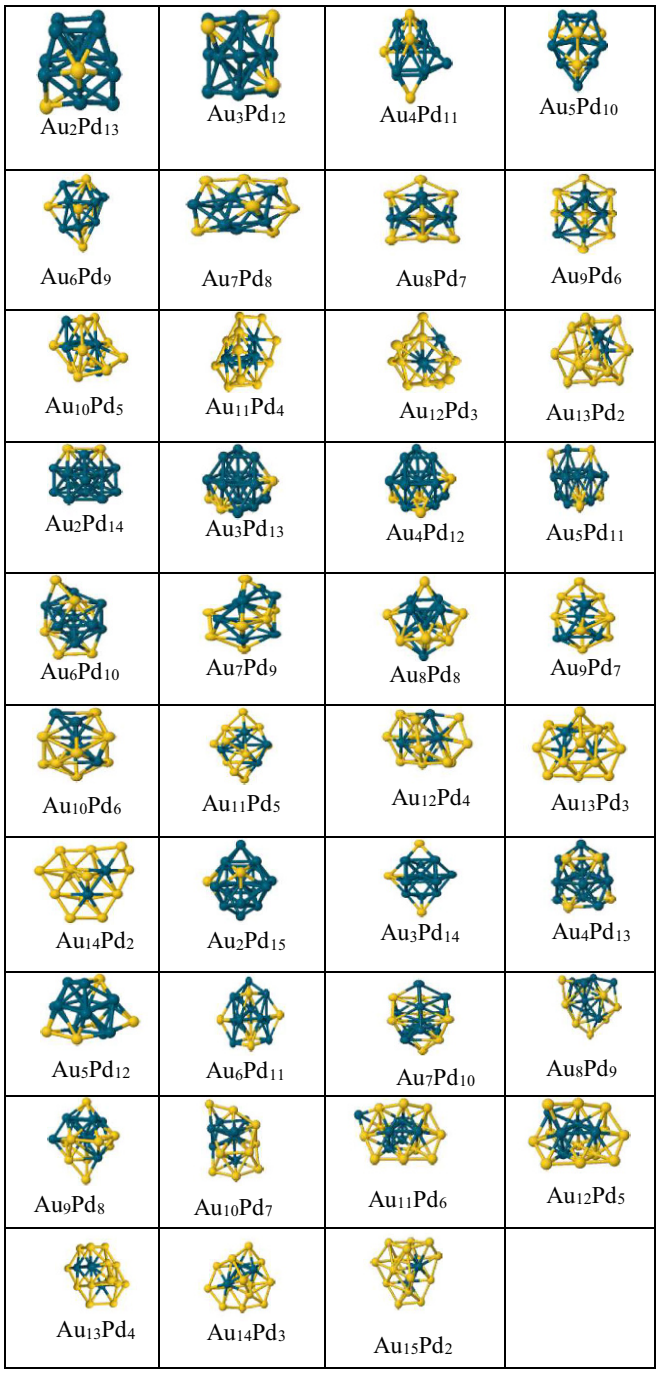

Fig. 7. Putative global minimum structures for all compositions (excluding mono-doping) of AuPd nanoalloys with sizes $N = 15$–17.

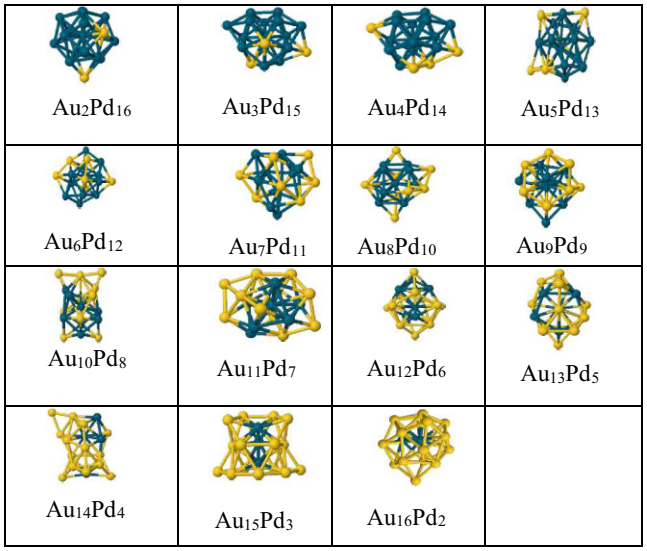

Fig. 8. Putative global minimum structures for all compositions (excluding mono-doping) of AuPd nanoalloys with size $N = 18$.

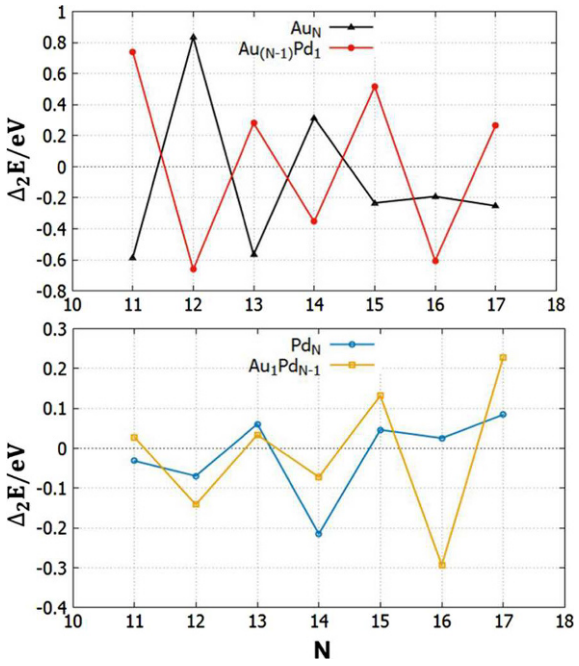

Fig. 9. Second difference in energy ($\Delta_2 E$) of pure Au and Pd-doped Au clusters (top); and pure Pd and Au-doped Pd clusters (bottom) with respect to the total number of atoms (N).

stabilities, corresponding to peaks in $\Delta_2 E$, with odd-numbered clusters being relatively unstable (troughs in $\Delta_2 E$). This even–odd behaviour is due to the fact that the Au atom has an unpaired s electron, and so reflects the greater stability of Au clusters (either 2D or 3D) with an even number of electrons, over those with an odd number [74–77]. The most stable cluster is 2D Au_{12}, although its $\Delta_2 E$ energy is lower (by 0.67 eV) than the magic size Au_6 observed recently [37]. Doping a single Pd atom into Au clusters shifts the stability from the even-number ($N = 12$, 14, and 16) clusters to odd-number ($N = 11$, 13, 15, and 17) clusters. This shift occurs because an odd-electron Au atom is replaced by an even-electron Pd atom, so clusters with odd values of N (e.g. $Au_{10}Pd_1$, which has the highest $\Delta_2 E$ value) now have an even number of electrons, and consequently are stable with respect to neighbouring cluster sizes.

As the Pd atom has an even number of electrons, there is no enhanced electronic stability for even N. In fact, odd numbered Pd_N clusters are relatively more stable than for

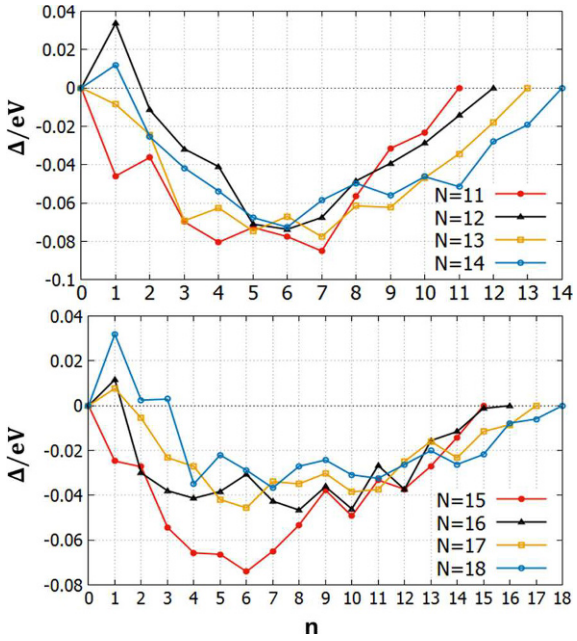

Fig. 10. Excess energy (Δ) as a function of the number of Pd atoms (n) for all compositions of $11 \leq N \leq 18$ for Au_mPd_n clusters, where $N = m + n$.

even N, which could be attributed to packing considerations. This behaviour is consistent with the significant effect of Pd atoms in weakening the odd–even fluctuation of stability of Ag and Cu clusters reported recently by Kahnouji et al. [78] Doping a single Au atom into Pd_N clusters generates odd-electron clusters for all values of N. The shape of the Δ_2E plot does not change and there is no shift in the odd–even pattern. Interestingly, for the larger sizes ($N = 15$–17), the extremes in Δ_2E are greater for the Au-doped clusters than for the corresponding pure Pd_N clusters. The size $N = 17$ shows the most relatively stable structure for both pure Pd and Au-doped Pd clusters, although Pd_6 has been predicted to have a Δ_2E value 0.34 eV higher than the Pd_{17} cluster [37].

The effect of mixing Au with Pd in medium-sized clusters is studied by calculating the excess energy, Δ. Excess energies as a function of the number of Pd atoms are shown in Figures 10 and 11 for all compositions of $11 \leq m + n \leq 18$ for Au_mPd_n clusters. Negative values of excess energies represent favourable mixing, whereas de-mixing is indicated by positive values of Δ.

For ($N = m + n = 11$) clusters, the best mixing (most negative Δ) is found at Au_4Pd_7, whereas Au_1Pd_{10} exhibits a weak mixing behaviour. All ($m + n = 12$) nanoalloys show a strong mixing tendency except $Au_{11}Pd_1$ and the strongest mixing is for 50% Pd composition. For ($m + n = 13$), Au_6Pd_7 shows the most energetically favourable mixing. For ($m + n = 14$), only $Au_{13}Pd_1$ shows a strong de-mixing tendency and the most favourable mixing is for Au_8Pd_6. All ($m + n = 15$) clusters favour mixing, with the strongest mixing for Au_9Pd_6. For ($m + n = 16$, 17 and 18), all Pd-doped Au clusters are energetically unfavourable compared to pure Pd and Au clusters, while the reverse is true for all other mixed clusters. The strongest mixing tendency at these sizes is observed for Au_8Pd_8, $Au_{11}Pd_6$ and $Au_{11}Pd_7$, though the magnitude of Δ is much smaller than for $m + n = 15$ (Au_9Pd_6). In fact, we find that the optimum values of Δ for $N = 11$–15 (approx. -0.075 to -0.085 eV) are quite similar but have approximately twice the magnitude of the larger clusters ($N = 16$–18).

The stabilities of nanoclusters relative to their constituent ground state atoms are obtained by calculating the binding energy per atom, E_b. According to the plots of E_b shown in Figures 12 and 13, the binding energy generally increases with increasing cluster size (though local switches in order along the y-axis correspond to peaks or troughs in the excess energy plots), as previously reported [35,37]. It can also be seen that the binding energy increases with increasing Pd composition (reflecting the stronger Pd–Pd and Pd–Au bonds compared to Au–Au), although the mono-Pd-doped Au clusters have lower E_b values than pure Au clusters for even sizes ($N = 12$, 14, 16, and 18 atoms). This is consistent with the shift in excess energies upon mono-doping of Pd into Au clusters seen in Figure 10. However, this disagrees with the relative stability observed for mixed clusters compared with their pure clusters for small sized Au–Pd clusters $N = 4$–10 except for $N = 6$, which is found to be a magic for pure Au and Pd clusters [37].

HOMO–LUMO gaps could indicate the structural stabilities of the clusters. High stability can be indicated by high HOMO–LUMO gaps. Figure S1 (see the Supporting Information) shows HOMO–LUMO gap versus number of Pd atoms for all clusters. For Au clusters, in line with Δ_2E results, the even-numbered clusters $N = 12$, 14, 16, and 18 atoms have high stabilities whereas the odd-numbered clusters are relatively unstable. HOMO–LUMO gaps of Pd clusters are range between (0.06–0.15 eV). For nanoalloys, higher HOMO–LUMO gaps correlate well with the suggested high stability (high mixing energy Δ) compositions for $N = 12$, 14, 16, and 17. However, HOMO–LUMO gaps disagree with the stability found for $N = 13$ and 18. For $N = 11$, the high HOMO–LUMO gaps observed for Au_7Pd_4, Au_8Pd_3 and $Au_{10}Pd_1$ disagree with Δ results except Au_7Pd_4 which is found to be stable in both. For $N = 15$, $Au_{11}Pd_4$ is found to be stable according to Δ and HOMO–LUMO gap whereas the results do not match for $Au_{14}Pd_1$.

The possible permutations of two different metals (Au and Pd) in the system can be investigated by the systematic homotop search. The number of homotops grows exponentially with the size of the cluster [38]. Hence many symmetry inequivalent homotops may have been missed by our BPGA-DFT search. In this context, we have studied the structural energies of proposed homotops of the mono-substituted clusters which are built based on their GM and minimized at the DFT level using the VASP code. Figures S2–S9 (see the Supporting Information) show the relative energies ΔE against symmetry inequivalent homotops for all mono-substituted clusters. For our system, the BPGA-DFT search for all mono-substituted

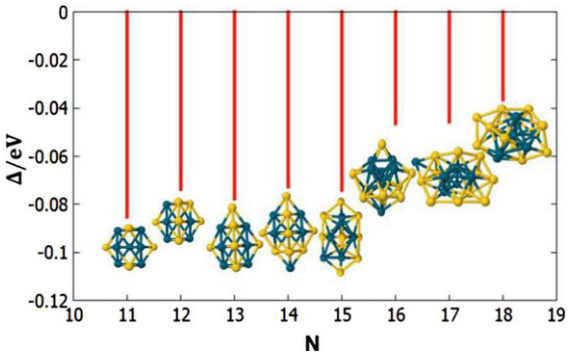

Fig. 11. Plot of the lowest excess energy (Δ), and the corresponding compositional isomer, calculated for each cluster size ($N = 11$–18) for Au_mPd_n clusters.

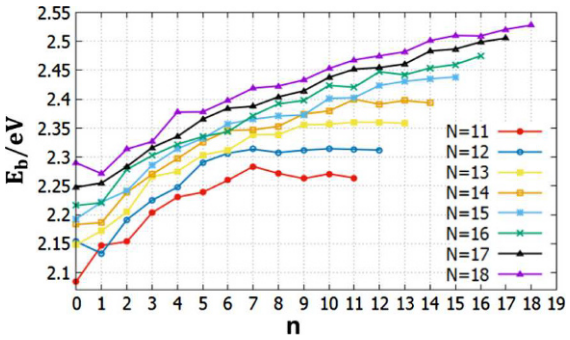

Fig. 12. Plot of binding energies of $Au_{(N-n)}Pd_n$ clusters for each cluster size $N = 11$–18 against the number of Pd atoms (n).

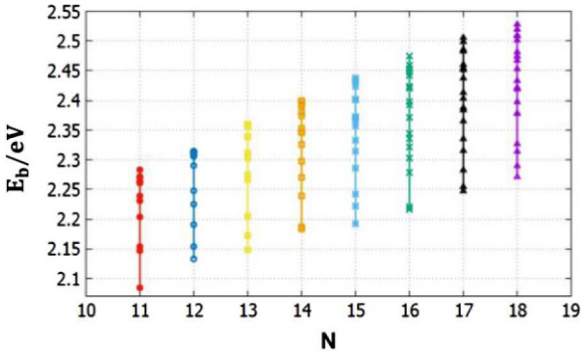

Fig. 13. The range of binding energies (E_b), for all compositions of $Au_{(N-n)}Pd_n$ clusters, plotted against the total number of atoms (N).

clusters Au_1Pd_n and Au_mPd_1 with 11 to 18 atoms, successfully found the lowest energy homotop as the global minimum.

4 Conclusions

We have applied the DFT based-Birmingham Parallel Genetic Algorithm (BPGA-DFT) to Au–Pd nanoalloys ranging from 11 to 18 atoms and compared them with their pure clusters in the same size range. The BPGA-DFT approach has successfully found the global minima of the studied clusters. A GM structures were reinforced by the systematic homotop search for singly doped clusters.

2D close-packed planar layer, condensed flattened cage, and pseudo-spherical hollow cage structure are identified to be the three generic structure types for pure Au clusters. Although all Pd clusters obtained here are 3D, their structural motifs are found to be size-dependent; as a structural transition occurs at $N = 15$ atoms from bilayer structures to filled cage structures. The structural behaviour for nanoalloys is controlled by the composition and size. Au atoms tend to be located in low-connectivity surface sites, in particular in capping sites, whereas Pd atoms generally prefer high-coordination positions in or close to the centre of the cluster.

The even-numbered Au clusters, Au_{12} (2D), Au_{14} (3D) and Au_{16} (3D) show high relative stability, corresponding to peaks in Δ_2E. There is no enhanced electronic stability for even-numbered Pd clusters. A strong tendency of Au–Pd clusters to alloy was predicted from calculated mixing energies, with the exception of some mono-Pd-doped Au clusters. The stabilities of cluster relative to their constituent increase with increasing cluster size and are found to be higher for Pd and Pd-rich clusters.

Supplementary Material

The Supporting Information includes energies, structures and point group symmetries (Tables S1–S5); Excess Energies Δ, Binding Energies E_b, and the second difference in energy Δ_2E (Tables S6–S9); the HOMO–LUMO gaps for all clusters (Fig. S1); and the relative energies ΔE for all symmetry inequivalent homotops of mono-substituted clusters (Figs. S2–S9).

H.A. Hussein is grateful to the University of Kufa and the Ministry of Higher Education and Scientific Research (Iraq) for the award of a PhD scholarship. Calculations were performed on the University of Birmingham's Blue-BEAR high-performance computer and ARCHER facilities, the UK National Supercomputing Service (http://www.archer.ac.uk) via membership of the UK's HPC Materials Chemistry Consortium, which is funded by EPSRC (EP/L000202), and "TOUCAN: Towards an Understanding of Catalysis on Nanoalloys" membership, which is funded by EPSRC under Critical Mass Grant EP/J010804/1. H.A. Hussein thanks Dr. Jack Davis for helpful advice and John Hey for valuable help.

Author contribution statement

R.L. Johnston designed the research project and supervised the work and H.A. Hussein carried out the calculations. All authors contributed to data interpretation and discussion of the results.

References

1. B. Hammer, J.K. Norskov, Nature **376**, 238 (1995)
2. F. Yang, D. Deng, X. Pan, Q. Fu, X. Bao, Natl. Sci. Rev. **2**, 183 (2015)
3. J.K. Edwards, B. Solsona, E. Ntainjua, A.F. Carley, A.A. Herzing, C.J. Kiely, G.J. Hutchings, Science **323**, 1037 (2009)
4. D.I. Enache, J.K. Edwards, P. Landon, B. Solsona-Espriu, A.F. Carley, A.A. Herzing, M. Watanabe, C.J. Kiely, D.W. Knight, G.J. Hutchings, Science **311**, 362 (2006)
5. X. Liu, M. Conte, M. Sankar, Q. He, D.M. Murphy, D. Morgan, R.L. Jenkins, D. Knight, K. Whiston, C.J. Kiely, G.J. Hutchings, Appl. Catal. A: Gen. **504**, 373 (2015)
6. I. Demiroglu, Z.Y. Li, L. Piccolo, R.L. Johnston, Catal. Sci. Technol. **6**, 6916 (2016)
7. L. Piccolo, Z.Y. Li, I. Demiroglu, F. Moyon, Z. Konuspayeva, G. Berhault, P. Afanasiev, W. Lefebvre, J. Yuan, R.L. Johnston, Sci. Rep. **6**, 35226 (2016)
8. L. Wang, Y. Yamauchi, J. Am. Chem. Soc. **132**, 13636 (2010)
9. Z. Peng, H. Yang, J. Am. Chem. Soc. **131**, 7542 (2009)
10. V. Mazumder, S. Sun, J. Am. Chem. Soc. **131**, 4588 (2009)
11. E. Antolini, Energy Environ. Sci. **2**, 915 (2009)
12. M. Shao, J. Power Sources **196**, 2433 (2011)
13. K. Zhang, Y. Xiang, X. Wu, L. Feng, W. He, J. Liu, W. Zhou S. Xie, Langmuir **25**, 1162 (2009)
14. Y. Mu, Y. Han, J. Wang, J. Wan G. Wang, Phys. Rev. A **84**, 053201 (2011)
15. X. Teng, Q. Wang, P. Liu, W. Han, A.I. Frenkel, W. Wen, N. Marinkovic, J.C. Hanson, J.A. Rodriguez, J. Am. Chem. Soc. **130**, 1093 (2008)
16. G. Schon, U. Simon, Colloid Polym. Sci. **273**, 202 (1995)
17. Y.W. Lee, M. Kim, Y. Kim, S.W. Kang, J. Lee, S.W. Han, J. Phys. Chem. C **114**, 7689 (2010)
18. J.W. Hong, Y.W. Lee, M. Kim, S.W. Kang, S.W. Han, Chem. Commun. **47**, 2553 (2011)
19. F. Wang, C. Li, L. Sun, H. Wu, T. Ming, J. Wang, J. C. Yu, C. Yan, J. Am. Chem. Soc. **133**, 1106 (2011)
20. D. Chen, C. Li, H. Liu, F. Ye, J. Yang, Sci. Rep. **5**, 11949 (2015)
21. C. Henry, C. Chapon, S. Giorgio, C. Goyhenex, in *Chemisorption and Reactivity on Supported Clusters and Thin Films*, 1st edn., edited by R.M. Lambert, P. Gianfranco (Springer, Netherlands, 1997), Vol. 331, p. 117
22. R. Ismail, R. Ferrando, R.L. Johnston, J. Phys. Chem. C **117**, 293 (2013)
23. L.O. Paz-Borbón, R.L. Johnston, G. Barcaro, A. Fortunelli, Eur. Phys. J. D **52**, 131 (2009)
24. A. Logsdail, L.O. Paz-Borbón, R.L. Johnston, J. Comput. Theor. Nanosci. **6**, 1 (2009)
25. V. Kaydashev, P. Ferrari, C. Heard, E. Janssens, R.L. Johnston, P. Lievens, Part. Part. Syst. Charact. **33**, 364 (2016)
26. S. Vajda, M.J. Pellin, J.P. Greeley, C.L. Marshall, L.A. Curtiss, G.A. Ballentine, J.W. Elam, S. Catillon-Mucherie, P.C. Redfern, F. Mehmood, P. Zapol, Nat. Mater. **8**, 213 (2009)
27. A. Shayeghi, R.L. Johnston, R. Schäfer, Phys. Chem. Chem. Phys. **15**, 19715 (2013)
28. P. Gruene, D.M. Rayner, B. Redlich, A.F.G. van der Meer, J.T. Lyon, G. Meijer, A. Fielicke, Science **321**, 674 (2008)
29. A.P. Woodham, A. Fielicke, in *Structure & Bonding: Gold Clusters, Colloids and Nano-Particles*, edited by M. Mingos (2014), Vol. 161, pp. 243–278
30. G.A. Bishea, M.D. Morse, J. Chem. Phys. **95**, 5646 (2001)
31. G.A. Bishea, M.D. Morse, J. Chem. Phys. **95**, 8779 (1991)
32. X. Xing, A. Hermann, X. Kuang, M. Ju, C. Lu, Y. Jin, X. Xia, G. Maroulis, Sci. Rep. **6**, 19656 (2016)
33. H. Huan, Y. Chen, T. Wang, X. Ye, J. Nanoparticle Res. **18**, 349 (2016)
34. F. Pittaway, L.O. Paz-Borbón, R.L. Johnston, H. Arslan, R. Ferrando, C. Mottet, G. Barcaro, A. Fortunelli, J. Phys. Chem. C **113**, 9141 (2009)
35. G. Zanti, D. Peeters, J. Phys. Chem. A **114**, 10345 (2010)
36. D. Palagin, J. Doye, Phys. Chem. Chem. Phys. **17**, 28010 (2015)
37. H.A. Hussein, B.A. Davis, R.L. Johnston, Phys. Chem. Chem. Phys. **18**, 26133 (2016)
38. R. Ferrando, J. Jellinek, R.L. Johnston, Chem. Rev. **108**, 845 (2008)
39. D. Zitoun, M. Respaud, M. Fromen, M.J. Casanove, P. Lecante, C. Amiens, B. Chaudret, Phys. Rev. Lett. **89**, 037203 (2002)
40. H. Cantera-Lóopez, J.M. Montejano-Carrizales, F. Aguilera-Granja, J.L. Morán-López, Eur. Phys. J. D **57**, 61 (2010)
41. J. Davis, A. Shayeghi, S.L. Horswell, R.L. Johnston, Nanoscale **7**, 14032 (2015)
42. F. Buendía, J.B.A. Davis, J.A. Vargas, M.R. Beltrán, R.L. Johnston, Phys. Chem. Chem. Phys. **18**, 22122 (2016)
43. I. Demiroglu, K. Yao, H.A. Hussein, R.L. Johnston, J. Phys. Chem. C **121**, 10773 (2017)
44. J.B.A. Davis, S.L. Horswell, R.L. Johnston, J. Phys. Chem. C **120**, 3759 (2016)
45. https://bitbucket.org/JBADavis/bpga/
46. R.L. Johnston, Dalton Trans. **4193** (2003)
47. A. Shayeghi, D. Götz, J.B.A. Davis, R. Schäfer, R.L. Johnston, Phys. Chem. Chem. Phys. **17**, 2104 (2015)
48. B. Bandow, B. Hartke, J. Phys. Chem. A **110**, 5809 (2006)
49. D. Deaven, K. Ho, Phys. Rev. Lett. **75**, 288 (1995)
50. G. Kresse, J. Hafner, Phys. Rev. B **47**, 558 (1993)
51. J. Perdew, K. Burke, Y. Wang, Phys. Rev. B **54**, 16533 (1996)
52. G. Kresse, Phys. Rev. B **59**, 1758 (1999)
53. M. Methfessel, A.T. Paxton, Phys. Rev. B **40**, 3616 (1989)
54. J. Wang, G. Wang, J. Zhao, Phys. Rev. B **66**, 035418 (2002)
55. Y. Dong, M. Springborg, Eur. Phys. J. D **43**, 15(2007)
56. H. Häkkinen, B. Yoon, U. Landman, X. Li, H.J. Zhai, L.S. Wang, J. Phys. Chem. A **107**, 6168 (2003)
57. B. Assadollahzadeh, P. Schwerdtfeger, J. Chem. Phys. **131**, 064306 (2009)
58. J. David, D. Guerra, A. Restrepo, Chem. Phys. Lett. **539–540**, 64 (2012)
59. V.B. Koutecky, J. Burda, R. Mitrić, M.G. Zampella, J. Chem. Phys. **117**, 3120 (2002)
60. Y.C. Choi, W.Y. Kim, H.M. Lee, K.S. Kim, J. Chem. Theor. Comput. **5**, 1216 (2009)
61. D.A. Gotz, R. Schafer, P. Schwerdtfeger, J. Comput. Chem. **34**, 1975 (2013)

62. M.P. Johansson, I. Warnke, A. Le, F. Furche, J. Phys. Chem. C **118**, 29370 (2014)
63. W. Fa, C. Luo, J. Dong, Phys. Rev. B **72**, 205428 (2005)
64. S. Bulusu, X.C. Zeng, J. Chem. Phys. **125**, 154303 (2006)
65. S. Bulusu, X. Li, L. Wang, X.C. Zeng, PNAS **103**, 8326 (2006)
66. M. J. Piotrowski, P. Piquini, J.L.F. Da Silva, Phys. Rev. B **81**, 155446 (2010)
67. Y. Sun, M. Zhang, Phys. Rev. A **79**, 043202 (2009)
68. J. Rogan, G. García, J.A. Valdivia, W. Orellana, A.H. Romero, R. Ramírez, M. Kiwi, Phys. Rev. B **72**, 115421 (2005)
69. A. Vega, J. Rogan, W. Orellana, G. Garc, Eur. Phys. J. D **44**, 125 (2007)
70. H. Zhang, D. Tian, J. Zhao, J. Chem. Phys. **129**, 114302 (2008)
71. F. Chen, R.L. Johnston, Acta Mater. **56**, 2374 (2008)
72. B. Zhu, G. Thrimurthulu, L. Delannoy, C. Louis, C. Mottet, J. Creuze, B. Legrand, H. Guesmi, J. Catal. **308**, 272 (2013)
73. A. Dhouib, H. Guesmi, Chem. Phys. Lett. **521**, 98 (2012)
74. K.J. Taylor, C.L. Pettiette-Hall, O. Cheshnovsky, R.E. Smalley, J. Chem. Phys. **96**, 3319 (1992)
75. T.H. Lee, K.M. Enin, J. Phys. Chem. **98**, 10023 (1994)
76. D. Stolcic, M. Fischer, G. Gantefo, Y.D. Kim, Q. Sun, P. Jena, J. Am. Chem. Soc. **125**, 2848 (2003)
77. D. Chan, R. Dietsche, G. Ganteför, Y. Dok, Chem. Phys. Lett. **457**, 391 (2008)
78. H. Kahnouji, H. Najafvandzadeh, S.J. Hashemifar, M. Alaei, Chem. Phys. Lett. **630**, 101 (2015)

Supporting Information of:

Application of a Parallel Genetic Algorithm to the global optimisation of medium-sized Au-Pd sub-nanometre clusters

Heider A. Hussein, Ilker Demiroglu, and Roy L. Johnston

May 2017

Tables S1-S5 contain energies, structures and point group symmetries for all studied clusters. Tables S6-S9 contain Excess Energies Δ, Binding Energies E_b, and the second difference in energy $\Delta_2 E$ for the studied clusters. Figure S1 shows the HOMO-LUMO gap versus numbers of Pd atom for all clusters. Figures S2-S9 display the relative energies for all symmetry inequivalent homotops of mono-substituted clusters.

Table S1:The energies, structures, and point groups for Au_N and Pd_N clusters, N= 11-18.

Composition	E / eV	Structure	Point Group
Au_{11}	-24.9726	Planar	C_1
Au_{12}	-28.0699	planar	D_{3h}
Au_{13}	-30.3331	Planar	C_1
Au_{14}	-33.1629	Flattened cage	C_{2v}
Au_{15}	-35.6779	Planar	C_{2v}
Au_{16}	-38.4264	Flattened cage	C_{2v}
Au_{17}	-41.3671	Hollow-cage	C_{2v}
Au_{18}	-44.5597	Hollow-cage	D_{4d}
Pd_{11}	-41.0965	Distorted hexagonal bilayer (HBL)	C_2
Pd_{12}	-45.4116	Buckled mono-planar (BMP)	C_1
Pd_{13}	-49.7966	Icosahedral fragment	C_2
Pd_{14}	-54.1211	Distorted hexagonal bilayer (HBL)	C_2
Pd_{15}	-58.6606	Buckled biplanar (BBP)	C_{2v}
Pd_{16}	-63.1540	Bicapped truncated decahedron (tDh)	C_{2v}
Pd_{17}	-67.6222	Spherical filled cage	C_{2v}
Pd_{18}	-72.0061	Spherical filled cage	C_{2v}

Table S2: The energies, structures, and point groups for all compositions of Au_mPd_n clusters, (m+n)= 11-13.

Composition	E / eV	Structure	Point Group
Au_1Pd_{10}	-39.8871	Icosahedral (Ih) fragment	C_{3v}
Au_2Pd_9	-38.5121	Bilayer-like	C_1
Au_3Pd_8	-37.2091	Hexagonal close-packed (hcp)	C_s
Au_4Pd_7	-36.1693	Hexagonal close-packed (hcp)	C_s
Au_5Pd_6	-34.6213	Hexagonal close-packed (hcp)	C_{2v}
Au_6Pd_5	-33.1024	Icosahedral (Ih) fragment	C_s
Au_7Pd_4	-31.7215	Icosahedral (Ih) fragment	C_{3v}
Au_8Pd_3	-30.1383	Icosahedral (Ih) fragment	C_s
Au_9Pd_2	-28.3030	Hexagonal bilayer (HBL) fragment	C_2
$Au_{10}Pd_1$	-26.9442	Planar	C_1
Au_1Pd_{11}	-44.1393	Icosahedral (Ih) fragment	C_1
Au_2Pd_{10}	-42.8671	Icosahedral (Ih) fragment	C_s
Au_3Pd_9	-41.5485	Fcc-like	C_1
Au_4Pd_8	-40.2130	Fcc-like	C_s
Au_5Pd_7	-38.9973	Fcc-like	C_2
Au_6Pd_6	-37.6259	Fcc-like	C_1
Au_7Pd_5	-36.1487	Fcc-like	C_2
Au_8Pd_4	-34.3432	Incomplete fcc-like	D_{3d}
Au_9Pd_3	-32.7873	Incomplete fcc-like	C_{3v}
$Au_{10}Pd_2$	-31.0987	Incomplete fcc-like	D_{3d}
$Au_{11}Pd_1$	-29.1113	Non-compact 3D	C_{2v}
Au_1Pd_{12}	-48.5333	Icosahedral based fragment	C_1
Au_2Pd_{11}	-47.2484	Icosahedral based fragment	C_1
Au_3Pd_{10}	-45.9154	Icosahedral based fragment	C_1
Au_4Pd_9	-44.6182	Fcc-like	C_s
Au_5Pd_8	-43.1107	Fcc-like incomplete octahedron	C_1
Au_6Pd_7	-41.8230	Fcc-like incomplete octahedron	C_s
Au_7Pd_6	-40.1881	3-layer hcp	C_s
Au_8Pd_5	-38.7905	Fcc-like incomplete octahedron	C_s
Au_9Pd_4	-37.1355	Fcc-like incomplete octahedron	C_s
$Au_{10}Pd_3$	-35.7262	Fcc-like incomplete octahedron	C_{3v}
$Au_{11}Pd_2$	-33.6461	Fcc-like	C_1
$Au_{12}Pd_1$	-31.9417	Flattened cage	C_1

Table S3: The energies, structures, and point groups for all compositions of Au_mPd_n clusters, (m+n)= 14-15.

Composition	E / eV	Structure	Point Group
Au_1Pd_{13}	-52.8938	Incomplete M_{19} double icosahedron	C_1
Au_2Pd_{12}	-51.5189	Distorted hexagonal bilayer (HBL)	C_1
Au_3Pd_{11}	-50.3511	Icosahedral based fragment	C_1
Au_4Pd_{10}	-48.7817	Fcc-fragment-like	C_s
Au_5Pd_9	-47.4217	Icosahedral based fragment	C_1
Au_6Pd_8	-45.8357	Fcc-fragment-like	C_s
Au_7Pd_7	-44.4632	Distorted hexagonal bilayer (HBL)	C_s
Au_8Pd_6	-43.1616	Fcc-like complete octahedron	C_s
Au_9Pd_5	-41.5954	Fcc-like complete octahedron	C_s
$Au_{10}Pd_4$	-39.9046	Fcc-fragment-like	C_{3v}
$Au_{11}Pd_3$	-38.2387	Flattened cage	C_1
$Au_{12}Pd_2$	-36.5149	Flattened cage	C_1
$Au_{13}Pd_1$	-34.4919	Flattened cage	C_1
Au_1Pd_{14}	-57.3312	Buckled biplanar (BBP)	C_s
Au_2Pd_{13}	-55.9744	Buckled biplanar (BBP)	C_1
Au_3Pd_{12}	-54.5825	Hexagonal close-packed (hcp)	C_1
Au_4Pd_{11}	-52.9772	Distorted fcc-like	C_1
Au_5Pd_{10}	-51.6720	Distorted fcc-like	C_s
Au_6Pd_9	-49.9539	Distorted fcc-like	C_1
Au_7Pd_8	-48.6409	Fused cage-like	C_1
Au_8Pd_7	-47.2713	Distorted hexagonal bilayer (HBL)	C_s
Au_9Pd_6	-45.8626	Distorted hexagonal bilayer (HBL)	C_1
$Au_{10}Pd_5$	-44.2016	Distorted fcc-like	C_1
$Au_{11}Pd_4$	-42.6470	Distorted fcc-like	C_1
$Au_{12}Pd_3$	-40.9309	Distorted fcc-like	C_1
$Au_{13}Pd_2$	-38.9792	Fused cage-like	C_1
$Au_{14}Pd_1$	-37.4451	Flattened cage	C_1

Table S4: The energies, structures, and point groups for all compositions of Au_mPd_n clusters, (m+n)= 16-17.

Composition	E / eV	Structure	Point Group
Au_1Pd_{15}	-61.7419	Bicapped truncated decahedron (tDh)	C_s
Au_2Pd_{14}	-60.2481	Hexagonal close-packed (hcp)	C_s
Au_3Pd_{13}	-58.7675	Hexagonal close-packed (hcp)	C_1
Au_4Pd_{12}	-57.5697	Hexagonal close-packed (hcp)	C_1
Au_5Pd_{11}	-55.8535	Hexagonal close-packed (hcp)	C_1
Au_6Pd_{10}	-54.6186	Compact pentagonal bipyramid with icosahedral	C_1
Au_7Pd_9	-52.9137	Compact pentagonal bipyramid with icosahedral	C_1
Au_8Pd_8	-51.5359	Spherical-like cage	C_1
Au_9Pd_7	-49.9264	Compact pentagonal bipyramid with icosahedral	C_1
$Au_{10}Pd_6$	-48.1901	Compact pentagonal bipyramid with icosahedral	C_1
$Au_{11}Pd_5$	-46.7666	Compact pentagonal bipyramid with icosahedral	C_1
$Au_{12}Pd_4$	-45.2696	hcp-based fragment	C_1
$Au_{13}Pd_3$	-43.6702	Spherical-like cage	C_1
$Au_{14}Pd_2$	-41.9981	Bicapped 13-atom close packed layer	C_1
$Au_{15}Pd_1$	-40.0203	Flattened cage	C_1
Au_1Pd_{16}	-66.2220	hcp-based fragment	C_1
Au_2Pd_{15}	-64.7300	Cage-like	C_1
Au_3Pd_{14}	-63.3849	Cage-like	C_1
Au_4Pd_{13}	-61.7151	Icosahedral based fragment	C_1
Au_5Pd_{12}	-60.3245	Intermediate structure between Au_4Pd_{13} and Au_6Pd_{11}	C_1
Au_6Pd_{11}	-58.9914	Capped hcp	C_1
Au_7Pd_{10}	-57.4650	Mixture of Icosahedraon and octahedron	C_1
Au_8Pd_9	-55.7808	Fused Icosahedral structures	C_1
Au_9Pd_8	-54.3155	Fcc like	C_1
$Au_{10}Pd_7$	-52.7544	Icosahedron based fragment	C_1
$Au_{11}Pd_6$	-51.4095	hcp-based fragment	C_1
$Au_{12}Pd_5$	-49.8011	hcp-based fragment	C_1
$Au_{13}Pd_4$	-48.0055	hcp-based fragment	C_1
$Au_{14}Pd_3$	-46.3950	Complex cage	C_1
$Au_{15}Pd_2$	-44.5505	Complex cage	C_1
$Au_{16}Pd_1$	-42.8786	Flattened cage	C_1

Table S5: The energies, structures, and point groups for all compositions of Au_mPd_n clusters, (m+n)=18.

Composition	E / eV	Structure	Point Group
Au_1Pd_{17}	-70.6521	Tri-capped buckled biplanar (BBP)	C_1
Au_2Pd_{16}	-69.0966	Filled spherical-like	C_1
Au_3Pd_{15}	-67.8241	Icosahedraon based fragment	C_1
Au_4Pd_{14}	-66.3788	Icosahedraon based fragment	C_1
Au_5Pd_{13}	-64.7440	Capped fused hexagonal bipyramid	C_1
Au_6Pd_{12}	-63.3306	Fused icosahedra structures	C_1
Au_7Pd_{11}	-61.9163	Fused hexagonal bipyramid and pentagonal bipyramid (heart-like)	C_1
Au_8Pd_{10}	-60.3633	Filled spherical-like	C_1
Au_9Pd_9	-58.7193	Filled spherical-like	C_1
$Au_{10}Pd_8$	-57.2446	Fused tri-capped buckled biplanar (BBP)	C_1
$Au_{11}Pd_7$	-55.8940	Fused hexagonal bipyramid structures (shell-like)	C_1
$Au_{12}Pd_6$	-54.2270	Filled spherical-like	C_1
$Au_{13}Pd_5$	-52.5806	Filled spherical-like	C_1
$Au_{14}Pd_4$	-51.2879	Fused icosahedra fragments (spherical-like cage)	C_1
$Au_{15}Pd_3$	-49.0812	Crown-like	C_s
$Au_{16}Pd_2$	-47.5646	Filled spherical-like	C_1
$Au_{17}Pd_1$	-45.7039	Flattened cage	C_1

Table S6: Excess Energy Δ, Binding Energy E_b and the second difference in energy $\Delta_2 E$ for 11-18 atoms.

Cluster	Excess Energy/eV	Second difference in energy/eV	Binding Energy/eV
Pd_{11}	0.0000	-0.0319	2.2638
Au_1Pd_{10}	-0.0233	0.0275	2.2708
Au_2Pd_9	-0.0315	—	2.2628
Au_3Pd_8	-0.0566	—	2.2715
Au_4Pd_7	-0.0850	—	2.2837
Au_5Pd_6	-0.0776	—	2.2599
Au_6Pd_5	-0.0727	—	2.2388
Au_7Pd_4	-0.0805	—	2.2302
Au_8Pd_3	-0.0698	—	2.2033
Au_9Pd_2	-0.0362	—	2.1534
$Au_{10}Pd_1$	-0.0459	0.7407	2.1468
Au_{11}	0.0000	-0.5858	2.0845
Pd_{12}	0.0000	-0.0698	2.3120
Au_1Pd_{11}	-0.0143	-0.1418	2.3132
Au_2Pd_{10}	-0.0288	—	2.3144
Au_3Pd_9	-0.0393	—	2.3118
Au_4Pd_8	-0.0484	—	2.3077
Au_5Pd_7	-0.0676	—	2.3136
Au_6Pd_6	-0.0737	—	2.3065
Au_7Pd_5	-0.07109	—	2.2906
Au_8Pd_4	-0.0410	—	2.2474
Au_9Pd_3	-0.0318	—	2.2249
$Au_{10}Pd_2$	-0.0115	—	2.1914
$Au_{11}Pd_1$	0.0336	-0.6634	2.1330
Au_{12}	0.0000	0.8339	2.1535
Pd_{13}	0.0000	0.0605	2.3582
Au_1Pd_{12}	-0.0179	0.0335	2.3600
Au_2Pd_{11}	-0.0343	—	2.3602
Au_3Pd_{10}	-0.0469	—	2.3566
Au_4Pd_9	-0.0623	—	2.3558
Au_5Pd_8	-0.0615	—	2.3388
Au_6Pd_7	-0.0776	—	2.3387
Au_7Pd_6	-0.0670	—	2.3119
Au_8Pd_5	-0.0747	—	2.3034
Au_9Pd_4	-0.0625	—	2.2750
$Au_{10}Pd_3$	-0.0693	—	2.2656
$Au_{11}Pd_2$	-0.0245	—	2.2045
$Au_{12}Pd_1$	-0.0085	0.2801	2.1724
Au_{13}	0.0000	-0.5665	2.1476

Table S7: Excess Energy Δ, Binding Energy E_b and the second difference in energy $\Delta_2 E$ for 11-18 atoms.

Cluster	Excess Energy/eV	Second difference in energy/eV	Binding Energy/eV
Pd_{14}	0.0000	-0.2151	2.3935
Au_1Pd_{13}	-0.0192	-0.0724	2.3978
Au_2Pd_{12}	-0.0279	—	2.3915
Au_3Pd_{11}	-0.0515	—	2.3999
Au_4Pd_{10}	-0.0463	—	2.3797
Au_5Pd_9	-0.0561	—	2.3745
Au_6Pd_8	-0.0497	—	2.3531
Au_7Pd_7	-0.0586	—	2.3470
Au_8Pd_6	-0.0726	—	2.3459
Au_9Pd_5	-0.0676	—	2.3259
$Au_{10}Pd_4$	-0.0538	—	2.2970
$Au_{11}Pd_3$	-0.0417	—	2.2699
$Au_{12}Pd_2$	-0.0255	—	2.2387
$Au_{13}Pd_1$	0.0119	-0.3545	2.1861
Au_{14}	0.0000	0.3148	2.1831
Pd_{15}	0.0000	0.0462	2.4384
Au_1Pd_{14}	-0.0132	0.1322	2.4353
Au_2Pd_{13}	-0.0252	—	2.4309
Au_3Pd_{12}	-0.0345	—	2.4239
Au_4Pd_{11}	-0.0296	—	2.4026
Au_5Pd_{10}	-0.0448	—	2.4014
Au_6Pd_9	-0.0324	—	2.3726
Au_7Pd_8	-0.0470	—	2.3709
Au_8Pd_7	-0.0578	—	2.3653
Au_9Pd_6	-0.0661	—	2.3572
$Au_{10}Pd_5$	-0.0575	—	2.3322
$Au_{11}Pd_4$	-0.0560	—	2.3143
$Au_{12}Pd_3$	-0.0437	—	2.2857
$Au_{13}Pd_2$	-0.0157	—	2.2414
$Au_{14}Pd_1$	-0.0124	0.5155	2.2216
Au_{15}	0.0000	-0.2335	2.1928

Table S8: Excess Energy Δ, Binding Energy E_b and the second difference in energy $\Delta_2 E$ for 11-18 atoms.

Cluster	Excess Energy/eV	Second difference in energy/eV	Binding Energy/eV
Pd_{16}	0.0000	0.0251	2.4749
Au_1Pd_{15}	-0.0011	-0.2937	2.4599
Au_2Pd_{14}	-0.0115	—	2.4541
Au_3Pd_{13}	-0.0156	—	2.4419
Au_4Pd_{12}	-0.0373	—	2.4475
Au_5Pd_{11}	-0.0266	—	2.4206
Au_6Pd_{10}	-0.0460	—	2.4239
Au_7Pd_9	-0.0361	—	2.3977
Au_8Pd_8	-0.0466	—	2.3920
Au_9Pd_7	-0.0426	—	2.3718
$Au_{10}Pd_6$	-0.0306	—	2.3437
$Au_{11}Pd_5$	-0.0382	—	2.3352
$Au_{12}Pd_4$	-0.0413	—	2.3220
$Au_{13}Pd_3$	-0.0379	—	2.3025
$Au_{14}Pd_2$	-0.0300	—	2.2784
$Au_{15}Pd_1$	0.0116	-0.6054	2.2205
Au_{16}	0.0000	-0.1920	2.2160
Pd_{17}	0.0000	0.0842	2.5055
Au_1Pd_{16}	-0.0084	0.2281	2.4988
Au_2Pd_{15}	-0.0115	—	2.4867
Au_3Pd_{14}	-0.0232	—	2.4833
Au_4Pd_{13}	-0.0159	—	2.4608
Au_5Pd_{12}	-0.0249	—	2.4546
Au_6Pd_{11}	-0.0373	—	2.4519
Au_7Pd_{10}	-0.0384	—	2.4378
Au_8Pd_9	-0.0302	—	2.4144
Au_9Pd_8	-0.0348	—	2.4039
$Au_{10}Pd_7$	-0.0339	—	2.3877
$Au_{11}Pd_6$	-0.0456	—	2.3843
$Au_{12}Pd_5$	-0.0418	—	2.3654
$Au_{13}Pd_4$	-0.0271	—	2.3354
$Au_{14}Pd_3$	-0.0232	—	2.3164
$Au_{15}Pd_2$	-0.0055	—	2.2836
$Au_{16}Pd_1$	0.0076	0.2651	2.2551
Au_{17}	0.0000	-0.2520	2.2477

Table S9: Excess Energy Δ, Binding Energy E_b and the second difference in energy $\Delta_2 E$ for 11-18 atoms.

Cluster	Excess Energy/eV	Second difference in energy/eV	Binding Energy/eV
Pd_{18}	0.0000	—	2.5281
Au_1Pd_{17}	-0.0059	—	2.5208
Au_2Pd_{16}	-0.0077	—	2.5094
Au_3Pd_{15}	-0.0218	—	2.5102
Au_4Pd_{14}	-0.0262	—	2.5014
Au_5Pd_{13}	-0.0201	—	2.4820
Au_6Pd_{12}	-0.0262	—	2.4750
Au_7Pd_{11}	-0.0324	—	2.4679
Au_8Pd_{10}	-0.0308	—	2.4531
Au_9Pd_9	-0.0242	—	2.4332
$Au_{10}Pd_8$	-0.0270	—	2.4227
$Au_{11}Pd_7$	-0.0367	—	2.4192
$Au_{12}Pd_6$	-0.0288	—	2.3981
$Au_{13}Pd_5$	-0.0220	—	2.3781
$Au_{14}Pd_4$	-0.0349	—	2.3777
$Au_{15}Pd_3$	0.0029	—	2.3266
$Au_{16}Pd_2$	0.0024	—	2.3138
$Au_{17}Pd_1$	0.0319	—	2.2712
Au_{18}	0.0000	—	2.2898

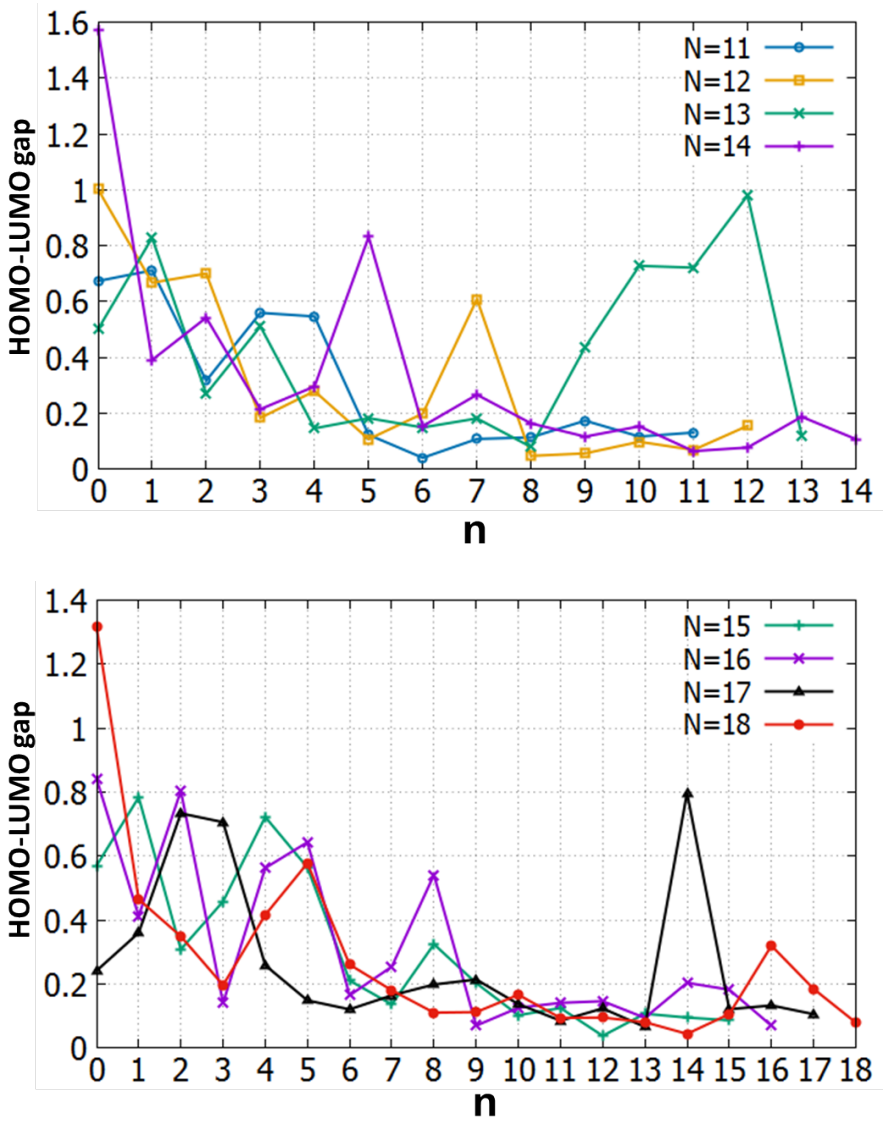

Figure (S1): HOMO-LUMO gap versus numbers of Pd atoms for N=11-18 $(Au,Pd)_N$ alloy clusters.

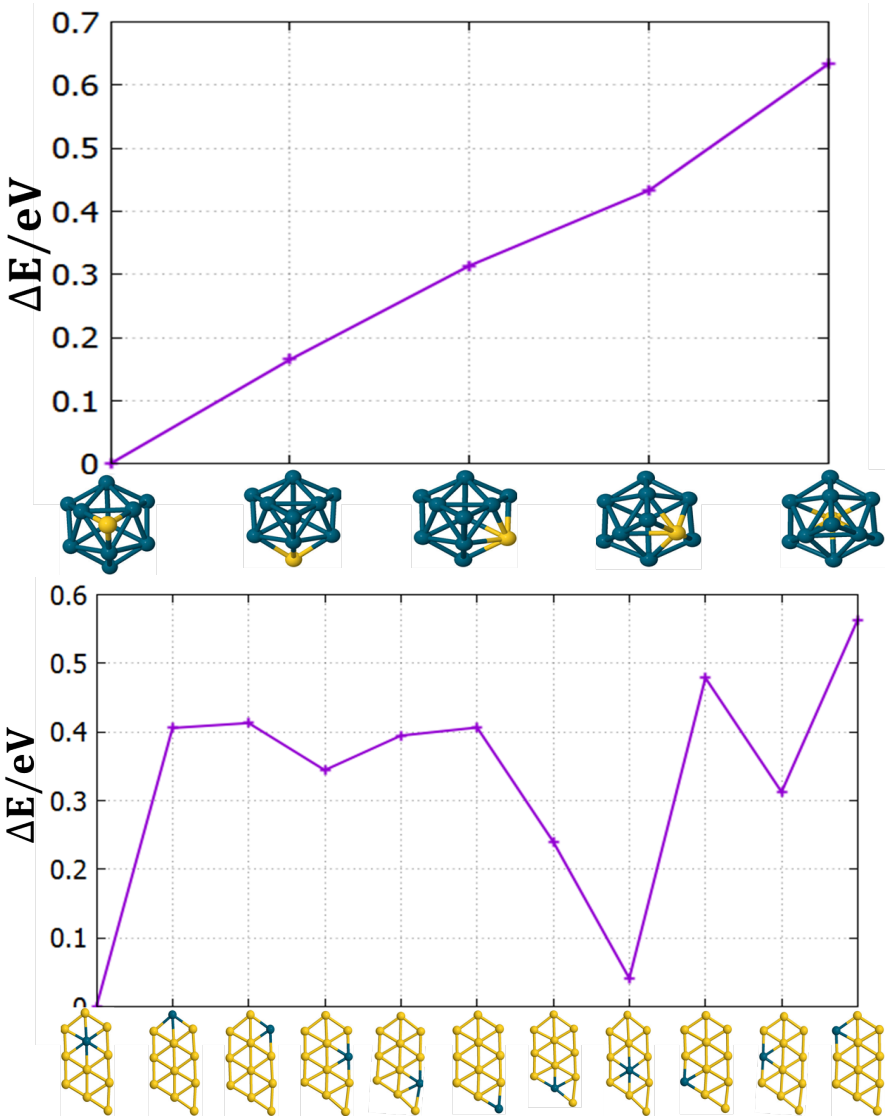

Figure (S2): The relative energies for all symmetry inequivalent homotops of Au_1Pd_{10} and $Au_{10}Pd_1$ clusters.

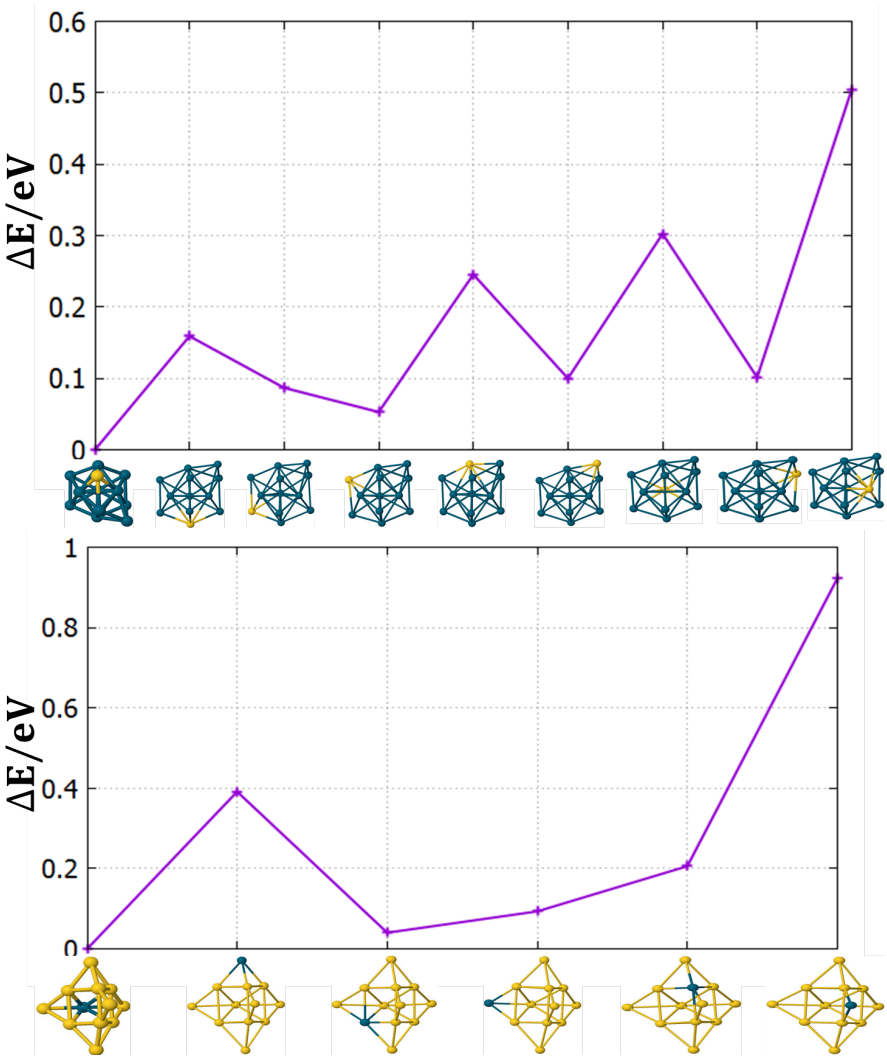

Figure (S3): The relative energies for all symmetry inequivalent homotops of Au_1Pd_{11} and $Au_{11}Pd_1$ clusters.

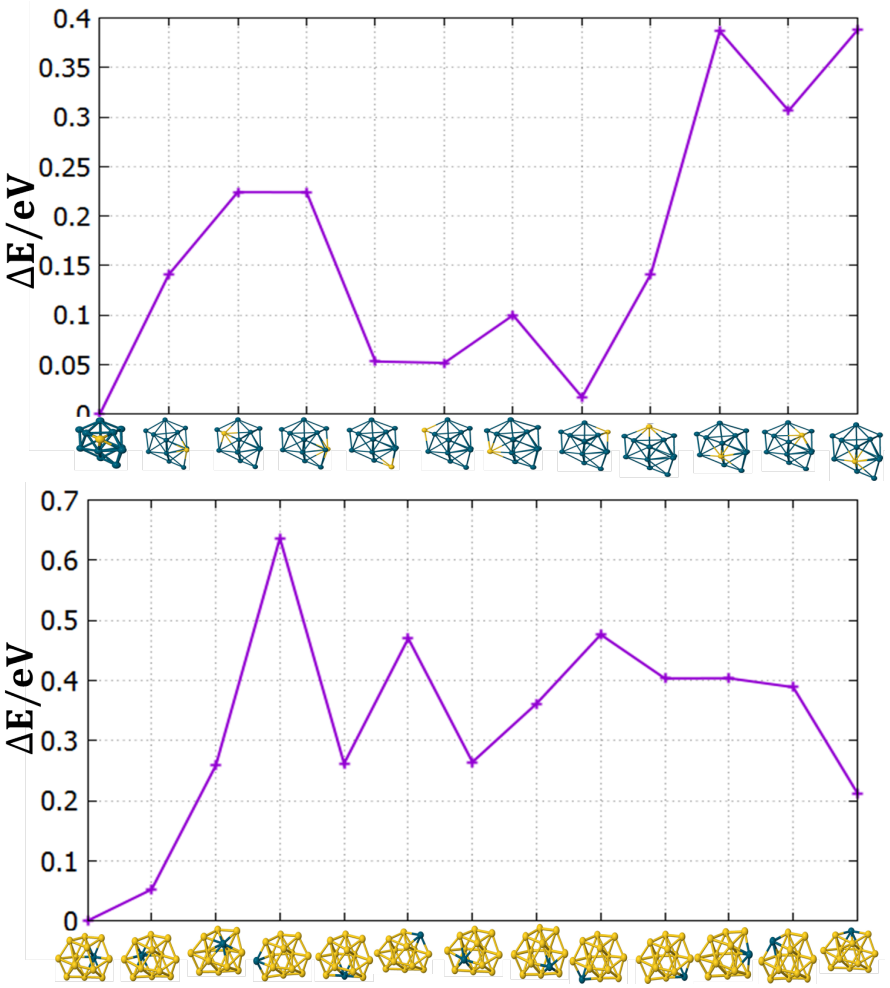

Figure (S4): The relative energies for all symmetry inequivalent homotops of Au_1Pd_{12} and $Au_{12}Pd_1$ clusters.

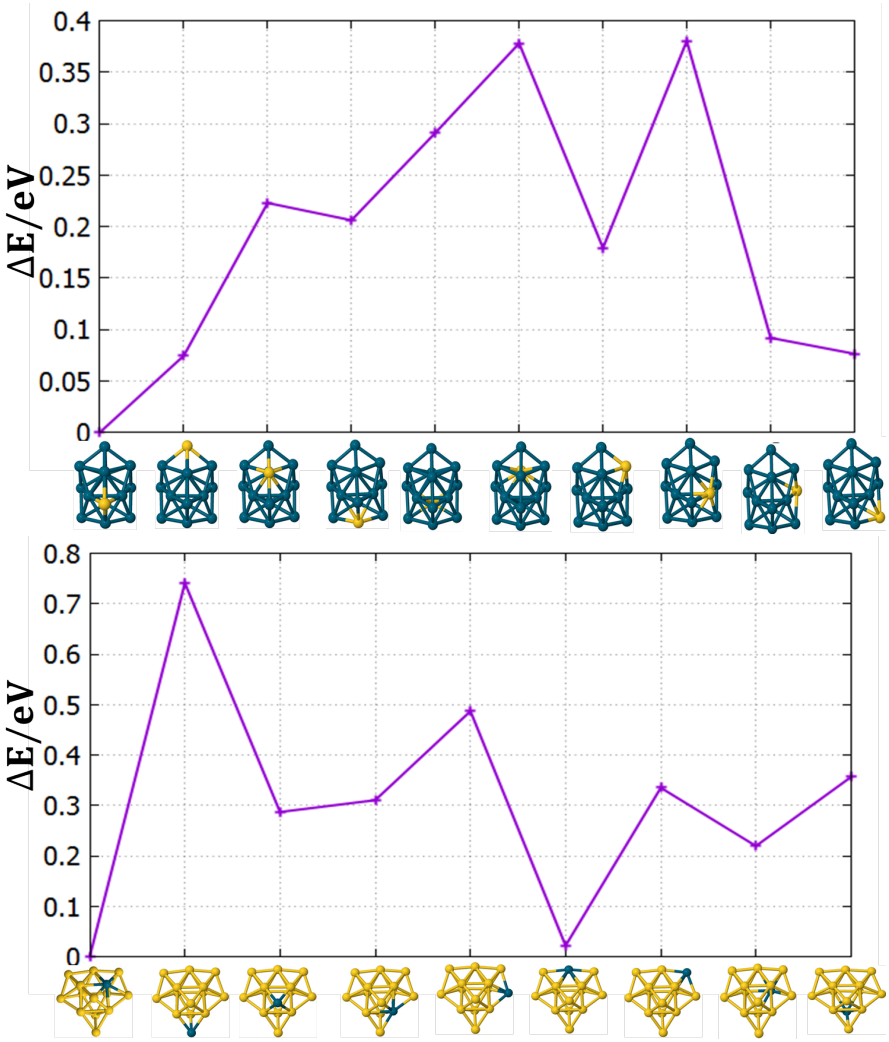

Figure (S5): The relative energies for all symmetry inequivalent homotops of Au_1Pd_{13} and $Au_{13}Pd_1$ clusters.

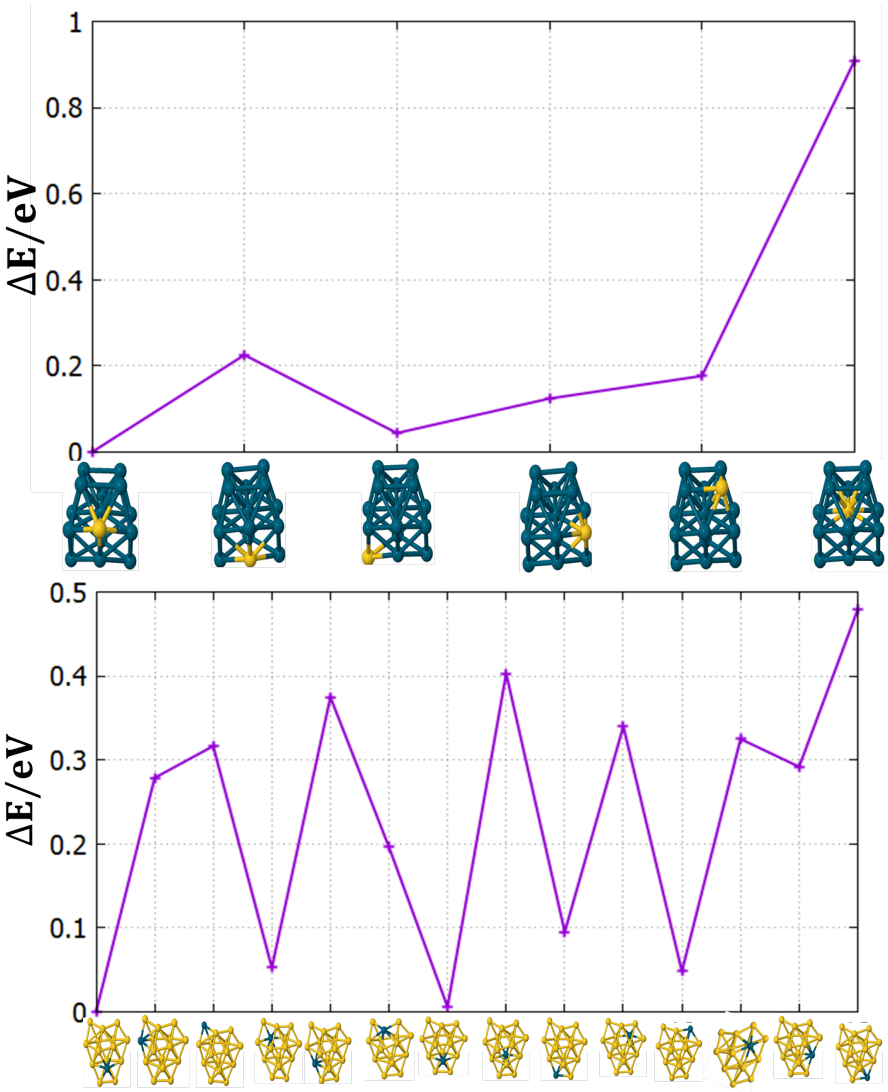

Figure (S6): The relative energies for all symmetry inequivalent homotops of Au_1Pd_{14} and $Au_{14}Pd_1$ clusters.

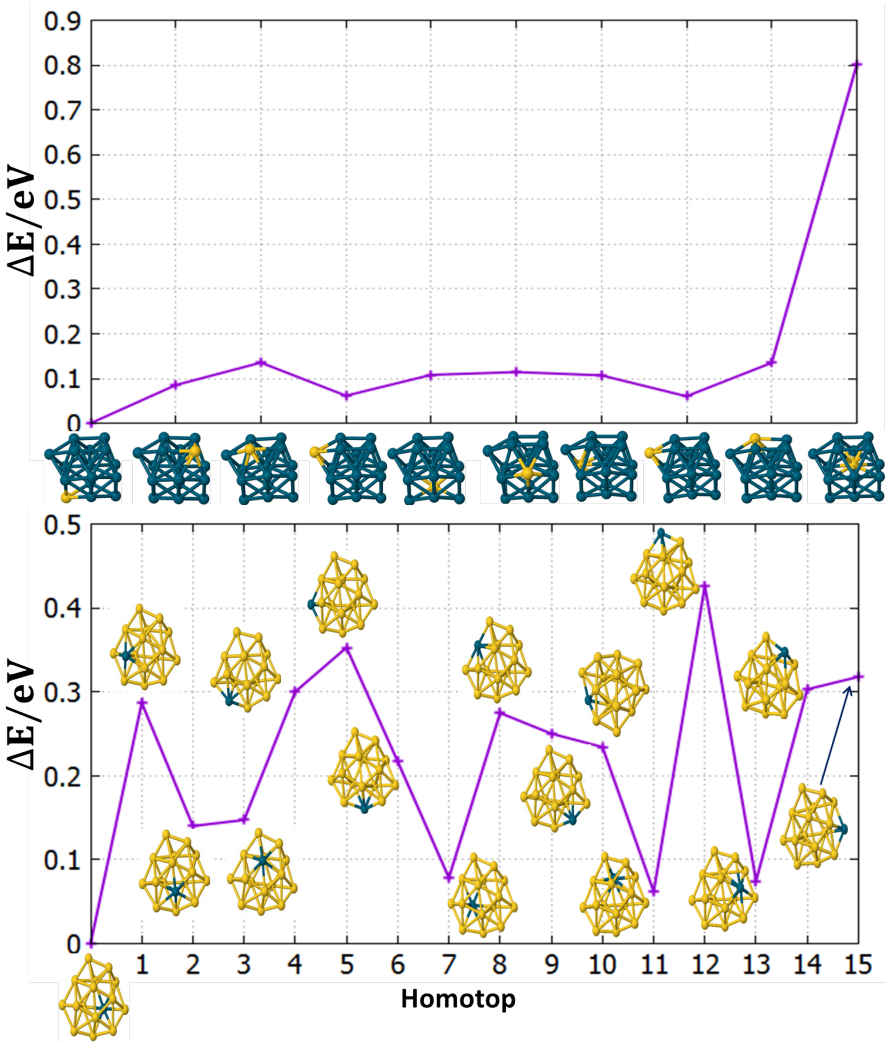

Figure (S7): The relative energies for all symmetry inequivalent homotops of Au_1Pd_{15} and $Au_{15}Pd_1$ clusters.

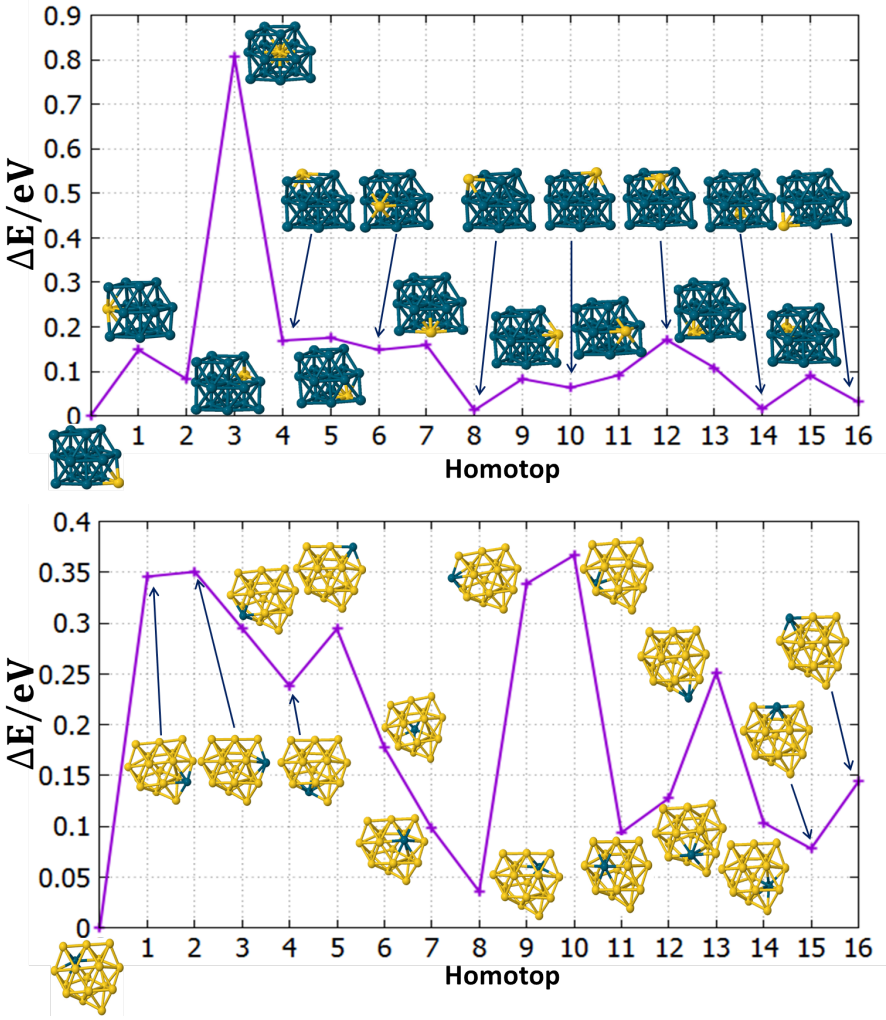

Figure (S8): The relative energies for all symmetry inequivalent homotops of Au_1Pd_{16} and $Au_{16}Pd_1$ clusters.

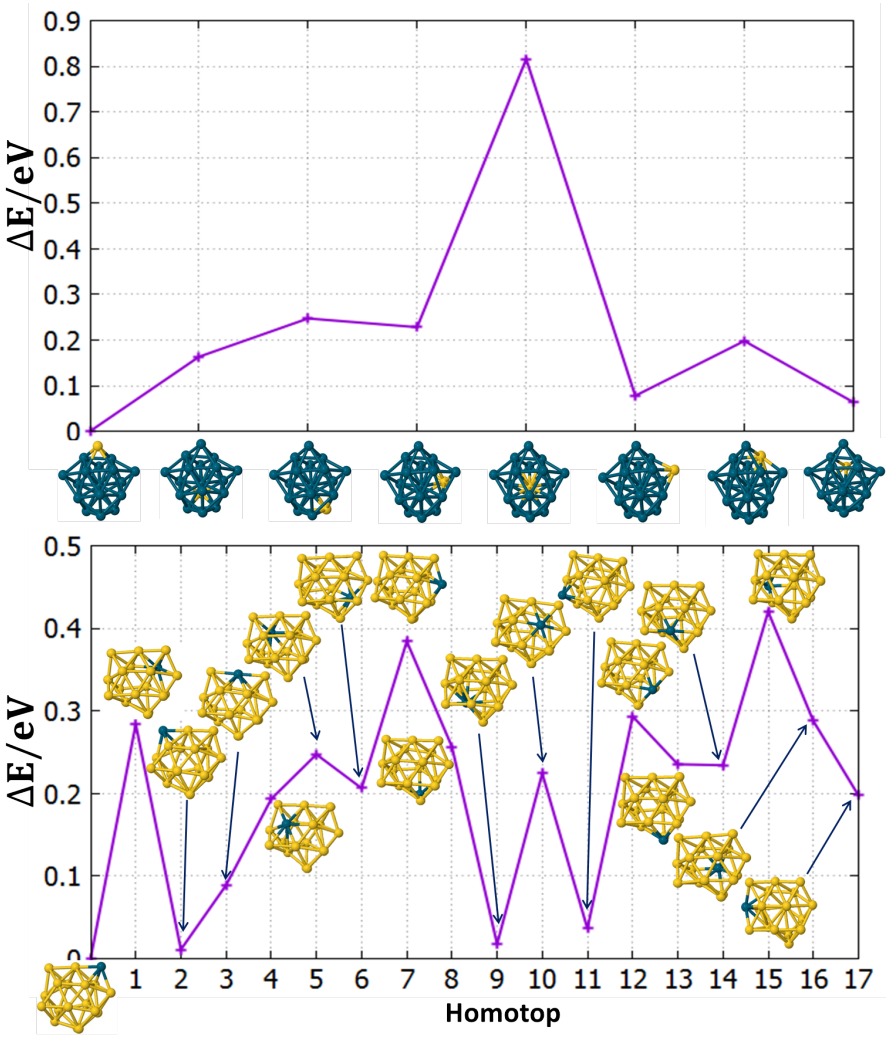

Figure (S9): The relative energies for all symmetry inequivalent homotops of Au_1Pd_{17} and $Au_{17}Pd_1$ clusters.

CHAPTER 4

STABILITY AND REACTIVITY OF MONO-CATIONIC PALLADIUM-DOPED GOLD SUBNANOMETRE CLUSTERS

4.1 Introduction

The catalytic application of ultra-small metallic particles is an emerging and increasingly developing area due to their high surface-to-volume ratios which provide and enhance distinct reactive properties along with an increased proportion of active sites which, can lead to alterations in their structural and electronic properties [1, 168–170]. Accordingly, metals which are catalytically inert on the bulk scale (or even at nanoscale), may become active on the subnanometre scale. For example, the inert bulk gold has shown high reactive properties in ultrasmall sizes, as previously evident and applied to CO oxidation reactions [171]. This has prompted the need to combine theory and experiment to understand the catalytic activity of the clusters. The higher catalytic activities of clusters on the subnanometre scale, relative to their larger counterparts, have helped to design more efficient catalysts with same type of homo-/hetero-geneous metals employed [48, 172, 173], and have led to cheaper catalysts [173].

The balance between stability, activity and selectivity is regarded as a challenging task for catalysts on both the nano- and subnanometre scales [174, 175]. However, this is a crucial requirement for industrial applications. While the elucidation of the stability

is not a trivial task in theory and is more complicated in practice, the selectivity and activity of a considerable number of metal particles have been effectively determined for particular reactions [170, 174, 176]. Doping a different type of metal atom into metal clusters and nanoparticles can enhance their stability, activity and selectivity [176–179]. Au_N, (N = 2-14), clusters have previously been shown an enhanced interaction with CO upon doping vanadium atoms because of the partially filled *d* orbitals of vanadium, which interact with the frontier filled and empty orbitals of CO, thus vanadium shows strong CO adsorption [177]. Stronger CO adsorption has been found when doping Pd atoms into smaller free Au_N (N = 2-3) clusters [178]. The enhanced reactivity has also been predicted for even-atom $Au_N{}^+$ ($N \leq 6$) clusters after doping a single atom of Pd [179]. Conversely, Cu, Ag and Y dopants were found to reduce the reactivity of Au clusters towards CO, due to the reduced (metal-CO) electron transfer which occurred upon doping [178, 180, 181].

In the following publications, we have established a systematic joint experimental and theoretical study to probe Pd dopant effects on both structure and stability (Publication 3) and reactivity with CO (Publication 4) of cationic gold clusters.

In Publication 3, we have combined photodissociation and decay channel analysis with DFT calculations to investigate the size dependent stability of palladium doped mono-cationic gold clusters. An excellent correspondence is obtained between experiments and computations, as the variation in abundance of the species found in the photofragmentation experiment is reproduced very well by the calculated second difference of energies. Fundamental questions related to simple and widely used concepts in physics, such as electron delocalization and quantum confinement are addressed. The enhanced stability of some clusters is explained in terms of the localization or delocalization of a *d* electron on the Pd atom. Theoretical search for the clusters, including those with enhanced stability, are introduced, explaining the "magic" sizes which are detected by mass spectrometry. The interplay between electronic shell structure and cluster geometry, as well as the modification of this shell structure by a Pd dopant atom, is understood - e.g. $PdAu_6^+$ is not strictly planar since the Pd atom occupies a site out of the plane defined by the six Au

atoms. Nevertheless, delocalization occurs mostly in the plane of the gold atoms and, therefore, a quasi-2D picture remains, as shown in Figure 4.1.

In Publication 4, we have presented a unique study combining mass spectrometric experiments, IR photodissociation spectroscopy, and DFT calculations to present a detailed examination of the Pd-doping influences on the interaction of one and two CO molecules on a series of mono-cationic gold clusters. The reactivity measurements and calculated binding energies have given a clear insight into the effect of a Pd dopant on the adsorption of CO. The unimolecular dissociation rates of CO are measured, indicating the reactivity of the cluster surface state. Under high-collision conditions, IR spectra are determined for cluster-CO complexes with one and two adsorbed CO molecules. Excellent correlation is found between the measured vibrational frequencies of CO and those calculated by theory, confirming the representative calculated structures and the preferred CO binding sites. The IR bands of the adsorbed CO molecules serve as a fingerprint of the preferred adsorption site.

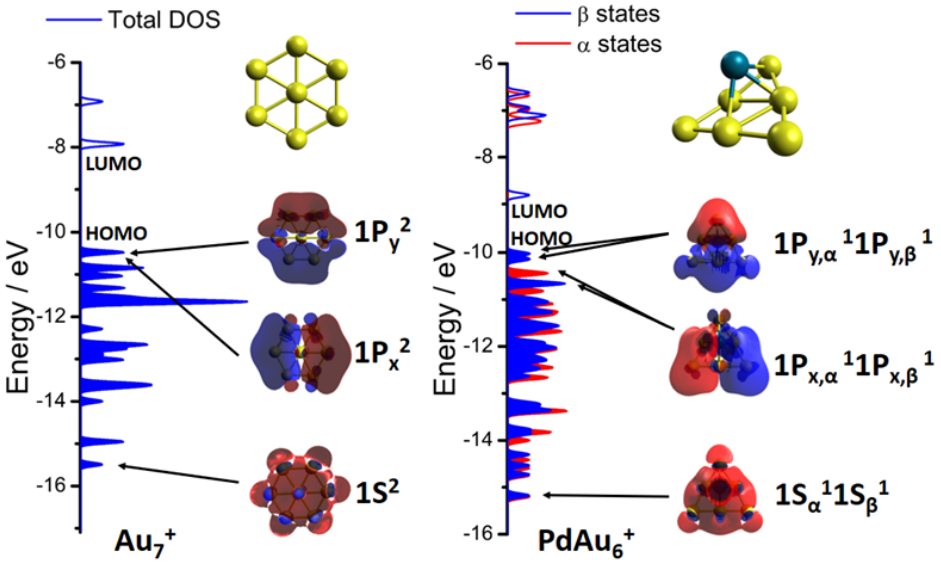

Figure 4.1: Total density of states of Au_7^+ (left) and $PdAu_6^+$ (right) clusters. Molecular orbitals of 1S and $1P_{x,y}$ character, corresponding to delocalized valence electrons, are plotted for each cluster. The HOMO-LUMO gap is shown.

4.2 Publication 3

Title

Effect of palladium doping on the stability and fragmentation patterns of cationic gold clusters

Authors

Piero Ferrari, Heider A. Hussein, Christopher Heard, Jan Vanbuel, Roy L. Johnston, Peter Lievens and Ewald Janssens

Journal Physical Review A

Volume 97

Pages 052508

DOI 10.1103/PhysRevA.97.052508

Submitted

12 December 2017

Published

21 May 2018

4.2.1 Author Contribution

The following publication is a collaborative work between groups at the Catholic University of Leuven (experiments) and the University of Birmingham (calculations). The au-

thor's contribution involved performing all global optimization calculations. All NWChem-DFT refinement calculations, including the minimizations and single-point energy calculations, were also performed by the author, except for the odd-atom clusters of Au_N^+, N≤13 and $PdAu_N^+$, N≤10, which were performed by Christopher Heard (Charles University, Prague). All the spin-states for all systems were optimised by the author. The simulation of all possible fragmentation channels were made by the author. The post-calculation analysis of the second differences in energies and dissociation energies were implemented by the author. The author contributed to the interpretation and discussion of the theoretical findings. The figures 2, 3b, 3d, 4b, and 4d were created by the author. The figures 5-8 in the paper and figure S1 in the supplemental material, were plotted based on the structures provided by the author. The tables of the calculated dissociation energies of the different fragmentation channels and XYZ coordinates of minimum-energy structures, which are listed in the supplemental material, were created by the author. The author wrote the computational part of section II, section IIIA and all results and discussions of the calculated dissociation energies in section IIIC.

Effect of palladium doping on the stability and fragmentation patterns of cationic gold clusters

P. Ferrari,[1] H. A. Hussein,[2,3] C. J. Heard,[4] J. Vanbuel,[1] R. L. Johnston,[2] P. Lievens,[1] and E. Janssens[1,*]

[1]*Laboratory of Solid State Physics and Magnetism, KU Leuven, 3001 Leuven, Belgium*

[2]*School of Chemistry, University of Birmingham, Edgbaston, Birmingham B15 2TT, United Kingdom*

[3]*Department of Chemistry, College of Science, University of Kufa, Najaf, Iraq*

[4]*Department of Physical and Macromolecular Chemistry, Charles University, 12843 Praha2, Czech Republic*

(Received 12 December 2017; published 21 May 2018)

We analyze in detail how the interplay between electronic structure and cluster geometry determines the stability and the fragmentation channels of single Pd-doped cationic Au clusters, $PdAu_{N-1}^+$ ($N = 2-20$). For this purpose, a combination of photofragmentation experiments and density functional theory calculations was employed. A remarkable agreement between the experiment and the calculations is obtained. Pd doping is found to modify the structure of the Au clusters, in particular altering the two-dimensional to three-dimensional transition size, with direct consequences on the stability of the clusters. Analysis of the electronic density of states of the clusters shows that depending on cluster size, Pd delocalizes one $4d$ electron, giving an enhanced stability to $PdAu_6^+$, or remains with all $4d^{10}$ electrons localized, closing an electronic shell in $PdAu_9^+$. Furthermore, it is observed that for most clusters, Au evaporation is the lowest-energy decay channel, although for some sizes Pd evaporation competes. In particular, $PdAu_7^+$ and $PdAu_9^+$ decay by Pd evaporation due to the high stability of the Au_7^+ and Au_9^+ fragmentation products.

DOI: 10.1103/PhysRevA.97.052508

I. INTRODUCTION

The search for stable cluster species has been an important subject in the study of small metallic clusters ever since the discovery that the stability of a cluster strongly depends on the number of constituent atoms. In 1984, Knight *et al.* [1] reported the surprising result that Na clusters composed of 8, 20, 40, and 58 atoms are significantly more stable than other sizes, describing them as "magic number" clusters. The observed stability pattern could be explained by phenomenological electronic shell models [2]. Electronic shells result from the confinement of delocalized valence electrons (one for each Na atom) within the small volume of the cluster. For a perfectly spherical "particle in a box," $1S$, $1P$, $1D$, $2S$, $1F$, $2P$, ... shells are formed, explaining the enhanced stability of the magic clusters, in the same way that noble gases are stable because of their closed electronic shells. The term "superatom" is sometimes adopted for this reason [3]. The geometry of most clusters, however, is quite different from a perfect sphere. A consequence of a lower structural symmetry is that electronic shell degeneracies are lifted, resulting in a subshell structure [4]. In quasi-two-dimensional (quasi-2D) structures, new magic numbers emerge by energetic destabilization of out-of-plane orbitals [5]. For example, six (closure of $1S$ and $1P_{x,y}$ shells) is a magic number for electrons that are confined in a two-dimensional triangular potential well [6]. The identification of stable clusters and the understanding of the interplay between localization and delocalization of valence electrons is of high importance for the development of novel applications using size-selected clusters.

Small gold clusters are ideal model systems to investigate the interplay between electronic magic numbers and cluster geometry. The heavy gold atom is subjected to strong relativistic effects, which reduce the $5d$-$6s$ energy separation, with direct consequences for the properties of gold clusters [7]. $5d$ electrons are partially involved in the bonding between the atoms and thus gold clusters adopt structures very different from clusters of other elements [8]. For example, ion mobility experiments have shown that negatively charged gold clusters are planar up to $N = 11$ [9], whereas recent calculations predicted that neutral species can be planar up to the surprisingly large number of 13 atoms [10]. For positively charged clusters, the 2D to 3D transition is known to take place at $N = 9$, with Au_8^+ the largest planar cluster [11].

These special features have consequences for the size-dependent stability pattern of gold clusters; electronic shell degeneracies associated with angular momentum are lost (while maintaining spin pairing) because of their rather asymmetric structures, and thus subshells open and close every time an atom (and, therefore, an electron) is added to the system. Hence, stability patterns of gold clusters depend strongly on size, possessing pronounced odd-even variations [12–14]. Interestingly, even though the hybridization between the d and s states in Au clusters is important, due to relativistic effects, simple electron counting rules for the valence electrons can explain their stability patterns quite well [15]. Another surprising feature of gold clusters is their reactivity. Even though bulk gold is one of the most noble elements of the periodic table, at the nano- and subnanoscale, Au particles become reactive and can act as catalysts for specific reactions, such as CO oxidation [16], methane activation [17], and hydrogen dissociation [18]. The stability of the catalyst is clearly of high importance.

*ewald.janssens@kuleuven.be

Doping can significantly influence the stability of a cluster; first, by altering the system's atomic structure, thus modifying the shape of the "box" confining the delocalized electrons, and second, by changing the number of valence electrons available for delocalization, which may lead to new shell closings [12,19,20]. From a fundamental point of view, Pd doping is a very interesting case for study because of its ground-state electronic configuration, with a closed $4d$ shell and no valence s electrons ($[\mathrm{Kr}]4d^{10}$). Photoelectron spectroscopy measurements on small Pd-doped anionic gold clusters, $\mathrm{PdAu}_N{}^-(N = 1–4)$, suggested that the Pd-dopant atom is excited to a $[\mathrm{Kr}]4d^9 5s^1$ state, after which the Pd valence s electron is delocalized and participates in the metallic bonding [21]. In addition, density functional theory (DFT) calculations on several cluster sizes in different charge states have shown that Pd doping can strongly influence both the atomic and the electronic structures of gold clusters [22–24]. Here we study the effect of Pd doping on the size-dependent stability of gold clusters. Pd doping is also interesting from a more applied point of view. Various studies have shown the influence of Pd in diverse properties of Au clusters, such as a quenching effect of the optical absorption in the visible range [25,26], an increase in the adsorption energies of molecules such as CO and O_2 [27], or an enhancement of the catalytic properties toward a variety of reactions [28–30]. Moreover, significant efforts have been devoted to the production and study of the properties of monolayer-protected Pd-doped Au clusters [31–35]. In all these clusters, the modification of the electronic structure upon doping plays a major role.

In this work, we combine mass spectrometric experiments with DFT calculations to investigate the effect of Pd doping on the stability patterns and the electronic structures of cationic $\mathrm{Au}_N{}^+$ ($N = 2–20$) clusters. The stability patterns of the pure and doped clusters as well as the preferred fragmentation channels are studied by photofragmentation. An extensive search for minimum-energy structures was conducted using DFT. The computational results are compared with the experimental findings, allowing better insight into the interplay between geometry and electronic structure of the clusters and the consequences thereof for their relative stability.

II. METHODS

A. Mass spectrometric experiments

Pure and Pd-doped $\mathrm{Au}_N{}^+$ clusters are produced by laser ablation and inert gas condensation. Their size distribution is analyzed by time-of-flight mass spectrometry, in a setup described in detail in Ref. [36]. A molecular beam containing both charged and neutral clusters is produced, but charged species are electrostatically removed from the beam. Only neutral species enter the mass spectrometer, where they are excited by a tightly focused excimer F_2 laser ($\lambda = 157$ nm), which triggers ionization and fragmentation. While the abundance distribution of clusters as produced in the source is strongly influenced by production conditions, such as ablating laser energy and carrier gas pressure, this is different for the spectra recorded after photofragmentation. The abundance of a specific cluster size relative to neighboring sizes in a photofragmentation experiment is sensitive to the relative dissociation energy of that cluster, and thus reflects its relative stability [37,38].

B. Theoretical calculations

An extensive search for minimum-energy structures (at the DFT level of theory) was performed for monometallic $\mathrm{Au}_N{}^+$ and Pd-doped $\mathrm{PdAu}_{N-1}{}^+$ clusters, in the extended $N = 2–20$ size range. This search was carried out using the Birmingham Parallel Genetic Algorithm (BPGA) [39,40], which employs a pool methodology to evaluate structures in parallel. In each run, multiple BPGA instances are implemented and, in each instance, a set of processes is run in parallel and independently [41,42]. First, numerous random geometries are generated to form a population [43]. Then, the generated structures of a given population are relaxed, followed by crossover and mutation operations being performed on individuals in the population. The newly generated structures are locally energy minimized at the DFT level and then the highest-energy isomers are replaced by any lower-energy isomers among the set of offspring and mutants. All the local energy minimizations mentioned above were conducted with Gamma-point DFT calculations employing the Vienna ab initio Simulation Package (VASP) [44]. Projected-augmented wave (PAW) pseudopotentials were used, with the generalized gradient approximation (GGA) Perdew-Burke-Ernzerhof (PBE) exchange-correlation functional [45,46]. A plane-wave basis set was implemented including spin polarization. The plane-wave cut-off energy was truncated at 400 eV. Methfessel-Paxton smearing, with a sigma value of 0.01 eV, was implemented to improve convergence [47]. The thresholds for the electronic energy and forces were set to 10^{-6} eV and 10^{-5} eV/Å, respectively. Spin states were optimized within VASP independently for each generated global minimum from BPGA. All clusters were found to exhibit the lowest possible spin state in the optimal electronic configurations. Finally, the energies of the lowest-energy VASP structures were recalculated using spin-unrestricted density functional calculations within the NWCHEM software package [48], employing the long-range-corrected LC-ωPBEh exchange-correlation functional and the extensive def2-TZVPP basis set within the corresponding effective core potential (def2-ECP) of Weigend and Ahlrichs [49–51].

III. RESULTS AND DISCUSSION

A. Photofragmentation results

Mass spectra of pure $\mathrm{Au}_N{}^+$ and doped $\mathrm{PdAu}_{N-1}{}^+$ clusters after photofragmentation are shown in Fig. 1. Stability patterns are clearly visible. For monometallic Au clusters, strong odd-even alterations in intensity are present, with higher intensities for clusters with an odd number of atoms (even number of $6s$ electrons). This pattern has been observed previously and is well understood in terms of the electronic shell model [2,12]. Two distinct maxima are seen for the photofragments $\mathrm{Au}_7{}^+$ and $\mathrm{Au}_9{}^+$, which possess stable closed electronic shells with six and eight delocalized electrons, respectively (see discussion later) [4,6]. For positively charged gold clusters, the 2D to 3D transition takes place at size $N = 9$, with $\mathrm{Au}_8{}^+$ being the largest planar cluster [11]. Additional, low-intensity signals on

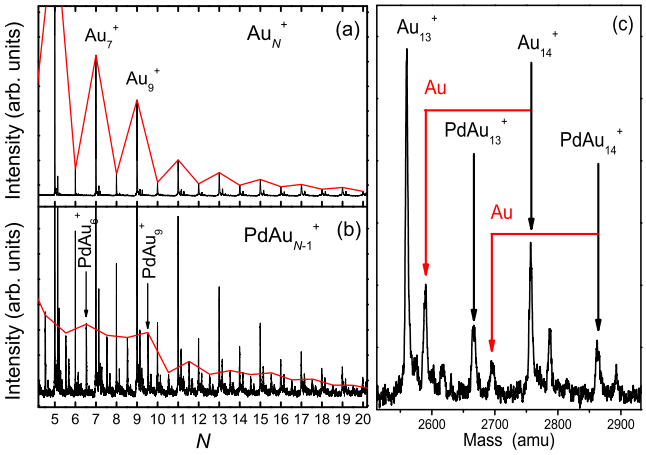

FIG. 1. Mass abundance spectra of clusters after photofragmentation with a tightly focused F_2 excimer laser ($\lambda = 157$ nm). (a) Au_N^+ clusters. (b) $PdAu_{N-1}^+$ clusters. Peaks are connected by a red line as a guide for the eye to visualize the size-to-size variations in intensity. (c) Zoom-in on (b) highlighting the pathways for metastable fragmentation of Au_{14}^+ and $PdAu_{14}^+$.

the right-hand side of each Au_N^+ cluster in the mass spectrum correspond to metastable fragments, as discussed later.

The mass spectrum of photofragmented $PdAu_{N-1}^+$ clusters [see Fig. 1(b)] demonstrates that the stability pattern is significantly altered by Pd doping. The most pronounced intensity drop is now found after size $N = 10$, instead of after $N = 9$ for the monometallic Au_N^+ clusters. This suggests that $PdAu_9^+$ has a relatively enhanced stability. Odd-even oscillations are seen in the abundances, but are less pronounced than for the monometallic gold clusters. For $N > 8$, the higher intensities are found for $PdAu_{N-1}^+$ clusters composed of an even number of atoms, while for Au_N^+ odd-N sizes are most intense. Replacing an odd-electron Au atom by an even-electron Pd atom means that even-N cationic clusters now have an even number of valence electrons. Interestingly, this odd-even pattern is broken below $N = 8$, with a local intensity maximum at $PdAu_6^+$, a cluster containing an odd number of atoms (and electrons).

Following multiple photon absorption, the internal energy of a cluster increases significantly, triggering fragmentation as a cooling (relaxation) mechanism [52]. Initially, fragmentation proceeds at a very high rate and thus the first fragmentation step takes place on a much faster time scale than the time scale of the time-of-flight mass spectrometry experiment (which is of the order of several microseconds). The photoexcited clusters are thus accelerated with the mass of those "instantaneous" fragmentation products. If no additional fragmentation steps occur before detection, the fragment is denoted as "prompt." These instantaneous or prompt fragments correspond to the species with the higher intensities in Fig. 1 and their size-to-size intensity variations reveal the electronic shell structure, as discussed above. Besides these prompt fragments, some clusters present in the molecular beam after photoexcitation are metastable. Such a cluster is the product of subsequent fragmentation steps, taking place on much longer time scales than prompt fragmentation because the internal energy of the cluster is now much lower [53]. A metastable fragment is recognizable in the mass spectrum as an additional peak next to the prompt clusters, as shown in Fig. 1(c). The apparently different mass of a metastable cluster is just a consequence of the fact that fragmentation taking place in free flight slightly changes the time of flight of the ion in the reflectron of the mass spectrometer (see Supplemental Material [54] for details).

Even though cluster stabilities can be investigated by the intensity of prompt fragments in a mass spectrum, information about the decay channel producing the fragments cannot be obtained by this approach. This is because the time of flight of a prompt fragment only depends on its mass after fragmentation. However, this is different for a metastable cluster, with a time of flight that depends on both the flight times of mother and daughter ions in the fragmentation process [53]. An example can be found in Fig. 1(c), which shows a zoom-in in Fig. 1(b). For instance, the decay channel $Au_{14}^+ \rightarrow Au_{13}^+ + Au$ leads to a metastable peak next to the prompt Au_{13}^+ cluster. Similarly, the fragmentation channel $PdAu_{14}^+ \rightarrow PdAu_{13}^+ + Au$ is identified by the presence of a metastable fragment visible after the prompt $PdAu_{13}^+$ cluster. A metastable fragment produced by the channel $PdAu_{14}^+ \rightarrow Au_{14}^+ + Pd$ would show in between the prompt Au_{14}^+ and the metastable Au_{15}^+ peaks, which is not observed. Thus, depending on the flight time of the metastable clusters, the decay channels can be identified.

B. Theoretical results

The lowest-energy structures obtained for Au_N^+ and $PdAu_{N-1}^+$ ($N = 2-20$) are shown in Fig. 2 and Cartesian coordinates are provided as supporting information. The cationic pure Au_N^+ geometries can be identified as planar fragments of hexagonal layers for N up to 8 atoms, 3D relaxed fcc bulk fragments for $N = 9-13$, and 3D hollow cage structures for $N = 14-20$. The obtained structures agree well with those found by combined ion mobility experiments and DFT calculations (in the $N < 14$ size range) [11], except for Au_8^+. For Au_8^+, a planar structure is predicted as the global minimum in our calculations, whereas the experiment assigned a 3D isomer as the species present in the molecular beam. Similar findings have been found elsewhere [55]. This 3D isomer has a relative energy of 0.023 eV in our calculations. Although this energy lies within the accuracy of DFT, possibly explaining the discrepancy, another possibility is that the ground-state structure is not the cluster produced in the experiment. Additional theoretical studies on the structures of cationic Au clusters can be found in the literature, although not for the entire size range presented here. Previously reported global minima agree in general with our results [56–59]. Compared with our recent global optimizations of neutral palladium-gold clusters [10,60], there is a significant effect of charge on the structural patterns. Losing one electron in pure neutral Au_N clusters is responsible for a shift of the 2D-3D crossover from $N = 14$ down to $N = 9$ [10,60,61].

Pd doping significantly alters the structures of the cationic Au clusters. The most remarkable structural change is the large decrease in the 2D to 3D transition size, which for the doped clusters is at the smallest possible size: $N = 4$. $PdAu_3^+$ has a tetrahedral geometry and all larger Pd-doped clusters are three dimensional, in clear contrast with Au_N^+.

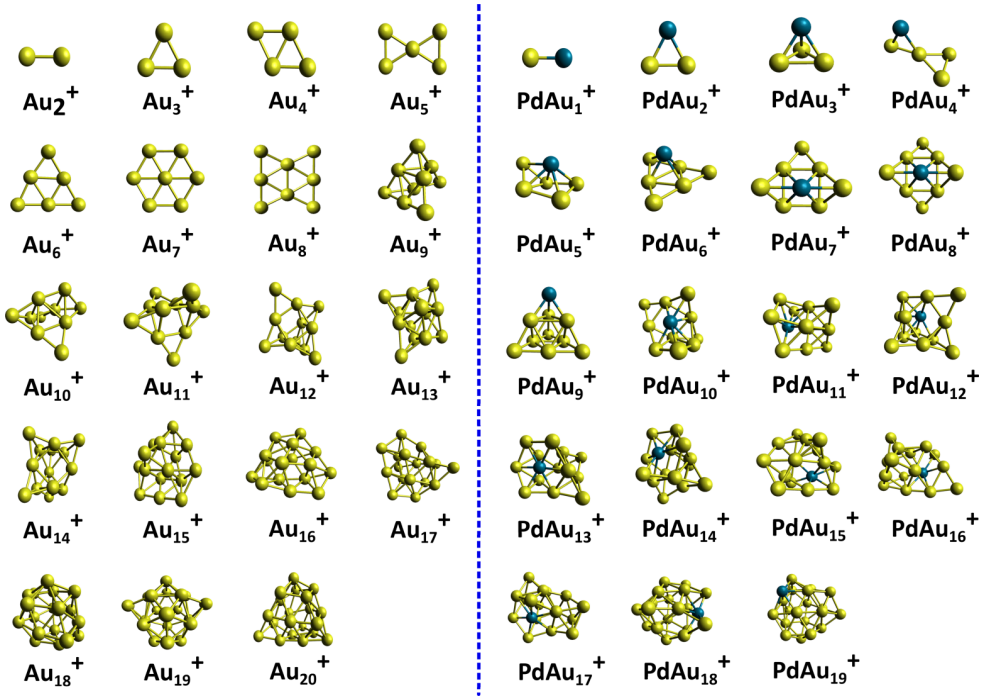

FIG. 2. Minimum-energy structures of Au_N^+ and $PdAu_{N-1}^+$ ($N = 2$–20) clusters. Au atoms are represented in yellow and Pd in blue.

This dopant-induced dimensional transition is consistent with previous studies [23,24]. Our predicted isomers satisfactorily concur with those presented by previous theoretical studies on Pd-doped Au clusters up to six atoms [25,62,63]; however, two differences are observed in the case of $PdAu_4^+$ and $PdAu_5^+$ clusters. Our $PdAu_4^+$ structure is found to show a 3D "twisted bow tie" as previously reported in Ref. [25], which does not agree with the M-like planar structure proposed in Ref. [63] or with the trigonal bipyramid structure suggested in Ref. [62]. The global minimum of $PdAu_5^+$ is found to be a capped square-based pyramid, while an edge-bridged trigonal bipyramid was previously proposed as the ground-state structure for this cluster [62]. For larger $PdAu_m^+(m > 6)$ clusters, we are unaware of theoretical or experimental studies to identify their detailed structures. For all sizes, the Pd atom occupies a high-coordination site in or close to the center of the cluster, as previously observed for the neutral species [10,60].

C. Stability patterns

Under the assumption that an evaporative decay chain proceeds through successive emission of monomers, the quantity $\ln(I_N/I_{N+1})$, with I_N corresponding to the intensity of cluster size N, provides information about relative stabilities [37,38]. This is different from the case in which cluster distributions are produced by a thermodynamic (quasi)equilibrium between growth and dissociation [4]. Values of $\ln(I_N/I_{N+1})$, as a function of cluster size, are plotted in Fig. 3 for the monometallic Au_N^+ [Fig. 3(a)] and doped $PdAu_{N-1}^+$ [Fig. 3(c)] clusters. From this figure, the previously mentioned size-to-size patterns can be discussed quantitatively; strong odd-even oscillations are found for Au_N^+, with pronounced maxima for Au_7^+ and Au_9^+, and local maxima for clusters composed of an odd number of atoms (even number of valence electrons). For the doped species, a maximum is found for $PdAu_9^+$, after which odd-even variations are present, with local maxima for clusters composed of an even number of atoms. For clusters smaller than $PdAu_8^+$, the pattern changes and a local maximum appears at $PdAu_6^+$. The reason for the deviation from the odd-even alternation in the $N = 6$–8 region for the Pd-doped clusters (both from theory and experiment) will be discussed later.

The observed stability pattern of the $PdAu_{N-1}^+$ clusters (with $N > 8$) can be described in terms of the electronic shell model. Assuming that all d electrons of the Pd-dopant atom (electronic configuration [Kr]$4d^{10}$) remain localized and that each Au atom delocalizes its $6s$ electron (one of which is lost in the cationic charge state), clusters with an even number of atoms have an even number of delocalized electrons and correspond to closed shells of itinerant electrons. In this interpretation, the stability maximum for $PdAu_9^+$ corresponds to a 3D magic number of electrons (eight), provided that $PdAu_9^+$ indeed has a 3D geometry, as the DFT calculations suggest (see Fig. 2). The stability pattern observed below $N = 8$ is less easy to interpret and requires a detailed analysis of the electronic structure of the clusters.

Information on the stability of a cluster relative to the neighboring sizes can be obtained from theory by calculating the second difference in energy ($\Delta_2 E$). For a cluster of size N, this quantity is defined as

$$\Delta_2 E = E(A_{N+1}^+) + E(A_{N-1}^+) - 2E(A_N^+), \qquad (1)$$

where A_N^+ is the cluster composed of N atoms and $E(A_N^+)$ is its total electronic energy. With this definition of $\Delta_2 E$, a cluster which is more stable than its closest neighbors has a positive $\Delta_2 E$ value. This quantity, as a function of cluster size, is plotted in Fig. 3 for Au_N^+ [Fig. 3(b)] and $PdAu_{N-1}^+$ [Fig. 3(d)].

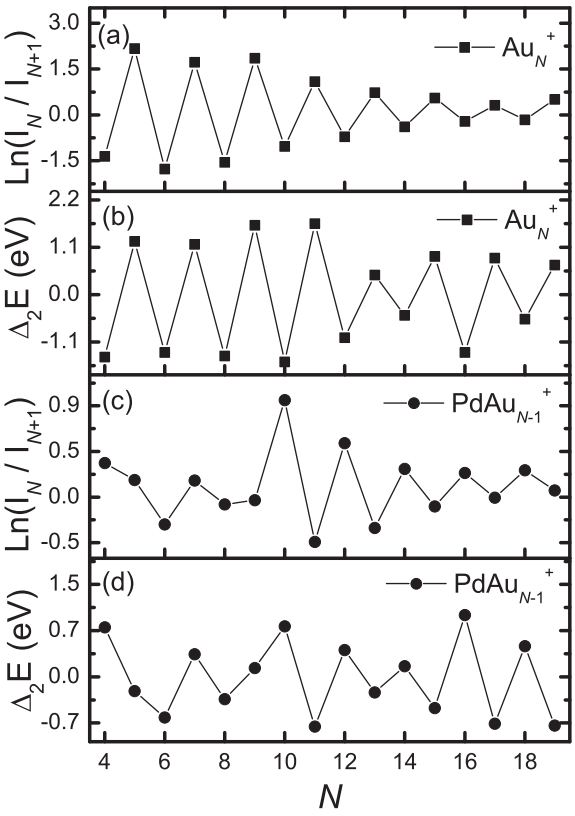

FIG. 3. Relative stability patterns of Au_N^+ and $PdAu_{N-1}^+$ clusters. Experimentally, stabilities are quantified by the quantity $\ln(I_N/I_{N+1})$, presented in (a) for Au_N^+ and in (c) for $PdAu_{N-1}^+$. Theoretically, relative stabilities are characterized by second differences in energy ($\Delta_2 E$), obtained from the density functional theory calculations. These are shown in (b) for Au_N^+ and in (d) for $PdAu_{N-1}^+$.

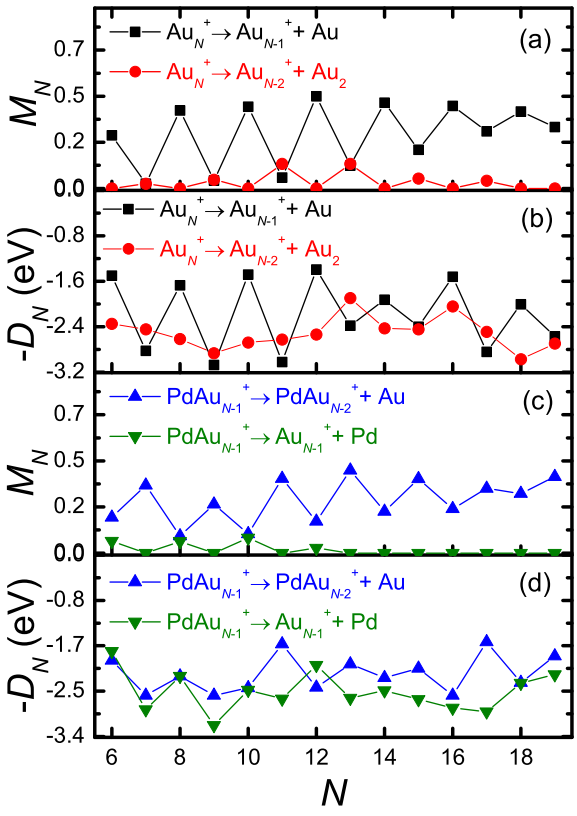

FIG. 4. Metastable fractions (M_N) obtained by the photofragmentation experiments. (a) Metastable fraction corresponding to monomer or dimer evaporation for the monometallic Au_N^+ clusters. (c) Metastable fraction corresponding to Au or Pd evaporation for $PdAu_{N-1}^+$ clusters. (b) Dissociation energies, as calculated by DFT, for monometallic Au_N^+ clusters corresponding to the removal of a neutral monomer or dimer. (d) Dissociation energies, as calculated by DFT, for Pd-doped $PdAu_{N-1}^+$ clusters corresponding to the removal of a neutral Au or Pd atom.

The abundance variations found in the photofragmentation experiment are reproduced very well by $\Delta_2 E$. Important features are as follows: (i) odd-even oscillations are present for all the Au_N^+ clusters, with higher stability for clusters composed of an odd number of atoms. (ii) Maxima are seen for Au_9^+ and Au_7^+. (iii) Upon Pd doping, odd-even oscillations are present for $N > 8$, with maxima for even N. (iv) The most pronounced maximum for the Pd-doped clusters corresponds to $PdAu_9^+$. (v) The odd-even pattern is broken for the Pd-doped clusters when $N < 8$, with a local maximum at $PdAu_6^+$. Taking into account the assumptions underlying Eq. (1), the agreement between theory and experiment is exceptional.

The decay channels for the fragmentation of Au_N^+ and $PdAu_{N-1}^+$ clusters, investigated through the measurement of metastable fragments, are compared in Fig. 4. Metastable fragmentation, as a function of cluster size, is characterized by the ratio of the intensity of metastable to prompt clusters of the same size (M_N). The decay channels of monometallic Au_N^+ clusters are known [12]; depending on cluster size, dimer loss competes with monomer evaporation. Figure 4(a) shows that Au_N^+ clusters composed of an even number of atoms decay only by monomer evaporation, whereas those composed of an odd number of atoms decay by both channels. This odd-even pattern in the decay channels of the clusters can be explained by their stability. When N is even, monomer evaporation is the preferred channel so that the fragmentation product is an odd-atom cationic cluster with a closed electronic shell (even number of electrons). Conversely, if N is odd, dimer evaporation is the channel which generates a closed-shell fragment cluster. For the Pd-doped clusters, no dimer evaporation is observed (above the noise level of the measurement), while Pd monomer evaporation is a competitive decay channel with Au evaporation for some sizes. Figure 4(c) shows the metastable fractions for the doped $PdAu_{N-1}^+$ clusters. Pd evaporation is observed for $PdAu_5^+$, $PdAu_7^+$, $PdAu_9^+$, and $PdAu_{11}^+$. This additional channel is especially competitive for $PdAu_7^+$ and $PdAu_9^+$, in which cases Pd loss generates the stable closed-shell Au_7^+ (6 electron) and Au_9^+ (8 electron) clusters, respectively. For all other clusters, Au monomer evaporation is the only observed decay channel. It worth nothing that in Fig. 4, information on decay channels is only presented for $N \geqslant 6$. The small heat capacity of cluster sizes $N < 6$ strongly suppresses metastable fragmentation.

The decay channels obtained from the experimental metastable fractions M_N can be compared with dissociation energies calculated by DFT, which are also shown in Fig. 4(b)

for Au_N^+ and Fig. 4(d) for $PdAu_{N-1}^+$. The dissociation energy D_N, of a cluster A_N^+ emitting a neutral fragment A_M, is defined as

$$D_N = E(A_{N-M}^+) + E(A_M) - E(A_N^+). \quad (2)$$

In these calculations, the reactant (A_N^+) and product (A_{N-M}^+) cluster ions are the lowest-energy structures found in our BPGA search (Fig. 2) and have energies calculated by reoptimization with NWChem. The neutral atomic or diatomic fragments emitted ($A_M, M = 1$ or 2) have also been energy minimized with NWChem. Only neutral monomers and dimers are considered in this analysis because the ionization energies of Au, Pd, Au_2, and PdAu are all significantly higher than those of the larger gold and Pd-doped gold clusters. Thus, the lower-energy dissociation channels will be those where the positive charge resides on the larger cluster fragments, rather than on the evaporated monomers or dimers. The calculated D_N's for the monomer and dimer evaporation channels of Au_N^+ and $PdAu_{N-1}^+$ clusters are listed in the Supplemental Material [54].

Considering the monomer decay channel of Au_N^+ clusters, a comparison of Figs. 4(a) and 4(b) shows excellent correlation between the measured metastable fractions (M_N) and the calculated dissociation energies (D_N). In the figure, the comparison is facilitated by plotting the opposite of D_N since in the simpler case in which fragmentation proceeds mainly by one channel, a high (low) value of D_N corresponds to a lower (higher) degree of metastable fragmentation. Turning to the dimer decay channel, we note that D_N values for dimer loss are significantly higher than those for monomer loss for even values of N, which is consistent with the experimental finding that dimer evaporation is not observed for even N. For odd values of N, dissociation energies for monomer evaporation are high, reflecting the stability of these even-electron closed-shell species. As the Au_2 dimer has an even number of electrons, dimer loss from a closed-shell cluster cation with an odd number of atoms generates a fragment which is also closed shell. Therefore, dissociation energies for dimer loss are mostly calculated to be lower than those for monomer evaporation, which is consistent with both decay channels being observed experimentally for odd N.

The calculated dissociation energies for monomer evaporation (loss of a single Au or Pd atom) from $PdAu_{N-1}^+$ are shown in Fig. 4(d). The D_N plot for Au loss shown in Fig. 4(d) does not exhibit the pronounced odd-even alternation observed experimentally for M_N in Fig. 4(c), though D_N values for Au evaporation are generally lower than for Pd evaporation, which is consistent with the experimental predominance of the Au evaporation channel. In contrast, a clear odd-even alternation in D_N is calculated for the evaporation of a Pd atom up to $N = 15$, with larger D_N for odd N. For the Pd-doped clusters, a direct quantitative comparison between the experimental M_N fractions and the calculated D_N energies is not possible. Because the Pd-doped species have a complicated competition between the emission of different types of atoms, deriving an equation directly linking M_N with D_N is not possible [12]. However, a good prediction of the energetically most favorable fragmentation channels and for which cases Pd loss will compete with Au emission is achieved. As shown in Fig. 4(d),

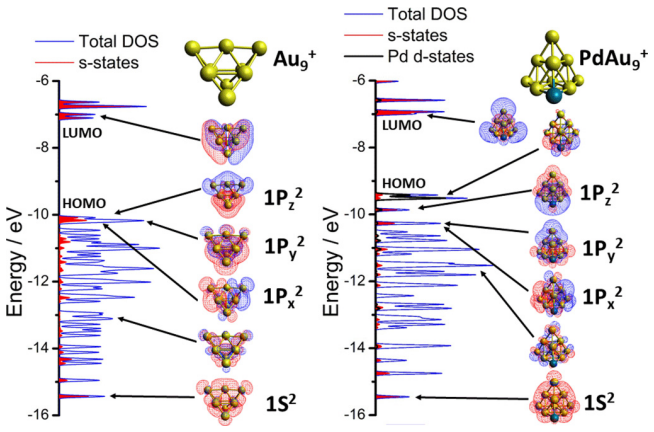

FIG. 5. Total density of states (blue line) of Au_9^+ (left) and $PdAu_9^+$ (right) clusters. The projection onto atomic *s* states is shaded red, whereas the projection onto Pd *d* states is shaded black. Molecular orbitals in which the electron density extends over the entire cluster are plotted and labeled based on their nodal character ($1S$ and $1P_{x,y,z}$). In addition, a molecular orbital in which a higher electron density on the different atoms and a zero or close-to-zero electron density in between the atoms of the cluster is identified. The HOMO and LUMO levels are labeled.

$PdAu_{N-1}^+$ clusters with even N generally have similar D_N energies for Au and Pd loss, in good agreement with the experimental M_N fractions of Fig. 4(c). This is particularly noticeable for $PdAu_7^+$ ($N = 8$) and $PdAu_9^+$ ($N = 10$), in which Pd evaporation competes so that the very stable clusters Au_7^+ and Au_9^+ are formed. According to the fragmentation experiments, there is no clear evidence for the evaporation of Au_2 or PdAu dimers from the Pd-doped clusters. As this may be due to experimental sensitivity problems, we have calculated the dissociation energies for evaporation of Au_2 and PdAu from $PdAu_{N-1}^+$ (see Supplemental Material [54]). In most cases, calculations indicate that D_N for dimer loss are higher than for monomer evaporation, with Au_2 loss favored over AuPd. It should be noted, however, that the calculated D_N for the evaporation of Au_2 from $PdAu_5^+$ is only 1.81 eV. In fact, the calculated energies for the evaporation of Au and Pd atoms and the Au_2 dimer from $PdAu_5^+$ are very similar, lying in the range 1.81–1.99 eV, so all three fragmentation channels may be competitive.

D. Electronic structure and magic numbers

In the extended size range studied, four clusters are particularly interesting in view of their apparent higher stability: Au_9^+, $PdAu_9^+$, Au_7^+, and $PdAu_6^+$. To understand why these clusters exhibit higher stability than the other species, a detailed analysis of their electronic structures was performed.

The 5*d* states in gold clusters are significantly hybridized with the valence 6*s* states [7]. As a result, the use of simple electron-counting rules to interpret the size-dependent stability of gold clusters is more complicated than, for example, for Na clusters. This is illustrated in the left panel of Fig. 5, showing the total density of states (DOS) of Au_9^+. Below the highest occupied molecular orbital (HOMO), many states form a dense band, composed of hybridized *d* and *s* states,

as a projection of the DOS reveals. At the top and bottom of this band, however, four states with high s character are found, i.e., at around −10 eV (three states) and −15.5 eV (one state). Inspection of these MOs show wave functions delocalized over the entire cluster that, based on their nodal character [20], can be classified as the $1S$ and $1P_{x,y,z}$ eigenstates of the "particle in a spherical box" [64]. These MOs are plotted in the figure, together with a (randomly chosen) MO of mainly d character, in which there is electron density localized on each atom of the cluster ("localized" here implies a MO with higher density on the different atoms and a zero or close-to-zero electron density in between the atoms). The doubly occupied $1S$ and $1P_{x,y,z}$ MOs (total of eight delocalized electrons) in the three-dimensional Au_9^+ cluster form a closed electronic shell structure, providing enhanced stability for the cluster. It is worth mentioning that in a potential with perfect radial symmetry, the $1P_x$,$1P_y$, and $1P_z$ eigenstates are degenerate; however, because of the reduced symmetry of the actual cluster structure, as compared to a sphere, the degeneracy of the $1P_{x,y,z}$ states is lifted (apart from in cubic and icosahedral point groups) so these three orbitals have slightly different energies in the cluster DOS [65].

The case of $PdAu_9^+$, presented in the right panel of Fig. 5, is similar to that of Au_9^+. Between −10.5 and −15 eV, many states of mainly d character form a dense band, with states of larger s contribution located below and above it. These states with large s contribution are delocalized over the entire cluster and can, based on their nodal character, be classified as the $1S$ and $1P_{x,y,z}$ MOs. In addition, a projection of the total DOS onto Pd d states (black shading) reveals minor Pd(d)-Au(d) hybridization and almost no Pd(d)-Au(s) hybridization. This supports the picture that in $PdAu_9^+$, the Pd remains with all its $4d^{10}$ electrons localized, whereas each Au atom delocalizes its $6s$ electron, giving a total of eight delocalized electrons. Interestingly, above the $1P_z$ MO, two occupied orbitals of mainly Pd(d) character are located, one of which is the highest occupied molecular orbital (HOMO) of the cluster. These states are poorly hybridized with Au(d) states due to a poor energy overlap, reducing the HOMO–lowest-unoccupied molecular orbital (LUMO) gap of $PdAu_9^+$ as compared to Au_9^+.

A similar analysis of the cluster DOS was performed for Au_7^+ and $PdAu_6^+$ and is presented in Fig. 6. The lowest-energy isomer of Au_7^+ (left panel of the figure) has a two-dimensional centered-hexagonal structure. This cluster has three doubly occupied MOs in which the wave function is delocalized over the entire cluster, resembling the lowest three eigenfunctions of a "particle in a circular box," based on their nodal character ($1S$ and $1P_{x,y}$) [5]. In a 2D cluster, the $1P_z$ orbital cannot be generated from a basis of s-type atomic orbitals so the electronic shell closure after filling $1S$ and $1P_{x,y}$ corresponds to six electrons [6,66]. In fact, the LUMO state of Au_7^+ resembles the 1D eigenstate of the particle in the circular box. Using the itinerant electron picture, each Au atom delocalizes its $6s$ electron, providing Au_7^+ with six itinerant electrons and enhanced stability. Similar arguments have been used to explain the high relative stability of specific flat boron clusters of different charge states [67,68].

Finally, we discuss the interesting case of $PdAu_6^+$ (right panel of Fig. 6). As for the previous clusters, the DOS is formed by a dense band of mainly d character (the d band),

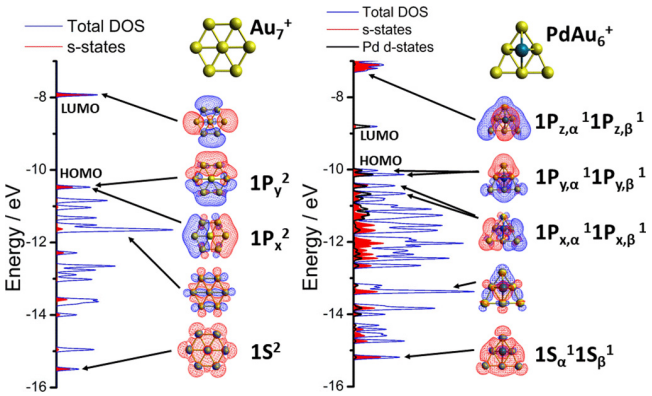

FIG. 6. Total density of states (blue line) of Au_7^+ (left) and $PdAu_6^+$ (right) clusters. A projection into atomic s states is shaded red, whereas a projection onto Pd d states is shaded black. Molecular orbitals in which the electron density extends over the entire cluster are plotted and labeled based on their nodal character ($1S$ and $1P_{x,y,z}$). In addition, a molecular orbital in which a higher electron density on the different atoms and a zero or close-to-zero electron density in between the atoms of the cluster is identified. The HOMO and LUMO levels are labeled.

and six orbitals (counting α and β orbitals for this odd-electron cluster) with a higher s contribution. A plot of these states reveal MOs delocalized over the entire cluster, resembling the $1S$ and $1P_{x,y}$ eigenstates of the particle in a triangular box, based on their nodal character [6]. These states are doubly occupied, suggesting, in the itinerant electron model, that Pd delocalizes one of its $4d^{10}$ electrons. Thus, $PdAu_6^+$ has a total of six itinerant electrons, with a closed 2D electronic shell and enhanced stability. A similar conclusion was drawn from photoelectron spectroscopy measurements on small anionic $PdAu_N^-$($N = 1$–4) clusters [21]. The very similar photoelectron spectra observed for anionic gold clusters and their Pd-doped equivalents suggested that in the doped clusters, one $4d$ Pd electron is promoted to a $5s$ electronic level and participates in the bonding with Au. A projection of the DOS of $PdAu_6^+$ onto Pd d states shows a very strong hybridization between Pd(d) and Au(s)-Au(d) states. In particular, the $1P_x$ and $1P_y$ MOs of the cluster possess a significant percentage of Pd(d) character, in clear contrast to the case of $PdAu_9^+$. This supports the simple picture that Pd donates one of its d electrons for delocalization and shell closing in the $PdAu_6^+$ cluster.

It should be noted, however, that the lowest-energy isomer of $PdAu_6^+$ is not strictly two dimensional since the Pd atom occupies a site out of the plane defined by the six gold atoms. Nevertheless, delocalization takes place mostly in the plane of the Au atoms, and thus a quasi-2D picture remains: this can be understood by the well-known high stability of the neutral Au_6 2D triangular cluster [60]. $PdAu_6^+$ can, therefore, reasonably be described as $(Pd^+)Au_6$. In $PdAu_6^+$, the $1P_z$ orbital (which is now possible due to the overall 3D topology) is destabilized, opening a significant HOMO-LUMO gap in the system's DOS. This gap, however, is smaller than in Au_9^+ since, as shown in the figure, the LUMO state is a MO of mainly Pd(d) character, which is poorly hybridized with Au(d) due to a poor energy overlap with the Au d band. The enhanced

stability of the odd-electron $PdAu_6^+$ cluster, which is due to the even-electron nature of the Au_6 triangle, is manifested in the local maximum in the second difference plot for $PdAu_6^+$ [Fig. 3(d)]. This also explains the reduced stability (relative to neighboring sizes) of the even-electron species $PdAu_5^+$ and $PdAu_7^+$, as predicted by the DFT calculations [Fig. 3(d)] and confirmed by the experiments [Fig. 3(c)].

An interesting comparison that enables a better understanding of the enhanced stability of $PdAu_6^+$ is the analysis of an isomer resembling the quasicircular structure of Au_7^+, comprising an Au hexagon with the Pd dopant at the center. A detailed analysis of this isomer, with a relative energy of +0.6 eV compared to the ground state, is presented in Appendix B. Remarkably, even though the Pd sits in the same plane as the Au framework, there is very weak hybridization between the Pd(d) and the Au(d)-Au(s) states, similar to the situation in $PdAu_9^+$. As a consequence, of the MOs which are delocalized over the entire cluster, only the $1S$ and $1P_x$ MOs are doubly occupied, whereas the $1P_y$ orbital is singly occupied. This implies a total of five itinerant electrons. Therefore, geometry has a determining role in the enhanced stability of $PdAu_6^+$, allowing good hybridization of the d states of Pd with the s and d bands of Au only for the 3D isomer.

It is interesting to consider how much electron correlation and relativistic effects determine the stability patterns observed in these clusters. To address this, calculations were performed on the four clusters Au_9^+, $PdAu_9^+$, Au_7^+, and $PdAu_6^+$ using single-determinant Hartree-Fock (HF) theory, in which electron correlation and relativistic effects are excluded. At the HF level, MOs which are delocalized over the entire cluster can be found in the cluster DOS. Their energies are all above the d band of the cluster. This is in sharp contrast with the DFT calculations discussed above, for which these delocalized orbitals are found within or even below (for the $1S$ MO) the d band. In the absence of relativistic effects, the d band of Au is lower in energy and does not hybridize with the s band. These results, shown in the Supplemental Material [54], can be expected to represent what would be observed, for instance, in Pd-doped Ag clusters, in which relativistic effects are much less important.

IV. CONCLUSIONS

In this work, we have employed a combined experimental and theoretical approach to determine and rationalize the stability trends of small Au_N^+ and $PdAu_{N-1}^+$ clusters in the $N = 5$–20 size range. The existence of "magic" clusters sizes at Au_7^+, Au_9^+, $PdAu_6^+$, and $PdAu_9^+$ is observed in both intensity profiles from mass spectrometry and metastable photofragmentation fractions. The increased stability of these clusters is attributed to electronic shell closings in a 2D and 3D confining potential. The ground-state structures of Au_7^+ and $PdAu_6^+$ represent perturbations of the particle in a circular potential, which exhibit closed-shell electronic structures with six delocalized electrons, while Au_9^+ and $PdAu_9^+$ exhibit structures close to that of the particle in a spherical potential, with a corresponding closed eight-electron shell. These conclusions are supported by detailed analysis of the cluster density of states. Oscillations in the stability of nonmagic clusters are observed experimentally for all investigated clusters according to the possibility of closure of the $5d$ orbital, with odd-numbered Au_N^+ clusters, and even $PdAu_{N-1}^+$ clusters more stable. Excellent agreement is found with theory, suggesting that the calculated structures are indeed global minima and are representative of the clusters produced in the experiment. Moreover, photofragmentation fractions are compared with calculated dissociation energies, with qualitative agreement, showing that the balance between monomer and dimer evaporation is controlled by the ability to maintain closed $5d$ shell daughter clusters. Furthermore, it is found that the evaporation of Pd atoms is suppressed in general, with exceptions for clusters in which this channel produces fragments of magic sizes.

In conclusion, we have demonstrated the significant effect of Pd doping on the stability and electron delocalization in small cationic Au clusters. These observations may be of relevance for the understanding of processes taking place in related systems, such as doped monolayer-protected clusters or larger bimetallic nanoparticles.

ACKNOWLEDGMENTS

This work was supported by the Research Foundation-Flanders (FWO) and the KU Leuven Research Council (GOA/14/007). P.F. acknowledges the FWO for financial support through a postdoctoral grant. J.V. thanks the FWO for doctoral financial support. H.A.H. is grateful to the University of Kufa and the Ministry of Higher Education and Scientific Research (Iraq) for financial support through the award of a Ph.D. scholarship. Calculations were performed at the University of Birmingham's Blue-BEAR high-performance computer [69], and the UK's national HPC facility ARCHER, through membership of the HPC Materials Chemistry Consortium, funded by EPSRC (Grant No. EP/L000202), and EPSRC Critical Mass Grant (Grant No. EP/J010804) "TOUCAN: Towards an Understanding of Catalysis on Nanoalloys."

APPENDIX A: DENSITY OF STATES OF $PdAu_7^+$ AND $PdAu_8^+$ CLUSTERS

In the left panel of Fig. 7, the analysis of $PdAu_7^+$ is presented. Four molecular orbitals in which the electron density is delocalized over the entire cluster can be identified in the cluster DOS. In clear contrast with $PdAu_9^+$ (Fig. 5), the $1P_z$ orbital is found to lie above the HOMO, and thus is empty. MOs $1S$ and $1P_{x,y}$ are doubly occupied, resulting in a total of six delocalized electrons. Since the cluster has a 3D geometry, the total number of six delocalized electrons does not correspond to a magic size. This is supported by the small HOMO-LUMO gap. The case of $PdAu_8^+$ (right panel of Fig. 7) is similar to $PdAu_7^+$, with the difference that this cluster is an open-shell system and thus α- and β-spin orbitals must be considered independently. Four orbitals of delocalized character over the entire cluster are found in the cluster DOS, with only the β-$1P_z$ orbital being empty. Therefore, $PdAu_8^+$ has seven delocalized electrons

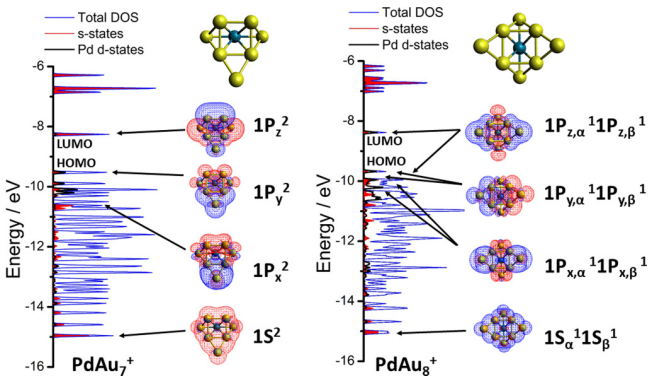

FIG. 7. Total density of states (blue line) of $PdAu_7^+$ (left) and $PdAu_8^+$ (right) clusters. A projection onto total *s* states is shaded red, whereas a projection onto Pd *d* states is shaded black. Molecular orbitals in which the electron density extends over the entire cluster are plotted and labeled based on their nodal character ($1S$ and $1P_{x,y,z}$). The HOMO and LUMO levels are labeled.

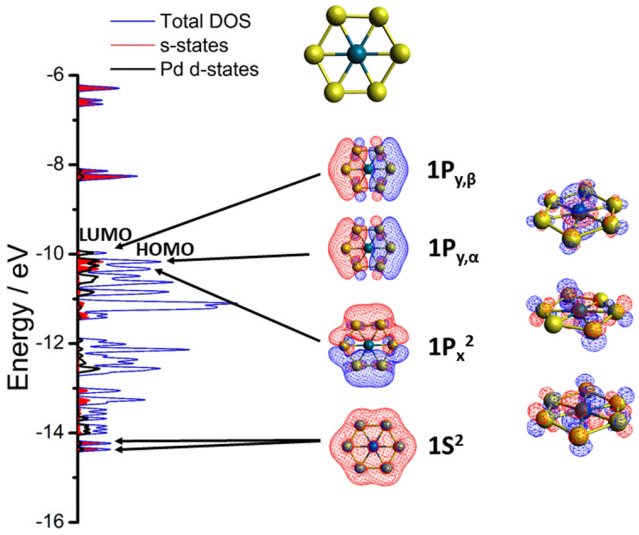

FIG. 8. Total density of states (blue line) of the planar hexagon isomer of $PdAu_6^+$, located 0.6 eV above the ground state. A projection onto total *s* states is shaded red, whereas a projection onto Pd *d* states is shaded black. Molecular orbitals in which the electron density extends over the entire cluster are plotted and labeled based on their nodal character ($1S$ and $1P_{x,y}$). In addition, three molecular orbitals in which a higher electron density on the different atoms and a zero or close-to-zero electron density in between the atoms of the cluster is shown.

APPENDIX B: PLANAR ISOMER OF $PdAu_6^+$

This isomer, with a relative energy of +0.6 eV compared to the ground state, comprises an Au hexagon with the Pd dopant at the center. The total density of states is shown in Fig. 8, with a projection onto total *s* and Pd *d* states. In this isomer, the hybridization of the Pd *d* states with Au *d* and Au *s* states is poor, as in the case of $PdAu_9^+$ presented in the main text. In fact, there are no MOs with high Au *s* character that simultaneously have large Pd contribution. This is reflected in the electronic structure of the isomer. The HOMO-LUMO gap of this cluster is very small since the $1P_{y,\beta}$ MO is empty. Thus, in the simplistic picture of itinerant electrons, Pd remains with all its *d* electrons localized, resulting in a total of five electrons which are delocalized over the entire cluster. Therefore, geometry plays a determining role in the electronic structure of the cluster and, thus, in its stability. Interestingly, DFT calculations on the neutral cluster show that this hexagonal structure is the ground state for neutral $PdAu_6$, instead of the triangular quasi-2D structure of the cation. By adding an extra electron, the system closes an electronic shell of delocalized valence electrons, providing enhanced stability for the planar structure.

[1] W. D. Knight, K. Clemenger, W. A. de Heer, W. A. Saunders, M. Y. Chou, and M. L. Cohen, Phys. Rev. Lett. **53**, 510 (1984).
[2] H. Häkkinen, Chem. Soc. Rev. **37**, 1847 (2008).
[3] A. C. Reber and S. N. Khanna, Acc. Chem. Res. **50**, 255 (2017).
[4] W. A. de Heer, Rev. Mod. Phys. **65**, 611 (1993).
[5] P. Atkins and R. Friedman, *Molecular Quantum Mechanics* (Oxford University Press, New York, 2011).
[6] E. Janssens, H. Tanaka, S. Neukermans, R. Silverans, and P. Lievens, New J. Phys. **5**, 46 (2003).
[7] P. Pyykko, Chem. Rev. **88**, 563 (1988).
[8] P. Gruene, D. M. Rayner, B. Redlich, A. F. G. van der Meer, J. T. Lyon, G. Meijer, and A. Fielicke, Science **321**, 674 (2008).
[9] F. Furche, R. Ahlrichs, P. Weis, C. Jacob, S. Gilb, T. Bierweiler, and M. M. Kappes, J. Chem. Phys. **117**, 6982 (2002).
[10] H. A. Hussein, I. Demiroglu, and R. L. Johnston, Eur. Phys. J. B **91**, 34 (2018)
[11] S. Gilb, P. Weis, F. Furche, R. Ahlrichs, and M. M. Kappes, J. Chem. Phys. **116**, 10 (2002).
[12] N. Veldeman, E. Janssens, K. Hansen, J. D. Haeck, R. E. Silverans, and P. Lievens, Faraday Discuss. **138**, 147 (2008).
[13] M. Vogel, K. Hansen, A. Herlert, and L. Schweikhard, Phys. Rev. A **66**, 033201 (2002).
[14] K. Hansen, A. Herlert, L. Schweikhard, and M. Vogel, Phys. Rev. A **73**, 063202 (2006).
[15] H. Häkkinen, Adv. Phys. **1**, 467 (2016).
[16] M. Haruta, T. Kobayashi, H. Sano, and N. Yamada, Chem. Lett. **16**, 405 (1987).
[17] S. M. Lang, T. M. Bernhardt, R. N. Barnett, and U. Landman, Angew. Chem. Int. Ed. **49**, 980 (2010).
[18] T. Fujitani, I. Nakamura, T. Akita, M. Okumura, and M. Haruta, Angew. Chem. Int. Ed. **48**, 9515 (2009).
[19] S. Neukermans, E. Janssens, H. Tanaka, R. E. Silverans, and P. Lievens, Phys. Rev. Lett. **90**, 033401 (2003).
[20] V. M. Medel, A. C. Reber, V. Chauhan, P. Sen, A. M. Köster, P. Calaminici, and S. N. Khanna, J. Am. Chem. Soc. **136**, 8229 (2014).
[21] K. Koyasu, M. Mitsui, A. Nakajima, and K. Kaya, Chem. Phys. Lett. **358**, 224 (2002).
[22] Z. J. Wu, S. H. Zhou, J. S. Shi, and S. Y. Zhang, Chem. Phys. Lett. **368**, 153 (2003).

[23] G. Zanti and D. Peeters, J. Phys. Chem. A **114**, 10345 (2010).
[24] D. W. Yuan, Y. Wang, and Z. Zeng, J. Chem, Phys. **122**, 114310 (2005).
[25] V. Kaydashev, P. Ferrari, C. Heard, E. Janssens, R. L. Johnston, and P. Lievens, Part. Part. Syst. Charact. **33**, 364 (2016).
[26] V. E. Kaydashev, E. Janssens, and P. Lievens, J. Chem. Phys. **142**, 034310 (2015).
[27] S. M. Lang, A. Frank, I. Fleischer, and T. M. Bernhardt, Eur. Phys. J. D **67**, 19 (2013).
[28] L. Luo, Z. Duan, H. Li, J. Kim, G. Henkelman, and R. Crooks, J. Am. Chem. Soc. M. **139**, 5538 (2017).
[29] S. Nishimura, Y. Yakita, M. Katayama, K. Higashimine, and K. Ebitani, Catal. Sci. Technol. **3**, 351 (2013).
[30] G. J. Hutchings and C. J. Kiely, Acc. Chem. Res. **46**, 1759 (2003).
[31] A. Bruma, F. R. Negreiros, S. Xie, T. Tsukuda, R. L. Johnston, A. Fortunelli, and Z. Y. Li, Nanoscale **5**, 9620 (2013).
[32] S. Xie, H. Tsunoyama, W. Kurashige, Y. Negishi, and T. Tsukuda, ACS Catal. **2**, 1519 (2012).
[33] Y. Negishi, W. Kurashige, Y. Niihori, T. Iwasa, and K. Nobusada, Phys. Chem. Chem. Phys. **12**, 6219 (2010).
[34] K. A. Kacprzak, L. Lehtovaara, J. Akola, O. Lopez-Acevedo, and H. Häkkinen, Phys. Chem. Chem. Phys. **11**, 7123 (2009).
[35] Y. Niihori, W. Kurashige, M. Matsuzaki, and Y. Negishi, Nanoscale **5**, 508 (2013).
[36] P. Ferrari, J. Vanbuel, Y. L. T. Li, E. Janssens, and P. Lievens, in *Gas Aggregation Synthesis of Nanoparticles*, edited by Y. Huttel (Wiley-VCH, Berlin, 2017).
[37] E. Janssens, T. Van Hoof, N. Veldeman, S. Neukermans, M. Hou, and P. Lievens, Int. J. Mass Spectrom. **252**, 38 (2006).
[38] S. Neukermans, X. Wang, N. Veldeman, E. Janssens, R. E. Silverman, and P. Lievens, Int. J. Mass Spectrom. **252**, 145 (2006).
[39] https://bitbucket.org/JBADavis/bpga (unpublished).
[40] R. L. Johnston, Dalton Trans. **22**, 4193 (2003).
[41] B. Bandow and B. Hartke, J. Phys. Chem. A **110**, 5809 (2006).
[42] A. Shayeghi, D. Götz, J. B. A. Davis, R. Schäfer, and R. L. Johnston, Phys. Chem. Chem. Phys. **17**, 2104 (2015).
[43] J. B. A. Davis, A. Shayeghi, S. L. Horswell, and R. L. Johnston, Nanoscale **7**, 14032 (2015).
[44] G. Kresse and J. Hafner, Phys. Rev. B **47**, 558 (1993).
[45] J. P. Perdew, K. Burke, and Y. Wang, Phys. Rev. B **54**, 16533 (1996).
[46] G. Kresse and D. Joubert, Phys. Rev. B **59**, 1758 (1999).
[47] M. Methfessel and A. T. Paxton, Phys. Rev. B **40**, 3616 (1989).
[48] M. Valiev, E. Bylaska, N. Govind, K. Kowalski, T. Straatsma, and H. V. Dam, Comput. Phys. Commun. **1181**, 1477 (2010).
[49] F. Weigend and R. Ahlrichs, Phys. Chem. Chem. Phys. **7**, 3297 (2005).
[50] O. Vydrov and G. Scuseria, J. Chem. Phys. **125**, 234109 (2006).
[51] M. Rohrdanz, K. Martins, and J. Herbert, J. Chem. Phys. **130**, 054112 (2009).
[52] K. Hansen, *Statistical Physics of Nanoparticles in the Gas Phase* (Springer Science & Business Media, Dordrecht, 2013).
[53] P. Ferrari, E. Janssens, P. Lievens, and K. Hansen, J. Chem. Phys. **143**, 224313 (2015).
[54] See Supplemental Material at http://link.aps.org/supplemental/10.1103/PhysRevA.97.052508 for Hartree-Fock calculations for $PdAu_6^+$, Au_7^+, $PdAu_9^+$ and Au_9^+; Determination of fragmentation channels; The calculated dissociation energies of the different fragmentation channels; and XYZ coordinates of minimum-energy structures.
[55] L. Ferrighi, B. Hammer, and G. K. H. Madsen, J. Am. Chem. Soc. **9**, 10605 (2009).
[56] F. Remacle and E. S. Kryachko, J. Chem. Phys. **122**, 044304 (2005).
[57] E. M. Fernández, J. M. Soler, I. L. Garzón, and L. C. Balbás, Phys. Rev. B **70**, 165403 (2004).
[58] X. Wu, L. Senapati, and S. K. Nayak, J. Chem. Phys. **117**, 4010 (2002).
[59] A. N. Gloess, H. Schneider, J. M. Weber, and M. M. Kappes, J. Chem. Phys. **128**, 114312 (2008).
[60] H. A. Hussein, J. B. A. Davis, and R. L. Johnston, Phys. Chem. Chem. Phys. **18**, 26133 (2016).
[61] C. J. Heard, A. Shayeghi, R. Schaefer, and R. L. Johnston, Z. Phys. Chem. **230**, 955 (2016).
[62] Y. Chen, X. Kuang, X. Sheng, H. Wang, P. Shao, and M. Zhong, Z. Naturforsch. A **68**, 651 (2013).
[63] E. M. Fernández and L. C. Balbás, J. Chem. Phys. **144**, 224308 (2016).
[64] V. M. Medel, J. U. Reveles, S. N. Khanna, V. Chauhan, P. Sen, and A. W. Castleman, Proc. Natl. Acad Sci. USA **108**, 10062 (2011).
[65] W. H. Blades, A. C. Reber, S. N. Khanna, L. López-Sosa, P. Calaminici, and A. M. Köster, J. Phys. Chem. A **121**, 2990 (2017).
[66] E. Janssens, S. Neukermans, and P. Lievens, Curr. Opin. Solid State Mater. Sci. **8**, 185 (2004).
[67] T. Ba Tai, R. W. A. Havenith, J. L. Teunissen, A. R. Dok, S. D. Hallaert, M. T. Nguyen, and A. Ceulemans, Inorg. Chem. **52**, 10595 (2013).
[68] B. Kiran, G. G. Kumar, M. T. K. A. K. Nguyen, and P. Jena, Inorg. Chem. **48**, 9965 (2009).
[69] http://www.birmingham.ac.uk/bear (unpublished).

Supporting Information

The effect of palladium doping on the stability and fragmentation patterns of cationic gold clusters

Piero Ferrari[a], Heider A. Hussein[b,c], Christopher J. Heard[d], Jan Vanbuel[a], Roy L. Johnston[b], Peter Lievens[a] and Ewald Janssens[a]

[a] Laboratory of Solid State Physics and Magnetism, KU Leuven, 3001 Leuven, Belgium
[b] School of Chemistry, University of Birmingham, Edgbaston, Birmingham B15 2TT, UK
[c] Department of Chemistry, College of Science, University of Kufa, Najaf, Iraq
[d] Department of Department of Physical and Macromolecular Chemistry, Charles University, 12843 Praha 2, Czech Republic

Content

1. Hartree-Fock calculations for $PdAu_6^+$, Au_7^+, $PdAu_9^+$ and Au_9^+.

In this section, we present calculations on Au_7^+, $PdAu_6^+$, Au_9^+ and $PdAu_9^+$, using the single determinant Hartree-Fock (HF) theory. These calculations are performed in order to investigate the role of charge correlation and relativistic effects on the results presented in the main text. As seen in Figure S1, the HF results are similar to those obtained by DFT, detailed in the main text. The clusters' DOS are composed of doubly occupied MOs in which the electron density is delocalized over the entire cluster. Based on their nodal character, these states can be labelled as the first eigenstates of electrons confined in a potential well.

An important difference between the HF results and the DFT calculations of the main text, are the energies of these delocalized MOs. Without relativistic effects, the *d*-band of Au is lower in energy and consequently, does not hybridize with the *s*-band. The HF results, therefore, show a very week *s*-*d* hybridization. This is particularly clear for the 1S MO, which under DFT is always located below the *d*-band, whereas at the HF level it is predicted to lie above this band.

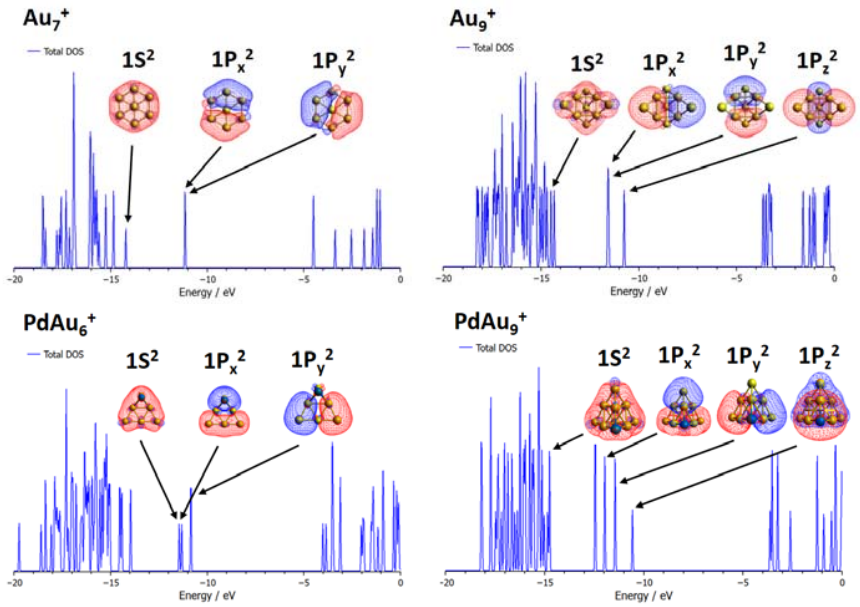

Figure S1. Total density of states (blue line) of Au_7^+, $PdAu_6^+$, Au_9^+ and $PdAu_9^+$, calculated by Hartree-Fock theory using the def2-SVP basis set. Molecular orbitals in which the electron density extends over the entire cluster are plotted and labeled based on their nodal character (1S and $1P_{x,y,z}$).

2. Determination of fragmentation channels

In this section, the equations used to determine the fragmentations channels of the clusters are detailed.

Figure S2 shows a scheme of the mass spectrometer. To improve time (or mass) resolution, the mass spectrometer makes use of a reflectron, in which clusters are decelerated and reflected before reaching a time-sensitive detector. This system is composed of three stages: laser excitation and ion extraction, free-flight, and reflection. As described in the main article, following laser excitation, the first step of fragmentation, or prompt fragmentation, takes place instantaneously. As a consequence, this fragmentation occurs in between the first two grids of the extraction stage of the mass spectrometer, where the laser excitation takes place. A prompt fragment, therefore, will be accelerated at the extraction and reflected with same mass. The total time-of-flight of a prompt fragment in the mass spectrometer can be easily calculated by solving the electrostatic equations of motion of this fragment. All dimensions and potentials are known as well as the mass and charge of the cluster. A similar analysis was presented already in Ref. [1], however, we will show here the most relevant equations.

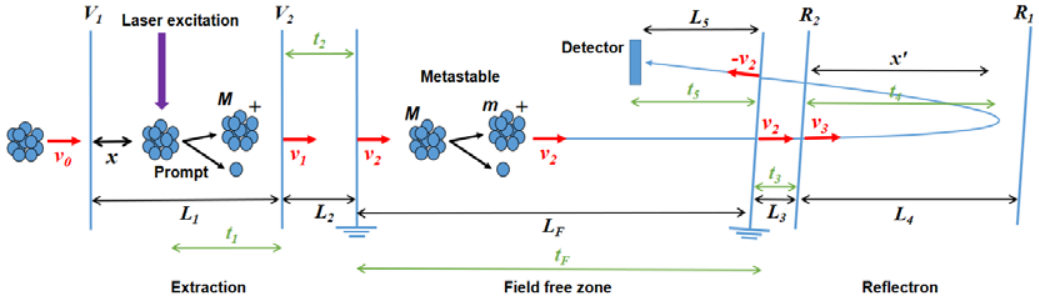

Figure S2. Schematic overview of the used reflectron time-of-flight mass spectrometer (not to scale), divided into three regions: laser excitation and ion extraction, free flight and ion reflection. Important lengths are L_1 = 21 mm, L_2 = 10 mm, L_3 = 10 mm, L_4 = 100 mm, L_5 = 790 mm, and L_F = 1230 mm. The distance *x*, measured from the first extraction electrode to the point of laser excitation, is approximately 10 mm. The applied voltages on the extraction and reflectron electrodes are V_1 = 3570 V, V_2 = 2550 V, R_1 = 3705 V, and R_2 = 2328 V. Times of flight and velocities are indicated by arrows in the figure. The length of arrows representing velocities do not correspond with their magnitude.

For excitation, a laser is directed in between the first two extraction grids, at a distance x, measured from the first extraction grid. This induces ionization and fragmentation. Positively charged clusters of mass M are accelerated in the first extraction zone by an electric field $(V_2 - V_1)/L_1$ with V_2 and V_1 the voltages applied on the first and second grid of the extraction (constant voltages are applied in these experiments). This results in a velocity v_1 at the second extraction grid. The time elapsed from laser excitation to the moment when clusters enter to the second extraction stage (t_1) is given by

$$t_1 = \frac{ML_1}{q(V_1 - V_2)}(v_1 - v_0) \qquad (S.1)$$

Then, clusters are accelerated by a potential difference V_2 since the third grid at the extraction stage is grounded. The flight time in this stage (t_2) corresponds to

$$t_2 = \frac{ML_2}{qV_2}(v_2 - v_1) \quad (\mathrm{S}.2)$$

During flight in the field free zone the velocity is constant. Therefore, the elapsed time t_F is simply,

$$t_F = \frac{L_F}{v_2} \quad (S.3)$$

Inside the reflectron an opposite potential is applied decreasing the clusters velocities. At the first reflectron stage, a potential difference R_2 is applied, leading to a flight time t_3 to travel the distance L_3 given by

$$t_3 = \frac{ML_3}{qR_2}(v_2 - v_3) \quad (\mathrm{S}.3)$$

At the second stage of the reflectron, clusters are decelerated by a field $(R_1 - R_2)/L_4$ with R_1 and R_2 the permanent voltages applied to the second and third grid of the reflectron, respectively. The time t_4 elapsed from the second reflectron plate to the stopping point x' is

$$t_4 = \frac{ML_4}{q(R_1 - R_2)}v_3 \quad (\mathrm{S}.4)$$

Finally, clusters exit the reflectron entering again the field free zone until they reach the detector, with a corresponding flight time t_5 given by,

$$t_5 = \frac{L_5}{v_2} \quad (\mathrm{S}.5)$$

The total time of flight T is thus calculated as

$$T = t_1 + t_2 + t_F + 2(t_3 + t_4) + t_5 \quad (S.6)$$

Eq. (S.6) determines the total time-of-flight of a prompt fragment for which the same mass M is used from laser excitation to detection. If metastable fragmentation takes place in free-flight, the velocity of the cluster is not changed [2], and the same Eq. (S.6) can be used to calculate the total time-of-flight of the metastable fragment, with the important difference that times t_3 and t_4 must be calculated with a different daughter mass, m, as depicted in Figure S2.

$$t_3{}' = \frac{mL_3}{qR_2}(v_2 - v_3) \quad (\mathrm{S}.7)$$

$$t_4{}' = \frac{mL_4}{q(R_1 - R_2)}v_3 \quad (\mathrm{S}.8)$$

The arrival time of the metastable fragments carries information about the decay channel, since their total time-of-flight is a function of both, the mass of the mother M, and the daughter m. To exemplify this, let's consider the cases presented in Figure 1c of the main article. Using Eq. (S.6) the total times-of-flight of the prompt fragments $PdAu_{13}^+$ and $PdAu_{14}^+$ are calculated as 146.4 µs and 152.8 µs,

respectively. This, however, is different if we consider a cluster produced by the metastable fragmentation of the mother $PdAu_{14}^{+}$; this cluster is extracted as $PdAu_{14}^{+}$ but reflected as the daughter of the fragmentation process, which can be either $PdAu_{14}^{+} \rightarrow PdAu_{13}^{+} + Au$ or $PdAu_{14}^{+} \rightarrow Au_{14}^{+} + Pd$. Because of the large difference in mass of the Au and Pd atoms, these two processes will lead to different flight times, because the mass m in Eqs. (S.7) and (S.8) will differ significantly from M in Eqs. (S1) and (S2). Using these expressions, the following times-of-flight are obtained: 147.1 µs for the loss of Au and 149.8 µs for the loss of Pd. In the experiments presented in the main article, only a peak at 147.1 µs is observed, proving that the fragmentation channel of $PdAu_{14}^{+}$ corresponds to the emission of a neutral Au monomer. It worth noting that in Figure 1c of the main article, the time axis was converted into a mass axis, although this does not affect the interpretation. A similar analysis can also be used to determine if evaporation of larger fragments, as dimers, competes with monomer decay.

3. The calculated dissociation energies of the different fragmentation channels

Reaction	Energy (eV)
$Au_3^+ \rightarrow Au_2^+ + Au$	3.25
$Au_4^+ \rightarrow Au_3^+ + Au$	1.31
$Au_5^+ \rightarrow Au_4^+ + Au$	2.76
$Au_6^+ \rightarrow Au_5^+ + Au$	1.52
$Au_7^+ \rightarrow Au_6^+ + Au$	2.86
$Au_8^+ \rightarrow Au_7^+ + Au$	1.69
$Au_9^+ \rightarrow Au_8^+ + Au$	3.11
$Au_{10}^+ \rightarrow Au_9^+ + Au$	1.50
$Au_{11}^+ \rightarrow Au_{10}^+ + Au$	3.06
$Au_{12}^+ \rightarrow Au_{11}^+ + Au$	1.41
$Au_{13}^+ \rightarrow Au_{12}^+ + Au$	2.41
$Au_{14}^+ \rightarrow Au_{13}^+ + Au$	1.95
$Au_{15}^+ \rightarrow Au_{14}^+ + Au$	2.43
$Au_{16}^+ \rightarrow Au_{15}^+ + Au$	1.54
$Au_{17}^+ \rightarrow Au_{16}^+ + Au$	2.88
$Au_{18}^+ \rightarrow Au_{17}^+ + Au$	2.03
$Au_{19}^+ \rightarrow Au_{18}^+ + Au$	2.60
$Au_{20}^+ \rightarrow Au_{19}^+ + Au$	1.91
$Au_2Pd_1^+ \rightarrow Au_2^+ + Pd$	2.96
$Au_3Pd_1^+ \rightarrow Au_3^+ + Pd$	2.17
$Au_4Pd_1^+ \rightarrow Au_4^+ + Pd$	2.59
$Au_5Pd_1^+ \rightarrow Au_5^+ + Pd$	1.78
$Au_6Pd_1^+ \rightarrow Au_6^+ + Pd$	2.86
$Au_7Pd_1^+ \rightarrow Au_7^+ + Pd$	2.24
$Au_8Pd_1^+ \rightarrow Au_8^+ + Pd$	3.15
$Au_9Pd_1^+ \rightarrow Au_9^+ + Pd$	2.50
$Au_{10}Pd_1^+ \rightarrow Au_{10}^+ + Pd$	2.66
$Au_{11}Pd_1^+ \rightarrow Au_{11}^+ + Pd$	2.04
$Au_{12}Pd_1^+ \rightarrow Au_{12}^+ + Pd$	2.65
$Au_{13}Pd_1^+ \rightarrow Au_{13}^+ + Pd$	2.51
$Au_{14}Pd_1^+ \rightarrow Au_{14}^+ + Pd$	2.67
$Au_{15}Pd_1^+ \rightarrow Au_{15}^+ + Pd$	2.83
$Au_{16}Pd_1^+ \rightarrow Au_{16}^+ + Pd$	2.90
$Au_{17}Pd_1^+ \rightarrow Au_{17}^+ + Pd$	2.37
$Au_{18}Pd_1^+ \rightarrow Au_{18}^+ + Pd$	2.21
$Au_{19}Pd_1^+ \rightarrow Au_{19}^+ + Pd$	2.26
$Au_2Pd_1^+ \rightarrow Au_1Pd_1^+ + Au$	6.59
$Au_3Pd_1^+ \rightarrow Au_2Pd_1^+ + Au$	2.51
$Au_4Pd_1^+ \rightarrow Au_3Pd_1^+ + Au$	1.72

$Au_5Pd_1^+$	→	$Au_4Pd_1^+ + Au$	1.95
$Au_6Pd_1^+$	→	$Au_5Pd_1^+ + Au$	2.60
$Au_7Pd_1^+$	→	$Au_6Pd_1^+ + Au$	2.24
$Au_8Pd_1^+$	→	$Au_7Pd_1^+ + Au$	2.60
$Au_9Pd_1^+$	→	$Au_8Pd_1^+ + Au$	2.46
$Au_{10}Pd_1^+$	→	$Au_9Pd_1^+ + Au$	1.65
$Au_{11}Pd_1^+$	→	$Au_{10}Pd_1^+ + Au$	2.45
$Au_{12}Pd_1^+$	→	$Au_{11}Pd_1^+ + Au$	2.02
$Au_{13}Pd_1^+$	→	$Au_{12}Pd_1^+ + Au$	2.27
$Au_{14}Pd_1^+$	→	$Au_{13}Pd_1^+ + Au$	2.10
$Au_{15}Pd_1^+$	→	$Au_{14}Pd_1^+ + Au$	2.60
$Au_{16}Pd_1^+$	→	$Au_{15}Pd_1^+ + Au$	1.61
$Au_{17}Pd_1^+$	→	$Au_{16}Pd_1^+ + Au$	2.36
$Au_{18}Pd_1^+$	→	$Au_{17}Pd_1^+ + Au$	1.87
$Au_{19}Pd_1^+$	→	$Au_{18}Pd_1^+ + Au$	2.65

Reaction			Energy (eV)
Au_3^+	→	$Au^+ + Au_2$	3.37
Au_4^+	→	$Au_2^+ + Au_2$	2.66
Au_5^+	→	$Au_3^+ + Au_2$	2.17
Au_6^+	→	$Au_4^+ + Au_2$	2.38
Au_7^+	→	$Au_5^+ + Au_2$	2.48
Au_8^+	→	$Au_6^+ + Au_2$	2.65
Au_9^+	→	$Au_7^+ + Au_2$	2.90
Au_{10}^+	→	$Au_8^+ + Au_2$	2.71
Au_{11}^+	→	$Au_9^+ + Au_2$	2.66
Au_{12}	→	$Au_{10}^+ + Au_2$	2.57
Au_{13}	→	$Au_{11}^+ + Au_2$	1.92
Au_{14}	→	$Au_{12}^+ + Au_2$	2.46
Au_{15}	→	$Au_{13}^+ + Au_2$	2.48
Au_{16}	→	$Au_{14}^+ + Au_2$	2.07
Au_{17}	→	$Au_{15}^+ + Au_2$	2.52
Au_{18}	→	$Au_{16}^+ + Au_2$	3.01
Au_{19}	→	$Au_{17}^+ + Au_2$	2.73
Au_{20}	→	$Au_{18}^+ + Au_2$	2.61
$Au_2Pd_1^+$	→	$Au^+ + PdAu$	3.90
$Au_3Pd_1^+$	→	$Au_2^+ + PdAu$	2.37
$Au_4Pd_1^+$	→	$Au_3^+ + PdAu$	3.02
$Au_5Pd_1^+$	→	$Au_4^+ + PdAu$	2.86
$Au_6Pd_1^+$	→	$Au_5^+ + PdAu$	3.58
$Au_7Pd_1^+$	→	$Au_6^+ + PdAu$	3.32

$Au_8Pd_1^+$	→	$Au_7^+ + PdAu$	4.09
$Au_9Pd_1^+$	→	$Au_8^+ + PdAu$	2.63
$Au_{10}Pd_1^+$	→	$Au_9^+ + PdAu$	3.58
$Au_{11}Pd_1^+$	→	$Au_{10}^+ + PdAu$	2.53
$Au_{12}Pd_1^+$	→	$Au_{11}^+ + PdAu$	3.40
$Au_{13}Pd_1^+$	→	$Au_{12}^+ + PdAu$	3.09
$Au_{14}Pd_1^+$	→	$Au_{13}^+ + PdAu$	3.73
$Au_{15}Pd_1^+$	→	$Au_{14}^+ + PdAu$	2.91
$Au_{16}Pd_1^+$	→	$Au_{15}^+ + PdAu$	3.73
$Au_{17}Pd_1^+$	→	$Au_{16}^+ + PdAu$	2.72
$Au_{18}Pd_1^+$	→	$Au_{17}^+ + PdAu$	3.33
$Au_{19}Pd_1^+$	→	$Au_{18}^+ + PdAu$	2.37
$Au_2Pd_1^+$	→	$Pd^+ + Au_2$	7.16
$Au_3Pd_1^+$	→	$Au_1Pd_1^+ + Au_2$	2.33
$Au_4Pd_1^+$	→	$Au_2Pd_1^+ + Au_2$	1.78
$Au_5Pd_1^+$	→	$Au_3Pd_1^+ + Au_2$	2.66
$Au_6Pd_1^+$	→	$Au_4Pd_1^+ + Au_2$	2.94
$Au_7Pd_1^+$	→	$Au_5Pd_1^+ + Au_2$	2.94
$Au_8Pd_1^+$	→	$Au_6Pd_1^+ + Au_2$	3.16
$Au_9Pd_1^+$	→	$Au_7Pd_1^+ + Au_2$	2.21
$Au_{10}Pd_1^+$	→	$Au_8Pd_1^+ + Au_2$	2.20
$Au_{11}Pd_1^+$	→	$Au_9Pd_1^+ + Au_2$	2.56
$Au_{12}Pd_1^+$	→	$Au_{10}Pd_1^+ + Au_2$	2.38
$Au_{13}Pd_1^+$	→	$Au_{11}Pd_1^+ + Au_2$	2.47
$Au_{14}Pd_1^+$	→	$Au_{12}Pd_1^+ + Au_2$	2.80
$Au_{15}Pd_1^+$	→	$Au_{13}Pd_1^+ + Au_2$	2.30
$Au_{16}Pd_1^+$	→	$Au_{14}Pd_1^+ + Au_2$	2.06
$Au_{17}Pd_1^+$	→	$Au_{15}Pd_1^+ + Au_2$	2.33
$Au_{18}Pd_1^+$	→	$Au_{16}Pd_1^+ + Au_2$	2.62
$Au_{19}Pd_1^+$	→	$Au_{17}Pd_1^+ + Au_2$	2.33

4. *XYZ* coordinates of minimum-energy structures

4.1. Au_N^+ clusters, *N*=2-20:

Au_2^+

Au	0.75633217	-0.79066243	-0.71379159
Au	-0.75633217	0.79066243	0.71379159

Au_3^+

Au	0.28795200	-0.83100282	-1.22798571
Au	0.61207735	1.37345513	0.14290605
Au	-0.90002935	-0.54245231	1.08507967

Au_4^+

Au	0.30042967	-1.03670287	0.77478118
Au	-0.29999035	1.03685982	-0.77476022
Au	-0.54494222	1.23657354	1.86601302
Au	0.54450290	-1.23673049	-1.86603398

Au_5^+

Au	-1.15716234	-1.62959222	-1.76690824
Au	1.39664191	-1.66340708	-1.54829961
Au	1.15663523	1.62206329	1.77362174
Au	-0.00037515	-0.00004857	0.00002346
Au	-1.39573965	1.67098458	1.54156265

Au_6^+

Au	-2.04135630	-0.07520849	-2.19285825
Au	0.04569588	1.17207958	-1.22450667
Au	-1.06434723	-1.09872976	0.00936620
Au	1.02171626	-0.00037452	1.13891992
Au	2.12071726	2.11652860	0.06063475
Au	-0.08242587	-2.11429542	2.20844405

Au_7^+

Au	-1.85434616	-0.05659725	-1.94209267
Au	-0.10791731	1.98183481	-1.80910465
Au	-1.85717023	-1.94083764	-0.02541593
Au	-0.00002991	-0.00048153	0.00051931
Au	1.87394150	1.92400240	0.00521967
Au	0.07200258	-1.95056956	1.84614930
Au	1.87351952	0.04264877	1.92472497

Au_8^+

Au	0.42078708	-2.63507847	-2.26172476
Au	-2.39472791	1.01744976	-2.33800303
Au	-0.52788025	-0.43258037	-1.22968817
Au	-1.41907687	1.84196395	-0.03877606
Au	1.41937080	-1.84173467	0.03861718
Au	0.52767633	0.43242557	1.22962325
Au	-0.42003880	2.63543538	2.26136399
Au	2.39388960	-1.01788115	2.33858760

Au_9^+

Au	1.93820705	1.08607021	-2.18326334
Au	-0.10890446	-0.62713260	-1.89889740
Au	-2.30339595	-2.03595868	-1.72883311
Au	0.11005180	1.69459865	-0.29993348
Au	1.95830450	-0.41821427	0.04008281
Au	-1.99572480	-0.15756784	0.06182205
Au	-1.73768422	2.00095771	1.63686026
Au	0.07148085	0.05133471	2.00081537
Au	2.06766523	-1.59408790	2.37134685

Au_{10}^+

Au	2.44644872	1.05926103	-2.44879698
Au	2.02535654	-0.64393759	-0.52301851
Au	-2.72329977	-2.32186442	-0.54478000
Au	0.41250525	1.55044336	-0.87783442
Au	-2.05147974	2.68853735	-0.79582328
Au	-0.27335195	-2.14720056	0.32359383
Au	-0.81710446	2.11986354	1.54589480
Au	0.70298636	-0.03807174	1.84052713
Au	-1.82608042	0.08643183	-0.05357499
Au	2.10401948	-2.35346280	1.53381242

Au_{11}^+

Au	1.61125263	1.66934435	-3.05722116
Au	-0.19354384	0.03944442	-2.11668955
Au	-2.23046208	-1.69880936	-2.10337910
Au	-0.30626597	-2.08472422	-0.28146381
Au	-2.12422620	0.04721504	-0.07583265
Au	1.55590070	1.37151581	-0.46750374
Au	1.34433545	-3.35689449	1.28556541
Au	1.44317148	-0.75269055	1.36778097
Au	-2.95617074	1.68755137	1.77227402
Au	-0.37471937	1.37928838	1.57337214

Au	2.23072795	1.69875924	2.10309747

Au_{12}^{+}

Au	0.21375139	2.34970142	0.43060108
Au	0.85002008	0.66005130	-1.68041619
Au	-3.11161905	-1.56155713	0.82314752
Au	2.73098814	2.24898197	-0.53092114
Au	1.15124698	-2.07796412	-0.88075961
Au	-1.40784906	-0.81284200	-1.15697874
Au	0.17204027	-1.42690360	-3.27362076
Au	-2.01168528	0.89750824	0.94667832
Au	-0.45942737	-1.36334358	1.38405513
Au	1.99766334	-2.48982338	1.61242291
Au	-1.92192117	3.46714691	1.46477821
Au	1.79679172	0.10904398	0.86101328

Au_{13}^{+}

Au	-0.73236137	-1.56812223	-3.13877233
Au	1.07368741	-0.04281101	-1.78854470
Au	-1.74714975	0.27538003	-1.50640236
Au	2.04979144	2.46955325	-1.50195870
Au	-0.36646957	-1.99811779	-0.47559984
Au	2.50859179	-1.90863660	-0.09027178
Au	-2.87730896	2.13723092	0.02630068
Au	-0.15552718	2.08056410	0.02530775
Au	2.15486202	0.72948403	0.60628502
Au	-1.59572108	0.12530036	1.33826874
Au	-1.63673163	-2.53462111	1.85807363
Au	0.58087451	1.42144774	2.75428024
Au	0.74346236	-1.18665168	1.89303365

Au_{14}^{+}

Au	6.497164535	8.573345090	3.387659715
Au	6.257602713	3.425220761	4.265286029
Au	6.307709169	6.122119957	4.545554053
Au	8.168129478	8.125212406	5.407823388
Au	5.347104203	8.307147965	5.866432279
Au	8.006958764	4.416627137	6.068410895
Au	5.132844120	4.540402216	6.460586054
Au	8.976730906	6.449665061	7.528256956
Au	7.203831683	8.584735403	8.025077055
Au	5.001950095	6.753721998	8.082290585
Au	4.700381426	9.447092587	8.280291455

Au	7.080982186	4.870318059	8.585497553
Au	9.774253846	9.045747086	7.364036848
Au	4.490730653	4.285017657	9.079170121

Au_{15}^{+}

Au	5.178141183	6.644890712	3.126248547
Au	7.323690673	4.843619354	3.230453754
Au	7.305757862	7.118784811	4.800894764
Au	5.485497231	5.016741576	5.357111777
Au	8.286987502	4.502040200	5.726518031
Au	4.241921933	8.016994939	5.224619644
Au	8.823103507	9.024317434	5.961200840
Au	6.340814597	8.656231857	6.935727139
Au	4.327933644	6.312520616	7.393711975
Au	8.378851505	6.825145525	7.455589697
Au	6.451183351	4.774886583	7.911695244
Au	9.205760816	4.330727879	8.270015896
Au	3.827703645	8.995394280	7.835250495
Au	5.707159094	7.594088572	9.409356586
Au	7.767604763	5.995728145	10.013718095

Au_{16}^{+}

Au	5.307652830	7.947954110	3.745540474
Au	3.924867605	5.601535117	3.776132502
Au	7.480169151	8.153972163	5.492501521
Au	6.472060064	5.645709586	4.908994617
Au	5.079910274	9.677266859	5.900880863
Au	4.286705072	4.196684346	6.074980122
Au	4.194238146	7.065690425	6.172902151
Au	8.898541078	8.388598860	7.913964382
Au	8.730820961	5.883338022	6.373613140
Au	6.803055193	3.838325362	7.032724226
Au	7.376773715	10.473659245	7.129865476
Au	10.411087934	6.254186675	8.533720973
Au	6.074059663	8.150604708	8.054641390
Au	9.127639450	3.832928361	8.351114334
Au	5.040686307	5.651570199	8.343070963
Au	7.615692704	6.061935711	9.019311818

Au_{17}^{+}

Au	7.283802007	4.454617766	3.454966025
Au	6.576149492	9.582598249	3.909901035
Au	6.339754837	6.866947023	4.096225226
Au	4.038744640	8.365487406	3.769392069
Au	8.192553355	8.577322361	5.831286552

Au	**6.042475641**	**4.605038857**	**5.874221688**
Au	**8.585236471**	**5.843235673**	**5.414676351**
Au	**3.726770707**	**6.271759524**	**5.422863697**
Au	**5.314702251**	**8.537141417**	**6.210422057**
Au	**9.308367182**	**6.964168491**	**7.752526682**
Au	**5.823586822**	**3.857630649**	**8.623894152**
Au	**3.600048679**	**4.079553521**	**7.021072591**
Au	**5.011441089**	**6.415055812**	**7.903029627**
Au	**8.362026152**	**4.339067245**	**7.670579164**
Au	**6.851449338**	**8.404873197**	**8.386386673**
Au	**7.273371472**	**5.938871512**	**9.637700003**
Au	**8.839945756**	**8.067057187**	**10.191283078**

Au_{18}^{+}

Au	**7.325473903**	**7.853367677**	**3.514886420**
Au	**5.047341373**	**9.391220604**	**4.189357380**
Au	**7.429174704**	**5.295738036**	**4.507570934**
Au	**5.051129706**	**6.705339838**	**4.705677476**
Au	**9.121718432**	**7.352722612**	**5.532097110**
Au	**9.917891999**	**4.698974855**	**5.561336701**
Au	**5.171219462**	**4.169812953**	**5.695347376**
Au	**7.120366971**	**9.221837171**	**5.964287720**
Au	**4.434272308**	**8.636060558**	**6.706538540**
Au	**3.484661622**	**6.046961266**	**6.890559626**
Au	**7.629241227**	**3.932946226**	**6.898849815**
Au	**8.898140968**	**8.704116516**	**7.961906629**
Au	**9.307832331**	**5.988290261**	**7.921503094**
Au	**5.497716383**	**4.959392653**	**8.365380149**
Au	**6.282369645**	**9.451348352**	**8.592402427**
Au	**7.837699067**	**4.373686670**	**9.636725453**
Au	**4.453636549**	**7.398148096**	**9.150964844**
Au	**7.180607085**	**7.010528589**	**9.395103645**

Au_{19}^{+}

Au	**9.619264912**	**5.741692846**	**4.111869955**
Au	**7.234296739**	**7.222898423**	**3.940102410**
Au	**4.911645311**	**5.826967823**	**3.884854414**
Au	**7.263768524**	**4.534207669**	**4.728713447**
Au	**7.232576752**	**9.701861109**	**5.037224393**
Au	**4.997226285**	**8.127071816**	**5.406648494**
Au	**9.278907399**	**7.899423079**	**5.730396528**
Au	**4.864869653**	**3.804031404**	**5.774063009**
Au	**3.343017773**	**6.072850426**	**6.216188579**
Au	**9.046037101**	**5.293335322**	**6.777077680**

Au	7.105488880	3.429910138	7.323185690
Au	5.661108635	9.946701720	7.370055747
Au	8.414856113	9.731411293	7.540047305
Au	4.412325359	7.664914393	8.131196586
Au	4.886650693	4.905668154	8.257885260
Au	9.475759561	7.385675633	8.502312274
Au	7.522757032	5.531844379	9.038362757
Au	5.332901833	6.413274338	10.474675462
Au	6.902451964	8.272171556	9.261049130

Au_{20}^{+}

Au	4.775382922	5.795907566	4.057230525
Au	7.378767623	6.595223693	3.411536122
Au	6.978904082	4.774507376	5.469108753
Au	5.429065130	8.460084504	4.107406050
Au	8.005591378	8.886665798	4.890291464
Au	9.222755626	6.364663921	5.408925520
Au	5.774844961	9.670863293	6.468815879
Au	4.158320137	7.340210611	6.294239858
Au	10.447822064	8.717277859	6.126218050
Au	4.361574606	4.553461013	6.441492009
Au	9.037455203	4.486589057	7.319590317
Au	8.358913196	9.745411745	7.549659091
Au	9.285190852	7.173201746	8.109148362
Au	4.317047629	8.719935853	8.645483126
Au	6.254013863	10.714648896	8.969585159
Au	5.151361646	6.114315252	8.625125248
Au	6.356167581	3.688937786	8.001441408
Au	6.970085911	8.105200567	9.391862995
Au	8.482391522	2.974471387	9.501219539
Au	7.701246472	5.565325926	9.658523960

4.2. $Au_{(N-1)}Pd_1^{+}$ clusters

$Au_1Pd_1^{+}$

Au	-0.61827907	-0.61812188	0.19445348
Pd	1.09465614	1.09437782	-0.34427769

$Au_2Pd_1^{+}$

Au	-0.30202190	-0.99376944	-0.93400431
Au	1.02418929	0.19842633	0.91547167
Pd	-1.22400356	1.32670134	0.01626793

$Au_3Pd_1^{+}$

Au	1.03601981	0.77329025	0.95608894

Au	-0.79961353	0.92186495	-1.04696206
Au	-0.86318021	-1.15910132	0.70507031
Pd	1.08260186	-0.92629563	-1.06080281

$Au_4Pd_1^+$

Au	-0.27252722	0.02059526	0.05950151
Au	-2.33324261	-0.01845414	1.63591128
Au	1.19776080	-1.13366458	-1.85007024
Au	1.45527714	1.38704448	-1.45310188
Pd	-0.08240092	-0.41711842	2.76597999

$Au_5Pd_1^+$

Au	-1.40082785	-0.67205312	-1.56154321
Au	0.94093241	-0.81588644	0.81436893
Au	0.94329418	0.88621612	-1.36246879
Au	-1.63591158	-1.75270828	0.80499307
Au	1.70380435	1.80636154	0.99802998
Pd	-0.94781710	0.94317868	0.55824039

$Au_6Pd_1^+$

Au	0.46665476	2.32289110	-1.95137165
Au	-0.70151951	0.02830266	-1.43386345
Au	1.37215892	-0.11087983	2.55806458
Au	-1.81598957	-2.29503941	-0.92602172
Au	1.30326736	1.10974772	0.20564409
Au	-0.00097642	-1.53269004	0.79111743
Pd	-1.05512321	0.80960464	1.30834620

$Au_7Pd_1^+$

Au	-1.67956878	-1.18171648	-1.10739164
Au	2.05606254	2.19618217	-1.41678493
Au	-0.38571815	1.30315437	-1.10681790
Au	-2.89275462	0.98961724	-0.14454572
Au	1.25335063	-1.15915554	2.54129294
Au	1.72174151	0.21224318	0.25896716
Au	0.43565314	-2.27678382	0.26179465
Pd	-0.87780314	-0.12144854	1.25872646

$Au_8Pd_1^+$

Au	1.66347093	-2.04335718	-2.31185088
Au	-1.95078296	0.40986754	-0.03764288
Au	0.07283782	0.00268165	-1.99254920
Au	-1.21093879	2.31897708	-1.73653151
Au	-0.20350287	-0.40670448	1.94110571
Au	1.82019617	-0.81369436	-0.01378649

Au	2.19673740	0.72656330	2.12263880
Au	-2.70173157	-1.16518078	1.90480971
Pd	0.53914232	1.66547631	0.21110294

$Au_9Pd_1^+$

Au	-1.65841071	-1.43934462	-2.38840992
Au	-1.87434288	0.21670054	-0.29890650
Au	-1.92652198	1.94250825	1.74415025
Au	2.54240318	1.63771580	-1.17523546
Au	0.35047293	1.84634738	0.34366364
Au	2.00734557	-0.45924001	0.50600726
Au	-0.23594685	-2.10246512	-0.14181521
Au	-0.37918399	-0.29645309	2.06511598
Au	0.49239256	0.05533833	-1.84510416
Pd	1.16945489	-2.40097445	2.04077103

$Au_{10}Pd_1^+$

Au	1.22362024	3.00231855	-2.62774609
Au	-0.42359827	2.30515172	-0.69616257
Au	-1.84957031	-2.78509594	-0.95475918
Au	2.97975033	-1.03305863	0.16095255
Au	0.62768261	-1.76875121	-0.80102793
Au	1.81704759	0.77258699	-1.40236271
Au	-1.64332527	-0.10154749	-0.72568880
Au	-0.39246704	-0.24966570	3.45220745
Au	-1.11565962	-1.76444416	1.45184551
Au	-1.62283097	1.43460337	1.54189814
Pd	0.72663216	0.31592592	1.04634677

$Au_{11}Pd_1^+$

Au	2.47629997	-2.38928131	-1.78262192
Au	0.56064440	-0.47939205	-2.22369462
Au	-1.12309640	1.57084007	-2.46570409
Au	0.25458827	-2.32207412	-0.17903735
Au	-2.25295148	2.39912924	0.00523567
Au	2.34648989	-0.41023504	-0.01853954
Au	0.47383894	1.73299742	-0.26301925
Au	2.26809853	1.57573940	1.75955926
Au	-1.72897583	-2.07734576	1.58238875
Au	-2.54985344	0.61133353	1.98902397
Au	0.16455271	-0.12957536	1.80366229
Pd	-1.53426852	-0.16547099	-0.37875071

$Au_{12}Pd_1^+$

Au	3.979187664	4.618647726	5.890593661

Au	6.063954015	4.181672056	4.132610413
Au	3.928993082	6.971500468	7.242412159
Au	8.176292584	8.032219123	5.490795133
Au	7.890169607	6.233932778	3.522245811
Au	8.062330079	4.968387907	5.920584824
Au	3.682214471	9.480692473	7.985488342
Au	8.669181944	9.464931551	7.748365938
Au	6.110666788	8.716384848	7.339753273
Au	8.350783919	4.222664938	8.510762365
Au	5.911540107	5.104319790	7.735003213
Au	8.114166522	6.852926347	8.046071196
Pd	5.834799763	6.595295171	5.314933623

$Au_{13}Pd_1^+$

Au	4.658600268	6.563749349	3.524977627
Au	4.191088780	4.364245538	5.143858565
Au	8.972629621	6.100866499	5.821559416
Au	8.195729383	5.645657945	8.565803939
Au	7.527768176	8.046639673	7.145304646
Au	5.084309967	9.138443784	7.524631806
Au	5.894669234	4.426368716	7.328120458
Au	10.092858062	7.385954876	7.961734206
Au	5.590486873	6.821149727	8.857583700
Au	6.330995328	4.430428555	10.006885077
Au	4.977933446	9.058647767	4.682754523
Au	6.831670739	4.900692543	4.746895942
Au	7.243119219	7.581709384	4.262844929
Pd	5.208104711	6.788278574	6.124094560

$Au_{14}Pd_1^+$

Au	9.609622837	8.301873409	5.829508433
Au	6.229853228	5.073530196	3.232281620
Au	4.691319517	9.684481388	5.054041785
Au	7.964528146	6.569608946	4.614842727
Au	5.132564811	7.023251520	4.705202489
Au	3.647653526	5.470341528	6.562247725
Au	9.024982793	4.436293149	6.090726910
Au	7.014797641	8.863896523	6.138185658
Au	4.556380951	8.026492265	7.212348852
Au	4.811996293	3.377373754	7.939338630
Au	7.497493988	3.820748654	8.238161192
Au	5.626012153	5.876715148	8.554821269
Au	8.140233126	6.603237741	7.484872336
Au	6.661109390	8.320520044	9.028289196

Pd	6.250168816	4.722390327	5.944310832

$Au_{15}Pd_1^+$

Au	8.175106129	5.000292952	3.626669949
Au	3.875394516	6.718089902	4.909032744
Au	7.537426997	9.930892843	5.221646231
Au	9.775260230	6.264118415	8.453317086
Au	3.483417493	4.178301142	6.048630053
Au	5.823150700	8.459846649	6.849901300
Au	7.114283580	7.286806038	4.597254614
Au	5.883502709	4.811767877	5.019977255
Au	5.024479975	9.044273530	4.280955183
Au	8.290035423	5.330492286	6.314830918
Au	8.627143289	8.164718750	6.958951355
Au	5.061096704	8.069478017	9.396567237
Au	4.391764210	6.215149013	7.590631247
Au	5.785363775	3.841951214	7.645520147
Au	8.229102381	3.951827335	8.704627852
Pd	7.012968510	6.397543623	8.509294504

$Au_{16}Pd_1^+$

Au	6.967247735	6.868673574	2.770325173
Au	9.168923164	6.580128444	6.864272282
Au	5.441175090	7.830672538	4.774711708
Au	9.475174868	9.366566174	6.809489153
Au	8.551192128	3.973549607	6.867138610
Au	7.761758986	8.250264286	8.723923376
Au	4.990493149	7.826664928	7.579727283
Au	8.369825311	8.156788912	4.644378889
Au	7.056405325	5.605139145	5.211706218
Au	4.339261310	5.566416280	5.958784673
Au	4.201512941	9.909096664	6.003266837
Au	6.828179933	9.679070671	6.484751066
Au	5.681052296	3.485972443	7.044037327
Au	7.460937717	1.563340772	7.165876939
Au	4.238441567	5.303004805	8.726600418
Au	5.714718128	7.171182509	10.150874283
Pd	6.780542741	5.779144096	7.998398052

$Au_{17}Pd_1^+$

Au	4.983808379	9.097099235	3.659591313
Au	3.757968232	6.534861647	3.547559313
Au	6.539176004	6.870831128	3.244321275

Au	**8.364265180**	**5.672500695**	**4.712760992**
Au	**5.487689363**	**4.937910564**	**4.943773859**
Au	**7.242022285**	**8.702016677**	**5.175102022**
Au	**4.557464093**	**7.619917658**	**5.912014562**
Au	**10.036473257**	**4.824921504**	**6.798649260**
Au	**7.341790495**	**4.170757614**	**6.797062407**
Au	**8.457503983**	**9.918519294**	**7.316040847**
Au	**8.873099094**	**7.282471079**	**6.893177182**
Au	**5.106916821**	**5.545678952**	**7.592907627**
Au	**8.471139906**	**5.514945643**	**8.992021293**
Au	**6.325083718**	**3.828814684**	**9.342788500**
Au	**8.405680613**	**8.217909098**	**9.594225717**
Au	**6.134805406**	**6.608858658**	**10.009062523**
Au	**3.888530415**	**7.705658021**	**8.668611341**
Pd	**6.354135984**	**8.295661714**	**7.815836563**

$Au_{18}Pd_1^+$

Au	**9.201672278**	**8.694844451**	**4.059772746**
Au	**6.067593572**	**4.279368886**	**4.671162187**
Au	**6.546941389**	**8.691452219**	**4.838095963**
Au	**3.689731549**	**5.181079694**	**5.692778063**
Au	**4.426750400**	**7.815502336**	**6.339524178**
Au	**8.262171308**	**4.744794137**	**6.509933745**
Au	**8.928685906**	**7.428141588**	**6.486674026**
Au	**5.562132379**	**4.196919350**	**7.404772966**
Au	**5.806129146**	**10.015964006**	**7.200520677**
Au	**8.057451725**	**8.980676635**	**8.651977028**
Au	**3.596670101**	**6.012596326**	**8.307526472**
Au	**7.677798148**	**3.560171727**	**8.942705495**
Au	**8.017132239**	**6.296013634**	**8.797151572**
Au	**5.567604066**	**7.840500148**	**8.900748899**
Au	**5.724354018**	**5.311009390**	**9.962739307**
Au	**8.622285691**	**3.764237891**	**4.018115930**
Au	**5.043937050**	**6.712577833**	**3.834808674**
Au	**8.390405284**	**10.210696978**	**6.227583687**
Pd	**7.845026556**	**6.343148869**	**4.200653736**

$Au_{19}Pd_1^+$

Au	**7.043629448**	**8.730039472**	**5.134048059**
Au	**4.331219396**	**6.807385774**	**6.777786415**
Au	**9.293907899**	**5.245736137**	**7.568520086**
Au	**6.317050618**	**10.579939633**	**7.050662317**
Au	**7.422003894**	**3.306633828**	**6.959529702**
Au	**5.027484430**	**4.410755643**	**7.832823156**

Au	**8.486830345**	**6.950649894**	**9.687100681**
Au	**8.739877941**	**9.393555259**	**7.163951416**
Au	**4.405895768**	**9.003076070**	**8.440714535**
Au	**7.353500098**	**4.535050479**	**9.436868437**
Au	**4.958970033**	**7.285392316**	**4.042176418**
Au	**6.160870221**	**5.234237289**	**5.435330611**
Au	**9.252433181**	**7.193934918**	**5.590371724**
Au	**4.293519539**	**9.339383471**	**5.681386043**
Au	**8.778036141**	**4.537813256**	**4.909056041**
Au	**10.664189051**	**7.570811376**	**7.940544301**
Au	**5.723329280**	**6.732671242**	**9.225265031**
Au	**9.654098307**	**9.434925674**	**9.760568656**
Au	**6.945935027**	**9.228958909**	**9.435021498**
Pd	**7.545770852**	**6.565218412**	**3.536176837**

4.3 Draft Publication 4

Title

Altering CO binding on Gold Cluster Cations by Pd-doping

Authors

Heider A. Abdulhussein, Piero Ferrari, Jan Vanbuel, Christopher Heard, André Fielicke, Peter Lievens, Ewald Janssens and Roy L. Johnston

4.3.1 Author Contribution

The study is a collaborative effort between groups at the Catholic University of Leuven, the Fritz Haber Institute of the Max Planck Society, Berlin and the University of Birmingham. All the global optimizations for free clusters and the spin-states optimizations for all cluster-carbonyl complexes were performed by the author. All possible complexes with one and two atop adsorbed CO molecules were constructed by the author, with an advisory role provided by Christopher Heard (Charles University, Prague). NWChem-DFT refinement calculations including; structural optimization, single-point energy, electronic distribution, vibrational spectra, were all implemented for free and CO-adsorbed clusters by the author, except odd-atom pure Au clusters with N$\leq$13, and odd-atom Pd-doped clusters with N$\leq$9, which were performed by Christopher Heard. The calculations to assess and compare various manually constructed adsorption sites, including: atop (terminal), edge-bridging (bridge) and face-capping (hollow) binding for $Au_N{}^+$(CO) and $PdAu_{N-1}{}^+$(CO), N= 3 and 4 clusters, were all performed by the author. The post-calculation analysis of the DFT calculated binding (adsorption) energies, CO stretching frequencies, the Mulliken and Löwdin charge populations, and bond lengths were all implemented by the author. All vibrational modes needed for the RRKM simulations were provided by the author. The author contributed to interpretation and discussion of the

theoretical findings. The figures 1, 3, 4, and 9 (Theory) in the paper and tables S1-S5 in the supplemental material, were all created by the author. The manuscript was written by the author, except for the experimental parts and section 3.2.

Journal Name

ARTICLE

Altering CO binding on Gold Cluster Cations by Pd-doping

Heider A. Abdulhussein,[a,b] Piero Ferrari,[c] Jan Vanbuel,[c] Christopher Heard,[d] André Fielicke,[e] Peter Lievens,[c] Ewald Janssens[c] and Roy L. Johnston*[a]

Received 00th January 20xx,
Accepted 00th January 20xx

DOI: 10.1039/x0xx00000x

www.rsc.org/

The introduction of dopant atoms into metal nanoparticles is an effective way to control the interaction with adsorbate molecules and is important in many catalytic processes. In this work, experimental and theoretical evidence of the influence of Pd doping on the bonding between small cationic Au_N ($N \leq 21$) clusters and CO is presented. The CO adsorption is studied by combining low-pressure collision cell reactivity and infrared multiple photon dissociation spectroscopy experiments with density functional theory calculations. Measured dissociation rates of the cluster-CO complex allow the estimation of cluster-CO binding energies, showing that Pd doping increases the CO adsorption energy to an extent that is size-dependent. These trends are reproduced by theoretical calculations. In agreement with theory, measurements of the C-O vibrational frequency suggest that for the doped $PdAu_{N-1}^+$ (N=3-5, 11) clusters, CO adsorbs on an Au atom, while for N = 6-10 and N= 12-14, CO interacts directly with the Pd dopant. A pronounced red-shifting of the C-O vibrational frequency is observed when CO interacts directly with the Pd dopant, indicating a significant back-donation of electron charge from Pd to CO. In contrast, the blue-shifted frequencies, observed when CO interacts with an Au atom, indicate that σ-donation dominates the Au-CO interaction. Studying such systems at the sub-nanometre scale enables a fundamental comprehension of the interactions between adsorbates, dopants and the host (Au) species at the atomic level.

1 Introduction

The surface of a catalyst is crucial for its catalytic activity and can be affected by many factors. The surface and core of nanoalloy systems usually differ in their chemical composition,[1] given that surface segregation is controlled by the surface free energy. However, the active surface state of a nanoalloy catalyst cannot be predicted only on the basis of surface energy. Other parameters, such as particle size and support effects, as well as the influence of adsorbates,[2,3] are important in determining the composition of the particle's surface. Under catalytic reaction conditions, these factors determine the surface segregation, thereby altering the structures and the local atomic compositions, and consequently the activities and selectivities of nanoalloy catalysts. This has been observed in a number of gold alloy systems.[4,5] For example, thermodynamically, Au tends to occupy surface sites on AuPd nanoalloys under vacuum conditions.[6–8] However, upon exposure to reactive gases, such as CO,[9,10] O_2,[11] NO,[6] and CO+O_2,[12] facile surface segregation of Pd occurs. The preference for Pd atom migration to the nanoalloy-substrate interface has also been investigated for AuPd nanoalloys on an oxide-support.[13,14] Such observations emphasize that the segregation mechanism is subtle, and hence it is necessary to combine a variety of different techniques to characterize the structures and reactivities of nanoalloys under industrial catalysis conditions.

Fundamental aspects of molecular adsorption and catalytic activity of nanoalloys can be investigated by studying small gas-phase clusters.[15–17,19] The ability to tune the size, composition and charge state of clusters in the gas-phase enables elucidating the specific role each of these parameters play in different reactions. From a theoretical point of view, small clusters at the sub-nanometre scale can be studied at a high level of theory.[15] The possibility of combining state-of-the-art experiments with high-level theory calculations allows the direct comparison of findings, by which one can gain important understanding of interactions and processes at the atomic scale.[18,19] Moreover, sub-nanometre clusters themselves often exhibit higher catalytic performance (activity and/or selectivity)[20] compared to their bulk and even nanoscale counterparts.[21,22] For example, Au_N clusters (N=8, 13 and 20) supported on MgO and $Mg(OH)_2$ surfaces have shown high catalytic activity for CO oxidation.[23–25]

The nature of CO adsorption on metallic clusters is strongly dependent on the type(s) of metal. Dissociative adsorption of CO is favoured on relatively electron deficient metals on the left-hand side of the periodic table[26,27] (e.g. V,[28] Nb,[29–32] Mo and Tc[30]). The more loosely bound electrons, coupled with the only partially filled d-bands of these early transition metals, make them more reactive. Also, for these more electropositive metals there is an increased possibility of coordination of CO via both the C and O atoms. These

[a] School of Chemistry, University of Birmingham, Edgbaston, Birmingham B15 2TT, UK. E-mail: r.l.johnston@bham.ac.uk.
[b] Department of Chemistry, College of Science, University of Kufa, Najaf, Iraq.
[c] Laboratory of Solid State Physics and Magnetism, KU Leuven, 3001 Leuven, Belgium. E-mail: ewlad.janssens@kuleuven.be.
[d] Department of Physical and Macromolecular Chemistry, Charles University, 12843 Praha 2, Czech Republic.
[e] Fritz-Haber-Institut der Max-Planck-Gesellschaft, Faradayweg 4-6, 14195 Berlin, Germany.
†Electronic Supplementary Information (ESI) available: See
DOI: 10.1039/x0xx00000x

factors combine to favour CO dissociation, resulting in adsorbed C and O atoms rather than an adsorbed molecule.[27,31,33,34] The gradual activation of the C-O bond when moving towards the early transition metals has been detected by IR spectroscopy of the cluster-CO complexes.[26,27,35] The bonding between CO and the metals on the right-hand side of the *d*-block, including Au[36,37] and Pd,[38] is treated by the Blyholder model,[39] where σ-donation of electron density from CO to the metal and π-backdonation from the metal to CO take place. Thus, they form weaker metal–CO bonds, leading to non-dissociative CO adsorption (the adsorbed CO molecules in such systems are easily desorbed, without dissociation, by raising the temperature[33,40]). The transition from dissociative to non-dissociative CO adsorption on transition metals has been previously identified at room temperature by Brodén et al.[26], suggesting that the transition shifts from iron in the 3d-block across technetium in the 4d-block towards tungsten in the heavier 5d elements.

Previous studies on Au clusters have shown that many of their physical and chemical properties can be tuned by the presence of a dopant atom.[41–44] The geometries,[45] optical properties,[46–48] and reactivities,[42,43,49–51] of doped Au clusters are, therefore, expected to be different from those of their pure Au counterparts. A significant amount of research has been performed on investigating doping and mixing effects on the reactivity of binary metallic nanoparticles with CO molecules. For AuPt clusters, the composition $Au_{0.27}Pt_{0.25}$ is found to show the highest adsorption strength of CO.[52] Adding a Pd dopant atom into cationic Au_N^+ clusters (*N*=2-20) is found to induce electronic and structural modifications, and results in very different stability patterns.[19] It has previously been shown that the interaction with CO is improved significantly by doping Pd atoms into smaller free Au_N (*N*=2-3) clusters.[53] The interaction is also enhanced for (*N*=4 and 6) but reduced for *N*=5 after doping a single Pd atom in the Au_N^+ clusters.[54] While doping a single atom of Au does not change the catalytic properties of the Pd_5 cluster for CO oxidation,[55] enhanced CO oxidation activity has been observed for Au_1Pd_4 deposited on a TiO_2(110) surface.[56] Stronger CO adsorption has also been predicted for doping vanadium into Au_N, (*N*= 2-14), clusters.[43] In contrast, doping copper, silver or yttrium atoms into Au clusters was found to reduce the cluster-CO interaction, which was attributed to a decrease in electron transfer between the metal cluster and the CO molecule.[53,57,58]

Formation of contiguous Pd sites, in particular forming dimers at the surface of AuPd(100) systems under high CO pressures, was investigated by Goodman and co-workers.[59,60] They demonstrated that Pd starts to segregate to the surface at a CO pressure of 10^{-3} Torr at 260 K. Zhu et al. [61] found evidence for CO-induced Pd surface enrichment, and in addition that, at low Pd concentrations, only Pd dimers and isolated Pd atoms are present on the surface of AuPd nanoparticles. These findings emphasize the importance of determining the surface structures and chemical ordering of nanoalloys under vacuum conditions and controlling these features under realistic operating conditions, in order to optimize catalyst performance. Although the segregation of Pd to an alloy surface in the presence of CO can be suggested by experimental[10,62] and theoretical[6,9,60,63] studies, knowledge of the effect of doping by single Pd atom on the coordination and surface reactivity of gold clusters towards CO gas, as well as the preferred location of the Pd atom, remains limited.

In this work, we combine low-pressure collision cell reactivity and infrared multiphoton dissociation spectroscopy experiments with density functional theory calculations to study in detail the influence of Pd-doping on the interaction of one and two CO molecules on a series of small cationic gold clusters Au_N^+, $N \leq 21$ atoms.

2 Methods

2.1 Theoretical calculation methods

The Birmingham Parallel Genetic Algorithm (BPGA),[64] combined with Density Functional Theory (DFT), has previously been employed for global optimization of cationic Au_N^+ and $PdAu_{N-1}^+$ (*N*=1-20) clusters.[19] The DFT calculations (Γ-point) are performed using the Vienna Ab initio Simulation Package (VASP),[65] employing projected-augmented wave (PAW) pseudopotentials and the PBE exchange correlation functional.[66,67] A plane-wave basis set is utilized, including spin polarization. The plane wave cut-off energy is truncated at 400 eV. To improve convergence, Methfessel-Paxton smearing, with a sigma value of 0.01 eV is used.[68] The thresholds for the electronic energy and forces are set to 10^{-6} eV and 10^{-5} eV/Å, respectively.

As shown in Figure 1, in BPGA a parallel evaluation of cluster structures is performed, using the so-called pool methodology.[71] Each BPGA run implements multiple GA instances which, in turn, run a set of parallel processes independently.[71,72] The initial population (a specified number of random structures) is generated from scratch and then subjected to geometrical relaxation (DFT local energy minimization). Crossover and mutation operations are then performed. Selection of individuals for crossover is achieved by tournament selection. The cut-and-splice method of Deaven and Ho[73] is used to perform the crossover. A homotop-swap option is adopted as a mutation operation for nanoalloys, while for the pure clusters a random-atom displacement mutation is employed. Fitness evaluation is then used to replace the highest energy isomers by the newly created lowest energy isomers among the set of offspring and mutants. The structure with the lowest energy, in the final population, is chosen as the global minimum (GM) geometry.

Considering all symmetry-inequivalent atomic sites in a particular cluster, all possible complexes with one and two atop adsorbed CO molecules are generated, for the putative GM located by the BPGA-DFT approach. All metal-CO complexes are then subjected to spin-unrestricted DFT local minimization using the orbital-based NWChem DFT package.[69] Def2-TZVPP basis set for all atoms; Au, Pd, C, and O, and the corresponding effective core potentials (def2-ECP) of Weigend and Ahlrichs are employed for Au and Pd.[70] The range separated hybrid exchange-correlation functional LC-*ω*PBEh is utilised.[71,72] The harmonic vibrational frequencies were calculated using the NWChem package, employing the same exchange correlation functional and basis set as in the geometry optimization step.[70] This allows the confirmation that the calculated structures are true energy minima (i.e. having no imaginary frequencies). Spin states are optimized for each cluster and cluster-CO complex. All the optimal electronic configurations are found to exhibit the lowest possible spin multiplicity, which

corresponds to either 2S+1 = 1 (singlet) for even electron counts or 2 (doublet) for the odd electron counts.

Binding energies of CO on the clusters are calculated as:

$$E_b = E_{CO} + E_{cluster} - E_{cluster-CO}, \quad (1)$$

where E_{CO}, $E_{cluster}$ and $E_{cluster\text{-}CO}$ are the energies of CO, the cluster and its corresponding CO complex, respectively.

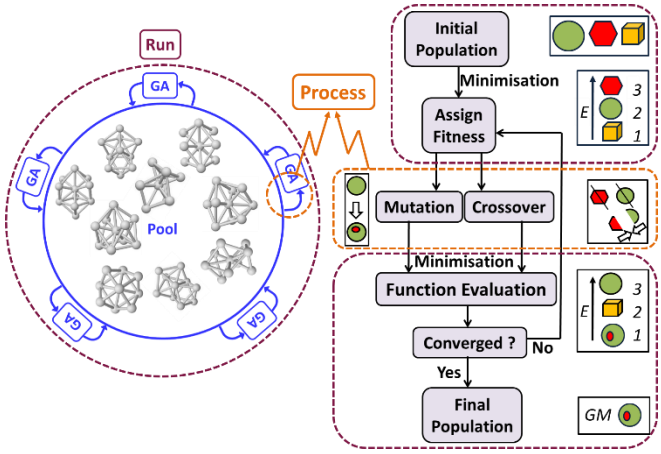

Fig. 1 Schematic representation of the BPGA programme. The left side shows the pool methodology, containing the structural database (within the blue circle) and defines the run (purple colour), and process (orange colour) concepts. The instance concept consists of carrying out the specified type of mutation or crossover (process), followed by DFT local minimization. The flow chart on the right side illustrates the GA operations.

2.2 Reactivity measurements

Reactivity measurements are performed in a dual-target dual-laser cluster setup described in detail elsewhere.[73] Two independent Au and Pd targets are ablated by two Nd:YAG lasers (532 nm, 10 Hz). Before ablation, He gas is introduced at the source by a pulsed valve (backing pressure of 7 bar). By collisions with He, the ablation plasma is cooled down, triggering cluster formation. This process is enhanced by a supersonic expansion into vacuum of the ablated plume, taking place through a conical nozzle that is kept at a temperature of 200 K by a flow of liquid N_2 and resistive heating. The cluster beam, composed of a mixture of pure Au_N^+ and single doped $PdAu_{N-1}^+$ clusters, is then interacting with CO gas in a low-pressure collision reaction cell (controlled pressures of CO, P_{CO}, in the 0-0.2 Pa range).[74] This leads to the formation of cluster–CO complexes, with each cluster adsorbing maximally one CO molecule. Finally, the distribution of pure clusters and their CO complexes is analyzed by reflectron time-of-flight (TOF) mass spectrometry. A typical example of a mass spectrum recorded under these conditions is presented in Figure 2.

Quantitative information on cluster reactivity is extracted based on a proposed model for adsorption. Since in the studied P_{CO} range at most one CO molecule is attached per cluster, no sequential adsorption of CO is considered. A detailed description of this model can be found in Refs.[75,76]. As a function of P_{CO}, the relative abundance of the $MAu_{N-1}^+(CO)$ [M=Au, Pd] complex with respect to the bare MAu_{N-1}^+ cluster is given by.

$$\frac{[MAu_{N-1}{}^+(CO)]}{[MAu_{N-1}{}^+]_0} = \frac{k_f P_{CO}}{k_f P_{CO} + k_D k_B T_{CO}} e^{-k_D t_2} \left(1 - e^{-\left(k_f \frac{P_{CO}}{k_B T_{CO}} + k_D\right) t_1}\right). \quad (2)$$

Here k_B is the Boltzmann constant, T_{CO} the temperature of the CO gas (e.g. room temperature), and t_1 and t_2 the times clusters spend inside the reaction cell and between the cell and the entrance to the time-of-flight mass spectrometer, respectively. k_f and k_d are the rates of formation and dissociation of a cluster-CO complex, respectively. The procedure follows by fitting Eq. (2) to the experimentally determined normalized abundances of cluster-CO complexes as a function of P_{CO} at the reaction cell, with k_d as fitting parameter. The rate of forward reaction, k_f, is approximated by hard-sphere collision theory.[42] Only for N=4 this procedure did not give a satisfactory fit of the experimental data, and both k_f and k_d had to be used as fitting parameters. For this cluster size a k_f coefficient slightly larger than the value corresponding to the hard sphere approximation is found, suggesting a role of electrostatic interactions in the CO adsorption process for this cluster size.

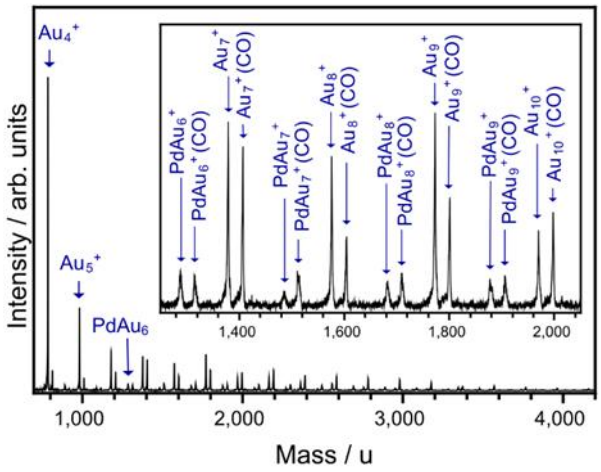

Fig. 2 Typical mass spectrum of Au_N^+ and $PdAu_{N-1}^+$ clusters and their CO complexes, formed in the low-pressure collision reaction cell. A zoom-in is shown for N=7-10. Clusters are exposed to a CO gas pressure of P_{CO} = 0.2 Pa.

2.3 Infrared multiphoton dissociation measurements

The frequencies of the internal C-O stretching mode (ν_{CO}) of cluster-CO complexes are measured by infrared multiple photon dissociation (IRMPD) spectroscopy, performed in a dual-target dual-laser cluster source setup coupled to the beamline of the Infrared Free Electron Laser at the Fritz Haber Institute of the Max Planck Society (FHI FEL).[77,78] A detailed description of the cluster source is given in Ref. [79], and its operational principles are similar to those of the cluster source used for the reactivity measurements. The main difference is that the CO gas is introduced via a reaction channel directly connected to the cluster source, using a pulsed valve at a backing pressure of 1 bar. In this way, clusters interact with CO in a high-collision regime and the complexes formed are thermalized by the

pressure of He. The source is operated at room temperature. In the studied size range *of N* = 5-14, each cluster attaches up to two or three CO molecules.

After production, the cluster beam is collimated by a 2 mm diameter skimmer, followed by a 1 mm diameter aperture. In between the clusters interact with focused, counter-propagating, IR laser beam delivered by the FHI FEL (5 Hz). Finally, clusters are analysed by reflectron TOF mass spectrometry and mass spectra are recorded with and without (reference spectra) exposure to the IR light. The FHI FEL is tuned in the 2050-2250 cm^{-1} frequency range and an average energy of 25 mJ/pp with a step size of 5 cm^{-1} is used during the measurements. When laser excitation takes place in resonance with the C-O stretching mode, multiple photon absorption heats up the cluster, via intra-molecular vibrational redistribution. Once the internal energy of the cluster is high enough, fragmentation occurs through the lowest-energy fragmentation channel, in this case the desorption of the CO molecule. This allows recording depletion spectra, by comparing cluster-CO complex intensities in mass spectra with and without laser interaction.

3 Results and discussion

3.1 Binding energies CO

The structures of CO complexes can be determined and their cluster-CO binding energies can be calculated theoretically. Various CO adsorption sites were considered in order to determine the lowest-energy configurations. Atop (terminal), edge-bridging (bridge) and face-capping (hollow) binding sites were compared for the $Au_N^+(CO)$ and $PdAu_{N-1}^+(CO)$ clusters with *N*=3 and 4. The relative binding energies of CO (ΔE_b), corresponding to the different adsorption sites, are listed in Table S1 of the Supplemental Material. Although the bridging site is preferred for $PdAu^+(CO)$, atop sites are found to be the preferred adsorption sites of CO for all the clusters with *N*=3 and 4. In addition, the Au atop site is found to have a ν_{CO} value closest to that measured by IRMPD for both $PdAu_3^+(CO)$ and $Au_4^+(CO)$ clusters (see below). Atop CO binding on Au was previously suggested for the $PdAu_2^+(CO)$ cluster.[53] Based on the correlation of calculated atop CO frequencies and experiment, only atop site adsorption is considered for the larger cluster-CO complexes.

Based on the structures located by our global optimization calculations and those reported recently,[19] all possible atop adsorption site configurations of CO on Au_N^+ (*N*=2-13) and $PdAu_{N-1}^+$ (*N*=2-10) clusters were calculated. The geometries of the lowest energy isomers are shown in Figure 3. The structures of complexes with two CO molecules adsorbed on atop sites have also been calculated for selected sizes (*N*=2-7 for Au_N^+ and *N*=4-7 for $PdAu_{N-1}^+$). Their lowest energy geometries are also shown in Figure 3. Although a large number of CO ligands can distort the frameworks of some metal clusters (e.g. $Au_5^+(CO)_{4,5}$ and $Au_6^+(CO)_{5,6}$), in order to maximize the number of Au-CO bonds,[36,80,81] the adsorption of one or two CO molecules typically does not lead to significant structural rearrangements. However, upon adsorption of a single CO molecule, the central structure of the doped $PdAu_7^+$ cluster undergoes a distortion from a square-based pyramid to a trigonal bipyramid. Also, for $PdAu_5^+$ there is a distortion from a bicapped tetrahedron for the bare cluster and mono-carbonyl species to a capped square-based pyramid for the dicarbonyl species. For the smallest clusters, the CO molecule is bound preferentially to a low-coordinated Au atom, while for *N*≥6 the Pd dopant becomes the preferred adsorption site.

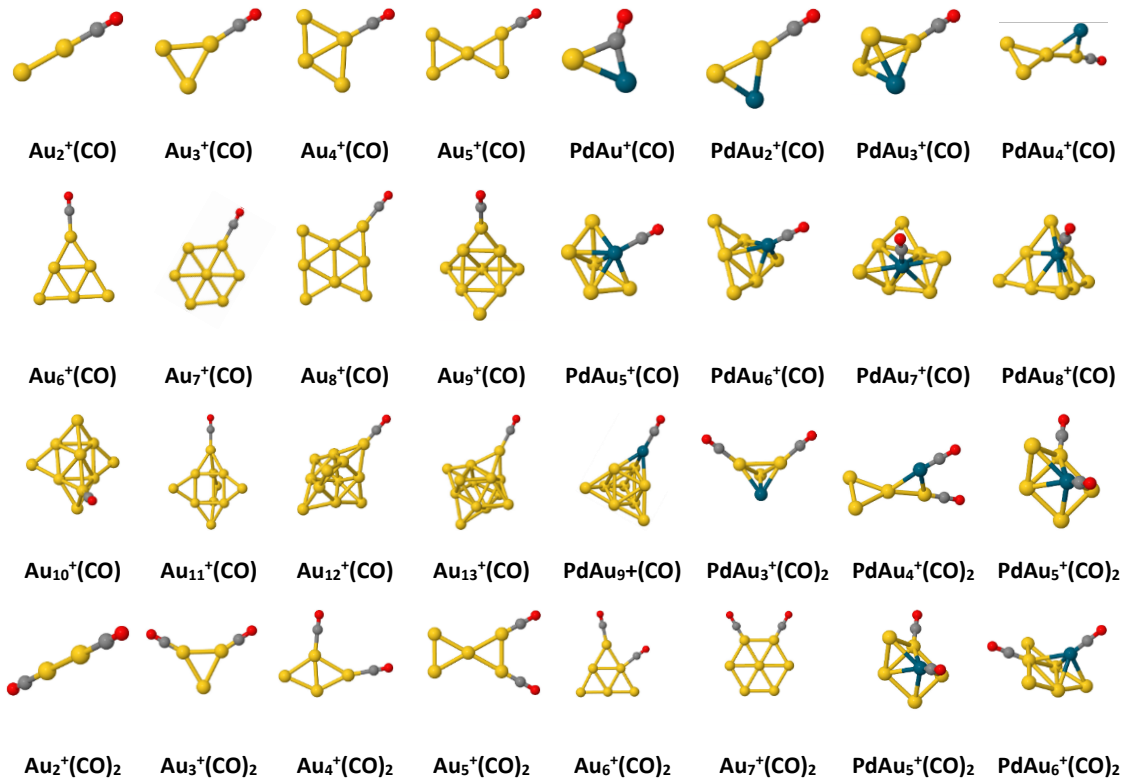

Fig. 3 Lowest-energy structures of $Au_N^+(CO)$ (*N*=2-13), $PdAu_{N-1}^+(CO)$ (*N*=2-10), $Au_N^+(CO)_2$, (*N*=2-7) and $PdAu_{N-1}^+(CO)_2$ (*N*=4-7) clusters. Au, Pd, C, and O are shown in yellow, blue, grey, and red, respectively.

Based on the lowest energy structures presented in Figure 3, CO binding energies were calculated via Eq. (1). A summary of the binding energies is presented graphically in Figure 4 and listed in Table S2 of the Supplemental Material. A very high E_b value is found for $PdAu^+(CO)$ (E_b=5.93 eV) with a bridging CO adsorption site between the Au and Pd atoms, opposite to $Au_2^+(CO)$ (E_b=1.93 eV) where CO adopts an atop configuration. In the N=3-5 size range, CO interacts directly with a Au atom in both $Au_N^+(CO)$ and $PdAu_{N-1}^+(CO)$. For N≥6, an odd-even variation (relative to the number of atoms) can be seen in the calculated binding energies E_b for $Au_N^+(CO)$ clusters. However, for sizes (N≥5), a significantly larger E_b is obtained for the Pd-doped species, as compared to the pure clusters composed of the same number of atoms, except for size N=7 which has almost the same value in both cases. Considering other CO adsorption sites, for $PdAu_6^+(CO)$ E_b is only 0.1 eV greater for the global minimum (Pd bound), while this difference is 0.15 eV in the case of $PdAu_8^+(CO)$. For the $PdAu^+(CO)$ cluster, CO adsorption on Au is 0.6 eV less stable than on Pd (which spontaneously deforms into the μ_2 bridging mode), though the Au-bound isomer was predicted to be the most stable structure by Deng and co-workers.[82] Overall, as seen in Figure 4, Pd-doping enhances the interaction of CO on the clusters, even in those cases where Au is the adsorption site.

The DFT calculations are complemented by mass spectrometric experiments. Already from the mass spectrum presented in Figure 2 a size-dependent effect of Pd-doping can be seen in the interaction of the clusters with CO. For example, for N=7 and 10 no clear influence of doping is visible (i.e. the ratio of the intensities of the cluster–CO complex and the bare cluster is comparable for Au_N^+ and $PdAu_{N-1}^+$). In contrast, a clear influence of the dopant is observed for N=8 and 9, with the intensity ratio of the CO complexes to the bare clusters being larger for $PdAu_{N-1}^+$ than for Au_N^+. These differences in the relative intensities of the bare clusters and their CO-complexes only qualitatively illustrate the effect of doping on the interaction of a cluster with CO. To quantify the effect of doping, pressure dependent relative abundances of the CO complexes are fitted using Eq. (2), as described in the Methods Section. This analysis gives the dissociation rates of CO, k_d, which are sensitive to the CO binding energy.

Examples of these fits are shown in Figure 5, for the pure gold clusters $Au_4^+(CO)$, $Au_8^+(CO)$ and $Au_{20}^+(CO)$ in panel (a) and for the doped clusters $PdAu_3^+(CO)$, $PdAu_7^+(CO)$ and $PdAu_{19}^+(CO)$ in panel (b). From the left panel of Figure 5 it can be observed that the relative intensity of the CO complexes is higher for larger clusters. This is a consequence of the reduced heat capacity of the smaller species; small clusters heat up more upon redistribution of the heat of formation of the CO complex (binding energy), thereby increasing k_d.[78] Thus, only clusters of the same size should be compared to exclude (to a first approximation) the effect of the different clusters heat capacities. The inclusion of heat capacity effects into the analysis is presented in section 3.2. A second observation from Figure 5 is the effect of doping on the CO adsorption, as observed also in Figure 2. While for N=8 the presence of Pd increases the adsorption of CO considerably, reduced reactivity is found upon doping Au_{20}^+. This suggests stronger binding of CO to $PdAu_7^+$ than to Au_8^+, with the opposite applying to the cases of $PdAu_{19}^+$ and Au_{20}^+.

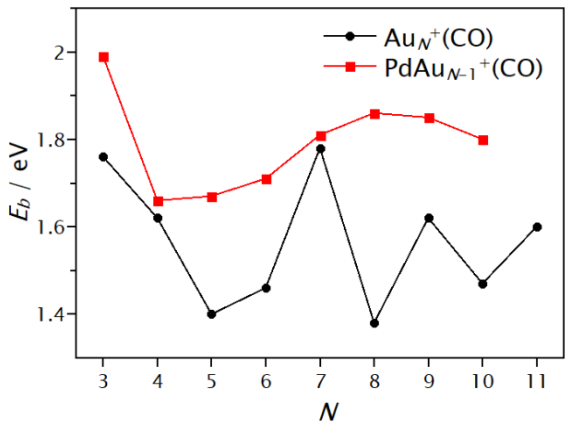

Fig. 4 Cluster-CO binding energies (E_b) calculated by DFT as a function of cluster size for $Au_N^+(CO)$ (N=3-11) and $PdAu_{N-1}^+(CO)$ (N=3-10).

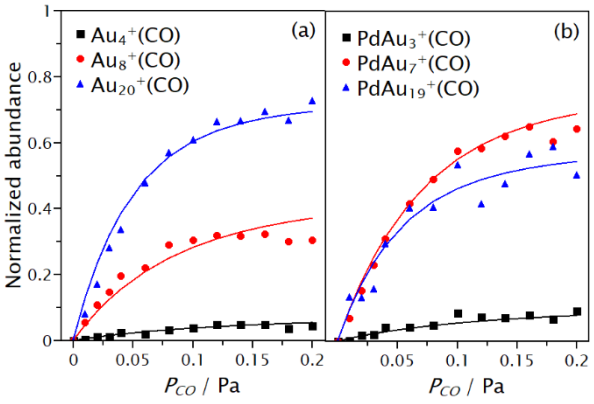

Fig. 5 Normalized abundances of $Au_4^+(CO)$, $Au_8^+(CO)$ and $Au_{20}^+(CO)$ in (a) and $PdAu_3^+(CO)$, $PdAu_7^+(CO)$ and $PdAu_{19}^+(CO)$ in (b), as a function of P_{CO} at the reaction cell. Points represent the experimental data, while solid lines are fits with Eq. (2).

A summary of the extracted k_d values is shown in Figure 6 for the pure Au_N^+ and single doped $PdAu_N^+$ clusters (N=4-21). First, an overall decrease of k_d with cluster size is observed. This, as discussed previously, is a consequence of the reduced heat capacity of the smaller clusters. Although the influence of Pd is not drastic for all sizes, some interesting cases are seen. For the sizes N=4, 5, 9 and in particular for N=8, reduced dissociation rates are observed upon doping. As a first approximation, this suggests that for these clusters the substitution of Au by Pd increases the CO binding energy. In contrast, for N=7, 10 and 18-21, dissociation rates are higher upon doping. For these sizes, Pd doping seems to reduce the CO binding energy. This experimental observation seems to be in disagreement with the DFT calculated binding energies E_b shown in Figure 4, where Pd doping was predicted to increase E_b, independent of cluster size. As discussed in the following section, the reason for this apparent discrepancy is that heat capacities are not yet accounted for.

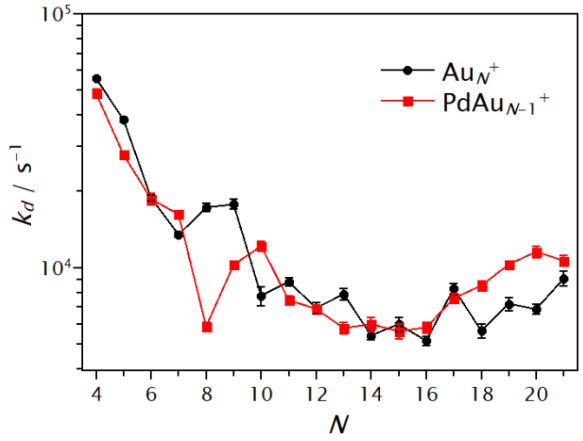

Fig. 6 Dissociation rates of CO for $Au_N^+(CO)$ (black circles) and $PdAu_{N-1}^+(CO)$ (red squares) clusters extracted by fitting Eq. (2) to the normalized abundance curves as a function of P_{CO}.

3.2 RRKM simulations for extracting CO binding energies

The CO binding energy is not the only factor that determines the rate at which CO will be desorb from a cluster. The effect of heat capacities should be included to compare with the DFT calculations, which provide E_b, with the k_d that is obtained from the mass spectrometric experiments. One possibility is to use Rice-Ramsperger-Kassel-Marcus (RRKM) theory.[83–85] In RRKM, a cluster is described as a set of s harmonic oscillators, one for each vibrational degree of freedom. One particular oscillator, the critical oscillator s_0, is selected to represent the reaction coordinate R of the dissociation process. For the clusters studied here, the critical oscillator is the cluster-CO vibration, which leads to dissociation of the complex. The total energy of the energized system (after CO adsorption), E, is assumed to be statistically distributed over the s oscillators and dissociation occurs when a fraction of the total energy E, larger than a critical energy E_0, is localized in s_0. In this case, E_0 is understood as the CO binding energy (calculated by DFT) and the heat capacity of a cluster depends on its vibrational degrees of freedom. By using statistical methods, an expression for the dissociation rate can be obtained. Thus, by knowing k_d and the vibrational frequencies of a cluster, the CO binding energy can be estimated and therefore, theoretical calculations can be directly compared with the experimental findings. This analysis was performed by using the MassKinetics software package.[86]

Results of this analysis are shown in Figure 7. In panel (a) an example of the procedure is presented, for the cluster size N=8. In the figure, simulated dissociation rates are plotted as a function of the critical energy E_0, which represents the CO binding energy E_b. As seen, k_d decreases with increasing E_0, as expected. Dotted lines represent the intersection of the experimentally determined rate and the corresponding critical energy associated with it. This process was performed for the clusters in the N=4-8 size range. For this analysis, the vibrational frequencies of the lowest energy structures calculated by DFT were used. The RRKM determined CO binding energies are given in Figure 7b. Despite the assumptions made in the RRKM analysis, the binding energies extracted by this approach and those calculated by DFT show the same trends. In both cases, an overall decrease in E_b with size is found, being more pronounced for Au_N^+, and most importantly, in all cases higher E_b are found for the Pd-doped clusters. The difference in E_b between Au_N^+ and $PdAu_{N-1}^+$ is found to be small for N=4-6 and larger for N=7 and 8. The effect of the Pd dopant atom for the N=5 and 6 size, however, seems to be smaller in the RRKM estimation than that found by DFT, while the reverse is observed for N=7.

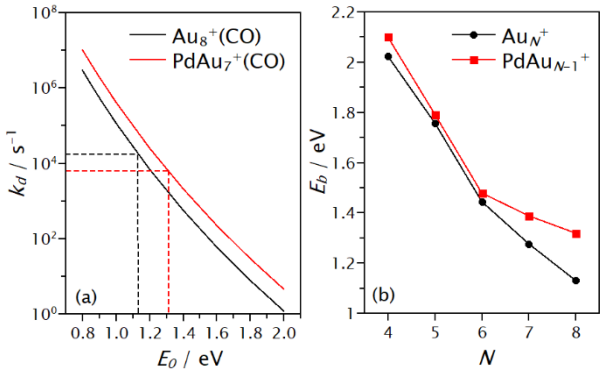

Fig. 7 (a) Dissociation rates as a function of the critical energy, simulated by RRKM theory for N=8. Dotted lines represent the intersection between the measured dissociation rates and the corresponding critical energy. (b) CO binding energies extracted by the RRKM analysis based on the experimental k_d rates.

3.3 Internal C-O stretching frequencies

The frequencies of the internal C-O stretching mode (ν_{CO}) for clusters adsorbing one or two CO molecules in the N=4-14 size range were measured by IRMPD spectroscopy. Knowledge of ν_{CO} alone is not sufficient to characterize the structure of a cluster. However, as discussed below, it allows the determination of the reactive site for CO adsorption (either an Au or a Pd atom).

Depending on cluster size, different behaviour of ν_{CO} with size is observed when comparing clusters with one or two CO molecules. This is exemplified in Figure 8, which shows depletion spectra recorded for the cluster sizes N=5 and N=7, both for the homoatomic (left) and Pd-doped species (right). For Au_5^+, a single absorption feature is observed around 2165 cm^{-1}, independently if the cluster adsorbs a single or two CO molecules. In $PdAu_4^+$, however, the ν_{CO} band of the first CO molecule (black curve) is at approximately 2165 cm^{-1}, as for Au_5^+, while for $PdAu_4^+(CO)_2$ (red curve) two distinct bands are observed. A maximum in depletion is found at 2165 cm^{-1}, in addition to a side peak close to 2120 cm^{-1}. This suggests that for this doped cluster the first CO molecule is bound to a Au atom in $PdAu_4^+$, while the second CO is adsorbed on the Pd dopant. The situation is different for N=7, as shown in the lower panels. As for the previous case, for the homoatomic Au cluster, bands for one and two adsorbed CO molecules are found at the same position, around 2160 cm^{-1}. However, for $PdAu_6^+$, ν_{CO} of the first adsorbed CO is red-shifted almost 30 cm^{-1}, whereas when two COs are adsorbed two distinctive bands are observed. This observation suggests that for $PdAu_6^+$ the first CO molecule is adsorbed on Pd, in contrast to $PdAu_4^+$, in agreement with our calculations.

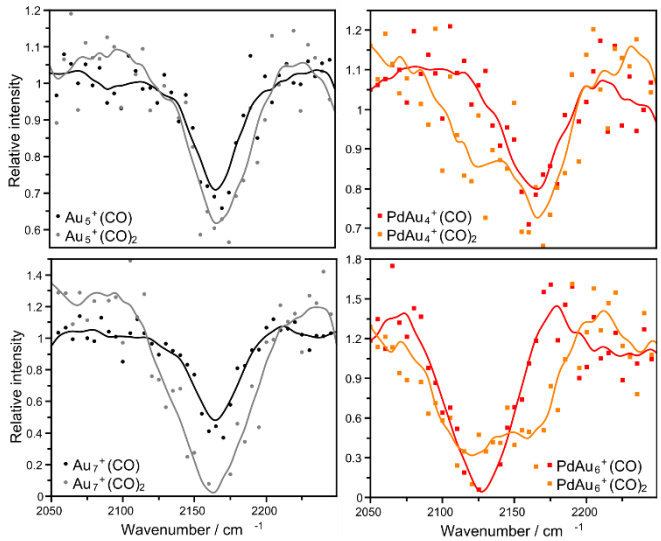

Fig. 8 Depletion spectra of $Au_N^+(CO)_p$ and $PdAu_{N-1}^+(CO)_p$ clusters with N=5,7 and p=1,2. Points represent the experimental data, while solid lines are an average of 4 adjacent points.

A summary of the vibrational frequencies determined by IRMPD of the first adsorbed CO molecule is shown in Figure 9. For the cluster sizes N=4, 5 and 11, depletion spectra suggest that the binding site of the first CO molecule is an Au atom, while for N=6-10 and 12-14, the first CO is proposed to be adsorbed on the Pd dopant.

We have also calculated the vibrational frequency of CO on the most favourable adsorption site on each cluster, using the same level of theory used in the final calculations of the cluster-CO complex structures, i.e. Def2-TZVPP/LC-ωPBEh. To correlate the calculated frequencies of CO with those experimentally measured here, the calculated frequencies of CO have been scaled by a factor 0.956 for all cluster sizes. This factor is determined based on the experimentally reported value of ν_{CO} for the free CO molecule, corresponding to 2143 cm^{-1}.[87] The scaled frequencies are listed in Table S2 of the Supplementary Material and plotted in the right panel of Figure 9. Although the calculated ν_{CO} frequencies are found to be slightly blue-shifted with respect to the experimental values, trends are very well reproduced by DFT. For the species with N=2, a very large gap is found, although in this particular case, this is a consequence of the bridge adsorption site found for $PdAu^+(CO)$. The similar values between the vibrational frequencies for $PdAu_{N-1}^+(CO)$ and $Au_N^+(CO)$ at sizes N=4,5 and 11 observed experimentally are also found in the theoretical calculations. For cluster sizes N=6-10, a larger gap is predicted by DFT, also in agreement with the experimental results. A comparison with previous theoretical calculations from literature is difficult, since studies of the adsorption of CO on cationic Pd doped Au clusters at the subnanometre scale are scarce. The small gap between the frequencies for the species at N=3 predicted here was suggested previously by Zhong et al.[54]. Zhong and co-workers[54] performed DFT calculations for $Pd_mAu_n^+(CO)$ (n+m<6) clusters at the B3PW91/6-311+G level. They found that CO binds to Pd in $PdAu_6^+$, in agreement with our findings.

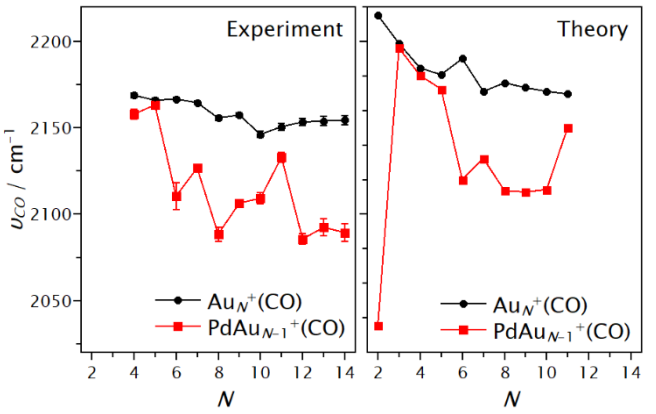

Fig. 9 Measured and calculated CO stretching frequencies, ν_{CO}, for the first adsorbed CO molecule on Au_N^+ and $PdAu_{N-1}^+$ clusters.

Therefore, Pd-CO binding is responsible for red-shifting the CO stretch of the larger clusters N≥6 (except for N=11), relative to that of the free CO molecule (2143 cm^{-1}). It has been shown that ν_{CO} for CO adsorbed on transition metal clusters can be decreased by replacing metal atoms with lower principal quantum numbers.[88] Hence, in agreement with our observation when Pd(4d) replaces Au(5d). An interpretation of this effect is provided by the Blyholder model[39], in which the metal-CO bonding is described by electron charge donation from the occupied 5σ orbital of CO to empty d-states of the metal, and back-donation of electron charge from occupied metal d-states to the 2π* antibonding orbital of CO, which is empty in the free molecule. In transition metal clusters, this model has successfully explained the adsorption of CO molecules, and provided a description for the observed red-shifted ν_{CO} frequencies of adsorbed COs, in comparison to the free molecule. The back-donation process partly populates the 2π* antibonding orbital of CO, which destabilizes the C-O bond thus lowering ν_{CO}. For CO bound to Pd, the lowered ν_{CO} frequencies suggest electron charge donation for the d-orbitals of Pd to CO. This is in agreement with previous calculations on the Pd-CO system, which predicted a decrease in ν_{CO} upon adsorption, although smaller than for other transition metals.[89] For the clusters where CO interacts directly with a Au atom, however, ν_{CO} frequencies are found higher than for the free CO molecule. This shows that back-donation of charge is not a determining factor in the interaction of CO with Au, which is mainly due to electron charge donation from CO to Au. The blue-shifting is due to the dominance of the repulsion between the filled 5σ HOMO of the CO molecule and a filled d-orbital on the Au atom, as described in Bagus' model.[88,90]

Tables S3 and S4 in the Supplementary Material list the partial charge distributions calculated with both the Mulliken and Löwdin partitioning methods for some of the bare clusters and their CO complexes. It is noted that except for $PdAu^+$, the Pd atom obtains significantly less positive charge than Au atoms, and occupies highly coordinated sites in order to maximise the electron charge transfer from Au to Pd. The adsorption of CO leads to an electronic rearrangement in the cluster which is small in magnitude. The unclear behaviour of charge distribution was previously reported by Joshi et al.[53] for dimeric and trimeric cationic AuPd clusters with an

adsorbed CO, and attributed to complex electron density transfer processes. The carbon atom is overall negatively charged in all cases. This charge is of the same magnitude regardless of cluster size. For Au-CO binding, Mulliken and Löwdin partial charges are C=-0.07e, O=+0.07e and C=-0.12e, O=+0.12e, respectively, and CO adsorbs preferentially to the Au atom that is more electron deficient. The oxygen atom is overall electron deficient and is again unaffected by the cluster size. This lack of size/structure sensitivity in CO electronics is in line with the lack of sensitivity of the M-C and C-O bond lengths across the cluster series. Multiple adsorption, as shown in the case of $Au_4^+(CO)_{1,2}$ (Table S5 in the Supplemental Material) does not lead to a significant change in electronic properties.

4 Conclusions

We have presented a study combining low-pressure collision cell reactivity and infrared multiphoton dissociation spectroscopy experiments with density functional theory calculations, to investigate the influence of Pd-doping on the interaction between CO molecules and small cationic gold clusters.

The rates of dissociation of formed cluster-CO complexes in the low-pressure collision cell were used to experimentally determine binding energies of CO on small cationic Au and Pd doped Au clusters. Hereto, an RRKM analysis was performed using as input parameters the dissociation rates of the CO-complexes and the vibrational frequencies of the clusters, calculated by DFT on the lowest energy structures. Pd doping is found to increase the CO binding energies irrespective of cluster size, although the extent of this increase is size-dependent. These findings agree remarkably well with binding energies determined by DFT.

Infrared multiphoton dissociation spectroscopy was used to characterize the internal C-O vibrational frequency and determine the CO adsorption site preference on the doped clusters. In clusters with *N*=4, 5 and 11 atoms, CO binds to a Au atom, whereas for clusters with *N*=6-10 and 12-14, CO binds to the Pd dopant, in agreement with theory.

This work highlights the subtle variations of adsorption preference and reactivity of clusters in the ultra-small "every-atom-counts" size regime. We find that multiple synergistic analysis methods are necessary to unambiguously describe the preferred adsorption modes and binding strengths for cluster-molecule interactions.

Conflicts of interest

There are no conflicts to declare.

Acknowledgements

H. A. A. is grateful to the University of Kufa and the Ministry of Higher Education and Scientific Research (Iraq) for financial support through the award of a PhD scholarship. P.F. and J.V. acknowledge the Research Foundation-Flanders (FWO) for a post-doctoral and doctoral grant, respectively. Calculations were performed on: the University of Birmingham's BlueBEAR high-performance computer (http://www.bear.bham.ac.uk/bluebear); ATHENA at HPC Midlands Plus, which is funded by the EPSRC through grant (EP/P020232); THOMAS, the UK Materials and Molecular Modelling Hub for computational resources, which is partially funded by EPSRC (EP/P020194/1); and ARCHER, the UK National Supercomputing Service (http://www.archer.ac.uk) via membership of the UK's HPC Materials Chemistry Consortium, which is funded by EPSRC (EP/L000202), and "TOUCAN: Towards an Understanding of Catalysis on Nanoalloys" membership, which is funded by EPSRC under Critical Mass Grant (EP/J010804/1). This work was supported by the FWO and the KU Leuven Research Council (GOA/14/007).

References

1 H. Zhang, T. Watanabe, M. Okumura, M. Haruta and N. Toshima, *Nat. Mater.*, 2012, **11**, 49–52.
2 T. V. de Bocarmé, T.-D. Chau, F. Tielens, J. Andrés, P. Gaspard, R. L. C. Wang, H. J. Kreuzer and N. Kruse, *J. Chem. Phys.*, 2006, **125**, 054703.
3 F. Tielens, J. Andrés, T.-D. Chau, T. V. de Bocarmé, N. Kruse and P. Geerlings, *Chem. Phys. Lett.*, 2006, **421**, 433–438.
4 M. García-Motaa and N. López, *Phys. Chem. Chem. Phys.*, 2011, **13**, 5790–5797.
5 S. A. Tenney, W. He, C. C. Roberts, J. S. Ratli, S. I. Shah, G. S. Shafai, V. Turkowski, T. S. Rahman and D. A. Chen, *J. Phys. Chem. C*, 2011, **115**, 11112–11123.
6 T. V. de Bocarme´, M. Moors, N. Kruse, I. S. Atanasov, M. Hou, A. Cerezo and G. D. W. Smith, *Ultramicroscopy*, 2009, **109**, 619–624.
7 Y. Gao, W. Huang, J. Woodford, L. Wang and X. C. Zeng, *J. Am. Chem. Soc.*, 2009, **131**, 9484–9485.
8 R. Ferrando, J. Jellinek and R. L. Johnston, *Chem. Rev.*, 2008, **108**, 846.
9 V. Soto-Verdugo and H. Metiu, *Surf. Sci.*, 2007, **601**, 5332–5339.
10 A. Hugon, L. Delannoy, J. Krafft and C. Louis, *J. Phys. Chem. C*, 2010, **114**, 10823.
11 A. Dhouib and H. Guesmi, *Chem. Phys. Lett.*, 2012, **521**, 98–103.
12 L. Delannoy, S. Giorgio, G. Mattei, C. R. Henry, N. El Kolli, C. Møthivier and C. Louis, *ChemCatChem*, 2013, **5**, 2707–2716.
13 R. Ismail, R. Ferrando and R. L. Johnston, *J. Phys. Chem. C*, 2013, **117**, 293.
14 H. A. Hussein, J. B. A. Davis and R. L. Johnston, *Phys. Chem. Chem. Phys.*, 2016, **18**, 26133–26143.
15 H. A. Hussein and R. L. Johnston, in *Frontiers of Nanoscience*, eds. S. T. Bromley and S. M. Woodley, Elsevier, Amsterdam, 2018, pp. 145–169.
16 S. Zhou, J. Li, M. Schlangen and H. Schwarz, *Angew. Chemie - Int. Ed.*, 2016, **55**, 10877–10880.
17 S. M. Lang, I. Fleischer, T. M. Bernhardt, R. N. Barnett and U. Landman, *J. Am. Chem. Soc.*, 2012, **134**, 20654–20659.
18 H. Schwarz, *Angew. Chemie - Int. Ed.*, 2015, **54**, 10090–10100.
19 P. Ferrari, H. A. Hussein, C. J. Heard, J. Vanbuel, R. L. Johnston, P. Lievens and E. Janssens, *Phys. Rev. A*, 2018, **97**, 052508.

20 J. Oliver-Meseguer, J. R. Cabrero-Antonino, I. Domínguez, A. Leyva-Pérez and A. Corma, *Science (80-.).*, 2012, **338**, 1452–1455.
21 B. Hammer and J. K. Norskov, *Nature*, 2002, **376**, 238–240.
22 F. Yang, D. Deng, X. Pan, Q. Fu and X. Bao, *Natl. Sci. Rev.*, 2015, **2**, 183–201.
23 A. Sanchez, S. Abbet, U. Heiz, W. D. Schneider, H. Häkkinen, R. N. Barnett and U. Landman, *J. Phys. Chem. A*, 1999, **103**, 9573–9578.
24 U. Heiz, A. Sanchez, S. Abbet and W. D. Schneider, *Eur. Phys. J. D*, 1999, **9**, 35–39.
25 D. A. H. Cunningham, W. Vogel, H. Kageyama, S. Tsubota and M. Haruta, *J. Catal.*, 1998, **177**, 1–10.
26 G. Brodén, T. N. Rhodin, C. Brucker, R. Benbow and Z. Hurych, *Surf. Sci.*, 1976, **59**, 593–611.
27 A. Fielicke, P. Gruene, G. Meijer and D. M. Rayner, *Surf. Sci.*, 2009, **603**, 1427–1433.
28 I. Swart, A. Fielicke, B. Redlich, G. Meijer, B. M. Weckhuysen and F. M. F. De Groot, *J. Am. Chem. Soc.*, 2007, **129**, 2516–2520.
29 D. B. Pedersen, D. M. Rayner, B. Simard, M. A. Addicoat, M. A. Buntine, G. F. Metha and A. Fielicke, *J. Phys. Chem. A*, 2004, **108**, 964–970.
30 M. A. Addicoat, M. A. Buntine, B. Yates and G. F. Metha, *J. Comput. Chem.*, 2008, **29**, 1497–1506.
31 A. S. Gentleman, M. A. Addicoat and G. F. Metha, *Aust. J. Chem.*, 2011, **64**, 1554.
32 Y. Xie, S. G. He, F. Dong and E. R. Bernstein, *J. Chem. Phys.*, 2008, **128**, 044306.
33 J. K. Nørskov, T. Bligaard, J. Rossmeisl and C. H. Christensen, *Nat. Chem.*, 2009, **1**, 37–46.
34 T. Wang, X.-X. Tian, Y.-W. Li, J. Wang, M. Beller and H. Jiao, *ACS Catal.*, 2014, **4**, 1991–2005.
35 J. T. Lyon, P. Gruene, A. Fielicke, G. Meijer and D. M. Rayner, *J. Chem. Phys.*, 2009, **131**, 184706.
36 A. Fielicke, G. Von Helden, G. Meijer, D. B. Pedersen, B. Simard and D. M. Rayner, *J. Am. Chem. Soc.*, 2005, **127**, 8416–8423.
37 A. Fielicke, G. Von Helden, G. Meijer, B. Simard and D. M. Rayner, *J. Phys. Chem. B*, 2005, **109**, 23935–23940.
38 P. Gruene, A. Fielicke, G. Meijer and D. M. Rayner, *Phys. Chem. Chem. Phys.*, 2008, **10**, 6144–6149.
39 G. Blyholder, *J. Phys. Chem.*, 1964, **68**, 2772–2777.
40 I. Chorkendorff and J. W. Niemantsverdriet, *Concepts of Modern Catalysis and Kinetics*, Wiley-VCH, Germany, 3rd edn., 2017.
41 P. Pyykkö and N. Runeberg, *Angew. Chem. Int. Edn*, 2002, **41**, 2174–2176.
42 P. Ferrari, L. M. Molina, V. E. Kaydashev, J. A. Alonso, P. Lievens and E. Janssens, *Angew. Chemie - Int. Ed.*, 2016, **55**, 11059–11063.
43 P. V. Nhat, T. B. Tai and M. T. Nguyen, *J. Chem. Phys.*, 2012, **137**, 164312.
44 H. T. Le, S. M. Lang, J. De Haeck, P. Lievens and E. Janssens, *Phys. Chem. Chem. Phys.*, 2012, **14**, 9350–9358.
45 P. Gruene, A. Fielicke, G. Meijer, E. Janssens, T. N. Vu, T. N. Minh and P. Lievens, *ChemPhysChem*, 2008, **9**, 703–706.
46 V. Kaydashev, P. Ferrari, C. Heard, E. Janssens, R. L. Johnston and P. Lievens, *Part. Part. Syst. Charact.*, 2016, **33**, 364–372.
47 A. Shayeghi, C. J. Heard, R. L. Johnston and R. Schäfer, *J. Chem. Phys.*, 2014, **140**, 054312.
48 V. E. Kaydashev, E. Janssens and P. Lievens, *J. Chem. Phys.*, 2015, **142**, 034310.
49 S. M. Lang, A. Frank and T. M. Bernhardt, *Int. J. Mass Spectrom.*, 2013, **354–355**, 365–371.
50 E. M. Fernández, M. B. Torres and L. C. Balbás, *Eur. Phys. J. D*, 2009, **52**, 135–138.
51 W. Zeng, J. Tang, P. Wang and Y. Pei, *RSC Adv.*, 2016, **6**, 55876–55877.
52 C. Song, Q. Ge and L. Wang, *J. Phys. Chem. B*, 2005, **109**, 22341–22350.
53 A. M. Joshi, M. H. Tucker, W. N. Delgass and K. T. Thomson, *J. Chem. Phys.*, 2006, **125**, 194707.
54 Y. M. Chen, X. Y. Kuang, X. W. Sheng, P. Shao, M. M. Zhong and H. Q. Wang, *Zeitschrift fur Naturforsch. - Sect. A J. Phys. Sci.*, 2013, **68**, 651–658.
55 D. Palagin and J. P. K. Doye, *Phys. Chem. Chem. Phys.*, 2015, **17**, 28010–28021.
56 J. Zhang and A. N. Alexandrova, *J. Phys. Chem. Lett.*, 2013, **4**, 2250–2255.
57 M. Neumaier, F. Weigend, O. Hampe and M. M. Kappes, *J. Chem. Phys.*, 2006, **125**, 104308.
58 Y. Zhao, Z. Li and J. Yang, *Phys. Chem. Chem. Phys.*, 2009, **11**, 2329–2334.
59 F. Gao, Y. Wang and D. W. Goodman, *J. Phys. Chem. C*, 2009, **113**, 14993–15000.
60 F. Gao, Y. Wang and D. W. Goodman, *J. Am. Chem. Soc.*, 2009, **131**, 5734–5735.
61 B. Zhu, G. Thrimurthulu, L. Delannoy, C. Louis, C. Mottet, J. Creuze, B. Legrand and H. Guesmi, *J. Catal.*, 2013, **308**, 272–281.
62 N. El Kolli, L. Delannoy and C. Louis, *J. Catal.*, 2013, **297**, 79–92.
63 P. S. West, R. L. Johnston, G. Barcaro and A. Fortunelli, *J. Phys. Chem. C*, 2010, **114**, 19678–19686.
64 J. Davis, A. Shayeghi, S. L. Horswell and R. L. Johnston, *Nanoscale*, 2015, **7**, 14032–14038.
65 G. Kresse and J. Hafner, *Phys. Rev. B*, 1993, **47**, 558–561.
66 J. Perdew, K. Burke and Y. Wang, *Phys. Rev. B*, 1996, **54**, 16533–16539.
67 G. Kresse, *Phys. Rev. B*, 1999, **59**, 1758–1775.
68 M. Methfessel and A. T. Paxton, *Phys. Rev. B*, 1989, **40**, 3616–3621.
69 M. Valiev, E. J. Bylaska, N. Govind, K. Kowalski, T. P. Straatsma, H. J. J. Van Dam, D. Wang, J. Nieplocha, E. Apra, T. L. Windus and W. A. De Jong, *Comput. Phys. Commun.*, 2010, **181**, 1477–1489.
70 F. Weigend and R. Ahlrichs, *Phys. Chem. Chem. Phys.*, 2005, **7**, 3297–3305.
71 O. A. Vydrov and G. E. Scuseria, *J. Chem. Phys.*, 2006, **125**, 234109.
72 M. A. Rohrdanz, K. M. Martins and J. M. Herbert, *J. Chem. Phys.*, 2009, **130**, 054112.
73 P. Ferrari, J. Vanbuel, Y. Li, T.-W. Liao, E. Janssens and P. Lievens, in *Gas aggregation synthesis of nanoparticles*, ed. Y. Huttel, Wiley-VCH, 2017, pp. 59–78.
74 E. Janssens, H. T. Le and P. Lievens, *Chem. - A Eur. J.*, 2015, **21**, 15256–15262.
75 H. T. Le, S. M. Lang, J. De Haeck, P. Lievens and E. Janssens, *Phys. Chem. Chem. Phys.*, 2012, **14**, 9350–9358.
76 J. De Haeck, N. Veldeman, P. Claes, E. Janssens, M. Andersson and P. Lievens, *J. Phys. Chem. A*, 2011, **115**, 2103–2109.

77 W. Schöllkopf, S. Gewinner, H. Junkes, A. Paarmann, G. von Helden, H. P. Bluem and A. M. M. Todd, in *Advances in X-ray Free-Electron Lasers Instrumentation III*, 2015, vol. 9512, p. 95121L.
78 W. Schöllkopf, S. Gewinner, W. Erlebach, H. Junkes, A. Liedke, G. Meijer, A. Paarmann, G. von Helden, H. Bluem, D. Dowell, R. Lange, J. Rathke, A. M. M. Todd, L. M. Young, U. Lehnert, P. Michel, W. Seidel, R. Wensch and S. C. Gottschalk, in *the 36th Free Electron Laser Conference*, Basel, 2014, pp. 629–634.
79 N. X. Truong, M. Haertelt, B. K. A. Jaeger, S. Gewinner, W. Schöllkopf, A. Fielicke and O. Dopfer, *Int. J. Mass Spectrom.*, 2016, **395**, 1–6.
80 A. P. Woodham and A. Fielicke, in *Gold Clusters, Colloids and Nanoparticles I. Structure and Bonding*, ed. D. M. P. Mingos, Springer, Cham, 2013, pp. 243–278.
81 X.-F. Yang, Y.-L. Wang, Y.-F. Zhao, A.-Q. Wang, T. Zhang and J. Li, *Phys. Chem. Chem. Phys.*, 2010, **12**, 3038.
82 X. Chen, R. F. Lu, E. J. Kan, Y. Z. Liu, C. Y. Xiao and K. M. Deng, *J. Mol. Model.*, 2014, **20**, 2313.
83 T. M. Bernhardt, J. Hagen, S. M. Lang, D. M. Popolan, L. D. Socaciu-Siebert and L. Wöste, *J. Phys. Chem. A*, 2009, **113**, 2724.
84 R. A. Marcus, *J. Chem. Phys.*, 1952, **20**, 359–364.
85 K. A. Holbrook, M. J. Pilling and S. H. Robertson, *Unimolecular Reactions*, John Wiley & Sons Ltd., Chichester, U.K., 2nd edn., 1996.
86 L. Drahos and K. Vékey, *J. Mass Spectrom.*, 2001, **36**, 237–263.
87 K. P. Huber and G. Herzberg, *Molecular Spectra And Molecular Structure, IV. Constants Of Diatomic Molecules*, Van Nostrand Reinhold, New York, 1979, vol. 5.
88 C. D. Zeinalipour-Yazdi, A. L. Cooksy and A. M. Efstathiou, *Surf. Sci.*, 2008, **602**, 1858–1862.
89 P. Schwerdtfeger, J. S. McFeaters, J. J. Moore, D. M. McPherson, R. P. Cooney, G. A. Bowmaker, M. Dolg and D. Andrae, *Langmuir*, 1991, **7**, 116–125.
90 P. S. Bagus, C. J. Nelin and C. W. Bauschlicher, *Phys. Rev. B*, 1983, **28**, 5423–5438.

Supporting Information

Altering CO binding on Gold Cluster Cations by Pd-doping

Heider A. Abdulhussein,[a,b] Piero Ferrari,[c] Jan Vanbuel,[c] Christopher Heard,[d] André Fielicke,[e] Peter Lievens,[c] Ewald Janssens[c] and Roy L. Johnston[a]

[a] School of Chemistry, University of Birmingham, Edgbaston, Birmingham B15 2TT, United Kingdom.
[b] Department of Chemistry, College of Science, University of Kufa, Najaf, Iraq.
[c] Laboratory of Solid State Physics and Magnetism, KU Leuven, 3001 Leuven, Belgium.
[d] Department of Physical and Macromolecular Chemistry, Charles University, 12843 Praha2, Czech Republic.
[e] Fritz-Haber-Institut der Max-Planck-Gesellschaft, Faradayweg 4-6, 14195 Berlin, Germany.

Content

1. Adsorption sites and their relative binding energies ΔE_b and the corresponding calculated frequencies for CO molecule on $Au_N^+(CO)$ and $PdAu_{N-1}^+(CO)$, N=3 and 4, clusters

Table S1: Adsorption sites and their relative binding energies ΔE_b, together with the corresponding calculated frequencies for a CO molecule on $Au_N^+(CO)$ and $PdAu_{N-1}^+(CO)$, N=3 and 4, clusters. The most favourable site for each cluster (having ΔE_b = 0.00 eV and nearest ν_{CO} to the corresponding measured value) is shown in bold.

Model	Site	ΔE_b / eV	ν_{CO} / cm^{-1}
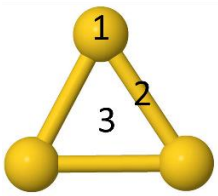	**1 (atop)**	**0.00**	**2198.77**
	2 (bridge)	0.11	2074.08
	3 (hollow)	0.13	1962.13
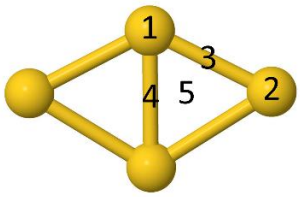	**1 (atop)**	**0.00**	**2184.57**
	2 (atop)	0.18	2192.81
	3 (bridge)	0.19	1961.22
	4 (bridge)	0.21	1893.45
	5 (hollow)	0.18	1969.51
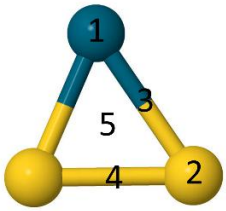	1 (atop)	0.23	2018.67
	2 (atop)	**0.00**	**2196.14**
	3 (bridge)	0.14	1938.70
	4 (bridge)	0.11	1959.22
	5 (hollow)	0.18	1880.78
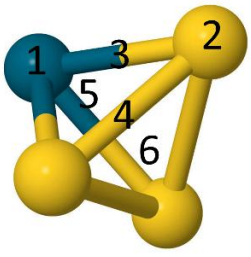	1 (atop)	0.25	1950.11
	2 (atop)	**0.00**	**2180.24**
	3 (bridge)	0.18	1992.02
	4 (bridge)	0.14	2030.27
	5 (hollow)	0.20	1971.10
	6 (hollow)	0.16	1997.76

2. Cluster-CO binding energies, CO stretching frequencies, and average bond lengths

Table S2: Cluster-CO binding energies, CO stretching frequencies, and average bond lengths of putative global minima of $Au_N^+(CO)$ and $PdAu_{N-1}^+(CO)$, *N*=2-11, clusters.

Species	Average Bond Length (Å)				E_b / eV	ν_{CO} / cm^{-1}
	Au-Au	Au-Pd	M-C	C-O		
$Au_2^+(CO)$	2.61	-----	1.93	1.12	1.93	2215.09
$Au_3^+(CO)$	2.63	------	1.95	1.12	1.76	2198.78
$Au_4^+(CO)$	2.68	-----	1.95	1.12	1.62	2184.57
$Au_5^+(CO)$	2.64	-----	1.94	1.12	1.40	2180.69
$Au_6^+(CO)$	2.66	-----	1.96	1.12	1.46	2189.97
$Au_7^+(CO)$	2.70	-----	1.96	1.12	1.78	2170.97
$Au_8^+(CO)$	2.67	-----	1.96	1.12	1.38	2175.98
$Au_9^+(CO)$	2.74	----	1.98	1.12	1.62	2173.18
$Au_{10}^+(CO)$	2.62	-----	1.96	1.12	1.47	2171.06
$Au_{11}^+(CO)$	2.71	----	1.97	1.12	1.60	2169.51
$PdAu^+(CO)$	-----	2.59	(Au-C=2.0980), (Pd-C=1.8576)	1.14	5.93	2035.40
$PdAu_2^+(CO)$	2.57	2.68	1.95	1.12	1.99	2196.14
$PdAu_3^+(CO)$	2.75	2.61	1.94	1.12	1.66	2180.25
$PdAu_4^+(CO)$	2.75	2.69	1.94	1.12	1.67	2172.35
$PdAu_5^+(CO)$	2.75	2.73	1.89	1.13	1.71	2119.99
$PdAu_6^+(CO)$	2.69	2.77	1.90	1.12	1.81	2132.16
$PdAu_7^+(CO)$	2.72	2.73	1.5	1.2	1.86	2113.70
$PdAu_8^+(CO)$	2.69	2.77	1.90	1.13	1.85	2112.78
$PdAu_9^+(CO)$	2.78	2.70	1.90	1.15	1.80	2114.21
$PdAu_{10}^+(CO)$	-----	-----	-----	-----	----	2150.22

3. Electronic distribution

Table S3: Partial charge distributions calculated with both the Mulliken and Löwdin portioning methods for $Au_N^+(CO)$ and $PdAu_{N-1}^+(CO)$, *N*=2 and 4, clusters and their corresponding free clusters.

Species	Numbering of the atoms	Type of atom	Charge Population Analysis		Structure
			Mulliken	Löwdin	
Au_2^+	1	Au	0.50	0.50	
	2	Au	0.50	0.50	
$Au_2^+(CO)$	1	Au	0.54	0.45	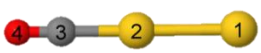
	2	Au	0.37	0.43	
	3	C	-0.09	-0.14	
	4	O	0.18	0.26	
$PdAu^+$	1	Au	0.45	0.40	
	2	Pd	0.55	0.60	
$PdAu^+(CO)$	1	Au	0.68	0.62	
	2	Pd	0.36	0.44	
	3	C	-0.16	-0.27	
	4	O	0.12	0.21	
Au_4^+	1	Au	0.23	0.13	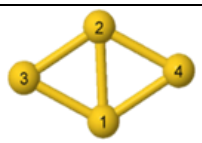
	2	Au	0.23	0.13	
	3	Au	0.27	0.37	
	4	Au	0.27	0.37	
$Au_4^+(CO)$	1	Au	0.03	0.29	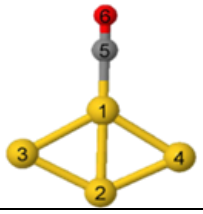
	2	Au	0.23	0.18	
	3	Au	0.34	0.22	
	4	Au	0.34	0.22	
	5	C	-0.09	-0.16	
	6	O	0.15	0.23	
$PdAu_3^+$	1	Au	0.37	0.33	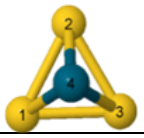
	2	Au	0.37	0.33	
	3	Au	0.37	0.33	
	4	Pd	-0.12	0.02	
$PdAu_3^+(CO)$	1	Au	0.19	0.41	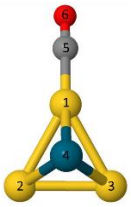
	2	Au	0.40	0.22	
	3	Au	0.40	0.25	
	4	Pd	-0.07	0.03	
	5	C	-0.07	-0.15	
	6	O	0.15	0.24	

Table S4: Partial charge distributions calculated with both the Mulliken and Löwdin portioning methods for $Au_N^+(CO)$ and $PdAu_{N-1}^+(CO)$, N=6, clusters and their corresponding free clusters.

Species	Numbering of the atoms	Type of atom	Charge Population Analysis		Structure
			Mulliken	Löwdin	
Au_6^+	1	Au	0.78	0.24	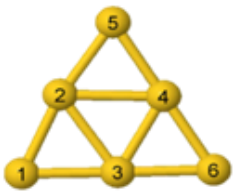
	2	Au	-0.35	0.07	
	3	Au	-0.53	0.14	
	4	Au	-0.53	0.14	
	5	Au	0.78	0.24	
	6	Au	0.85	0.17	
$Au_6^+(CO)$	1	Au	0.19	0.32	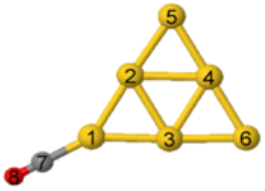
	2	Au	-0.15	0.06	
	3	Au	-0.15	0.06	
	4	Au	-0.38	0.13	
	5	Au	0.71	0.17	
	6	Au	0.71	0.17	
	7	C	-0.07	-0.14	
	8	O	0.15	0.24	
$PdAu_5^+$	1	Au	0.30	0.23	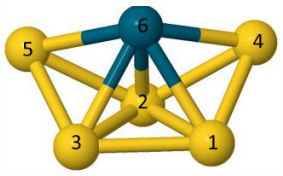
	2	Au	0.31	0.24	
	3	Au	0.29	0.24	
	4	Au	0.28	0.22	
	5	Au	0.29	0.21	
	6	Pd	-0.47	-0.15	
$PdAu_5^+(CO)$	1	Au	0.12	0.16	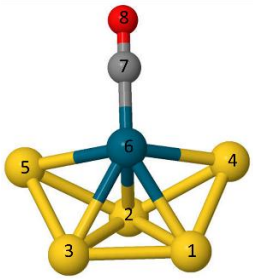
	2	Au	0.11	0.15	
	3	Au	0.10	0.17	
	4	Au	0.26	0.19	
	5	Au	0.27	0.19	
	6	Pd	0.12	0.02	
	7	C	-0.07	-0.13	
	8	O	0.15	0.25	

Table S5: Partial charge distributions calculated with both the Mulliken and Löwdin portioning methods for $Au_4^+(CO)_{1,2}$ clusters and their energetically competitive isomers (labelled by *) and their corresponding free cluster.

Species	Numbering of the atoms	Type of atom	Charge Population Analysis		Structure
			Mulliken	Löwdin	
Au_4^+	1	Au	0.23	0.13	
	2	Au	0.23	0.13	
	3	Au	0.27	0.37	
	4	Au	0.27	0.37	
$Au_4^+(CO)$	1	Au	0.03	0.29	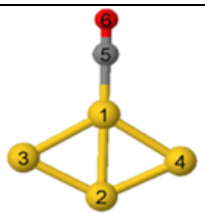
	2	Au	0.23	0.18	
	3	Au	0.34	0.22	
	4	Au	0.34	0.22	
	5	C	-0.09	-0.16	
	6	O	0.15	0.23	
$Au_4^+(CO)$*	1	Au	0.25	0.23	
	2	Au	0.28	0.18	
	3	Au	0.28	0.18	
	4	Au	0.12	0.32	
	5	C	-0.08	-0.15	
	6	O	0.16	0.24	
$Au_4^+(CO)_2$	1	Au	0.33	0.13	
	2	Au	0.13	0.29	
	3	Au	0.27	0.15	
	4	Au	0.13	0.29	
	5	C	-0.09	-0.17	
	6	O	0.14	0.23	
	7	C	-0.07	-0.15	
	8	O	0.15	0.23	
$Au_4^+(CO)_2$*	1	Au	0.21	0.09	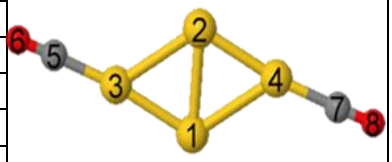
	2	Au	0.21	0.09	
	3	Au	0.24	0.34	
	4	Au	0.24	0.34	
	5	C	-0.1	-0.16	
	6	O	0.15	0.23	
	7	C	-0.1	-0.16	
	8	O	0.15	0.23	
$Au_4^+(CO)_2$*	1	Au	0.17	0.29	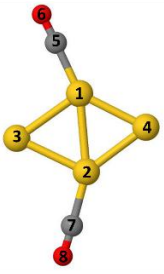
	2	Au	0.17	0.29	
	3	Au	0.26	0.14	
	4	Au	0.27	0.13	
	5	C	-0.07	-0.15	
	6	O	0.15	0.23	
	7	C	-0.09	-0.16	
	8	O	0.14	0.23	

CHAPTER 5

PHYSICO-CHEMICAL INSIGHTS INTO GAS-PHASE AND OXIDE-SUPPORTED SUBNANOMETRE GOLD-COPPER CLUSTERS

5.1 Introduction

Gold and copper are metals that are well-known for their utility in catalysis. Both atoms belong to the same group of the periodic table: the coinage group metals. The filled d orbitals and the singly occupied s valence orbital of the coinage metals impart a predominantly noble behaviour. Although, the atoms have a similar chemistry, their cluster characteristics are highly different. At small sizes, their pure clusters, for example, show different 2D-3D crossover points [182,183]. The explanation for this difference is attributed to the higher relativistic contraction of the valence s orbitals in Au than in Cu, which enhances s-d hybridisation [182,183], increasing the stability of 2D configurations (raising the 2D-3D crossover size). This also plays a significant role in decreasing the nobility (enhancing reactivity) of the coinage metal clusters at ultrasmall sizes. Such differences are reflected in their catalytic activities [184]. Copper-based catalysts have shown a distinct catalytic role in oxidation and hydrogenation reactions [104, 105] (e.g. in the oxidation of alcohols to aldehydes [185]). The catalytic activity of small gold clusters has led to a step change in catalysis: gold catalysts have been used in hydrogenation reactions and many organic transformations [186], but have been especially important in selective oxidation

reactions [187].

Bimetallic AuCu clusters have been developed to improve the catalytic properties [31]. However, the main problem with Cu-based catalysts is their dispersion during the reaction and reduction processes [184,188]. Supporting the catalyst on a surface can help in this context. However, the catalytic activity can be affected by the interaction with the support. Alteration in the density of electronic states and metal oxidation states, and even geometric distortion of the clusters, are all possible upon surface-adsorption [166, 167]. The study presented here aims to investigate such inherent surface effects. Additionally, gold-copper clusters on the subnanometre scale are regarded as ideal simplified models to rationalize the optical [189] and catalytic properties of their larger systems [190, 191]. Moreover, they are in the quantum regime, where quantum effects are observed and where "every atom counts" [192, 193], which can lead to unique catalytic properties and applications.

In Publication 5, the Mexican Enhanced Genetic Algorithm (MEGA), the recently developed GA-DFT code, is applied to ultrasmall AuCu clusters in order to rationalize their highly efficient catalytic properties. The global minima of gas-phase and MgO(100) supported AuCu clusters with 3-10 atoms are identified. Individual adatoms and supported dimers are also studied. A large number of calculations, including an extensive structural search, for a wide variety of compositions, and the exploration of different spin states, have been carried out. The structures of the isolated (gas-phase) clusters are compared with those supported on (defect-free) MgO(100) and reasons for the observed structural changes are rationalized. Where appropriate, comparison is made to previous studies. The interplay between the mixing of the component cluster atoms and their interactions with the oxide interface is investigated. Figure 5.1 shows the predicted difference in bond lengths between free and supported Au_3Cu_1 and Au_1Cu_4 clusters. The most favourable adsorption orientations for all supported atoms, dimers and clusters are predicted and compared, in terms of their adsorption energies, preferential metal-oxygen interactions, and electron transfer.

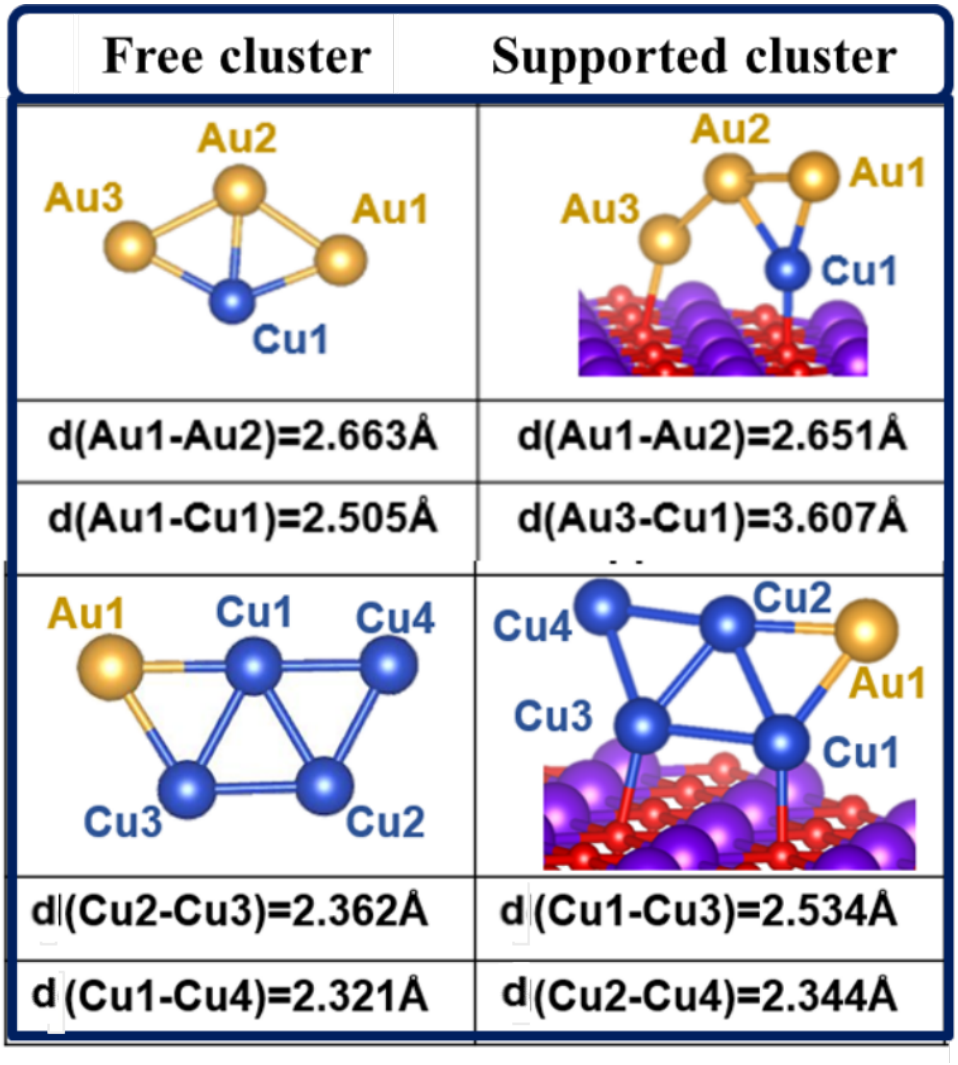

Figure 5.1: Comparison between bond lengths, d, for free and supported Au_3Cu_1 and Au_1Cu_4 clusters. A clear increase of the bond lengths between atoms that are in direct binding with the substrate can be recognised, in particular for Au_3Cu_1, which has an elongated Au-Cu bond bridging two O atoms on the surface.

5.2 Publication 5

Title

Physico-Chemical Insights into Gas-Phase and Oxide-Supported Sub-Nanometre AuCu Clusters

Authors

Heider A. Hussein, Mansi Gao, Yiyun Hou, Sarah L. Horswell and Roy L. Johnston

Journal Zeitschrift für Physikalische Chemie

Volume 233

Pages 813-843

DOI 10.1515/zpch-2018-1356

Submitted

29 November 2018

Accepted

28 January 2019

5.2.1 Author Contribution

The author supervised the work of Yiyun Hou, who carried out the global optimizations of the free clusters, and of Mansi Gao, who performed the global optimizations of the

supported clusters with N≤6. The author installed the MEGA code and made amendments to the code required for the systems of study. The global optimizations of the supported clusters were subsequently extended up to N=10 and performed by the author. Calculations, including reoptimisation of all unconverged isomers, homotop searches, local minimisation calculations for alternative potentially competitive isomers, zero-point energy and spin states optimizations, were all conducted by the author. The post-calculation analysis of the spin states, structures, bond lengths, energetics, homotop, calculated quantum molecular descriptors, and HOMO-LUMO energy gaps, were all contributed to and implemented by the author. The figures 3-11 in the paper and figures S1, S2, and S6-S11, as well as tables S1, S2, and S5-S10 of the supplemental material, were all created by the author. The paper was written by the author.

Heider A. Hussein, Mansi Gao, Yiyun Hou, Sarah L. Horswell and Roy L. Johnston*

Physico-Chemical Insights into Gas-Phase and Oxide-Supported Sub-Nanometre AuCu Clusters

https://doi.org/10.1515/zpch-2018-1356
Received November 29, 2018; accepted January 28, 2019

Abstract: Catalysis by AuCu nanoclusters is a promising scientific field. However, our fundamental understanding of the underlying mechanisms of mixing in AuCu clusters at the sub-nanometre scale and their physico-chemical properties in both the gas-phase and on oxide supports is limited. We have identified the global minima of gas-phase and MgO(100)-supported AuCu clusters with 3–10 atoms using the Mexican Enhanced Genetic Algorithm coupled with density functional theory. Au and Cu adatoms and supported dimers have been also simulated at the same level of theory. The most stable composition, as calculated from mixing and binding energies, is obtained when the Cu proportion is close to 50%. The structures of the most stable free AuCu clusters exhibit Cu-core/Au-shell segregation. On the MgO surface however, there is a preference for Cu atoms to lie at the cluster-substrate interface. Due to the interplay between the number of interfacial Cu atoms and surface-induced cluster rearrangement, on the MgO surface 3D structures become more stable than 2D structures. The O-site of MgO surface is found to be the most favourable adsorption site for both metals. All dimers favour vertical (V) configurations on the surface and their adsorption energies are in the order: $\underline{\text{Au}}\text{Cu} < \text{Cu}\underline{\text{Cu}} < \text{Au}\underline{\text{Au}} < \text{Au}\underline{\text{Cu}}$ (where the underlined atom is bound to the O-site). For both adatoms and AuCu dimers, adsorption via Cu is more favourable than Au-adsorbed configurations, but, this disagrees with the ordering for the pure dimers due to a combination of electron transfer and the metal-on-top effect. Binding energy (and second difference) and HOMO-LUMO gap calculations show that even-atom (even-electron) clusters are more stable than the neighbouring odd-atom (odd- electron) clusters, which is expected for closed- and open-shell

***Corresponding author: Roy L. Johnston,** School of Chemistry, University of Birmingham, Birmingham B15 2TT, UK, e-mail: r.l.johnston@bham.ac.uk
Heider A. Hussein: School of Chemistry, University of Birmingham, Birmingham B15 2TT, UK; and Department of Chemistry, College of Science, University of Kufa, Najaf, Iraq
Mansi Gao, Yiyun Hou and Sarah L. Horswell: School of Chemistry, University of Birmingham, Birmingham B15 2TT, UK

systems. Supporting AuCu clusters on the MgO(100) surface decreases the charge transfer between Au and Cu atoms calculated in free clusters. The results of this study may serve as a foundation for designing better AuCu catalysts.

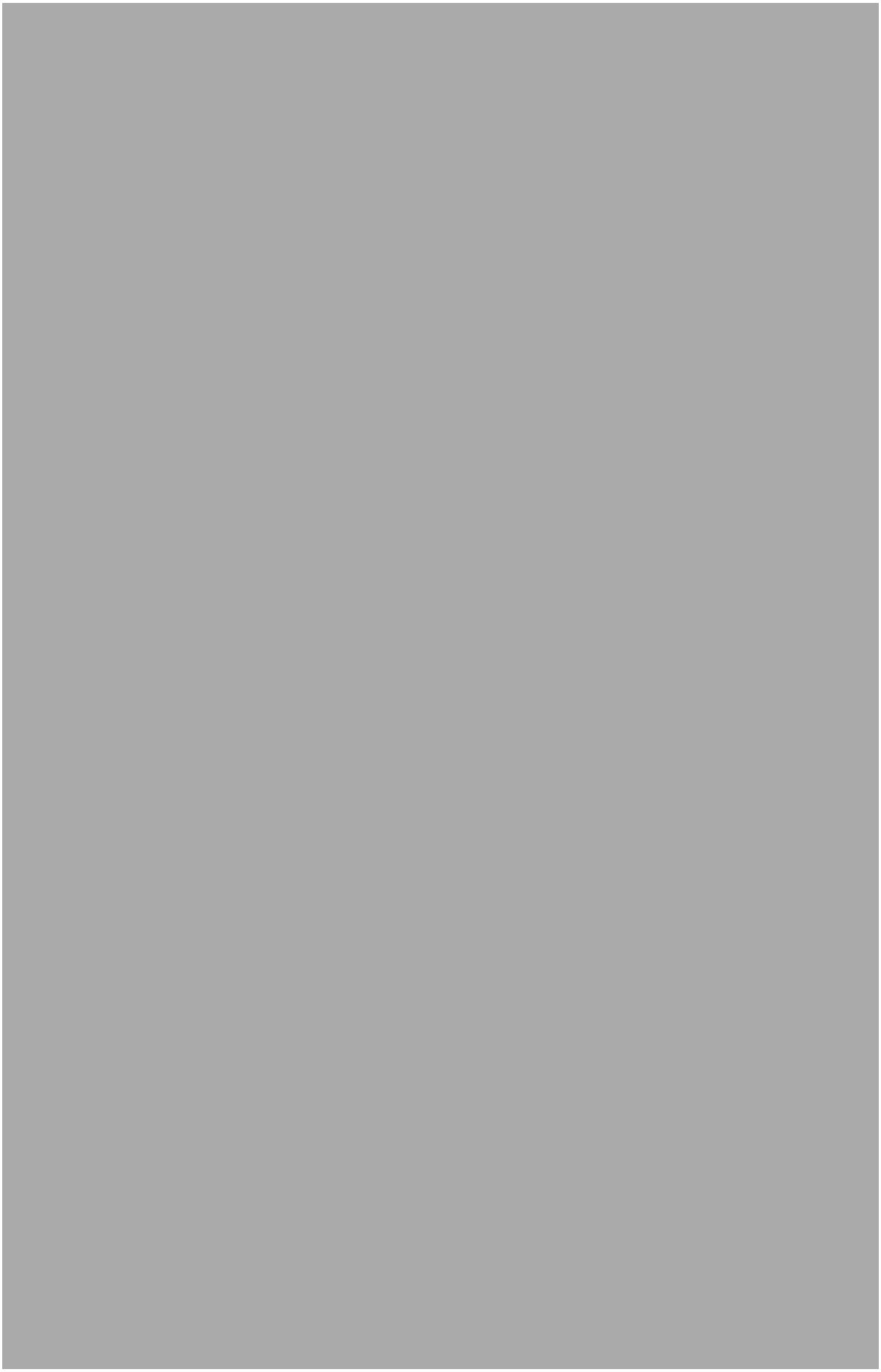

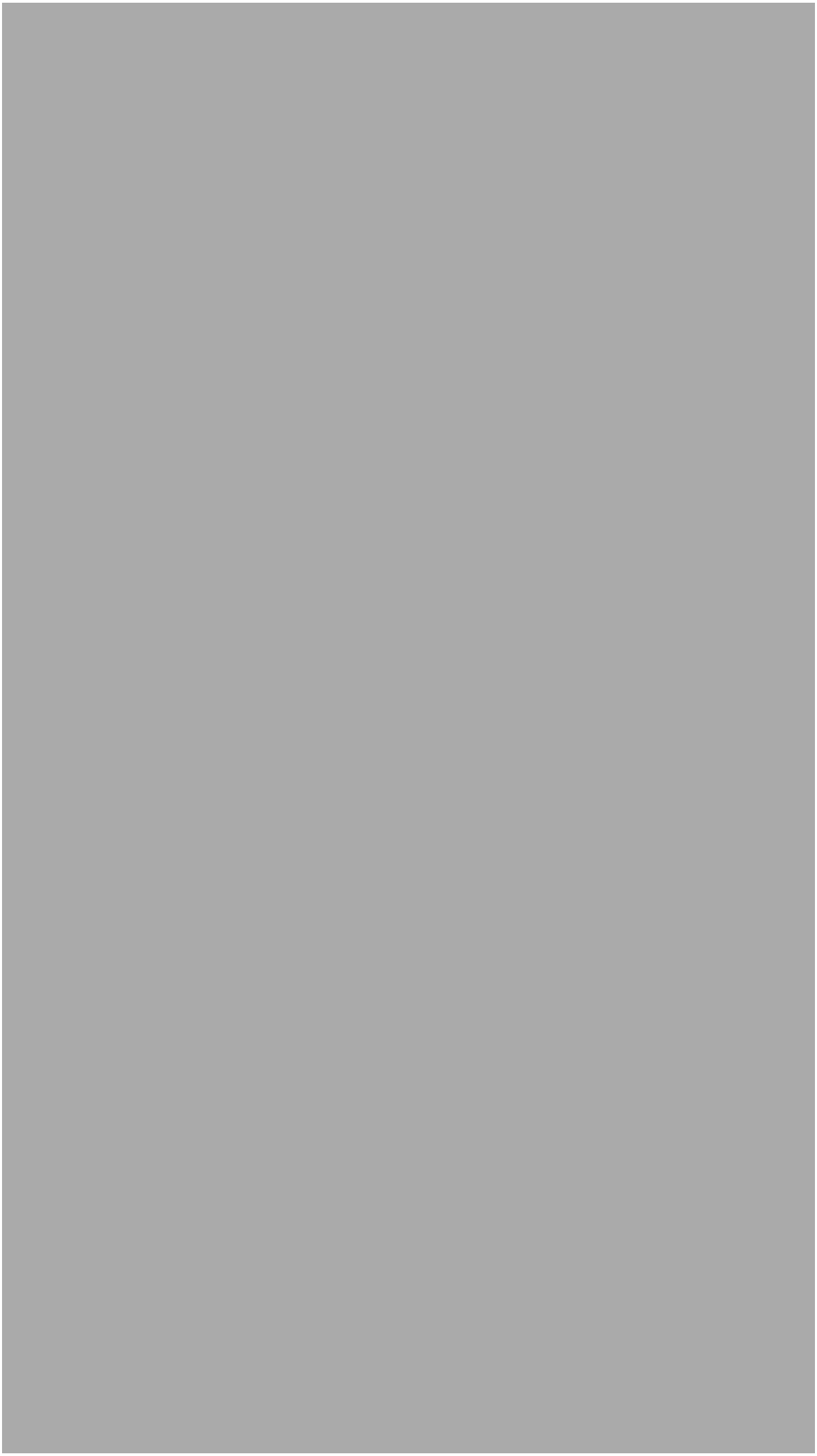

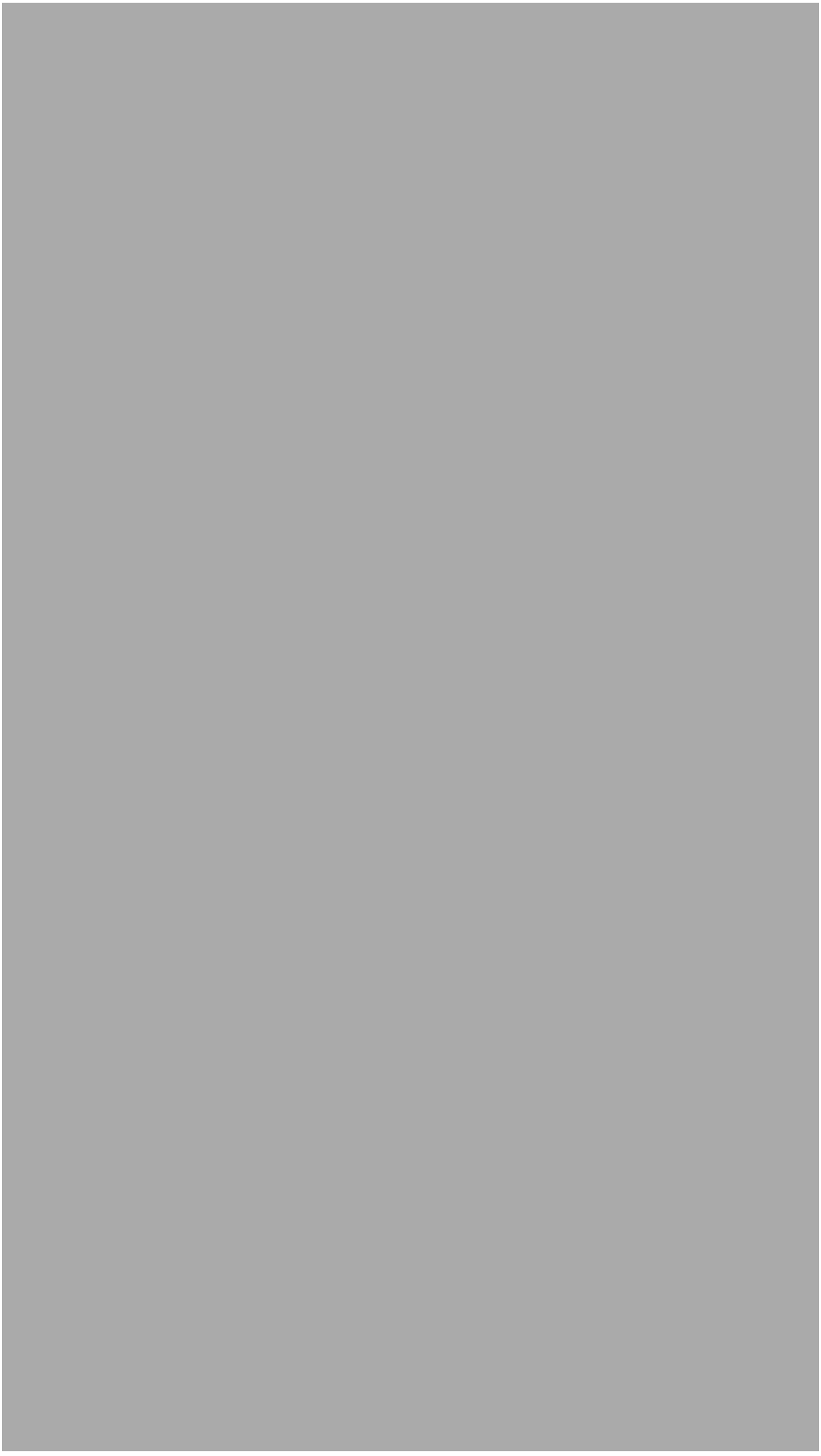

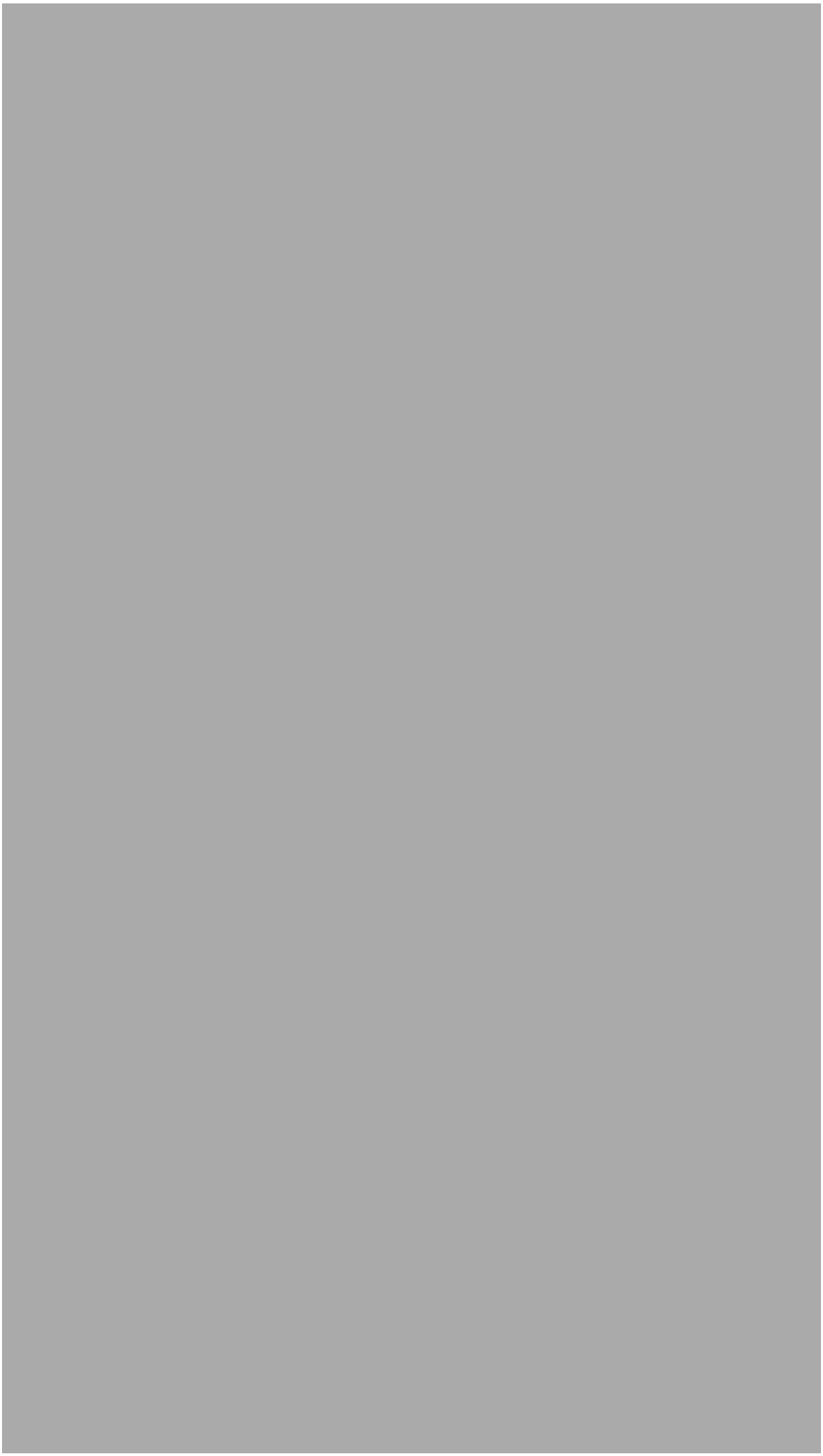

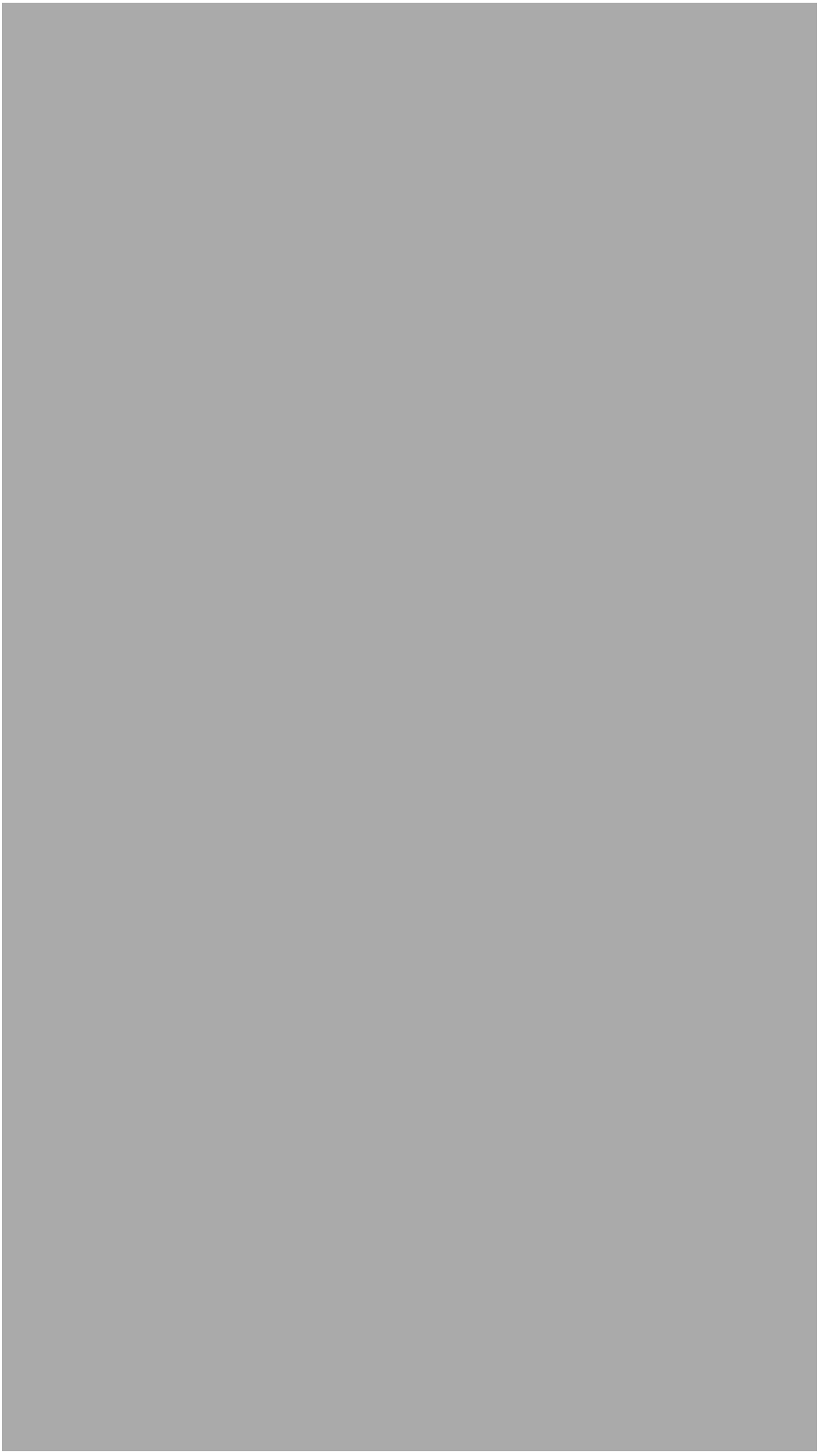

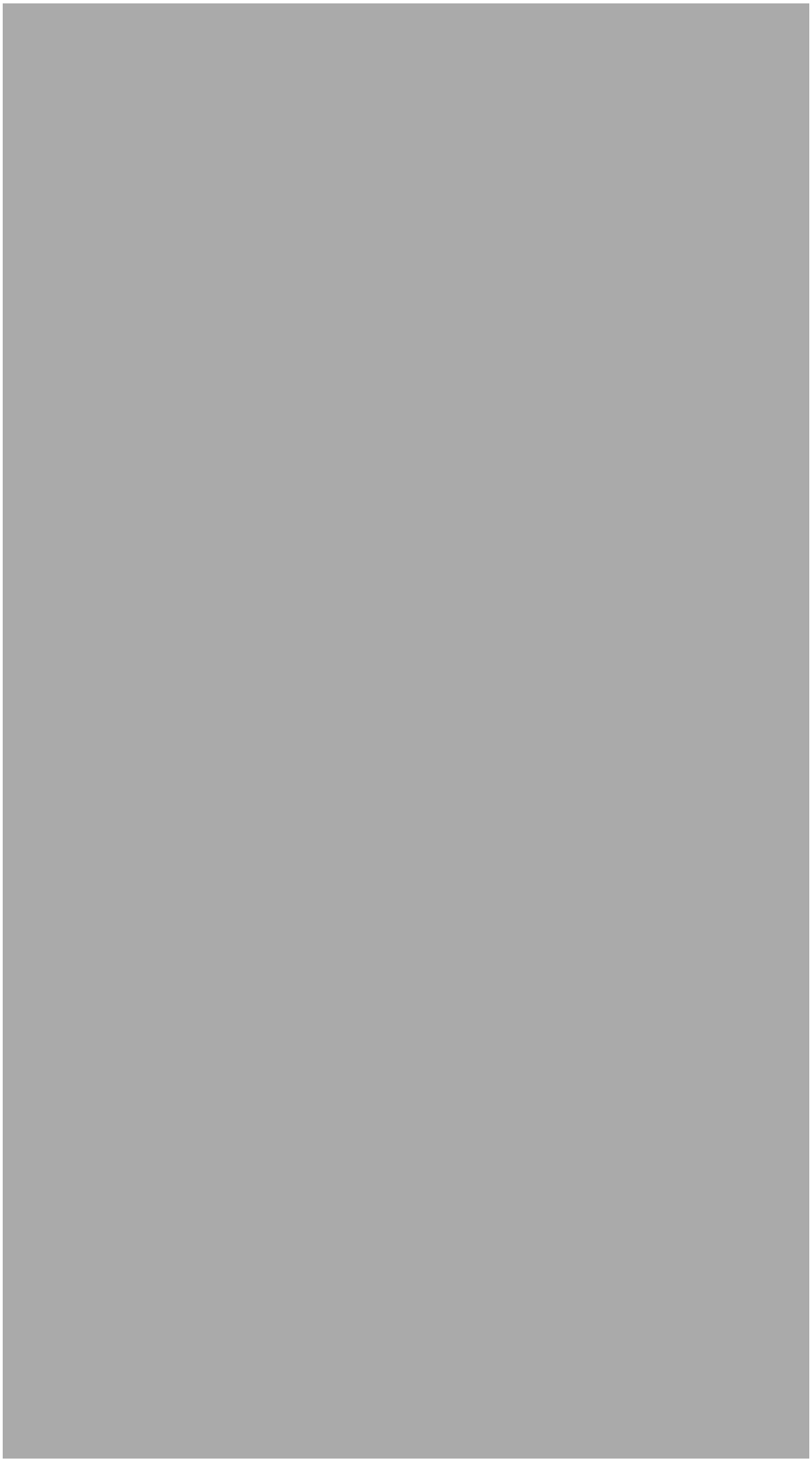

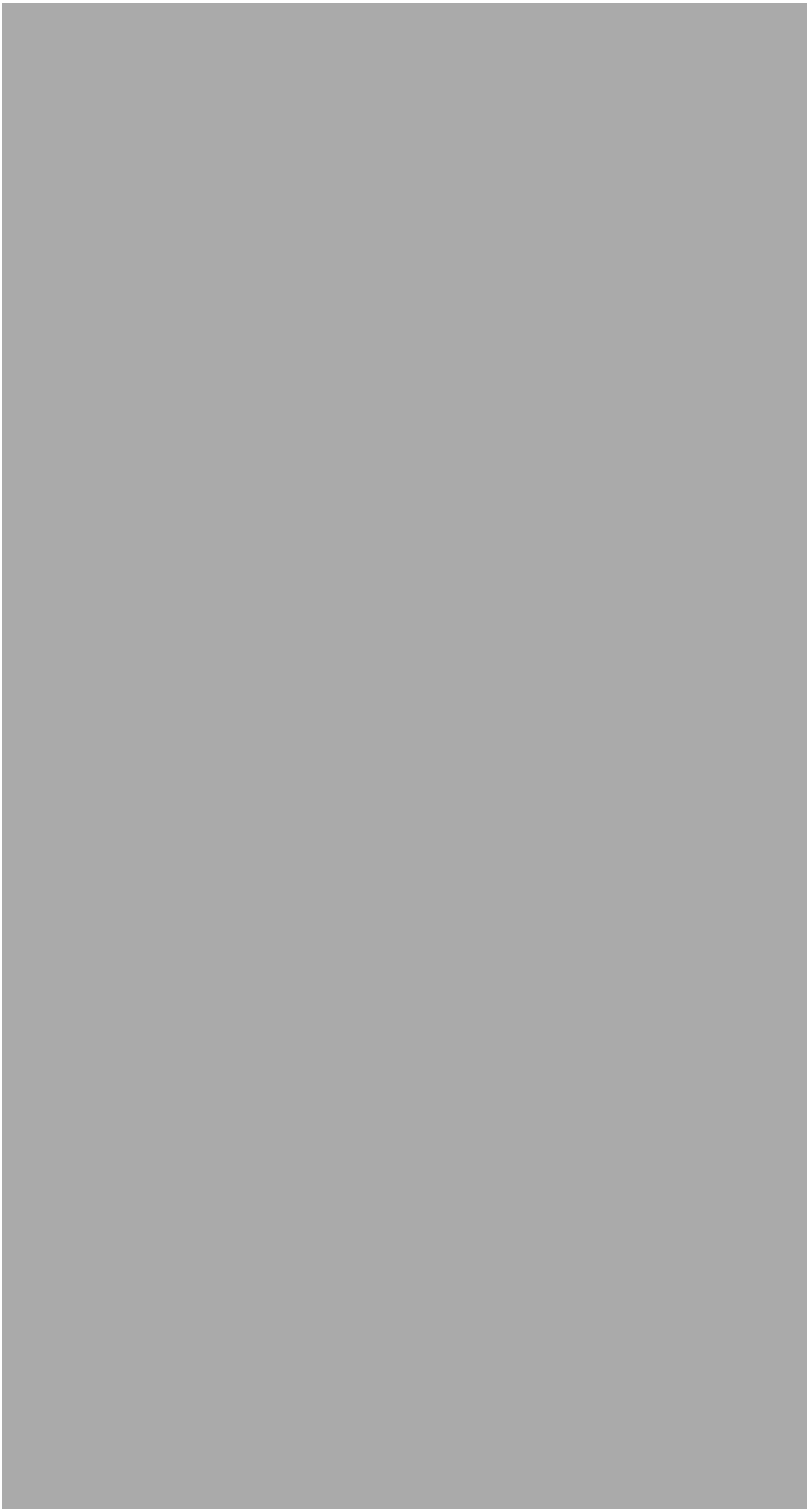

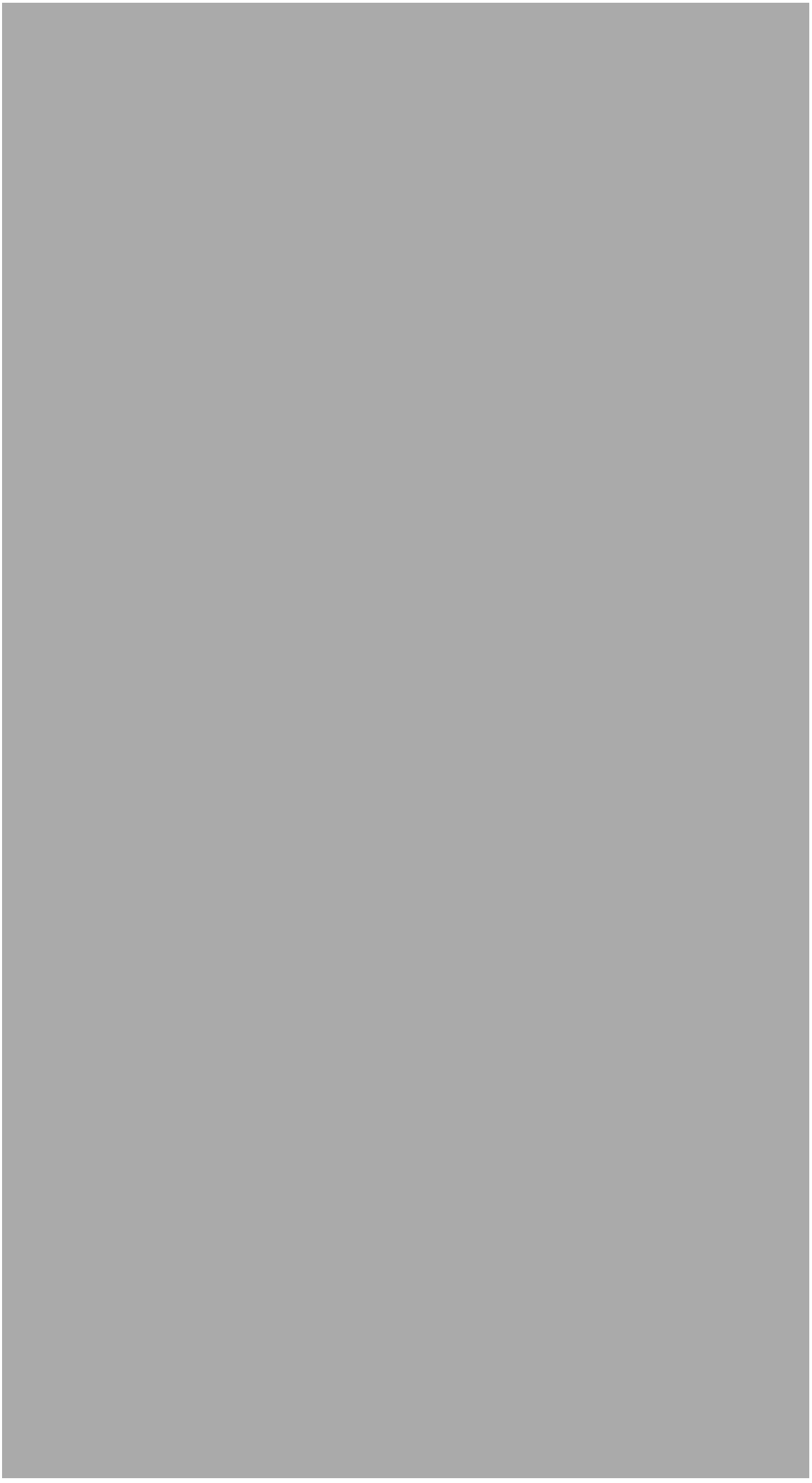

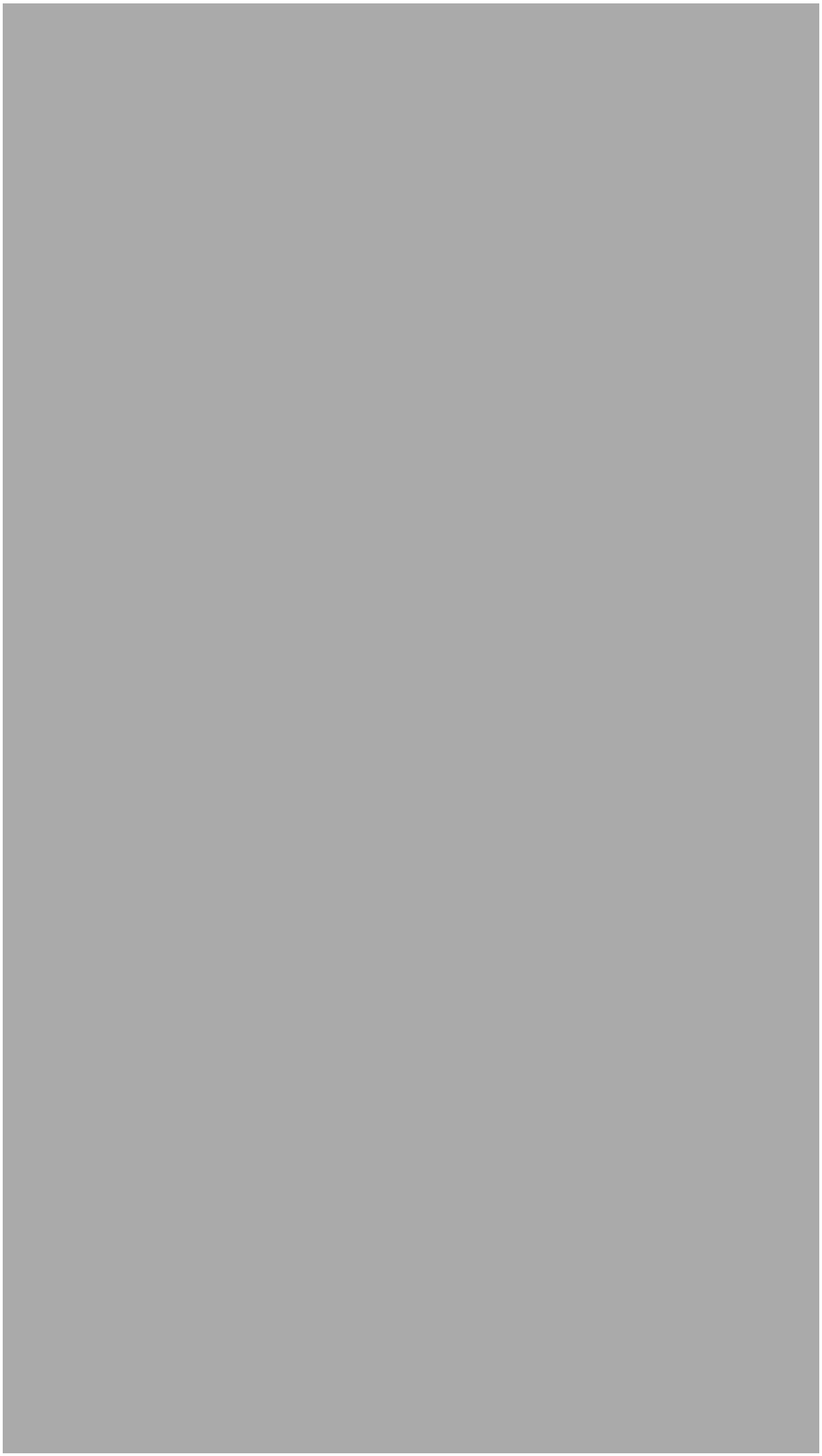

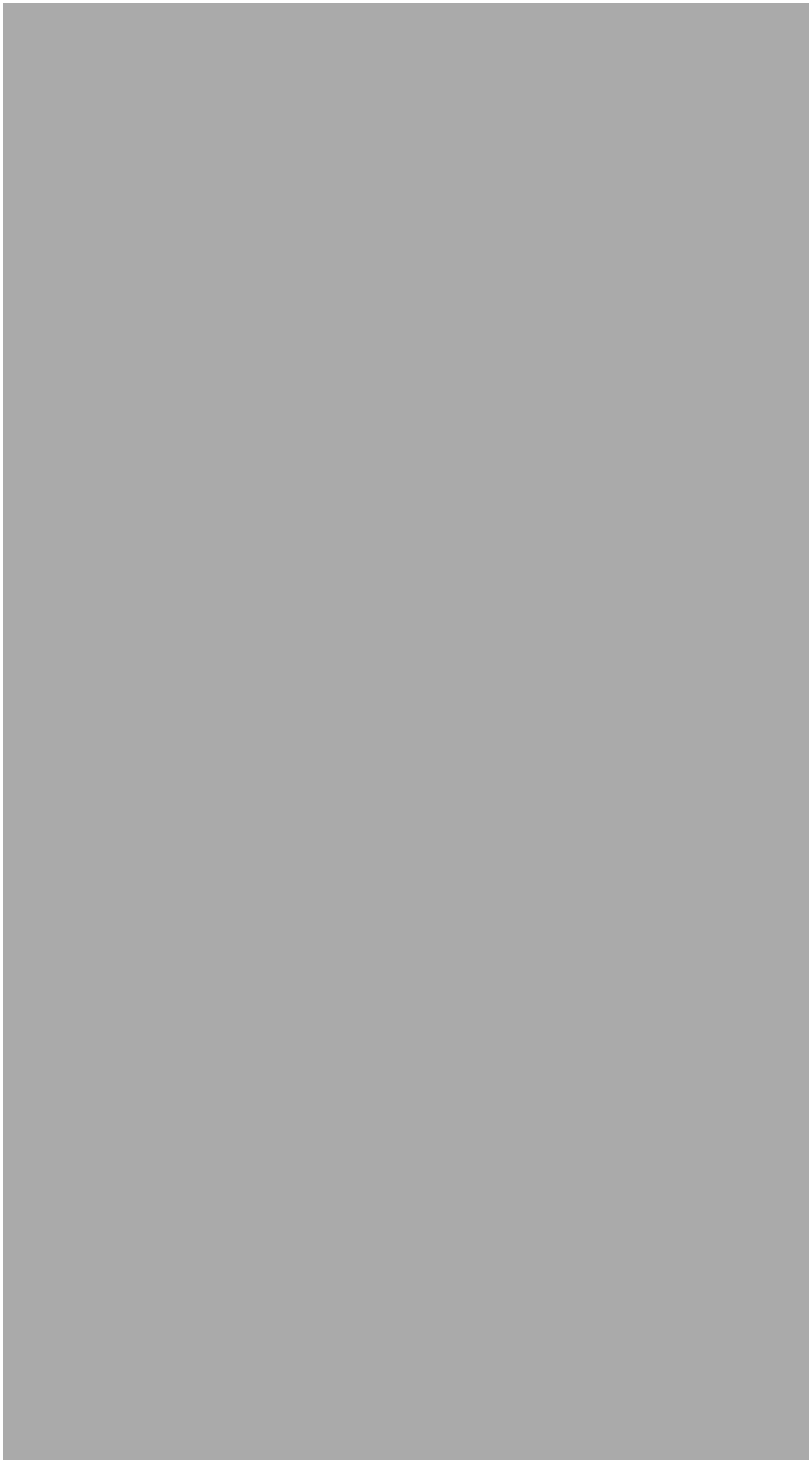

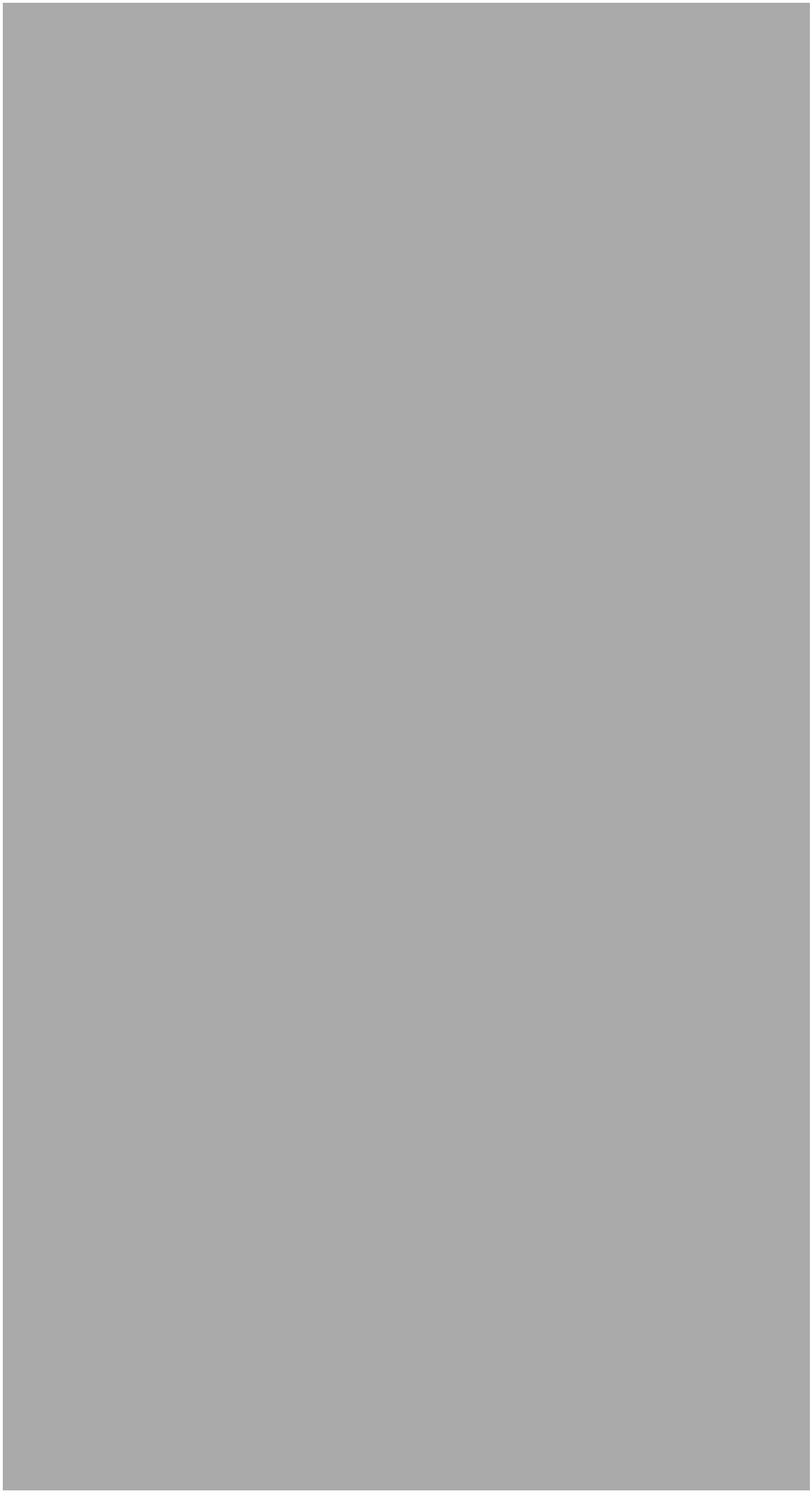

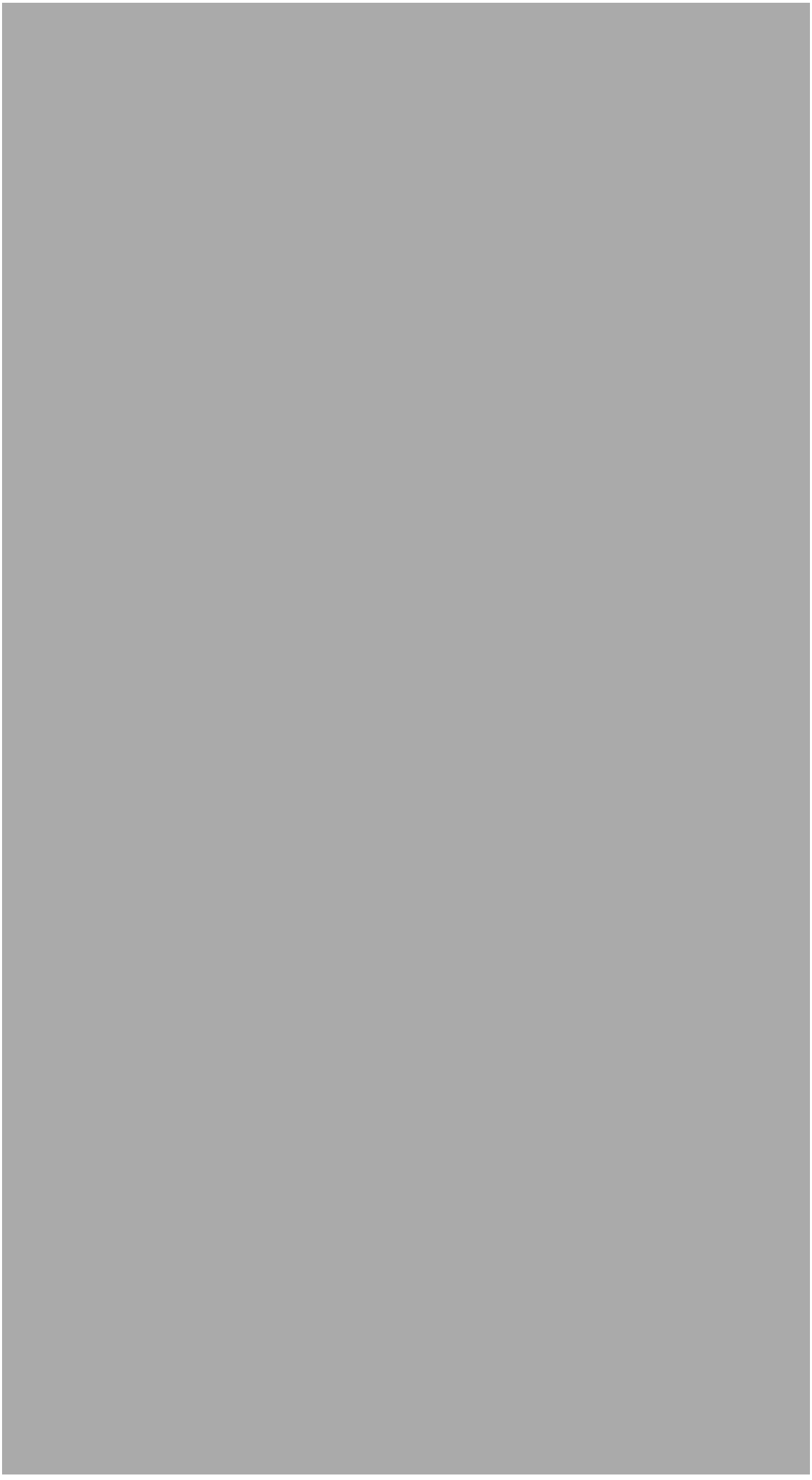

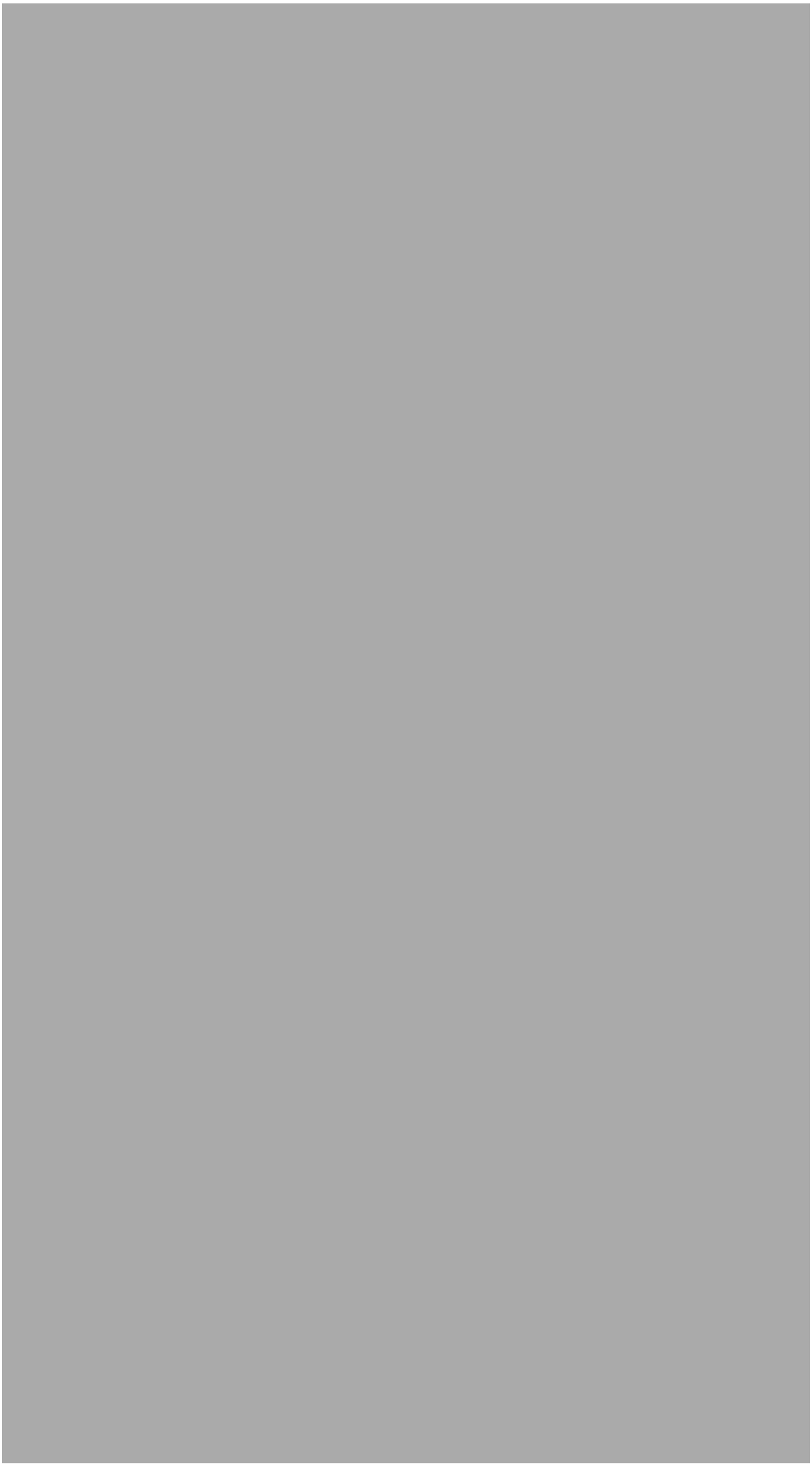

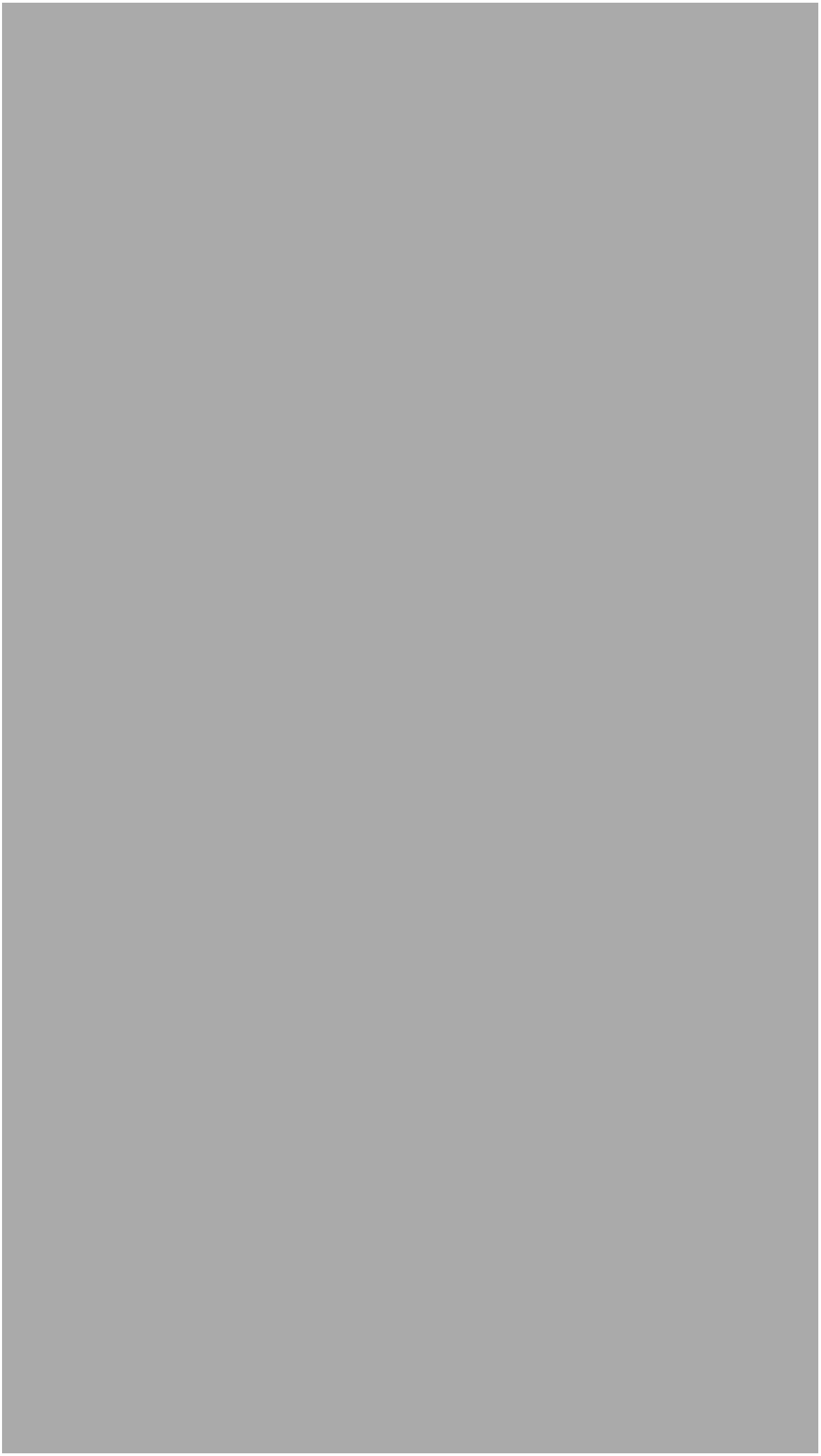

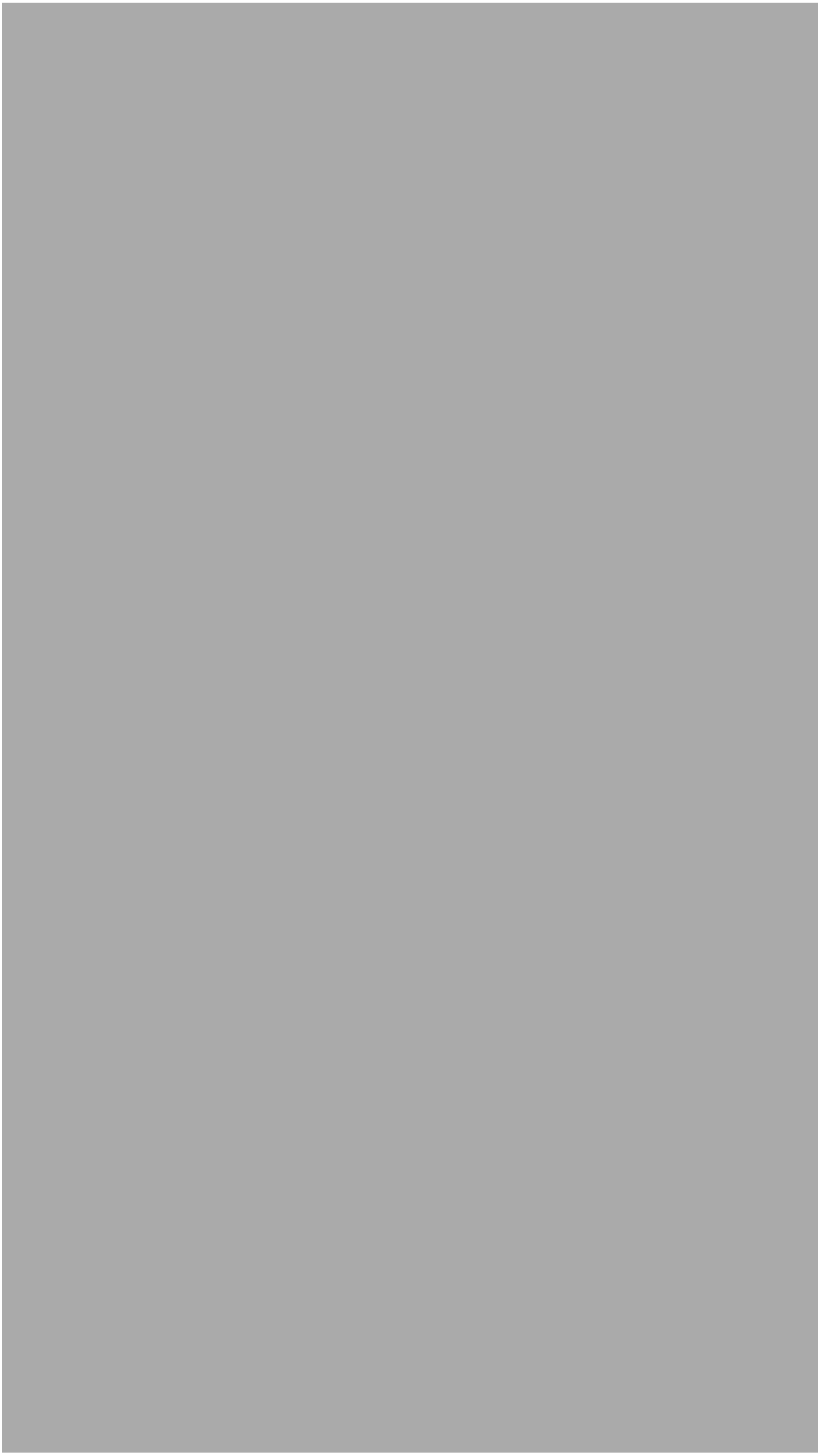

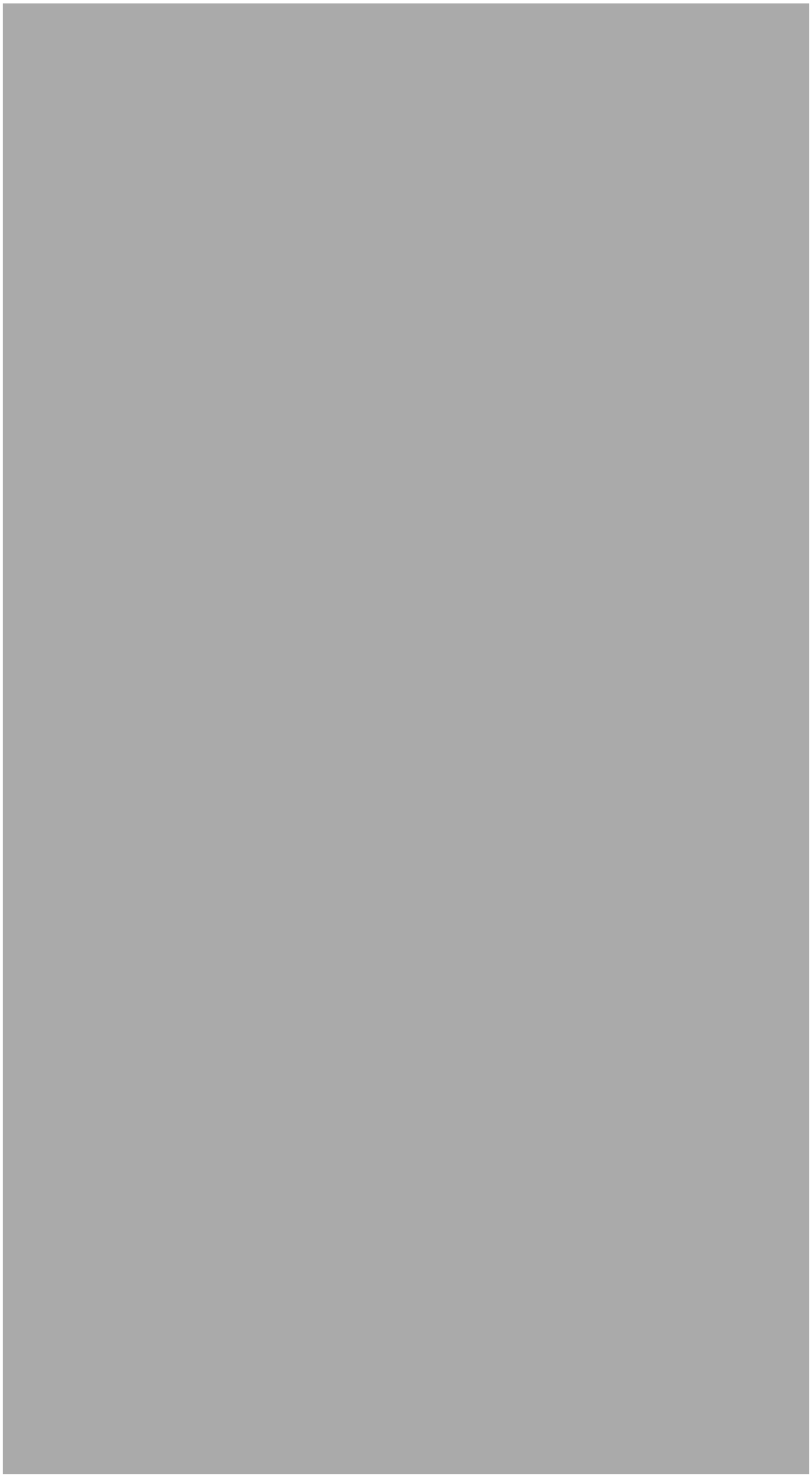

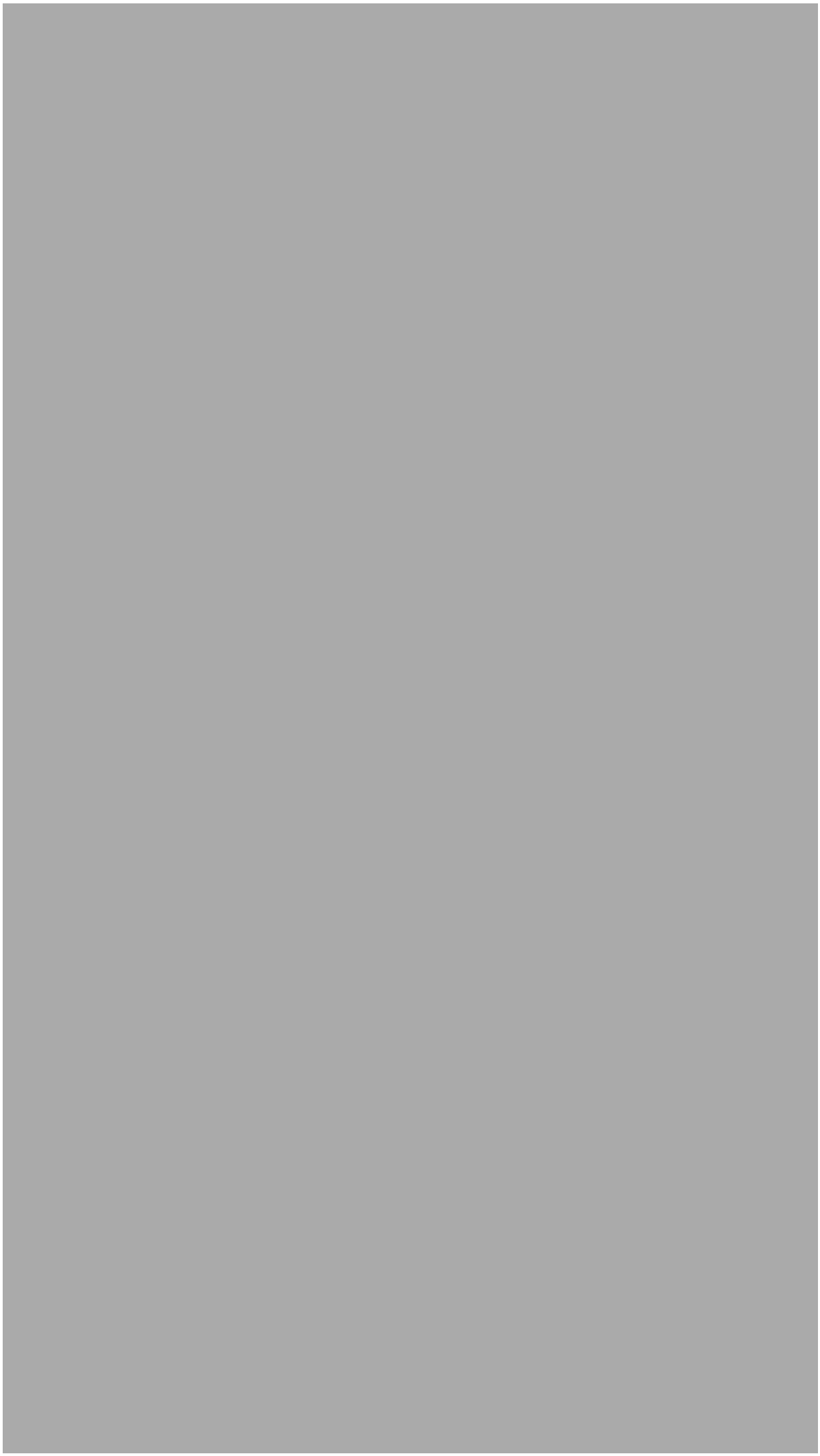

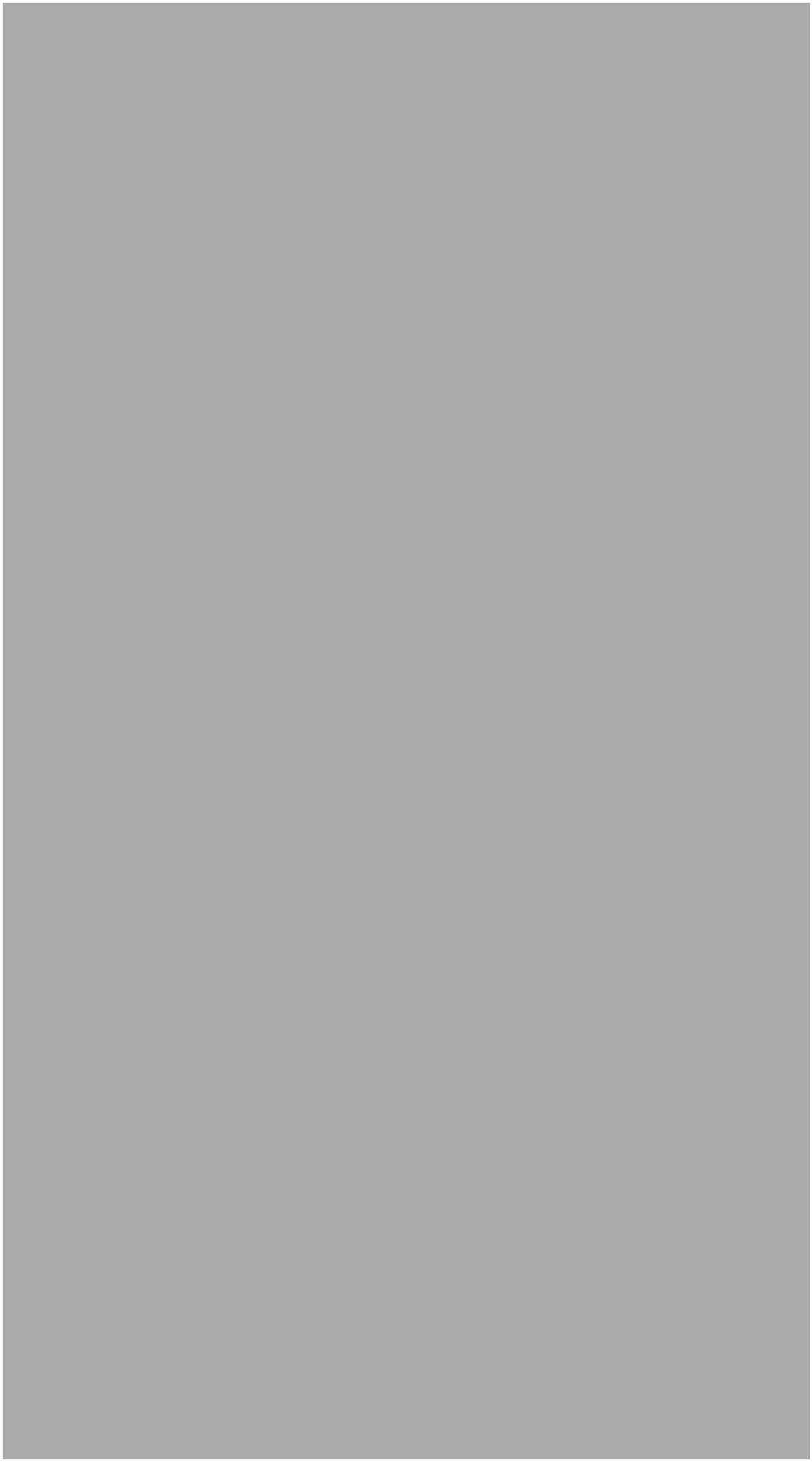

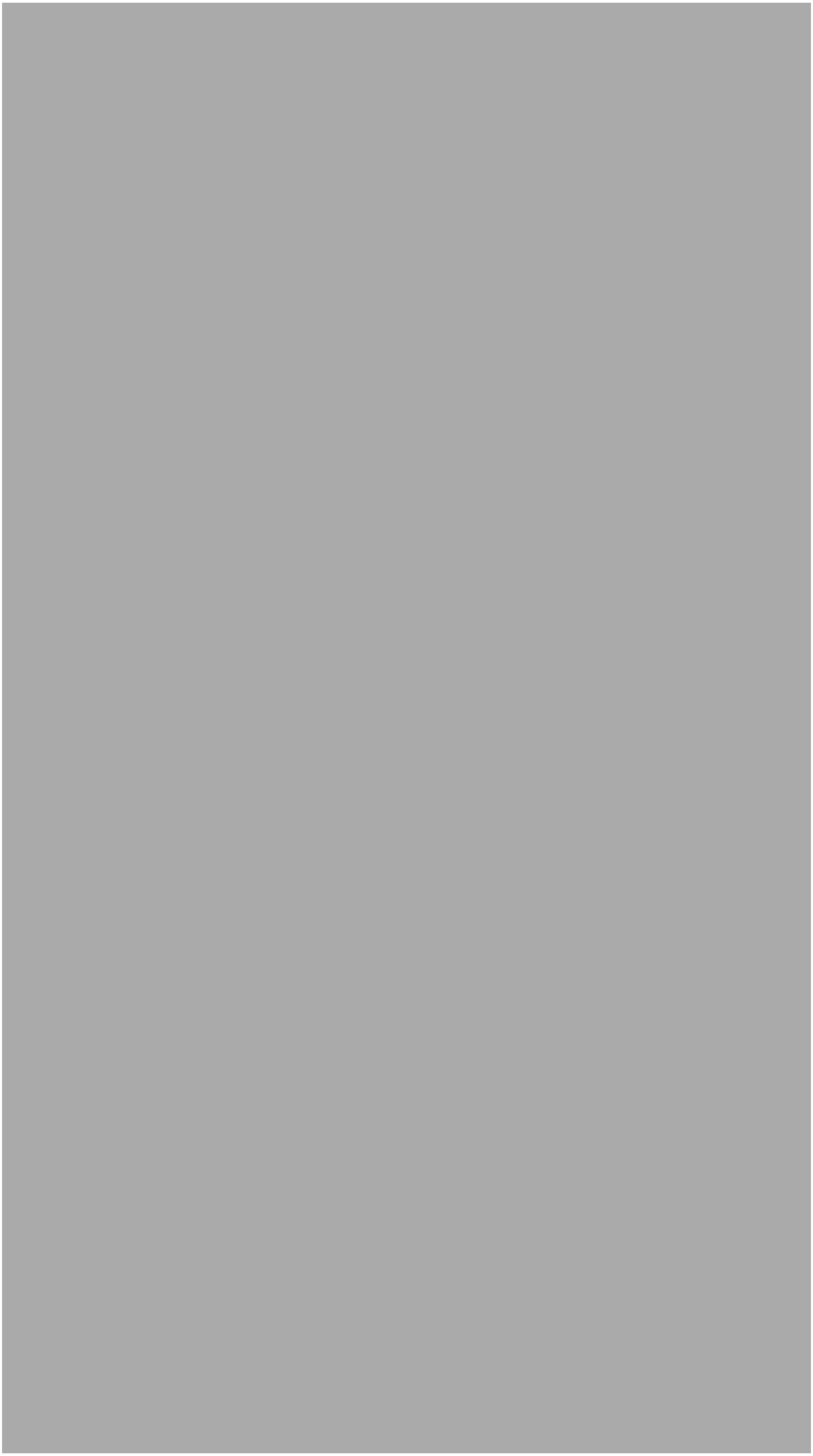

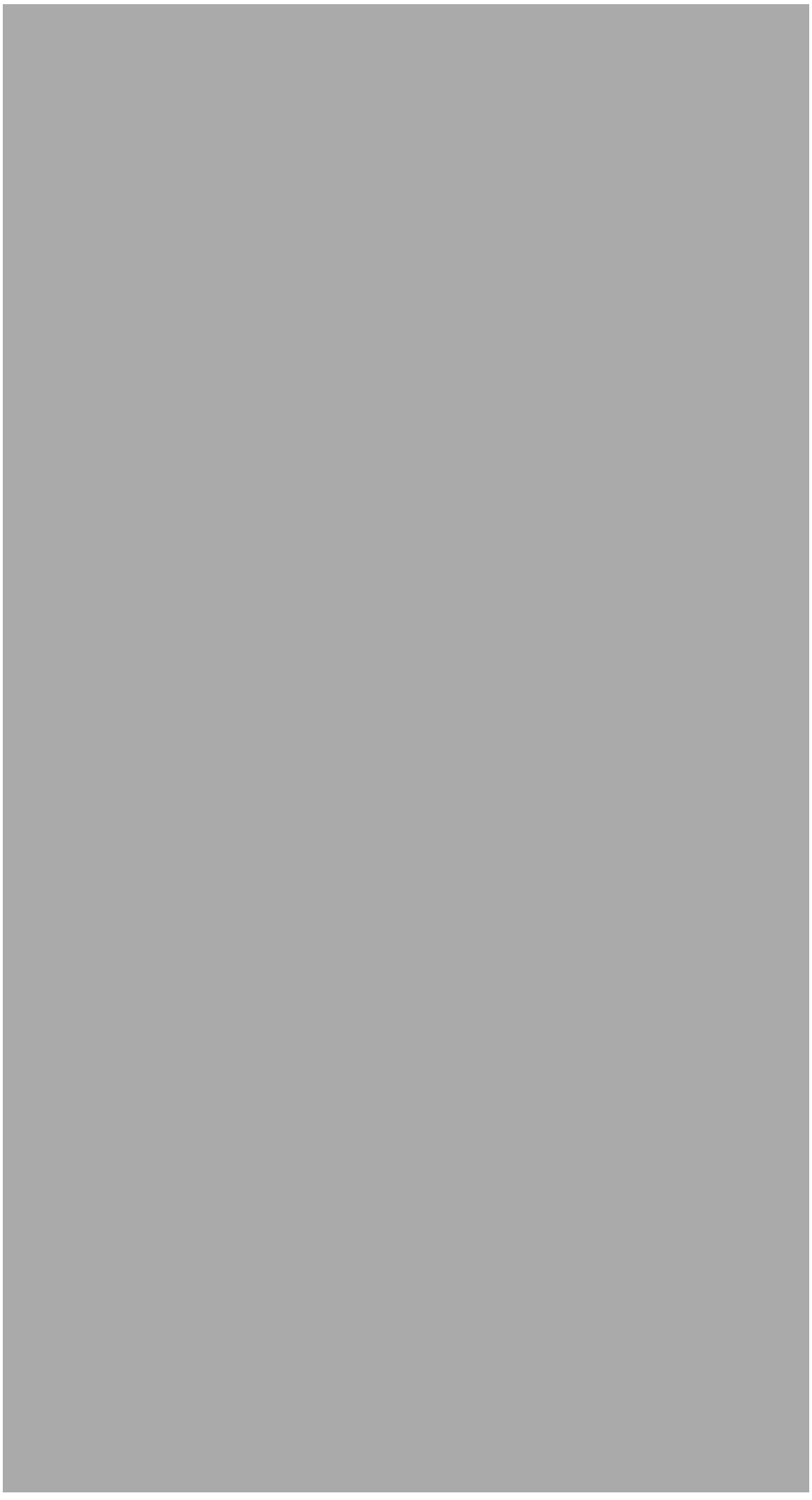

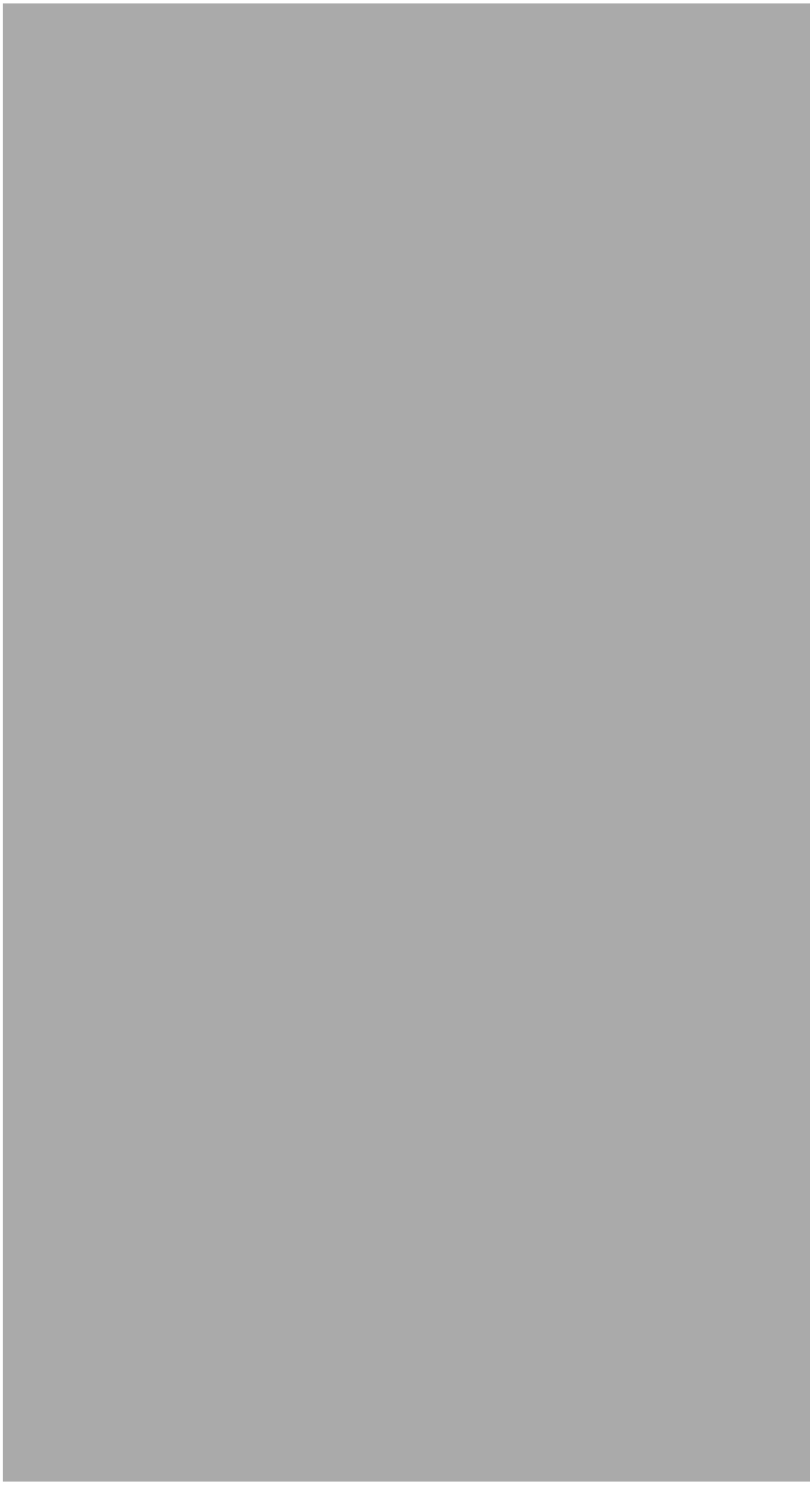

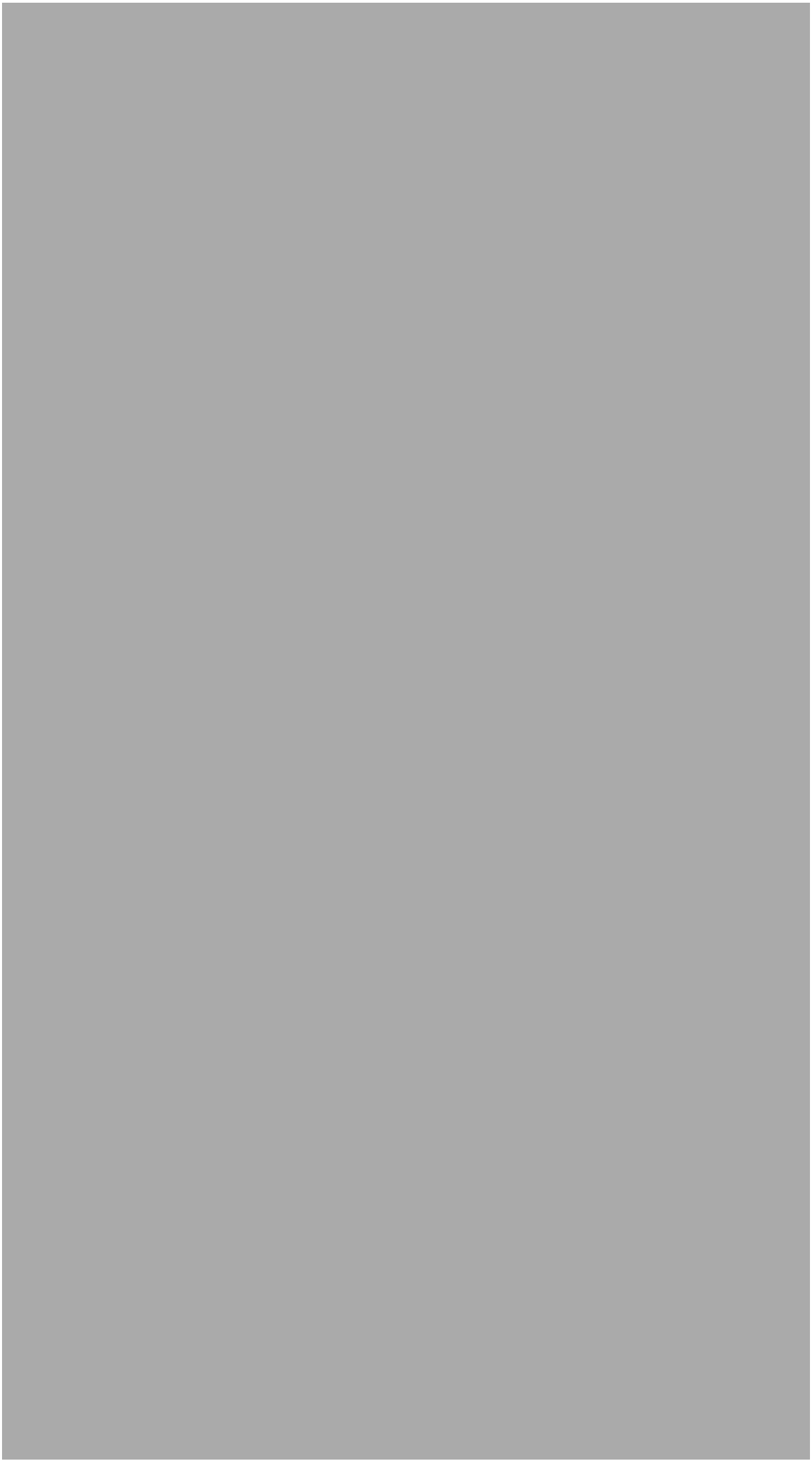

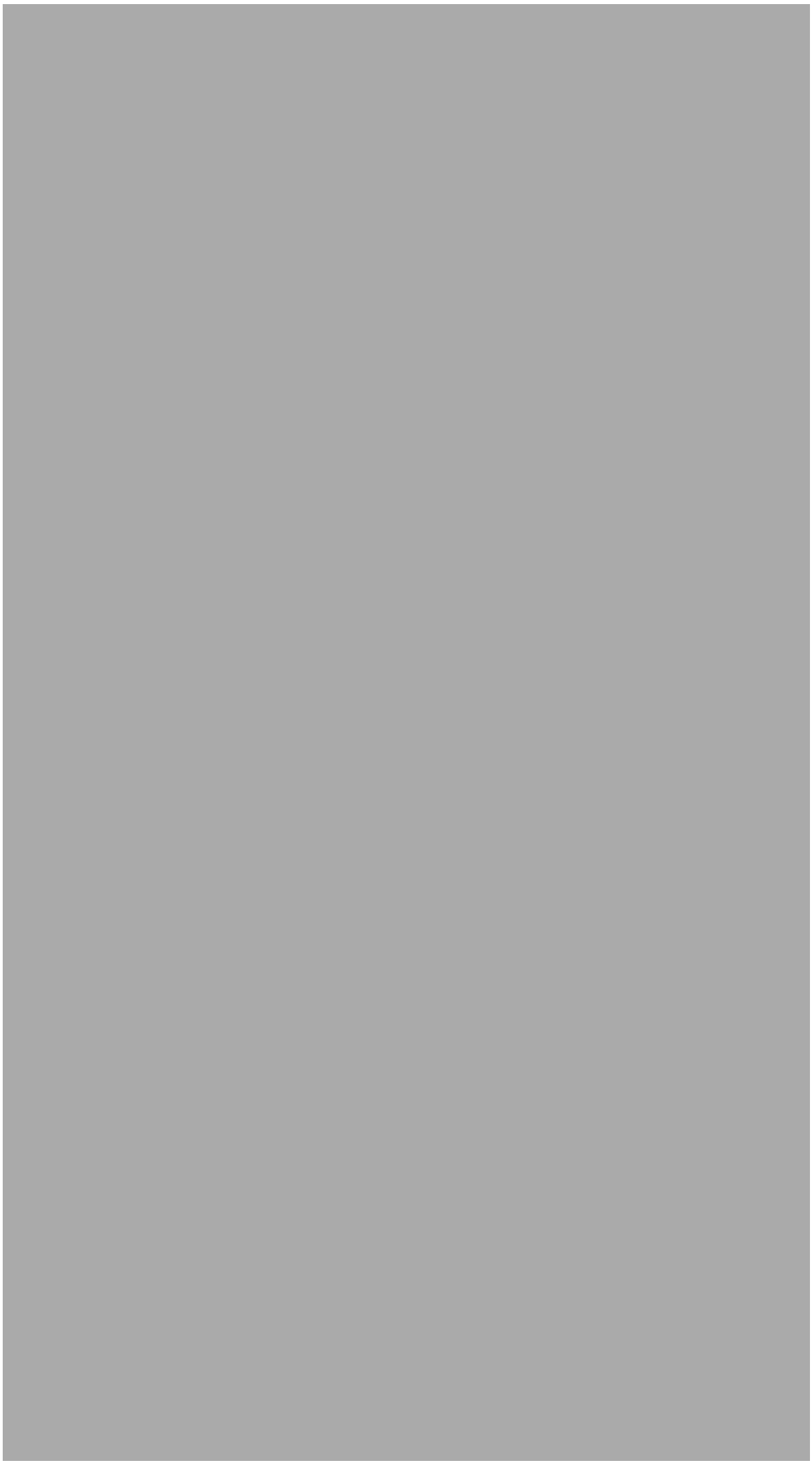

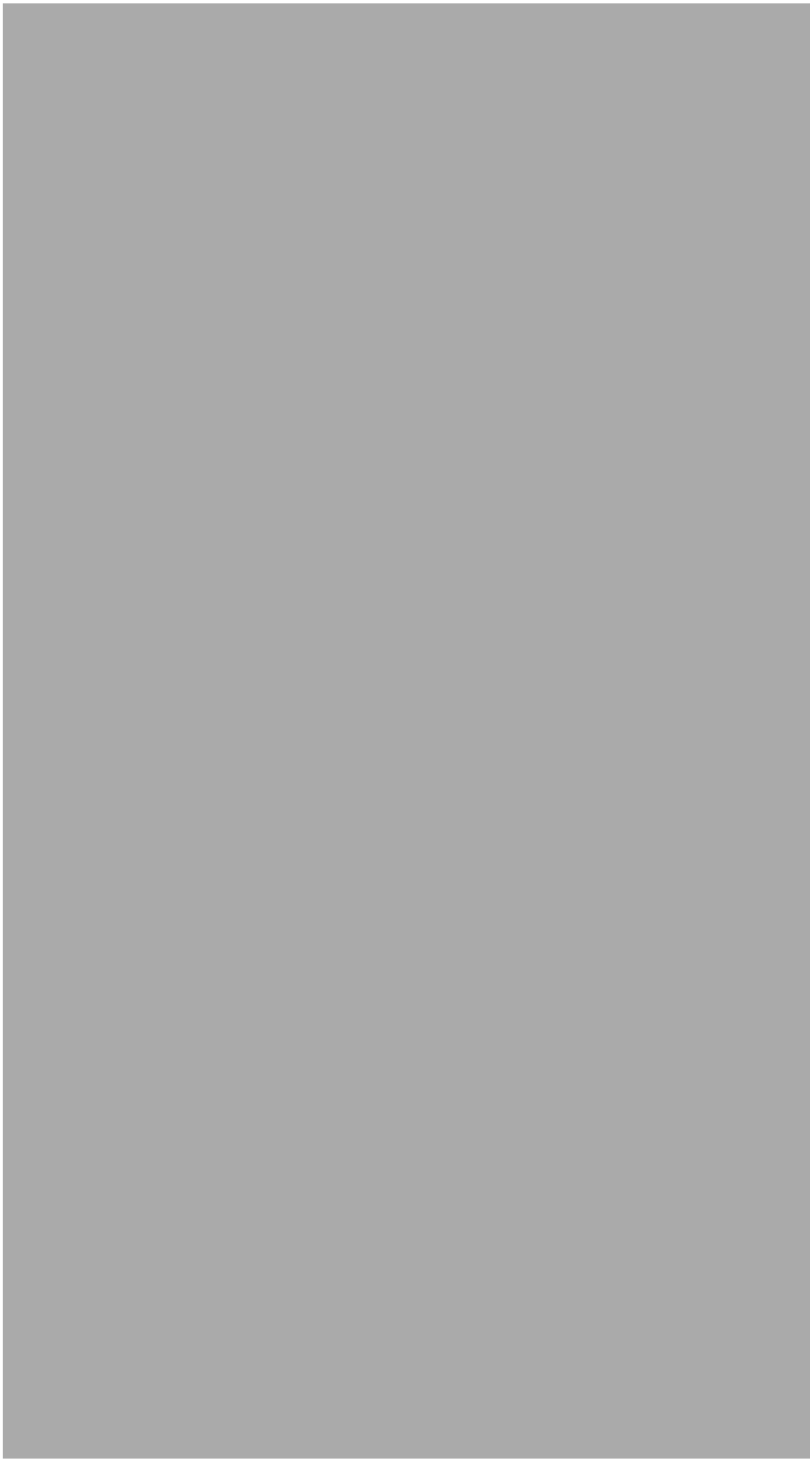

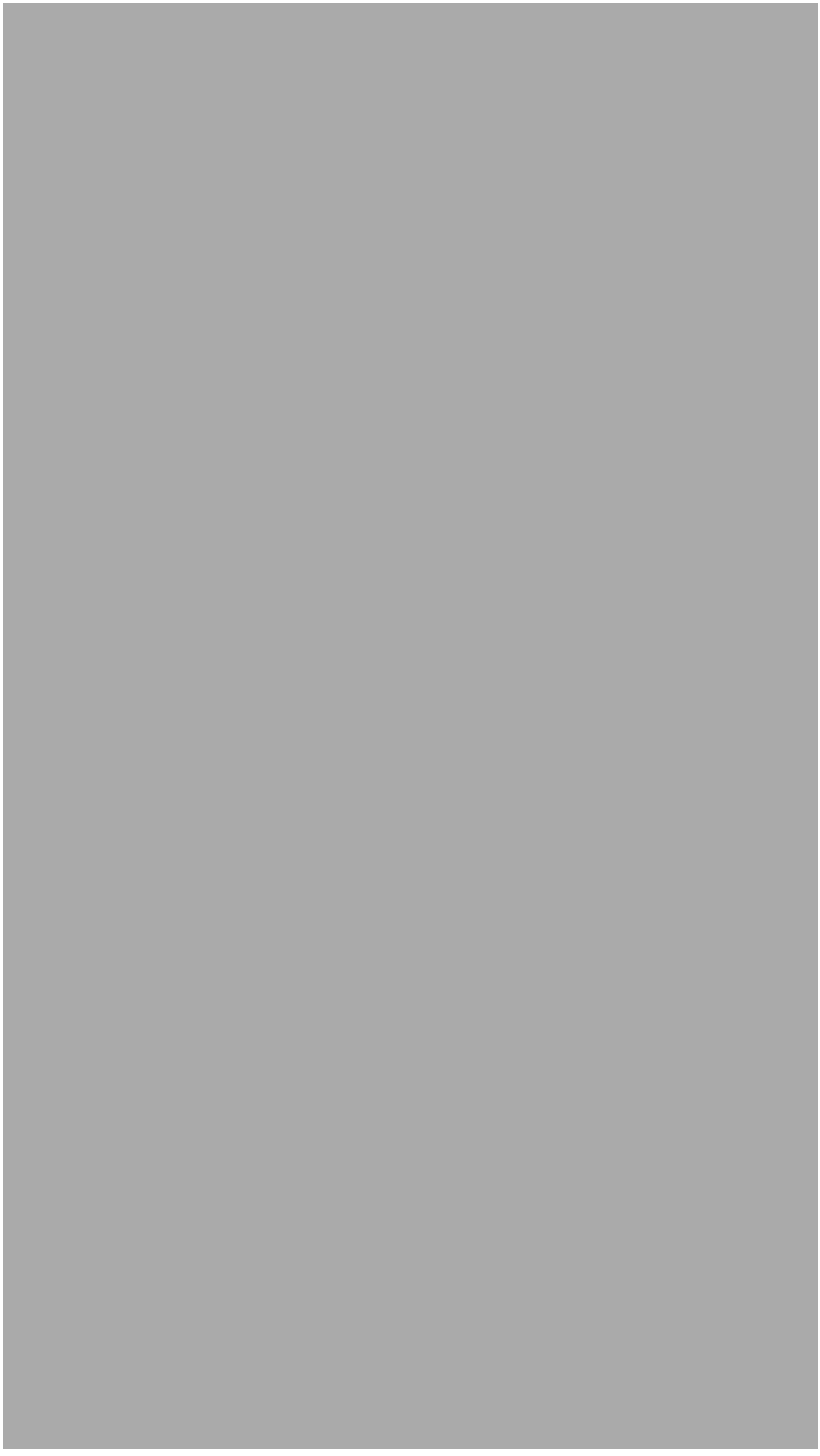

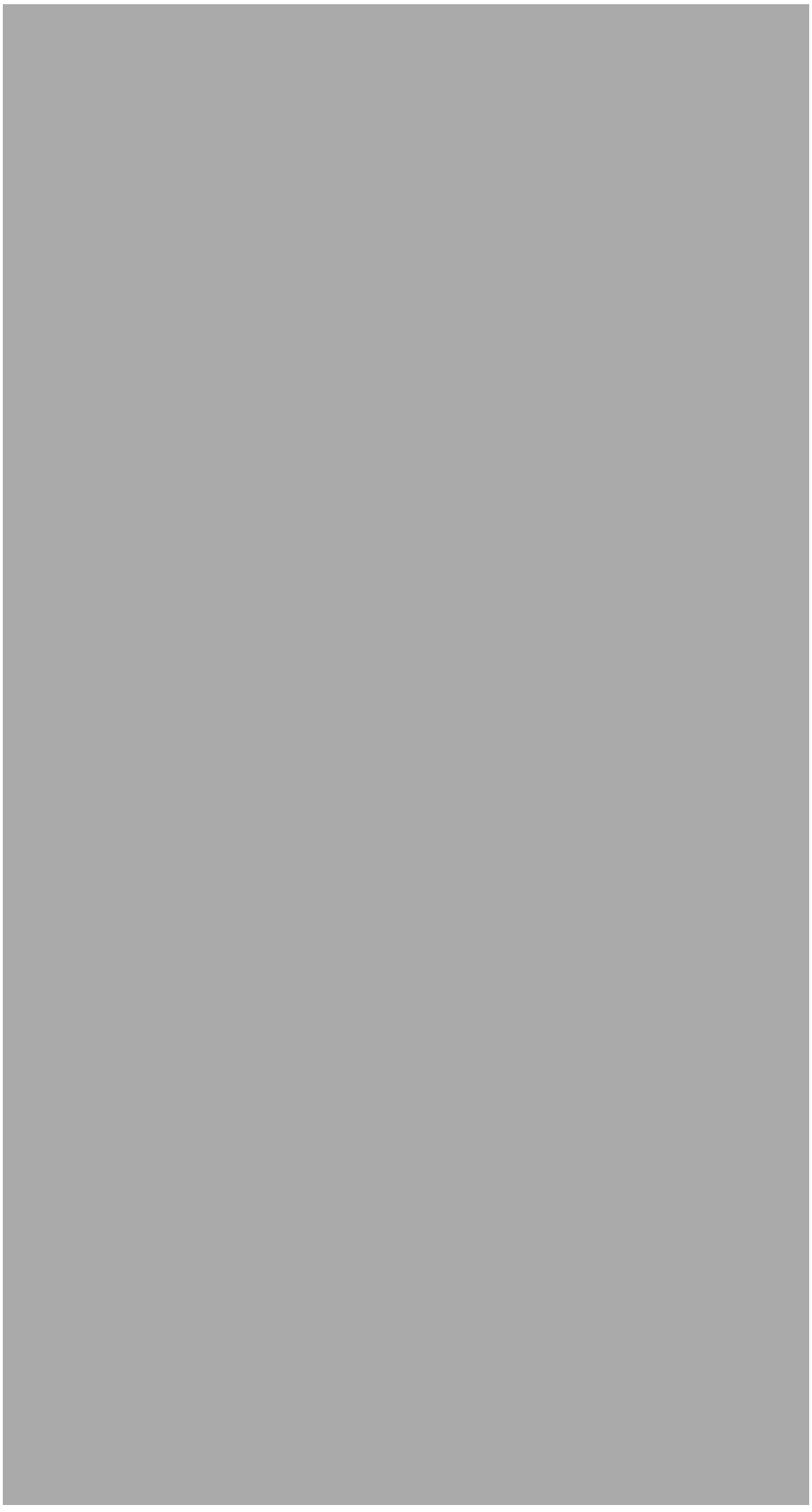

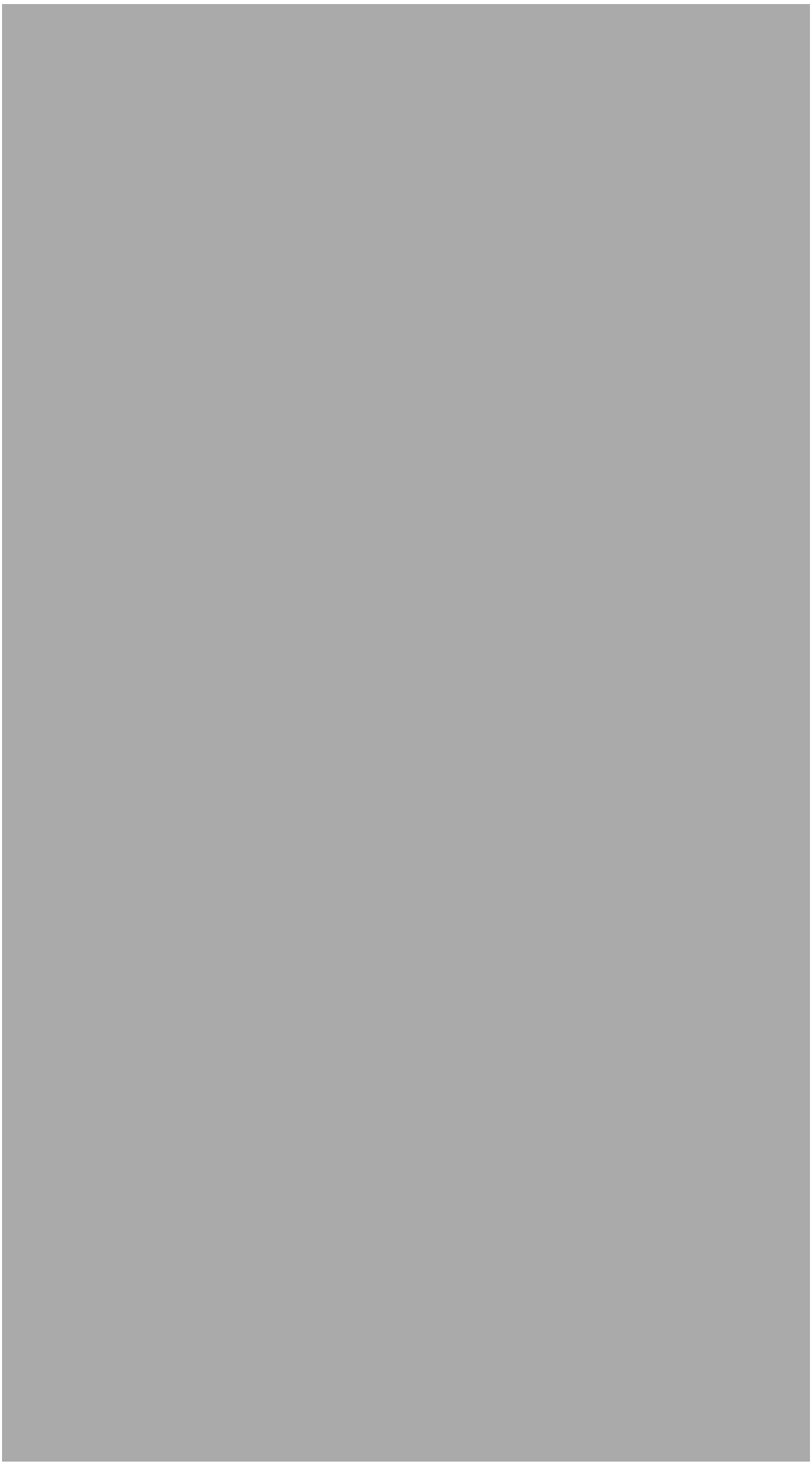

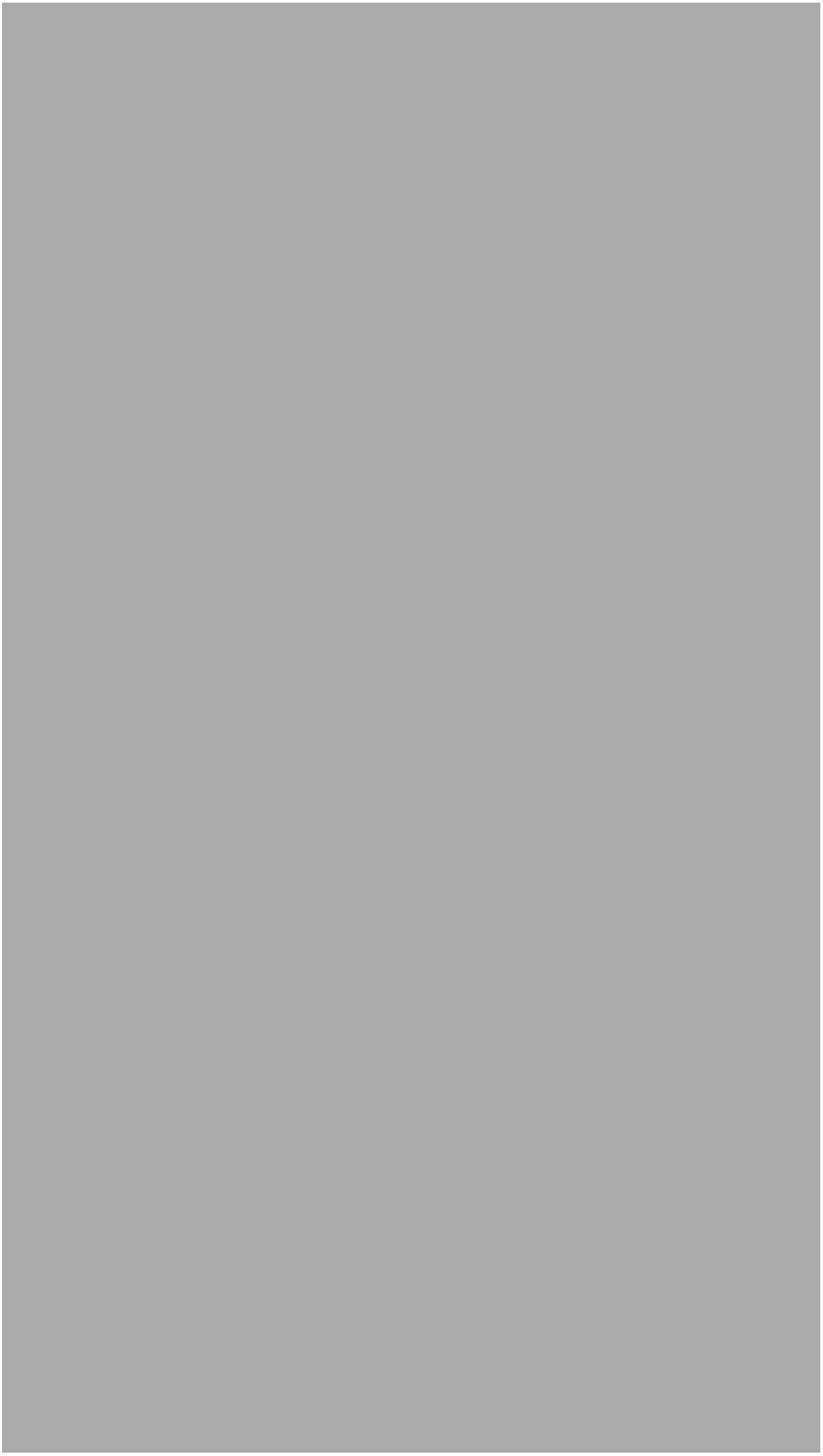

Supporting Information

Physico-chemical insights into gas-phase and oxide-supported sub-nanometre AuCu clusters

Heider A. Hussein,[1,2] Mansi Gao,[1] Yiyun Hou,[1] Sarah L. Horswell,[1] Roy L. Johnston[1]

[1] School of Chemistry, University of Birmingham, Edgbaston, Birmingham B15 2TT, UK
[2] Department of Chemistry, College of Science, University of Kufa, Najaf, Iraq

Content

1. Determination of the optimal spin states

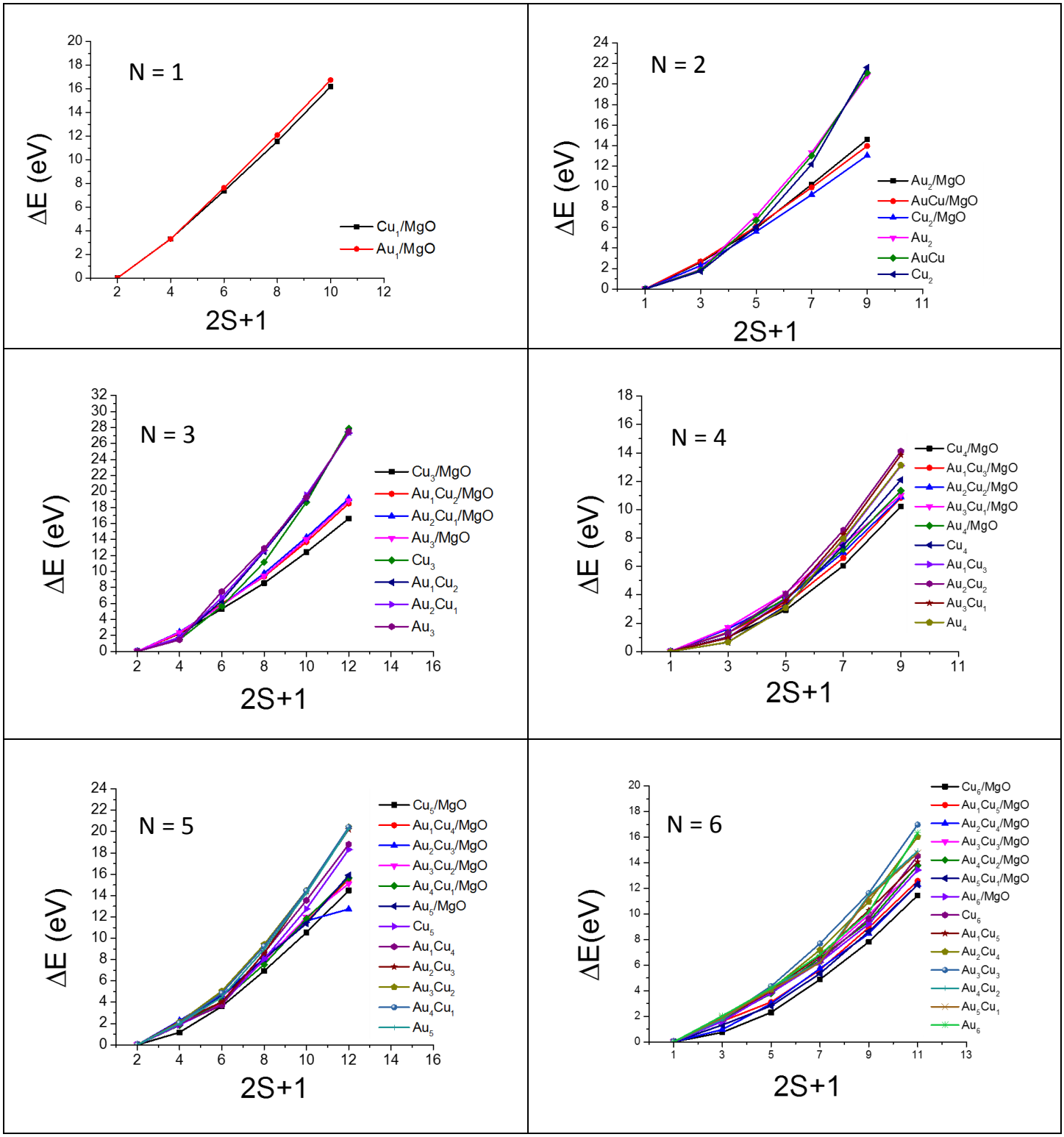

Fig S1. Relative energies as a function of spin state for free and supported atoms, dimers and clusters (N = 3-6).

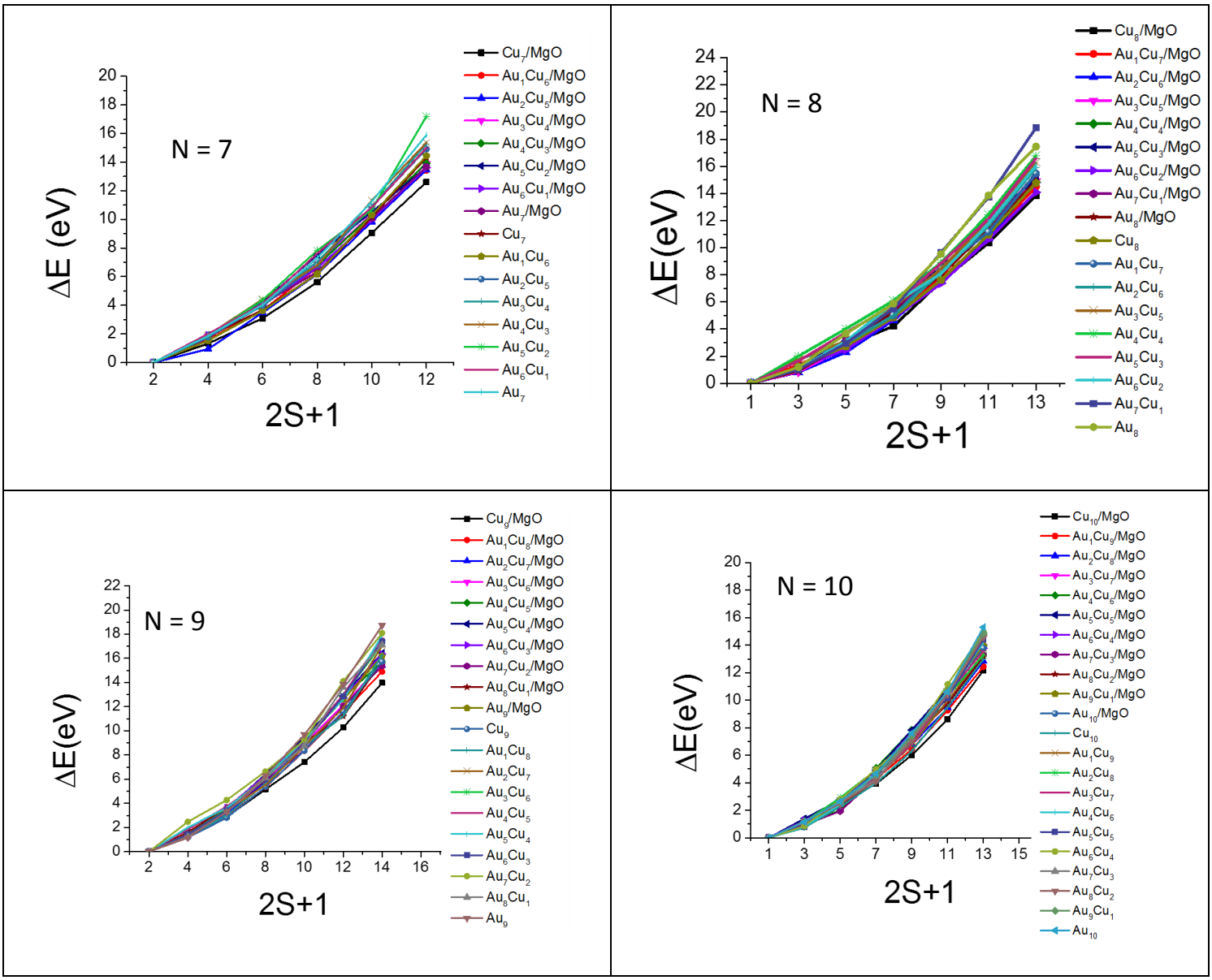

Fig S2. Relative energies as a function of spin state for free and supported clusters (N = 7-10).

2. Energies and point groups of free clusters

Table S1. Energies and point groups of Au_N and Cu_N clusters, N = 3-10.

Cluster	E / eV	Point group	Cluster	E / eV	Point group
Au_3	-4.23	C_{2v}	Cu_3	-4.41	C_{2v}
Au_4	-6.92	D_{2h}	Cu_4	-7.33	D_{2h}
Au_5	-9.38	C_{2v}	Cu_5	-9.83	C_{2v}
Au_6	-12.68	D_{3h}	Cu_6	-12.94	D_{3h}
Au_7	-14.51	C_s	Cu_7	-15.97	D_{5h}
Au_8	-17.53	D_{2d}	Cu_8	-19.06	D_{2d}
Au_9	-19.62	C_{2v}	Cu_9	-21.41	C_s
Au_{10}	-22.62	D_{2h}	Cu_{10}	-24.55	D_{2d}

Table S2. Energies and point groups of AuCu clusters, N = 3-10.

Cluster	E / eV	Point group	Cluster	E / eV	Point group
N = 3			N = 8		
Au_1Cu_2	-4.773	C_{2v}	Au_1Cu_7	-19.257	C_{3v}
Au_2Cu_1	-4.730	C_{2h}	Au_2Cu_6	-19.495	C_{2v}
N = 4			Au_3Cu_5	-19.740	C_{3v}
Au_1Cu_3	-7.820	C_{2v}	Au_4Cu_4	-19.984	T_d
Au_2Cu_2	-8.230	D_{2h}	Au_5Cu_3	-19.269	C_{3v}
Au_3Cu_1	-7.640	C_{2v}	Au_6Cu_2	-18.537	D_2
N = 5			Au_7Cu_1	-18.030	C_{2v}
Au_1Cu_4	-10.184	C_s	N = 9		
Au_2Cu_3	-10.519	C_{2v}	Au_1Cu_8	-21.733	C_s
Au_3Cu_2	-10.401	C_s	Au_2Cu_7	-21.891	C_{2v}
Au_4Cu_1	-10.007	C_{2v}	Au_3Cu_6	-22.171	C_{3v}
N = 6			Au_4Cu_5	-22.140	C_s
Au_1Cu_5	-13.358	C_{2v}	Au_5Cu_4	-22.089	C_{2v}
Au_2Cu_4	-13.749	C_{2v}	Au_6Cu_3	-21.403	C_s
Au_3Cu_3	-14.107	D_{3h}	Au_7Cu_2	-20.814	C_{2v}
Au_4Cu_2	-13.719	C_{2h}	Au_8Cu_1	-20.287	C_2
Au_5Cu_1	-13.242	C_{2h}	N = 10		
N = 7			Au_1Cu_9	-24.923	C_{2v}
Au_1Cu_6	-16.018	C_{2v}	Au_2Cu_8	-25.209	C_2
Au_2Cu_5	-16.196	C_s	Au_3Cu_7	-25.256	C_1
Au_3Cu_4	-16.411	C_{3v}	Au_4Cu_6	-25.348	C_s
Au_4Cu_3	-16.018	C_s	Au_5Cu_5	-25.327	C_s
Au_5Cu_2	-15.591	C_s	Au_6Cu_4	-24.916	C_s
Au_6Cu_1	-15.134	C_s	Au_7Cu_3	-24.331	C_2
			Au_8Cu_2	-23.705	C_1
			Au_9Cu_1	-23.198	C_{2v}

3. Energies of free and supported atoms and dimers and M-M and M-O bond lengths for supported dimers

Table S3. Energies of free and supported atoms and dimers of AuCu system.

Free species	E / eV	Supported-species	E / eV
Au	-0.184	Au@MgO(100)	-412.957
Cu	-0.241	Cu@MgO(100)	-413.036
Au_2	-2.705	Au_2@MgO(100)	-415.972
Cu_2	-2.747	Cu_2@MgO(100)	-415.882
AuCu	-2.946	AuCu@MgO(100)	-416.387

Table S4. Bond lengths of M-M and M-O of supported dimers of AuCu system.

P-configuration					
Au_2@MgO(100)		Cu_2@MgO(100)		AuCu@MgO(100)	
Au(1)-Au(2)/Å	2.550	Cu(1)-Cu(2) /Å	2.272	Au-Cu/Å	2.443
Au(1)-O/Å	2.956	Cu(1)-O/Å	2.148	Au-O/Å	3.620
Au(2)-O/Å	2.970	Cu(2)-O/Å	2.151	Cu-O/Å	2.343
V-configuration					
Au_2@MgO(100)		Cu_2@MgO(100)		AuCu@MgO(100)	
Au-Au / Å	2.500	Cu-Cu / Å	2.235	Au-**Cu** / Å	2.380
Au-O / Å	2.199	Cu-O / Å	1.958	Cu-O / Å	1.976

4. Adsorption energies for sites and orientations of adatoms and dimers

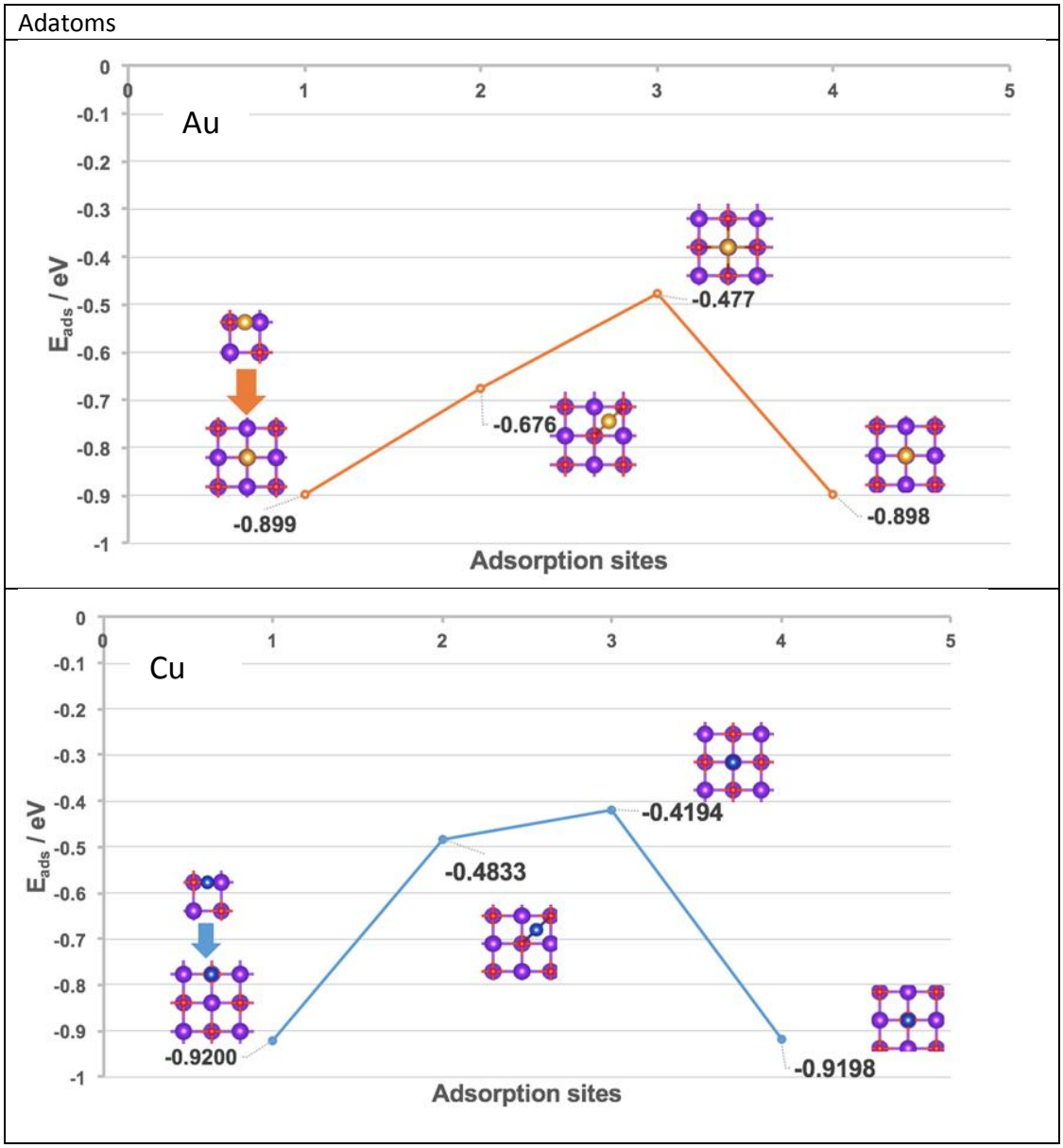

Fig S3. Adsorption energies of Au and Cu adatoms as a function of different starting positions.

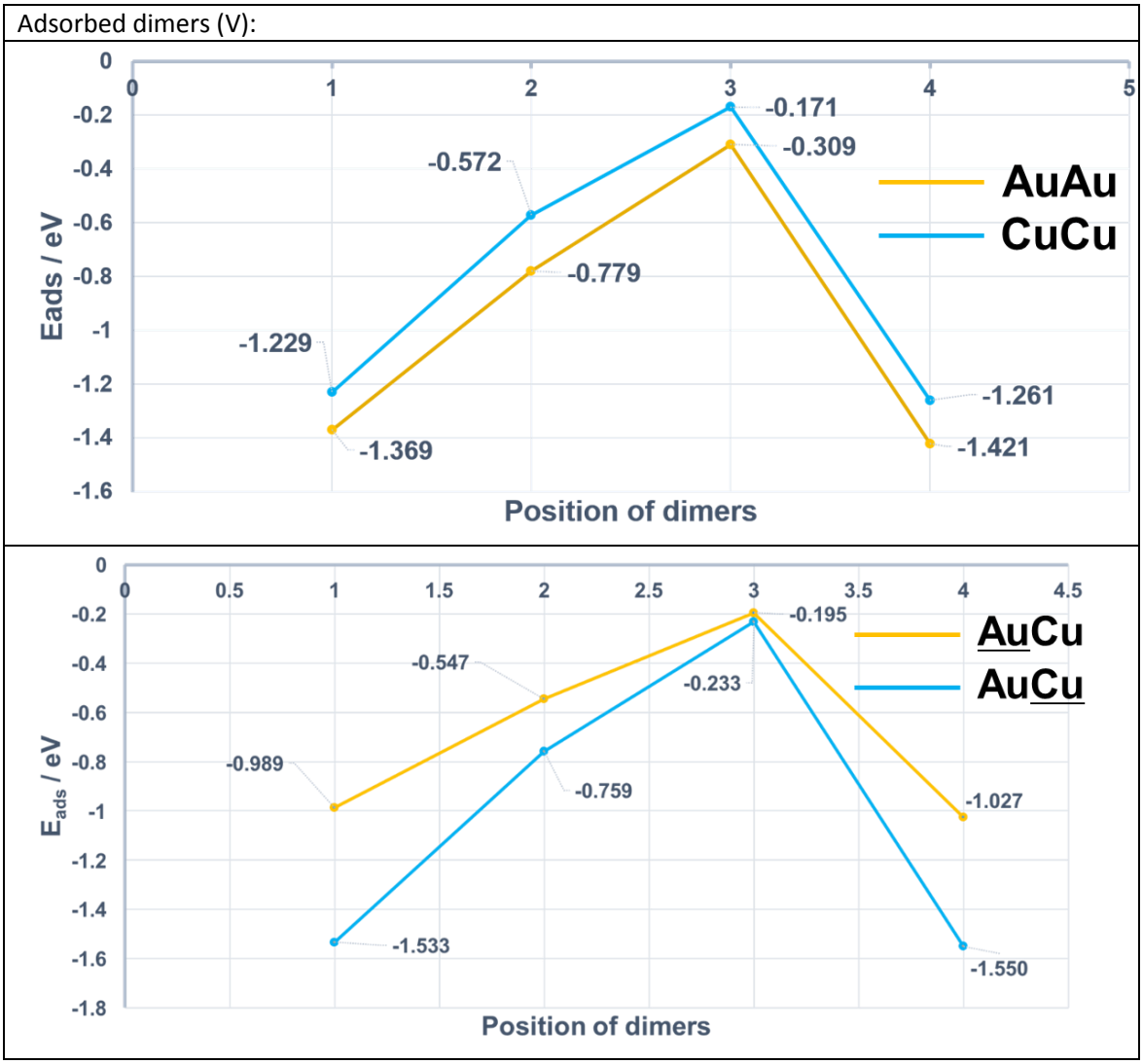

Fig S4. Adsorption energies of supported vertical (V) Au_2, Cu_2 and AuCu dimers as a function of different starting positions. For the AuCu dimers, the underlined atom is in contact with the support.

Adsorbed dimers (P):

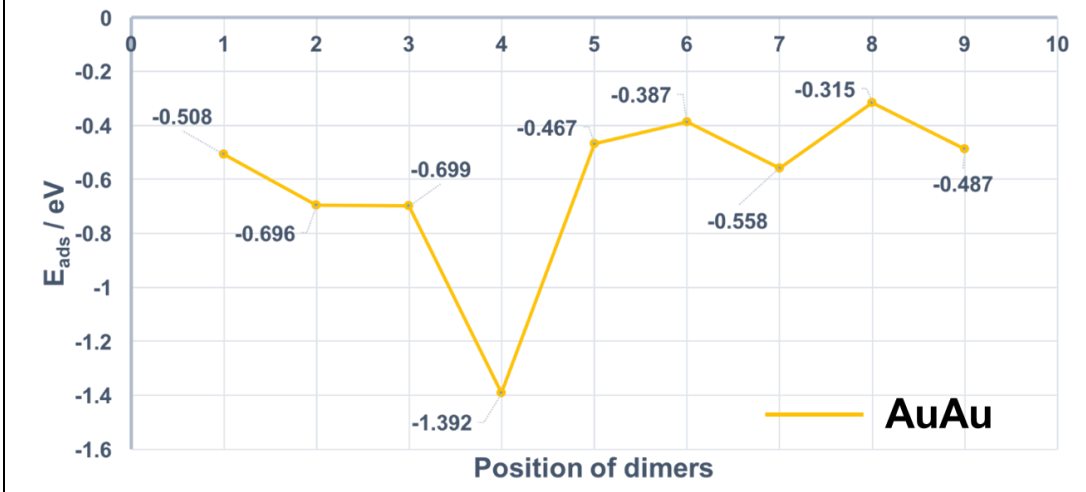

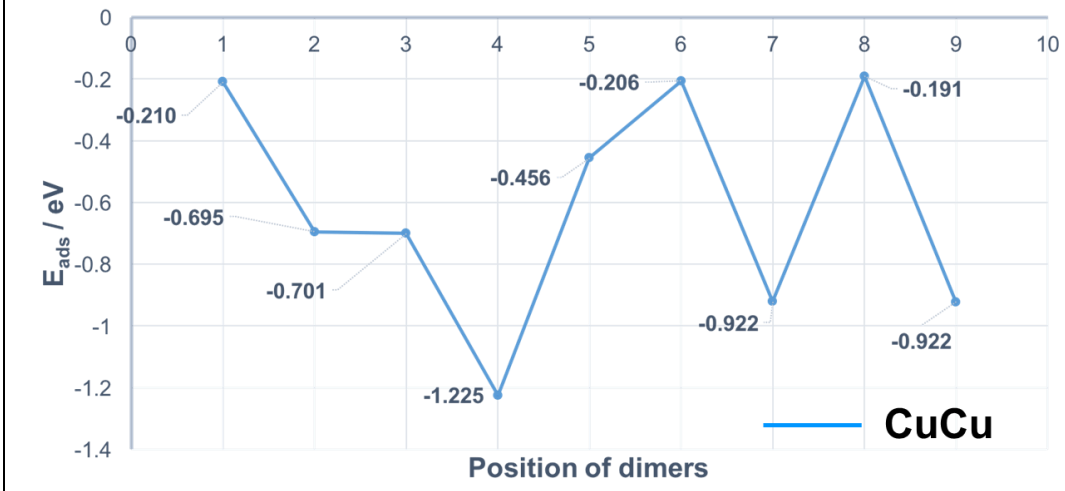

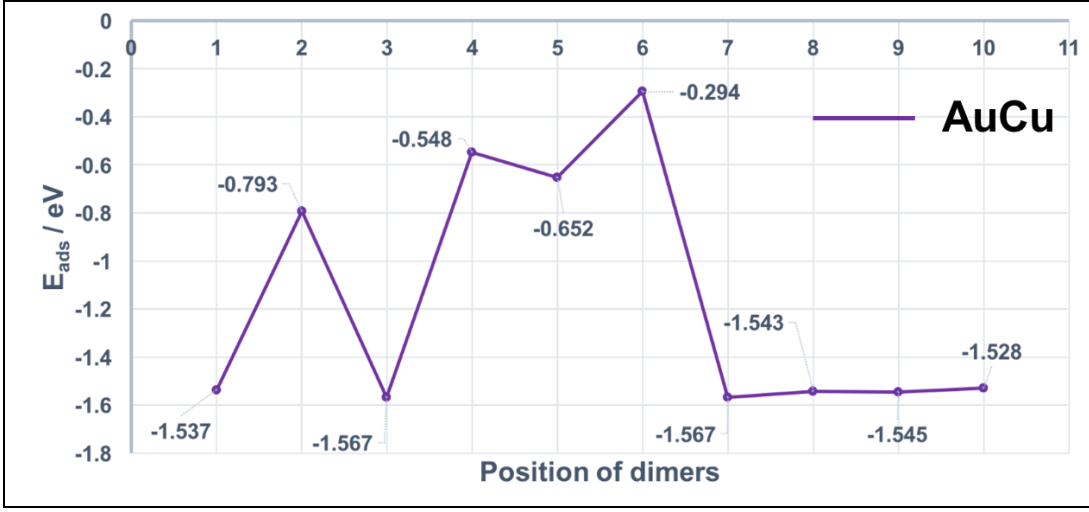

Fig S5. Adsorption energies of supported parallel (P) Au_2, Cu_2 and AuCu dimers as a function of different starting positions.

5. Homotop search

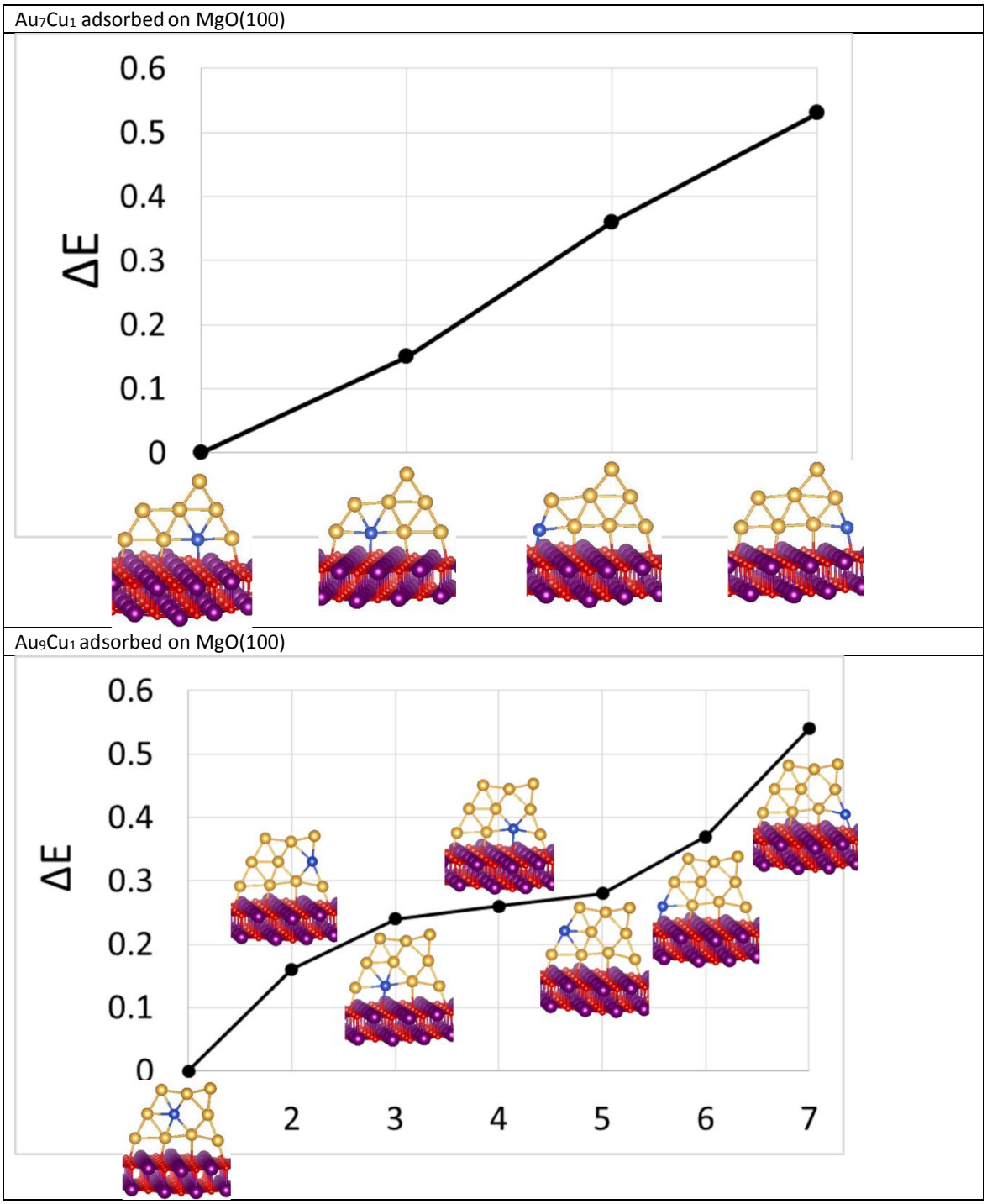

Fig S6. The relative energies for selected homotops of MgO(100)-supported Au_7Cu_1 and Au_9Cu_1 clusters.

6. Energies of gas-phase and supported dimers and GM of AuCu clusters

Table S5. Excess Energy Δ and Binding Energy E_b (gas-phase only), Adsorption Energy E_{ads} (surface-supported only), and second difference in energy Δ_2E for 2-7 atoms.

	Gas Phase			Surface Supported	
Cluster	Δ / eV	Δ_2E / eV	E_b / eV	Δ_2E / eV	E_{ads} / eV
N = 2					
Cu_2	0.0	0.835	1.1316	0.835	-1.261
Au_1Cu_1	-0.220	-----	1.259	-----	-1.566
Au_2	0.0	0.987	1.168	1.078	-1.420
N = 3					
Cu_3	0.0	-1.246	1.230	-0.855	-1.847
Au_1Cu_2	-0.416	-1.219	1.368	-1.136	-2.271
Au_2Cu_1	-0.432	-1.124	1.373	-0.882	-1.981
Au_3	0.0	-1.154	1.228	-1.025	-1.968
N = 4					
Cu_4	0.0	0.418	1.591	0.552	-2.084
Au_1Cu_3	-0.589	0.682	1.727	0.974	-2.136
Au_2Cu_2	-1.099	-----	1.844	-----	-1.828
Au_3Cu_1	-0.611	0.541	1.710	0.955	-2.410
Au_4	0.0	0.225	1.546	0.832	-2.394
N = 5					
Cu_5	0.0	-0.619	1.724	-0.723	-2.540
Au_1Cu_4	-0.442	-0.809	1.806	-1.103	-2.003
Au_2Cu_3	-0.865	-----	1.884	-----	-2.189
Au_3Cu_2	-0.835	-----	1.872	-----	-2.329
Au_4Cu_1	-0.529	-0.867	1.805	-1.436	-1.966
Au_5	0.0	-0.836	1.693	-1.179	-2.178
N = 6					
Cu_6	0.0	0.088	1.916	0.424	-2.640
Au_1Cu_5	-0.453	0.513	1.994	0.714	-2.285
Au_2Cu_4	-0.888	-----	2.068	-----	-2.791
Au_3Cu_3	-1.288	-----	2.137	-----	-2.352
Au_4Cu_2	-0.944	-----	2.082	-----	-1.908
Au_5Cu_1	-0.510	1.343	2.012	1.820	-1.987
Au_6	0.0	1.474	1.929	1.354	-1.809
N = 7					
Cu_7	0.0	-0.059	2.040	-0.369	-2.466
Au_1Cu_6	-0.251	-0.578	2.054	-0.749	-2.360
Au_2Cu_5	-0.637	-----	2.088	-----	-3.165
Au_3Cu_4	-1.061	-----	2.127	-----	-2.168
Au_4Cu_3	-0.877	-----	2.079	-----	-2.368
Au_5Cu_2	-0.660	-----	2.026	-----	-2.638
Au_6Cu_1	-0.412	-1.004	1.969	-1.183	-2.210
Au_7	0.0	-1.197	1.888	-0.996	-1.994

Table S6. Excess Energy Δ and Binding Energy E_b (gas-phase only), Adsorption Energy E_{ads} (surface-supported only), and second difference in energy Δ_2E for 8-10 atoms.

	Gas Phase			Surface Supported	
Cluster	Δ / eV	Δ_2E / eV	E_b / eV	Δ_2E / eV	E_{ads} / eV
N = 8					
Cu_8	0.0	0.736	2.141	0.640	-2.505
Au_1Cu_7	-0.384	0.763	2.172	0.960	-2.675
Au_2Cu_6	-0.813	-----	2.209	-----	-3.326
Au_3Cu_5	-1.249	-----	2.247	-----	-3.409
Au_4Cu_4	-1.684	-----	2.284	-----	-3.183
Au_5Cu_3	-1.160	-----	2.202	-----	-2.490
Au_6Cu_2	-0.619	-----	2.118	-----	-2.149
Au_7Cu_1	-0.304	0.639	2.061	0.705	-2.400
Au_8	0.0	0.934	2.007	0.569	-2.441
N = 9					
Cu_9	0.0	-0.782	2.137	-0.518	-2.979
Au_1Cu_8	-0.516	-0.714	2.179	-0.841	-2.889
Au_2Cu_7	-0.873	-----	2.203	-----	-2.905
Au_3Cu_6	-1.353	-----	2.240	-----	-2.967
Au_4Cu_5	-1.521	-----	2.243	-----	-3.430
Au_5Cu_4	-1.670	-----	2.244	-----	-3.777
Au_6Cu_3	-1.183	-----	2.174	-----	-3.310
Au_7Cu_2	-0.793	-----	2.115	-----	-3.147
Au_8Cu_1	-0.466	-0.654	2.063	-0.963	-3.027
Au_9	0.0	-0.914	1.995	-0.464	-2.401
N = 10					
Cu_{10}	0.0	-----	2.213	-----	-3.121
Au_1Cu_9	-0.565	-----	2.256	-----	-3.088
Au_2Cu_8	-1.044	-----	2.290	-----	-3.257
Au_3Cu_7	-1.284	-----	2.300	-----	-3.047
Au_4Cu_6	-1.568	-----	2.315	-----	-3.130
Au_5Cu_5	-1.739	-----	2.319	-----	-2.989
Au_6Cu_4	-1.522	-----	2.284	-----	-3.136
Au_7Cu_3	-1.129	-----	2.231	-----	-2.975
Au_8Cu_2	-0.695	-----	2.174	-----	-3.270
Au_9Cu_1	-0.382	-----	2.129	-----	-2.255
Au_{10}	0.0	-----	2.077	-----	-2.338

7. Second difference in energy

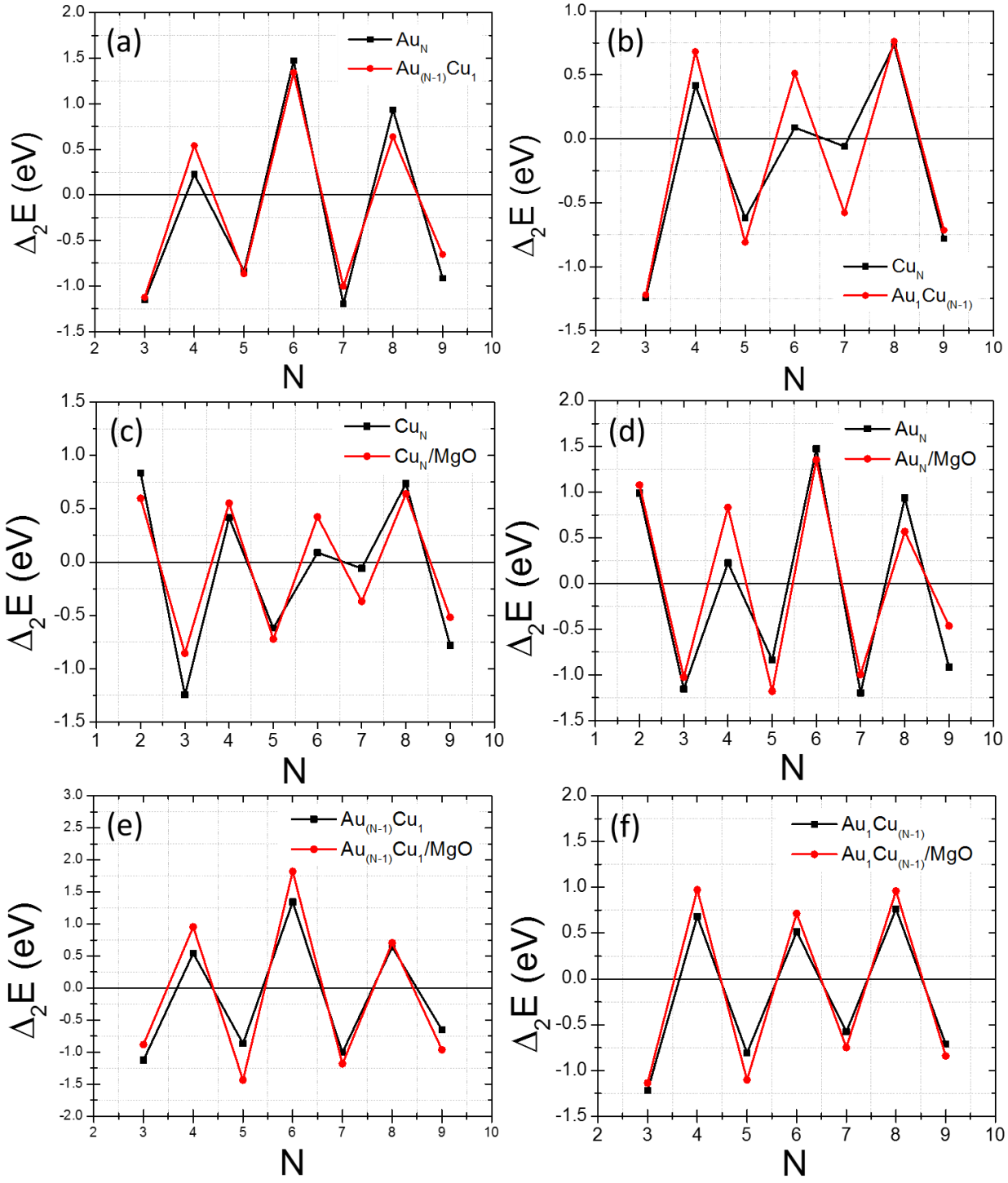

Fig S7. Second difference in energy Δ_2E for free and supported pure and mono-substituted AuCu clusters.

8. Excess and binding energies for all compositions of AuCu clusters

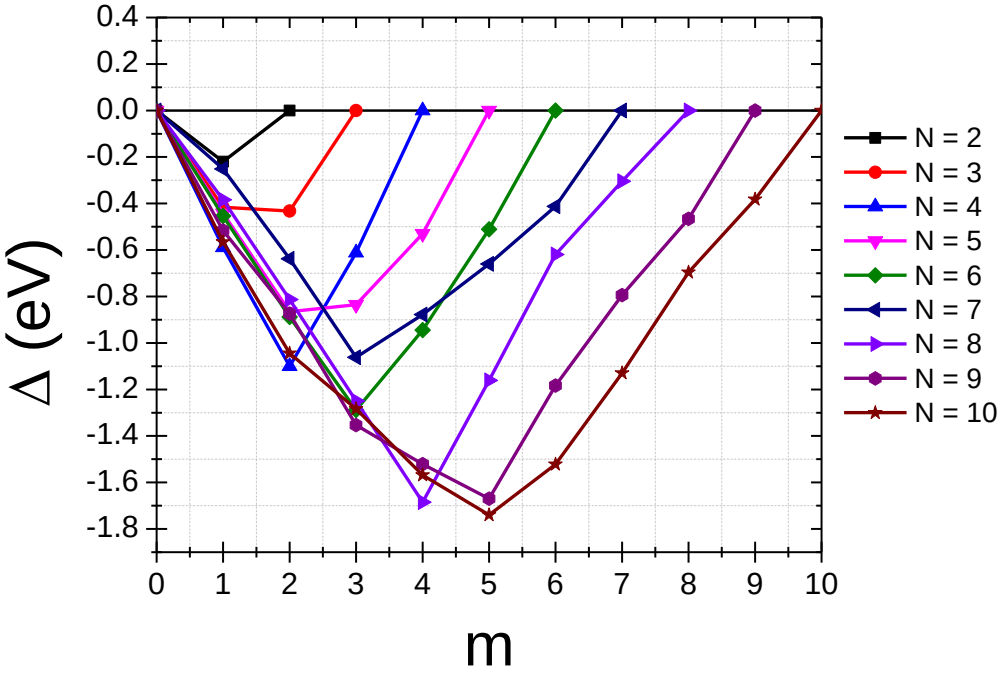

Fig S8. Plot of excess (mixing) energy Δ against the number of Au atoms (m) for free AuCu clusters, with N = 2-10.

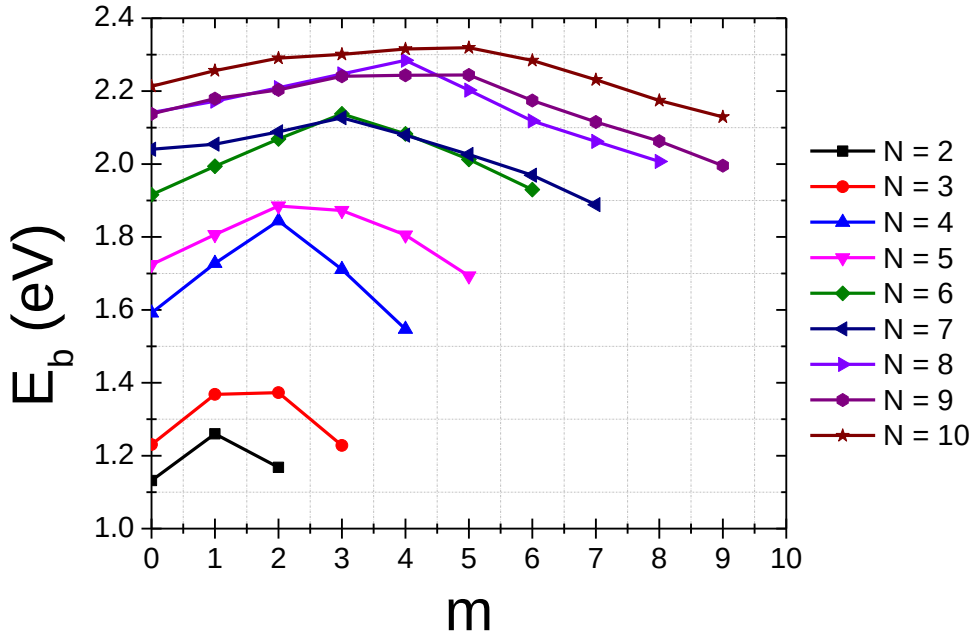

Fig S9. Plot of binding energy E_b against the number of Au atoms (m) for free AuCu clusters, with N = 2-10.

9. Calculated quantum molecular descriptors for free and supported AuCu clusters

Table S7. Calculated quantum molecular descriptors for free atoms, dimers and clusters (N = 3-6).

	Gas Phase						
Cluster	*I* / eV	*A* / eV	χ / eV	μ / eV	η / eV	*S* / eV	ω / eV
N = 1							
Cu_1	4.839	4.016	4.428	-4.428	0.411	1.215	23.835
Au_1	6.630	5.296	5.963	-5.963	0.667	0.749	26.660
N = 2							
Cu_2	4.599	3.072	3.836	-3.836	0.763	0.655	9.641
Au_1Cu_1	5.202	3.580	4.391	-4.391	0.810	0.616	11.890
Au_2	6.159	4.2	5.179	-5.179	0.979	0.510	13.693
N = 3							
Cu_3	3.561	3.314	3.437	-3.437	0.123	4.053	47.904
Au_1Cu_2	4.015	3.408	3.711	-3.711	0.303	1.647	22.692
Au_2Cu_1	4.324	3.562	3.943	-3.943	0.381	1.3118	20.396
Au_3	6.011	5.271	5.641	-5.641	0.37	1.351	43.002
N = 4							
Cu_4	4.373	3.426	3.899	-3.899	0.473	1.056	16.060
Au_1Cu_3	4.635	3.351	3.993	-3.993	0.642	0.778	12.416
Au_2Cu_2	4.897	3.372	4.134	-4.134	0.762	0.656	11.216
Au_3Cu_1	5.090	3.835	4.462	-4.462	0.627	0.796	15.864
Au_4	5.179	4.190	4.685	-4.685	0.494	1.011	22.207
N = 5							
Cu_5	4.623	3.740	4.181	-4.181	0.441	1.133	17.487
Au_1Cu_4	4.798	3.915	4.356	-4.356	0.441	1.132	18.981
Au_2Cu_3	4.961	4.147	4.554	-4.554	0.407	1.228	20.746
Au_3Cu_2	5.151	4.444	4.798	-4.798	0.353	1.415	23.021
Au_4Cu_1	5.434	4.622	5.028	-5.028	0.405	1.232	25.285
Au_5	5.521	4.610	5.065	-5.065	0.455	1.098	25.663
N = 6							
Cu_6	4.518	2.738	3.628	-3.628	0.889	0.561	7.397
Au_1Cu_5	4.697	2.956	3.827	-3.827	0.870	0.574	8.415
Au_2Cu_4	4.697	2.956	3.827	-3.827	0.870	0.574	8.415
Au_3Cu_3	4.954	3.238	4.096	-4.096	0.858	0.582	9.777
Au_4Cu_2	5.091	3.536	4.313	-4.313	0.777	0.642	11.963
Au_5Cu_1	5.042	3.412	4.227	-4.227	0.815	0.613	10.961
Au_6	5.471	3.429	4.4504	-4.450	1.020	0.489	9.702

Table S8. Calculated quantum molecular descriptors for free clusters (N = 7-10).

	Gas Phase						
Cluster	*I* / eV	*A* / eV	χ / eV	μ / eV	η / eV	*S* / eV	ω / eV
N = 7							
Cu_7	4.567	3.517	4.042	-4.042	0.524	0.952	15.568
Au_1Cu_6	3.851	2.914	3.382	-3.382	0.468	1.067	12.213
Au_2Cu_5	4.801	3.765	4.283	-4.283	0.5184	0.964	17.694
Au_3Cu_4	4.945	3.817	4.381	-4.381	0.564	0.885	17.008
Au_4Cu_3	5.165	4.327	4.746	-4.746	0.418	1.194	26.906
Au_5Cu_2	5.336	4.611	4.974	-4.974	0.362	1.379	34.126
Au_6Cu_1	5.230	4.411	4.821	-4.821	0.409	1.221	28.394
Au_7	5.480	4.544	5.012	-5.012	0.468	1.068	26.838
N = 8							
Cu_8	4.374	2.909	3.641	-3.641	0.732	0.682	9.053
Au_1Cu_7	4.535	2.641	3.588	-3.588	0.947	0.527	6.797
Au_2Cu_6	4.602	2.682	3.642	-3.642	0.960	0.520	6.908
Au_3Cu_5	4.749	2.765	3.757	-3.757	0.991	0.504	7.114
Au_4Cu_4	4.935	2.878	3.906	-3.906	1.028	0.486	7.419
Au_5Cu_3	5.011	3.269	4.140	-4.140	0.870	0.574	9.841
Au_6Cu_2	4.909	3.864	4.386	-4.386	0.522	0.957	18.417
Au_7Cu_1	4.934	3.916	4.425	-4.425	0.508	0.982	19.248
Au_8	5.297	3.915	4.606	-4.606	0.690	0.723	15.357
N = 9							
Cu_9	4.364	3.623	3.993	-3.993	0.370	1.349	21.525
Au_1Cu_8	4.438	3.907	4.172	-4.172	0.265	1.882	32.775
Au_2Cu_7	3.500	2.978	3.239	-3.239	0.261	1.915	20.097
Au_3Cu_6	3.601	3.031	3.316	-3.316	0.285	1.754	19.300
Au_4Cu_5	3.821	2.804	3.313	-3.313	0.508	0.983	10.792
Au_5Cu_4	3.831	2.868	3.350	-3.350	0.481	1.037	11.647
Au_6Cu_3	3.932	3.269	3.601	-3.601	0.331	1.509	19.577
Au_7Cu_2	5.194	4.423	4.809	-4.809	0.385	1.296	29.995
Au_8Cu_1	5.134	4.400	4.767	-4.767	0.367	1.362	30.960
Au_9	4.899	4.061	4.480	-4.480	0.419	1.193	23.948
N = 10							
Cu_{10}	3.918	2.938	3.428	-3.428	0.490	1.019	11.984
Au_1Cu_9	4.286	3.006	3.646	-3.646	0.640	0.780	10.380
Au_2Cu_8	4.269	2.873	3.571	-3.571	0.698	0.716	9.134
Au_3Cu_7	4.332	3.100	3.716	-3.716	0.616	0.811	11.209
Au_4Cu_6	4.271	3.264	3.768	-3.768	0.503	0.993	14.103
Au_5Cu_5	4.650	3.295	3.972	-3.972	0.677	0.737	11.645
Au_6Cu_4	4.683	3.662	4.173	-4.173	0.510	0.979	17.057
Au_7Cu_3	4.733	3.254	3.994	-3.994	0.739	0.676	10.789
Au_8Cu_2	4.903	3.598	4.250	-4.250	0.652	0.766	13.843
Au_9Cu_1	5.453	4.128	4.791	-4.791	0.662	0.754	17.327
Au_{10}	5.202	3.925	4.564	-4.564	0.638	0.783	16.316

Table S9. Calculated quantum molecular descriptors for supported atoms, dimers and clusters (N = 3-6).

	Surface Supported						
Cluster	I / eV	A / eV	χ / eV	μ / eV	η / eV	S / eV	ω / eV
N = 1							
Cu_1	3.394	2.049	2.721	-2.721	0.672	0.743	5.507
Au_1	1.987	0.140	1.064	-1.064	0.923	0.541	0.613
N = 2							
Cu_2	2.468	0.3396	1.4038	-1.403	1.064	0.469	0.925
Au_1Cu_1	3.2462	0.4844	1.8653	-1.865	1.380	0.362	1.259
Au_2	3.4024	0.9465	2.17445	-2.174	1.227	0.407	1.925
N = 3							
Cu_3	0.217	-0.579	-0.181	0.181	0.398	1.255	0.041
Au_1Cu_2	0.395	-0.445	-0.025	0.025	0.420	1.188	0.0007
Au_2Cu_1	0.395	-0.445	-0.025	0.025	0.420	1.188	0.0007
Au_3	0.928	-0.020	0.454	-0.454	0.474	1.054	0.217
N = 4							
Cu_4	0.984	-0.365	0.309	-0.309	0.674	0.741	0.071
Au_1Cu_3	1.158	-0.525	0.316	-0.316	0.841	0.594	0.059
Au_2Cu_2	1.708	-0.303	0.702	-0.702	1.006	0.496	0.245
Au_3Cu_1	1.99	-0.123	0.933	-0.933	1.056	0.473	0.412
Au_4	2.188	0.438	1.313	-1.313	0.874	0.571	0.986
N = 5							
Cu_5	0.107	-0.632	-0.262	0.262	0.370	1.350	0.092
Au_1Cu_4	0.503	-0.378	0.062	-0.062	0.440	1.134	0.004
Au_2Cu_3	0.596	-0.495	0.050	-0.050	0.545	0.916	0.002
Au_3Cu_2	0.728	-0.103	0.312	-0.312	0.416	1.201	0.117
Au_4Cu_1	0.849	0.148	0.499	-0.499	0.350	1.426	0.355
Au_5	0.821	-0.113	0.353	-0.353	0.467	1.069	0.133
N = 6							
Cu_6	0.436	-0.488	-0.026	0.026	0.462	1.080	0.0007
Au_1Cu_5	1.500	-0.037	0.731	-0.731	0.768	0.650	0.347
Au_2Cu_4	1.145	-0.525	0.31	-0.31	0.835	0.598	0.057
Au_3Cu_3	1.228	-0.395	0.416	-0.416	0.811	0.615	0.106
Au_4Cu_2	1.829	0.242	1.035	-1.035	0.793	0.630	0.676
Au_5Cu_1	1.500	-0.037	0.731	-0.731	0.768	0.650	0.347
Au_6	2.034	0.365	1.200	-1.200	0.834	0.599	0.863

Table S10. Calculated quantum molecular descriptors for supported clusters (N = 7-10).

	Surface Supported						
Cluster	I / eV	A / eV	χ / eV	μ / eV	η / eV	S / eV	ω / eV
N = 7							
Cu_7	0.029	-0.543	-0.257	0.257	0.286	1.747	0.115
Au_1Cu_6	1.416	0.681	1.048	-1.048	0.367	1.360	1.496
Au_2Cu_5	0.871	0.345	0.608	-0.608	0.263	1.900	0.704
Au_3Cu_4	0.419	-0.276	0.071	-0.071	0.348	1.436	0.007
Au_4Cu_3	0.682	-0.326	0.177	-0.177	0.504	0.991	0.031
Au_5Cu_2	1.740	0.945	1.343	-1.343	0.397	1.257	2.268
Au_6Cu_1	2.395	1.456	1.925	-1.925	0.469	1.065	3.950
Au_7	2.380	1.592	1.986	-1.986	0.393	1.269	5.009
N = 8							
Cu_8	1.033	-0.195	0.419	-0.419	0.614	0.813	0.143
Au_1Cu_7	1.138	-0.190	0.473	-0.473	0.664	0.752	0.168
Au_2Cu_6	1.238	-0.094	0.572	-0.572	0.666	0.750	0.245
Au_3Cu_5	1.223	-0.083	0.569	-0.569	0.653	0.765	0.248
Au_4Cu_4	1.399	0.055	0.727	-0.727	0.671	0.744	0.393
Au_5Cu_3	2.283	0.539	1.411	-1.411	0.871	0.573	1.142
Au_6Cu_2	2.181	0.858	1.519	-1.519	0.661	0.756	1.745
Au_7Cu_1	2.506	1.419	1.963	-1.963	0.543	0.920	3.545
Au_8	1.910	0.887	1.399	-1.399	0.511	0.977	1.914
N = 9							
Cu_9	0.299	-0.170	0.064	-0.064	0.235	2.125	0.008
Au_1Cu_8	0.814	0.204	0.509	-0.509	0.304	1.640	0.425
Au_2Cu_7	0.961	0.121	0.541	-0.541	0.420	1.190	0.349
Au_3Cu_6	0.279	-0.503	-0.111	0.111	0.391	1.278	0.015
Au_4Cu_5	1.505	0.495	1.0003	-1.0003	0.505	0.990	0.990
Au_5Cu_4	1.297	0.470	0.884	-0.884	0.413	1.209	0.945
Au_6Cu_3	1.483	0.566	1.025	-1.025	0.458	1.090	1.146
Au_7Cu_2	1.882	1.074	1.478	-1.478	0.404	1.236	2.703
Au_8Cu_1	2.405	1.355	1.880	-1.880	0.524	0.952	3.367
Au_9	2.180	1.664	1.922	-1.922	0.258	1.937	7.165
N = 10							
Cu_{10}	0.867	-0.184	0.341	-0.341	0.525	0.951	0.110
Au_1Cu_9	0.961	-0.297	0.331	-0.331	0.629	0.794	0.087
Au_2Cu_8	1.095	-0.120	0.487	-0.487	0.607	0.822	0.195
Au_3Cu_7	1.187	-0.212	0.487	-0.487	0.700	0.714	0.169
Au_4Cu_6	1.311	-0.156	0.577	-0.577	0.733	0.681	0.227
Au_5Cu_5	1.439	-0.115	0.661	-0.661	0.777	0.642	0.281
Au_6Cu_4	1.416	-0.078	0.669	-0.669	0.747	0.668	0.299
Au_7Cu_3	1.726	0.666	1.196	-1.196	0.529	0.943	1.350
Au_8Cu_2	1.594	0.483	1.039	-1.039	0.555	0.899	0.971
Au_9Cu_1	2.222	1.258	1.740	-1.740	0.482	1.036	3.140
Au_{10}	2.256	1.246	1.751	-1.751	0.504	0.990	3.038

10. Linear regression analysis of Δ_{HL} against the computed softness

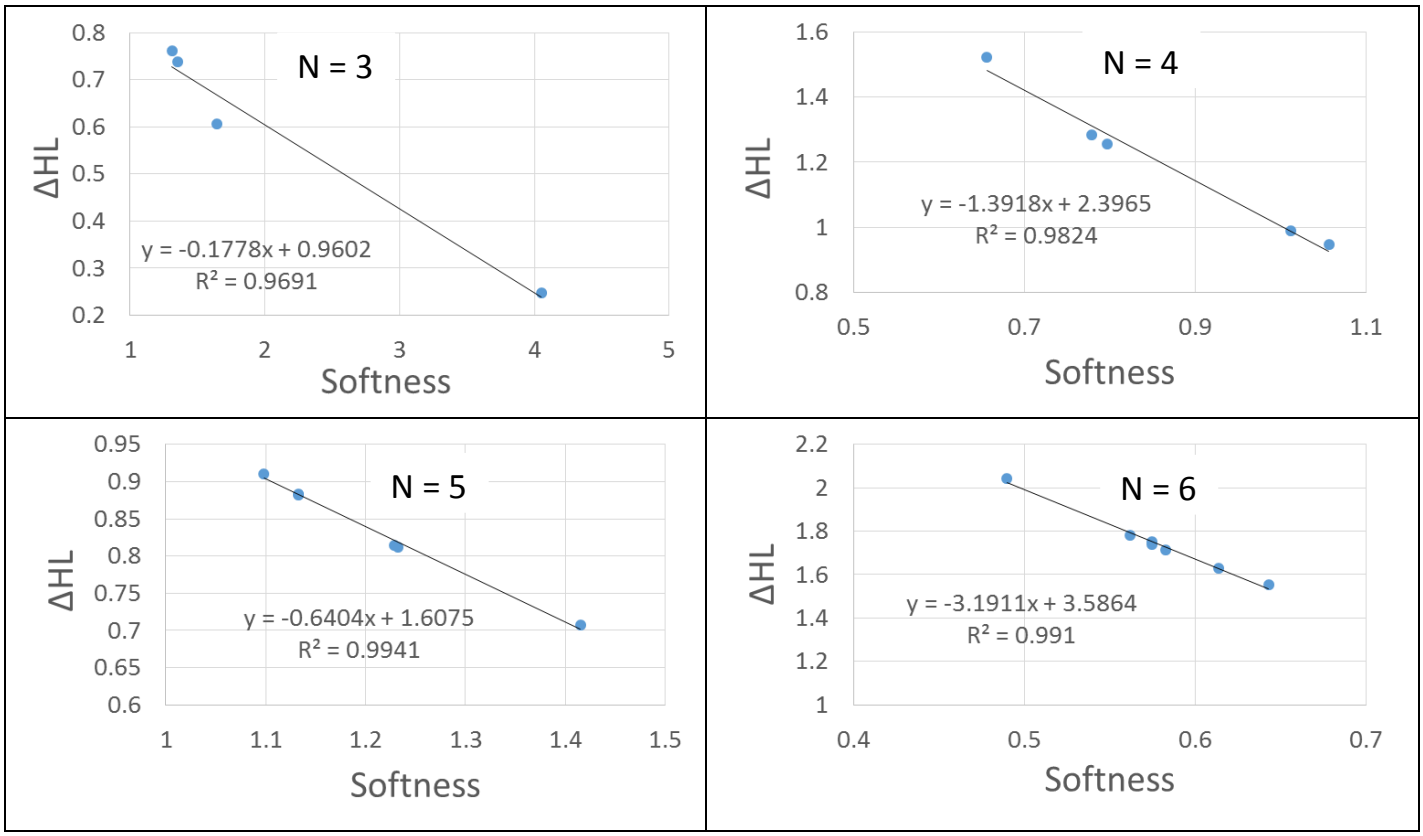

Fig S10. Linear correlation plot between HOMO-LUMO gaps and softness for free AuCu clusters (N= 3-6).

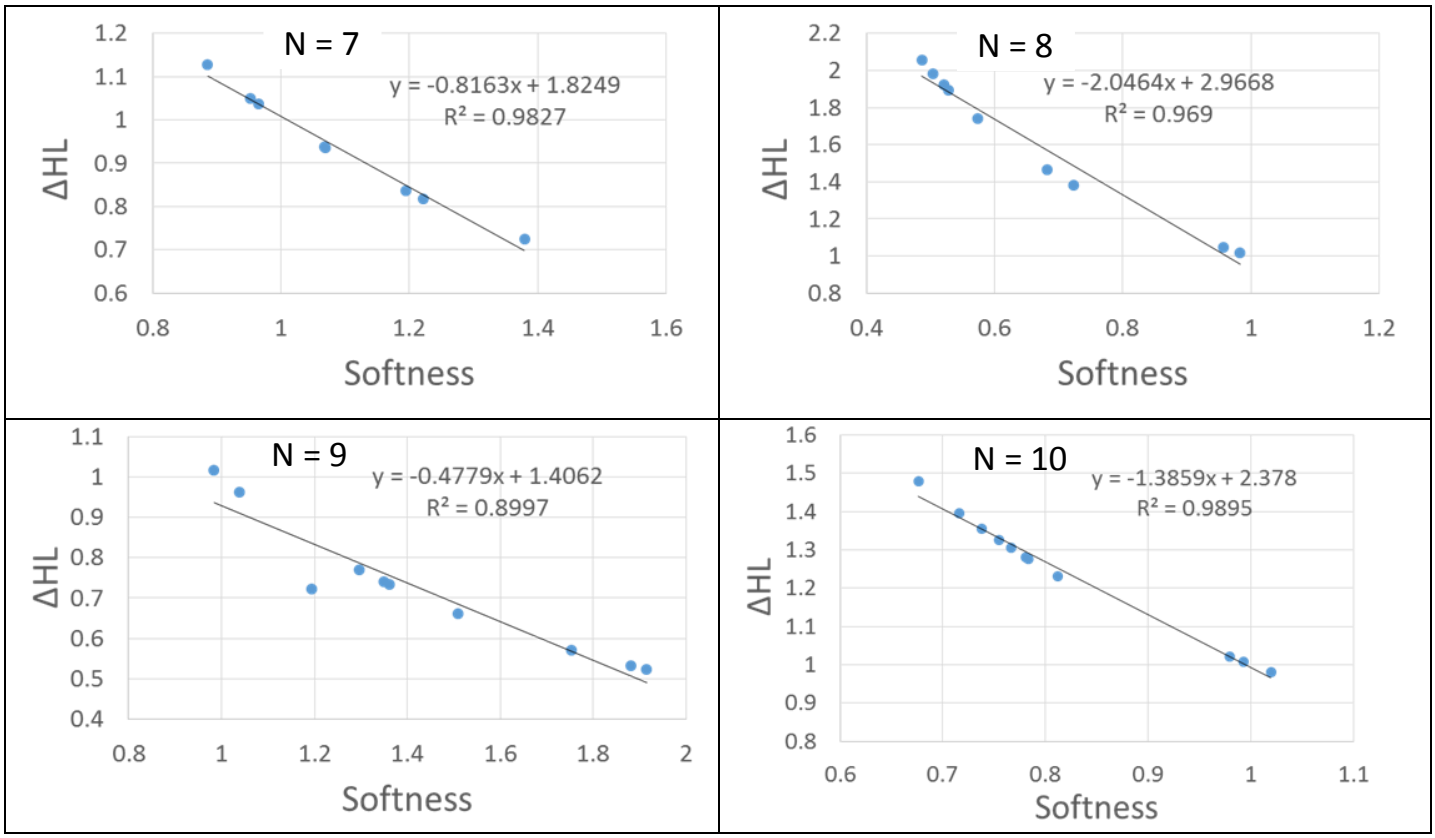

Fig S11. A linear correlation plot between HOMO–LUMO gap and softness for AuCu clusters (N = 7-10).

CHAPTER 6

DFT GLOBAL OPTIMIZATION OF GAS-PHASE SUBNANOMETER RUTHENIUM-PLATINUM CLUSTERS

6.1 Introduction

Platinum catalysts have been employed extensively in electrochemical fuel cells, in particular for direct methanol fuel cells [194]. As fuel cells are regarded among the most promising non-fossil fuel alternatives for power generation technology [195, 196], the use of Pt catalysts in this field has attracted substantial attention [197]. However, these catalysts have properties which need to be optimised in order to improve the catalytic performance. The formation of CO intermediates during the methanol oxidation reaction and the high cost of Pt are the most common drawbacks [198]. Inclusion of Ru atoms into Pt clusters can reduce the cost effectively and can be employed to minimize CO poisoning of the fuel cell [199]. Ru has been shown to be a selective catalyst for reaction of CO with H_2 to form CH_4 and H_2O (methanation) [200–202]. RuPt nanoalloys have, therefore, been introduced as promising electrode catalysts in order to improve the fuel cell performance in converting chemical energy to electrical energy and selectively activating the CO methanation (higher CO tolerance) [203], which is essential for the future viability of the fuel cell.

It is known that the catalytic performance of nanosized RuPt particles, in the elec-

trochemical reactions, is highly influenced by their sizes, composition, and the catalyst structure and morphology [204,205]. High catalytic performance has been previously suggested for RuPt systems that have a surface composition of 1:1 [204, 206, 207]. However, the optimal surface activity has been suggested by Gasteiger et al. for RuPt clusters that have the stoichiometric composition, Ru:Pt = 0.10:0.90 [208, 209]. Hence, the choice of optimal parameters required to optimise effective RuPt electrocatalysts remains an open question.

In Publication 6, a combination of DFT for energy calculations (VASP software, standard basis set and pseudopotential, and a standard choice of functional, PBE) and a genetic algorithm for structure optimization is employed to study the geometric structures and energies of RuPt clusters in the size range N=2-8, for all possible compositions. The structural evolution of the pure Pt and Ru clusters, as well as their binary clusters, is discussed. The low-lying isomers are also calculated and examples of their structures and energetics are presented. The spin multiplicities are optimized within the VASP code for each structure generated during the global optimization. The preferred cluster sites for Ru atoms are identified and compared to those of Pt atoms and rationalized in terms of the various metal-metal bond strengths. Bader charges are calculated, which show charge transfer from Ru to Pt. In addition to binding energies, second differences in energy and mixing energies, the stabilities of certain nanoalloy compositions is supported by a study of the HOMO-LUMO gaps.

6.2 Publication 6

Title

DFT Global Optimization of Gas-Phase Subnanometer Ru-Pt Clusters

Authors

Ilker Demiroglu, Kezi Yao, Heider A Hussein and Roy L. Johnston

Journal Journal of Physical Chemistry C

Volume 121

Pages 10773-10780

DOI 10.1021/acs.jpcc.6b11329

Submitted

10 November 2016

Accepted

22 December 2016

6.2.1 Author Contribution

The author co-supervised the calculations of Kezi Yao. The author installed the BPGA-DFT code and made amendments to the code required for the systems of study, as well as having an advisory role in the calculations. The author contributed to the discussion of the results and revised the initial draft of the article.

THE JOURNAL OF PHYSICAL CHEMISTRY C

Article

pubs.acs.org/JPCC

DFT Global Optimization of Gas-Phase Subnanometer Ru−Pt Clusters

Ilker Demiroglu, Kezi Yao, Heider A Hussein, and Roy L. Johnston*

School of Chemistry, University of Birmingham, Edgbaston, Birmingham B15 2TT, United Kingdom

Supporting Information

ABSTRACT: The global optimization of subnanometer Ru−Pt binary nanoalloys in the size range 2−8 atoms is systematically investigated using the Birmingham Parallel Genetic Algorithm (BPGA). The effect of size and composition on the structures, stabilities and mixing properties of Ru−Pt nanoalloys are discussed. The results revealed that the maximum mixing tendency is achieved for 40−50% Ru compositions. Global minimum structures show that the Ru atoms prefer to occupy central and core positions and maximize coordination number and the number of strong Ru−Ru bonds.

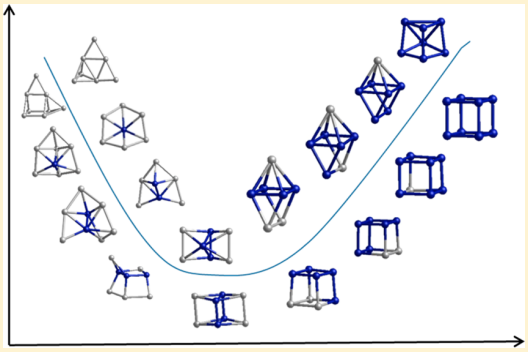

INTRODUCTION

Subnanometer noble metal clusters are of great importance due to their extraordinary structural and electronic properties, which are intermediate between atomic and nanoparticular systems.[1] The interest in subnanometer clusters is growing, especially in the field of catalysis, owing to recent experimental results suggesting high selectivity and activity toward specific reactions,[2−4] as well as advances in experimental procedures that allow size selectivity of subnanometer clusters.[5] One example is platinum (Pt) for which Vajda et al. have shown up to 2 orders of magnitude higher catalytic activities than previous Pt catalysts for the selective oxidative dehydrogenation of propane.[4]

Platinum is the key component in catalysts for low temperature methanol electro-oxidation, which is of great interest for direct methanol fuel cells.[6] However, pure platinum catalysts suffer from two main drawbacks: high cost and CO-poisoning.[7] Addition of another metal has been investigated, either to reduce the usage of comparatively expensive platinum or to improve CO tolerance. To optimize the catalysts, various bimetallic alloys have been tested for their catalytic properties, including Pt−Ni,[8] Pt−Co,[9] and Pt−Ru.[10−12] Among all these electrode materials, Pt−Ru catalysts have showed promising catalytic activities toward fuel cell applications[13,14] and higher CO tolerance.[15]

Pt in the bulk exhibits face-centered cubic (fcc) packing, while bulk Ru is hexagonal close-packed (hcp). The binary Ru−Pt phase diagram[16] suggests a fcc-type structure when Pt is above 40%, a hcp-type structure when Pt is below 20% and a coexisting hcp(Ru-rich)-fcc(Pt-rich) phase region for intermediate compositions. This phase diagram refers to solids at a temperature above 1000 °C, which is much higher than normal temperatures for Pt−Ru nanoalloy (NAs) synthesis and postsynthesis treatment. In addition, nanosize alloys sometimes show distinct structures from their bulk counterparts.[17,18] The atomic-scale structures of Pt−Ru nanoalloys, therefore, cannot be simply defined by their composition. Experimental conditions and synthetic methods also play important roles here. In the literature, composition-induced structural changes[19,20] were shown for Pt−Ru nanoalloys and mixed structures were obtained at low temperatures. Nevertheless, a high-temperature treatment after synthesis[21−23] showed Pt segregation to the surface, leading to "core-shell" particles and it has been shown that core−shell Ru@Pt nanoalloys have higher catalytic activity for CO oxidation than mixed Ru−Pt nanoparticles.[24]

Since the catalytic activities of nanoalloys are closely related to their sizes and structures, it is important to rationalize the relationship between structures and catalytic properties as well as mixing patterns at the nanoscale. Theoretical studies here can give an insight into size and structural effects on catalyst stability and activity. Although in the literature there have been a number of experimental and theoretical studies of pure subnanometer Ru[25−33] and Pt[4,34−39] clusters, to our knowledge there has been no theoretical study of subnanometer Ru−Pt alloys.

In this study, low energy structures of subnanometer Ru−Pt alloys have been systematically studied by global optimization at the DFT level within the Birmingham Parallel Genetic Algorithm (BPGA).

Special Issue: ISSPIC XVIII: International Symposium on Small Particles and Inorganic Clusters 2016

Received: November 10, 2016
Revised: December 22, 2016
Published: December 22, 2016

METHODOLOGY

The BPGA-DFT[40,41] approach was applied to obtain low energy structures of $(Ru,Pt)_N$ alloy clusters in the size range $N = 3-8$, as well as pure Ru_N and Pt_N clusters. This method is an open-source genetic algorithm, improving on the Birmingham Cluster Genetic Algorithm (BCGA), a genetic algorithm for determining the lowest energy structures of nanoparticles and nanoalloys directly at the DFT level.[42] BPGA employs a pool methodology[43] to evaluate structures in parallel instead of based on generations. In each run, multiple BPGA instances are implemented, and in each instance, a set of processes are run in parallel and independently. Initially a number of random structures (10 in this study) are generated and geometrically relaxed (by local energy minimization at the DFT level) to form a population. Once the local minimization of the initial pool structures has been completed, the crossover and mutation operations of the genetic algorithm begin for each instance. In each instance, either a pair of clusters are taken from the pool according to "roulette-wheel" selection[42] for the crossover operation to generate an "offspring" structure or a single cluster is taken for mutation. Offspring structures are produced through weighted crossover according to the Deaven and Ho "cut and splice" method.[44] Mutated clusters are either obtained by displacing some of the atoms randomly or swapping different types of atoms in alloy clusters. The newly generated structures are then locally minimized to compare with existing structures in the pool and the pool is updated whenever a new cluster is found that is lower in energy.

All the DFT-level local minimizations mentioned above were performed with a plane wave basis set, as implemented in the Vienna ab initio Simulation Package (VASP),[45−48] including spin polarization. Spin states are optimized within VASP independently for each generated structure from BPGA during global optimization. The exchange-correlation energy was calculated using the generalized gradient approximation (GGA), with the Perdew−Burke−Ernzerhof (PBE)[49] exchange-correlation functional. The interaction between valence electrons and ionic cores was described by the projector augmented wave (PAW) method.[50,51] Methfessel-Paxton smearing, with a sigma value of 0.01 eV, was implemented to improve convergence of metallic systems.[52]

For the comparison of the energetics of different composition nanoalloys, a mixing (or excess) energy term (Δ) was calculated, which is expressed as

$$\Delta = E_{tot}(A_mB_n) - m\frac{E_{tot}(A_{m+n})}{m+n} - n\frac{E_{tot}(B_{m+n})}{m+n}$$

where the total energy (E_{tot}) of the nanoalloy A_mB_n is compared to the pure metal clusters of A and B of the same size ($m + n$). Hence, a negative value of Δ means an energy decrease upon mixing and therefore favorable mixing, whereas positive values indicate a demixing tendency.

The stability of each cluster, relative to its neighbors, is indicated by the second difference in energy Δ_2E, which is given by

$$\Delta_2E = E_{tot}(A_{N+1}) + E_{tot}(A_{N-1}) - 2E_{tot}(A_N)$$

where A is Ru or Pt, $E_{tot}(A_N)$ corresponds to the total energy of the N-atom cluster, and $E_{tot}(A_{N+1})$ and $E_{tot}(A_{N-1})$ are the neighboring clusters when increased one atom more and decreased one atom less, respectively.

The average binding energy per atom E_b is given by

$$E_b = -\frac{1}{N}[E_{tot}(A_mB_n) - mE_{tot}(A_1) - nE_{tot}(B_1)]$$

where m and n are the numbers of A and B atoms; $E_{tot}(A_1)$, and $E_{tot}(B_1)$ are the electronic energies of a single Ru or Pt atom; and N is the total number of atoms ($N = m + n$).

RESULTS

Ru Clusters. The lowest energy structures obtained from global optimization for pure Ru_N clusters ($3 \le N \le 12$) are shown in Figure 1. Overall, the global minimum clusters and their corresponding spin multiplicities are in good agreement with structures suggested in previous theoretical works.[25−29]

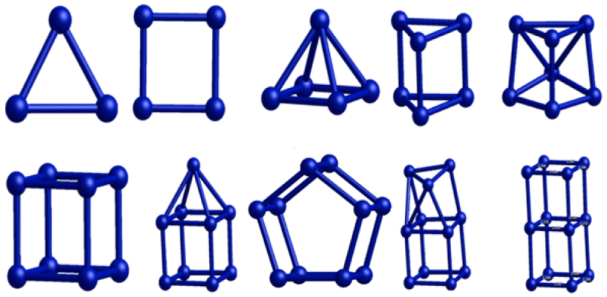

Figure 1. Global minima structures for pure Ru clusters $3 \le N \le 12$.

Ru_3 is an equilateral triangle (D_{3h}) and Ru_4 is also planar, while the larger sizes adopt 3D structures. Ru_4 is a rectangle with bond lengths of 2.24 and 2.15 Å. Ru_5 is a square pyramid (C_{4v}) and Ru_6 is a trigonal prism (D_{3h}) again with high symmetries as for Ru_3 and Ru_4 (see Table 1).

Table 1. Binding Energies E_b, Point Groups, and Spin Multiplicities $(2S + 1)$ for the Global Minimum Ru_N Clusters

cluster	point group	E_b (eV)	$(2S + 1)$
Ru_3	D_{3h}	2.66	7
Ru_4	D_{2h}	3.24	1
Ru_5	C_{4v}	3.50	1
Ru_6	D_{3h}	3.78	5
Ru_7	C_s	3.97	7
Ru_8	O_h	4.34	5
Ru_9	C_{4v}	4.26	9
Ru_{10}	D_{5h}	4.36	1
Ru_{11}	C_1	4.37	1
Ru_{12}	D_{4h}	4.54	5

The first low symmetry structure is Ru_7 with point group C_s, which is in agreement with the cationic Ar-tagged species Ru_7Ar^+ observed in gas phase experiments.[33] Ru_8 is found to be cubic (with full O_h symmetry), while Ru_9 has an additional Ru atom capping a face of the cube (C_{4v} symmetry). These structures are in agreement with recent experiments on both cationic[33] and anionic[28] clusters, which indicate the occurrence of cubic structures for certain nuclearities. The lowest energy structure for Ru_{10} is found to be pentagonal prism (D_{5h}), as in previous theoretical studies.[25,27,29] However, a doubly capped cube has been shown to give a better fit to electron diffraction measurements for anionic Ru_{10}^- clusters.[28] The lowest energy structure for Ru_{11} is found to be a cube with three atoms on the top face, missing one atom to complete the double cube, leading to the lowest (C_1) symmetry. Ru_{12} is found to be a

DOI: 10.1021/acs.jpcc.6b11329
J. Phys. Chem. C 2017, 121, 10773−10780

double cube (D_{4h}) with the edges of the middle square being shorter than the top and bottom layers which are equal. Most of our results agree well with anionic or cationic clusters investigated experimentally, except for Ru_{10}^- and Ru_{12}^-, in which the configurations that fit the experimental results best have lower symmetry point groups than we have found for the neutral clusters. When we compared the effect of charge for Ru_8 (see Supporting Information, Figure 1), while Ru_8^- preserved the perfect cubic structure, Ru_8^+ distorted into a squashed cube (with D_{4h} symmetry).

According to Table 1, the binding energies of the clusters increase with increasing cluster size, as expected, to converge on the bulk cohesive energy (calculated value = 6.78 eV). However, the higher binding energy calculated for Ru_8 than Ru_9 indicates the extra stability of the cubic structure of Ru_8. This extra stability is also confirmed by fitting binding energies as a function of $n^{1/3}$ for small clusters (see Supporting Information, Figure 2). Although the cubic Ru_8 has the highest positive residual, indicating a "magic" size, larger cubic clusters Ru_{11} and Ru_{12} have negative residuals, indicating reduced relative stability.

Pt Clusters. Figure 2 shows the lowest energy structures of pure Pt_N clusters ($3 \le N \le 10$). In addition to the equilateral

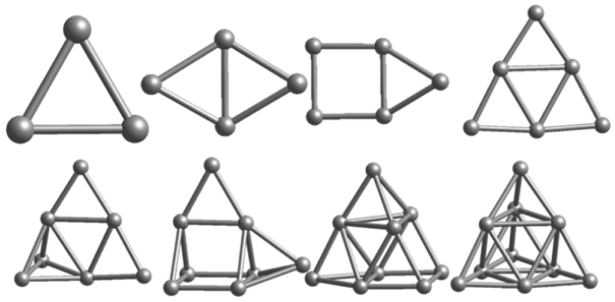

Figure 2. Global minima structures for pure Pt clusters $3 \le N \le 10$.

triangular Pt_3 (D_{3h}), the lowest isomer of Pt_6 is also planar (D_{3h}), while Pt_4 has a slightly bent rhombus configuration and Pt_5 is an edge-bridged square with a slight bending out of the square plane. The global minimum configuration of Pt_7 is based on the planar structure of Pt_6, with an outer triangle capped to generate a 3D structure (with C_s symmetry).

For both Pt_8 and Pt_9, global optimization leads to 3D structures, which are the same structures previously predicted[35] for Pt_8^+ and Pt_9^+ cations, though there are quasi-2D structures which are nearly degenerate with the 3D isomers. The 3D Pt_8 and Pt_9 structures are both based on the structure of Pt_6 mentioned above, with the planar structure of Pt_6 capped to form 3D triangular structures tending toward a tetrahedral structure. The 2D Pt_9 isomer is a 3×3 square lattice.[34−36] Pt_{10} is found to be the tetrahedral (T_d) structure, corresponding to a small fragment of fcc packing.

Overall, our low energy structures and their corresponding spin multiplicities compare well with previous studies.[34−36,38,39] For the high symmetry structures of Pt_3, Pt_6, and Pt_{10} (see Table 2), all previous studies have shown the same lowest energy structures, while nonglobal optimization studies[34,36,38,39] did not considered some of the lowest energy structures for other sizes. However, most of lowest energy isomers presented here are in good agreement with a previous global optimization study.[35] Although it has been reported that all global minima up

Table 2. Binding Energies E_b, Point Groups, and Spin Multiplicities ($2S + 1$) for the Global Minimum Pt_N Clusters

cluster	point group	E_b (eV)	$(2S + 1)$
Pt_3	D_{3h}	2.51	1
Pt_4	C_{2v}	2.80	5
Pt_5	C_s	3.05	3
Pt_6	D_{3h}	3.31	3
Pt_7	C_s	3.41	5
Pt_8 (2D)	C_1	3.51	3
Pt_8 (3D)	C_s	3.51	1
Pt_9 (2D)	D_{4h}	3.65	5
Pt_9 (3D)	C_{2v}	3.65	7
Pt_{10}	T_d	3.80	9

to Pt_9 are planar for neutral Pt clusters, here it is shown that 3D clusters become competitive after Pt_7, that is, having almost the same binding energies as their planar counterparts. As for Ru clusters, binding energies of Pt clusters increase with increasing cluster size to converge on the bulk cohesive energy (calculated value = 5.58 eV) and the fit to $n^{-1/3}$ reveals the extra stability of Pt_3, Pt_6, and Pt_{10} clusters with positive residuals (see Supporting Information, Figure 3).

Ru−Pt Clusters. The global minima for all compositions of Ru_mPt_n clusters for $3 \le m + n \le 8$, are shown in Figure 3. For all sizes and compositions, due to the high cohesive energy of Ru (as shown in Table 3), the Ru atoms prefer to occupy core-like positions with higher coordination numbers. Moreover, when there is more than one Ru atom, Ru atoms tend to occupy adjacent positions, due to the stronger Ru−Ru bonds.

All the favored structures of Ru_mPt_1 are similar to the pure Ru clusters of the same size (Ru_{m+1}), except for Ru_6Pt_1, in which the Pt atom caps one of the square faces of the trigonal prism structure of Ru_6. Ru_1Pt_3, Ru_1Pt_4, and Ru_1Pt_5 resemble the pure Pt clusters, while Ru_1Pt_7 and Ru_1Pt_6 both possess a Ru atom with high coordination number and differ significantly from the corresponding pure-Pt clusters. In Ru_1Pt_2, the triangle opens up and the Pt−Pt distance becomes 3.77 Å from the value of 2.46 Å in Pt_3, while the Pt−Ru distances are 2.23 Å. In contrast, for Ru_2Pt_1, the Ru−Ru distance is smaller (2.12 Å) than Ru_3 (2.24 Å), while the Ru−Pt distances are 2.48 Å. For $(Ru,Pt)_4$, the rhombus structure of Pt_4 is preserved until all but one Pt atom is replaced with Ru, at which point the structure converts to a distorted square structure similar to Ru_4. Similarly, for $(Ru,Pt)_5$ and $(Ru,Pt)_6$, pure Pt structures are preserved until more than 50% replacement of Ru, while an intermediate nonplanar trapezoidal structure is observed for Ru_3Pt_2 before adopting the square pyramidal pure Pt structure. Ru_4Pt_2 is an edge-bridged square pyramid, which has same coordination numbers (three and four) as Ru_3Pt_2.

For $(Ru,Pt)_7$, the structure of Ru_1Pt_6 has a Ru atom surrounded by six Pt atoms, so that the Ru atom obtain the maximum coordination number. In this structure, six Pt atoms around the Ru atoms form a chairlike configuration, in which the Ru atom sits ~0.5 Å out of the vertical plane. In Ru_2Pt_5, the additional Ru atom moves toward to the center and binds to two extra Pt atoms while displacing the central Ru atom out of the plane. Ru_3Pt_4 is two square pyramids sharing a triangular Ru_3 face, ensuring the three Ru atoms are bonded together and have high coordination numbers. The structures of Ru_4Pt_3 and Ru_5Pt_2 resemble the Ru_6Pt_1 structure, corresponding to a trigonal prism with a square Ru_4 face capped by a Pt atom. For $(Ru,Pt)_8$, when the composition is 50%, the structure is a

DOI: 10.1021/acs.jpcc.6b11329
J. Phys. Chem. C 2017, 121, 10773−10780

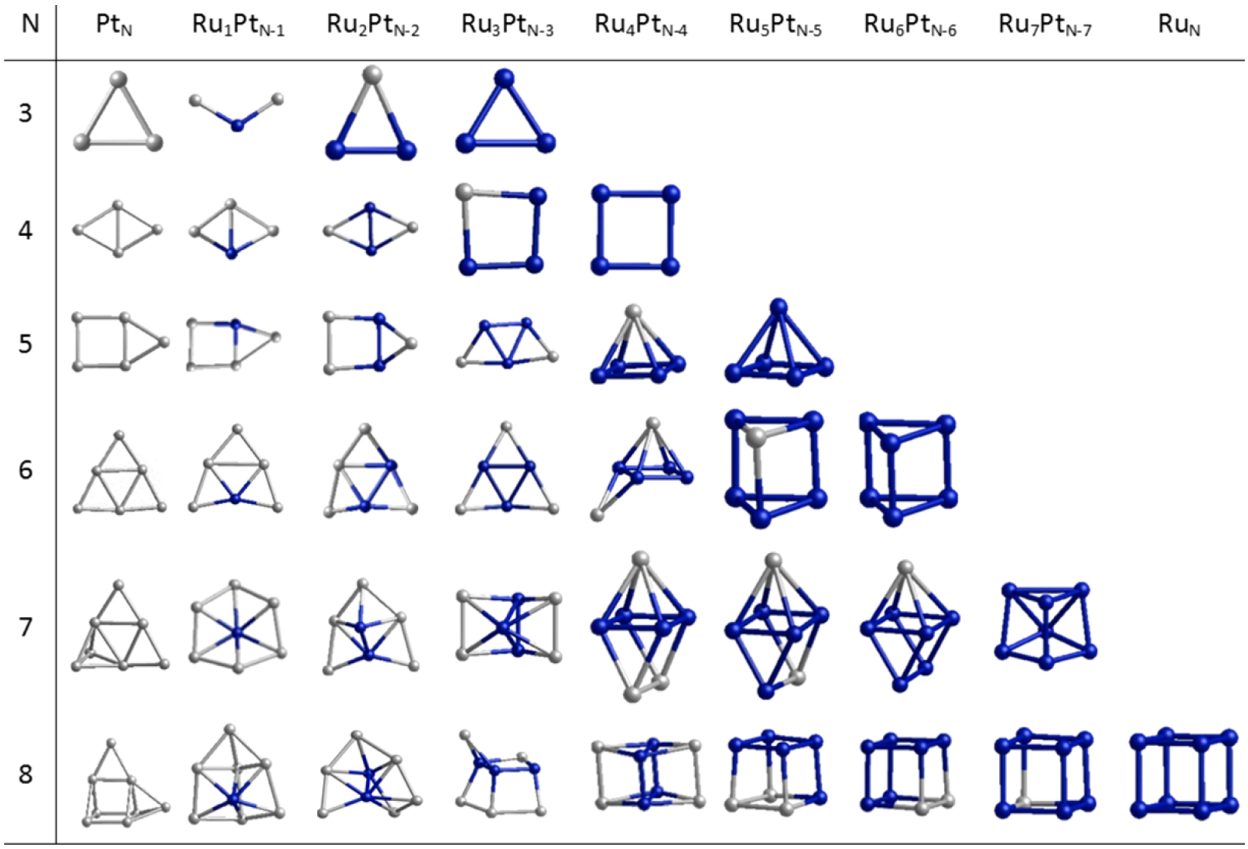

Figure 3. Global minima structures for all composition of Ru−Pt clusters $3 \leq N \leq 8$.

Table 3. Bond Lengths and Binding Energies of Ru−Ru, Ru−Pt, and Pt−Pt Dimers, As Well As Cohesive Energies of Bulk Ru and Pt

dimer	bond length (Å)	binding energy (eV)
Ru−Ru	2.04	2.00
Ru−Pt	2.25	2.13
Pt−Pt	2.32	1.94
bulk	bond length (Å)	cohesive energy (eV)
Ru	2.65 and 2.72	6.78
Ru (exp.)[53]	2.64 and 2.71	6.74
Pt	2.80	5.58
Pt (exp.)[53]	2.77	5.84

distorted cube, corresponding to two trigonal prisms sharing a square Ru_4 face. As the Ru percentage increases, the structure becomes more cubic.

Apart from sizes $n = 4$ and 5, pure Ru_n clusters have higher spin multiplicities than pure Pt_n clusters (see Tables 1 and 2). Upon alloying (Table 4), as Ru replaces Pt, spin multiplicities increase in general for $(RuPt)_n$ clusters up to 40% Ru composition (see Supporting Information, Figure 4). For $(Ru,Pt)_4$, $(Ru,Pt)_5$, and $(Ru,Pt)_6$, spin multiplicities on Ru doping of the Pt structure start to decrease when the Ru structure starts to dominate the alloy geometry. For $(Ru,Pt)_7$, spin multiplicities do not follow the trend as all the alloy structures are significantly different than the pure Ru or pure Pt geometries. For $(Ru,Pt)_8$, spin multiplicities become maximal as the cubic Ru structure dominates the alloy geometry, but decreases for pure Ru.

Energetic Analysis. The relative stabilities of the clusters can be studied by calculating the second difference in energy ($\Delta_2 E$), which indicates the stability of an N atom cluster with respect to neighboring sizes. Figure 4 shows the plot of second difference in energy as a function of cluster size for pure Ru and pure Pt clusters, respectively. The significant positive peaks indicate the relatively stable clusters.

Figure 4 reveals that Ru_8 and Pt_6 clusters are significantly more stable relative to their neighbors, suggesting they are "magic" sizes in the considered subnanometer regime. However, note that the energetic range for Ru clusters (approximately 5.0 eV) is larger than for Pt clusters (approximately 1.0 eV) and also the binding energy versus cluster size fit (see Supporting Information, Figure 3) reveals higher stability for tetrahedral Pt_{10} than planar Pt_6. For Ru clusters, the second difference energies also reveal an even−odd alternation, where even number of Ru clusters are more stable than the neighboring odd number clusters.

The effect of mixing Ru with Pt in small clusters is studied by calculating the mixing energy, Δ. Mixing energies as a function to the number of Ru atoms for all compositions of $3 \leq m + n \leq 8$ for Ru_mPt_n clusters are plotted in Figure 5. Negative values of mixing energy indicate a favorable mixing, whereas demixing is represented by positive values.

For $(Ru,Pt)_3$, both alloy composition shows a mixing tendency. All compositions for $(Ru,Pt)_4$ clusters also favor mixing except for Ru_3Pt_1, in which the dopant Pt atom distorts the rectangular structure of Ru. For $(Ru,Pt)_5$ clusters, high Pt compositions show more negative mixing energies than high Ru compositions, and the mixing tendency is maximum for 40%

DOI: 10.1021/acs.jpcc.6b11329
J. Phys. Chem. C 2017, 121, 10773−10780

Table 4. Binding Energies E_b, Point Groups, and Spin Multiplicities $(2S + 1)$ for the Global Minimum Ru_mPt_n Clusters

cluster	point group	E_b (eV)	$(2S + 1)$
Ru_1Pt_2	C_{2v}	2.64	5
Ru_2Pt_1	C_{2v}	2.70	5
Ru_1Pt_3	C_1	3.00	7
Ru_2Pt_2	C_{2v}	3.18	7
Ru_3Pt_1	C_{2v}	3.10	3
Ru_1Pt_4	C_1	3.20	5
Ru_2Pt_3	C_s	3.34	7
Ru_3Pt_2	C_1	3.37	7
Ru_4Pt_1	C_{4v}	3.43	5
Ru_1Pt_5	C_{2v}	3.40	3
Ru_2Pt_4	C_1	3.52	7
Ru_3Pt_3	C_s	3.59	5
Ru_4Pt_2	C_s	3.63	5
Ru_5Pt_1	C_s	3.71	7
Ru_1Pt_6	C_s	3.53	5
Ru_2Pt_5	C_s	3.65	3
Ru_3Pt_4	C_{2v}	3.76	3
Ru_4Pt_3	C_{2v}	3.82	3
Ru_5Pt_2	C_s	3.87	5
Ru_6Pt_1	C_{2v}	3.94	3
Ru_1Pt_7	C_s	3.63	5
Ru_2Pt_6	C_1	3.74	5
Ru_3Pt_5	C_1	3.83	3
Ru_4Pt_4	D_{2h}	3.99	3
Ru_5Pt_3	C_s	4.05	7
Ru_6Pt_2	C_{2v}	4.17	7
Ru_7Pt_1	C_{3v}	4.26	7

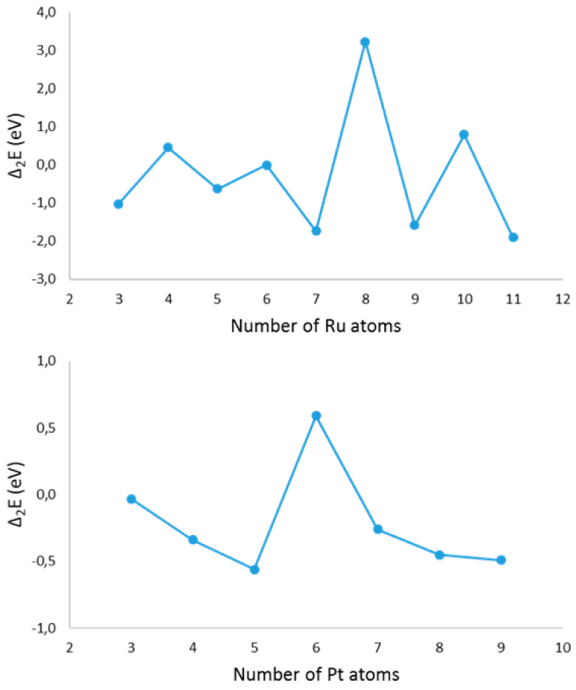

Figure 4. Second difference in energy (Δ_2E) of Ru (top) and Pt clusters (bottom) with respect to the number of atoms.

Ru. Similarly, the Ru_2Pt_4 composition is found to have the maximum mixing tendency for $(Ru,Pt)_6$ clusters, which has a 33% Ru composition, while the second best was found for 50% composition, whereas for other compositions the mixing energies were found to be close to zero.

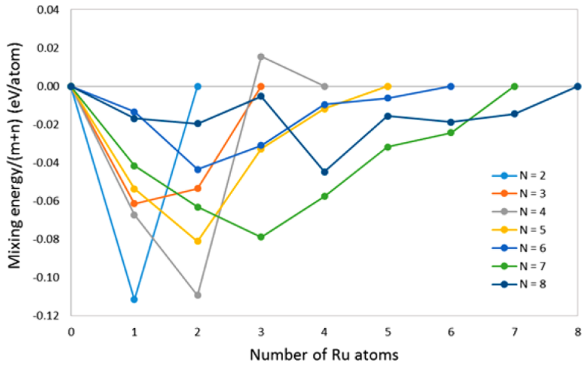

Figure 5. Mixing energies as a function of number of Ru atoms for all compositions of $3 \leq m + n \leq 8$ for Ru_mPt_n clusters.

For $(Ru,Pt)_7$, the Ru_3Pt_4 structure has the maximum mixing tendency, followed by the two neighboring compositions. Again, in $(Ru,Pt)_8$, the 50% configuration favors mixing more than the other compositions. Pt-rich compositions for $(Ru,Pt)_8$ are found to have reduced mixing tendencies than the Ru-rich configurations because of the magic size of pure Ru_8. The largest mixing energy is found for Ru_1Pt_1, and Ru_2Pt_2, followed by Ru_1Pt_2, Ru_2Pt_3, and Ru_3Pt_4. For $(Ru,Pt)_6$ clusters mixing tendency is lower than for $(Ru,Pt)_5$ and $(Ru,Pt)_7$, in general, because of the magic size of pure Pt_6, as in the Ru_8 case.

Figure 5 also reveals that alloy clusters with even numbers of Ru atoms usually lie below the line connecting its neighbors. That is to say, clusters with even numbers of Ru atoms favor mixing more than the adjacent clusters, which have odd number of Ru atoms. This also fits with the even−odd stability order of pure Ru clusters (see Figure 4); however, the trend is not as clear as for the pure Ru clusters.

The binding energy per atom (E_b), which is related to the stability of nanoclusters, is shown in Figure 6. According to the

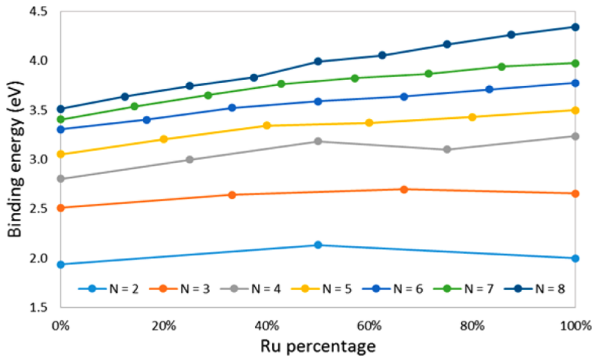

Figure 6. Binding energies of Ru−Pt clusters for each size $N = 2$−8 against the Ru composition.

figure, binding energy increases with increasing cluster size. The binding energy also increases with increasing Ru composition except for the Ru dimer, Ru_3, and Ru_3Pt_1, which is in agreement with the higher cohesive energy of Ru than Pt. From the binding energy plot, it can be seen that values for 40−50% Ru compositions are slightly higher than the connecting lines, which indicates higher stabilities at these compositions. Mixing

DOI: 10.1021/acs.jpcc.6b11329
J. Phys. Chem. C 2017, 121, 10773−10780

energy and second difference in energy values for nanoalloy clusters also confirm this trend. In the second difference energy plot in Figure 7, there are positive peaks for 50% Ru compositions of $(Ru,Pt)_4$ and $(Ru,Pt)_8$, while the peaks are at around 40% Ru composition for $(Ru,Pt)_5$, $(Ru,Pt)_6$, and $(Ru,Pt)_7$.

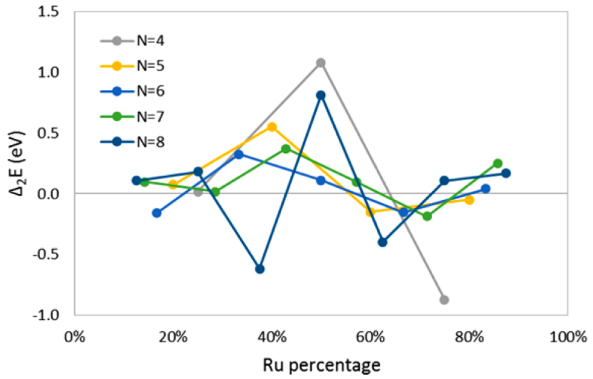

Figure 7. Second difference in energy (Δ_2E) of $(RuPt)_N$ clusters for N = 4−8 with respect to Ru composition.

HOMO−LUMO gaps are often used as an indicator for the structural stabilities of small clusters, with higher HOMO−LUMO gaps usually indicating higher stabilities. However, our calculations revealed that the HOMO−LUMO gaps are smallest for the "magic" sizes of Pt_6 and Ru_8 for pure metal clusters (see Supporting Information, Figure 5). For alloy clusters, higher HOMO−LUMO gaps correlate well with the suggested high stable compositions of $(Ru,Pt)_4$, $(Ru,Pt)_6$, and $(Ru,Pt)_7$. However, smaller HOMO−LUMO gaps are found for $(Ru,Pt)_5$ and $(Ru,Pt)_8$.

Although the trends discussed here only consider the lowest energy (global minimum) clusters, global optimization calculations also revealed several low-lying isomers of alloy clusters. For the higher stability compositions for each size (Ru_2Pt_2, Ru_2Pt_3, Ru_2Pt_4, Ru_3Pt_4, and Ru_4Pt_4), no low-lying isomers were found within a binding energy range of 0.3 eV. Several low-lying isomers are found, however, for less stable alloy clusters. For example, for $(Ru,Pt)_6$, low lying isomers found for Ru_3Pt_3 and Ru_4Pt_2 with 0.03 eV energy difference with corresponding global minima structures (see Supporting Information, Table 3). While Ru_3Pt_3 isomer is a distorted structure of global minima Ru_3Pt_3, Ru_4Pt_2 isomer is again an edge-capped square pyramid structure as in the global minimum Ru_4Pt_2, only with a different edge capped. Similarly for $(Ru,Pt)_7$, low-lying isomers are found for Ru_4Pt_3 and Ru_5Pt_2, which have the same geometric structure as the highly stable Ru_3Pt_4 composition.

Bader charge analysis[54] shows that there is a 0.41 e^- charge transfer from Ru to Pt in the RuPt dimer. For Ru_mPt_1 clusters, calculated Ru−Pt charge transfers are between 0.4 and 0.5 e^-, while for Ru_1Pt_n clusters there is higher charge transfer (between 0.7 and 0.9 e^-). Charge transfer also increases as the composition get closer to 50% for alloy clusters (see Supporting Information, Figure 6). Ru−Pt charge transfer may play a role in strengthening Ru−Pt interactions and may also contribute to the stabilization of cluster isomers with Ru atoms occupying central positions, surrounded by Pt.

CONCLUSIONS

We have performed a computational study of Ru−Pt nanoalloys ranging from 3 to 8 atoms and compared them with pure Ru and Pt clusters in the same size range. The structural properties and energetics of bimetallic Ru−Pt nanoalloys have been studied within the framework of the BPGA-DFT approach that performs a global optimization search for the lowest energy configuration for each size and composition directly at the DFT level.

The calculations reveal that Ru atoms prefer central and adjacent positions due to stronger Ru−Ru bonds than Pt−Pt bonds, while the Pt atoms occupy peripheral positions. This, together with shorter Ru−Ru bond lengths, also predicts that "core-shell" Ru@Pt structures would become thermodynamically more stable as the cluster size increases. Energetic analysis shows that Ru compositions of 40−50% exhibit more favorable mixing than Ru-rich or Pt-rich compositions.

In future work, this study will be extended to larger bimetallic Ru−Pt nanoalloys, to investigate core−shell Ru−Pt structure formation.

ASSOCIATED CONTENT

Supporting Information

The Supporting Information is available free of charge on the ACS Publications website at DOI: 10.1021/acs.jpcc.6b11329.

All the Cartesian coordinates and energy values for considered subnanometer clusters (PDF).

AUTHOR INFORMATION

Corresponding Author

*E-mail: r.l.johnston@bham.ac.uk. Tel.: +44 121 414 7477.

ORCID

Ilker Demiroglu: 0000-0001-7801-4566

Roy L. Johnston: 0000-0003-4019-9280

Notes

The authors declare no competing financial interest.

ACKNOWLEDGMENTS

We acknowledge the Engineering and Physical Sciences Research Council, U.K. (EPSRC), for funding under Critical Mass Grant EP/J010804/1 "TOUCAN: Towards an Understanding of Catalysis on Nanoalloys". Calculations were performed on the following HPC facilities: The University of Birmingham BlueBEAR facility (see http://www.bear.bham.ac.uk/bluebear for more details) and the UK's national HPC facility, ARCHER, both via membership of the UK's HPC Materials Chemistry Consortium, which is funded by EPSRC (EP/L000202), and via the TOUCAN Grant. I.D. and K.Y. also thank Zhen Yao for her valuable help.

REFERENCES

(1) Ferrando, R.; Jellinek, J.; Johnston, R. L. Nanoalloys: From Theory to Applications of Alloy Clusters and Nanoparticles. *Chem. Rev.* **2008**, *108*, 845−910.

(2) Lei, Y.; Mehmood, F.; Lee, S.; Greeley, J.; Lee, B.; Seifert, S.; Winans, R. E.; Elam, J. W.; Meyer, R. J.; Redfern, P. C.; et al. Increased Silver Activity for Direct Propylene Epoxidation via Subnanometer Size Effects. *Science (Washington, DC, U. S.)* **2010**, *328*, 224−228.

(3) Oliver-Meseguer, J.; Cabrero-Antonino, J. R.; Domínguez, I.; Leyva-Pérez, A.; Corma, A. Small Gold Clusters Formed in Solution Give Reaction Turnover Numbers of 10(7) at Room Temperature. *Science* **2012**, *338*, 1452.

DOI: 10.1021/acs.jpcc.6b11329
J. Phys. Chem. C 2017, 121, 10773−10780

(4) Vajda, S.; Pellin, M. J.; Greeley, J. P.; Marshall, C. L.; Curtiss, L. A.; Ballentine, G. A.; Elam, J. W.; Catillon-Mucherie, S.; Redfern, P. C.; Mehmood, F.; et al. Subnanometre Platinum Clusters as Highly Active and Selective Catalysts for the Oxidative Dehydrogenation of Propane. *Nat. Mater.* **2009**, *8*, 213−216.
(5) Lu, Y.; Chen, W. Sub-Nanometre Sized Metal Clusters: From Synthetic Challenges to the Unique Property Discoveries. *Chem. Soc. Rev.* **2012**, *41*, 3594−3623.
(6) Steele, B. C. H.; Heinzel, A. Materials for Fuel-Cell Technologies. *Nature* **2001**, *414*, 345−352.
(7) Lemons, R. A. Fuel Cells for Transportation. *J. Power Sources* **1990**, *29*, 251−264.
(8) Mathiyarasu, J.; Remona, A. M.; Mani, A.; Phani, K. L. N.; Yegnaraman, V.; Phani, M. K. L. N. Exploration of Electrodeposited Platinum Alloy Catalysts for Methanol Electro-Oxidation in 0.5 M H_2SO_4: Pt-Ni System. *J. Solid State Electrochem.* **2004**, *8*, 968−975.
(9) Antolini, E.; Salgado, J. R. C.; Gonzalez, E. R. The Stability of Pt-M (M = First Row Transition Metal) Alloy Catalysts and Its Effect on the Activity in Low Temperature Fuel Cells. A Literature Review and Tests on a Pt-Co Catalyst. *J. Power Sources* **2006**, *160*, 957−968.
(10) Watanabe, M.; Motoo, S. Electrocatalysis by Ad-Atoms. *J. Electroanal. Chem. Interfacial Electrochem.* **1975**, *60*, 275−283.
(11) Watanabe, M.; Uchida, M.; Motoo, S. Preparation of Highly Dispersed Pt + Ru Alloy Clusters and the Activity for the Electrooxidation of Methanol. *J. Electroanal. Chem. Interfacial Electrochem.* **1987**, *229*, 395−406.
(12) Chu, D. Methanol Electro-Oxidation on Unsupported Pt-Ru Alloys at Different Temperatures. *J. Electrochem. Soc.* **1996**, *143*, 1685.
(13) Aricò, A. S.; Srinivasan, S.; Antonucci, V. DMFCs: From Fundamental Aspects to Technology Development. *Fuel Cells* **2001**, *1*, 133−161.
(14) Liu, H.; Song, C.; Zhang, L.; Zhang, J.; Wang, H.; Wilkinson, D. P. A Review of Anode Catalysis in the Direct Methanol Fuel Cell. *J. Power Sources* **2006**, *155*, 95−110.
(15) Brankovic, S. R.; Wang, J. X.; Adzic, R. R. Pt Submonolayers on Ru Nanoparticles - A Novel Low Pt Loading, High CO Tolerance Fuel Cell Electrocatalyst. *Electrochem. Solid-State Lett.* **2001**, *4*, A217−A220.
(16) Massalski, T. B.; Okamoto, H.; Subramanian, P. R. *Binary Alloy Phase Diagrams*; ASM International: OH, 1990.
(17) Busani, R.; Folkers, M.; Cheshnovsky, O. Direct Observation of Band-Gap Closure in Mercury Clusters. *Phys. Rev. Lett.* **1998**, *81*, 3836−3839.
(18) Jellinek, J.; Acioli, P. H. Magnesium Clusters: Structural and Electronic Properties and the Size-Induced Nonmetal-to-Metal Transition. *J. Phys. Chem. A* **2002**, *106*, 10919−10925.
(19) Pan, C.; Dassenoy, F.; Casanove, M.-J.; Philippot, K.; Amiens, C.; Lecante, P.; Mosset, A.; Chaudret, B. A New Synthetic Method toward Bimetallic Ruthenium Platinum Nanoparticles; Composition Induced Structural Changes. *J. Phys. Chem. B* **1999**, *103*, 10098−10101.
(20) Liu, Z.; Ling, X. Y.; Su, X.; Lee, J. Y. Carbon-Supported Pt and PtRu Nanoparticles as Catalysts for a Direct Methanol Fuel Cell. *J. Phys. Chem. B* **2004**, *108*, 8234−8240.
(21) Nashner, M. S.; Frenkel, A. I.; Somerville, D.; Hills, C. W.; Shapley, J. R.; Nuzzo, R. G. Core Shell Inversion during Nucleation and Growth of Bimetallic Pt/Ru Nanoparticles. *J. Am. Chem. Soc.* **1998**, *120*, 8093−8101.
(22) Jeon, T.-Y.; Lee, K.-S.; Yoo, S. J.; Cho, Y.-H.; Kang, S. H.; Sung, Y.-E. Effect of Surface Segregation on the Methanol Oxidation Reaction in Carbon-Supported Pt-Ru Alloy Nanoparticles. *Langmuir* **2010**, *26*, 9123−9129.
(23) Zhang, H.; Zheng, Z.; Ma, C.; Zheng, J.; Zhang, N.; Li, Y.; Chen, B. H. Tuning Surface Properties and Catalytic Performances of Pt-Ru Bimetallic Nanoparticles by Thermal Treatment. *ChemCatChem* **2015**, *7*, 245−249.
(24) Alayoglu, S.; Nilekar, A. U.; Mavrikakis, M.; Eichhorn, B. Ru−Pt Core−shell Nanoparticles for Preferential Oxidation of Carbon Monoxide in Hydrogen. *Nat. Mater.* **2008**, *7*, 333−338.
(25) Aguilera-Granja, F.; Balbás, L. C.; Vega, A. Study of the Structural and Electronic Properties of RhN and RuN Clusters (N < 20) within the Density Functional Theory. *J. Phys. Chem. A* **2009**, *113*, 13483−13491.
(26) Bae, Y.-C.; Osanai, H.; Kumar, V.; Kawazoe, Y. Atomic Structures and Magnetic Behavior of Small Ruthenium Clusters. *Mater. Trans.* **2005**, *46*, 159−162.
(27) Li, S.; Li, H.; Liu, J.; Xue, X.; Tian, Y.; He, H.; Jia, Y. Structural and Electronic Properties of Run Clusters (n = 2−14) Studied by First-Principles Calculations. *Phys. Rev. B: Condens. Matter Mater. Phys.* **2007**, *76*, 45410.
(28) Waldt, E.; Hehn, A.-S.; Ahlrichs, R.; Kappes, M. M.; Schooss, D. Structural Evolution of Small Ruthenium Cluster Anions. *J. Chem. Phys.* **2015**, *142*, 24319.
(29) Zhang, W.; Zhao, H.; Wang, L. The Simple Cubic Structure of Ruthenium Clusters. *J. Phys. Chem. B* **2004**, *108*, 2140−2147.
(30) Kerpal, C.; Harding, D. J.; Lyon, J. T.; Meijer, G.; Fielicke, A. N2 Activation by Neutral Ruthenium Clusters. *J. Phys. Chem. C* **2013**, *117*, 12153−12158.
(31) Lang, S. M.; Bernhardt, T. M.; Krstič, M.; Bonačič-Koutecký, V. The Origin of the Selectivity and Activity of Ruthenium-Cluster Catalysts for Fuel-Cell Feed-Gas Purification: A Gas-Phase Approach. *Angew. Chem., Int. Ed.* **2014**, *53*, 5467−5471.
(32) Shetty, S.; Jansen, A. P. J.; van Santen, R. A. Magnetic, Bonding and Structural Behavior of Ru12 and Ru13 Clusters: Is Ru12 Magic? *J. Mol. Struct.: THEOCHEM* **2010**, *954*, 109−114.
(33) Kerpal, C.; Harding, D. J.; Rayner, D. M.; Lyon, J. T.; Fielicke, A. Far-IR Spectra and Structures of Small Cationic Ruthenium Clusters: Evidence for Cubic Motifs. *J. Phys. Chem. C* **2015**, *119*, 10869−10875.
(34) Bhattacharyya, K.; Majumder, C. Growth Pattern and Bonding Trends in Ptn (N = 2−13) Clusters: Theoretical Investigation Based on First Principle Calculations. *Chem. Phys. Lett.* **2007**, *446*, 374−379.
(35) Chaves, A. S.; Rondina, G. G.; Piotrowski, M. J.; Tereshchuk, P.; Da Silva, J. L. F. The Role of Charge States in the Atomic Structure of Cun and Ptn (N = 2−14 Atoms) Clusters: A DFT Investigation. *J. Phys. Chem. A* **2014**, *118*, 10813−10821.
(36) Kumar, V.; Kawazoe, Y. Evolution of Atomic and Electronic Structure of Pt Clusters: Planar, Layered, Pyramidal, Cage, Cubic, and Octahedral Growth. *Phys. Rev. B: Condens. Matter Mater. Phys.* **2008**, *77*, 205418.
(37) Negreiros, F. R.; Fabris, S. Role of Cluster Morphology in the Dynamics and Reactivity of Subnanometer Pt Clusters Supported on Ceria Surfaces. *J. Phys. Chem. C* **2014**, *118*, 21014−21020.
(38) Nie, A.; Wu, J.; Zhou, C.; Yao, S.; Luo, C.; Forrey, R. C.; Cheng, H. Structural Evolution of Subnano Platinum Clusters. *Int. J. Quantum Chem.* **2007**, *107*, 219−224.
(39) Xiao, L.; Wang, L. Structures of Platinum Clusters: Planar or Spherical. *J. Phys. Chem. A* **2004**, *108*, 8605−8614.
(40) JBADavis/BPGA — Bitbucket; https://bitbucket.org/JBADavis/bpga/ (accessed March 15, 2016).
(41) Davis, J.; Shayeghi, A.; Horswell, S. L.; Johnston, R. L. The Birmingham Parallel Genetic Algorithm and Its Application to the Direct DFT Global Optimisation of IrN (N = 10 − 20) Clusters. *Nanoscale* **2015**, *7*, 14032−14038.
(42) Johnston, R. L. Evolving Better Nanoparticles: Genetic Algorithms for Optimising Cluster Geometries. *Dalt. Trans.* **2003**, *70*, 4193.
(43) Bandow, B.; Hartke, B. Larger Water Clusters with Edges and Corners on Their Way to Ice: Structural Trends Elucidated with an Improved Parallel Evolutionary Algorithm. *J. Phys. Chem. A* **2006**, *110*, 5809−5822.
(44) Deaven, D. M.; Ho, K. M. Molecular Geometry Optimization with a Genetic Algorithm. *Phys. Rev. Lett.* **1995**, *75*, 288−291.
(45) Kresse, G.; Furthmüller, J. Efficiency of Ab-Initio Total Energy Calculations for Metals and Semiconductors Using a Plane-Wave Basis Set. *Comput. Mater. Sci.* **1996**, *6*, 15−50.

DOI: 10.1021/acs.jpcc.6b11329
J. Phys. Chem. C 2017, 121, 10773−10780

(46) Kresse, G.; Furthmüller, J. Efficient Iterative Schemes for Ab Initio Total-Energy Calculations Using a Plane-Wave Basis Set. *Phys. Rev. B: Condens. Matter Mater. Phys.* **1996**, *54*, 11169−11186.
(47) Kresse, G.; Hafner, J. Ab Initio Molecular-Dynamics Simulation of the Liquid-Metalamorphous- Semiconductor Transition in Germanium. *Phys. Rev. B: Condens. Matter Mater. Phys.* **1994**, *49*, 14251−14269.
(48) Kresse, G.; Hafner, J. Ab Initio Molecular Dynamics for Liquid Metals. *Phys. Rev. B: Condens. Matter Mater. Phys.* **1993**, *47*, 558−561.
(49) Perdew, J. P.; Burke, K.; Ernzerhof, M. Generalized Gradient Approximation Made Simple. *Phys. Rev. Lett.* **1996**, *77*, 3865−3868.
(50) Kresse, G. From Ultrasoft Pseudopotentials to the Projector Augmented-Wave Method. *Phys. Rev. B: Condens. Matter Mater. Phys.* **1999**, *59*, 1758−1775.
(51) Blöchl, P. E. Projector Augmented-Wave Method. *Phys. Rev. B: Condens. Matter Mater. Phys.* **1994**, *50*, 17953−17979.
(52) Methfessel, M.; Paxton, A. T. High-Precision Sampling for Brillouin-Zone Integration in Metals. *Phys. Rev. B: Condens. Matter Mater. Phys.* **1989**, *40*, 3616−3621.
(53) Kittel, C. *Introduction to Solid State Physics*; Wiley: New York, 2005.
(54) Tang, W.; Sanville, E.; Henkelman, G. A Grid-Based Bader Analysis Algorithm without Lattice Bias. *J. Phys.: Condens. Matter* **2009**, *21*, 84204.

DOI: 10.1021/acs.jpcc.6b11329
J. Phys. Chem. C 2017, 121, 10773−10780

DFT Global Optimization of Gas-Phase Subnanometer Ru-Pt Clusters

Ilker Demiroglu, Kezi Yao, Heider A. Hussein, Roy L. Johnston*

School of Chemistry, University of Birmingham, Edgbaston, Birmingham B15 2TT, U.K.

Supporting Information

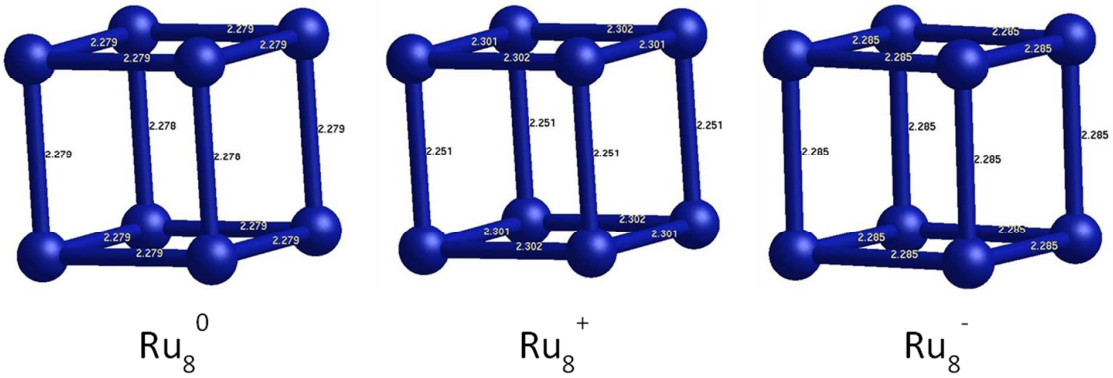

Figure 1. Structures and bond lengths of neutral, cationic, and anionic Ru_8 clusters.

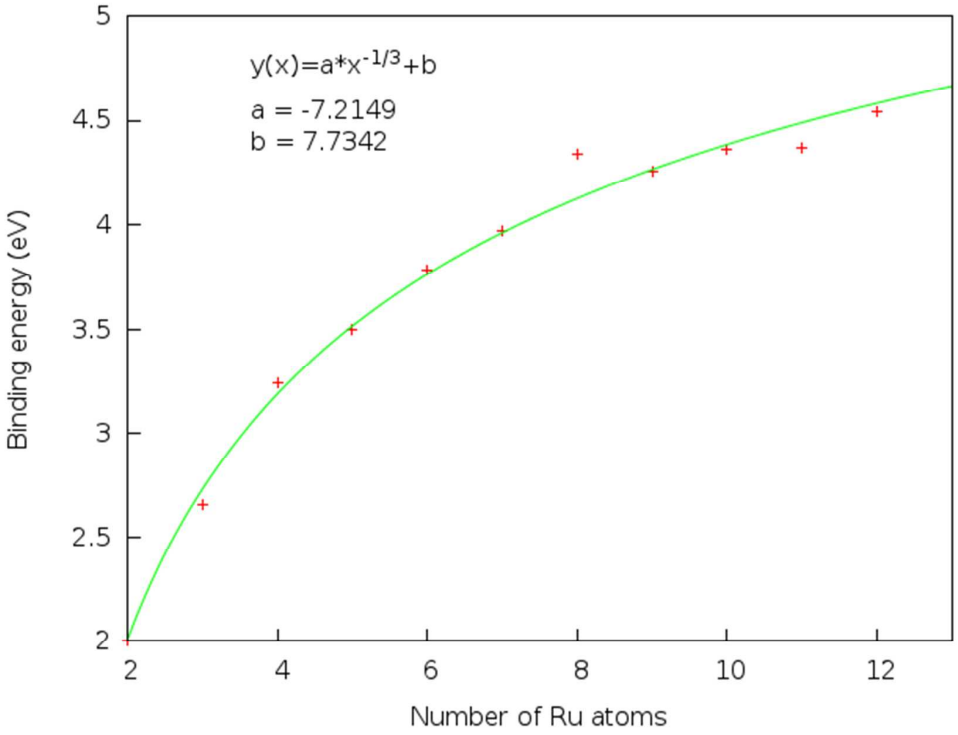

Figure 2. Binding energy versus number of atom graph for Ru_N clusters.

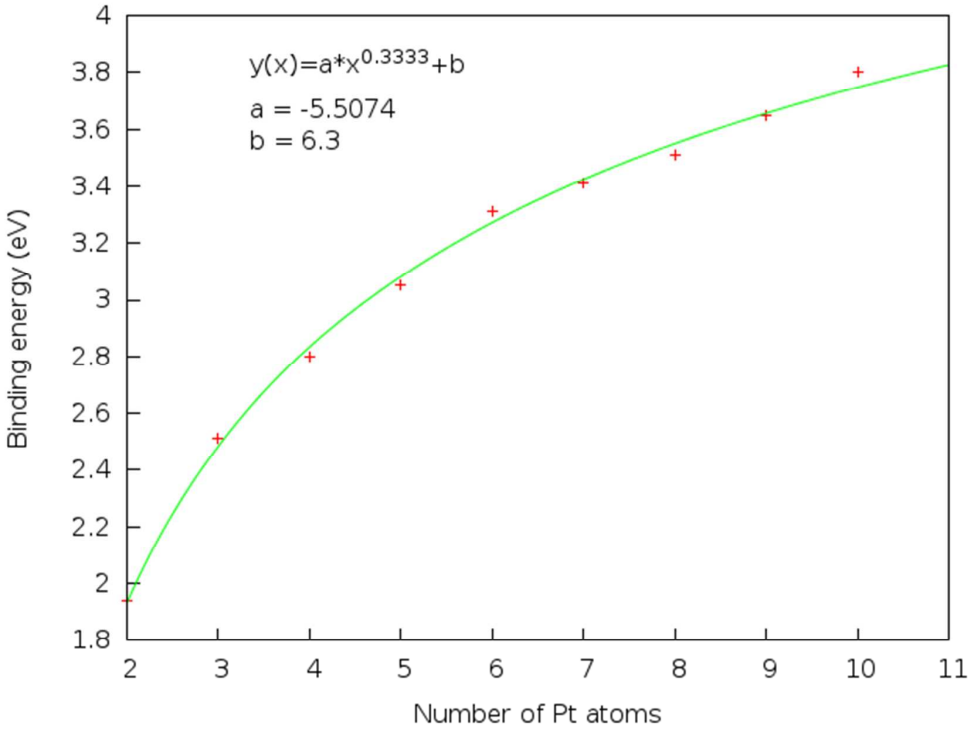

Figure 3. Binding energy versus number of atom graph for Pt_N clusters.

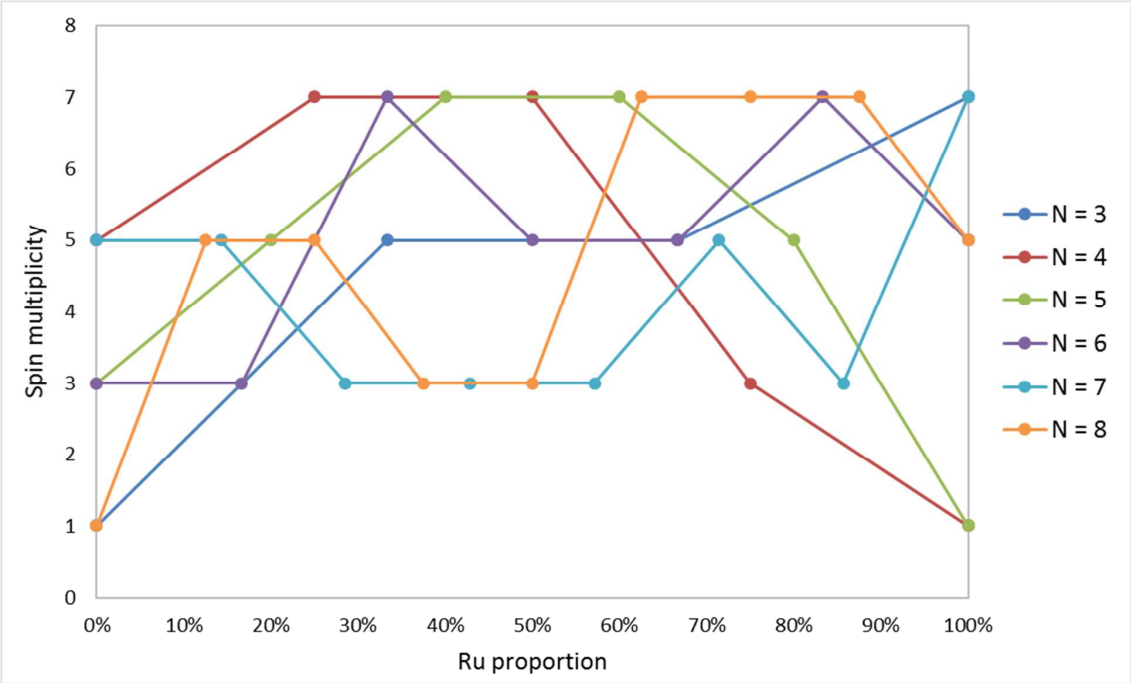

Figure 4. Spin multiplicities versus Ru proportion for $(Ru,Pt)_N$ alloy clusters.

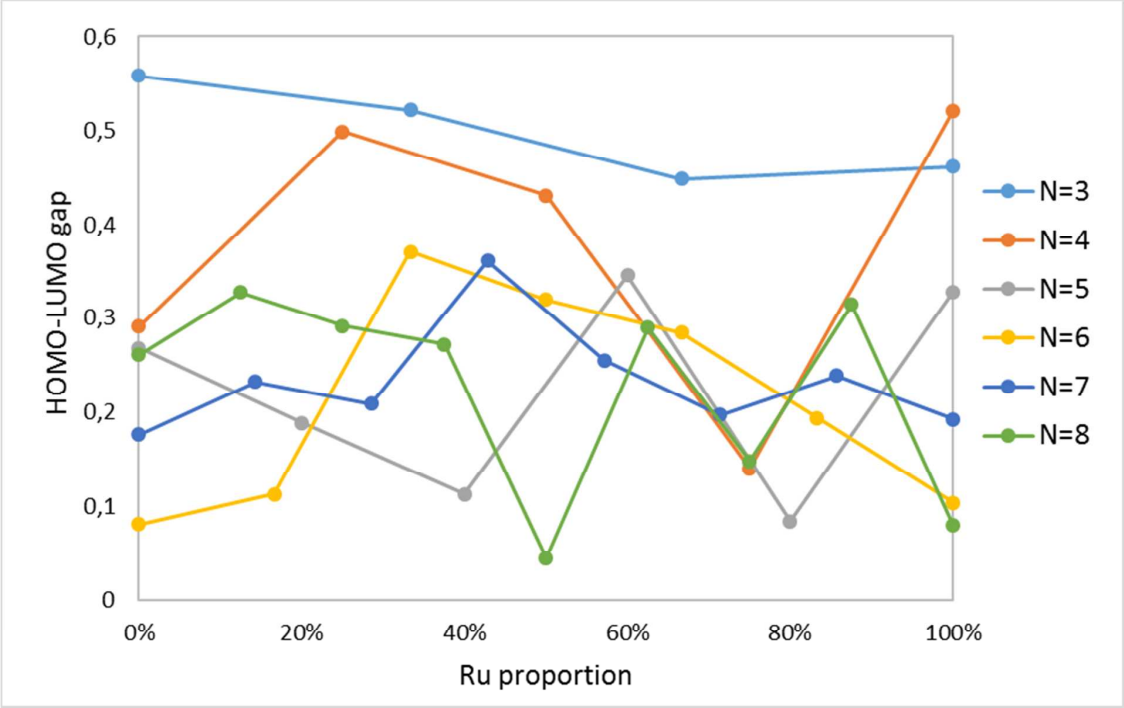

Figure 5. HOMO-LUMO gap versus Ru proportion for $(Ru,Pt)_N$ alloy clusters.

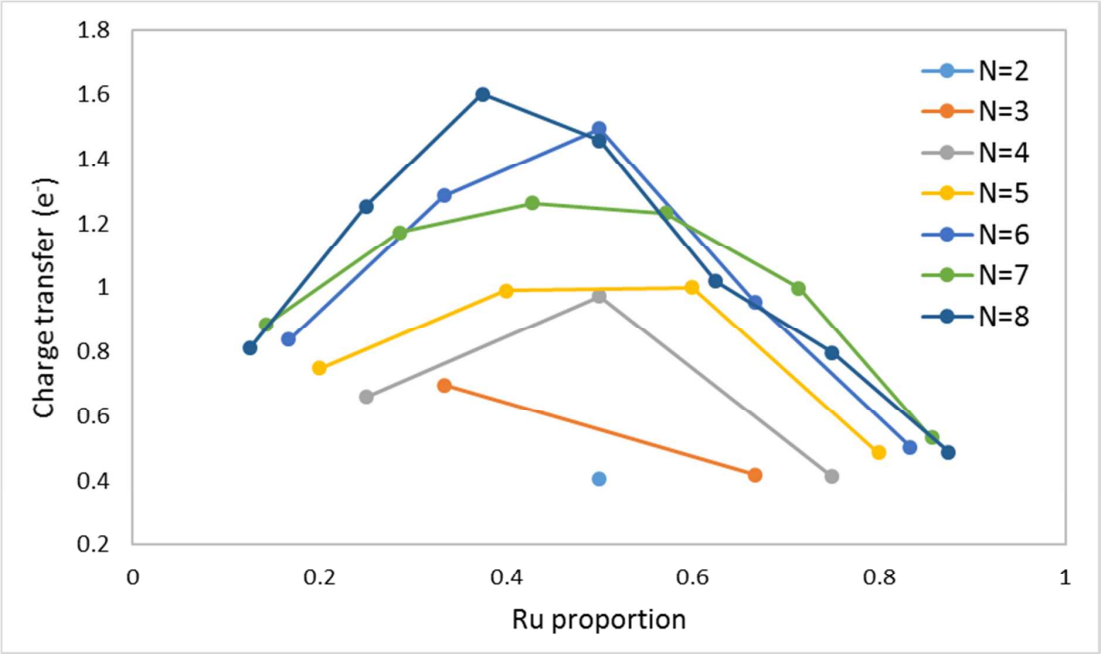

Figure 6. Charge transfer from Ru to Pt versus Ru proportion for $(Ru,Pt)_N$ alloy clusters.

Table 1. Second difference energy (Δ_2E) values of pure Ru and pure Pt clusters.

cluster	Δ_2E (eV)	cluster	Δ_2E (eV)
Ru_3	-1.02	Pt_3	-0.03
Ru_4	0.45	Pt_4	-0.34
Ru_5	-0.63	Pt_5	-0.56
Ru_6	0.00	Pt_6	0.59
Ru_7	-1.73	Pt_7	-0.26
Ru_8	3.23	Pt_8	-0.45
Ru_9	-1.59	Pt_9	-0.49
Ru_{10}	0.79		
Ru_{11}	-1.90		

Table 2. Mixing energy (Δ) and second difference energy (Δ_2E) values of RuPt nanoalloy clusters.

cluster	Δ (eV)	Δ_2E (eV)
Ru_1Pt_1	-0.33	0.67
Ru_1Pt_2	-0.25	0.22
Ru_2Pt_1	-0.27	0.29
Ru_1Pt_3	-0.34	-0.87
Ru_2Pt_2	-0.66	1.08
Ru_3Pt_1	0.11	0.02
Ru_1Pt_4	-0.32	-0.05
Ru_2Pt_3	-0.57	-0.15
Ru_3Pt_2	-0.26	0.55
Ru_4Pt_1	-0.11	0.08
Ru_1Pt_5	-0.09	0.04
Ru_2Pt_4	-0.35	-0.15
Ru_3Pt_3	-0.28	0.11
Ru_4Pt_2	-0.10	0.32
Ru_5Pt_1	-0.07	-0.16
Ru_1Pt_6	-0.33	0.25
Ru_2Pt_5	-0.57	-0.19
Ru_3Pt_4	-0.79	0.10
Ru_4Pt_3	-0.63	0.37
Ru_5Pt_2	-0.38	0.02
Ru_6Pt_1	-0.32	0.10
Ru_1Pt_7	-0.15	0.17
Ru_2Pt_6	-0.20	0.11

Table 3. Lowest energy isomers for some compositions of the Ru-Pt nanoalloys.

Ru_1Pt_5	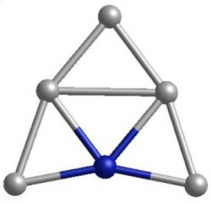 ΔE = 0 eV	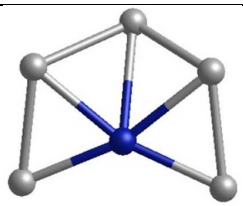 ΔE = 0.32 eV	
Ru_2Pt_6	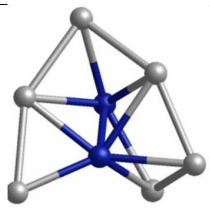 ΔE = 0 eV	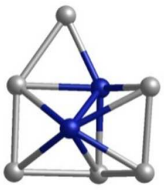 ΔE = 0.07 eV	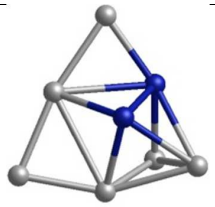 ΔE = 0.08 eV
Ru_3Pt_3	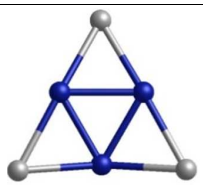 ΔE = 0 eV	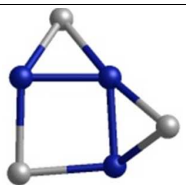 ΔE = 0.03 eV	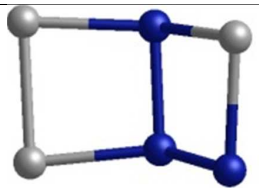 ΔE = 0.06 eV
Ru_4Pt_2	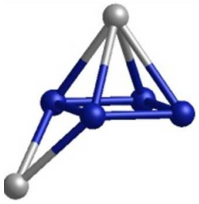 ΔE = 0 eV	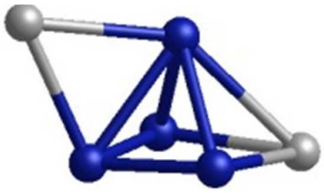 ΔE = 0.03	
Ru_4Pt_3	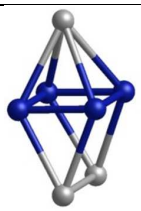 ΔE = 0 eV	 ΔE = 0.14 eV	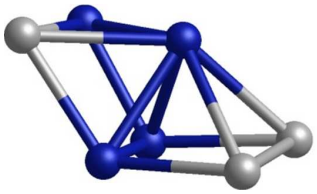 ΔE = 0.20 eV
Ru_4Pt_4	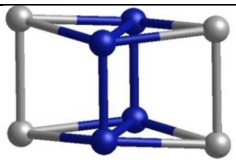 ΔE = 0 eV	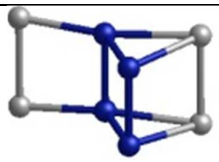 ΔE = 0.52 eV	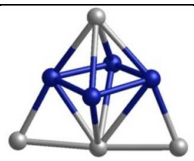 ΔE = 0.63 eV

Ru_5Pt_2	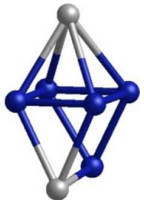 ΔE = 0 eV	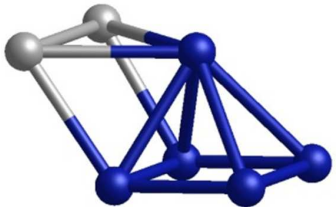 ΔE = 0.07 eV	
Ru_5Pt_3	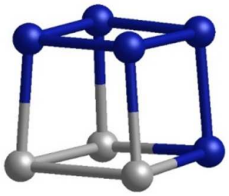 ΔE = 0 eV	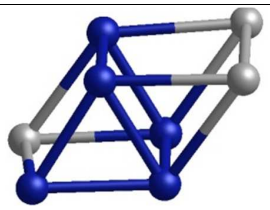 ΔE = 0.14 eV	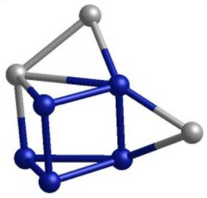 ΔE = 0.19 eV

Coordinates of global minimum clusters (Å):

```
Pt2
cartesian coordinates:
Pt 0.0000 0.0000 2.5586
Pt 0.0000 0.0000 0.2414

Pt3
cartesian coordinates:
Pt 4.5143 5.4095 6.5152
Pt 6.6237 4.6204 5.5186
Pt 5.4792 6.5873 4.5834

Pt4
cartesian coordinates:
Pt 5.4231 6.6007 6.8602
Pt 4.3187 4.4950 6.0916
Pt 7.7006 7.0408 5.9309
Pt 6.1691 5.4750 4.7288

Pt5
cartesian coordinates:
Pt 6.2691 4.8129 7.9578
Pt 7.2682 6.5983 6.5996
Pt 4.5393 4.5018 6.2412
Pt 5.5427 6.3284 4.9341
Pt 6.9843 8.3622 4.8709
```

Pt6
cartesian coordinates:
Pt 6.0152 6.0913 7.8320
Pt 7.5996 4.2488 7.7076
Pt 4.4963 7.9831 7.7009
Pt 7.3918 5.4850 5.6340
Pt 5.6531 7.4920 5.6063
Pt 6.9931 6.8490 3.6684

Pt7
cartesian coordinates:
Pt 8.3302 4.8196 7.9992
Pt 6.1612 5.9329 7.7209
Pt 5.1262 8.2734 7.4899
Pt 3.8326 6.2589 6.7118
Pt 7.9197 5.6074 5.7282
Pt 5.7775 7.1444 5.2894
Pt 7.3068 6.4178 3.5150

Pt8
cartesian coordinates:
Pt 8.3270 6.7565 8.9062
Pt 5.8994 6.2812 8.3884
Pt 8.1752 8.8980 7.5925
Pt 5.7483 8.4013 7.0899
Pt 3.9250 6.5950 6.7426
Pt 8.7408 6.7035 6.3601
Pt 6.3668 6.2498 5.8936
Pt 8.1188 5.4161 4.3280

Pt9
cartesian coordinates:
Pt 7.8107 7.7767 8.4922
Pt 5.9270 6.0697 8.1060
Pt 3.9333 5.2005 6.8181
Pt 6.0394 8.1101 6.6516
Pt 8.1494 6.3278 6.4665
Pt 6.1828 4.4675 5.9132
Pt 4.0498 7.3205 5.3041
Pt 6.2817 6.5017 4.4441
Pt 8.2560 4.8554 4.4343

Pt10
cartesian coordinates:
Pt 8.1122 7.3282 8.1224
Pt 5.9408 6.0220 8.0439
Pt 3.8024 4.7232 7.6496
Pt 7.9872 5.6304 6.2424
Pt 6.5642 7.9913 6.2280
Pt 5.6425 4.2170 5.9800
Pt 4.2155 6.5745 5.9680
Pt 7.5624 4.0179 4.3350
Pt 4.9459 8.3452 4.3052
Pt 6.2672 6.1909 4.1660

Ru2
cartesian coordinates:
Ru 0.0000 0.0000 2.4203
Ru 0.0000 0.0000 0.3797

Ru3
cartesian coordinates:
Ru 5.1644 4.5795 6.2742
Ru 6.6378 6.2027 5.8224
Ru 4.7094 5.7293 4.4150

Ru4
cartesian coordinates:
Ru 5.0605 5.1033 6.9703
Ru 6.7993 4.6203 5.7680
Ru 4.6038 6.7828 5.6352
Ru 6.3425 6.2998 4.4327

Ru5
cartesian coordinates:
Ru 6.4875 6.8319 6.6627
Ru 4.7224 5.1351 6.6535
Ru 7.0384 4.7721 5.9394
Ru 4.9196 6.9792 5.0514
Ru 5.4681 4.9176 4.3290

Ru6
cartesian coordinates:
Ru 5.7971 7.3165 6.9825
Ru 4.5845 5.3443 6.9002
Ru 7.6254 6.1931 6.2411
Ru 6.3744 4.2483 6.1870
Ru 4.7124 6.7920 5.0035
Ru 6.5008 5.7004 4.2803

Ru7
cartesian coordinates:
Ru 6.4821 5.5886 7.7691
Ru 5.0169 7.2303 7.1861
Ru 7.9707 6.4088 6.2519
Ru 5.5983 4.2588 6.1449
Ru 6.3626 7.8164 5.4304
Ru 4.4008 6.0338 5.3346
Ru 6.8509 5.3455 4.5651

Ru8
cartesian coordinates:
Ru 5.4805 5.8834 8.0675
Ru 6.6728 7.8092 7.7309
Ru 7.1328 4.6784 7.0371
Ru 8.3252 6.6039 6.7027
Ru 4.4523 6.1760 6.0782
Ru 5.6472 8.0990 5.7393
Ru 6.1038 4.9709 5.0479
Ru 7.3002 6.8938 4.7112

Ru9
cartesian coordinates:
Ru 6.3395 6.6663 8.5514
Ru 4.6110 5.6250 7.4424
Ru 7.8472 5.6359 7.2031
Ru 6.2227 8.4355 7.0938
Ru 6.0630 4.5783 6.0657
Ru 4.4677 7.4118 6.0101
Ru 7.7115 7.4531 5.7069
Ru 8.1683 5.1355 4.6905
Ru 5.9154 6.4048 4.5824

Ru10
cartesian coordinates:
Ru 7.4631 6.5767 8.4620
Ru 5.3684 5.5822 8.2384
Ru 6.6920 8.4051 7.5475
Ru 4.5972 7.4097 7.3258
Ru 8.6834 6.1256 6.5295
Ru 5.2935 4.5167 6.1664
Ru 7.9118 7.9547 5.6164
Ru 4.5223 6.3434 5.2542
Ru 7.3435 4.8533 5.1107
Ru 6.5733 6.6811 4.1976

Ru11
cartesian coordinates:
Ru 7.2271 6.1947 8.7953
Ru 5.0088 5.7495 8.5112
Ru 7.8004 4.3717 7.4584
Ru 5.6001 3.8727 7.2082
Ru 7.1809 7.4966 6.8769
Ru 4.9364 7.0610 6.6234
Ru 7.6754 5.7645 5.4935
Ru 5.5152 5.2013 5.3162
Ru 6.2002 8.9658 5.2508
Ru 4.9455 7.1118 3.9781
Ru 7.1838 7.4842 3.7616

Ru12
cartesian coordinates:
Ru 5.5681 5.8587 8.2310
Ru 6.7617 7.7800 7.8967
Ru 7.2155 4.6577 7.2062
Ru 8.4081 6.5797 6.8727
Ru 4.4929 6.1816 6.0704
Ru 5.6563 8.0603 5.7386
Ru 6.1029 5.0065 5.0651
Ru 7.2650 6.8851 4.7337
Ru 3.3416 6.4774 3.9489
Ru 4.5291 8.4005 3.6029
Ru 4.9877 5.2756 2.9174
Ru 6.1731 7.1988 2.5723

Ru1Pt1
cartesian coordinates:
Ru 0.0000 0.0000 0.2729
Pt 0.0000 0.0000 2.5271

Ru1Pt2
cartesian coordinates:
Ru 5.6319 4.7793 5.5969
Pt 4.3175 5.9653 6.9784
Pt 7.2096 6.0019 4.5667

Ru1Pt3
cartesian coordinates:
Ru 5.2403 5.0492 4.9055
Pt 6.9474 4.1909 6.3793
Pt 6.7331 6.7165 6.0140
Pt 4.2488 7.1470 5.5697

Ru1Pt4
cartesian coordinates:
Ru 5.3836 5.6156 5.8430
Pt 5.5742 3.7373 7.2650
Pt 7.2555 5.8504 7.1479
Pt 7.6567 8.1365 6.2324
Pt 5.6046 7.8315 4.9526

Ru1Pt5
cartesian coordinates:
Ru 7.5323 6.1663 5.8534
Pt 6.4455 6.6990 8.0209
Pt 8.9162 6.3917 7.7634
Pt 4.0744 6.8564 7.4926
Pt 5.1531 6.3133 5.3139
Pt 6.9846 5.7994 3.6074

Ru1Pt6
cartesian coordinates:
Ru 6.5422 6.2217 5.7865
Pt 8.5525 6.0185 7.3124
Pt 7.0834 8.0989 7.2627
Pt 6.7901 4.2033 7.1600
Pt 4.1331 6.4436 5.3610
Pt 5.5816 8.5074 5.2712
Pt 5.1894 4.1532 5.1985

Ru1Pt7
cartesian coordinates:
Ru 7.0944 6.8442 7.5075
Pt 6.1498 4.5679 7.4112
Pt 8.7028 5.0016 6.9880
Pt 3.7894 5.4603 6.9082
Pt 4.8948 7.7834 6.9050
Pt 7.1151 9.0732 6.3735
Pt 5.7966 5.9886 5.2906
Pt 8.2140 6.9391 5.2403

Ru2Pt1
cartesian coordinates:
Ru 6.2881 6.8269 5.4648
Ru 4.9227 5.8553 4.1610
Pt 5.4287 4.6479 6.2700

Ru2Pt2
cartesian coordinates:
Ru 5.0512 5.3199 6.2961
Ru 6.6695 6.4714 5.2748
Pt 5.8916 7.3431 7.4458
Pt 5.7905 4.4779 4.1007

Ru2Pt3
cartesian coordinates:
Ru 5.6909 6.9844 6.5250
Ru 4.4755 5.5665 5.3347
Pt 7.2970 5.3289 7.1075
Pt 5.9472 3.7476 5.7609
Pt 4.8788 7.8023 4.3107

Ru2Pt4
cartesian coordinates:
Ru 5.9031 6.3569 7.5686
Ru 7.4144 5.8257 5.8039
Pt 7.9871 5.2628 8.1287
Pt 4.6711 8.3635 7.3376
Pt 5.1552 6.9527 5.2612
Pt 6.2517 5.1535 3.8383

Ru2Pt5
cartesian coordinates:
Ru 5.8413 6.3284 7.1199
Ru 7.7166 6.5038 5.9968
Pt 5.7481 4.2727 8.2961
Pt 4.7146 8.4256 7.0734
Pt 6.5350 4.2603 5.8418
Pt 5.6350 7.4493 4.8772
Pt 7.1229 5.6578 3.7443

Ru2Pt6
cartesian coordinates:
Ru 5.8038 7.2264 6.9291
Ru 6.3249 5.0557 6.7435
Pt 6.1343 8.0584 9.1237
Pt 7.9851 6.6455 8.0137
Pt 8.6585 5.3337 5.9138
Pt 4.2285 7.1588 5.0552
Pt 4.7526 4.6590 4.9512
Pt 6.7702 6.5989 4.6797

Ru3Pt1
cartesian coordinates:
Ru 5.9334 6.6481 6.7473
Ru 7.1986 5.0274 6.1884
Ru 5.9292 4.2650 4.6562
Pt 4.3551 6.0002 5.0853

Ru3Pt2
cartesian coordinates:
Ru 5.9365 6.0423 7.7349
Ru 5.6849 7.7155 6.1463
Ru 6.0760 5.5276 5.4759
Pt 4.7621 4.0050 6.9172
Pt 7.3819 7.3209 4.3723

Ru3Pt3
cartesian coordinates:
Ru 5.4071 5.9136 7.0885
Ru 6.8095 7.6912 6.4996
Ru 7.4747 5.4852 6.0917
Pt 6.5173 3.7802 7.5829
Pt 4.4975 8.2445 6.9043
Pt 8.6190 7.3928 4.9365

Ru3Pt4
cartesian coordinates:
Ru 5.0498 7.3135 6.5221
Ru 6.8297 5.7286 6.4533
Ru 4.9904 5.7676 4.9370
Pt 5.0123 5.6679 8.3476
Pt 4.9436 3.9038 6.5398
Pt 7.1981 8.2350 5.7618
Pt 7.1307 6.4723 3.9531

Ru3Pt5
cartesian coordinates:
Ru 7.2808 6.8310 8.4013
Ru 7.8900 6.7883 6.2177
Ru 6.6488 8.4232 5.6300
Pt 6.2556 4.7398 8.2421
Pt 9.6226 7.0665 8.0230
Pt 6.0089 8.7595 7.9710
Pt 6.2787 5.1505 5.7059
Pt 5.2147 7.0267 4.3282

Ru4Pt1
cartesian coordinates:
Ru 7.1714 5.9404 6.8395
Ru 5.5954 7.4165 6.3265
Ru 6.9669 5.0304 4.8255
Ru 5.4179 6.5333 4.2943
Pt 4.8095 4.9287 6.2888

Ru4Pt2
cartesian coordinates:
Ru 6.9982 4.6779 7.2555
Ru 5.0781 5.4041 6.4184
Ru 8.1176 6.2200 6.0552
Ru 6.2060 6.9578 5.2025
Pt 6.3222 7.2172 7.7668
Pt 4.6754 5.4315 3.9824

Ru4Pt3
cartesian coordinates:
Ru 5.7540 6.6930 7.6263
Ru 5.3520 4.7739 6.6180
Ru 7.4355 7.0645 6.2462
Ru 7.0305 5.1465 5.2335
Pt 7.7587 4.9030 7.8087
Pt 3.9923 6.7816 5.7782
Pt 5.9450 7.2173 4.1809

Ru4Pt4
cartesian coordinates:
Ru 5.0095 6.0737 7.1888
Ru 6.0111 7.8368 6.3308
Ru 6.5768 4.7495 6.2905
Ru 7.5816 6.5118 5.4355
Pt 6.9408 5.4587 8.6888
Pt 8.1226 7.5349 7.6799
Pt 4.4612 5.0571 4.9339
Pt 5.6363 7.1226 3.9313

Ru5Pt1
cartesian coordinates:
Ru 5.0060 6.3974 7.5879
Ru 6.5382 4.8350 7.1902
Ru 6.2131 7.8619 6.1819
Ru 7.6944 6.2326 5.8505
Ru 4.4299 6.6364 5.3485
Pt 5.8978 4.8233 4.7225

Ru5Pt2
cartesian coordinates:
Ru 5.2090 6.5366 7.2375
Ru 7.0236 5.2599 7.2295
Ru 8.2726 6.7555 5.9050
Ru 5.0639 6.4212 5.0276
Ru 6.8725 5.1378 4.9318
Pt 4.7249 4.0932 6.2868
Pt 6.4167 8.3702 5.9378

Ru5Pt3
cartesian coordinates:
Ru 4.8883 5.5530 7.6215
Ru 6.4900 8.2433 6.6337
Ru 4.3583 7.4681 6.5850
Ru 6.8540 7.3347 4.5999
Ru 4.7203 6.6052 4.5169
Pt 7.2047 6.2968 7.8018
Pt 7.6818 5.3017 5.4772
Pt 5.2425 4.4840 5.4584

Ru6Pt1
cartesian coordinates:
Ru 7.0738 7.4572 6.8537
Ru 4.7328 6.9146 6.5281
Ru 7.6347 5.6078 5.8063
Ru 5.3189 5.0711 5.4839
Ru 5.9029 8.2210 4.9686
Ru 6.4839 6.3785 3.8602
Pt 6.2135 5.0739 7.9812

Ru6Pt2
cartesian coordinates:
Ru 6.5719 5.6379 8.1117
Ru 5.1576 7.3933 7.7901
Ru 8.0445 6.5538 6.6688
Ru 6.6395 8.3149 6.3470
Ru 4.1106 6.3664 6.0480
Ru 5.5864 7.2873 4.6095
Pt 5.4298 4.3858 6.4036
Pt 7.1182 5.4345 4.7504

Ru7Pt1
cartesian coordinates:
Ru 7.1473 5.9207 8.2868
Ru 6.3839 7.9426 7.5844
Ru 5.3534 4.9180 7.3186
Ru 4.5567 6.9469 6.6744
Ru 8.3107 5.6952 6.3511
Ru 7.6036 7.7470 5.6776
Ru 6.5419 4.6321 5.4028
Pt 5.7033 6.7438 4.5405

CHAPTER 7

CONCLUSIONS AND OUTLOOK

7.1 Conclusions

Subnanometre clusters (SNCs) are important for understanding larger clusters and nanoparticles, as well as for the growing number of applications of SNCs themselves. However, the study of SNCs is complicated, due to the importance of finite size quantum mechanical effects, such as orbital hybridisation, magnetism, and orbital shell closing, giving rise to physical and chemical properties that do not vary monotonically with size - i.e. "every atom counts".

This thesis has presented publications devoted to the fundamental understanding of the catalytic properties of pure and heteroatomic SNCs, including prediction of their geometries and electronic structures, exploration of their interactions with metal oxide surfaces and small ligands, and investigation of surface and ligand effects on their alloying properties.

A range of SNCs (of varying sizes) have been studied, as detailed in the attached publications, aided by the growth of computational techniques and computing power. The stable motifs of the clusters have been searched using a range of local and global optimisation methodologies, including recently developed genetic algorithm (GA) codes, coupled with the density functional theory method (DFT), which employ parallel computing techniques. To explore the evolution of cluster properties as a function of cluster size,

the effect of dopant metals, variation of oxidation states, and incorporation of substrates, the GA-DFT approach has proven to be a very useful tool.

In Chapter 3, we have used DFT-based Birmingham Parallel Genetic Algorithm (BPGA) calculations to locate the GM of binary Au-Pd SNCs, in order to predict their structural properties. The structures of pure Au clusters are size-dependent, showing 2D close-packed planar layers for 4-13 and 15 atoms; condensed flattened cage structures for 14 and 16 atoms; and pseudo-spherical hollow cage structures for 17 and 18 atoms. As for pure Au clusters, there are three generic structure types for pure Pd clusters, represented by deltahedral motifs for up to 10 atoms; bilayer structures for 11-15 atoms; and filled-cage structures for 16-18 atoms. For mixed clusters, the structural properties are found to depend both on cluster size and composition. The Au atoms occupy low-connectivity sites on the outside of the cluster, whereas Pd atoms tend to aggregate in the core of the cluster in high-coordination sites. The high mixing tendency of Au and Pd atoms is evident in the mixing energies except for the 6-atom nanoalloys due to the high stability of the "magic number" pure Au_6 and Pd_6 clusters.

The use of DFT has also allowed BPGA to capture the effect of the MgO(100) surface on the stability and structural behaviour of AuPd SNCs. Significant differences are observed between the lowest-energy supported and free clusters for some clusters due to the stabilisation of geometries which maximise the number of the stronger (Pd-O) bonds and the quenching of electron spin. As for free Au clusters, the GM for supported Au clusters are found to remain 2D on the MgO(100) surface, and, due to the "metal-on-top" effect, they lie roughly perpendicular to the surface. The Pd and Pd-rich clusters are found to be highly influenced by their interaction with the support, showing (3D-3D) structural alterations or (3D-2D) structural transitions for most of their supported species. Such effects are very interesting for catalytic applications because they maximize the exposed surface area. Adsorption calculations also suggest the use of the supported AuPd clusters in catalytic applications due to their ability to suppress cluster sintering by anchoring them to the surface via the stronger Pd-O bonds.

In Chapter 4, a synergy between theory and experiment is successfully employed to investigate the Pd dopant effects on the stability of mono-cationic Au SNCs and their reactivity towards CO gas.

The stabilities of the free cationic clusters have been studied by combining molecular beam experiments with BPGA-DFT calculations. Using DFT-based global optimization, the putative ground state structures for Au_N^+ and $PdAu_{(N-1)}^+$ SNCs with N=2-20 are determined. Magic clusters sizes are detected, by mass spectra and metastable photofragmentation fractions, at N =7 and 9 for the pure clusters and at N=7 and 10 atoms for the doped clusters. These magic sizes are also captured by the density functional energetics. A delocalisation of its six s electrons, closing the 2D electronic shell, is found to give an enhanced stability for both Au_7^+ and $PdAu_6^+$, whereas the closed shell electronic structures with eight delocalized electrons are exhibited for the 3D Au_9^+ and $PdAu_9^+$ clusters. The very good correlation, between the experimental stability patterns after photofragmentation and the calculated second difference in energies, suggests greater stability for odd N (even number of electrons) of Au_N^+ and for even N (even number of electrons) of $PdAu_{N-1}^+$ with N $\geq$10. Such theory/experiment agreement has confirmed that the global minima located by BPGA-DFT approach are indeed representative of the clusters obtained by the experiment. The reported photofragmentation channels of monomer and dimer evaporation show how the closed 5d shell daughter clusters can dominate over the other species (open shell) due to their relative stability. It is suggested also that if the produced fragments are magic sizes, the preferential evaporation of the unique Pd atom can be found, otherwise it is suppressed.

Combining mass spectrometric experiments, IR multiphoton dissociation spectroscopy and DFT calculations, we have presented a clear insight into the Pd-doping effects on the reactivity of Au_N^+, N$\leq$21, clusters towards one and two CO molecules. Based on DFT calculations, adsorption of CO on these clusters has been proposed to occur on atop (terminal) sites. The effect of Pd-doping is found to be size dependent, with a similar trend observed for the pure Au and Pd-doped clusters. It was observed that Pd-doped clusters

exhibit stronger CO binding (enhanced reactivity), even when the CO molecule is not directly bound to the Pd atom, in agreement with RRKM simulations, though greater enhancement of binding is observed for CO bound to Pd. The unimolecular dissociation rates of CO, which are sensitive to the CO binding energy (as well as heat capacities), have been measured and found to be higher for the larger clusters. The increase in the dissociation rates is attributed to the reduced heat capacity of the smaller clusters as they undergo greater heating upon redistribution of the heat of formation of the CO complex. Upon doping with Pd, reduced dissociation rates are observed for sizes N=4, 5, 8, and 9, while they are higher for N=7, 10 and N=18-21.

The preferred adsorption site was indicated by the measured IR bands of CO adsorbed species, under high-collision conditions. For pure Au clusters and some Pd-doped clusters, υ_{CO} is around 2165 cm^{-1}, indicating Au-CO binding, while υ_{CO} of around 2120 cm^{-1} indicates Pd-CO binding. The existence of bands for one and two adsorbed CO molecules at the same position ($\approx$ 2165 cm^{-1}) indicates that the adsorption occurred on the same type of atom (Au). For $PdAu_4^+(CO)_2$, we have deduced that the first CO molecule is adsorbed on Au atom and the second CO is bound to Pd, while in $PdAu_6^+(CO)_2$ the first CO molecule is adsorbed on Pd and the second on Au. Excellent agreement has been found between the calculated CO stretching frequencies and those measured by experiment, concluding that the CO binding site is a Au atom for $PdAu_{N-1}^+(CO)$, N=3-5 and 11, and is the Pd atom for N=6-10. Due to this correlation, the calculated structures, including the proposed atop sites, are considered to be representative of the clusters detected in the experiment. For Pd-bound clusters, the red-shifted values of υ_{CO} relative to that of the gas-phase CO molecule (2143 cm^{-1}) confirms clearly the contribution of Pd dopant in binding with CO. The high red shift (31-60 cm^{-1}), observed for sizes N=6, 8-10, and 12-14 atoms, suggests that π-back-donation dominates over electrostatic interactions. The uniformly blue-shifted values of υ_{CO} (higher than for free CO) obtained for the pure $Au_N^+(CO)$ clusters, suggest that the effect of π-back-donation is minimal, due to the stability of the filled 5d shell, and the repulsive interaction

between the 5σ HOMO of CO and a filled d orbital of the Au atom dominates.

The recently introduced version of the GA-DFT code, MEGA-DFT, is adapted to AuCu SNCs in Chapter 5. A computational study of mixed AuCu clusters consisting of 1 to 10 atoms, for all possible compositions, as free and supported on a rigid substrate of MgO(100) surface, is presented. The key structures for AuCu clusters at N=3-6 atoms are suggested to be planar. Changes from 2D to 3D configurations are observed in Au_N clusters, N=7-9, when doping more than two Cu atoms. All clusters with N=10 are found to be 3D, except for the pure and single-Cu-doped clusters. Factors, such as, larger size, higher electronegativity, and lower surface energy, for Au compared with Cu atoms, can synergistically contribute to explain the observed interior high-connectivity aggregation of Cu and the peripheral low-connectivity segregation of Au. Cu@Au core-shell segregation is, therefore, suggested and confirmed by the highest mixing tendency predicted close or at the stoichiometric composition, Au:Cu = 1:1.

On the oxide-support, the atop O-site is proposed to be the most favourable adsorption site. Cu adatoms show a higher tendency (relative to Au adatoms) to be adsorbed on the surface. The vertical orientation is found to be the preferred configuration for all adsorbed dimers due to the "metal-on-top" effect. For the adsorbed hetero-atomic dimers, it is suggested that Au is on top of Cu due to the difference in electronegativity which leads to Cu-Au electron transfer and thus strengthening the interaction of the positively charged Cu with the oxide anion. However, owing to the greater "metal-on-top" effect in Au systems, pure Au dimers exhibit stronger adsorption on the surface than the Cu dimer. The comparative adsorption energies for all supported dimers show the order: **Au**Cu< **Cu**Cu<**Au**Au<Au**Cu** (where the bold atom is bound to the oxide interface). For supported clusters, it has been shown that Cu segregation at the interface is energetically favoured, but some Au atoms are also present at the interface due to the flattening on the surface for some smaller Au-rich clusters, which also results in more freedom and flexibility to bond easily with atoms of the surface. The enhanced stability for both free and supported even-number clusters is observed in the second difference of energy

and HOMO-LUMO gap calculations. The analysis of the computed electronegativity and electrophilicity indices have shown that the electrons of Cu and Cu-rich clusters are more loosely bound than in pure Au and Au-rich clusters of the same size. In the free binary clusters, Cu-to-Au electron transfer is predicted. For the supported clusters, however, there is overall MgO-to-cluster electron transfer and the supported binary clusters show reduced Cu-to-Au electron transfer relative to the free clusters.

Ru-Pt binary nanoalloys have been studied in Chapter 6. The framework of the BPGA-DFT approach is employed to systematically perform global optimization on the pure and mixed SNCs ranging from 3 to 8 atoms. The structural properties and energetics of the clusters are studied. Adjacent aggregation of Ru atoms is predicted at the core of the clusters, whereas the peripheral dispersion is found for Pt atoms due to the weaker Pt-Pt bonds. Ru@Pt core-shell structures are, therefore, proposed for such sizes and also thermodynamically expected for larger clusters. The most favorable mixing is found at compositions which have approximately 40-50 % Ru atoms.

7.2 Additional Studies

In addition to the results reported in Chapters 3-6, the following two studies have also been carried out during the course of my PhD studies.

The CO adsorption and mixing properties of Pd-Ir nanoalloys have been studied [210] at the nanoscale - a copy of a resultant publication is included in the Appendix. DFT calculations were employed to investigate the properties of 38-atom and 79-atom truncated octahedral (TO) Pd-Ir nanoalloys. For both the 38-atom and 79-atom systems, the following stability order was concluded: $Pd_{shell}Ir_{core}$ > $Pd_{cup}Ir_{ball}$ > sandwich-Pd > Janus > sandwich-Ir > ordered ≈ $Pd_{ball}Ir_{cup}$ > $Pd_{core}Ir_{shell}$. Upon the adsorption with CO, Ir atoms were predicted to show higher interaction with CO than that of Pd atoms.

A study has been conducted on scandium SNCs [211]. Computational analysis of the electronic and structural properties of Sc clusters was performed, in an attempt to

answer the outstanding scientific questions: how do the d electrons interact in the Sc system and is it more analogous to either an s^1 metal (e.g. Na) or an s^2p^1 metal (e.g. Al)?. This has involved the determination of how localized or delocalized the electrons are in these clusters, as a function of charge, spin state and size.

7.3 Outlook

We have shown the significant utility of employing various local and global optimisation strategies (where possible, combined with complementary experiments) to achieve a good atomistic understanding of clusters and nanoalloy properties. Such studies can serve as a foundation for other similar systems, such as larger nanoalloys, ligated clusters, and clusters deposited on metal oxide surfaces, which may lead to the expansion of varied novel applications (e.g. few-atom or even single-atom catalysis).

It will be of interest to undertake theoretical studies in the future to support further research involving cluster beam photodepletion and photodetachment experiments. The goal of such projects is to explore the dependence of optical properties of subnanometre metal clusters on size, charge state, and doping. Characteristing the individual roles of doping and charge on an isoelectronic system of nanoalloys is one of the proposed studies. AuAg clusters could be employed, as they may be produced in the photofragmentation beam/mass spectrometry apparatus used for our current studies of similar metal systems. Sizes up to 20 atoms should be selected as well-studied archetypical ultrasmall clusters, so direct comparisons to our current theoretical/experimental work can be made. For the theoretical investigations, GA-DFT global optimisation should be employed for all sizes of $\mathrm{Au}_m\mathrm{Ag}^z_{(20-m)}$, $z = +1, 0, -1$, clusters. Refinement using several exchange-correlation functionals should be conducted to investigate the correlation with experimental findings. For example, compared with the standard GGA functionals, Minnesota type functionals have shown better performance in treating high-coordination, compact structures. Studying the system in the three charge states $(+1, 0, -1)$ is interesting, because charge

influences the critical cluster size at which the 2D-3D transition occurs - e.g. negative charge tends to increase the critical size. The high electronegativity which sustains the negative charge and the tendency towards planarity have been already observed for similar metal systems - e.g. CuAu clusters which are studied in the present work, suggest that any doping by less electronegative metals can induce 3D structures at smaller sizes (as found also for cationic clusters). By isolating the effects of doping and charge, one can characterise and understand such structural transitions. Calculating the ionisation potentials for the differently charged species, the electronic behaviour can be screened and compared with photoelectron spectroscopy measurements.

We have already performed preliminary studies on AuFe clusters, focussing on designing improved catalysts for CO_2 hydrogenation, based on nanoscale and sub-nanometre metal clusters. Atomistic modeling based on DFT calculations are employed to structurally distinguish the active catalytic motifs of the AuFe@TiO_2 (110) system. This includes tuning the dimensions of the metal cluster (i.e. from nanoscale to sub-nanometre) and the dimensionality (from 3D to 2D or even 1D). Such non-isoelectronic doping of Fe atoms into Au clusters leads to changes in the structures and dimensionality of the clusters. Quantum effects can also be studied, for example the effect of spin and the electronic decomposition of the orbitals, which can give insight into the factors influencing size-dependent trends.

The extension of the energy landscape analysis to larger nanoalloys is a further research direction. Studying the evolution of the size and doping of the clusters, and mapping their consequent energy landscapes, enable the quantification of the growth of complexity. The rearrangement pathways of the mixed metal clusters, which can be investigated by mapping the landscape, can provide an insight into the kinetics of such rearrangements.

LIST OF REFERENCES

[1] Whitesides, G. M. *Small* **1**(2), 172–179 (2005).

[2] Volokitin, Y., Sinzig, J., de Jongh, L. J., Schmid, G., Vargaftik, M. N., and Moiseevi, I. I. *Nature* **384**, 621–623 (1996).

[3] Ferrara, M. A., Dardano, P., De Stefano, L., Rea, I., Coppola, G., Rendina, I., Congestri, R., Antonucci, A., De Stefano, M., and De Tommasi, E. *Plos One* **9**(7), e103750 (2014).

[4] Vasundhara, K., Achary, S. N., Deshpande, S. K., Babu, P. D., Meena, S. S., and Tyagi, A. K. *Journal of Applied Physics* **113**(19), 194101–1 (2013).

[5] Piccolo, L., Li, Z. Y., Demiroglu, I., Moyon, F., Konuspayeva, Z., Berhault, G., Afanasiev, P., Lefebvre, W., Yuan, J., and Johnston, R. L. *Scientific Reports* **6**, 35226 (2016).

[6] Demiroglu, I., Li, Z. Y., Piccolo, L., and Johnston, R. L. *Catalysis Science and Technology* **6**(18), 6916–6931 (2016).

[7] Young, A., Amin, M., Petros, J., Natan, M., Shuming Nie, and Wang, M. In *2005 IEEE Engineering in Medicine and Biology 27th Annual Conference*, number July 2015, 723–726, (2005).

[8] Rozhkova, E. A., Ulasov, I., Lai, B., Dimitrijevic, N. M., Lesniak, M. S., and Rajh, T. *Nano Letters* **9**(9), 3337–3342 (2009).

[9] Pillarisetty, R. *Nature* **479**(7373), 324–328 (2011).

[10] Ostrikov, K. *IEEE Transactions on Plasma Science* **35**(2), 127–136 (2007).

[11] Li, Y., Liu, Q., and Shen, W. *Dalton Transactions* **40**(22), 5811 (2011).

[12] Redl, F. X., Cho, K.-S., Murray, C. B., and O'Brien, S. *Nature* **423**(6943), 968–971 (2003).

[13] Browning, N. D., Chisholm, M. F., and Pennycook, S. J. *Nature* **366**(6451), 143–146 (1993).

[14] Li, Z. Y., Young, N. P., Di Vece, M., Palomba, S., Palmer, R. E., Bleloch, A. L., Curley, B. C., Johnston, R. L., Jiang, J., and Yuan, J. *Nature* **451**(7174), 46–48 (2008).

[15] Selvakumar, R., Seethalakshmi, N., Thavamani, P., Naidu, R., and Megharaj, M. *RSC Adv.* **4**(94), 52156–52169 (2014).

[16] Patra, J. K. and Baek, K.-H. *Journal of Nanomaterials* **2014**, 417305 (2014).

[17] Johnston, R. *Atomic and Molecular Clusters*. Taylor & Francis, 1 edition, (2002).

[18] Richard, C., Catlow, A., Bell, R. G., and Gale, J. D. *Journal of Materials Chemistry* **4**(6), 781 (1994).

[19] Heard, C. J. and Johnston, R. L. In *Clusters: Structure, Bonding and Reactivity,* Nguyen, M. and Kiran, B., editors, chapter 1, 1–52. Springer, Cham1 edition (2017).

[20] He, R., Wang, Y.-C., Wang, X., Wang, Z., Liu, G., Zhou, W., Wen, L., Li, Q., Wang, X., Chen, X., Zeng, J., and Hou, J. G. *Nature communications* **5**, 4327 (2014).

[21] Baletto, F. and Ferrando, R. *Reviews of Modern Physics* **77**(1), 371–423 (2005).

[22] Sumiyama, K., Suzuki, K., Makhlouf, S., Wakoh, K., Kamiyama, T., Yamamuro, S., Konno, T., Xu, Y., Sakurai, M., and Hihara, T. *Journal of Non-Crystalline Solids* **192-193**, 539–545 (1995).

[23] Urayasu, T. K., Okayama, H. D., and Kashiwa, N. G. *United States Patent* , 1–6 (1988).

[24] Bozzolo, G., Ferrante, J., Noebe, R. D., Good, B., Honecy, F. S., and Abel, P. *Computational Materials Science* **15**(2), 169–195 (1999).

[25] Ruban, A., Skriver, H., and Nørskov, J. *Physical Review B* **59**(24), 15990–16000 (1999).

[26] Teng, X., Wang, Q., Liu, P., Han, W., Frenkel, A. I., Wen, W., Marinkovic, N., Hanson, J. C., and Rodriguez, J. a. *Journal of the American Chemical Society* **130**(3), 1093–1101 (2008).

[27] Schön, G. and Simon, U. *Colloid & Polymer Science* **273**(3), 202–218 (1995).

[28] Radillo-Díaz, A., Coronado, Y., Pérez, L. A., and Garzón, I. L. *The European Physical Journal D* **52**(1-3), 127–130 (2009).

[29] Frias, J. C., Ma, Y., Williams, K. J., Fayad, Z. A., and Fisher, E. A. *Nano Letters* **6**(10), 2220–2224 (2006).

[30] Sastry, M., Swami, A., Mandal, S., and Selvakannan, P. *Journal of Materials Chemistry* **15**(31), 3161 (2005).

[31] Ferrando, R., Jellinek, J., and Johnston, R. L. *Chemical Reviews* **108**, 846 (2008).

[32] Johnston, R. L. *Dalton Transactions* (22), 4193–4207 (2003).

[33] Rossi, G., Rapallo, A., Mottet, C., Fortunelli, A., Baletto, F., and Fernando, R. *Physical Review Letters* **93**(10), 105503 (2004).

[34] Mackay, A. *Acta Crystallographica* **15**(9), 916–918 (1962).

[35] Wales, D. J., Doye, J. P. K., Dullweber, A., Hodges, M. P., Calvo, F. Y. N. F., Hernández-Rojas, J., and Middleton, T. F. *The Cambridge Cluster Database,* (URL http://www-wales.ch.cam.ac.uk/CCD.html), Accessed: 27–04–2019.

[36] Weiher, N., Bus, E., Delannoy, L., Louis, C., Ramaker, D. E., Miller, J. T., and van Bokhoven, J. A. *Journal of Catalysis* **240**(2), 100–107 (2006).

[37] Hinz, A., Larsson, P.-O., Skårman, B., and Andersson, A. *Applied Catalysis B: Environmental* **34**(2), 161–178 (2001).

[38] Dupuis, V., Favre, L., Stanescu, S., Tuaillon-Combes, J., Bernstein, E., and Perez, A. *Journal of Physics: Condensed Matter* **16**(22), S2231–S2240 (2004).

[39] Hussein, H. A. and L. Johnston, R. In *Frontiers of Nanoscience,* Bromley, S. T. and Woodley, S. M., editors, chapter 4, 145–169. Elsevier, Amsterdam (2018).

[40] Vajda, S., Pellin, M. J., Greeley, J. P., Marshall, C. L., Curtiss, L. A., Ballentine, G. A., Elam, J. W., Catillon-Mucherie, S., Redfern, P. C., Mehmood, F., and Zapol, P. *Nature Materials* **8**(3), 213–216 (2009).

[41] Heiz, U., Vanolli, F., Sanchez, A., and Schneider, W. D. *Journal of the American Chemical Society* **120**(37), 9668–9671 (1998).

[42] Bonnemann, H. and Richards, R. M. *Eur. J. Inorg. Chem.* , 2455–2480 (2001).

[43] DiCenzo, S. and Wertheim, G. In *Clusters of Atoms and Molecules,* Haberland, H., editor, 362. Berlin, Springerii edition (1994).

[44] Lu, Y. and Chen, W. *Chemical Society Reviews* **41**(9), 3594 (2012).

[45] Götz, D. A., Heiles, S., Johnston, R. L., and Schäfer, R. *Journal of Chemical Physics* **136**(18), 29–31 (2012).

[46] Neyman, K. M., Inntam, C., Gordienko, A. B., Yudanov, I. V., and Rösch, N. *Journal of Chemical Physics* **122**, 174705 (2005).

[47] Heiles, S. and Johnston, R. L. *International Journal of Quantum Chemistry* **113**(18), 2091–2109 (2013).

[48] Jäger, M., Schäfer, R., and Johnston, R. L. *Advances in Physics: X* **3**, S100009 (2018).

[49] Woodley, S. M. In *Structure and Bonding*, volume 110, 95–132. (2004).

[50] Woodley, S. M. and Catlow, R. *Nature Materials* **7**(12), 937–946 (2008).

[51] Lazauskas, T., Sokol, A. A., and Woodley, S. M. *Nanoscale* **9**(11), 3850–3864 (2017).

[52] Escher, S. G. E. T., Lazauskas, T., Zwijnenburg, M. A., and Woodley, S. M. *Computational and Theoretical Chemistry* **1107**, 74–81 (2017).

[53] Cartwright, H. M. In *structure and bonding*, volume 110, chapter 1, 1–32. Springer-Verlag Berlin Heidelberg1 edition (2004).

[54] Hartke, B. *Journal of Physical Chemistry* **97**(39), 9973–9976 (1993).

[55] Hartke, B. *Chemical Physics Letters* **258**(1-2), 144–148 (1996).

[56] McGarrah, D. B. and Judson, R. S. *Journal of Computational Chemistry* **14**(11), 1385–1395 (1993).

[57] Brodmeier, T. and Pretsch, E. *Journal of Computational Chemistry* **15**(6), 588–595 (1994).

[58] Wang, B., Yin, S., Wang, G., Buldum, A., and Zhao, J. *Physical Review Letters* **86**(10), 2046–2049 (2001).

[59] Wang, B., Wang, G., and Zhao, J. *Physical Review B* **65**(23), 1–5 (2002).

[60] Wang, B., Wang, G., Ren, Y., Wang, J., and Zhao, J. *J. Phys.: Cond. Mat.* **13**, L403–L408 (2001).

[61] Fu, R. T., Esfarjani, K., Hashi, Y., Wu, J., Sun, X., and Kawazoe, Y. *Sci. Rep. Res. Inst. Tohoku Univ. Ser. A-Phys. Chem. Metall.* **44**, 77–81 (1997).

[62] Landree, E., Collazo-Davila, C., and Marks, L. D. *Acta Crystallographica Section B: Structural Science* **53**, 916–922 (1997).

[63] M. Woodley, S., D. Battle, P., D. Gale, J., and Richard A. Catlow, C. *Physical Chemistry Chemical Physics* **1**, 2535–2542 (1999).

[64] Woodley, S. M., Catlow, C. R. A., Battle, P. D., and Gale, J. D. *Chemical Communications* **4**, 22–23 (2004).

[65] Woodley, S. M. *Phys. Chem. Chem. Phys.* **6**, 1823–1829 (2004).

[66] Harris, K. D. *Computational Materials Science* **45**, 16–20 (2009).

[67] Paszkowicz, W., Harris, K. D., and Johnston, R. L. *Computational Materials Science* **45**, ix–x (2009).

[68] Zhou, Z. and Harris, K. D. *Computational Materials Science* **45**, 118–121 (2009).

[69] Harris, K. D. M., Johnston, R. L., and Habershon, S. In *Structure and Bonding*, volume 110, 55–94. (2004).

[70] Zhou, Z. and Harris, K. D. *Physical Chemistry Chemical Physics* **10**, 7262–7269 (2008).

[71] Harris, K. D. *Materials and Manufacturing Processes* **24**, 293–302 (2009).

[72] Pintér, J. D. In *Verlag Nonconvex Optimization and its Applications,* Doye, J. P. K., editor, volume 85, chapter 5, 103–139. Springer, US (2006).

[73] Jellinek, J. and Krissinel, E. *Chemical Physics Letters* **258**(1-2), 283–292 (1996).

[74] Xiao, Y. and Williams, D. E. *Chem. Phys. Lett.* **215**, 17–24 (1993).

[75] Hartke, B. *Physical Chemistry Chemical Physics* **5**(2), 275–284 (2003).

[76] Hartke, B., Flad, H.-J., and Dolg, M. *Phys. Chem. Chem. Phys.* **3**, 5121–5129 (2001).

[77] Zeiri, Y. *Physical Review E* **51**(4), 2769–2772 (1995).

[78] Deaven, D. and Ho, K. *Physical Review Letters* **75**(2), 288–291 (1995).

[79] Wales, D. J. and Doye, J. P. *Journal of Physical Chemistry A* **101**(28), 5111–5116 (1997).

[80] Tuson, A. and Clark, D. In *Evolutionary Algorithms in Molecular Design,* Clark, D. E., editor, chapter 12, 241. Wiley-VCH, Weinheim (2000).

[81] Heard, C. J., Heiles, S., and Johnston, R. L. *Nanoscale* **6**, 11777–11788 (2014).

[82] Davis, J., Shayeghi, A., Horswell, S. L., and Johnston, R. L. *Nanoscale* **7**, 14032–14038 (2015).

[83] Roberts, C., Johnston, R. L., and Wilson, N. T. *Theoretical Chemistry Accounts* **104**(2), 123–130 (2000).

[84] Doye, J. P. K. and Wales, D. J. *Journal of the Chemical Society, Faraday Transactions* **93**(24), 4233–4243 (1997).

[85] Giannozzi, P., Baroni, S., Bonini, N., Calandra, M., Car, R., Cavazzoni, C., Ceresoli, D., Chiarotti, G. L., Cococcioni, M., Dabo, I., Dal Corso, A., De Gironcoli, S., Fabris, S., Fratesi, G., Gebauer, R., Gerstmann, U., Gougoussis, C., Kokalj, A., Lazzeri, M., Martin-Samos, L., Marzari, N., Mauri, F., Mazzarello, R., Paolini, S., Pasquarello, A., Paulatto, L., Sbraccia, C., Scandolo, S., Sclauzero, G., Seitsonen, A. P., Smogunov, A., Umari, P., and Wentzcovitch, R. M. *Journal of Physics Condensed Matter* **21**(39), 395502 (2009).

[86] Valiev, M., Bylaska, E. J., Govind, N., Kowalski, K., Straatsma, T. P., Van Dam, H. J., Wang, D., Nieplocha, J., Apra, E., Windus, T. L., and De Jong, W. A. *Computer Physics Communications* **181**(9), 1477–1489 (2010).

[87] Heiles, S., Logsdail, A. J., Schäfer, R., and Johnston, R. L. *Nanoscale* **4**(4), 1109–1115 (2012).

[88] Heard, C. *Structural and Electronic Characterisation of Sub-nanometre Metal Particles*. PhD thesis, University of Birmingham, (2014).

[89] Heard, C. J., Vajda, S., and Johnston, R. L. *Journal of Physical Chemistry C* **118**(7), 3581–3589 (2014).

[90] Kresse, G. and Hafner, J. *Physical Review B* **47**(1), 558–561 (1993).

[91] Kresse, G. and Hafner, J. *Physical Review B* **49**, 14251–14269 (1994).

[92] Kresse, G. and Furthmüller, J. *Computufional Murerials Science* **6**, 15–50 (1996).

[93] Kresse, G. and Furthmüller, J. *Physical Review B - Condensed Matter and Materials Physics* **54**, 11169–11186 (1996).

[94] Du, J., Sun, X., Chen, J., and Jiang, G. *J Phys Chem A* **114**(49), 12825–12833 (2010).

[95] Pawluk, T., Hirata, Y., and Wang, L. *The Journal of Physical Chemistry B* **109**(44), 20817–20823 (2005).

[96] Zhang, W., Xiao, L., Hirata, Y., Pawluk, T., and Wang, L. *Chemical Physics Letters* **383**(1-2), 67–71 (2004).

[97] Davis, J. B. A., Horswell, S. L., and Johnston, R. L. *Journal of Physical Chemistry C* **120**, 3759–3765 (2016).

[98] Hussein, H. A., Davis, J. B. A., and Johnston, R. L. *Phys. Chem. Chem. Phys.* **18**(37), 26133–26143 (2016).

[99] Vargas, J. A., Buendía, F., and Beltrán, M. R. *Journal of Physical Chemistry C* **121**(20), 10982–10991 (2017).

[100] Shao, N., Huang, W., Gao, Y., Wang, L. M., Li, X., Wang, L. S., and Zeng, X. C. *Journal of the American Chemical Society* **132**(18), 6596–6605 (2010).

[101] Jäger, M., Schäfer, R., and Johnston, R. L. *Nanoscale* **11**, 9042–9052 (2019).

[102] Ferrando, R., Johnston, R. L., and Louis, C. *Physical Chemistry Chemical Physics* **17**(42), 27920–27921 (2015).

[103] Shan, S., Luo, J., Wu, J., Kang, N., Zhao, W., Cronk, H., Zhao, Y., Joseph, P., Petkov, V., and Zhong, C. J. *RSC Advances* **4**(80), 42654–42669 (2014).

[104] Iwai, H., Umeki, T., Yokomatsu, M., and Egawa, C. *Surface Science* **602**, 2541–2546 (2008).

[105] Pérez-Hernández, R., Mondragón Galicia, G., Mendoza Anaya, D., Palacios, J., Angeles-Chavez, C., and Arenas-Alatorre, J. *International Journal of Hydrogen Energy* **33**, 4569–4576 (2008).

[106] Roduner, E. *Chemical Society Reviews* **35**(7), 583–592 (2006).

[107] Wales, D. J. *Energy Landscapes with Application to Clusters, Biomolecules and Glasses*. Cambridge University Press, 1 edition, (2003).

[108] Schön, J. C., Čančarević, Ž. P., Hannemann, A., and Jansen, M. *Journal of Chemical Physics* **128**(19), 194712 (2008).

[109] Wevers, M. A., Schön, J. C., and Jansen, M. *Journal of Physics Condensed Matter* **11**(33), 6487–6499 (1999).

[110] Hey, J. C., Doyle, E. J., Chen, Y., and Johnston, R. L. *Philosophical Transactions of the Royal Society A* **376**, 20170154 (2018).

[111] Smeeton, L., Hey, J., and Johnston, R. *Inorganics* **5**, 20 (2017).

[112] Hey, J. C., Smeeton, L. C., Oakley, M. T., and Johnston, R. L. *Journal of Physical Chemistry A* **120**, 4008–4015 (2016).

[113] Neelamraju, S., Oakley, M. T., and Johnston, R. L. *Journal of Chemical Physics* **143**, 165103 (2015).

[114] Schön, J. C., Wevers, M. A., and Jansen, M. *Journal of Physics Condensed Matter* **15**, 5479–5486 (2003).

[115] Hellmann, H. *Einführung in die Quantenchemie*. Springer Spektrum, Berlin, Heidelberg, (2017).

[116] Feynman, R. P. *Physical Review* **56**, 340–343 (1939).

[117] Feibelman, P. J. *Physical Review B* **35**, 2626–2646 (1987).

[118] Duan, Z. and Wang, G. *J. Phys.: Condens. Matter* **23**, 475301 (2011).

[119] Clark, D. E. In *Rational Drug Design: Novel Methodology and Practical Applications*, volume 719, 255–270. (1999).

[120] Shayeghi, A., Götz, D., Davis, J. B. A., Schäfer, R., and Johnston, R. L. *Phys. Chem. Chem. Phys.* **17**(3), 2104–2112 (2015).

[121] Henrik Grönbeck and Broqvist, P. *J. Chem. Phys.* **119**(7), 3896 (2003).

[122] Ferrando, R. and Fortunelli, A. *J. Phys.: Condens. Matter* **21**(26), 264001 (2009).

[123] Ismail, R., Ferrando, R., and Johnston, R. L. *The Journal of Physical Chemistry C* **117**, 293–301 (2013).

[124] Barcaro, G. and Fortunelli, A. *Journal of Chemical Theory and Computation* **1**(5), 972–985 (2005).

[125] Vilhelmsen, L. B. and Hammer, B. *Journal of Chemical Physics* **141**(4), 044711 (2014).

[126] Richard M. Martin. *Electronic Structure: Basic Theory and Practical Methods.* Cambridge University Press, Cambridge, UK, (2004).

[127] Robert Evarestov. *Quantum Chemistry of Solids: The LCAO First Principles Treatment of Crystals.* Springer-Verlag, Berlin, Heidelberg, 1 edition, (2007).

[128] Booth, G. H., Grüneis, A., Kresse, G., and Alavi, A. *Nature* **493**, 365–370 (2013).

[129] Fulde, P. *Nature Physics* **12**, 106–107 (2016).

[130] Häkkinen, H., Yoon, B., Landman, U., Li, X., Zhai, H. J., and Wang, L. S. *Journal of Physical Chemistry A* **107**, 6168–6175 (2003).

[131] Hohenberg, P. and Kohn, W. *Phys. Rev.* **136**, B864–B871 (1964).

[132] Kohn, W. and Sham, L. J. *Physical Review A* **140**, 1133–1138 (1965).

[133] Perdew, J. P. and Kurth, S. In *A Primer in Density Functional Theory,* Fiolhais, C., Nogueira, F., and Marques, M. A., editors, volume 620, chapter 1, 1–55. Springer-Verlag, Berlin, Heidelberg,1st edition (2003).

[134] Burke, K. *Journal of Chemical Physics* **136**, 150901 (2012).

[135] Cohen, A. J., Mori-Sánchez, P., and Yang, W. *Chemical Reviews* **112**, 289–320 (2012).

[136] Perdew, J. P. and Zunger, A. *Physical Review B* **23**, 5048–5079 (1981).

[137] Perdew, J. P., Burke, K., and Ernzerhof, M. *Physical Review Letters* **77**, 3865–3868 (1996).

[138] Haas, P., Tran, F., Blaha, P., and Schwarz, K. *Physical Review B* **83**(20), 205117 (2011).

[139] Philipsen, P. and Baerends, E. *Physical Review B* **54**(8), 5326–5333 (1996).

[140] Liptak, M. D. and Shields, G. C. *International Journal of Quantum Chemistry* **105**, 580–587 (2005).

[141] Neugebauer, J. and Hickel, T. *Wiley Interdisciplinary Reviews: Computational Molecular Science* **3**, 438–448 (2013).

[142] Molina, L. M. and Hammer, B. *Physical Review Letters* **90**(20), 206102 (2003).

[143] Yudanov, I. V., Sahnoun, R., Neyman, K. M., Rösch, N., Hoffmann, J., Schauermann, S., Johánek, V., Unterhalt, H., Rupprechter, G., Libuda, J., and Freund, H. J. *Journal of Physical Chemistry B* **107**, 255–264 (2003).

[144] Rohrdanz, M. A., Martins, K. M., and Herbert, J. M. *Journal of Chemical Physics* **130**, 054112 (2009).

[145] Reske, R., Duca, M., Oezaslan, M., Schouten, K. J. P., Koper, M. T. M., and Strasser, P. *Journal of Physical Chemistry Letters* **4**, 2410–2413 (2013).

[146] Refaely-Abramson, S., Baer, R., and Kronik, L. *Physical Review B* **84**, 075144 (2011).

[147] Pastore, M., Mosconi, E., Angelis, F. D., and Grätzel, M. *J. Phys. Chem. C* **114**, 7205–7212 (2010).

[148] Vydrov, O. A. and Scuseria, G. E. *Journal of Chemical Physics* **125**, 234109 (2006).

[149] Verga, L. G. and Skylaris, C. K. In *Frontiers of Nanoscience,* Bromley, S. T. and Woodley, S. M., editors, volume 12, chapter 8, 239–293. Elsevier Ltd., Amsterdam,1st edition (2018).

[150] Barca, G. M. and Loos, P. F. *Journal of Chemical Physics* **147**, 024103 (2017).

[151] *Basis Set Exchange.* (URL https://bse.pnl.gov/bse/portal), Accessed: 27–04–2019.

[152] Weigend, F. and Ahlrichs, R. *Physical Chemistry Chemical Physics* **7**, 3297–3305 (2005).

[153] Blöchl, P. E. *Physical Review B* **50**, 17953–17979 (1994).

[154] Shimizu, K., Sawabe, K., and Satsuma, A. *Catalysis Science and Technology* **1**, 331–341 (2011).

[155] Muratsugu, S., Yamaguchi, A., Yokota, G.-i., Maenoa, T., and Tada, M. *Chemical Communications* **54**, 4842–4845 (2018).

[156] Takahashi, M., Koizumi, H., Chun, W.-J., Kori, M., Imaoka, T., and Yamamoto, K. *Science Advances* **3**, e1700101 (2017).

[157] Xu, H., Cheng, D., Gao, Y., and Zeng, X. C. *ACS Catalysis* **8**, 9702–9710 (2018).

[158] Xu, C. Q., Lee, M. S., Wang, Y. G., Cantu, D. C., Li, J., Glezakou, V. A., and Rousseau, R. *ACS Nano* **11**, 1649–1658 (2017).

[159] Fang, J., Li, J., Zhang, B., Yuan, X., Asakura, H., Tanaka, T., Teramura, K., Xie, J., and Yan, N. *Nanoscale* **7**, 6325–6333 (2015).

[160] Zhu, L., Jiang, Y., Zheng, J., Zhang, N., Yu, C., Li, Y., Pao, C. W., Chen, J. L., Jin, C., Lee, J. F., Zhong, C. J., and Chen, B. H. *Small* **11**, 4385–4393 (2015).

[161] Hussein, H. A., Gao, M., Hou, Y., Horswell, S. L., and Johnston, R. L. *Z. Phys. Chem.* (2019), DOI:10.1515/zpch–2018–1356.

[162] Moseler, M., Häkkinen, H., and Landman, U. *Physical Review Letters* **89**, 176103 (2002).

[163] Poh, S. M., Zhao, X., Tan, S. J. R., Fu, D., Fei, W., Chu, L., Jiadong, D., Zhou, W., Pennycook, S. J., Neto, A. H. C., and Loh, K. P. *ACS Nano* **12**, 7562–7570 (2018).

[164] Ndlovu, G. F., Roos, W. D., Wang, Z. M., Asante, J. K., Mashapa, M. G., Jafta, C. J., Mwakikunga, B. W., and Hillie, K. T. *Nanoscale Research Letters* **7**, 173 (2012).

[165] Bromann, K., Félix, C., Brune, H., Harbich, W., Monot, R., Buttet, J., and Kern, K. *Science* **274**, 956–958 (2002).

[166] Razouk, R. I. and Mikhail, R. S. *Journal of Physical Chemistry* **61**(7), 886–891 (1957).

[167] Thanh, N. T., Maclean, N., and Mahiddine, S. *Chemical Reviews* **114**(15), 7610–7630 (2014).

[168] Zhang, H., Watanabe, T., Okumura, M., Haruta, M., and Toshima, N. *Nature Materials* **11**, 49–52 (2012).

[169] Bazzi, R., Flores-Gonzalez, M., Louis, C., Lebbou, K., Dujardin, C., Brenier, A., Zhang, W., Tillement, O., Bernstein, E., and Perriat, P. *Journal of Luminescence* **102-103**, 445–450 (2003).

[170] Allian, A. D., Takanabe, K., Fujdala, K. L., Hao, X., Truex, T. J., Cai, J., Buda, C., Neurock, M., and Iglesia, E. *Journal of the American Chemical Society* **133**, 4498–4517 (2011).

[171] Oliver-Meseguer, J., Cabrero-Antonino, J. R., Domínguez, I., Leyva-Pérez, A., and Corma, A. *Science* **338**, 1452–1455 (2012).

[172] Parkinson, G. S. *Catalysis Letters* **149**, 1137–1146 (2019).

[173] Baletto, F. *Journal of physics. Condensed matter* **31**, 113001 (2019).

[174] Chen, H. Y. T., Chou, J. P., Lin, C. Y., Hu, C. W., Yang, Y. T., and Chen, T. Y. *Nanoscale* **9**, 7207–7216 (2017).

[175] Kim, Y.-T., Lopes, P. P., Park, S.-A., Lee, A.-Y., Lim, J., Lee, H., Back, S., Jung, Y., Danilovic, N., Stamenkovic, V., Erlebacher, J., Snyder, J., and Markovic, N. M. *Nature Communications* **8**, 1449 (2017).

[176] Song, C., Ge, Q., and Wang, L. *Journal of Physical Chemistry B* **109**, 22341–22350 (2005).

[177] Nhat, P. V., Tai, T. B., and Nguyen, M. T. *Journal of Chemical Physics* **137**, 164312 (2012).

[178] Joshi, A. M., Tucker, M. H., Delgass, W. N., and Thomson, K. T. *Journal of Chemical Physics* **125**, 194707 (2006).

[179] Chen, Y. M., Kuang, X. Y., Sheng, X. W., Shao, P., Zhong, M. M., and Wang, H. Q. *Zeitschrift fur Naturforschung - Section A Journal of Physical Sciences* **68**, 651–658 (2013).

[180] Neumaier, M., Weigend, F., Hampe, O., and Kappes, M. M. *Journal of Chemical Physics* **125**, 104308 (2006).

[181] Zhao, Y., Li, Z., and Yang, J. *Physical Chemistry Chemical Physics* **11**, 2329–2334 (2009).

[182] Remacle, F. and Kryachko, E. S. *Journal of Chemical Physics* **122**, 044304 (2005).

[183] Jug, K., Zimmermann, B., Calaminici, P., and Köster, A. M. *Journal of Chemical Physics* **116**, 4497–4507 (2002).

[184] Bracey, C. L., Ellis, P. R., and Hutchings, G. J. *Chemical Society Reviews* **38**, 2231–2243 (2009).

[185] Yoo, W.-J. and Li, C.-J. *Tetrahedron Letters* **48**, 1033–1035 (2007).

[186] Corma, A. and Garcia, H. *Chemical Society Reviews* **37**, 2096–2126 (2008).

[187] Bond, G. C., Louis, C., and Thompson, D. T. *Catalysis by Gold*, volume 6. Imperial College Press, London, (2006).

[188] Basile, A., Parmaliana, A., Tosti, S., Iulianelli, A., Gallucci, F., Espro, C., and Spooren, J. *Catalysis Today* **137**, 17–22 (2008).

[189] Heard, C. J. and Johnston, R. L. *European Physical Journal D* **67**(2), 34 (2013).

[190] Ma, L., Melander, M., Weckman, T., Laasonen, K., and Akola, J. *J. Phys. Chem. C* **120**, 26747 (2016).

[191] Ma, L., Laasonen, K., and Akola, J. *Journal of Physical Chemistry C* **121**(20), 10876 (2017).

[192] Heiz, U., Sanchez, A., Abbet, S., and Schneider, W. D. *Journal of the American Chemical Society* **121**(13), 3214–3217 (1999).

[193] Landman, U. *Proceedings of the National Academy of Sciences* **102**(19), 6671–6678 (2005).

[194] Steele, B. C. H. and Heinzel, A. *Nature* **414**, 345–352 (2001).

[195] Sharma, S. and Pollet, B. G. *Journal of Power Sources* **208**, 96–119 (2012).

[196] Karim, N. A., Kamarudin, S. K., Shyuan, L. K., Yaakob, Z., Daud, W. R., and Kadhum, A. A. *Journal of Power Sources* **288**, 461–472 (2015).

[197] Ramli, Z. A. and Kamarudin, S. K. *Nanoscale Research Letters* **13**, 410 (2018).

[198] Lemons, R. A. *Journal of Power Sources* **29**, 251–264 (1990).

[199] Lang, S. M., Bernhardt, T. M., Krstic, M., and Bonačic-Koutecký, V. *Angewandte Chemie - International Edition* **53**, 5467 (2014).

[200] Eckle, S., Denkwitz, Y., and Behm, R. J. *Journal of Catalysis* **269**, 255–268 (2010).

[201] Tada, S., Kikuchi, R., Urasaki, K., and Satokawa, S. *Applied Catalysis A: General* **404**, 149–154 (2011).

[202] Eckle, S., Augustin, M., Anfang, H. G., and Behm, R. J. *Catalysis Today* **181**, 40–51 (2012).

[203] Mishra, A. and Prasad, R. *Bulletin of Chemical Reaction Engineering and Catalysis* **6**, 1–14 (2011).

[204] Watanabe, M., Uchida, M., and Motoo, S. *J. Electroanal. Chem. Interfacial Electrochem.* **229**, 395–406 (1987).

[205] Stoupin, S., Rivera, H., Li, Z., Segre, C. U., Korzeniewski, C., Dominick J. Casadonte, J., Inoue, H., and Smotkin, E. S. *Physical Chemistry Chemical Physics* **10**, 6430–6437 (2008).

[206] Chu, D. and Gilman, S. *Journal of The Electrochemical Society* **143**, 1685 (1996).

[207] Aricò, A. S., Antonucci, P. L., Modica, E., Baglio, V., Kim, H., and Antonucci, V. *Electrochimica Acta* **47**, 3723–3732 (2002).

[208] Gasteiger, H. A., Markovic, N., Ross, P. N., and Cairns, E. J. *The Journal of Physical Chemistry* **97**, 12020–12029 (1993).

[209] Gasteiger, H. A., Markovic, N., Jr, P. N. R., and Cairns, E. J. *Electrochimica Acta* **39**, 1825–1832 (1994).

[210] Fan, T. E., Demiroglu, I., Hussein, H. A., Liu, T. D., and Johnston, R. L. *Physical Chemistry Chemical Physics* **19**, 27090–27098 (2017).

[211] Abdulhussein, H. A., Gilmour, J. T. A., Gaston, N., and Johnston, R. L. *under preparation* .

APPENDIX

Book Chapter

and Additional Publication

CHAPTER

4 The DFT-genetic algorithm approach for global optimization of subnanometer bimetallic clusters

Heider A. Hussein[*,†], **Roy L. Johnston**[*,1]

[*]*School of Chemistry, University of Birmingham, Birmingham, United Kingdom*

[†]*Department of Chemistry, Faculty of Science, University of Kufa, Najaf, Iraq*

[1]*Corresponding author: e-mail address: r.l.johnston@bham.ac.uk*

CHAPTER OUTLINE

Frontiers of Nanoscience, Volume 12, ISSN 1876-2778, https://doi.org/10.1016/B978-0-08-102232-0.00004-X

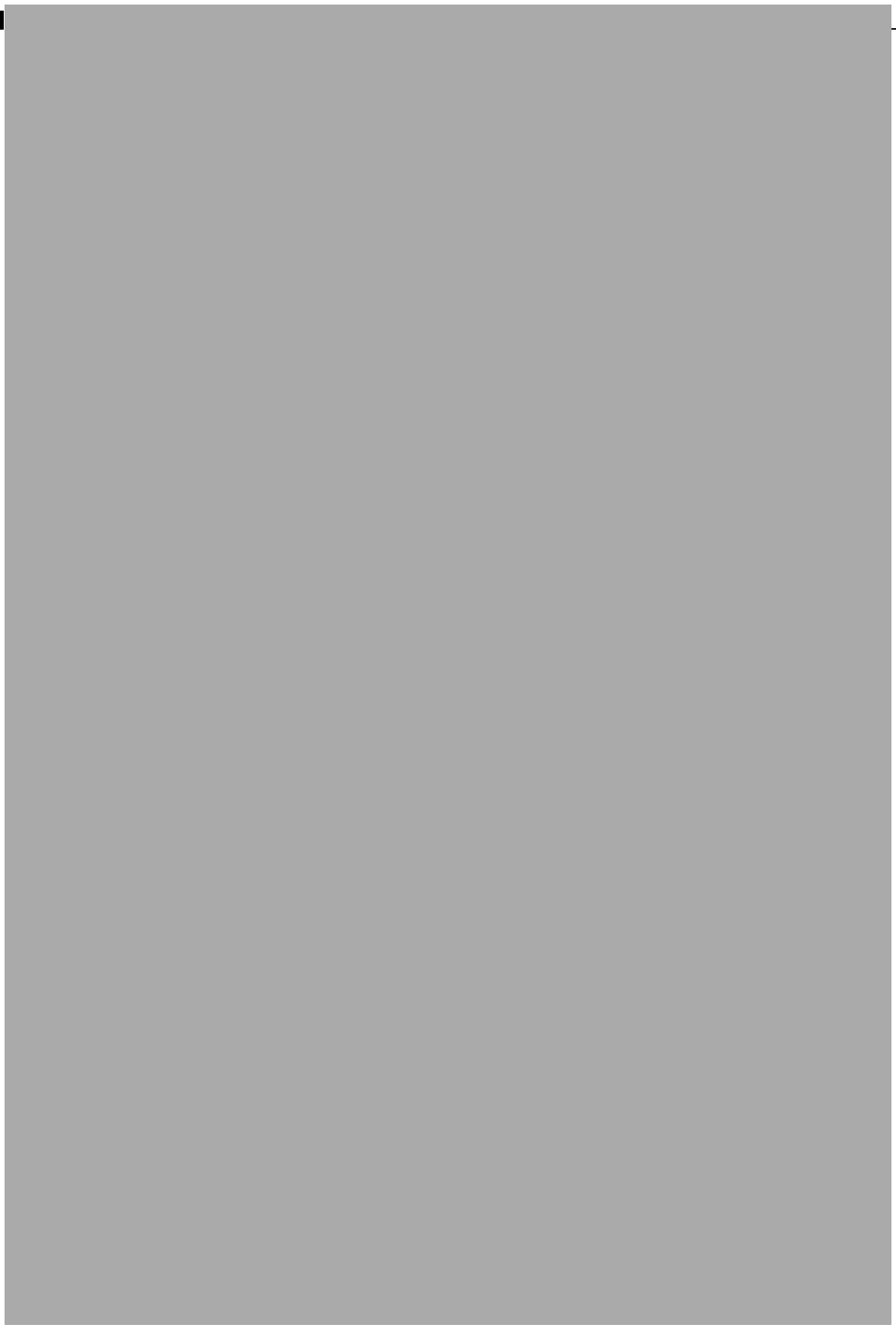

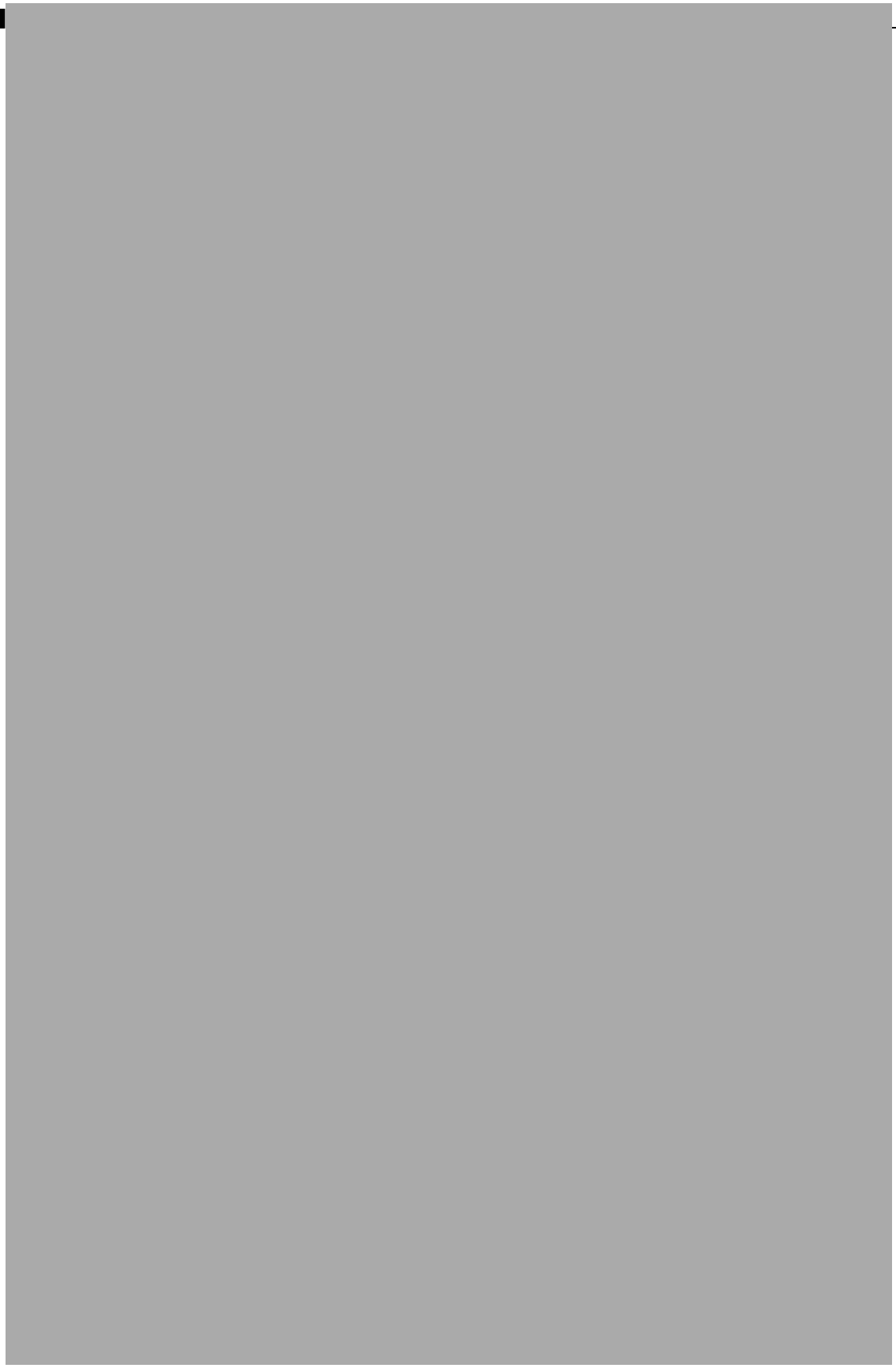

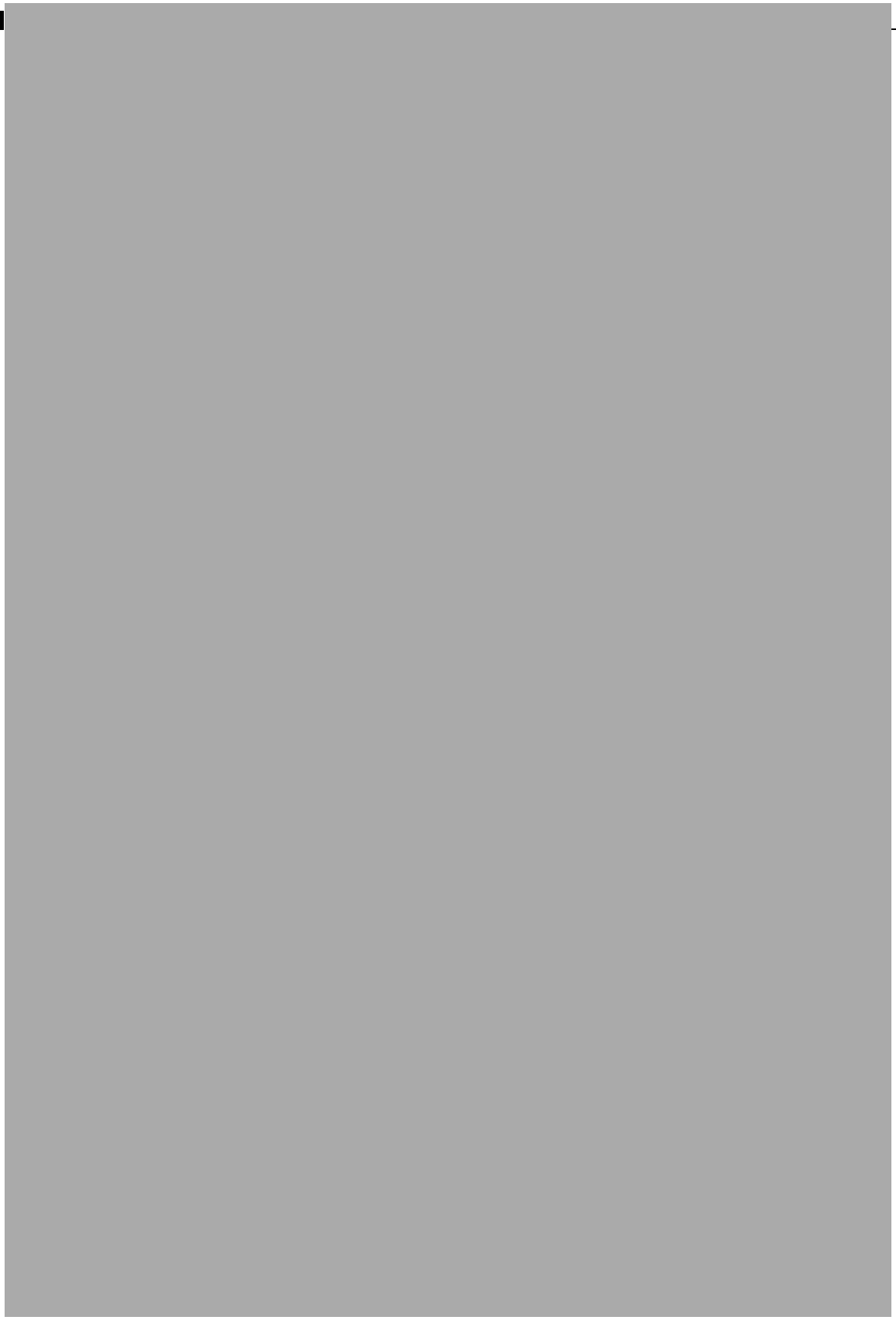

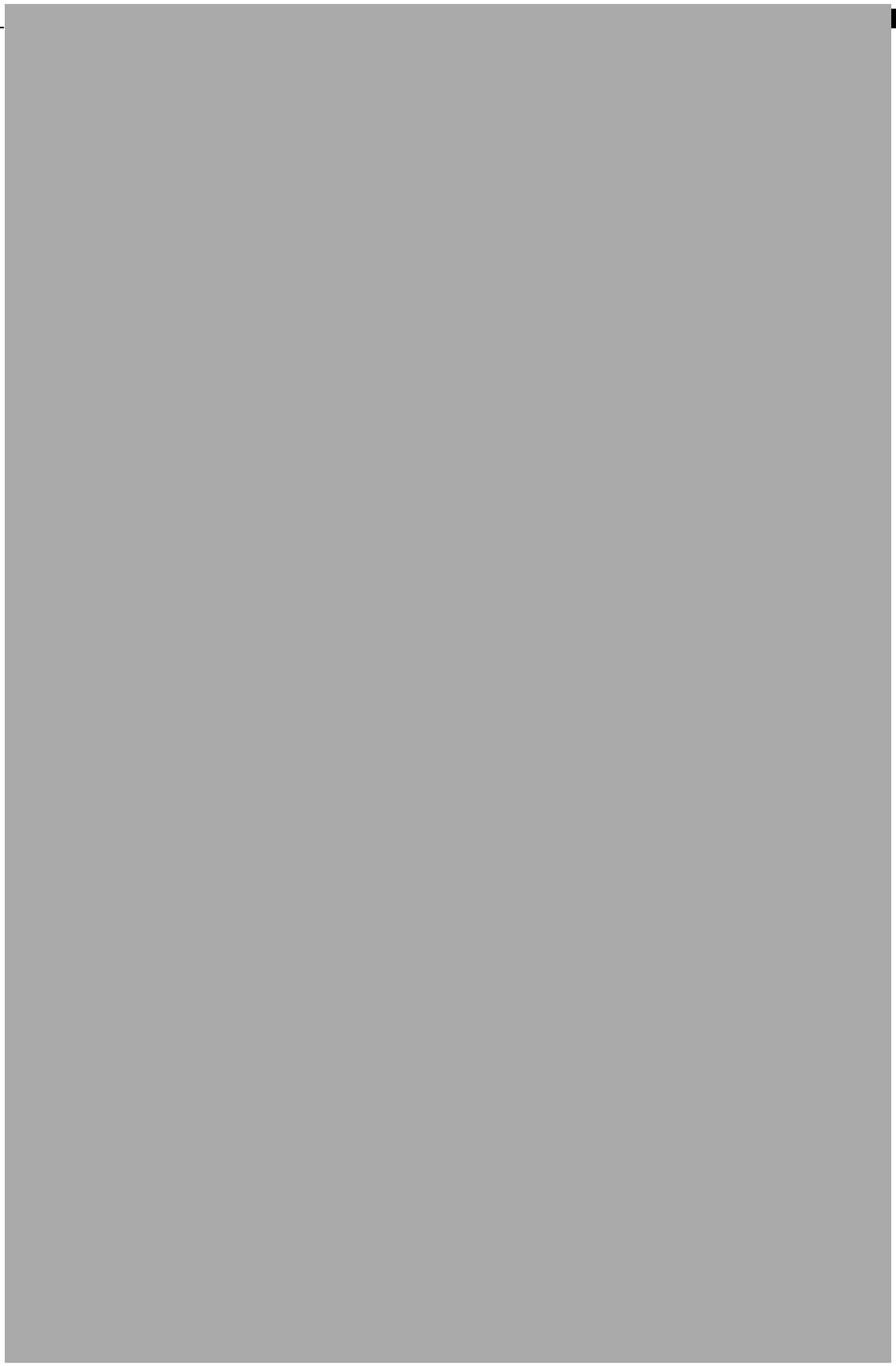

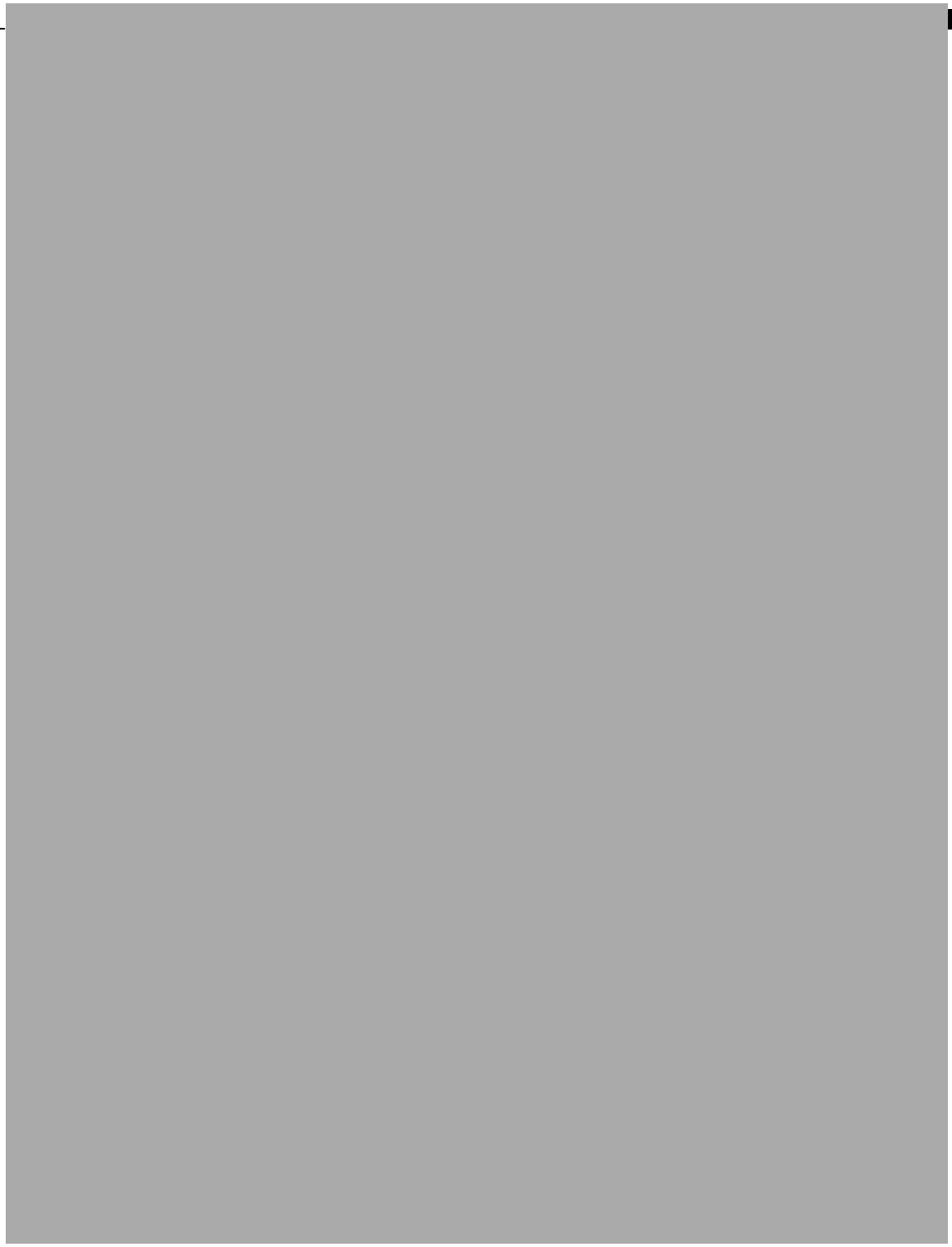

PCCP

PAPER

View Article Online
View Journal | View Issue

Cite this: *Phys. Chem. Chem. Phys.*, 2017, **19**, 27090

DFT study of the structure, chemical ordering and molecular adsorption of Pd–Ir nanoalloys†

Tian-E Fan,[ab] Ilker Demiroglu,[b] Heider A. Hussein,[bc] Tun-Dong Liu*[a] and Roy L. Johnston*[b]

Received 17th July 2017,
Accepted 25th September 2017

DOI: 10.1039/c7cp04811d

rsc.li/pccp

The structures and surface adsorption sites of Pd–Ir nanoalloys are crucial to the understanding of their catalytic performance because they can affect the activity and selectivity of nanocatalysts. In this article, density functional theory (DFT) calculations are performed on bare Pd–Ir nanoalloys to systematically explore their stability and chemical ordering properties, before studying the adsorption of CO on the nanoalloys. First, the structural stability of 38-atom and 79-atom truncated octahedral (TO) Pd–Ir nanoalloys are investigated. Then the adsorption properties and preferred adsorption sites of CO on 38-atom Pd–Ir nanoalloys are considered. The $Pd_{shell}Ir_{core}$ structure, which has the lowest energy of all the considered isomers, exhibits the highest structural stability, while the $Pd_{core}Ir_{shell}$ configuration is the least stable. In addition, the adsorption strength of CO on Ir atoms is found to be greater than on Pd for Pd–Ir nanoclusters. The preferred adsorption sites of CO on pure Pd and Ir clusters are in agreement with calculations and experiments on extended Pd and Ir surfaces. In addition, d-band center and charge effects on CO adsorption strength on Pd–Ir nanoalloys are analyzed by comparison with pure clusters. The study provides a valuable theoretical insight into catalytically active Pd–Ir nanoalloys.

1. Introduction

Nanosized clusters or nanoparticles are new materials, which differ from individual atoms and bulk materials; showing unique chemical and physical properties.[1] Metal nanoclusters are of interest as catalysts due to their high surface–volume ratio and high proportion of low-coordinated active sites.[2] Among metallic nanoclusters, palladium–iridium (Pd–Ir) nanoalloys have been considered as important catalysts in a number of chemical and physical applications.[3–8] For example, Pd–Ir nanoalloys act as catalysts for a range of organic reactions, including olefin hydrogenation and tetralin hydro-conversion through selective ring opening.[9] They are also applied in the preferential oxidation of CO for the elimination of impurities in H_2 production.[10] Palladium (Pd) is regarded as one of the best catalysts, owing to its excellent reactivity and stability, being the only bulk metal that can form a hydride phase at ambient temperature and pressure.[11] Pd–Ir is a demixing system in the bulk, exhibiting miscibility gaps with relatively high critical temperatures,[12,13] but miscibility is enhanced at the nanoscale.[7,9] Nanoalloying Pd and Ir not only enhances the catalytic activity, due to the synergistic effect of atomic configuration and electronic structures of the component metals, but also improves the selectivity of catalysts.[14]

For Pd–Ir nanoalloys, their (geometric and electronic) structures are crucial to the understanding of their catalytic performances because the activity and selectivity are closely associated with structure. The catalytic performance also depends on composition, surface segregation and chemical ordering, and these characteristics of alloyed NPs can be controlled to tune their optical, electrical, and catalytic properties.[15–17] Moreover, both theory and experiment show that the binding of ligands can change the chemical ordering and the structures of nanoalloys.[18–20] The surface sites and the bonding of adsorbates under reaction conditions can also affect the surface structure and change the activity and the selectivity of nanocatalysts. Surface segregation of Pd has been reported to occur in the presence of reactive gases such as CO and O_2,[21,22] and the binding of CO molecules is commonly used as a probe to identify the nature of metal surface adsorption sites.[23,24] Pd–Ir nanoalloys are often used as catalysts in the preferential oxidation of CO (PROX).[8,10]

The Pd–Ir system has rarely been studied computationally,[25–29] and relatively few catalytic studies have been devoted to Pd–Ir nanoalloys.[9,27,30] In this study, the structure and chemical ordering of bare and CO-adsorbed Pd–Ir nanoalloys have been investigated theoretically by using density functional theory (DFT). The mixing energy and the effect of CO adsorption on

[a] *Department of Automation, Xiamen University, Xiamen, 361005, China. E-mail: ltd@xmu.edu.cn*
[b] *School of Chemistry, University of Birmingham, Edgbaston, Birmingham B15 2TT, UK. E-mail: r.l.johnston@bham.ac.uk*
[c] *Department of Chemistry, College of Science, University of Kufa, Najaf, Iraq*

† Electronic supplementary information (ESI) available. See DOI: 10.1039/c7cp04811d

Pd–Ir nanoalloys have been considered. Since the d-band model[31] is particularly important for understanding metal–adsorbate bond formation and trends in reactivity, the d-band center is calculated to analyze the adsorption strength caused by metal–adsorbate interaction. This article is structured as follows. Section 2 briefly describes the calculation methods. Section 3 presents the calculated results, discussion and comparison with available experimental results for bare Pd–Ir and CO-adsorbed Pd–Ir nanoalloys. The main conclusions are summarized in the fourth section.

2. Methodology

2.1 Model

In our atomistic calculation, the (fcc packing) truncated octahedron (TO) having six {100} and eight {111} facets, has been chosen as the nanoparticle model to study 38-atom and 79-atom Pd–Ir nanoalloys (Fig. 1). The TO structure is frequently adopted in theoretical and experimental studies,[32,33] because of its high symmetry (O_h) and it being a fragment of a face-centered cubic crystal (fcc). The sizes of 38 and 79 atoms have been selected to describe the trend of structural stability for Pd–Ir nanoalloys with different compositions and configurations, which enables predictions for larger experimental fcc-based nanoparticles.

Binary nanoalloys present increasing structural complexity compared with unary nanoclusters because the two components can have variable compositions and exhibit various chemical ordering patterns.[14] For example, there are ordered, Janus, ball–cup, core–shell, sandwich structures and so on in nanoalloys,[34] some structures are shown in Fig. 2. Here, the preferred position for a single Pd or Ir dopant in 38-atom and 79-atom nanoclusters is first investigated, considering the unique positions for single-atom substitutions. These dopant sites are shown in Fig. 1 for the 79-atom TO.

For other compositions, we have constructed several configurations for 38-atom and 79-atom Pd–Ir nanoalloys. The configurations studied for 38-TO are shown in Fig. 2. The ball–cup structures are generated by embedding (but not completely covering) one type of atom in the other.[35] The Janus alloy particle is formed by dividing the TO structure into discrete Pt and Ir regions, sharing a single (approximately) planar interface. The cluster Janus-$Pd_{19}Ir_{19}$ has a perfect half Pd and half Ir structure. Ordered structures are created by alternating Pd and Ir layers in the (100) or (111) directions and by occupying different fcc crystal positions with Pd or Ir. The core–shell structures have a core of one metal, completely surrounded by a shell of the other metal. Sandwich structures have a layer of one metal, sandwiched by layers of the other metal. In addition, to compare relative stabilities of different clusters with the same compositions, we also build the hex and centroid structures. For example, hex-$Pd_{32}Ir_6$ has 6 Ir atoms forming a hexagonal ring surrounding one of the (111) facets of TO_{38}, while centroid-$Pd_{32}Ir_6$ has 6 Ir atoms occupying the centres of 6 (111) facets of TO, in a D_{3d} symmetry arrangement.

For molecular adsorption studies, the CO molecule has been chosen for adsorption on TO 38-atom Pd–Ir nanoalloys. The possible adsorption sites on the surface of TO-shaped nanoparticles are grouped into eight symmetry-inequivalent sites, as shown in Fig. 3. The sites include both (111) and (100) facets. 1 and 2 are the atop sites, on the center of the (111) facet and the edge atom between (111) and (100) facets, respectively. 3, 4 and 5 are bridge sites, respectively on the (111) facet, between the (111) and (100) facets, and between two (111) facets. 6 and 7 are (fcc) and (hcp) hollow sites on the (111) facet, 8 is the hollow site on the (100) facet. Calculations are performed by placing a single CO molecule at each of these sites and carrying out local DFT minimization.

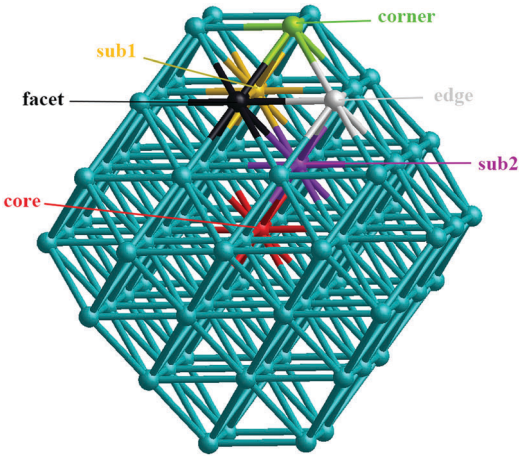

Fig. 1 Unique positions for single-atom doping in 79-atom TO nanoparticles.

2.2 DFT calculations

In this study, all calculations are performed using the DFT method, as implemented in the Vienna ab initio Simulation Package (VASP) code.[36] The interaction between valence electrons and ionic cores is described by the projector augmented wave (PAW) method.[37,38] The generalized gradient approximation (GGA) is employed within the Perdew–Burke–Ernzerhof (PBE) parameterization for the exchange–correlation energy functional.[39] All the calculations are spin-polarized, and the valence electrons are treated explicitly. To avoid spurious periodic interactions, the bare clusters are placed into a sufficiently large supercell to ensure $\sim$10 Å separation by vacuum. All calculated clusters are locally geometrical optimized at the DFT level, where all cluster atoms, are relaxed until the forces on the atoms are lower than 0.01 eV $Å^{-1}$, and the electronic ground states are determined by requiring a total energy convergence of 10^{-6} eV. In order to test the correctness of our computational methodology (VASP/PBE), a comparison of calculated and experimental lattice parameters (a), cohesive energies (E_c) and bulk modulus (B) for bulk fcc Pd and Ir has been made. As shown in the ESI,† the experimental and calculated values are in good agreement.

2.3 Energies

For the stability comparison of Pd–Ir nanoalloys with different compositions and different configurations, a mixing (or excess)

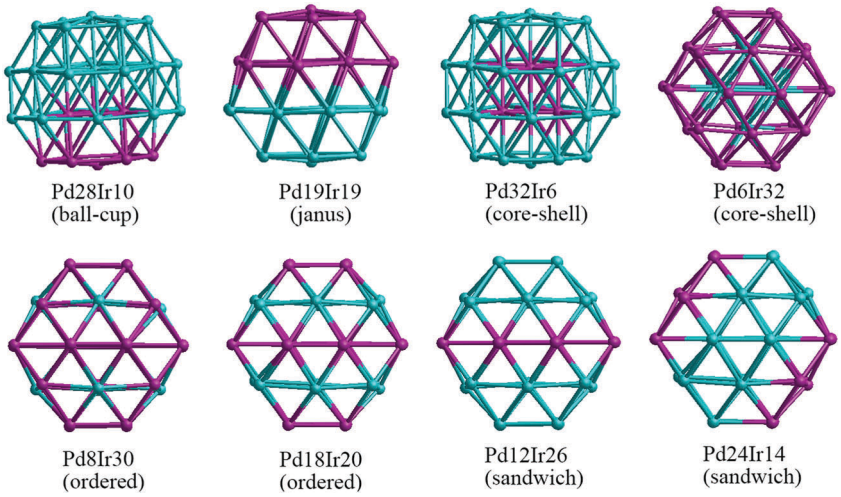

Fig. 2 38-TO Pd–Ir nanoalloys with different compositions and configurations. In this (and later figures) Pd atoms are shown in blue and Ir atoms in purple.

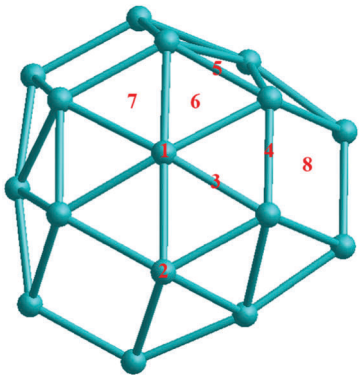

Fig. 3 The eight unique sites for CO molecular adsorption on the surface of 38-atom TO Pd–Ir nanoalloys.

energy term (Δ) is calculated using:[40]

$$\Delta = E_{\mathrm{tot}}(\mathrm{Pd}_m\mathrm{Ir}_n) - m\frac{E_{\mathrm{tot}}(\mathrm{Pd}_{m+n})}{m+n} - n\frac{E_{\mathrm{tot}}(\mathrm{Ir}_{m+n})}{m+n} \quad (1)$$

where $E_{\mathrm{tot}}(\mathrm{Pd}_m\mathrm{Ir}_n)$ denotes the total energy of $\mathrm{Pd}_m\mathrm{Ir}_n$ nanoalloys, $E_{\mathrm{tot}}(\mathrm{Pd}_{m+n})$ and $E_{\mathrm{tot}}(\mathrm{Ir}_{m+n})$ are the energies of pure Pd and Ir clusters with the same size $(m + n)$ as $\mathrm{Pd}_m\mathrm{Ir}_n$. m and n are the number of atoms of metal Pd and Ir, respectively. A negative value of mixing energy (Δ) means an energy decrease after mixing and therefore favorable mixing, whereas positive values indicate a demixing tendency.

The average binding energy E_{b} is given by:

$$E_{\mathrm{b}} = \frac{1}{N}[mE_{\mathrm{Pd}} + nE_{\mathrm{Ir}} - E(\mathrm{Pd}_m\mathrm{Ir}_n)] \quad (2)$$

where m and n are the numbers of Pd and Ir atoms, E_{Pd} and E_{Ir} are the electronic energies of a single Pd or Ir atom. N is the total number of atoms, $N = m + n$.

The adsorption energy of a CO molecule on Pd–Ir clusters is calculated as the difference between the total energies of the combined system and separated ones, which is expressed by:

$$E_{\mathrm{ads}} = E_{\mathrm{tot}}(\mathrm{combined}) - E_{\mathrm{tot}}(\mathrm{cluster}) - E_{\mathrm{tot}}(\mathrm{adsorbate}) \quad (3)$$

where E_{tot}(combined) is the total energy of CO adsorbed on the Pd–Ir cluster, E_{tot}(cluster) is the energy of the locally-minimized bare Pd–Ir cluster and E_{tot}(adsorbate) is the energy of an isolated CO molecule.

To compare the properties of alloyed clusters and pure clusters, the d-band center is calculated as:[28,41]

$$d_{\mathrm{center}} = \frac{\int \rho E \mathrm{d}E}{\rho \mathrm{d}E} \quad (4)$$

where ρ is the d-band density, E is the d-band energy, ρdE is the number of states. The d_{center} values are calculated only for the (111) facets of the clusters, to allow a comparison between alloyed and pure clusters.

3. Results and discussion

3.1 Bare Pd–Ir nanoalloys

First, to investigate the site preference for Pd and Ir dopants in the TO Pd–Ir nanoalloys, we calculate the mixing energy of Pd–Ir nanoalloys with only one dopant atom. The results are listed in Table 1. For the 38-TO cluster, a single Ir dopant in the Pd cluster preferentially occupies a core site (having the most negative Δ value), but it is most unfavourable in the corner (with largest positive Δ). Conversely, the most favourable

Table 1 Mixing energies (Δ/eV) of single dopants in 38-atom and 79-atom TO clusters. In each case, the preferred (most negative Δ) sites are indicated in bold and the least stable (most positive Δ) sites in italics

Position	$Pd_{37}Ir_1$	Pd_1Ir_{37}	$Pd_{78}Ir_1$	Pd_1Ir_{78}
Core	**−0.412**	*1.170*	**−0.181**	*1.596*
Facet	−0.055	0.318	0.216	0.292
Corner	*0.449*	**−0.088**	*0.803*	**−0.348**
Edge	—	—	0.453	0.225
Sub1	—	—	−0.069	0.682
Sub2	—	—	−0.117	0.853

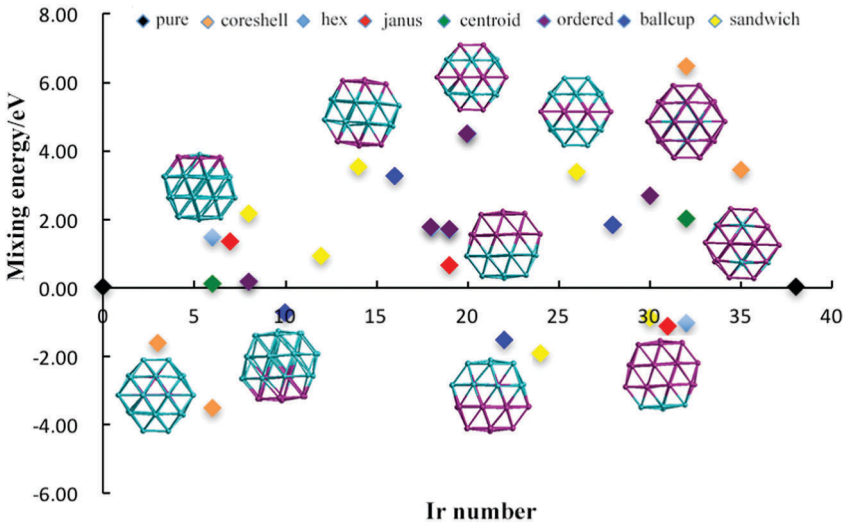

Fig. 4 Mixing energy of 38-TO Pd–Ir nanoalloys with different compositions and configurations. Different colours represent different configurations.

position for a Pd dopant is the corner site, and it is demixing in the core site. The results (in terms of most and least stable sites) for 79-TO are the same as for 38-TO. The stability order for a single Ir dopant in 79-TO Pd clusters is core > subsurface > facet > edge > corner. On the contrary, for a Pd dopant, the stability order is corner > edge > facet > subsurface > core, only the corner position has negative mixing energy, which is similar to the Pd dopant in TO-38 Pd–Ir nanoalloys.

The observed dopant site preferences are in agreement with the higher cohesive energy of Ir (6.93 eV) than Pd (3.94 eV);[42] the fact that the metal–metal bond strengths are in the order Ir–Ir > Ir–Pd > Pd–Pd;[43] and the lower (111) surface energy of Pd (0.824 eV per atom) compared to Ir (1.225 eV per atom).[44]

The relative structural stabilities of Pd–Ir nanoalloys is determined by calculating the mixing energies for different compositions and configurations, as shown in Fig. 4 and 5. Fig. 4 describes the variation of mixing energies of 38-atom Pd–Ir nanoalloys with increasing Ir composition. From this figure, one can see that the $Pd_{shell}Ir_{core}$ structure is the most stable configuration of all the isomers considered (having the most negative) mixing energy, because the Pd atoms on the surface are beneficial to lowering the total energy of Pd–Ir nanoalloys. This is consistent with the results for single dopants in Pd–Ir clusters, since Ir atoms preferentially occupy core sites. Conversely, the $Pd_{core}Ir_{shell}$ isomer is the least stable structure, which is also consistent with the site preference of Pd doping, which is unfavourable in core sites. In addition, for different chemical orderings of Pd–Ir nanoalloys with the same composition, taking hex-$Pd_{32}Ir_6$, centroid-$Pd_{32}Ir_6$ and core–shell-$Pd_{32}Ir_6$ nanoalloys as examples, one can see the mixing energy (Δ) of hex > centroid > core–shell structures, which means for the same compositions, the stability of core–shell > centroid > hex. Similarly, the stability of Janus-$Pd_{19}Ir_{19}$ is higher than that of ordered-$Pd_{19}Ir_{19}$, because of the much higher strength of the Ir–Ir bonds.

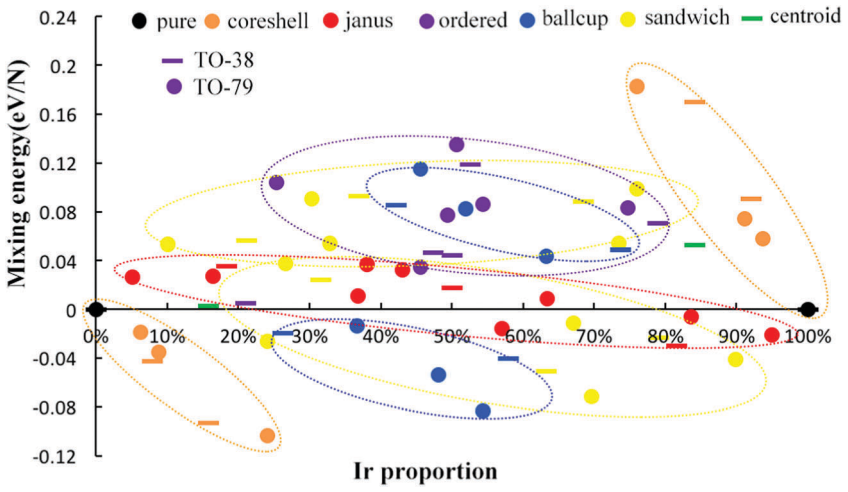

Fig. 5 Comparison of mixing energy per atom for 38-TO and 79-TO Pd–Ir nanoalloys with different compositions and configurations. Different colors represent different configurations, the bar symbol denotes the 38-TO Pd–Ir system, and the circle symbol denotes the 79-TO Pd–Ir system.

Moreover, for the Janus-type configurations with different compositions, Ir-rich clusters are most stable among all considered compositions. For ordered-structures, the Pd-rich cluster has the lowest mixing energy (0.176 eV) among all ordered structures. Interestingly, for both sandwich-type and ball–cup-type arrangements, the slightly Ir-rich structures have lowest mixing energies with mixing energies of −1.904 eV and −1.525 eV, respectively.

To investigate the structural stability of Pd–Ir nanoalloys with different compositions and configurations, we calculate the mixing energies per atom of 38-atom and 79-atom Pd–Ir alloys with increasing Ir composition. As shown in Fig. 5, the stability trend found for 38-TO also applies for 79-TO Pd–Ir nanoclusters. The same configurations of 38-atom and 79-atom Pd–Ir clusters are grouped in the coloured ellipses. Interestingly, for the core–shell group, one can see that the mixing energies of the core–shell structures and the corresponding pure clusters form a straight line for both $Pd_{shell}Ir_{core}$ and $Pd_{core}Ir_{shell}$. Since Ir atoms prefer to occupy core sites, when the core sites of the $Pd_{shell}Ir_{core}$ structure are gradually replaced by Pd atoms, the mixing energy of the core–shell structure increases, until $\Delta = 0$ eV for the pure Pd clusters. To distinguish the stability of sandwich structures sandwiched by Pd atoms or Ir atoms, we divide them into sandwich-Pd structures (Pd sandwiching Ir) and sandwich-Ir ones (Ir sandwiching Pd). The general stability order for both 38-atom and 79-atom Pd–Ir nanoalloys is $Pd_{shell}Ir_{core}$ > $Pd_{cup}Ir_{ball}$ > sandwich-Pd > Janus > sandwich-Ir > ordered ≈ $Pd_{ball}Ir_{cup}$ > $Pd_{core}Ir_{shell}$. Although the mixing energies of the sandwich-type and Janus-type structures range from positive to negative values with increasing Ir proportion, the other arrangements either have all positive or all negative Δ values, indicating the consistency of the mixing or demixing tendency of a given configuration.

To further measure the stability of Pd–Ir clusters with different compositions and configurations, we calculate the average binding energy of alloy Pd–Ir clusters, as shown in Fig. 6. It can be clearly observed that the average binding energies of Pd–Ir clusters increase as the proportion of Ir becomes larger, because Ir–Ir and Pd–Ir bonds are stronger than Pd–Pd bonds. From this figure, we can obtain the stability order of Pd–Ir clusters: $Pd_{core}Ir_{shell}$ > sandwich-Pd > $Pd_{cup}Ir_{ball}$ > ordered > $Pd_{ball}Ir_{cup}$ > $Pd_{core}Ir_{shell}$. By comparing the results of the average binding energy and mixing energy calculations, only the order of the ball–cup and sandwich configurations are reversed.

3.2 CO adsorption

To investigate the best adsorption site of a CO molecule on TO 38-atom Pd–Ir nanoalloys and the effect of alloying on CO adsorption strength, we compare the adsorption energies (E_{ads}) of CO on several alloying configurations with pure Pd_{38} and Ir_{38} TO clusters in eight surface adsorption sites, as shown in Table 2. As a representative for alloyed clusters, core–shell ($Pd_{32}Ir_6$ and Pd_6Ir_{32}) and Janus ($Pd_{19}Ir_{19}$–Pd and $Pd_{19}Ir_{19}$–Ir) clusters are selected.

For the pure Pd cluster, the preferred position for adsorption of the CO molecule is site 6 (the fcc-hollow on the (111) facet), which has the most negative adsorption energy −2.12 eV, followed by the bridge site between two (111) facets (site 5, −2.11 eV). This agrees with a previous study showing that fcc and hcp hollow sites are the favoured sites for CO on the extended Pd(111) surface, and the bridge site is the second most stable.[45] Our calculations of CO adsorption on extended Pd(111), Pd(100), Ir(111) and Ir(100) surfaces, also show that hollow sites are preferred on Pd(111) surfaces with E_{ads} = −2.05 eV and −2.07 eV for fcc hollow and hcp hollow sites, respectively, as shown in Table 3. For the Pd(100) surface, the bridge-adsorption site is energetically most favourable for CO adsorption, in agreement with CO previous study.[46] The adsorption on the bridge site on the (111) facet (site 3) of the pure Pd cluster also has a reported adsorption energy of −2.12 eV, since CO adsorption on the (111)-bridge is unstable

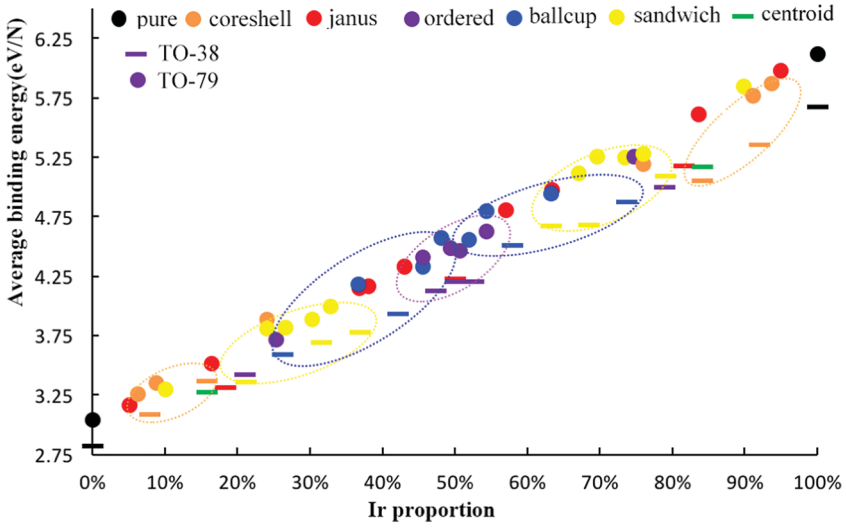

Fig. 6 The average binding energy per atom for 38-TO and 79-TO Pd–Ir nanoalloys with different compositions and configurations. Different colors represent different configurations, the bar symbol denotes the 38-TO Pd–Ir system, and the circle symbol denotes the 79-TO Pd–Ir system.

Table 2 Adsorption energy (E_{ads}/eV) of CO molecule adsorption on 38-atom Pd–Ir nanoalloys. The best site for each structure (the most negative E_{ads}) is shown in bold and sites from which the CO relaxes to an alternative site are shown in italics

Site	Pure Pd	$Pd_{shell}Ir_{core}$	Janus-Pd	Janus-Ir	$Pd_{core}Ir_{shell}$	Pure Ir
1 (centre-atop)	−1.31	−1.51	−1.49	**−2.75**	−2.60	−2.47
2 (edge-atop)	−1.64	−1.67	−1.69	−2.59	**−2.75**	**−2.58**
3 (111-bridge)	*−2.12*	−1.82	*−2.16*	−1.99	−2.06	−1.96
4 (111–100 bridge)	−1.95	−1.92	**−2.17**	−2.32	−2.37	−2.45
5 (111–111 bridge)	−2.11	−2.03	−2.01	−2.28	−2.41	−2.25
6 (fcc-hollow)	**−2.12**	**−2.05**	−2.16	*−2.75*	*−2.06*	*−2.24*
7 (hcp-hollow)	−2.02	−1.97	−2.14	*−1.99*	*−2.06*	*−2.44*
8 (fourfold-hollow)	−1.96	−1.75	*−2.16*	*−2.41*	*−2.37*	*−2.45*

Table 3 Adsorption energy (E_{ads}/eV) of CO adsorbed on extended Pd and Ir surfaces. The best CO adsorption site for each surface is shown in bold. "—" means there are no four-fold/three-fold hollow sites on the 111/100 extended surfaces

Site	Pd(111)	Pd(100)	Ir(111)	Ir(100)
Atop	−1.43	−1.51	**−1.99**	**−2.28**
Bridge	−2.04	**−1.94**	−1.65	−2.12
fcc/hcp-hollow	**−2.05**/**−2.07**	—	−1.59/−1.67	—
Four-fold-hollow	—	−1.89	—	−1.74

(the site is not a local minimum), and the CO molecule relaxes to a neighbouring fcc-hollow (site 6).

For the pure Ir_{38} cluster, the atop site on the edge (site 2) is found to be the favoured position, followed by the atop site in the centre of the (111) facet. This result agrees with the extended Ir surface calculations listed in Table 3, where the atop sites are found to be preferred on both the Ir(111) and Ir(100) surfaces. In previous computational and experimental studies of CO on Ir surfaces, the atop site was reported to be the most favourable site for CO on Ir(111) and Ir(100) surfaces.[47,48] It is worth noting that on the pure Ir cluster, the CO molecule in hollow sites (the (111)-fcc-hollow, (111)-hcp-hollow and (100)-fourfold-hollow) all relax to neighbouring bridge positions (site 4 or site 5), probably because the corner atoms of the (111) facet have lower coordination numbers and bind CO more strongly. CO binding on the pure Ir cluster is significantly stronger (with more negative E_{ads} values) than on the pure Pd cluster for all adsorption sites. Comparing the adsorption energies for the most strongly binding sites for Ir_{38} and Pd_{38}, E_{ads} is 0.46 eV lower for Ir_{38} than Pd_{38}.

Moving to Pd–Ir nanoalloys, for the core–shell type, the fcc-hollow position (site 6) of CO on the $Pd_{shell}Ir_{core}$ ($Pd_{32}Ir_6$) cluster is found to be the preferred site, as for the pure Pd cluster, followed by the bridge position between two (111) facets (site 5). The adsorption strength of CO on the $Pd_{shell}Ir_{core}$ cluster is lower than on the pure Pd cluster, for all sites except the atop sites. For the $Pd_{core}Ir_{shell}$ (Pd_6Ir_{32}) cluster, the edge atop site (site 2) is found to be the most favourable, as for the pure Ir cluster. For almost all sites, the adsorption strength of CO on $Pd_{core}Ir_{shell}$ is stronger than on the pure Ir cluster, except for those sites where CO relaxes to other sites. The difference in the adsorption energies for the best sites on the $Pd_{core}Ir_{shell}$ and $Pd_{shell}Ir_{core}$ clusters is greater (0.70 eV) than for the pure metal clusters (0.46 eV), reflecting the strengthening of Ir–CO and weakening of Pd–CO binding on going from the pure to the core–shell clusters.

For Janus structures ($Pd_{19}Ir_{19}$), the underlying Pd or Ir layers again affect the adsorption strength of CO on the other metal, but in a less straightforward way than for the core–shell clusters. As seen in Table 2, the adsorption energies of CO on Janus-Pd (*i.e.* the Pd part of the Janus cluster) are generally more negative (indicating stronger Pd–CO binding). The bridge site between the (111) and (100) facets is the preferred site for CO on Janus-Pd (site 4), different from the pure Pd cluster and $Pd_{shell}Ir_{core}$ cluster, which favour the fcc-hollow (site 6), though the difference in E_{ads} is only 0.01 eV. The adsorption energies on Janus-Ir (*i.e.* the Ir part of the Janus cluster) are generally more negative (indicating stronger Ir–CO binding) than for the pure Ir cluster. The strongest binding site (more negative adsorption energy) is the centre-atop position (site 1), in contrast to the pure Ir and $Pd_{core}Ir_{shell}$ clusters, which favour the edge-atop position (site 2). Again, the adsorption of CO on Ir is significantly greater than on Pd, with a difference in E_{ads} of the favoured sites of 0.58 eV (*i.e.* intermediate between that for pure and core–shell clusters).

From Table 2, we see that the fcc hollow site (site 6) is energetically the most favorable position for CO adsorption on Pd, except for the Janus-Pd cluster, while the atop site on the edge (site 2) is found to be the most favorable site for Ir, except the Janus-Ir cluster. Therefore, for comparison of the adsorption strength of CO for several alloying configurations and the pure clusters, we select several Pd–Ir configurations with CO adsorption on sites 2 and 6 as representatives, as shown in Fig. 7. Comparing the pure clusters with core–shell and Janus nanoalloys, we observe that the adsorption strength on one particular metal (Pd or Ir) is affected by the presence of the other metal, whether it is in direct contact with the adsorbing metal atom or not.

For CO adsorption on Pd, the situation is complex. Due to the presence of Ir atoms, the CO adsorption strength on the $Pd_{shell}Ir_{core}$ cluster decreases (E_{ads} becomes less negative) while on the Janus-Pd cluster the adsorption strength is greater (more negative E_{ads}) compared to pure Pd_{38}. For CO adsorption on Ir, CO molecules adsorbed on the fcc hollow site (site 6) relax to other positions, but the adsorption strength on both $Pd_{core}Ir_{shell}$ and Janus-Ir clusters still increases compared to pure Ir_{38}, indicating a positive effect of the underlying Pd atoms. Comparing these results with previous studies of CO adsorption on Au–Rh nanoalloys,[45] the strengthening of Ir–CO

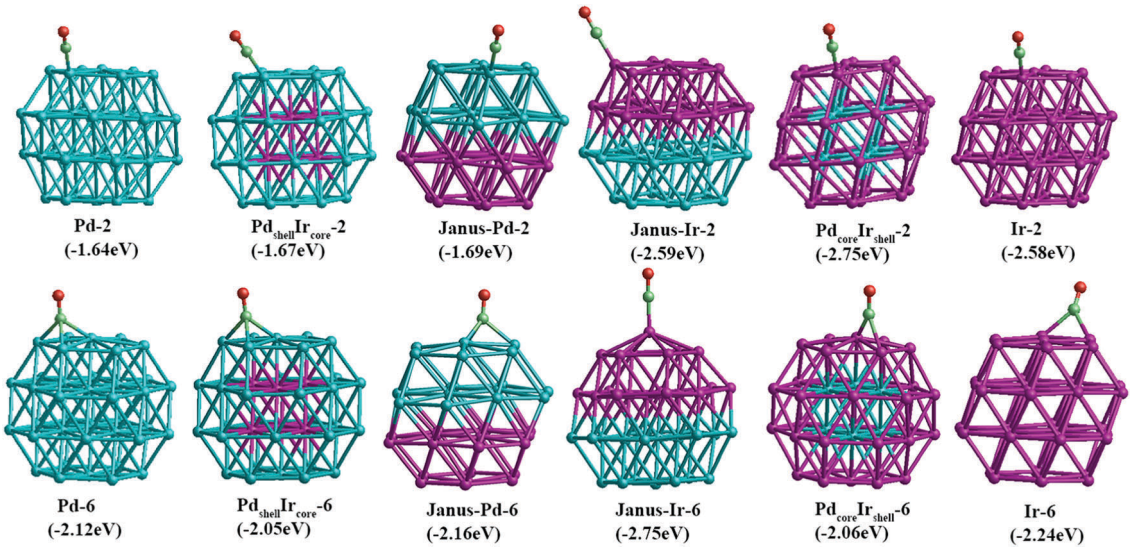

Fig. 7 Adsorption energies and structures of CO on edge-atop (site 2) and fcc hollow (site 6) sites for 38-atom TO pure Pd and Ir cluster and core–shell and Janus Pd–Ir nanoalloys.

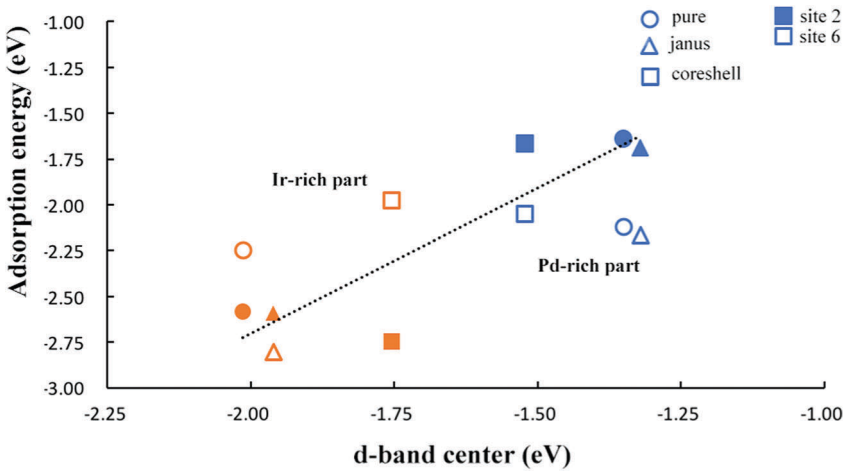

Fig. 8 Plot of d-band center against adsorption energy (E_{ads}) for CO molecular adsorption on Pd–Ir nanoalloys. Different shapes represent different configurations. The light blue color denotes CO on Pd and the orange color denotes CO on Ir. CO on sites 2 and 6 are shown as shaded and empty symbols, respectively.

binding in the presence of Pd and the weakening of Pd–CO binding in the presence of Ir as seen for the $Pd_{shell}Ir_{core}$ cluster, could be attributed to a mechanical (strain) effect, whereby (as the metal–metal bond strengths are in the order Ir–Ir > Ir–Pd > Pd–Pd) underlying Ir atoms impose greater rigidity to the Pd atoms, decreasing the Pd–CO binding. Conversely, underlying Pd atoms reduce the rigidity of the Ir atoms, allowing stronger Ir–CO binding. However, this argument doesn't apply for all binding sites, and, in particular, does not apply to Janus-Pd, where the presence of Ir leads to an increase in Pd–CO binding strength (more negative E_{ads}). Therefore, electronic effects must also be investigated.

3.3 Alloying effect on adsorption strength

To further investigate trends in the adsorption strength of CO molecular adsorption on pure clusters and Pd–Ir nanoalloys, we calculate the d-band centers of several Pd–Ir configurations. Fig. 8, shows the relationship between CO adsorption energies and the d-band centers of the clusters. According to the definition of the d-band model, an upshift in the d-band center (less negative value) is expected to correspond to stronger CO adsorption strength (more negative E_{ads}). For adsorption of CO on Pd, it follows the relationship of d-band center and adsorption strength by comparing the d-band centers of $Pd_{shell}Ir_{core}$ and Janus-Pd clusters with pure Pd_{38}. Since we can clearly observe a significant downshift in the d-band centre for $Pd_{shell}Ir_{core}$ and a small upshift for Janus-Pd, which corresponds to weaker CO adsorption on $Pd_{shell}Ir_{core}$ and stronger adsorption on Janus-Pd, compared to Pd_{38}.

For CO adsorption on Ir, we observe an upshift of the d-band centers for both Janus-Ir and $Pd_{core}Ir_{shell}$ clusters, when compared with pure Ir_{38}, for both sites, though the upshift for

Table 4 The d-band centers (eV) and layer charges (|e|) of bare TO 38-atom Pd–Ir clusters, together with charge transfer (|e|) to CO, C–O and M–CO distances (Å), and adsorption energies (eV) on site 2 (edge-atop) and site 6 (fcc-hollow) of CO on Pd–Ir clusters

Cluster	*d*-Center	Layer charge	Charge transfer	d_{C-O}	d_{M-C}	E_{ads}
Site 2						
Pure-Pd	−1.351	0.183	−0.413	1.162	1.842	−1.641
$Pd_{shell}Ir_{core}$	−1.522	0.201	−0.414	1.163	1.854	−1.667
Janus-Pd	−1.320	0.314	−0.405	1.162	1.853	−1.693
Janus-Ir	−1.960	0.075	−0.598	1.173	1.838	−2.593
$Pd_{core}Ir_{shell}$	−1.755	0.270	−0.577	1.171	1.839	−2.747
Pure-Ir	−2.014	0.448	−0.551	1.172	1.839	−2.584
Site 6						
Pure-Pd	−1.351	0.183	−0.589	1.198	2.081, 2.037, 2.036	−2.118
$Pd_{shell}Ir_{core}$	−1.522	0.201	−0.581	1.197	2.051, 2.054, 2.088	−2.050
Janus-Pd	−1.320	0.314	−0.590	1.2	2.052, 2.033, 2.052	−2.164
Janus-Ir	−1.960	0.075	−0.608	1.174	1.801	−2.750
$Pd_{core}Ir_{shell}$	−1.755	0.270	−0.665	1.191	2.043, 2.065	−2.063
Pure-Ir	−2.014	0.448	−0.646	1.193	2.026, 2.026	−2.244

Janus-Ir is small. This follows the change of adsorption strength, since the adsorption of CO on Ir is stronger (more negative E_{ads}) for all alloy configurations on site 2 compared to pure Ir_{38}, consistent with the prediction of the d-band model. However, for CO adsorption on site 6, the Ir-rich clusters do not always follow the trend of d-band center and adsorption strength, because CO adsorption on site 6 of Ir-rich clusters is unstable, CO moving to other sites. Fig. 8 also shows that the adsorption strength on site 6 is stronger than on site 2 for Pd–CO binding, while for Ir–CO binding, the adsorption strength on site 2 is not always better than on site 6 since CO on hollow sites is generally not stable, relaxing to neighboring sites (*e.g.* bridging sites), as can be seen in Fig. 7.

To analyze the charge effect on the adsorption strength of alloy clusters relative to their corresponding pure clusters, we calculate the charges on the (111) layer of bare clusters and charge transfer between clusters and the CO adsorbate. These, along with the d-band centers and the metal–CO and C–O distances are shown in Table 4. The Pd layer charges for $Pd_{shell}Ir_{core}$ and Janus-Pd clusters are more positive than for the pure Pd cluster due to the effect of alloying with Ir. Conversely, the Ir layer charges become less positive when alloyed with Pd, though the electronegativity of Ir is equal to Pd (having the value 2.20). Meanwhile, the charge transferred from Janus-Ir and $Pd_{core}Ir_{shell}$ clusters CO adsorbed on site 2 is more negative than for the pure Ir cluster. Perhaps, as Ir has fewer d electrons than Pd, this leads to d electron transfer from Pd to Ir.

4. Conclusions

The mixing properties of bare Pd–Ir clusters, the adsorption effect and preferred adsorption sites of the CO molecule on 38-atom Pd–Ir nanoclusters have been investigated theoretically using DFT methods. In agreement with the lower surface and cohesive energy of Pd than Ir, the calculations show that $Pd_{shell}Ir_{core}$ clusters are the most stable structures and $Pd_{cup}Ir_{ball}$ clusters are the second most stable, with negative mixing energies for all considered isomers, while $Pd_{core}Ir_{shell}$ is the highest energy configuration, with large positive mixing energies. These results are also consistent with the site preference for Pd and Ir dopants in the TO Pd–Ir nanoalloys. The general stability order for both 38-atom and 79-atom Pd–Ir nanoclusters is $Pd_{shell}Ir_{core}$ > $Pd_{cup}Ir_{ball}$ > sandwich-Pd > Janus > sandwich-Ir > ordered ≈ $Pd_{ball}Ir_{cup}$ > $Pd_{core}Ir_{shell}$. Moreover, the Ir atoms exhibit significantly stronger adsorption of CO molecules than Pd atoms. The preferred binding site of CO on the pure Pd cluster is the fcc-hollow on the (111) facet, while the atop site on the edge atom between (111) and (100) facets is found to be the most favorable position for CO on the pure Ir cluster. These results agree with the favored binding sites for CO on extended Pd and Ir surfaces. In addition, the d-band center of the pure and nanoalloy clusters has been calculated to understand the adsorption strength of CO molecules on different clusters. Adsorption strength is found to follow the position of the d-band center in most, but not all cases. Charge effects have also been studied, correlating with the increase or decrease of adsorption strength, but the possible role of mechanical (strain) effects remains to be determined.

In future studies, we will investigate the effect of oxide supports (such as Al_2O_3) on the structures and stabilities of Pd–Ir nanoalloys and on the adsorption of CO and other molecules, as well as reactions between adsorbed molecules.

Conflicts of interest

There are no conflicts to declare.

Acknowledgements

RLJ is grateful to Dr Laurent Piccolo (University of Lyon 1, France) for useful discussions. This work was funded by the Graduate School of Xiamen University (T.-E Fan). H. A. Hussein is grateful to the University of Kufa and the Ministry of Higher Education and Scientific Research (Iraq) for the award of a PhD scholarship. Calculations were performed on the following HPC facilities: The University of Birmingham BlueBear facility (http://www.bear.bham.ac.uk/bluebear) and the UK's national

HPC facility, ARCHER, *via* membership of the UK's HPC Materials Chemistry Consortium, which is funded by EPSRC (EP/L000202), and the EPSRC Critical Mass Grant (EP/J010804/1) TOUCAN.

References

1 R. W. Murray, *Chem. Rev.*, 2008, **108**, 2688.
2 B. Hammerand and J. K. Norskov, *Nature*, 1995, **376**, 238.
3 K. Persson, A. Ersson, K. Jansson, N. Iverlund and S. Jaras, *J. Catal.*, 2005, **231**, 139.
4 A. S. Rocha, E. L. Moreno, G. P. M. da Silva, J. L. Zotin and A. C. Faro Jr., *Catal. Today*, 2008, **133**, 394.
5 S. Y. Shen, T. S. Zhao and J. B. Xu, *Electrochim. Acta*, 2010, **55**, 9179.
6 Y. M. Lopez-De Jesús, C. E. Johnson, J. R. Monnier and C. T. Williams, *Top. Catal.*, 2010, **53**, 1132.
7 F. Morfin, S. Nassreddine, J. L. Rousset and L. Piccolo, *ACS Catal.*, 2012, **2**, 2161.
8 C. Zlotea, F. Morfin, T. S. Nguyen, N. T. Nguyen, J. Nelayah, C. Ricolleau, M. Latroche and L. Piccolo, *Nanoscale*, 2014, **6**, 9955.
9 L. Piccolo, S. Nassreddine, M. Aouine, C. Ulhaq and C. Geantet, *J. Catal.*, 2012, **292**, 173.
10 F. Morfin, S. Nassreddine, J. L. Rousset and L. Piccolo, *ACS Catal.*, 2012, **2**, 2161.
11 L. Piccolo, S. Nassreddine, G. Toussaint and C. Geantet, *ChemSusChem*, 2012, **5**, 1717.
12 P. E. A. Turchi, V. Drchal and J. Kudrnovský, *Phys. Rev. B: Condens. Matter Mater. Phys.*, 2006, **74**, 064202.
13 B. Kolb, S. Müller, D. B. Botts and G. L. W. Hart, *Phys. Rev. B: Condens. Matter Mater. Phys.*, 2006, **74**, 144206.
14 R. Ferrando, J. Jellinek and R. L. Johnston, *Chem. Rev.*, 2008, **108**, 845.
15 S. Alayoglu, A. U. Nilekar, M. Mavrikakis and B. Eichhorn, *Nat. Mater.*, 2008, **7**, 333.
16 L. Kesavan, R. Tiruvalam, M. H. Ab Rahim, M. I. Bin Saiman, D. I. Enache, R. L. Jenkins, N. Dimitratos, J. A. Lopez-Sanchez, S. H. Taylor, D. W. Knight, C. J. Kiely and G. J. Hutchings, *Science*, 2011, **331**, 195.
17 S. Khanal, N. Bhattarai, J. J. Velazquez-Salazar, D. Bahena, G. Soldano, A. Ponce, M. M. Mariscal, S. Mejia-Rosalesc and M. Jose-Yacaman, *Nanoscale*, 2013, **5**, 12456.
18 K. J. Andersson, F. Calle-Vallejo, J. Rossmeisl and I. Chorkendorff, *J. Am. Chem. Soc.*, 2009, **131**, 2404.
19 F. Tao, M. E. Grass, Y. Zhang, D. R. Butcher, J. R. Renzas, Z. Liu, J. Y. Chung, B. S. Mun, M. Salmeron and G. A. Somorjai, *Science*, 2008, **322**, 932.
20 F. Tao, M. E. Grass, Y. Zhang, D. R. Butcher, F. Aksoy, S. Aloni, V. Altoe, S. Alayoglu, J. R. Renzas, C. Tsung, Z. Zhu, Z. Liu, M. Salmeron and G. A. Somorjai, *J. Am. Chem. Soc.*, 2010, **132**, 8697.
21 V. Soto-Verdugo and H. Metiu, *Surf. Sci.*, 2007, **601**, 5332.
22 A. Dhouib and H. Guesmi, *Chem. Phys. Lett.*, 2012, **521**, 98.
23 G. Ertl, M. Neumann and K. M. Streit, *Surf. Sci.*, 1977, **64**, 393.
24 O. Cairon and H. Guesmi, *Phys. Chem. Chem. Phys.*, 2011, **13**, 11430.
25 W. Bouderbala, A.-G. Boudjahem and A. Soltani, *Mol. Phys.*, 2014, **112**, 1789.
26 J. B. A. Davis, S. L. Horswell, L. Piccolo and R. L. Johnston, *J. Organomet. Chem.*, 2015, **792**, 190.
27 J. B. A. Davis, S. L. Horswell and R. L. Johnston, *J. Phys. Chem. A*, 2013, **118**, 208.
28 J. B. A. Davis, R. L. Johnston, L. Rubinovich and M. Polak, *J. Chem. Phys.*, 2014, **141**, 224307.
29 T. H. Andriamiharintsoa, A. Rakotomahevitra, L. Piccolo and C. Goyhenex, *J. Nanopart. Res.*, 2015, **17**, 217.
30 B. Coq and F. J. Figueras, *J. Mol. Catal. A: Chem.*, 2001, **173**, 117.
31 L. L. Wang and D. D. Johnson, *J. Am. Chem. Soc.*, 2009, **131**, 14023.
32 Y. Sun, B. Wiley, Z. Y. Li and Y. Xia, *J. Am. Chem. Soc.*, 2004, **126**, 9399.
33 F. Baletto, C. Mottet and R. Ferrando, *Phys. Rev. Lett.*, 2003, **90**, 135504.
34 D. Cheng, W. Wang, S. Huang and D. Cao, *J. Phys. Chem. C*, 2008, **112**, 4855.
35 L. O. Paz-Borbon, A. Gupta and R. L. Johnston, *J. Mater. Chem.*, 2008, **18**, 4154.
36 G. Kresse and J. Hafner, *Phys. Rev. B: Condens. Matter Mater. Phys.*, 1993, **47**, 558.
37 P. E. Blöchl, *Phys. Rev. B: Condens. Matter Mater. Phys.*, 1994, **50**, 17953.
38 G. Kresse and D. Joubert, *Phys. Rev. B: Condens. Matter Mater. Phys.*, 1999, **59**, 1758.
39 J. P. Perdew, K. Burke and M. Ernzerhof, *Phys. Rev. Lett.*, 1996, **77**, 3865.
40 R. Ferrando, A. Fortunelli and G. Rossi, *Phys. Rev. B: Condens. Matter Mater. Phys.*, 2005, **72**, 085449.
41 I. Demiroglu, Z. Y. Li, L. Piccolo and R. L. Johnston, *Catal. Sci. Technol.*, 2016, **6**, 6916.
42 V. Rosato, M. Guillope and B. Legrand, *Philos. Mag. A*, 1989, **59**, 321.
43 J. E. Bercaw, A. C. Durrell, H. B. Gray, J. C. Green, N. Hazari, J. A. Labinger and J. R. Winkler, *Inorg. Chem.*, 2010, **49**, 1801.
44 L. Vitos, A. V. Ruban, H. L. Skriver and J. Kollar, *Surf. Sci.*, 1998, **411**, 186.
45 D. Loffreda, D. Simon and P. Sautet, *Surf. Sci.*, 1999, **425**, 68.
46 A. Eichler and J. Hafner, *Phys. Rev. B: Condens. Matter Mater. Phys.*, 1998, **57**, 10110.
47 W. P. Krekelberg, J. Greeley and M. Mavrikakis, *J. Phys. Chem. B*, 2004, **108**, 987.
48 I. A. Erikat, B. A. Hamad and J. M. Khalifeh, *Eur. Phys. J. B*, 2009, **67**, 35.

Supporting Information of:

DFT study of the structure, chemical ordering and molecular adsorption of Pd-Ir nanoalloys

Tian-E Fan,[a,b] Ilker Demiroglu,[b] Heider A. Hussein,[b, c] Tun-Dong Liu,[a*] Roy L. Johnston[b*]

[a]*Department of Automation, Xiamen University, Xiamen, 361005, China. E-mail: ltd@xmu.edu.cn*

[b]*School of Chemistry, University of Birmingham, Edgbaston, Birmingham B15 2TT, UK. E-mail: r.l.johnston@bham.ac.uk*

[c]*Department of Chemistry, College of Science, University of Kufa, Najaf, Iraq*

Table 1. Detailed comparison of the lattice constant, cohesive energy, and bulk modulus for bulk Pd (fcc) and Ir (fcc) with experimental and theoretical data.

		This method	Reference (PBE)	Experiment
Lattice parameter	Pd	3.940	3.95[3]	3.88[1]
(Å)	Ir	3.872	3.89[5]	3.84[6]
Cohesive energy	Pd	3.743	3.63[3]	3.89[2]
(eV/atom)	Ir	7.351	8.96[5]	6.94[2]
Bulk modulu	Pd	168.96	166[4]	181[2]
(GPa)	Ir	345.78	340[5]	355[7]

[1] J. Heyd, G. E. Scuseria, J. Chem. Phys., 2004, 121, 1187.

[2] C. Kittel, Introduction to solid state physics (Wiley, 2005).

[3] J. L. F. D. Silva, C. Stampfl, M. Scheffler, Surf. Sci., 2006, 600, 703.

[4] M. Ropo, K. Kokko, L. Vitos, Phys. Rev. B, 2008, 77, 195445.

[5] I. A. Erikat, B. A. Hamad, J. M. Khalifeh, Eur. Phys. J. B, 2009, 67, 35.

[6] C. Kittel, Introduction to Solid State Physics (Wiley, New York,1971).

[7] D.R. Lide, CRC Handbook of chemistry and physics, 80th edition (CRC Press, Boca Raton, 1999–2000).